CRANFIELD UNIVERSITY

CRANFIELD DEFENCE AND SECURITY

Department of Engineering & Applied Science

Aeromechanical Systems Group

PhD

Academic Year 2010 - 2011

Nathan Daniel Blagdon Phillips

Experimental Unsteady Aerodynamics Relevant to Insect-inspired Flapping-wing Micro Air Vehicles

Supervisor:

Professor Kevin Knowles

April 2011

Abstract

Small hand-held micro air vehicles (*MAVs*) can serve many functions unsuitable for a manned vehicle, and can be inexpensive and easily deployed. *MAVs* for indoor applications are underdeveloped due to their demanding requirements. Indoor requirements are best met by a flapping-wing micro air vehicle (*FMAV*) based on insect-like flapping-wing flight, which offers abilities of sustained hover, aerial agility, and energy efficiency. *FMAV* development is hampered by a lack of understanding of insect-like flapping-wing aerodynamics, particularly at the *FMAV* scale. An experimental programme at the *FMAV* scale (Reynolds number on the order of 10^4) was undertaken, investigating: leading-edge vortex (*LEV*) stability, flapping kinematic effects on lift and the flowfield, and wing planform shape effects on the flowfield. For these experiments, an apparatus employing a novel flapping mechanism was developed, which achieved variable three-degree-of-freedom insect-like wing motions (flapping kinematics) with a high degree of repeatability in air up to a $20Hz$ flapping frequency. Mean lift measurements and spatially dense volumetric flowfield measurements using stereoscopic particle image velocimetry (*PIV*) were performed while various flapping kinematic parameters and wing planform were altered, to observe their effects. Three-dimensional vortex axis trajectories were reconstructed, revealing vortex characteristics such as axial velocity and vorticity, and flow evolution patterns. The first key result was the observation of a stable *LEV* at the *FMAV* scale which contributed to half of the mean lift. The *LEV* exhibited vortex breakdown, but still augmented lift as Reynolds number was increased indicating that *FMAVs* can exploit this lifting mechanism. The second key result was the identification of the trends of mean lift versus the tested kinematic parameters at the *FMAV* scale, and appropriate values for *FMAV* design. Appropriate values for lift generation, while taking mechanical practicalities into account, included a flat wingtip trajectory with zero plunge amplitude (Θ), angle of attack at mid-stroke (α_{mid}) of $\sim 45^\circ$, rotation phase (τ) of +5.5%, and maximum flapping frequency and stroke amplitude.

To
my Dad, for sparking my interest in flight

Acknowledgements

This work would not have been possible were it not for the many people who provided me with invaluable help, advice and support. A big thank you is owed to the following:

To my supervisor Professor Kevin Knowles for his advice, guidance, and support in all aspects of this endeavor.

To Professor John Hetherington as well as my supervisor, for their support in the patenting of the developed flapping mechanism.

To Professor Rafał Żbikowski for his helpful advice and support.

To my lab mate Dr. Graham Stabler, to whom I owe a heart-felt thank you for his invaluable help and advice in this project and especially in the development of the flapperatus. Also, thank you for teaching me about various aspects of electronics, parallel kinematics, microcontrollers, microcontroller programming, and how to free-line skate.

To my former lab mates Tanmay and Bidur, for the many well needed coffee breaks over the past years. I think we are all now experts on the operation and maintenance of Flavia coffee machines.

To Dr. Salman Ansari for teaching me how to use LaTeX, and for arranging the loan of the *PIV* measurement equipment from the EPSRC equipment loan pool.

To Dr. Simon Ritchie for teaching me the technique of *PIV*.

To Dr. Nicholas J. Lawson for the loan of his high-speed cameras.

To Dave Wasley for laser interlocking the lab area, and Dr. Mark Finnis for the use of his LIC software.

To Brian Duguid, Mike Goodland and all of the machinists in the workshop for their excellent work in the manufacturing of all the components for the flapperatus.

To Mike Corboy from Omron for performing various requested tests, and his help in tuning the servo motors.

To the 102.1 the Edge Toronto radio station, and my canary 'Charlie' for providing the soundtrack to my thesis write up.

To the Fancy Tea cafe for our ritual Friday lunch time traditional breakfasts, and introducing me to black pudding.

To Pia for being with me on this PhD marathon, and putting up with the mountains of papers and books in our flat during my write up.

Finally, thank you to my family and friends back home for their support and encouragement.

Preface

This thesis presents an experimental study which addresses a number of questions with regards to insect-like flapping-wing aerodynamics at the flapping-wing micro air vehicle (*FMAV*) scale. In particular, the stability of the leading-edge vortex (*LEV*) at this scale, effects of flapping kinematics on mean lift and the flow structures generated, and effects of wing planform shape on the flow structures, are addressed. The main contributions of this thesis are outlined below, followed by publications, patents and awards that have come out of this work. Finally, the thesis structure is described.

0.1 Contributions

The main contributions of the work performed by the author are as follows:

- The design, development and analysis of a novel, patent-pending flapping mechanism which enables separate control of each of the three rotational degrees of freedom of a flapping wing, thus allowing flapping kinematics to be altered. The mechanism is a three-degree-of-freedom parallel spherical design, and it possesses unique characteristics that are advantageous for this application, which include: large workspace (range of motion of the wing), minimised inertial loads and vibrations due to location of the centre of mass of all components at the centre of rotation, ability to achieve very high rotational accelerations of the wing, low backlash, and few (7) moving parts.

- The design and development of a first-of-its-kind experimental apparatus, which employs the aforementioned flapping mechanism to drive a flapping wing in air. The apparatus consists of cable drives, servo motors and control hardware to drive the mechanism, and integrates with measurement devices to measure mechanism position, wing position, lift forces, and flowfield velocities. This apparatus has demonstrated a never-before-seen ability to mimic insect-like flapping-wing kinematics smoothly with a high degree of

repeatability up to a 20Hz flapping frequency in air, with separate control of the wing's three degrees of freedom, and variable kinematics.

- Experimental setup and the collection of a spatially-dense set of 3D flowfield measurements on an insect-like flapping wing operating at the $FMAV$ scale. Flow velocities were measured at each point in space throughout a dense 3D grid representing a volume enclosing the wing. From these data, the form of 3D vortex core structures, and axis trajectories were reconstructed, particularly those of the 3D leading-edge vortex (LEV) and tip vortex.

- Identification of a stable LEV, on an insect-like flapping wing operating at the $FMAV$ scale.

- Identification of the presence of a secondary LEV of opposite sense to the primary LEV, on an insect-like flapping wing at the $FMAV$ scale.

- More detailed experimental measurement than hitherto reported of the lift contribution from the 3D LEV.

- Recovery of characteristics of vortices generated by an insect-like flapping wing from 3D vortex axis trajectories. Calculated characteristics for a given vortex include axial velocity, tangential velocity, axial vorticity, helix angle, circulation, and vortex diameter.

- Experimental characterisation of vortex breakdown in the LEV on an insect-like flapping-wing at the $FMAV$ scale. It is shown how the helix angle in the LEV surpasses a critical value, axial velocity levels drop and vortex diameter rises, indicating vortex breakdown.

- Experimental identification of an axial 'blowing' effect originating from the tip vortex, which causes vortex breakdown in the LEV on an insect-like flapping wing.

- Demonstration that the tip vortex re-energises the LEV when they merge, which suppresses vortex breakdown.

- Experimental identification of flapping kinematic effects on mean lift at the $FMAV$ scale, and identification of optimal values for various kinematic parameters for generating lift.

- Identification of the effects of flapping kinematics on 3*D* flow structures generated by an insect-like flapping wing. These include effects on flow evolution, vortex breakdown in the *LEV*, and *LEV* axial velocity.
- Calculation of axial accelerations due to viscous, Euler, Coriolis, and centrifugal forces along the 3*D LEV* axis.
- Identification of the suppression of *LEV* formation inboard for a forward-swept leading edge.

0.2 Publications & Patent

This work has led to a patent application and a number of publications as listed below:

- Phillips, N. (2010). Three Degree-of-Freedom Parallel Spherical Mechanism for Payload Orienting Applications. UK Patent GB2464147 (pending).
- Phillips, N. & Knowles, K. (2010d). Reynolds Number and Stroke Amplitude Effects on the Leading-edge Vortex on an Insect-like Flapping Wing. In *International Powered Lift Conference*, 5-7 October, Philadelphia, PA, USA. AHS International.
- Phillips, N. & Knowles, K. (2010c). Formation of Vortices and Spanwise Flow on an Insect-like Flapping Wing throughout a Flapping Half Cycle. In *Aerodynamics Conference*, 27-28 July, Bristol, UK. Royal Aeronautical Society. *(also invited for submission to the Aeronautical Journal)*.
- Phillips, N. & Knowles, K. (2010b). Effect of Wing Planform Shape on the Flow Structures of an Insect-like Flapping Wing in Hover. In *27th International Congress of the Aeronautical Sciences (ICAS) 2010*, 19-24 September, Nice, France.
- Phillips, N. & Knowles, K. (2010a). Effect of Flapping Kinematics on the Mean Lift of an Insect-like Flapping wing. Accepted for *Proc. IMechE, Part G, Journal of Aerospace Engineering*. *(invited paper)*.

- Phillips, N. & Knowles, K. (2009). Effect of Flapping Kinematics on the Mean Lift Generated by an Insect-like Flapping Wing. In *CEAS European Air and Space Conference*, 26-29 October, Manchester, UK. Royal Aeronautical Society.

- Phillips, N. & Knowles, K. (2008). Progress in the Development of an Adjustable, Insect-like Flapping-wing Apparatus Utilising a Three Degree-of-Freedom Parallel Spherical Mechanism. In *International Powered Lift Conference*, 22-24 July, London, UK. Royal Aeronautical Society.

Additional publication related to this work, and contributed to by the author:

- Ansari, S. A., Phillips, N., Stabler, G., Wilkins, P. C., Żbikowski, R., & Knowles, K. (2009). Experimental Investigation of Some Aspects of Insect-like Flapping Flight Aerodynamics for Application to Micro Air Vehicles. *Experiments in Fluids, Special Issue: Animal Locomotion-The Physics of Flying, 46(5), 777-798. (invited paper)*.

0.3 Awards

This work has received the awards listed below:

- 1^{st} Place in the IMechE Western Aerospace Centre Prize Competition 2011, Bristol UK.

- 2^{nd} Place in the 9^{th} Osborne Reynolds Recent Postgraduate & Research Student Award 2011, London UK.

0.4 Thesis Outline

This thesis is comprised of three main parts and a set of appendices. The first part provides an introduction and relevant background, starting with an introduction to *MAVs* and the motivation for their development (Chapter 1) with a particular focus on *FMAVs*. This is followed by background material on insect-like flight

and a literature review (Chapter 2). Lastly, the research aims of the thesis and the methodology used are given (Chapter 3).

The second part focuses on experimentation, beginning with the design and development of the experimental flapping-wing apparatus, termed the 'flapperatus', used for experiments (Chapter 4). This is followed by the experimental programme (§ 5.1), procedures (§ 5.2), and analysis of the data (Chapter 5). This includes a discussion of the employed *PIV* processing and analysis (§ 5.3), and an uncertainty analysis of measurements performed in the study (§ 5.4).

The last part contains the results of the experimental study and a discussion (Chapter 6). Following this, conclusions are given (Chapter 7), including *FMAV* design recommendations derived from this work (§ 7.1), as well as recommendations for future work (§ 7.2).

Appendices at the end of the thesis present functions which define flapping kinematics (Appendix A), and a derivation of the flapping mechanism kinematics (Appendix B). The non-intrusive flowfield measurement technique of particle image velocimetry (*PIV*) is described (Appendix C), as well as the developed vortex axis identification procedure and vortex point-joining algorithm (Appendix D). In addition, the methods by which vortex parameters including helix angle and vortex diameter were calculated along a vortex axis are given (Appendix E), as well as supplementary figures (Appendix F). Lastly, extra terms which arise in the Navier-Stokes equations due to the fact that flow velocities are viewed in a rotating and accelerating frame are derived (Appendix G).

Contents

List of Tables

List of Figures

Nomenclature

All units are as indicated in brackets unless otherwise stated. A & B are generic variables

Latin Alphabet

a	acceleration (m/s^2)
AB	angle subtended by line segment between generic points A and B on the surface of a sphere (rad)
AR	aspect ratio, $2R^2/S$
b	distance of wing root from centre of rotation (m)
C	correlation value, see Equation C.1
C	cosine of angle subtended by line segment 'DZ' on the surface of a sphere, see Equation B.19
c	chord length (m)
$\bar{C}_L$	mean lift coefficient, $\bar{L}/0.5\rho\bar{v}_{tip}^2 S$
d	vortex diameter (m)
DA	denominator of expression for $\dot{\beta_A}$, see Equation B.32 & B.36
E	cosine of angle subtended by line segment 'AE' on the surface of a sphere, see Equation B.67 & B.70
F	cosine of angle subtended by line segment 'BC' on the surface of a sphere, see Equation B.63
f	flapping frequency (Hz)
I	array of pixel intensity levels
i	unit vector in x direction
j	unit vector in y direction

K	vortex axis identification score, see Equation D.1 (*rad*)
$\mathbf{k}$	unit vector in z direction
L	lift (N)
$\bar{L}$	mean lift over a flapping cycle (N)
l	distance from centre of rotation to wingtip, $b + R$ (m)
LA	angle subtended by link LA on the surface of a sphere (*rad*)
n	interrogation window size, see Equation C.1 (pixels)
n	sample size, see Equation 5.22
n_A	point A
NA	numerator of expression for $\dot{\beta}_A$, see Equation B.30 & B.34
P	coefficient of power-two term of characteristic equation of velocity gradient tensor, see Equation 5.7 ($1/s^2$)
Q	coefficient of power-one term of characteristic equation of velocity gradient tensor, see Equations 5.6 & 5.8 ($1/s^2$)
q	multiplier of the square of the mean wingtip speed used as a threshold when plotting Q isosurfaces ($1/m^2$)
R	length of one wing from root to tip, (m)
$\mathfrak{R}$	coefficient of power-zero term of characteristic equation of velocity gradient tensor, see Equation 5.9 ($1/s^2$)
Re	Reynolds number, $\frac{\bar{v}_{tip}\bar{c}}{\nu}$
S	planform area of one wing (m^2)
S	sine of angle subtended by line segment 'DZ' on the surface of a sphere, see Equation B.20
S	symmetric part of velocity gradient tensor, see Equation 5.3 ($1/s^2$)
T	flapping period (s)

t	time (s)
$T_{A/B}$	transformation matrix from frame B to frame A
T_{LA} or T_B	input torque on link LA, or torque in direction B (Nm)
∇v	velocity gradient tensor
$\mathbf{v}$	velocity (m/s)
$\mathbf{w}$	vorticity ($1/s$)
X, Y, Z	alternative orthogonal axis system
x, y, z	orthogonal axis system

Greek Symbols

α	pitch angle (rad)
β or $\beta_{A,B}$	angle between two vectors, or angle between vectors A and B (rad)
β_A	generic angle between two segments of a great circle on the surface of a sphere (rad)
$\Delta\phi_A$	difference between generic stroke angle ϕ_A and wing stroke angle ϕ (rad)
δA	error on A
Γ	circulation, see Equation 6.1 (m^2/s)
γ	helix angle, see Equation 2.2 (rad)
λ	viewing angle of camera in the $x_{cam}y_{cam}$ plane to point n in the measurement plane (rad)
μ	dynamic viscosity of fluid (Ns/m^2)
ν	kinematic viscosity of fluid, μ/ρ (m^2/s)
Ω	angular velocity (rad/s)
Ω	antisymmetric part of velocity gradient tensor, see Equation 5.4 ($1/s^2$)

Φ	stroke amplitude (*rad*)
ϕ	stroke angle (*rad*)
ψ	inclination angle of link (*rad*)
ψ	phase angle between stroke and plunge kinematics (*rad*)
ρ	fluid density (kg/m^3)
σ	standard deviation
τ	rotation phase (% of flapping period T)
Θ	plunge amplitude (*rad*)
θ	plunge angle (*rad*)
ς	fraction of flapping period with constant pitch
ζ	viewing angle of camera in the $x_{cam}z_{cam}$ plane to point n in the measurement plane (*rad*)

Superscripts

L	left camera
R	right camera

Subscripts

0	$x_0y_0z_0$ coordinate system fixed to wing (strokes), see Figure G.1
1	xyz coordinate system fixed to wing (strokes and plunges), see Figure 2.4
a	axial component
cam	$x_{cam}y_{cam}z_{cam}$ measurement coordinate system fixed to camera, see Figure 4.27
$cent$	centrifugal
cor	Coriolis

cr	centre of rotation
eul	Euler
flx	flex
I	inertial $X_I Y_I Z_I$ coordinate system, see Figure 2.4
imgL	$x_{imgL} y_{imgL} z_{imgL}$ coordinate system fixed to image plane of left camera, see Figure C.3
imgR	$x_{imgR} y_{imgR} z_{imgR}$ coordinate system fixed to image plane of right camera, see Figure C.3
LA	link *LA*
max	maximum
mec	flapping mechanism output
*mec*1	$x_{mec1} y_{mec1} z_{mec1}$ flapping mechanism output coordinate system (strokes and plunges), see Figure 4.7
*mec*2	$x_{mec2} y_{mec2} z_{mec2}$ flapping mechanism output coordinate system (strokes, plunges and pitches), see Figure 4.7
mid	mid-stroke
min	minimum
r	radial component
t	tangential component
tip	wingtip
va	$x_{va} y_{va} z_{va}$ local coordinate system at point n on a vortex axis, see Figure 6.1
w	$x_w y_w z_w$ coordinate system fixed to wing (strokes, plunges and pitches), see Figure 2.4
wng	wing

Notation

$(\mathbf{A})_B$	vector $\mathbf{A}$ with respect to frame B
$\bar{A}$	mean
$\ddot{A}$	second time derivative
$\dot{A}$ or dA/dt	first time derivative
$\frac{\partial A}{\partial B}$	partial derivative of A with respect to B
$\mathbf{A} \cdot \nabla \mathbf{A}$	convective derivative
$\mathbf{A}$	vector
A_x, A_y, A_z	components of vector $\mathbf{A}$ in xyz frame
A_{x0}, A_{y0}, A_{z0}	components of vector $\mathbf{A}$ in $x_0y_0z_0$ frame
$A_{xcam}, A_{ycam}, A_{zcam}$	components of vector $\mathbf{A}$ in $x_{cam}y_{cam}z_{cam}$ frame
A_{xw}, A_{yw}, A_{zw}	components of vector $\mathbf{A}$ in $x_wy_wz_w$ frame
$D\mathbf{A}/Dt$	substantial derivative, $d\mathbf{A}/dt + \mathbf{A} \cdot \nabla \mathbf{A}$

Abbreviations

$2D$	two-dimensional
$3D$	three-dimensional
CCD	charge-coupled device
CFD	computational fluid dynamics
CI	confidence interval
DOF	degrees of freedom
FMAV	flapping-wing micro air vehicle
KHI	Kelvin-Helmholtz instability
KHV	Kelvin-Helmholtz vortex

LEV	leading-edge vortex
LIC	Line Integral Convolution
MAV	micro air vehicle
PIV	particle image velocimetry
PPR	pulses per revolution
PTV	pitching vortex
rms	root mean square
RPM	revolutions per minute
RTV	root vortex
STPV	stopping vortex
STRV	starting vortex
TPV	tip vortex
UAV	unmanned air vehicle
UFLIC	Unsteady Flow Line Integral Convolution
VTOL	vertical take-off and landing

Chapter 1

Introduction

This first chapter begins with the origin of the micro air vehicle (*MAV*), followed by a discussion of various *MAV* applications, requirements, and types. The motivation for developing flapping wing micro air vehicles (*FMAVs*) in particular is then presented. Lastly, an account of *FMAV* research and development up to this point at Cranfield University will be given.

1.1 Origin of the MAV

Autonomous or remotely-controlled unmanned vehicles are useful in many situations which are either too hazardous for human presence, or are simply impossible for a manned vehicle to achieve. For example, bomb disposal robots eliminate the hazards for the human operator, while still allowing the task to be performed. Meanwhile, some tasks are simply impossible for a human, such as very long endurance reconnaissance flights that last days, or inspection in small areas such as inside pipes, in which cases unmanned vehicles are suitable.

In the realm of aeronautics, unmanned air vehicles, or *UAVs*, began in World War I as self-guided airplanes carrying a warhead to deliver to a target, and were later used as radio-controlled target drones, and flying bombs in World War II (Mueller, 2009). Small UAVs (below 6m wingspan and 25kg Mueller & DeLaurier (2003)) later became possible with the advent of better and smaller components such as small combustion engines, and radio receivers. An advantage of a smaller *UAV* is that the vehicle becomes less expensive and, hence, expendable. Ultimately, miniaturisation of electric motors, sensors, receivers and actuators progressed to the point that even smaller *UAVs* became a reality (Mueller, 2009). In the early 1990*s* following a feasibility study on small flying vehicles from *RAND*, the Defense Advanced Research Projects Agency (*DARPA*) held a workshop where a 15.24cm (6in) flying vehicle weighing no more than 90 grams was proposed (McMichael & Francis, 1997). Such a small vehicle was termed a micro air vehicle, or *MAV*. The advantage of such a vehicle whether for

military or civilian applications would lie in its small size, as it could be carried and deployed by a single operator, would be inexpensive and mass produced, and could be fitted with sensors of many types for remote sensing. Since their initial conception, the development of *MAVs* has taken off, and there is great interest in developing these vehicles for a number of applications.

1.2 MAV Applications

There are many applications for *MAVs*, both military and civilian. A number of such uses are discussed in Davis et al. (1996) and Galiński & Żbikowski (2007), some of which will be discussed here.

Reconnaissance One of the obvious applications for *MAVs* is outdoor reconnaissance. Ground-level troops could easily carry and deploy a *MAV* fitted with a small camera, which could be used on the battlefield to locate enemy positions to achieve better situational awareness, and result in fewer casualties. A vehicle of this size would be very stealthy as its radar signature would be very small or even undetectable due to its small size, low flying speed, and low power signature (Davis et al., 1996). Indoor reconnaissance missions could also be achieved by a *MAV*. A hover-capable *MAV* would be able to operate in dense urban environments, and go so far as to even fly inside buildings to carry out mission objectives. This capability would be useful in civilian law enforcement in hostage situations or "drug busts". In such scenarios, a stealthy *MAV* would be able to fly into the building of interest before a raid and locate all of the combatants. This would give invaluable information for planning the raid to minimise casualties and achieve main objectives such as saving hostages.

Survivor Searching Many search and rescue situations are complicated by the need to search over vast areas. For example, in a scenario where either survivors are stranded at sea or in vast uninhabited areas and their location is unknown, one or a number of search and rescue aircraft must manually scan the area. With such large areas to cover, the search and rescue teams may not be able to search the whole area before the survivors expire. In

such a situation, many *MAVs* fitted with conventional or thermal-imaging cameras, could be deployed in a swarm that would be able to work together and scan a vast area much faster, purely because of their great numbers. Furthermore, search *MAVs* would be able to get closer to the ground in environments that are hazardous to manned aircraft, such as in mountainous and densely wooded areas. This would improve chances of locating survivors. Hover-capable *MAVs* could be used for searching for survivors in indoor environments or other confined spaces. For example, if a building is on fire, or has collapsed in the aftermath of an earthquake, search and rescue crews could deploy *MAVs* to help locate survivors, as they would be able to fly through very confined spaces that are too small for a human.

Inspection in Environmentally Hazardous Areas Inspection in areas which are too hazardous for a human presence, could be accomplished with an *MAV*. For example, in a situation where there is a radiation or hazardous gas leak inside a facility, a *MAV* could be fitted with the appropriate sensors and deployed to locate the source of the problem and potentially rectify it without putting humans at risk.

Structural Health Monitoring Large structures such as bridges have to be continually inspected for cracks and fatigue. This inspection is carried out manually by a single inspector, or inspection crew, which can be complicated by areas that are difficult to access. An *MAV* or number of *MAVs*, with the ability to hover and perch on the structure, could be used to access difficult areas so that an easier, and less hazardous remote inspection could be performed. Furthermore, health monitoring of large distances of pipeline could be performed with *MAVs* fitted with sensors to detect leaks.

Space Exploration Because of their small size and light weight, *MAVs* would be perfect for space exploration, which places particularly high costs on volume and weight of the launch payload. *MAVs* would be useful in this application as they would enable exploration of areas that are difficult to reach with land rovers. In addition, a long-endurance *MAV* would be able to explore much larger areas, and even potentially have the capability of repeated takeoffs and landings to inspect key areas of interest more closely.

1.3 MAV Requirements

From the previous section, it can be seen that *MAV* applications generally fall into three types:

1. outdoor
2. outdoor with hover
3. indoor with hover

For outdoor applications in general, in addition to the small size and weight requirements of $\sim 150mm$ and 90 grams laid out by *DARPA*, a flight speed of $10 - 15m/s$ necessary to overcome winds, and an endurance of $20 - 60$ minutes are required (Davis et al., 1996). Adding the need for hover leads to much more challenging requirements, especially for indoor applications where there are other additional complications. It is for this reason that *MAVs* for indoor applications are relatively underdeveloped. *MAVs* for outdoor, and outdoor with hover applications already exist, whereas suitable *MAVs* for indoor applications are only starting to emerge. As the topic of this thesis is related to *MAVs* intended for indoor applications as we will see later, only the requirements for this application will be described. Including requirements laid out by *DARPA* for the AeroVironment Inc. Phase II Nano Hummingbird Project (AeroVironment, 2011b), the requirements for an *MAV* for use in indoor environments are as follows:

Small Size and Low Weight The wingspan should be $\sim 150mm$ and it should weigh less than 90 grams.

Ability to Operate at Low Speeds The vehicle should be able to operate at low flying speeds. This implies that in addition to generating a sustaining lift force at low speeds, the vehicle must still possess directional control at low speed.

Sustained Hover Capability The vehicle should be able to sustain hover. This also requires that the vehicle is able to transition from forward flight to hover, and then back again. In addition, a hover capability also requires that the vehicle still has directional control during hover.

Ability to Operate in Confined Spaces The *MAV* should be able to operate in confined spaces, which requires good stability, maneuverability and precise control. In addition, this requires that the vehicles operates well close to obstacles, such as walls, floors, and ceilings.

Vertical Takeoff and Landing (VTOL) Capability The vehicle should be able to takeoff and land vertically, which is a necessary requirement for operation in confined spaces.

Ability to Transition from Outdoor to Indoor Environment and Back Although the vehicle is intended for indoor use, it will experience periods at the start and end of its mission when it is entering and leaving a building. Hence, it will be in an outdoor environment for brief periods of time. Thus, the vehicle should be capable of transitioning between these environments, which requires the ability to tolerate gusts and winds when entering and exiting a building.

Energy Efficiency The vehicle should be as energy efficient as possible so as to maximise endurance.

Ability to Carry Sensors The vehicle should have the ability to carry sensors required for the mission, such as a camera. To achieve this, the vehicle must be designed with the payload (sensor) weight in mind, so that it will be able to generate enough lift for sustained flight.

Autonomous Operation or 'Heads-Down' Remote Control The vehicle must either be capable of operating and guiding itself to achieve the mission goals, or it must enable 'heads-down' remote control in which the operator is able to pilot the vehicle with only a video feed from the *MAV*.

Low Noise Signature For covert operations, the vehicle should be as quiet as possible so as to minimise the possibility of detection.

1.4 MAV Types

The different types of *MAVs* developed thus far for various applications will now be described. These include fixed, rotary, and flapping wing *MAVs*.

1.4.1 Fixed Wing

Fixed wing *MAVs* are simply very small airplanes that use a fixed lifting surface with control surfaces to provide directional control and a propulsion system. They are intended to be used for comparatively long endurance outdoor missions. A large number of different fixed-wing *MAV* designs have been developed, thus only a few examples will be presented here.

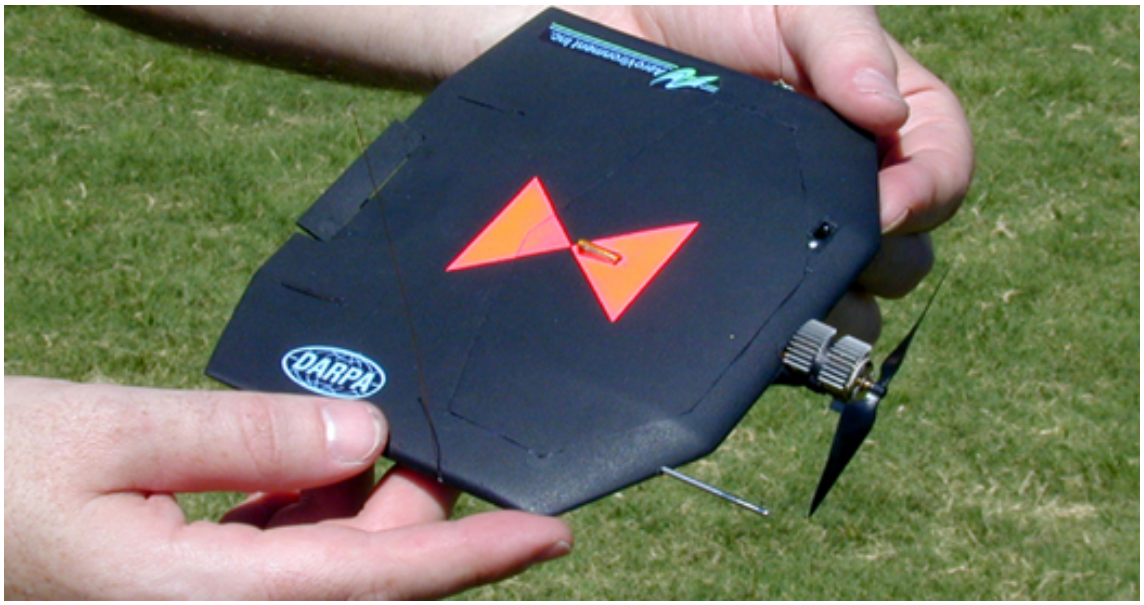

Figure 1.1: AeroVironment's Black Widow (AeroVironment, 2011c)

One of the most active researchers in unmanned air systems in general, AeroVironment Inc., produced a six inch size ($\sim 150mm$), three ounce ($\sim 85gram$) *MAV* called the Black Widow (Figure 1.1), in the 1990*s* soon after *DARPA's* initial proposal for a vehicle of this type (AeroVironment, 2011c). It had an endurance of 30 minutes, range of $1.8km$, maximum altitude of 800 feet ($\sim 244m$), and carried a video camera providing a live video feed to the ground. The success of this project earned the design team and their leader Matt Keennon, several awards.

Another key researcher in fixed wing *UAVs* and *MAVs*, the Naval Research Laboratory (*NRL*), has produced a number of *MAV* designs. Shown in Figure 1.2 are different versions of their MITE (Micro Tactical Expendable) *MAV*, with varying wingspans for carrying different payloads (Kellogg et al., 2001). For the MITE2 version, with a camera payload, they reported a flight time of over 20 minutes,

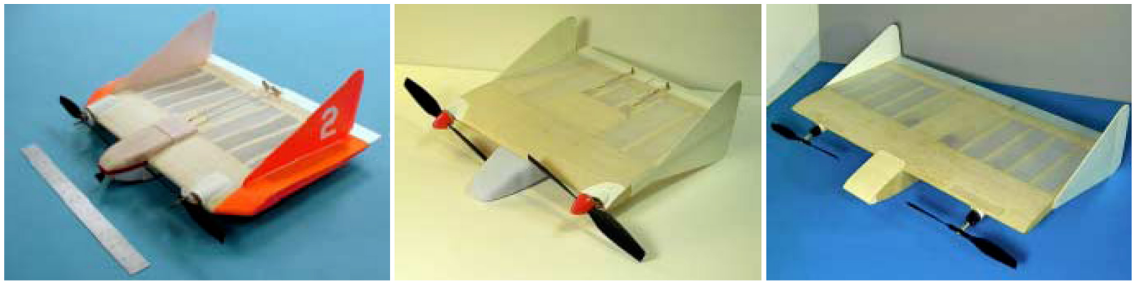

Figure 1.2: Naval Research Laborator's MITE *MAVs*; from left to right, the *MAVs* are MITE2, MITE3, MITE4 (Kellogg et al., 2001)

Figure 1.3: Gust resistant MAV (Galiński et al., 2010)

and flight speeds from 10 to 20mph ($\sim 9m/s$).

A more recent example of a fixed wing *MAV* is the gust-resistant *MAV* of Galiński et al. (2010) illustrated in Figure 1.3. The design features a cranked delta wing, with a propeller in the wing which elevates lift coefficients and enables it to fly controllably at very high angles of attack. The authors reported an issue with with the propeller that caused the vehicle to roll and fly off path with a change in motor speed; however, a second stage prototype using contra-rotating propellers is proposed which would eliminate this problem.

1.4.2 Rotary Wing

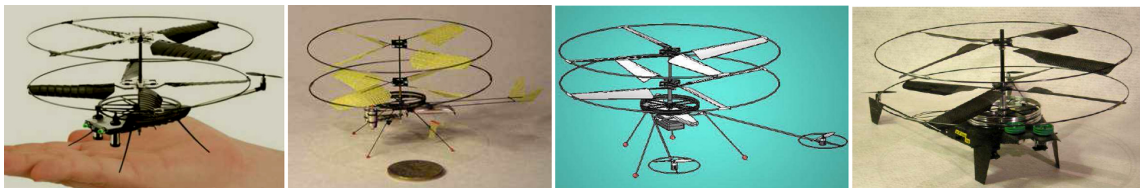

Figure 1.4: Rotary wing *MAVs* of Prox Dynamics; from left to right: Micro Mosquito toy, Nanoflyer, *PD* – 250*L* flying science platform, ProxFlyer *MAV* for US army (Muren, 2008)

Rotary-wing *MAVs* are essentially small helicopters. These vehicles are mainly intended for short endurance outdoor missions requiring a hover capability. As with fixed-wing *MAVs*, many different rotary-wing *MAVs* have been developed, only a few of which will be mentioned here.

Figure 1.5: *PD* – 100 Black Hornet by Prox Dynamics; carrying case (left) ; vehicle right (ProxDynamics, 2011)

A very active developer of rotary wing *MAVs* is Prox Dynamics, headed by Petter Muren. He formulated a novel solution for passive stability, called the Proxflyer system, which uses a special coaxial rotor hub design that achieves passive stability without the need for gyros or servos (Muren, 2008). With this system, a number of vehicle designs which can typically fly for up to 10 minutes have been developed for areas ranging from the military to the toy market as illustrated in Figure 1.4. Currently, Prox Dynamics is developing their '*PD* – 100 Black Hornet' rotary wing *MAV* design as shown in Figure 1.5 (ProxDynamics, 2011). This is intended for military applications, giving soldiers on the ground the abilities to perform reconnaissance inside buildings and urban areas, and to gain a bird's eye view of an area. It will have a 120*mm* rotor diameter, 15 gram weight, 10m/s maximum speed and an endurance of up to 30 minutes.

Figure 1.6: Rotary wing *MAVs* of Ascending Technologies Gmbh (AscTech, 2011)

Many other companies and organisations have arisen that specialise in developing rotary wing *MAVs*. A popular configuration is to use multiple rotors, typically four, spaced around a central hub which is referred to as a quadrotor. Ascending Technologies Gmbh (also known as AscTech) specialises in rotary-wing *MAVs* of this type for a number of applications. Some of their designs are illustrated in Figure 1.6, which are typically mounted with a camera for applications including industrial inspection, surveying and aerial photography (AscTech, 2011). Recently, with a partner company LaserMotive, they broke a world record and achieved a continuous flight of over twelve hours using a ground based laser to power the vehicle (AscTech, 2010).

Figure 1.7: AR Drone by Parrot with different body casings (Parrot, 2011)

The company Parrot has also developed a similar quadrotor *MAV* called the AR Drone, pictured in Figure 1.7. Although intended as a toy, it has all the capabilities required for many practical applications. It is equipped with two onboard video cameras (front and vertical), an ultrasound altimeter, and can be flown with an iPod device with a touchscreen, which also displays the live video feed from the vehicle (Parrot, 2011).

1.4.3 Flapping Wing

A flapping wing *MAV* or, *FMAV* is a vehicle that employs a pair (or two pairs) of insect-like flapping wings. As will be discussed in the next section, this mode of flight offers the abilities of sustained hover and agile manoeuvres in confined spaces, which is why *FMAVs* are intended for indoor applications. A detailed review of flapping-wing devices and *FMAVs* will be given in Chapter 2, thus to avoid undue repetition, only one example of a *FMAV* will be given here.

Figure 1.8: Nano Hummingbird by AeroVironment (AeroVironment, 2011b)

The very first *FMAV* that truly mimics the insect-like mode of flight has only very recently emerged, and is the 'Nano Hummingbird' of AeroVironment Inc. shown in Figure 1.8 (AeroVironment, 2011a). Although designed to resemble a hummingbird, it exploits an insect-like mode of flight, as hummingbirds and insects use very similar flapping wing kinematics. This is the first *FMAV* that truly mimics insect flight in the sense that it uses only a pair of flapping wings to achieve all the required propulsion and control, just as insects do. As will be seen in Chapter 2, past *FMAVs* that have achieved free-flight employed a tail for directional control. The Nano Hummingbird is equipped with an onboard video camera which provides a live video feed to the operator, has a wingspan of 160*mm*, weighs 19 grams in total, and has a flight time of 11 minutes. The vehicle successfully achieved all of the Phase II requirements laid out by *DARPA*, some

of which include a sustained hover capability, ability to tolerate winds, hover endurance of 8 minutes, and the ability to fly from an outdoor environment to indoors and back again.

1.5 Motivation for FMAV Development

Although a number of *MAV* solutions for outdoor missions either with or without hover already exist, suitable *MAVs* for indoor missions are comparatively under-developed due to the challenging requirements imposed by an indoor environment. No system has successfully demonstrated all of the abilities required for these missions, until very recently by AeroVironment. However, there is still a great need for further research and development on *MAVs* for indoor applications, as this area has only just begun.

As indoor missions require hover, rotary wing *MAVs* and *FMAVs* are potential solutions. However, compared to rotary wing *MAVs*, *FMAVs* are apparently more efficient. A comparison of the energy requirements for different *MAV* types was performed by Woods et al. (2001) using formulated expressions for power required. It was found that at flight velocities below approximately $15m/s$ (which is the case for indoor flight), flapping wings require less power for sustained flight than rotary wings as illustrated in Figure 1.9. The horizontal line segment at the low flight velocity end of the flapping wing curve arises from a separate expression for required power in the hover condition. This is needed because the expression for necessary power for higher flight velocities goes to infinity as flight velocity approaches zero (Woods et al., 2001). In this study, the different *MAV* types were also tested for power required for a number of mission scenarios including an urban, battlefield, and artillery spotting scenario, in which loitering time, payload weight and windspeed were varied. It was found that flapping wings were best for missions requiring long loitering times, and that flapping wings were more efficient than rotary wings in the presence of wind, but only up to a windspeed of approximately $15m/s$ (Woods et al., 2001). Experiments with free-flying *FMAVs* have also shown the benefits of flapping wings compared to rotary wings. The *FMAV* of Zdunich et al. (2007) showed higher thrust-to-power ratios for flapping wings in comparison to a rotary wing at higher disk loadings (ratio of *FMAV* weight to area swept by wings). They explained that this would

give such a vehicle the ability to carry a significant payload, and that it would perform well in gusts and turbulence. Thus, given these benefits of flapping wings over a rotary wing, an *FMAV* would be a better solution than a rotary wing *MAV*, as it would be more efficient and offer a longer endurance. Furthermore, it is clearly observed in nature with two-winged insects (Diptera) that this mode of flight offers the unique abilities of sustaining hover, and performing complex and agile manoeuvrers in confined spaces. An *FMAV* that exploits the insect-like mode of flight would therefore successfully meet many of the requirements outlined for indoor applications in § 1.3. Hence, the motivation for developing *FMAVs* is to use them for indoor applications, as they show a particular suitability for this environment.

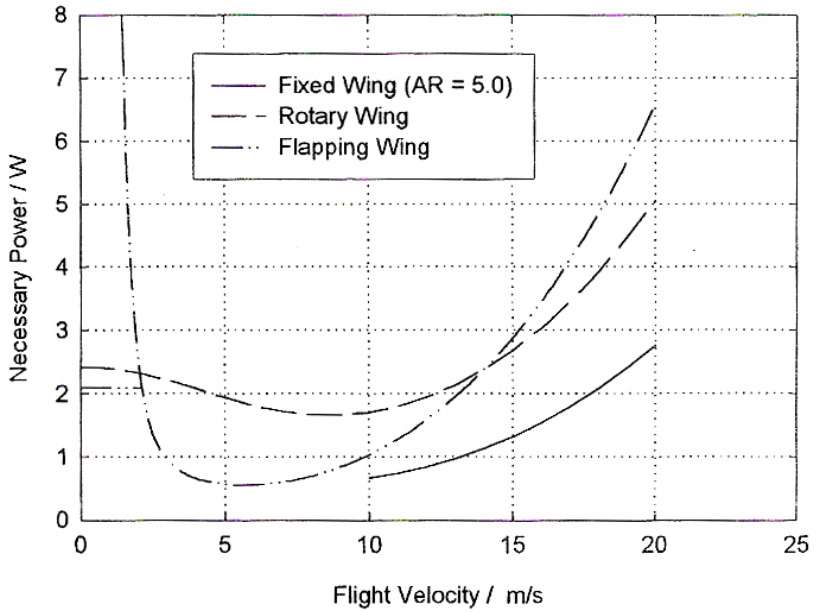

Figure 1.9: Power required versus flight velocity for fixed, rotary and flapping wing *MAVs* (Woods et al., 2001)

One of the impediments to the development of *FMAVs* is the lack of physical understanding of various aspects of insect-like flapping wing aerodynamics, which has been highlighted by Żbikowski (2002). For instance, effects of wing design and flapping kinematics on the aerodynamic forces and flows have not been adequately explored and understood as we will see in the next chapters. Such knowledge is a necessary prerequisite for *FMAV* design. To advance the understanding of insect-like flapping wing aerodynamics to a level which can facilitate design and development of *FMAVs*, further experimental studies on the

subject are required. The focus of this thesis, therefore, is to answer a number of fundamental questions on insect-like flight relevant to *FMAV* development, through an experimental study. These questions will be posed later in Chapter 3.

1.6 FMAV Research & Development at Cranfield

Cranfield University at Shrivenham has been an active researcher on insect-like flight, with relevance to *FMAVs*. Analytical modeling of insect-like flight began with the work of Pedersen (2003), who developed a blade element based indicial-Polhamus model which predicted aerodynamic forces on a flapping wing. The model was 2*D* (thus, no spanwise flow and tip vortex), and proved to be over simplified, as it did not correctly model the flow physics, and showed discrepancies with experimental data (see Pedersen (2003) for details of this model). Later work of Ansari (2004) also took an analytical approach using a nonlinear unsteady model, which was also blade element based, but used radial chords instead of straight ones (see Ansari (2004) for details of this model). This model predicted aerodynamic forces in addition to generating flow visualisation. It proved to be a great improvement over the model of Pedersen, as 2*D* flow visualisations, and predicted forces agreed very well with experimental data. A parametric study was performed with this model, in which kinematic parameters and wing design were varied to determine an optimal wing planform, and flapping kinematics. There were, however, still limitations to this model as it was quasi-2*D*, and thus could not capture spanwise flow and the tip vortex, which are both very prominent features of the flowfield on insect-like wings. Work by Wilkins (2008) took a *CFD* approach, combined with some basic experiments. This study focused on impulsive start and pure sweeping motion of an insect-like wing, both in 2*D* and 3*D*, which appropriately captured spanwise flow and the tip vortex. Effects studied were that of Reynolds number, angle of attack, wing planform, and aspect ratio to name a few. Results yielded useful conclusions relating to the stability of the leading-edge vortex (*LEV*), which we will see later in Chapter 2. Other work at Cranfield has produced a number of flapping-wing demonstrators, which replicate insect-like wing motions (Galiński & Żbikowski, 2005, 2007)

which we will see later in Chapter 2. The work in this thesis represents the first major experimental study on insect-like flight at Cranfield.

Chapter 2

Background & Literature Survey

In this chapter, all of the necessary background to the subject of insect flight will be presented. This begins with a discussion on insect flapping-wing kinematics, in which various aspects related to an insect's wing motion will be described. Following this, aerodynamic mechanisms and phenomena experienced by insects will be discussed. Observed kinematic effects such as the effect of Reynolds number, will be presented next. Lastly, a review of flapping wing mechanical models ('flappers') that have been developed to date for various purposes will be given, followed by a summary of this chapter.

2.1 Insect Flapping Wing Kinematics

Necessary background on insect flapping wing kinematics will first be presented. This begins with a discussion on the flapping cycle, which is followed by a description of the coordinate systems used, and how the instantaneous wing position is defined. Definitions of kinematic parameters describing a given insect's flapping wing motion are then given and, lastly a short description of insect manoeuvres is presented.

2.1.1 Flapping Cycle

An insect's cyclic flapping motion consists of four phases: downstroke, supination, upstroke, and pronation. These are illustrated in Figure 2.1. The downstroke is a translation of the wing at a relatively constant angle of attack from its most aft and dorsal position to its most forward and ventral position. The wing accelerates from the beginning of the downstroke to a constant or peak angular velocity around mid-stroke, after which the wing begins to decelerate. At the end of the downstroke supination occurs, which is when the wing rapidly comes to a stop and reverses its direction and angle of attack so that the wing's underside becomes the topside for the subsequent half-stroke. The wing then translates

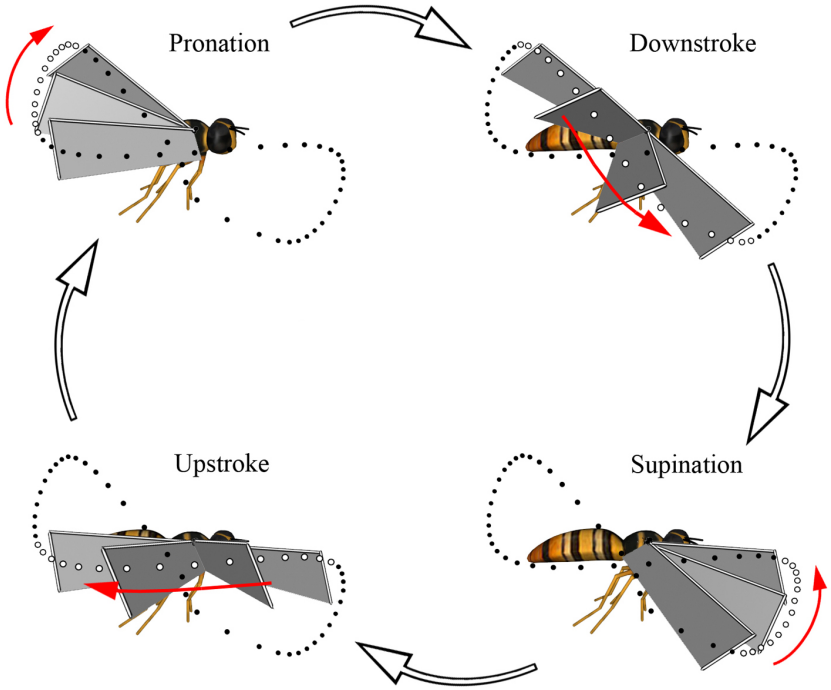

Figure 2.1: Phases of insect flapping cycle

with a relatively constant angle of attack back to its most aft and dorsal position, which is the upstroke. Similar to the downstroke, the wing accelerates to around mid-stroke and then begins decelerating. Finally, at the end of the upstroke, the wing pronates, which is when it again rapidly comes to a stop and reverses its direction and angle of attack in preparation for the next half-stroke. Thus, an insect's flapping motion consists of two 'translation' phases (downstroke and upstroke) with relatively constant angle of attack, and two 'rotation' phases (supination and pronation) in between. The translation phases last 80 – 90% of the flapping period T, while the remaining phases encompassing pitch reversal take up the rest (Ellington, 1984b).

The path that the wingtip traces during the flapping cycle takes the form of irregular self-intersecting shapes, typically resembling a figure-of-eight. Some examples of wingtip trajectories from high-speed footage of insects are shown in Figure 2.2. The wingtip trajectory can take on many shapes, including ellipses, arcs and banana-type shapes, in addition to a figure-of-eight. Some species of insects exhibit common wingtip paths between individuals, whereas in others, the trajectory of the wingtip can be very different between individuals (Ellington,

Figure 2.2: Wingtip trajectories of a hoverfly (left) and bumble bee (right) (Ellington, 1984b); red lines indicate instantaneous orientation of wing chord showing angle of attack; red cross indicates position of wing base

1984b).

2.1.2 Definition of Wing Position & Coordinate Systems

Upon examining an insect's flapping cycle, it is evident that an insect's wing motion is the composition of three separate motions. As illustrated in Figure 2.3, these are a fore and aft stroking motion (stroke), an up and down plunging motion (plunge), and a pitching motion (pitch) about the pitch axis to vary the wing's angle of attack. The stroking motion will also be referred to here as sweep. From Figure 2.4, the wing's position in the stroke, plunge and pitch directions are the stroke angle ϕ, plunge angle θ and pitch angle α respectively. Before these angles are described further, a few coordinate systems must first be defined using Figure 2.4.

As will be discussed later at the end of this chapter, this thesis only deals with insect flight during hover, thus, the insect's body is always considered fixed. The inertial $X_I Y_I Z_I$ frame (fixed to the earth) is aligned with insect's body such that the X_I, Y_I, Z_I axes coincide with the insect's forward, lateral (starboard), and vertical directions respectively. Also, the Z_I axis, $X_I Y_I$ plane are respectively normal and parallel to the earth's surface. The stroke plane can be thought of as a plane of fit through the wing base and the curve defining the path of the wingtip. As this thesis only deals with flight in hover, the stroke plane is always considered to be

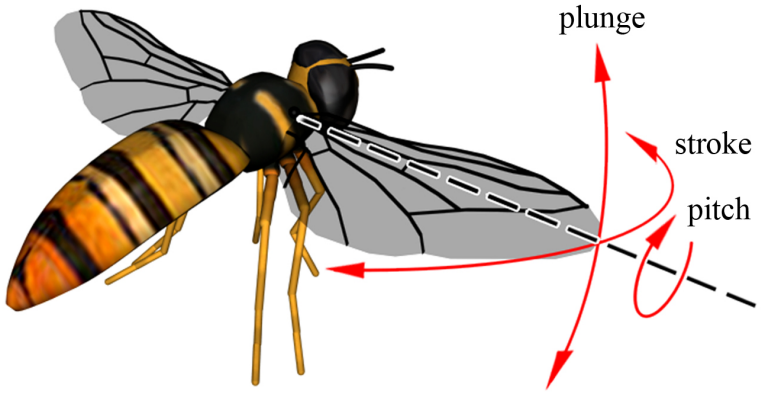

Figure 2.3: Definition of stroke, plunge and pitch

parallel with the $X_I Y_I$ plane. Using the starboard wing, the xyz frame is fixed to the wing (but does not pitch with the wing) such that the x axis is aligned with the wing's pitch axis, the y axis is always parallel to the $X_I Y_I$ plane and points forward, and the z axis is perpendicular to the two. The remaining $x_w y_w z_w$ frame is fixed to the wing (and pitches with the wing), where the x_w axis coincides with the x and pitch axes, the y_w axis always points from trailing edge to leading edge, and z_w is normal to the wing surface.

Returning to the definition of the angles defining wing position, the stroke angle ϕ, is the angle from the X_I (lateral) axis to the projection of the wing's pitch axis on the stroke ($X_I Y_I$) plane as illustrated in Figure 2.4. The positive stroke direction is in the Z_I direction, thus a positive stroke angle is forward of the X_I axis, and a negative stroke angle is aft. The plunge angle θ is the angle between the pitch axis and the stroke plane. The direction of positive plunge is in the $-y$ direction, hence, the plunge angle is positive when the wing is above the stroke plane, and negative when it is below. Pitch α, is the wing's geometric angle of attack relative to the $-y$ axis, and the direction of increasing pitch is in the $-x_w$ direction as seen in Figure 2.4. For example, the wing has 0° and 180° pitch angles when the y_w axis (pointing from trailing to leading edge) coincides with the $-y$ and y directions respectively. Thus, the pitch angle is greater than 90° on the downstroke and less than 90° on the upstroke.

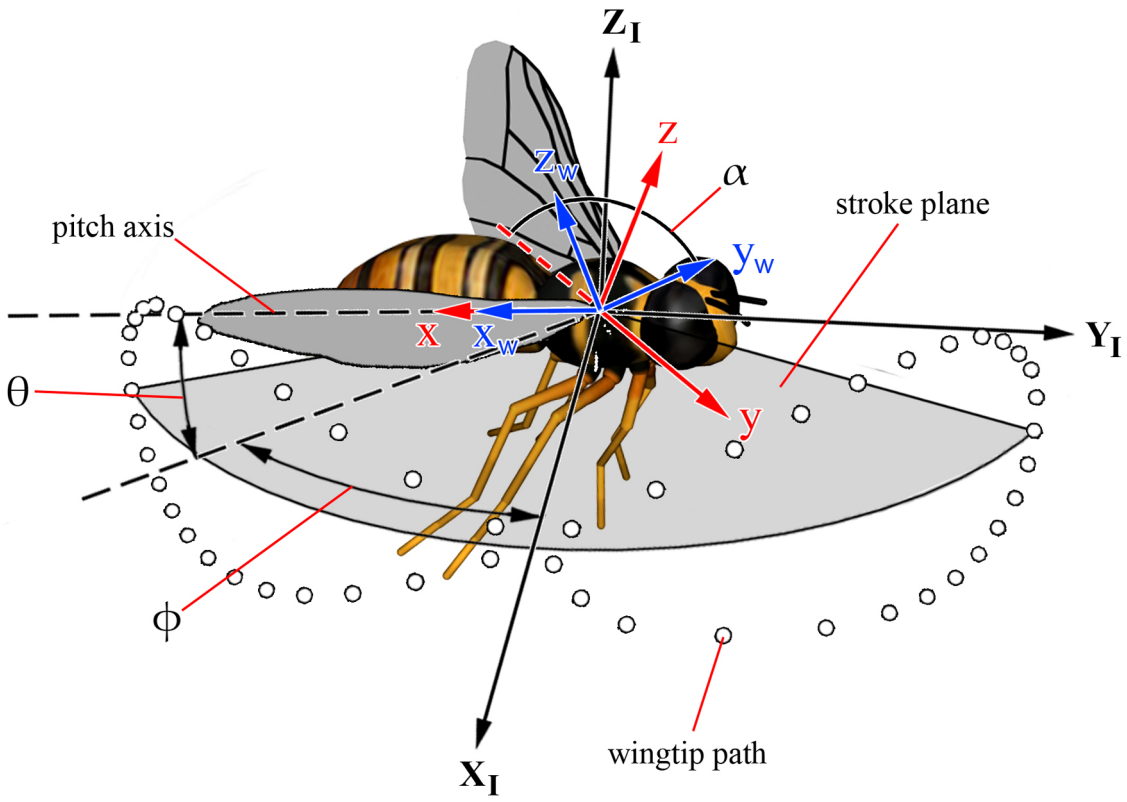

Figure 2.4: Definition of wing position and coordinate systems

2.1.3 Kinematic Parameters

An insect's flapping kinematics may be described using a number of kinematic parameters. These include flapping frequency, stroke amplitude, plunge amplitude, angle of attack at mid-stroke, and rotation phase, which will all be described now.

Flapping Frequency Flapping frequency f, simply describes the number of flapping cycles in a second. Insects execute a flapping cycle with frequencies ranging from $5-200Hz$. The general trend is that an insect's mass is inversely proportional to its flapping frequency, thus larger insects have lower flapping frequencies (Azuma, 2006). For example, fruit flies exhibit flapping frequencies of $240Hz$, whereas hummingbirds which are 10000 times heavier, flap at $15Hz$ (ibid.). As noted in the previous chapter, hummingbirds use insect-like kinematics and, thus, exploit the same mode of flight.

Stroke Amplitude From the wingtip trajectories shown earlier, it can be seen that an insect's wing motion is mostly a stroking motion, with pitching at either end of the stroke and small amounts of plunging. The extent of the stroking motions is measured by the stroke amplitude Φ, which is simply the angle between the maximum and minimum stroke angles. Insects exhibit stroke amplitudes as high as 180° (Weis-Fogh, 1973) and as low as 66° (Ellington, 1984b). However, for most insects, the stroke amplitude is about 120° (Weis-Fogh, 1973). Insects can vary their stroke amplitude, as it has been reported that hawkmoths increase their stroke amplitude when in hover (Willmott & Ellington, 1997), and increasing the stroke amplitude on one wing can initiate a turn (Brackenbury, 1995).

Plunge Amplitude Similar to stroke amplitude, the extent of wing plunging is the plunge amplitude Θ, described as the angle between the maximum and minimum plunge angles. Observed plunge amplitudes are always much smaller than stroke amplitudes (Ellington, 1984b). For example, upon examination of results from Willmott & Ellington (1997), for a hawkmoth, the maximum plunge amplitude is approximately 20°, compared to a ~ 115° stroke amplitude.

Angle of Attack at Mid-Stroke Angle of attack at mid-stroke α_{mid} describes the wing's angle of attack when it is at the mid-stroke position, which is the mean stroke angle $\bar{\phi}$. Insect wings twist along their span such that during the 'translation' phases of the flapping cycle, the angle of attack (pitch angle) at the wingtip is $10 - 20°$ lower (more horizontal) than at the wing root (Ellington, 1984b). The angle of attack at mid-stroke at 70% span ranges from $35 - 45°$, but is usually around 35° (ibid.). For the downstroke, these angles would simply be subtracted from 180° to obtain the equivalent values. In this thesis, symmetric pitching kinematics are always used, an example of which is an α_{mid} of 45° and 135°, on the upstroke and downstroke respectively, giving the same effective angle of attack of 45°. α_{mid} is always quoted as the angle that is less than 90°.

Rotation Phase The timing of the pitch reversal with stroke reversal in insects has been observed to be variable. Hoverflies show a changing location of

the middle point of pronation (time at which the angle of attack is 90°) so that it occurs after the end of the upstroke, which implies that insects can pitch their wings on command, and pitch reversal is not purely the result of inertia (Ellington, 1984b). To modulate aerodynamic forces for manoeuvres, insects can advance or delay supination relative to stroke reversal (Dickinson et al., 1999). In this thesis, the timing of pitch reversal with stroke reversal is termed the rotation phase τ. Here it is defined as a percentage of the flapping period T, where a positive sign implies that pitch reversal (pronation and supination) begins early whereas a negative sign indicates that pitch reversal is delayed. For example, at a 20Hz flapping frequency, a rotation phase of 5% means that the wing begins pitching early so that it reaches a 90° angle of attack 2.5ms before reaching the end of the stroke.

The manner in which flapping kinematics are defined as a function of these kinematic parameters is given in Appendix A.

2.1.4 Manoeuvres

Insects achieve manoeuvres using a number of methods. Since, over a flapping cycle, the resultant force acts nearly perpendicular to the stroke plane, forward/back or lateral accelerations can be achieved by respectively pitching or rolling the stroke plane relative to the insect body (Ellington, 1984b). Tilting the stroke plane in this manner tilts the resultant force over a flapping cycle in the direction of the desired acceleration. Sudden forward or back accelerations can also result from sudden increases in angle of attack on the upstroke or downstroke respectively, creating a rowing-type effect in the direction of acceleration (ibid.). Yawing in fruit flies has been observed to be the result of advancing supination on the wing on the outside of the turn, and delaying supination on the other (Dickinson et al., 1993). Pitching moments about the lateral axis are achieved in insects by shifting the mean stroke angle forward or aft (Ellington, 1984b). Shifting the mean stroke angle aft yaws the stroke plane of both wings back, creating a nose-down moment. A nose-up moment is caused by the opposite, by shifting the mean stroke angle forward. Banking (rolling) is achieved by insects by either increasing the stroke amplitude (with fixed flapping frequency, keeping the wings in phase), or

increasing angle of attack on the outside of the roll (Brackenbury, 1995). Increasing the stroke amplitude on one wing with fixed flapping frequency, requires the wing to travel further in the same period of time, thus increasing its speed and hence lift on that side.

2.2 Aerodynamic Mechanisms & Phenomena

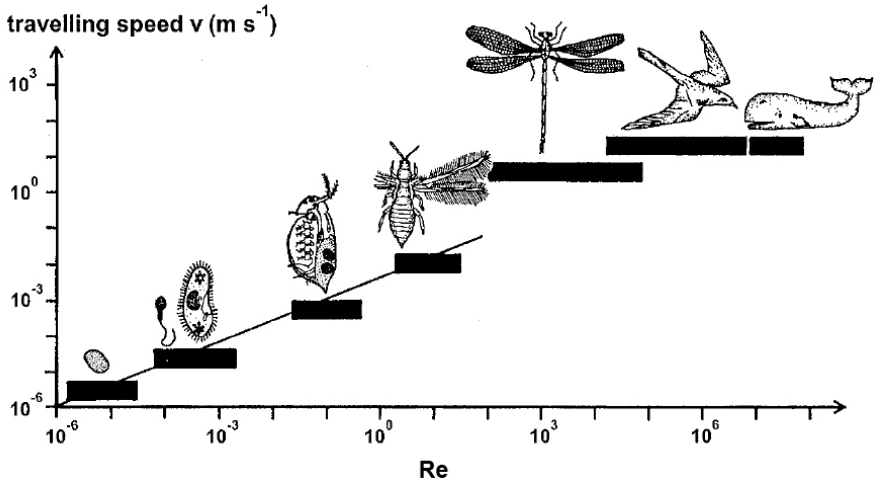

Figure 2.5: Reynolds numbers in the animal kingdom ranging from bacteria (left) to whales (right) (adapted from Nachtigall (1977))

Insects achieve high lift using a number of aerodynamic mechanisms. These will be discussed, in addition to relevant aerodynamic phenomena. These include, Kelvin's circulation theorem, the Wagner and Kramer effects, 'added mass', wake capture, clap and fling manoeuvre, the leading-edge vortex, and vortex breakdown. However, before proceeding, we must first define Reynolds number (Re) which is the ratio of inertial forces to viscous forces given as $Re = vl/\nu$. Here, v is the velocity of the fluid with respect to the body, l is a characteristic length, and ν is the kinematic viscosity. After Ellington (1984d), the characteristic velocity is taken as the mean wingtip speed $\bar{v}_{tip}$, and the characteristic length is taken as the mean chord $\bar{c}$, thus:

$$Re = \frac{\bar{v}_{tip}\bar{c}}{\nu} \tag{2.1}$$

As seen in Figure 2.5, insects operate at Reynolds numbers up to the order of 10^4 where they overlap with small birds. *FMAVs* operate at this upper end, at Reynolds numbers on the order of 10^4. For example, the Nano Hummingbird by Aerovironment, is very comparable in weight to the hummingbird *Patagona gigas* (only differing by 1 gram) which, in nature, operates at Re = 15000 (Azuma, 2006).

2.2.1 Kelvin's Circulation Theorem

Kelvin's circulation theorem states that in a control volume made up of the same fluid elements the time rate of change of circulation must always be zero (Anderson, 2001). For instance, when a wing accelerates from rest, it develops circulation that generates lift, and to balance this, a starting vortex of equal and opposite circulation to the wing-bound circulation must be shed. This is of little interest to conventional aircraft, as starting vortices are left far behind at the point of takeoff. However, insect-like flapping wings only travel a few chord lengths beyond their starting position, so starting vortices are a prominent characteristic of the flow-field generated. Kelvin's circulation theorem comes into play any time there is an increase or decrease in lift. For instance, when the wing's angle of attack rises during pitch reversal and lift increases, a pitching vortex of the same strength and opposite sense to the wing-bound circulation increase must shed. Similarly, when lift falls either due to an angle of attack reduction, or as a result of the wing coming to a rest, a vortex with a strength proportional to the reduction in wing-bound circulation, and with the same sense, is shed. In the case of a wing coming to rest, this is manifested as a stopping vortex.

2.2.2 Wagner Effect

As mentioned previously, when a wing starts from rest, a starting vortex forms at the trailing edge. The impact of this starting vortex is to slow the growth of lift. This is the Wagner effect (Wagner, 1925). The result of this is that lift on the wing

grows gradually to its steady-state value, as the starting vortex is left behind in the wake and hence has decreasing influence. This is relevant to insect-like flight because starting vortices are shed at the start of each half-stroke, which will have an impact on lift.

2.2.3 Kramer Effect

The study of Kramer (1932) investigated the effect on an airfoil from a sudden increase in angle of attack. Rather than pitching a wing rapidly, a sudden angle of attack increase was achieved by rapidly changing the direction of the oncoming flow using a set of louvres at the upstream end of the test section in an open-loop wind tunnel. By suddenly changing the angle of the louvres, angle of attack increases in the pitch-up direction of up to $220 deg/s$ were achieved on a wing in the test section. It was found that a rapid increase in angle of attack from $0°$ to an angle beyond stall of $30°$, was accompanied by a sudden increase in lift coefficient to a level beyond steady state values. This is the Kramer effect. It addition, the maximum lift coefficient achieved was proportional to the rate of angle of attack increase. The cause for this effect was attributed to the fact that following the sudden increase in incidence, there was a lag in the flow separation and it did not all separate at once. During a flapping cycle, an insect's wing makes use of this effect when it suddenly pitches up at the end of a half-stroke as it begins reversing pitch. Sometimes this effect is negative, where at the end of pitch reversal the wing rapidly pitches down causing lift to suddenly fall.

2.2.4 Added Mass

When an insect accelerates its wing from rest, it not only experiences the inertial reaction force from accelerating the wing mass, but also an inertial reaction force from accelerating the fluid around it. The extra force from accelerating this 'added' mass of fluid is known as added mass (also known as apparent mass). This added mass can be comparable to the wing mass itself for some insects (Ellington, 1984a), and is affected by wing geometry and flapping kinematics (Dudley, 2000). This effect also comes into play at the end of a half-stroke when the wing must decelerate an 'added' mass of fluid, in addition to the wing itself.

Added mass will affect instantaneous forces on the wing; however, if flapping kinematics are symmetric, as the usually are, then inertial forces from the wing and added mass will average out, and have no effect on mean forces (Ellington, 1984a).

2.2.5 Wake Capture

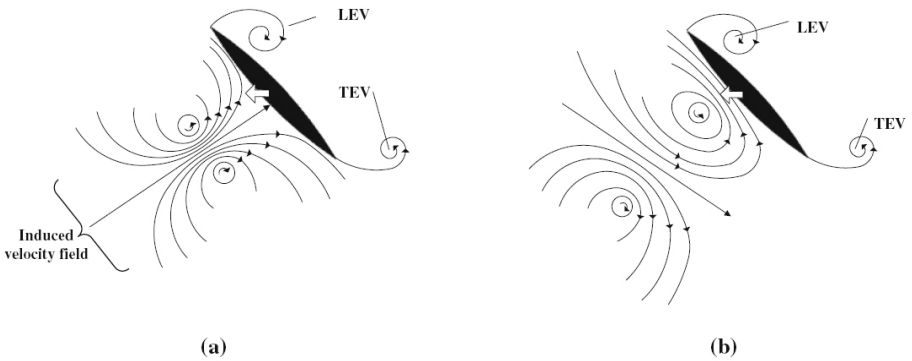

Figure 2.6: Two types of wake capture (adapted from Lua et al. (2011)); (a) wing-wake interaction with counter-rotating vortex pair; (b) and with a single vortex

Another aerodynamic mechanism that is thought to be exploited by insects is wake capture. This mechanism was studied in experiments by Birch & Dickinson (2003) in which the wings of a dynamically-scaled model of a fruit fly were accelerated from rest in the presence of the wake from a previous half stroke, and also in the absence of any wake. Their results showed that when a wing is accelerated from rest into its wake, the resulting lift is much greater than in the wake-free case. It was suggested by Dickinson that this increase in lift results from the wing recapturing shed vorticity from the previous half stroke, which adds to the wing's bound vorticity and enhances lift. This is what he called 'wake capture'. Wake capture was demonstrated in a later study in which the flapping-wing was brought to rest at the end of a half-stroke while the wing was pitched early (a positive rotation phase). The result was that when the wing came to rest it had the appropriate angle of attack to receive (capture) the previously shed wake and generate lift, resulting in lift generation for a short while after the wing was brought to rest (Dickinson et al., 1999). There is, however, some controversy over the effect of wake capture, and whether it enhances lift, has little effect, or impedes lift. It was found in *CFD* studies by Sun (2005) that wake capture is detrimental

to lift, and by Aono & Liu (2006) that it has little effect. A recent study of Lua et al. (2011) involving a 2*D* translating and pitching wing, has shed some light on this as it was found that interaction of the wing with the wake can either lead to augmented or decreased lift, depending on whether a single vortex or pair of counter rotating vortices are encountered. A counter rotating pair (Figure 2.6a) was found to increase the oncoming flow velocity on the underside of the wing, and increase lift, whereas a single vortex (Figure 2.6b) close to the wing underside would decrease lift momentarily. It was suggested by the investigators that lift can be enhanced by correctly timing the wing stroke to encounter the desired structures.

2.2.6 Clap and Fling

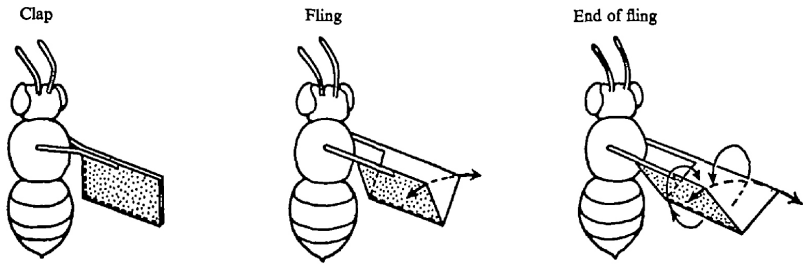

Figure 2.7: 'Clap-and-fling' manoeuvre from Weis-Fogh (1973)

During the pronation stage of the flapping cycle insects can exploit a lifting mechanism called the 'clap and fling' manoeuvre, which was proposed by Weis-Fogh (1973) and Lighthill (1973). Referring to Figure 2.7, during pronation when the upper surfaces of the wings are in contact with both leading edges pointing forward, the wings fold apart as pronation continues towards the downstroke, forming a 'V' with the two wing chords. As this happens, fluid rushes into fill the gap which immediately creates a bound circulation on both wings, but of opposite sense. When the wings then translate apart, the starting vortices from each wing add to the bound vorticity of the neighbouring wing, thus the gradual growth in circulation resulting from the Wagner effect is subdued and the wing-bound circulation reaches levels higher than those seen during the translation (Ellington, 1984c). This is the 'fling' portion of the clap and fling mechanism. The 'clap'

refers to the wings coming together at pronation, in which the leading edges first come together to form an inverted 'V' shape. As the rest of the wing upper surfaces come together, a jet of fluid is ejected downwards as the inverted 'V' closes, leading to an increase in lift (Ellington, 1984c). The clap can last between $20 - 25\%$ of the flapping period (Ellington, 1984b). This mechanism is thought to be exploited by numerous insects as well as birds which bring their wing tips very close together (or even touch) during pronation.

Other variations of the clap and fling exist, such as the 'peel' in which the wings peel apart like two pieces of paper rather than rigidly flinging open. This was proposed by Ellington (1984c), who had observed wings of moths and butterflies to peel apart in this manner. Another variation is the 'near clap and fling (or peel)' in which the upper wing surfaces do not come into contact, but come very close or even touch at the tailing edges.

2.2.7 Leading-edge Vortex (LEV)

The transient high lift produced during translation phases (downstroke & upstroke) of the flapping cycle originates largely from a leading-edge vortex, or *LEV*, that forms at the leading edge of an insect-like flapping wing. This is similar in some ways to the *LEVs* observed on delta wings. Due to the high angle of attack, the flow separates at the leading edge and then rolls up into a vortex that grows in size towards the wingtip where it merges with the tip vortex. The presence of this vortex further increases the flow velocity over the topside of the wing, hence reducing pressure and increasing lift. It has been said that the *LEV* is responsible for up to two thirds of the lift generated (van den Berg & Ellington, 1997a).

The *LEV* was first reported by Maxworthy (1979), who performed experiments on the 'fling' portion of the 'clap-and-fling' manoeuvre described previously. It was reported that as the wings swept, a 'separation-vortex' (the *LEV*) formed on the upper surface each wing, which developed a flow through its axis that transported vorticity out of it and into the tip vortex. This is pictured in Figure 2.8. Maxworthy realised that this axial flow prevented the *LEV* from shedding by transporting vorticity away and into the tip vortex, whereas in the $2D$ case (a $2D$

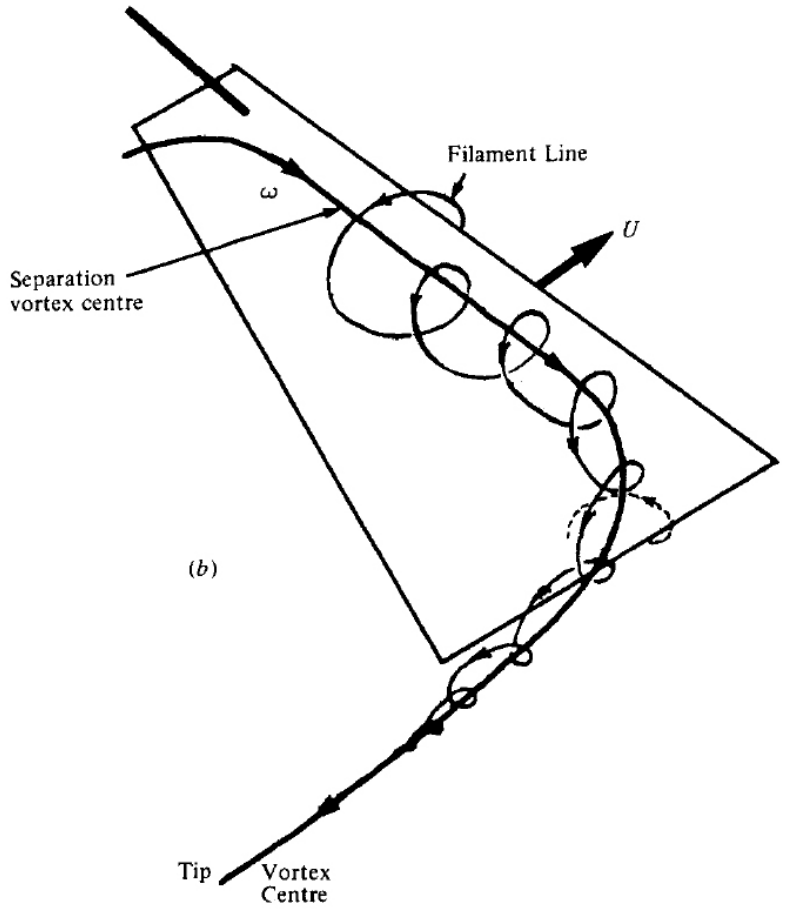

Figure 2.8: First observation of the leading-edge vortex on a flapping wing by Maxworthy (1979); 'separation vortex' (the *LEV*) feeds into the tip vortex

translating wing, as opposed to a 3*D* sweeping wing), vorticity is removed by a buildup and subsequent shedding of vorticity.

Flow visualisations of live insects have shown the existence of the *LEV*. In the studies of Ellington et al. (1996) and Willmott et al. (1997), an *LEV* was reported to be present on the wing of a hawkmoth that fed into the tip vortex. Spanwise (axial) flow was reported to be present above the wing, which decreased in strength towards the end of a half-stroke. In addition, the size of the *LEV* was said to grow towards the wingtip, and also throughout a half-stroke, but despite this, it did not grow so large that it became unstable and shed. This was attributed to the spanwise flow that transported vorticity into the tip vortex. Additional flow visualisations on a mechanical model of a hawkmoth, called the 'flapper', by Ellington and his colleagues, also observed the formation of a *LEV*. Again, it

was seen to grow in size towards the wingtip, and grow throughout a half-stroke (Ellington et al., 1996). They also reported that the *LEV* remained attached until the middle of a half-stroke (mid-stroke), where the *LEV* broke down outboard and the outboard portion of the *LEV* soon shed towards the end of the half-stroke. The same observations of the *LEV* were made in later studies also using the 'flapper' (van den Berg & Ellington, 1997b,a).

Axial flow velocities in the *LEV* have been reported in a number of studies to be comparable to the mean wingtip speed (Ellington et al., 1996; van den Berg & Ellington, 1997a; Ramasamy & Leishman, 2006), and even as high as two times the mean wingtip speed (Lu & Shen, 2008). It was suggested that axial flow through the *LEV* is the result of either centrifugal forces, a favourable pressure gradient along the vortex core, or a combination of the two (Ellington et al., 1996; van den Berg & Ellington, 1997a). An axial pressure gradient through the *LEV* has been confirmed in *CFD* studies of Wilkins (2008) and Wilkins & Knowles (2009). The pressure in the *LEV* core decreases towards the tip due to the increase in wing tangential velocity from root to tip. The higher flow speeds (and hence lower pressures) in the stronger tip-ward end of the *LEV* induces a flow from the weaker (and relatively higher pressure) root-ward end of the *LEV*. In the case of a 2*D* translating wing, the oncoming flow velocity at every chord is the same, thus no axial pressure gradient and hence, no axial flow forms. It has been observed in studies of Birch & Dickinson (2001), that at low Reynolds numbers (Re = 160) spanwise flow is very weak on a revolving wing. This led to the conclusion that the structure of the LEV and the strength of the spanwise flow is Reynolds number dependent. This appears to be true as an experiment by Ramasamy & Leishman (2006) which used a very similar wing geometry to that used by (Birch & Dickinson, 2003), saw a strong spanwise flow at Re = 15500.

The stability of the *LEV* is somewhat controversial. In the case of a 2*D* translating wing, the *LEV* is always reported to be unstable, as it sheds within the first few chord lengths of travel (see e.g. Dickinson & Götz (1993), Wilkins (2008)). In the case of a 3*D* wing, some studies report it to be stable, while others report that it sheds. Experiments by Lentink & Dickinson (2009), linearly translated a 3*D* wing with and without a swept leading edge and found that the *LEV* shed, leading to the conclusion that the presence of a tip vortex is not enough to stabilise the *LEV*. Only when the wing is rotated (swept), is the *LEV* stable. This

was also found by Wilkins (2008) who showed the *LEV* on a 3*D* translating wing to be unstable, but stable when revolved (swept). Dickinson and his colleagues have experimented up to Reynolds numbers on the order of 10^4 (Re = 14000) with their model fruit fly wing, and consistently reported that the *LEV* is stable for a 3*D* revolving wing (see e.g. Birch et al. (2004), Poelma et al. (2006), Lentink & Dickinson (2009)). Experiments by Ellington and his co-workers with their 'flapper' using a model Hawkmoth wing at Re = 8000 reported a stable *LEV* for the first half of a downstroke (Ellington et al., 1996; van den Berg & Ellington, 1997b,a), which then shed in the second half and a new one formed. In later experiments testing a hawkmoth and tapered planform using a more simplified propeller-like test rig, which simply revolved a wing continuously, found that lift coefficients above Re = 10000 did not increase (Ellington & Usherwood, 2001). Purely from the aerodynamic force data, they tentatively concluded that above Re = 10000 the *LEV* lacks the axial flow required to stabilise it and it becomes turbulent and periodically grows and breaks away rather than remaining stable. In a later experiment using a similar setup using a different versions of a revolving hawkmoth wing ($AR = 5.66-6.33$) at Re = 8071 it was found that the *LEV* is stable, even under continual revolutions (Usherwood & Ellington, 2002a). A follow up study tested wings with different aspect ratios and different Reynolds numbers ranging from 1100 to 26000, but could not comment on *LEV* stability as no flow visualisation was performed, only force measurements (Usherwood & Ellington, 2002b). Flow visualisation of the mechanical flapping wing model of Tarascio et al. (2005), Ramasamy et al. (2005) and Ramasamy & Leishman (2006) from $Re = 8000 - 19500$, saw periodic shedding of the *LEV*. Over the Reynolds number range of $160 - 3200$, studies of Lu et al. (2006) observed two *LEVs* to be present over a flapping wing, and later at Re = 1624 they saw multiple *LEV* structures (Lu & Shen, 2008). At even higher Reynolds numbers from $Re = 10000 - 60000$, experiments of Jones & Babinsky (2010, 2011) showed continuous shedding of the *LEV*. Thus, the general trend appears to be that for Reynolds numbers below 10000, the *LEV* is typically reported to be stable, whereas above 10000 conflicting reports of *LEV* stability arise. This is of particular interest to *FMAVs* as they will operate at Reynolds numbers on the order of 10^4, and the stability of the *LEV* can potentially impact performance.

2.2.8 Vortex Breakdown

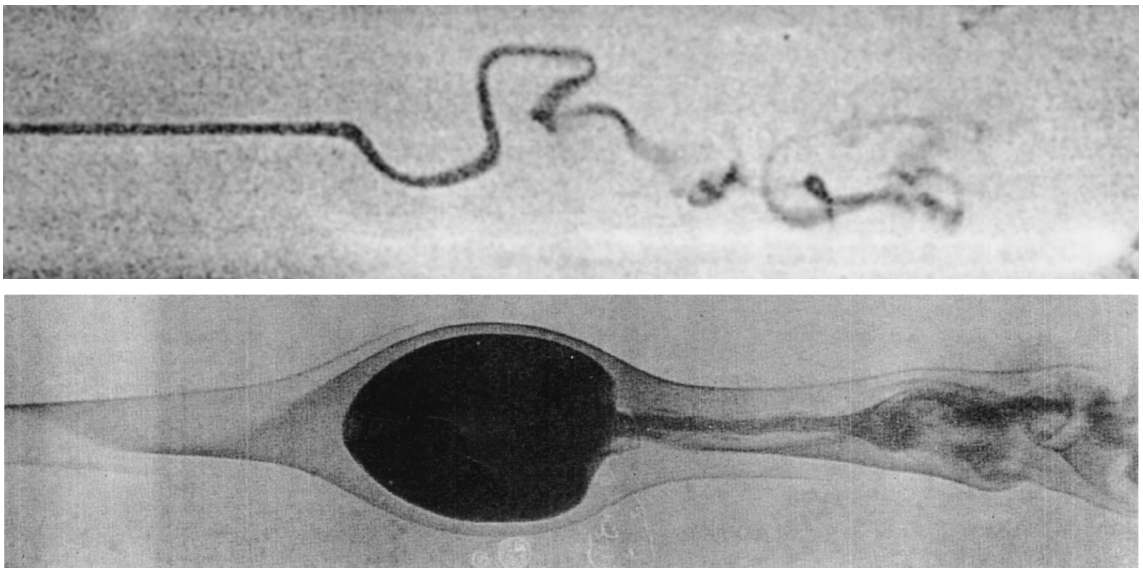

Figure 2.9: Spiral-type vortex breakdown (top) from Leibovich (1978); bubble-type vortex breakdown (bottom) from Sarpkaya (1971)

Vortex breakdown has been seen to occur in the *LEV* in numerous experiments on insect-like flapping wings. Before discussing breakdown with regards to flapping flight, the phenomenon will first be discussed. Vortex breakdown (also known as vortex burst) pictured in Figure 2.9, is generally described as an abrupt change in the core structure of a swirling flow (Benjamin, 1962). More specifically, it is characterised by the formation of a stagnation point on the vortex axis followed by a region of reversed axial flow (Leibovich, 1984), which is accompanied by a sudden increase in vortex size. It was first observed to occur on the LEVs over a delta wing by Peckham & Atkinson (1957). The occurrence of vortex breakdown is either desirable or undesirable depending on the application. In swirl combustion systems it is beneficial because it improves mixing, whereas breakdown of the LEV over delta wings is undesirable as it decreases lift and causes buffeting (Escudier, 1988).

Forms & Structure

There are two main types of vortex breakdown: spiral-type and bubble-type which are illustrated in Figure 2.9. The spiral-type occurs first when a breakdown-

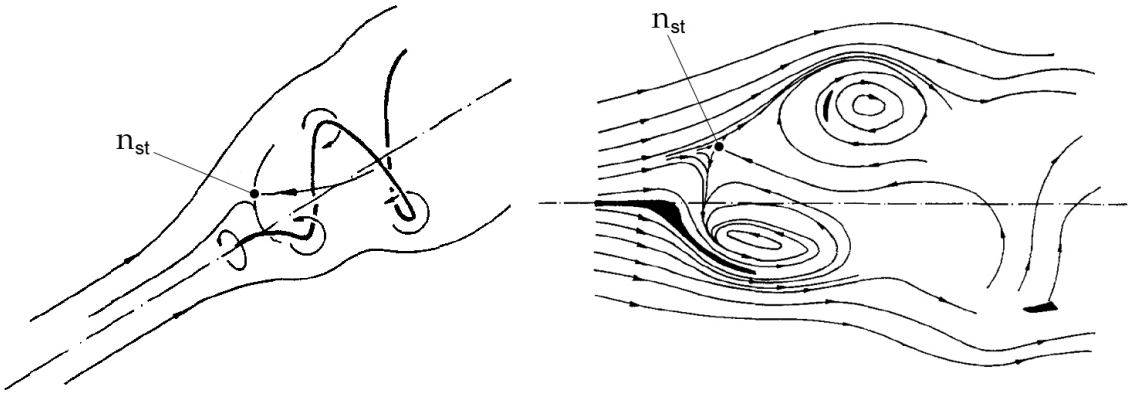

Figure 2.10: Schematic diagram of spiral-type breakdown (left) adapted from Brücker (1993); cross-section through flowfield of spiral-type breakdown (right) adapted from Brücker (1993); the stagnation point in both figures is denoted by the point n_{st}

free vortex reaches a sufficient level of swirl (Lucca-Negro & O'Doherty, 2001), which will be discussed later. Here, swirl describes the ratio between the tangential and axial velocity components of the vortex. The structure of the spiral type breakdown is given in Figure 2.10. It can be seen that after a certain point, the initially straight vortex axis forms a kink to one side and then coils up. The sense of the coiling of the axis has been observed to be the same, and in other cases opposite to the sense of rotation of the undisturbed vortex core. A definite explanation as to why this discrepancy occurs has yet to be given (Lucca-Negro & O'Doherty, 2001). The present discussion will focus on those which coil in the opposite sense to the rotation of the vortex core (as illustrated in Figure 2.10). This sense of coiling appears to be more common and is the manner in which the vortex axis coils over delta wings (Lambourne & Bryer, 1961). Just downstream of the initial kink in the vortex axis is a region of reversed axial flow. It can be seen in Figure 2.10 that the vortex-induced velocity at the centre of the coiled vortex axis is in the same direction as this reversed axial flow. In addition, as a consequence of the coiling of the vortex axis, the stagnation point is located off the vortex axis (Brücker, 1993). This is illustrated in Figure 2.10.

If the swirl level is increased further, the breakdown transitions from a spiral-type to bubble-type, which is accompanied by a shift in the breakdown location further upstream (Lucca-Negro & O'Doherty, 2001). The bubble-type exhibits a larger increase in vortex core size beyond the breakdown location compared to the spiral-type (Leibovich, 1984). Figure 2.11 illustrates the structure of the bubble,

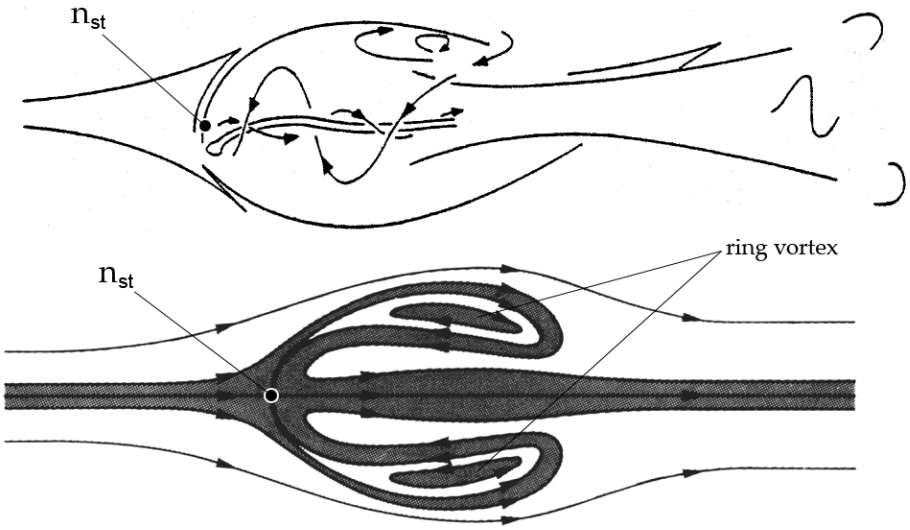

Figure 2.11: Schematic diagram of bubble-type breakdown (top) adapted from Uchida et al. (1985); cross-section through flowfield of bubble-type breakdown (bottom) adapted from Escudier (1988); the stagnation point in both figures is denoted by the point n_{st}

where it can be seen that the flow is axisymmetric, the stagnation point is on the vortex axis unlike the spiral-type, and a vortex ring exists at the downstream end of the bubble. After performing flowfield measurements of the transition from spiral-type to bubble-type, Brücker (1993) argued that during this transition the winding of the coiled vortex becomes more compressed and as this happens the flow becomes more axisymmetric and the stagnation point approaches the vortex axis. When this coil is compressed enough it forms a vortex ring which has an increased level of vorticity in its circumferential direction because the vorticity along the coil has been concentrated into a single ring. As a result of this, the level of reversed axial flow is increased (as the vortex-induced velocity at the centre of this ring is in the opposite direction to the upstream axial flow) and the breakdown location moves upstream. Beyond this type of breakdown, additional increases in swirl only have the effect of moving the bubble-type breakdown structure further upstream (Lucca-Negro & O'Doherty, 2001).

Factors Affecting Vortex Breakdown

The phenomenon of vortex breakdown is not entirely understood, and a generally accepted explanation of the exact cause of vortex breakdown has yet to be reached (Lucca-Negro & O'Doherty, 2001). However, it is generally accepted that the

occurrence of vortex breakdown is dictated by two factors: the swirl level and axial pressure gradient (Gursul et al., 2007). Swirl level is represented by some parameter describing the ratio of tangential velocity to axial velocity of the vortex. A commonly used measure of swirl level is the helix angle, given by:

$$\gamma = tan^{-1}(v_t/v_a) \tag{2.2}$$

Here, v_t is the tangential velocity component, and v_a is the axial velocity component. It has been shown that vortex breakdown occurs when the helix angle reaches a critical value of approximately 50° (Délery, 1994). As mentioned, the axial pressure gradient, which results from downstream conditions is the other factor contributing to the occurrence of breakdown. This pressure gradient is influenced by the presence of solid boundaries on or near the vortex axis, and by the existence of downstream flow traveling in the opposite axial direction. The presence of either of these makes the pressure gradient more adverse, and if the pressure gradient is adverse enough then a stagnation point will form on the vortex axis resulting in breakdown. Experiments by Werlé (1960), illustrated this by triggering vortex breakdown in the LEV over a delta wing by placing a solid disk downstream in the LEV and in another experiment by blowing a jet of air in the axial direction opposite to the travel of the LEV. It should be noted that if the helix angle is below the critical helix angle of 50° mentioned previously, vortex breakdown is not necessarily absent. This is because for a greater adverse pressure gradient, a lesser degree of swirl is required for breakdown (Hall, 1972).

Independent changes in swirl level or pressure gradient can either incite or suppress vortex breakdown. This is the basis for flow control methods for delaying vortex breakdown over delta wings, where such methods rely on altering either the swirl level or pressure gradient (Gursul et al., 2007). For example, either blowing or sucking along the vortex axis in the same direction as the vortex axial velocity will alleviate the adverse pressure gradient and can even completely suppress breakdown, which has been shown experimentally by Werlé (1960). Such a method was employed on the Concorde where breakdown of the LEVs over the wings was eliminated with the aid of the exhaust from the engines (Mitchell & Délery, 2001). Here the exhaust created trailing-edge blowing in the same direction as the LEV axial velocity, which acted to alter the adverse pressure gradient

favourably.

Vortex Breakdown in Insect-like Flight

Probably the first reported occurrence of breakdown in the LEV on an insect-like wing took place in experiments by Ellington et al. (1996) with their mechanical 'flapper' executing Hawkmoth-like flapping kinematics at $Re \approx 1000$. It was observed with smoke streaklines released from the wing root that the LEV broke down around 60 – 70% of the wing length, after which it connected to the tip vortex. In another experiment by van den Berg & Ellington (1997a) (also performed with their 'flapper') the LEV was again observed to breakdown around the same location. In this study, the helix angle was measured from the 'clearly defined' streaklines (the streaklines before the breakdown location) through the LEV, which was found to be 45.9° with a standard deviation of ±11.9°. Since then, breakdown of the LEV has been reported in numerous other experiments, which have mostly been performed at Reynolds numbers of the order of 10^3. It is typically seen that breakdown initiates at or around mid-stroke, where the location on the wing at which breakdown occurs appears to vary. Observations have reported breakdown to occur at approximately 75% of the wing length (van den Berg & Ellington, 1997b), 50% wing length (Lu & Shen, 2008; Lentink & Dickinson, 2009), and 35% of the wing length (Lu et al., 2006). This discrepancy in breakdown location is possibly in part a result of the fact that over these various studies, the breakdown location has been determined in a qualitative way, with different methods. That is, rather than locating the breakdown location quantitatively (i.e. the point at which axial flow stagnates and reverses), the breakdown location has typically been qualitatively determined as the point where streaklines either dissipate or suddenly follow a greater radius of curvature, or when a vortex criterion isosurface disappears, all of which may lead to a different result. After mid-stroke when the wing decelerates, breakdown of the LEV has consistently been seen to move inboard (van den Berg & Ellington, 1997b; Lu & Shen, 2008; Lentink & Dickinson, 2009). As for the effect of breakdown on aerodynamic forces, the experiments of Lentink & Dickinson (2009) found that lift coefficients were higher at a Reynolds number where breakdown had occurred (Re = 1400) compared to a lower Reynolds number where breakdown was absent (Re = 110). Thus, they concluded that vortex breakdown did not negatively impact force production.

CFD studies have also observed breakdown or hints of the occurrence of breakdown (Liu et al., 1998; Wilkins, 2008). The study of Liu et al. (1998) replicated the experiment of van den Berg & Ellington (1997a) but computationally. Immediately after mid-stroke they observed breakdown of the LEV between $60-70\%$ of the wing length and also reported an adverse pressure gradient which they attributed to a balance between the spanwise pressure gradient and the pressure gradient originating from the wing tip. It should be noted that in most of the reported incidences of breakdown of the LEV on insect-like wings, no attempt has been made to classify which type of breakdown has occurred. However, upon inspection of results from such studies, it appears that only the spiral-type breakdown has been observed.

2.3 Kinematic Effects

Studies on insect-like flight to date have observed a number of effects due to various kinematic parameters. These include effects from Reynolds number, angle of attack, rotation phase, stroke amplitude, plunge amplitude and wingtip kinematics. Such effects will now be discussed, in that order.

2.3.1 Reynolds Number

Experiments by Dickinson & Götz (1993) measured forces on a $2D$ translating and pitching wing, immersed in liquid over the range $Re = 120-1400$, and found that lift and drag coefficients rose with increasing Reynolds number. This led to the conclusion that lift augmentation increases with Re. A later experiment using a $3D$ revolving (sweeping) wing at $Re = 120\&1400$ gave a similar story, where lift and drag coefficients were larger at higher Reynolds number (Birch et al., 2004). Up to an even higher Reynolds number range from $Re = 110-14000$, testing a flapping and continually rotating (sweeping) wing, the same trend was observed for all cases where aerodynamic coefficients increased with Re (Lentink & Dickinson, 2009). However, the rate of increase of lift and drag coefficients declined with increasing Re, as force coefficients at $Re = 1400\&14000$ were similar. The waving (sweeping) wing experiment of Jones & Babinsky (2011), showed similar lift coefficients at $Re = 30000$ and $Re = 60000$ over various angles of attack.

A similar result was obtained in the study of Ellington & Usherwood (2001) testing different revolving wings from $Re = 10000 - 50000$. The general trend for all wings tested was that in the range $Re = 20000 - 50000$ lift and drag coefficients are relatively unchanged. However at $Re = 10000$ lift and drag coefficients were at their peak, as they were generally higher respectively at high and low angles of attack for two of the planforms tested (manduca and taper). These findings later led to the conclusion of a critical Reynolds number of 10000, above which the flow will become turbulent and lift coefficients will drop by a factor of three (Ellington, 2006). However, this conclusion was later rejected by Usherwood (2009) who showed that at even higher Reynolds numbers, model pigeon wings ($Re = 10800\&54000$) saw very similar force coefficients to those of a hawkmoth ($Re = 8000$). In computational studies, the work of Wilkins (2008) found that on a $3D$ revolving wing, lift coefficients increase up to $Re = 2500$, and remain constant thereafter.

In terms of the effect on the *LEV*, as mentioned earlier in § 2.2.7, there are observed discrepancies in *LEV* stability above $Re \approx 10000$. Also, axial flow in the *LEV* core is minimal at low Reynolds number of 160 (Birch & Dickinson, 2001), it exhibits higher values as *Re* increases, but has been postulated to be absent at $Re > 1000$ resulting in vortex shedding (Ellington & Usherwood, 2001). Although axial flow has been confirmed on a flapping wing at $Re = 14000$ (Lentink & Dickinson, 2009). Other observed Reynolds number effects are that *LEVs* grow more quickly at low *Re* (Jones & Babinsky, 2011), and even a dual *LEV* structure has been observed to form at $Re \geq 640$ (Lu et al., 2006).

From the previous discussions, it can be seen that a number of discrepancies exist in regards to Reynolds number effects. These include conflicting reports of effects on aerodynamic forces, and effects on the flow, such as potential effects on *LEV* stability, and axial flow.

2.3.2 Angle of Attack

It has been consistently reported that lift coefficient peaks between an angle of attack of $40 - 50°$, declining on either side of this value, whereas drag coefficient continually rises as the angle of attack approaches 90°. This is true for the $2D$ case of a translating wing (Dickinson & Götz, 1993; Wilkins, 2008), as well as $3D$

flapping wings, or continually revolving wings (Sane & Dickinson, 2001; Ellington & Usherwood, 2001; Usherwood & Ellington, 2002a; Wilkins, 2008). Even in the case of varying wing geometry and aspect ratio, lift coefficient still peaks in this angle of attack range and drag coefficient continually climbs (Usherwood & Ellington, 2002b).

In *CFD* studies by Wilkins (2008), it was found that increasing the angle of attack on an impulsively-swept wing increased the stable size of the *LEV*. Smoke visualisations on a continually revolving wing at $Re \approx 8000$ by Usherwood & Ellington (2002a) saw no separated flow (*LEV*) below an angle of attack of 10°. Above this, the *LEV* and axial flow through its core soon developed. At the highest angle of attack of 90° a stable *LEV* in addition to a stable trailing-edge vortex, both possessing strong axial flows, were present. Observations by Lu et al. (2006) on a flapping wing at $Re = 1624$ revealed the formation of a dual *LEV* structure for angles of attack around 30° and above.

2.3.3 Rotation Phase

The first investigation of rotation phase appears to be that of Dickinson et al. (1999), in which pitch reversal was advanced, symmetric, and delayed relative to stroke reversal, which respectively correspond to a positive, zero, and negative rotation phase. Experiments were performed at $Re = 140$, and it was found that when pitch reversal was advanced, higher mean lift coefficients were achieved, and that delaying pitch reversal gave the lowest lift. These results were replicated in a *CFD* simulation of the same wing type (fruit fly) at $Re = 136$ by Sun & Tang (2002b), and again in another study at $Re = 147$ (Sun & Tang, 2002a) in which it was found that the power required per unit of lift increased as pitch reversal was advanced. A similar *CFD* study by Ramamurti & Sandberg (2002), with a fruit fly wing planform, at a similar Reynolds number ($Re = 136$), also found that advanced pitch reversals lead to higher lift, followed by a symmetric and delayed pitch reversal which performed the worst. The study of Sane & Dickinson (2001) investigated this further experimentally, where a range of rotation phases were tested at a Reynolds number on the order of 10^2. It was found that a rotation phase of 5% was optimal, as mean lift coefficient fell on either side of this value (Sane & Dickinson, 2001). In the same year, experiments by Sunada et al. (2001)

on a $2D$ translating and pitching wing at Re = 1000 found that maximum lift was achieved with a 0% rotation phase, whereas peak efficiency (lift per power required) was obtained at a value of 12.5%. Consistent with the trends found by Sane & Dickinson (2001), results from the analytical model of Ansari et al. (2008b) found a rotation phase of 5% to be optimal for two different wing geometries.

2.3.4 Stroke Amplitude

Investigation of stroke amplitude effects are few. Experiments by Sane & Dickinson (2001) performed at Reynolds numbers on the order of 10^2, varied stroke amplitude with a fixed flapping frequency. It was found that when increasing the stroke amplitude, the normal force rises, but the normal force coefficient falls. Regarding lift and drag components, they found that increasing stroke amplitude increased lift coefficients, and decreased drag coefficients. The analytical model of Ansari et al. (2008b) similarly found that increasing stroke amplitude with a fixed flapping frequency led to a rise in both lift and drag forces. Computational investigations of Meng et al. (2010) studied effects due to wing corrugation, and varied stroke amplitude, but with a fixed Reynolds number of 1800, as opposed to a fixed flapping frequency. Only effects due to corrugation are discussed rather than stroke amplitude effects; however, upon examination of their results, mean drag coefficient declines with increasing stroke amplitude, whereas mean lift coefficient falls by about 0.3 for a 110° increase in stroke amplitude.

In flow visualisations of Tarascio et al. (2005) on their flapper operating at Re = 8000, stroke amplitude was varied. However, they observed no changes in the flowfield, as they reported that vortices were continually shed regardless of stroke amplitude. The effect of stroke amplitude on the flowfield mainly comes down to the stability of the *LEV* which, as has been mentioned earlier, is a controversial subject. As discussed, some studies observed the *LEV* to be stable for continual revolutions (infinite stroke amplitude), while in others it sheds almost immediately.

2.3.5 Plunge Amplitude and Wingtip Kinematics

Plunge amplitude effects are relatively unexplored. In experiments by Sane & Dickinson (2001) at Reynolds numbers on the order of 10^2, figure-of-eight and oval wingtip trajectories with increasing plunge amplitude were investigated for their effects on forces. A figure-of-eight trajectory can be followed in two ways, by either rising or descending at the start of a half stroke. It was found that for both trajectories, including the mentioned two ways of following a figure-of-eight, increasing the plunge amplitude from zero (from a flat wingtip trajectory) led to a decrease in both mean lift and drag coefficients, but had little effect on the mean lift to drag coefficient ratio. The parametric study of Ansari (2004) using his analytical model, examined a figure-of-eight, concave, and convex arc wingtip trajectory, and varied the plunge amplitude of these. Increasing the plunge amplitude for figure-of-eight kinematics in which the wing rises at the start of half-stroke, showed a decline in lift and rise in drag. Achieving a figure-of-eight trajectory in the other manner by descending at the start of a half-stroke gave comparatively higher lift and drag, but effects from changing plunge amplitude with this case were not given. For the concave arc (wingtip follows a 'u' shape) increasing plunge amplitude generally led to a rise in lift and a larger rise in drag. The convex arc (wingtip follows an inverted 'u') saw lift fall slightly with rising plunge amplitude, whereas drag fell comparatively more, which led to particularly higher lift to drag ratios at higher plunge amplitude. Another study, by Berman & Wang (2007) also using an analytical model, used an optimisation algorithm and varied kinematic parameters to converge on an optimal set of kinematics that would minimise power consumption for a fruitfly, a bumblebee and a hawkmoth. A sensitivity study of one of the optimal sets of kinematics showed that increasing the plunge amplitude (with figure-of-eight wingtip kinematics) led to a continual rise in lift and power required. The recent experimental study by Ania et al. (2011) measured forces using their 'RotaFlap' mechanism which flapped a wing through a figure-of-eight trajectory up to $Re \approx 3700$. Although the resultant force coefficient was found not to change significantly with Re, it exhibited much smaller resultant force coefficients of at most 0.7 compared to values of around 3 (even at very high plunge amplitudes) found by Sane & Dickinson (2001) at lower Reynolds number (Re on the order of 10^2).

2.4 Flapping Wing Mechanical Models

In experiments concerning the aerodynamics of insect-like flight with applications for FMAVs in mind, mechanical flapping wing models (or 'flappers') that emulate insect-like flapping-wing motion are very useful. Unlike working with real insects, a mechanical flapper gives the experimenter control over flapping kinematics, and forces can be measured from individual wings. Furthermore, mechanical flappers (which operate in air) serve as a stepping stone towards a fully functional *FMAV*. For these reasons, experiments performed with mechanical flappers are a key part of advancing the understanding of insect-like flapping-wing flight necessary for the development of a working *FMAV*. In such experiments arguably one of the most important aspects is the design and operation of the flapper, and the experimental apparatus as a whole. This section will perform a review of different mechanical flappers that have been made thus far that emulate insect-like wing motion, and what they were used for. The section begins with a review of submerged flappers (flappers that operate in a liquid), followed by flappers that operate in air. Free-flying flappers are then discussed, which are flappers that can actually sustain free-flight.

2.4.1 Submerged Flappers

One of the advantages of performing experiments in a liquid is that, in comparison to working in a gas, the more viscous nature of a liquid allows the subject of the experiment to be slowed down much more for a given physical size of the subject, while still preserving the Reynolds number (due to the lower kinematic viscosity). This is advantageous because slowing down the experiment makes it much easier to visualise unsteady effects. In addition, liquid flows can be seeded more easily, and make it easier to separate aerodynamic forces from inertial forces as the inertial forces (from accelerating the body, not the fluid) become relatively smaller. This section will discuss mechanical flappers that have operated in a liquid, starting with early and recent two-dimensional flappers, followed by early and recent three-dimensional flappers.

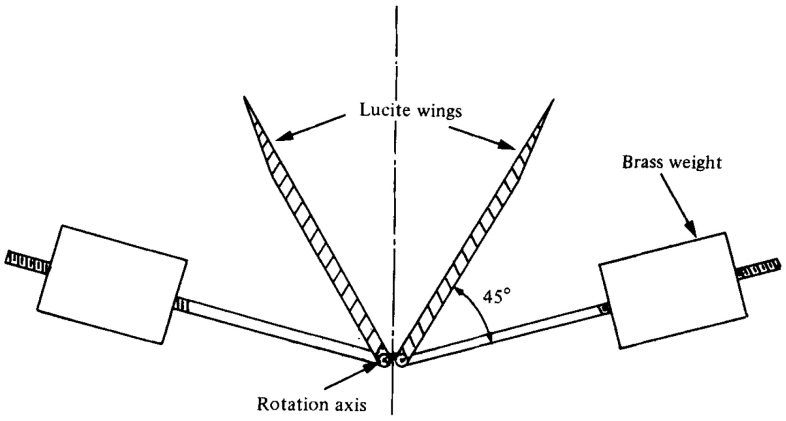

Figure 2.12: 2D experimental apparatus of Maxworthy (1979)

2D Flappers

Early Flappers

The earliest experiment of this kind appears to be that of Maxworthy (1979) who studied the 'clap-and-fling' mechanism formulated by Weis-Fogh (1973) and Lighthill (1973). In his experiments, Maxworthy used a 2*D* and a 3*D* apparatus, the latter of which will be described later. The 2*D* apparatus (Figure 2.12) consisted of two rectangular wings pivoted at their trailing edges and each attached to a rod with a brass weight to drive the wing rotation and 'fling' the wings apart from a closed position. Experiments were performed in water and later glycerine (to simulate Re = 13000 and Re = 32, respectively) and flow visualisation was performed using dye and neutrally buoyant wax beads illuminated with a light sheet perpendicular to the wingspan, and later parallel to the wingspan. 'Streak photographs' of the flow were taken at various points following the release of the wings. Here, a 'streak photograph' is obtained when the exposure of the film is set such that streaks on the image are produced resulting from the motions of the particles during the exposure. From the length and direction of the streaks on the image, and from the known time of exposure, Maxworthy was able to determine local fluid velocities and ultimately circulation in different areas of interest.

In the same year, a two-dimensional water tank experiment was also performed by Savage et al. (1979). Savage and his colleagues studied the unsteady flow resulting from a 2*D* flapping wing in a water tank undergoing an idealised dragonfly-like flapping wing motion at an average Reynolds number of app-

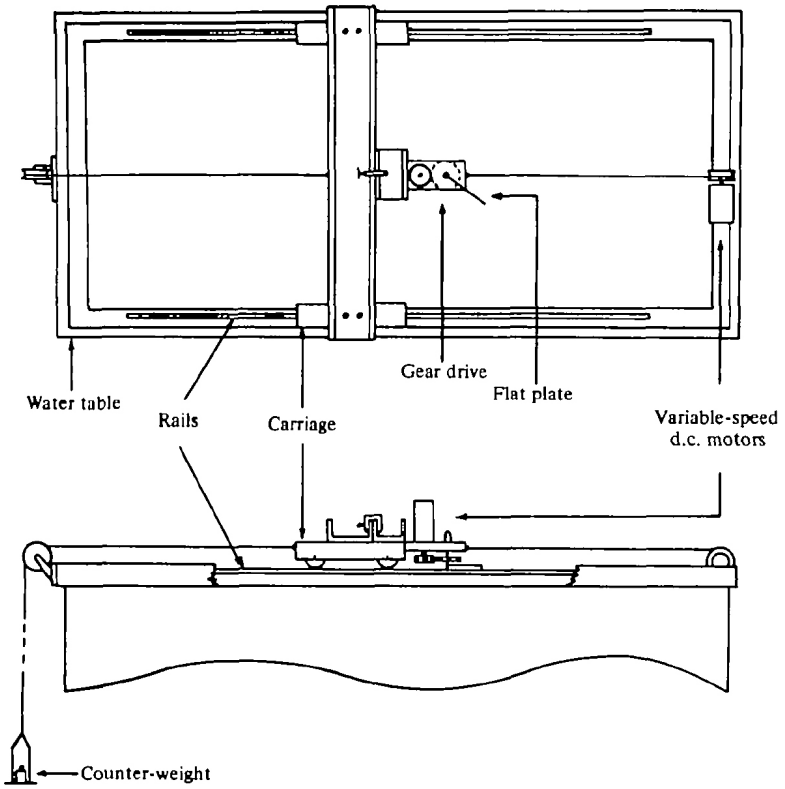

Figure 2.13: 2D experimental apparatus of Savage et al. (1979)

roximately 6000. Their experimental apparatus consisted of a rectangular wing mounted vertically in a water tank, where pitch and stroke control of the wing were achieved via two separate motors. As noted previously, this was a two-dimensional experiment as the wing purely translated. An illustration of the apparatus is given in Figure 2.13.

Savage and his colleagues studied the flow induced by the flapping wing by seeding the water surface with markers of 'confetti comprising the residue from computer card punching operations' (Savage et al., 1979). Photographs were then taken of the water surface at different points in the flapping cycle to produce streak photographs. These were then converted to vector maps, where the positions and strengths of vortices in the flow field were determined and ultimately forces were analysed using potential flow theory.

Less than a decade later, another water tank-based experiment concerning the clap-and-fling was performed by Spedding & Maxworthy (1986). In their experiment, they used an apparatus submersed in water, comprising of two rectangular

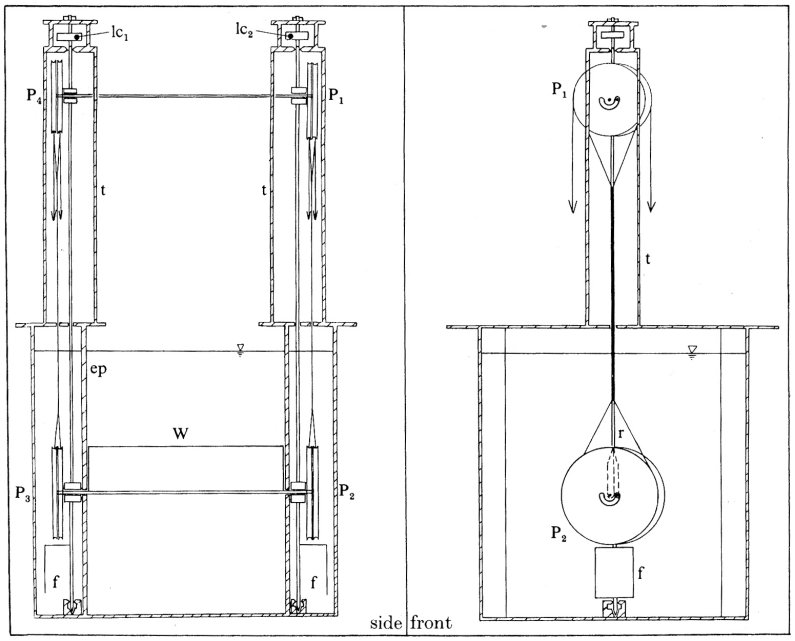

Figure 2.14: 2D experimental apparatus of Spedding & Maxworthy (1986)

wings pivoted at their trailing edges which would 'fling' apart using hanging weights. The apparatus was supported within the water by 'floats' to make the system neutrally buoyant, and enable lift to be measured via a connection to load cells with pushrods. Flow visualisation was performed by seeding the tank with polystyrene beads and illuminating the flow with a sheet of light at the mid span to produce streak photographs, and vector maps at different points following the wing rotation.

Recent Flappers

Following the work of Maxworthy, Spedding and Savage, there have been numerous 2*D* water tank based experiments which have utilised experimental apparatuses very similar to the one used by Savage et al. (1979). That is, an apparatus that generally consists of a wing in a water tank which is mounted to a motor-driven translating platform to produce stroking (or pure plunging) motions, while the wing pitches passively or via a motor. Studies that used this type of apparatus include those of Dickinson & Götz (1993), Sunada et al. (2001), Heathcote (2007), Beckwith & Babinsky (2009), and Wilkins (2008). Illustrations of their respective apparatuses are given in Figure 2.15.

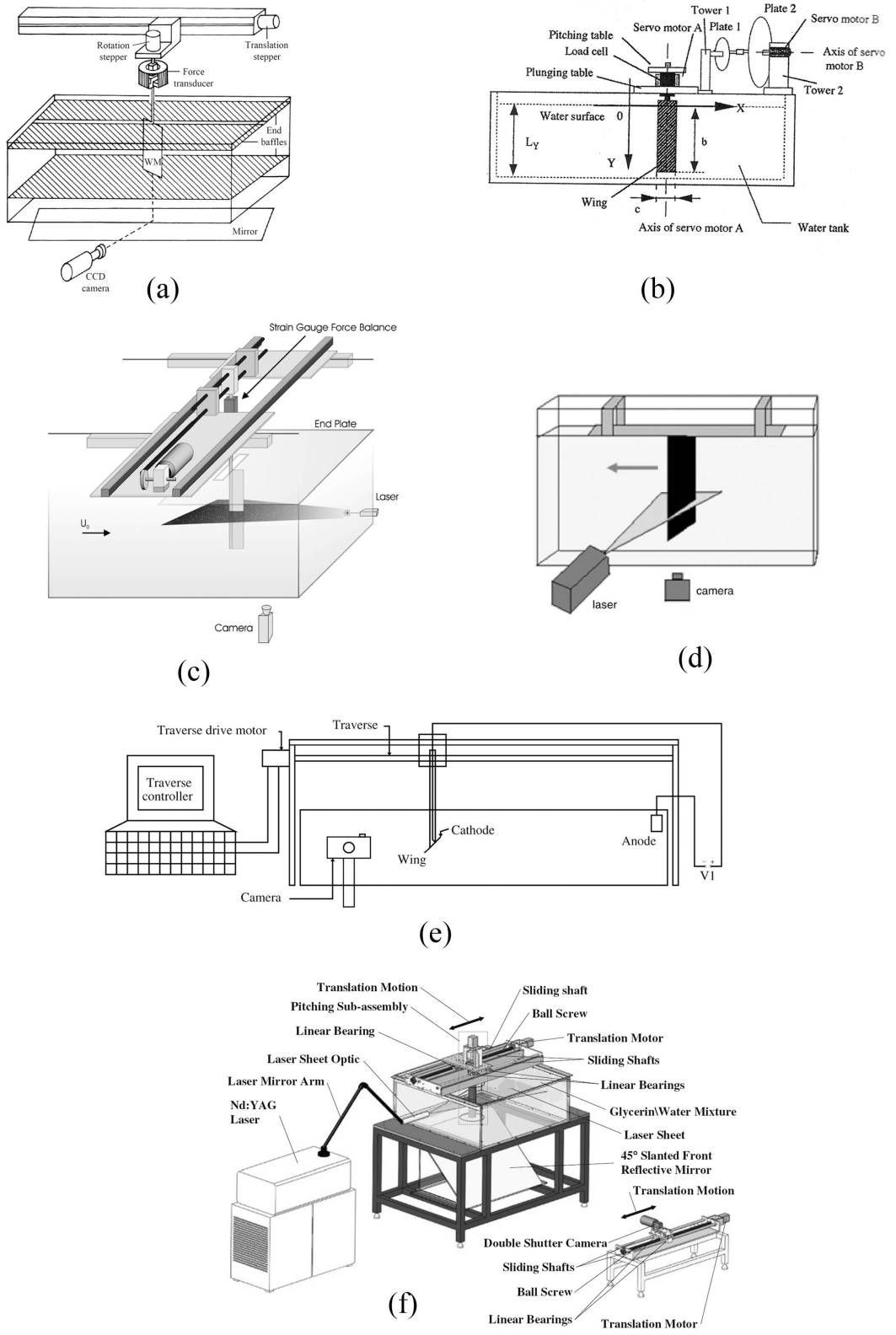

Figure 2.15: 2D experimental apparatuses of a) Dickinson & Götz (1993); b) Sunada et al. (2001); c) Heathcote (2007); d) Beckwith & Babinsky (2009); e) Wilkins (2008); f) Lua et al. (2011)

These apparatuses are very similar in design and function. Most were equipped with a force balance at the root to measure forces and some used a separate motor for pitch control, depending upon the nature of the experiment. These have been used to perform flowfield measurement via *PIV*, or flow visualisation with hydrogen bubbles. Aspects studied, include effects due to wing rotation (Dickinson & Götz, 1993), stroke and pitch phase effects (Sunada et al., 2001), chordwise flexibility effects (Heathcote, 2007), flows of an impulsively started wing (Wilkins, 2008; Beckwith & Babinsky, 2009), and wake capture effects (Lua et al., 2011).

3D Flappers

Early Flappers

The earliest three-dimensional experiment of this kind appears to be that of Maxworthy (1979) who studied the 'clap-and-fling' mechanism. In addition to building a two-dimensional apparatus as discussed above, in this study, Maxworthy also built a three-dimensional apparatus. This consisted of two vertical rods which could pivot on bearings. Perpendicularly attached to each rod was another rod on which wings pivoted freely via teflon bearings. The wings were made rigid and had 'stops' to limit the angle of attack of each wing to approximately 30°. During the experiment, the wings would start off together with their upper surfaces touching, and then the wings would fold apart by rotating the two vertical rods by their handles through desired sweep angles. Thus, this experiment studied the 'fling' portion of the 'clap-and-fling' mechanism, as well as the subsequent translation of the wings through a sweep. As mentioned, the wings pivoted freely until a certain point where they were held at a constant angle of attack of approximately 30° via stops. Figure 2.16 gives an illustration of this apparatus.

As with the two-dimensional apparatus mentioned above, this apparatus was immersed separately in water and glycerine, flow visualisation was performed using dye and wax beads, and streak photographs were taken which were used to determine flow velocities and circulation in desired areas.

Recent Flappers

The next three-dimensional flapping apparatus that operated in a liquid appeared twenty years later in the experiments of Dickinson et al. (1999). In their ex-

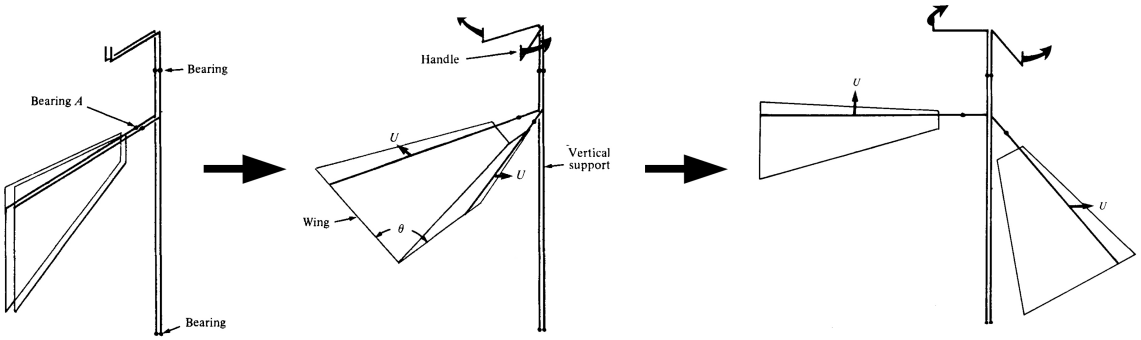

Figure 2.16: 3D experimental apparatus of Maxworthy (1979)

periments, Dickinson and his colleagues used a mechanical flapping wing model dubbed the 'Robofly', which has become by far the most successful flapping-wing apparatus operating in a liquid. This apparatus has been used in a number of studies, with many different researchers since its creation and it continues to yield valuable results. The design of the apparatus consisted of two wings modeled, from a fruit fly, each controlled by three stepper motors via three coaxial drive shafts connecting to a gearbox. Each wing had three degrees of freedom, and thus the apparatus could achieve a wide range of flapping kinematics with either symmetric or asymmetric wing motions by simply programming a desired velocity profile for the six motors. There is no mention made of how the sweeping, plunging and pitching motions were produced from the rotations of the drive shafts, but it is implied by the 'gearbox' connecting to the wing that a collection of gears were used. To measure aerodynamic forces, a two-dimensional force balance was located at the root of one of the wings. Studies with this apparatus have relied on flowfield measurements with particle image velocimetry (PIV) and force measurements. An illustration of the apparatus is given in Figure 2.17.

Since the development of the 'Robofly' by Dickinson and his colleagues, there have been numerous three-dimensional flapping-wing apparatuses that operate quite similarly. Three of these are the apparatuses used in the studies of Maybury & Lehmann (2004), Yamamoto & Isogai (2005) and Lu et al. (2007) illustrated in Figure 2.18. It can be seen, however, that these apparatuses differed from Dickinson's Robofly in the sense that two wings were used in tandem to simulate dragon-fly like flapping wing motion, and were oriented vertically in a tank or water tunnel. In addition, the wings on each one of these apparatuses had two degrees of freedom rather than three, thus only sweeping and pitching motions

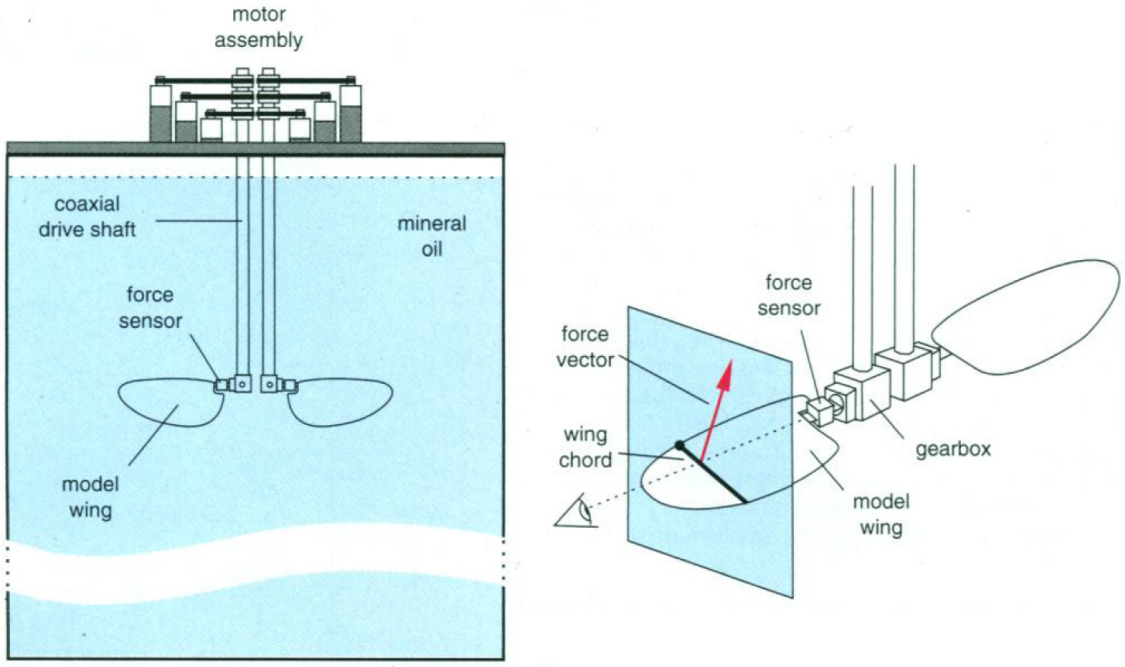

Figure 2.17: 3D experimental apparatus of Dickinson et al. (1999)

were possible for each wing. Like the Robofly, however, with the exception of the apparatus of Lu et al. (2007), they could measure aerodynamic forces via a force sensing element at the root.

Recently developed three-dimensional flapping wing apparatuses which use either a single wing or a single pair of wings (and thus are of more interest in this case) include those of Luc-Bouhali (2006), Lu et al. (2006), Wilkins (2008), Nagai & Hayase (2009), and Jones & Babinsky (2011) which are illustrated in Figure 2.19. As with the more recent 2*D* apparatuses, these are all very similar

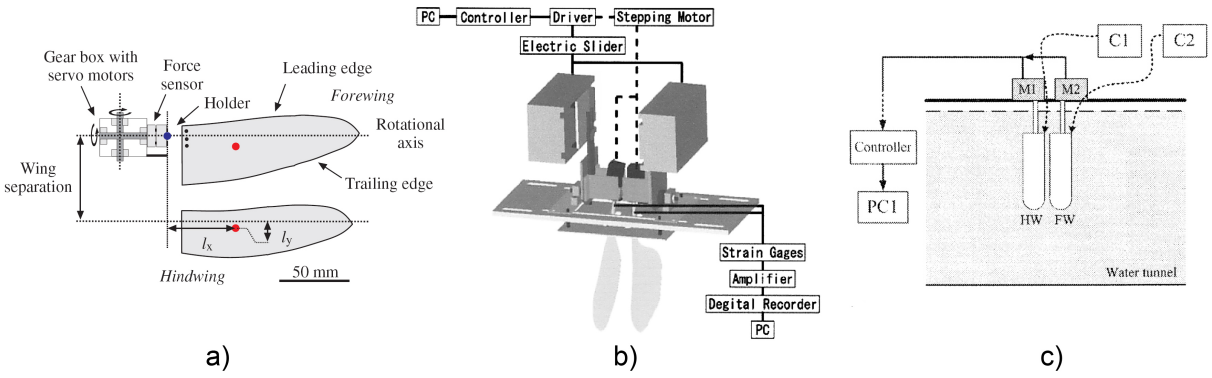

Figure 2.18: 3D experimental apparatuses of a) Maybury & Lehmann (2004); b) Yamamoto & Isogai (2005); c) Lu et al. (2007)

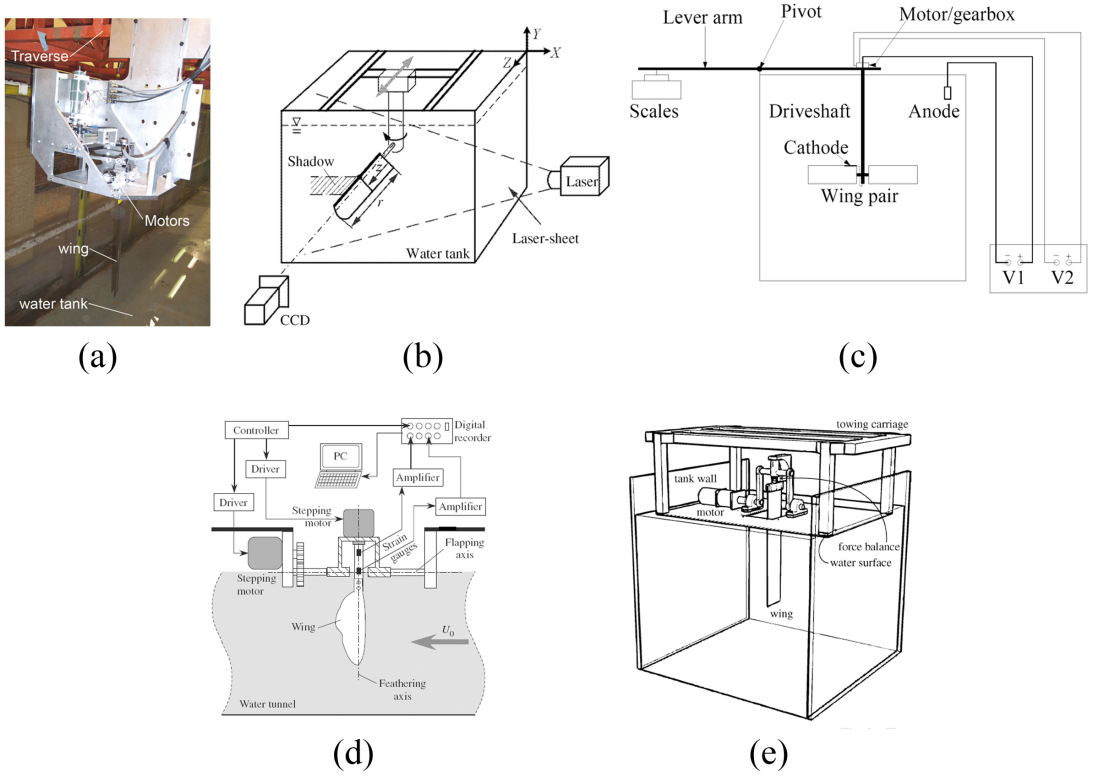

Figure 2.19: 3D experimental apparatuses of a) Luc-Bouhali (2006); b) Lu et al. (2006); c) Wilkins (2008); d) Nagai & Hayase (2009); e) Jones & Babinsky (2011)

with most employing a force balance at the root for measuring wing forces, and some utilise a separate motor to enable wing pitching. In most of the studies with these devices, flowfield measurements via *PIV* were performed. Topics that were investigated include force and flowfield measurement (Luc-Bouhali, 2006), kinematic and aspect ratio effects (Lu et al., 2006), flow from an impulsively swept wing (Wilkins, 2008), stroke plane inclination and advanced ratio effects (Nagai & Hayase, 2009), and Reynolds number and angle of attack effects (Jones & Babinsky, 2011).

A recent flapper that operates in liquid is the 'RotaFlap' mechanism of Ania et al. (2011) shown in Figure 2.20. It employs a patented mechanism consisting of a housing with a set of shafts and bevel gears. Two of the shafts (40 & 42 in Figure 2.20) connect to flapping wings as illustrated, whereas the other shaft (102) remains stationary and the housing (100) is driven to continually rotate (not reciprocate) about the stationary shaft. The result is that as the housing rotates, the wings are subjected to two simultaneous rotations about two perpendicular

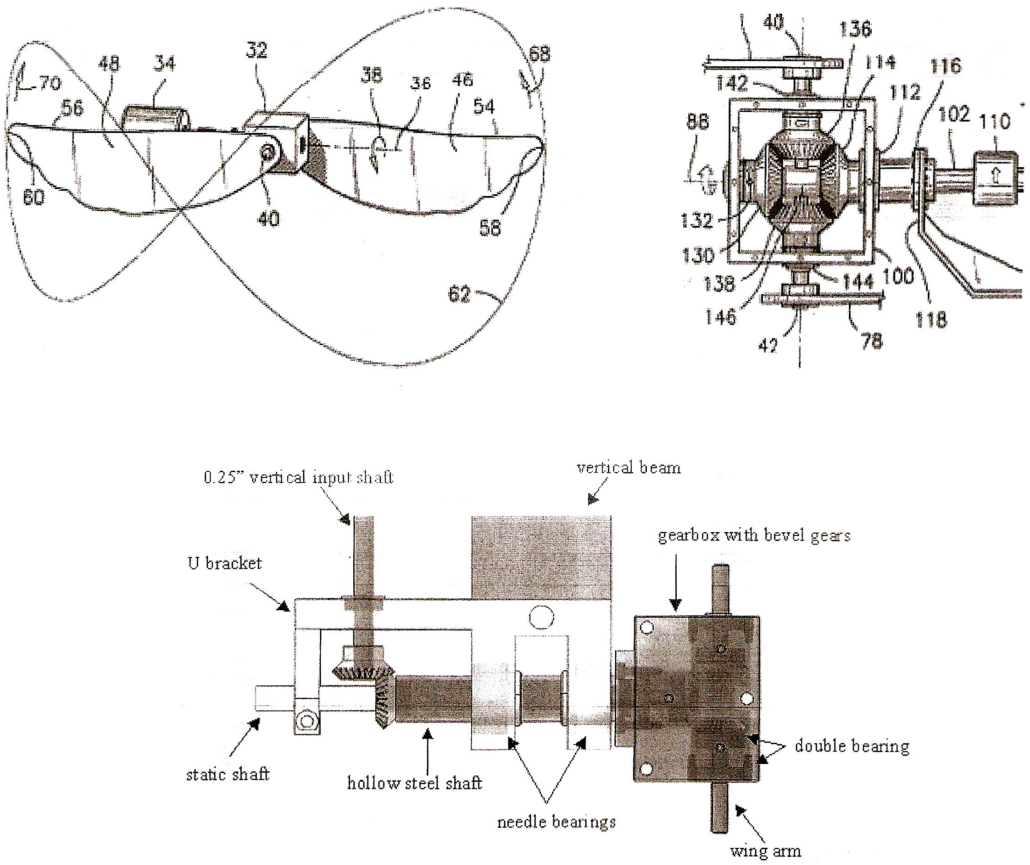

Figure 2.20: RotaFlap of Ania et al. (2011); images from original patent (top); flapping mechanism (bottom)

axes, which when combined, result in a figure-of-eight wingtip trajectory for each wing. However, as shown, both wings will always be 180° out of phase. This was used in experiments in mineral oil, and aerodynamic forces were measured over a range of flapping frequencies.

2.4.2 Air Flappers

The advantage of a flapper that works in air from the point of view of FMAVs, is that if the flapper is at the FMAV scale, there is no debate about dynamic similarity. Furthermore, as mentioned previously, this type of flapper serves as a stepping stone towards a working FMAV prototype. For example, lessons learnt in the development of flappers that work in air, may be applied to FMAVs since they will have similar issues. This section will now discuss flappers that have operated

in air, beginning with early flappers, then the more recent flappers.

Early Flappers

The first experiment concerning insect flight using a mechanical apparatus in air was that of Bennett (1966). His experimental apparatus consisted of a wing made of music wire and cellophane tape which was swept back and forth by an oscillating shaft driven by a pulley. The wing could pitch passively, but was limited to certain angles of attack by using 'stops'. It could flap at a frequency of $46Hz$, with a 144° stroke amplitude. An illustration of his apparatus is given in Figure 2.21. This was used to measure the induced velocities above and below the wing, which was accomplished with a hot-wire anemometer. Using the measured velocities, the time-averaged lift acting on the wing was inferred using momentum theory.

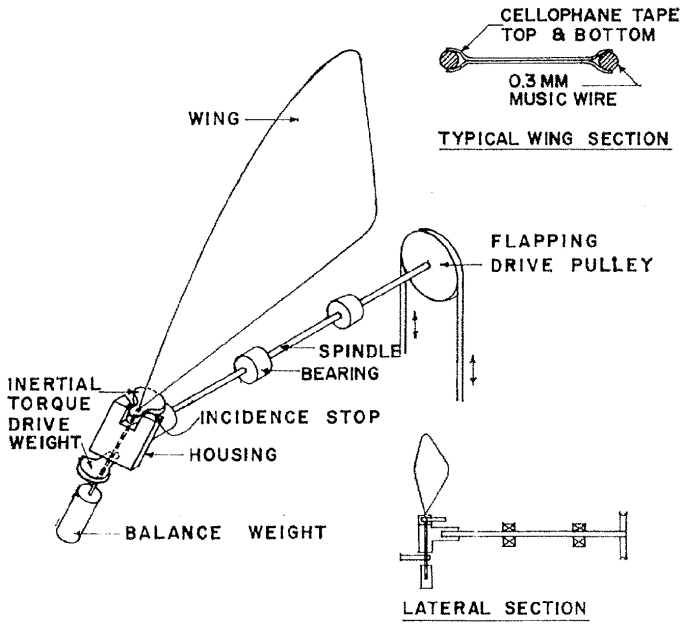

Figure 2.21: Experimental apparatus of Bennett (1966)

Four years later, Bennett performed another flapping-wing experiment in air, using a new mechanical apparatus (Bennett, 1970). His new apparatus was similar to the previous one, except it was improved to give control of wing pitching. This improvement was possibly prompted by the fact that in the original apparatus in which wing pitching was passive, the wing took too long to reach a constant

angle of attack (Bennett, 1966). The new apparatus consisted of a wing which swept back and forth driven by a shaft via a toothed belt drive. The wing's angle of attack was varied via a cam which pivoted a follower arm that pushed a bobbin up and down on the shaft. Nylon threads connected the bobbin to a pulley fixed to the wing spar, so that the motion of the bobbin up and down the shaft caused by the cam-driven follower would make the wing pitch. Figure 2.22 gives an illustration of Bennett's apparatus. As with his previous experiment, this apparatus was used to measure induced velocities above and below the wing to deduce the lifting forces acting on the wing using momentum theory.

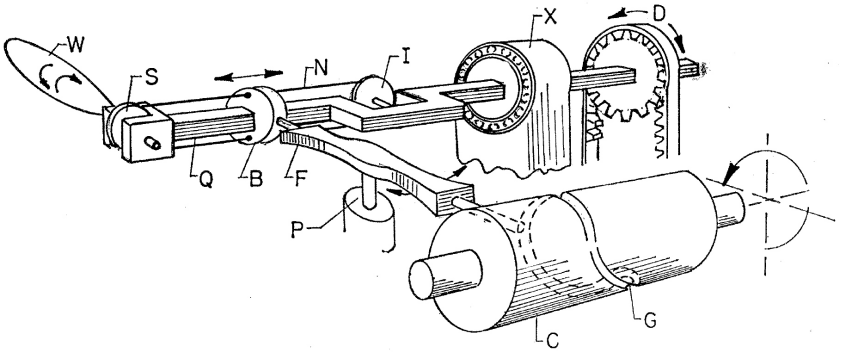

Apparatus schematic. Mechanism to control incidence of simulated *Melolontha vulgaris*. Not to scale. *W*, Wing; *S*, incidence sheave; *N*, nylon cord; *B*, bobbin; *C*, incidence cam; *G*, groove; *F*, follower arm; *P*, pivot; *I*, idler; *D*, flapping drive; *X*, bearing support; *Q*, square shaft.

Figure 2.22: Experimental apparatus of Bennett (1970)

Bennett performed another flapping wing experiment using a mechanical flapper seven years later (Bennett, 1977). The focus of this new experiment was to study the 'clap-and-fling' mechanism proposed by Weis-Fogh (1973) and Lighthill (1973). The apparatus that he used for this was quite different than the previous two. This new apparatus comprised of a rectangular wing freely pivoted at the end of a long arm. The wing was held up against a stationary image plane by a 'trigger' chord while a rubber band attached to the arm was stretched in the other direction, causing the wing to 'peel' away from the image plane when released. Thus, this experiment studied the 'fling' portion of the 'clap-and-fling' mechanism in 2D as was later studied in experiments by Maxworthy (1979) and Spedding & Maxworthy (1986). The purpose of the image plane was to simulate the effect of two wings 'flinging' apart, and removing the image plane allowed Bennett to study a 'clapless' wing. To measure the angle of attack and translation of the wing, potentiometers were used at the wing pivot and the pivot of the arm. In addition,

the rate of change of the angle of attack was controlled by a 'snubber' chord. An illustration of the apparatus is given in Figure 2.23. This apparatus was used to measure the induced velocities under the wing using a hot-wire anemometer, and estimate relative lift forces.

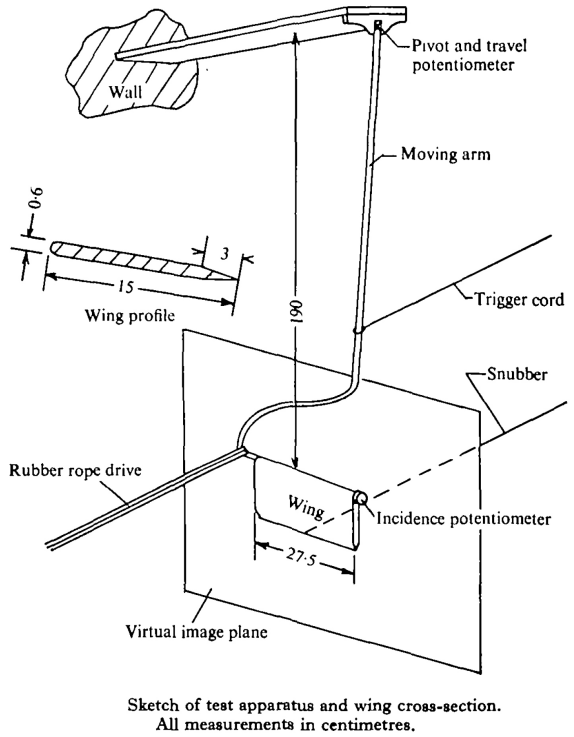

Figure 2.23: Experimental apparatus of Bennett (1977)

The next experiments which used a mechanical flapping apparatus in air were those of Saharon & Luttges (1987) and Saharon & Luttges (1988). Both studies were concerned with dragonfly-like flight. The earlier study focused on the effects of wing pitching and plunging from a single dragonfly-like wing on the unsteady flow. On the other hand, the second study utilised a pair of wings in tandem and observed the effect on the flow by changing various parameters like flapping frequency, plunging amplitude and phase difference between the two wings. In the earlier study the apparatus consisted of a single wing extending through a side wall in a wind tunnel that was driven to plunge up and down and pitch via a motor-driven scotch yoke and slider-driven universal joint. The apparatus in the second study instead employed a pair of wings in tandem. An illustration of the apparatus used in the later study (Saharon & Luttges, 1988) is given in Figure 2.24.

Due to the limited illustrations of the apparatuses used by Saharon & Luttges,

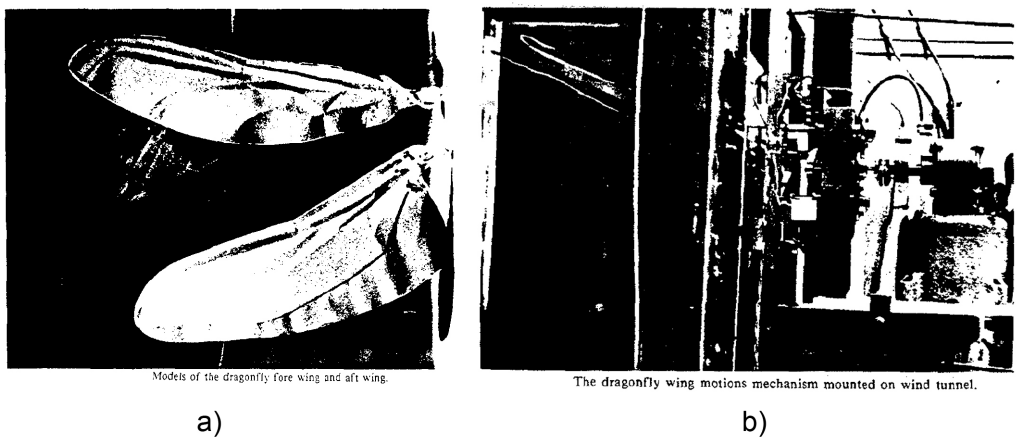

Figure 2.24: Experimental apparatus of Saharon & Luttges (1988); a) wing models used; b) experimental apparatus

it is difficult to tell exactly how the mechanisms controlling the wings worked. In both studies, the apparatuses were used for flow visualisation with smoke in conjunction with a synchronised strobe lamp to illuminate the flow at desired points in the flapping cycle

Recent Flappers

Around a decade after the work of Saharon and Luttges, the experiment of Ellington et al. (1996) was performed using arguably the most famous mechanical flapping wing model that operated in air, called simply the 'flapper'. The design of this flapper consisted of a pair of mechanical wings modeled from the hawkmoth *Manduca sexta*, but scaled up approximately ten times. Each wing had four degrees of freedom enabling sweeping and plunging motions, as well as individual pitching motions of the fore and hind sections of the wing. This was accomplished by a complicated mechanism of bevel gears and yokes driven by a set of four coaxial drive shafts in turn driven by four motors. Here, the outer drive shaft controlled the sweeping motion of the wing, the middle drive shaft controlled the plunging motion, and the inner two drive shafts controlled the pitching motions of the two segments of the wing. In addition, the motions of the two wings were coupled so that the wing motions mirrored each other. Figure 2.25 gives an illustration of the 'flapper' used by Ellington and his colleagues. This mechanical model was used in numerous studies for studying the nature of

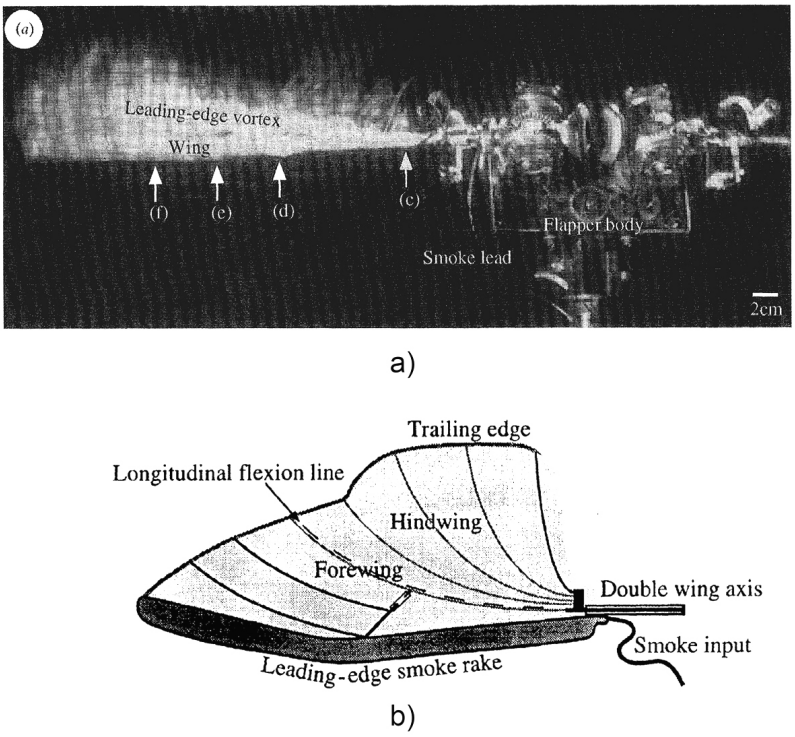

Figure 2.25: Experimental apparatus of (Ellington et al., 1996); a) flapper; b) wing model

the leading-edge vortex by performing flow visualisation with smoke released along the leading edge of the wings.

Five years following the experiments of Ellington et al. (1996) with their mechanical model of the hawkmoth *Manduca sexta*, another study involving Ellington was performed that utilised a mechanical flapping apparatus in air, which was that of Ellington & Usherwood (2001). Their apparatus is illustrated in Figure 2.26a, which consisted of a continually revolving wing driven by a motor (like a propeller). Lift measurements were achieved by placing the apparatus on a balance, and torque measurements (used to deduce drag) were performed by transmitting torque through a beam to a force balance. Lift and drag coefficients were measured on different wing designs over a range of angles of attack and Reynolds numbers. Similar versions of this apparatus were later used in Usherwood & Ellington (2002a), Usherwood & Ellington (2002b), and Usherwood (2009) which are shown respectively in Figure 2.26b-d. In all cases, lift and torque measurements were achieved via a connection to a force balance, either via a pivoted arm or by direct mounting of the apparatus to a balance. These rigs were used to measure lift and drag coefficients on continually revolving wings at

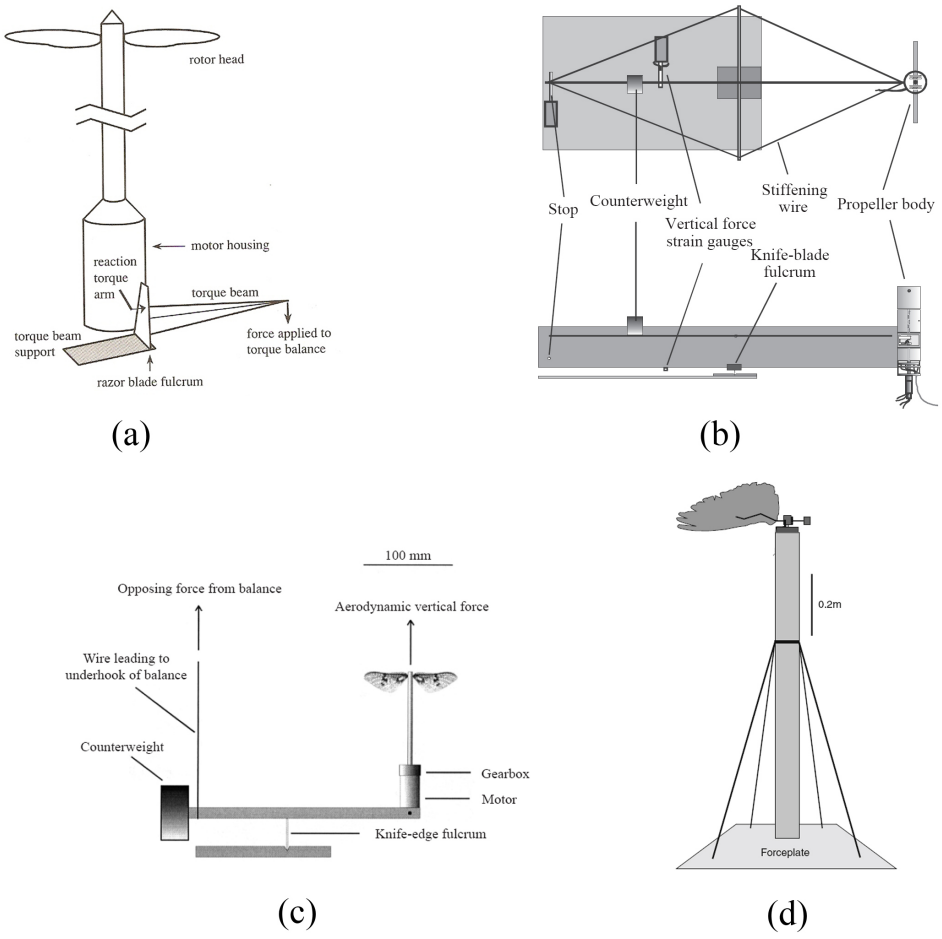

Figure 2.26: Revolving wing apparatuses of a) Ellington & Usherwood (2001); b) Usherwood & Ellington (2002a); c) Usherwood & Ellington (2002b); d)Usherwood (2009)

different angles of attack and Reynolds numbers.

In the same year, the first prototype of a mechanical flapper called the 'Micromechanical Flying Insect' or 'MFI' emerged (Yan et al., 2001). Since the initial prototype, there have been several improvements and versions but the basic operation and form of the flapper is the same, and the latest version of the MFI is illustrated in Figure 2.27. The basic design consists of four four-bar mechanisms (2 per wing) each driven by its own piezoelectric actuator. Each four-bar mechanism pair is then coupled to a wing via a 'differential' which is a folded structure of carbon fibre forming a mechanism with two input links. When these two input links of the differential are actuated in the same direction the wing sweeps, and when they are actuated in opposite directions the wing twists, hence changing its angle of attack. The lengths of the links in each four-bar linkage are

such that they each form a double-rocker mechanism, and a small oscillation on the input link (from the actuator) produce a large oscillation at the output link (connected to the wing differential). Each actuator pair oscillates slightly out of phase, hence causing the connecting four-bar linkages to oscillate out of phase which then translates to cyclic sweeping and pitching motions of the wing via the differential. The purpose of the MFI is eventually to be a flying, stable and autonomous FMAV, and thus this flapper is more of an FMAV prototype than an experimental test bed. Latest improvements to the MFI include optimal kinematics for the actuators driving the four-bar linkages and lower wing inertia resulting in a wing beat frequency of 275Hz producing a total of 1400μN of lift (Steltz et al., 2007).

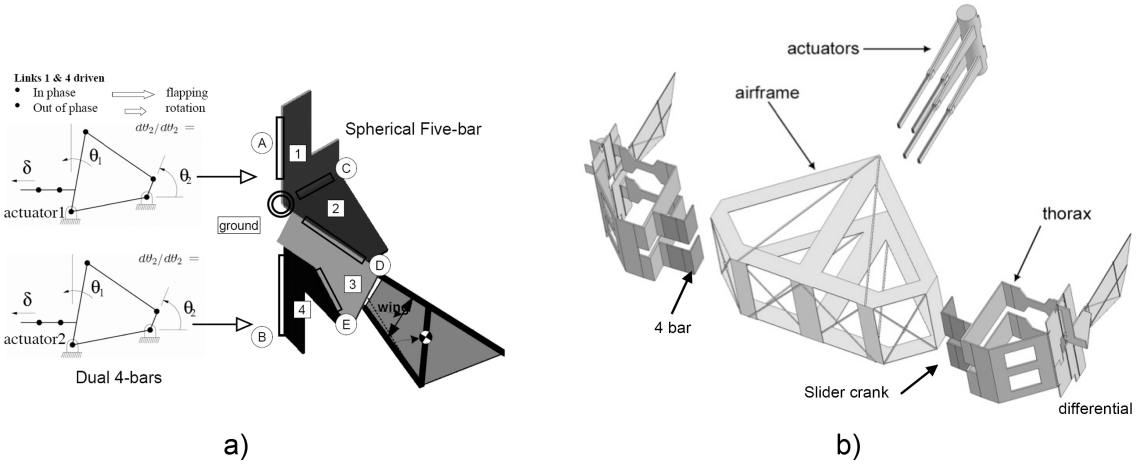

Figure 2.27: Micromechanical Flying Insect (MFI); a) details of flapping mechanism; b) exploded view of complete MFI

The next mechanical flappers of interest are those of Żbikowski et al. (2005) and Galiński & Żbikowski (2005), dubbed 'flapper Mk1' and 'flapper Mk2' respectively as illustrated in Figure 2.28. These were built as flapping-wing technology demonstrators to be used as research test beds as well as precursor FMAV designs. Both flappers had wings with three ranges of motion, that is, they could both produce sweeping, plunging and pitching motions. However, their wing trajectories were both fixed such that the wing tip followed a figure-of-eight with symmetric pitch reversal. The first flapper Mk1 produced flapping wing motion via a complex drive train that drove a Watt's straight-line mechanism in which the midpoint of one of the links followed a figure-of-eight trajectory. This link was connected to two wings via sockets that interfaced with the wing spars so that

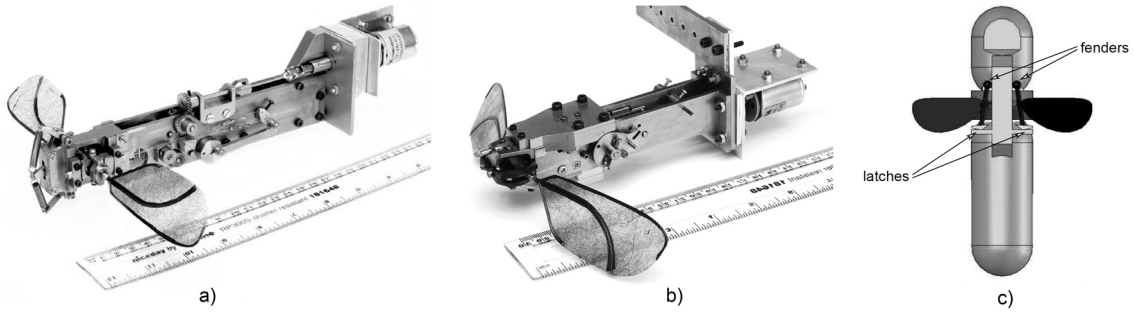

Figure 2.28: a) Flapper Mk1 of Żbikowski et al. (2005); b) Flapper Mk2 of Galiński & Żbikowski (2005); c) conceptual flapper redesign of Galiński et al. (2007)

the figure-of-eight motion of the link was translated to the wings. Pitch reversal was achieved with a Geneva wheel that drove a cable drive interfacing with the wing spar. The second flapper Mk2 had a mechanism significantly different from the first. In this flapper, wing sweeping and plunging motions were achieved by two spherical scotch yokes that interfaced with the wing root. One of the yokes was oriented horizontally to raise the wing and produce plunging motions, while the other yoke was oriented vertically to sweep the wing back and forth. The spherical yokes flapping each wing were driven by a complex drive train and a single motor. Pitch reversal in this design was produced via articulating a link connecting to universal joints interfacing with the root of each wing spar. Both flappers have been used for flow visualisation as well as flow field measurements via *PIV*.

A concept of a flapper redesign was later made by Galiński et al. (2007) (Figure 2.28c) that would avoid problems with resonance that the flapper Mk2 experienced when it reached a flapping frequency of approximately 15*Hz*, and avoid the large power consumption seen as flapping frequency increased. This new conceptual redesign consisted of two wings each oscillated by a resonating spring driven by an ultrasonic motor. The concept for controlling pitch reversal was to use a series of latches and fenders (stops) on the wing to force wing rotation at desired points.

The next noteworthy mechanical flapping wing apparatus that operated in air, was that of Tarascio et al. (2005). An illustration of their mechanical flapper is given in Figure 2.29. Their design consisted of a single motor driving a scotch yoke that flapped the wings back and forth, while pitch reversal was achieved by using rods fixed to the root of the wing that came into contact with stops at

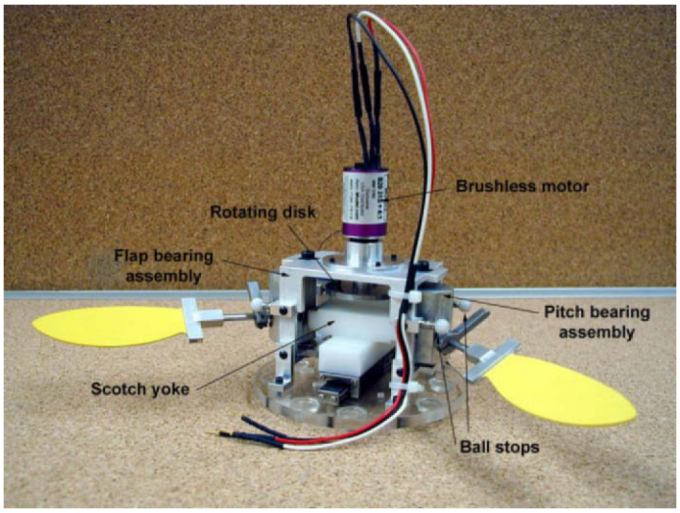

Figure 2.29: Mechanical flapper of Tarascio et al. (2005)

either end of a stroke. When the wings were at mid-stroke, they were held fixed at a constant angle of attack by a cam attached to each wing spar. The cams were designed to give the wing a desired angle of attack at mid stroke, and to be bi-stable so that the wing would be in either one of two positions which were set by the stationary stops. This apparatus was used to investigate the nature and stability of the leading-edge vortex as well as other vortical wake structures induced by a pair of flapping wings using flow field measurements via *PIV*.

Just a year later a mechanical flapping wing model was also developed by Conn et al. (2006). Their mechanical flapper featured a parallel crank-rocker (PCR) flapping mechanism, an illustration of which is given in Figure 2.30 along with the flapper itself. The design of this mechanism used two crank-rockers driven out of phase by a motor. The follower of one of the crank-rockers was continuous with the leading-edge spar of the wing, while the follower of the other crank-rocker extended through a slotted rod fixed to the wing root. Thus, by driving the two crank-rockers slightly out of phase, the followers and hence the wing would simultaneously sweep back and forth as well as pitch at either ends of a stroke. This was similar to the operation of the MFI, where instead of two out-of-phase double-rocker mechanisms, two out-of-phase crank-rocker mechanisms were used. Like many other flappers, the motion of the flapper of Conn and his colleagues was fixed during operation, although kinematics could be altered prior to operation by changing the phase angle between the two crank-

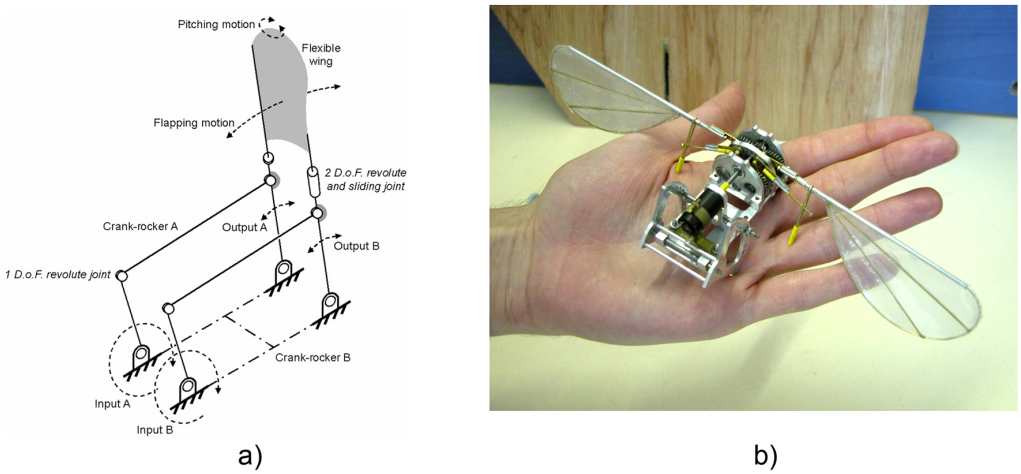

Figure 2.30: Mechanical flapper of Conn et al. (2006); a) parallel crank-rocker mechanism; b) working flapper

rockers. This mechanical flapper was used to measure forces as well as perform flow visualisation to study the flow induced by flapping wings. Most recently, it has been fitted with a more powerful motor which has increased the flapping frequency from 7.15Hz to 13.2Hz (Conn et al., 2008).

Following the MFI mentioned earlier, another flapper emerged (from some of the same researchers) using the same technology as the MFI. An illustration of this flapper is shown in Figure 2.31 and it achieved powered flight (Wood, 2008); although, it was tethered to an external power source and it was not free-flight as it slid up two vertical wires. However, it was later argued that this 'liftoff' may have been the result of standing waves in the guide wires rather than aerodynamic lift, as it was shown that a simple pager motor (no wings) can travel up two vertical wires due to standing waves (Marks, 2009). The operation of this flapper is similar to the MFI, but much more simplified as it has only one piezoelectric actuator driving two wings which have passive wing pitching.

In the same year as the aforementioned Mk1 and Mk2 flapper by Żbikowski and Galiński, a mechanical flapping-wing model was developed by Banala & Agrawal (2005) that could also produce three-dimensional wing motions in which the wing tip traced a figure-of-eight. Their design consisted of a planar five-bar linkage in combination with a four-bar linkage and is illustrated in Figure 2.32. Here the five-bar linkage (ABCDE) produced the sweeping and plunging motions while the four bar linkage (CBFG) produced the pitching motions. The motions of this system of linkages were transmitted to the wings via universal joints and

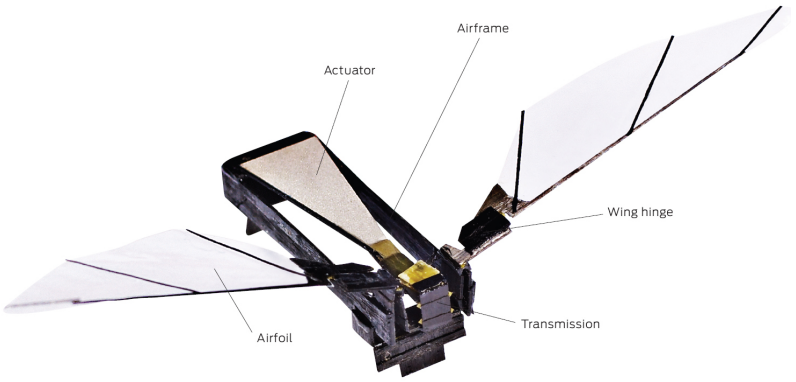

Figure 2.31: Mechanical flapper of Wood (2008)

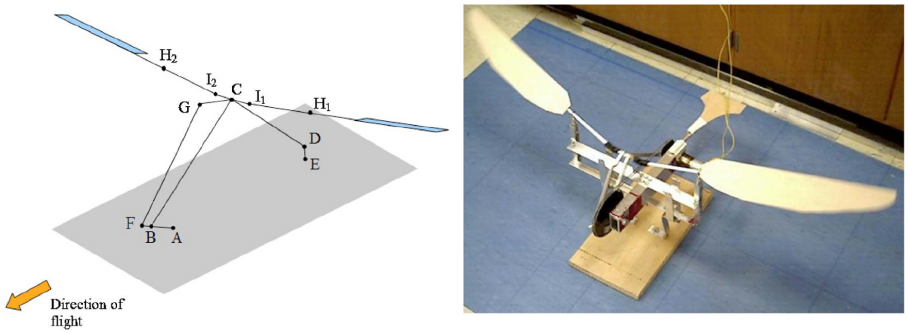

Figure 2.32: Mechanical flapper of Banala & Agrawal (2005)

telescopic segments coupling the wing spar with the mechanism. The purpose of this mechanical model was to mimic the wing motion of a hawkmoth, and to eventually serve as the flapping mechanism for a flying prototype.

Another mechanical flapper worth mentioning is that of McIntosh et al. (2006) which is illustrated in Figure 2.33. Their design consisted of two wings that swept back and forth via two crank-rockers driven by a motor. To vary the wing pitch, each wing spar extended to connect to a follower via a spring, where the follower had a cam on the end that followed a guide as the wing swept. The guide was designed so that when the wing was at the appropriate point in the flapping cycle, the wing would pitch as a consequence of the cam following the profile of the guide. This mechanical flapper was used to measure forces generated by the wings and is intended to be ultimately used on an actual hovering MAV.

The next flapping wing model to be mentioned is that of Syaifuddin et al. (2006). Their design which is given in Figure 2.34 consisted of two wings actuated by a pair of four-bar linkages. Each four-bar linkage constituted a double-rocker

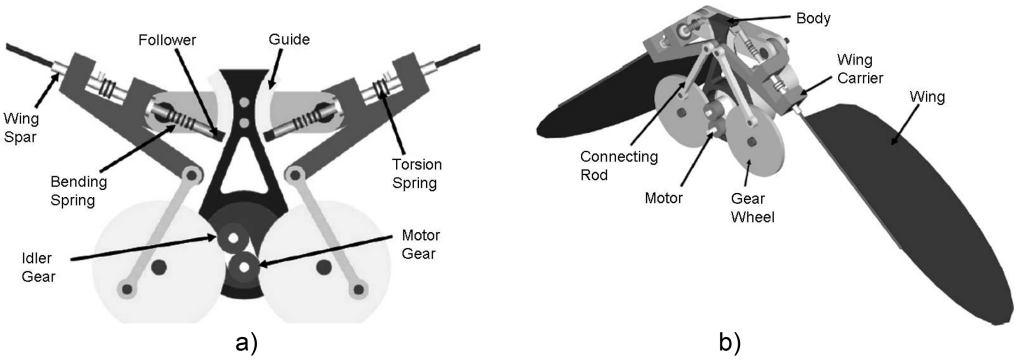

Figure 2.33: Mechanical flapper of McIntosh et al. (2006); a) details of flapping mechanism; b) assembled flapper

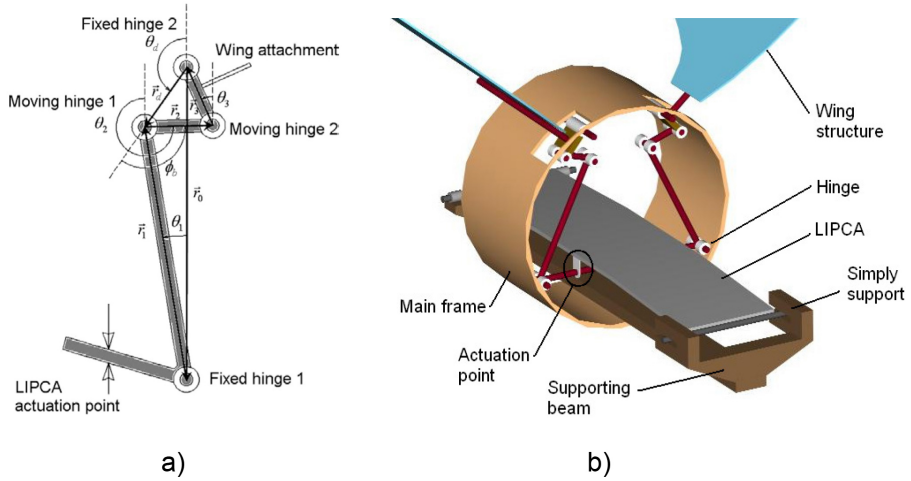

Figure 2.34: Mechanical flapper of Syaifuddin et al. (2006); a) details of flapping mechanism; b) assembled flapper

mechanism that was actuated at one end by an oscillating piezoceramic actuator and at the other end flapped a wing. The lengths of the linkages were chosen such that the small oscillations of the actuator were translated into large oscillations of the wings, similar to what was done with the MFI. Wing pitching was passive, but was limited to certain angles of attack by stoppers at the wing pivots. This mechanical flapper was used to measure lift forces produced by the wings and perform flow visualisation with smoke. In a later study, it was used to to observe effects of wing rotation, wing corrugation and the 'clap-and-fling' manoeuvre on the lift it produced (Nguyen et al., 2008).

The last mechanical flapper that will be mentioned here is the mechanical flapper of Warkentin & DeLaurier (2007) which featured two pairs of wings in tandem like a dragonfly as shown in Figure 2.35. The wings were flapped up

Figure 2.35: Mechanical flapper of Warkentin & DeLaurier (2007); a) details of flapping mechanism; b) assembled flapper

and down via a crank-rocker mechanism driving each wing, while wing pitching was passive. The purpose of this flapper was to study the effect on thrust and efficiency from changing the phase angle and wing spacing between the wing pairs.

2.4.3 Free-Flying Flappers

This section will discuss insect-like mechanical flappers that have achieved free-flight. The section begins with a discussion of the early free-flying flappers, followed by an overview of the more recent ones.

Early Flappers

Probably the first free-flying mechanical flapper that mimicked insect-like flight was the CIA funded 'Insectothopter' which was developed in the 1970*s* (Adkins, 2008). This was a dragonfly-sized mechanical flapper with two pairs of wings, and looked very similar to a real dragonfly as illustrated in Figure 2.36. The Insectothopter was powered by a flapping mechanism consisting of a leaf spring and a 'power bag' in which lithium nitrate crystals were used to produce a gas to inflate the bag. As the bag would inflate, the leaf spring would be deflected and at a certain point the power bag would then deflate and the leaf spring would return to its neutral position where the bag would re-inflate and the cycle would repeat. The motion of the leaf spring was coupled to the wings to produce flapping motion, and the gas produced in the bag was vented aft to produce extra thrust.

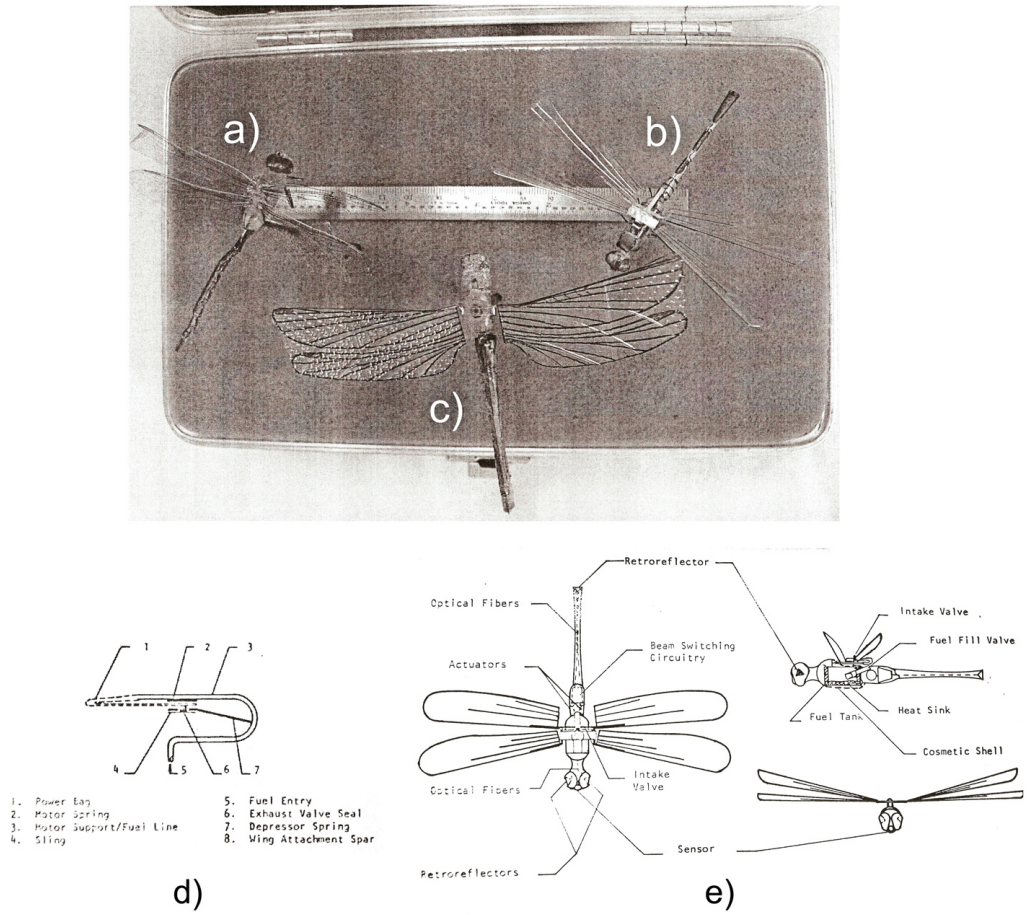

Figure 2.36: DARPA and CIA funded mechanical flappers; a) real dragonfly; b) Insectothopter; c) Insectothopter; d) flapping mechanism of Insectothopter; e) schematic of Insectothopter

With this added thrust, the Insectothopter could achieve a range of 200m and fly for 60s with a 1gram launch weight. The purpose of the Insectothopter was to be launched over walls and fences and to perform reconnaissance using an onboard 'optical microphone'.

In 1985, a rubber band-powered 'Canard Biplane' ornithopter was made by Frank Kieser, which in the same year set a world record for indoor free-flight duration (Jones et al., 2004). An illustration of his flapper is given in Figure 2.37. The design consisted of two pairs of wings on top of each other, as opposed to a tandem configuration like a dragonfly, and had a canard for longitudinal stability. The rubber band drove a crank-rocker mechanism for each wing pair which caused the starboard and port wing pairs to cyclically open and close. Although this was called an ornithopter, it was insect-like in the sense that it made use of the 'clap-and-fling' mechanism identified by Weis-Fogh (1973) and

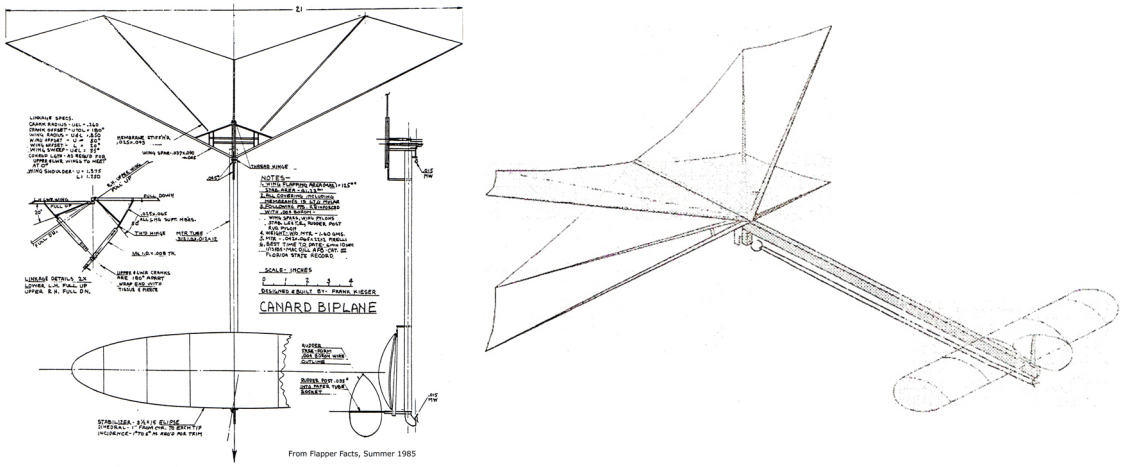

Figure 2.37: Kieser's canard biplane flapper (Kieser, 1985)

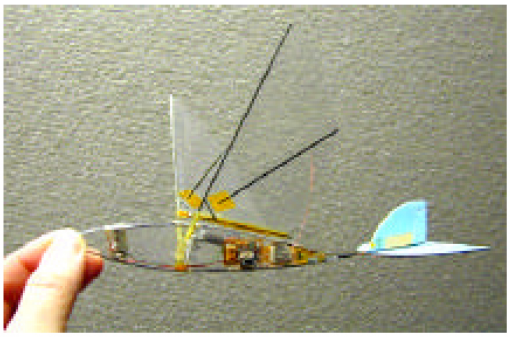

Figure 2.38: AeroVironment Inc.'s Microbat

Lighthill (1973).

The next insect-like mechanical flapper that could sustain free-flight was AeroVironment Inc.'s 'Microbat' MAV which was the first palm-sized ornithopter and flew for the first time in 1998 (Pornsin-Sirirak et al., 2001). An illustration of the Microbat is shown in Figure 2.38. Although the Microbat was referred to as an ornithopter and had a tail, it was arguably an entomopter since it had a flapping frequency in the insect range of 30Hz (Keennon & Grasmeyer, 2003). In addition, leading-edge vortices were observed over the wings in wind tunnel tests using smoke, where the leading-edge vortex is typically characteristic of insect-like aerodynamics in contrast to bird-like aerodynamics where the flow is generally attached (Zdunich et al., 2007). The Microbat was powered by a small electric motor that drove a simple crank-rocker mechanism to drive the wings up and down, and wing pitching was passive.

Recent Flappers

Figure 2.39: DelFly (Mols, 2005)

One of the more recent free-flight capable mechanical flappers is the 'DelFly' from Delft University of Technology built in 2005 (Mols, 2005), and pictured in Figure 2.39. The DelFly weighed between 15 and 21 grams, and had two pairs of wings on top of each other as the rubber band powered ornithopter of Kieser in 1985 did. Wing flapping was achieved via a small electric motor that drove a crank-rocker mechanism for each pair of wings, and wing pitch was passive. For control, it had a V-tail which was actuated via onboard servos. In addition, it had an on-board camera so it could be remotely operated.

Another free-flying flapper with the same wing configuration as the DelFly and Kieser's ornithopter, was the 'Mentor' MAV which was developed at the University of Toronto in collaboration with SRI International (Zdunich et al., 2007). This is pictured in Figure 2.40, and the design of the Mentor flapper consisted of a single motor driving two crank-rockers that flapped two pairs of wings with passive wing pitch. Like the DelFly it also had a tail for control. The purpose of the Mentor flapper was to produce a flapping-wing design for an FMAV prompted by DARPA's initiative to develop working MAVs.

Another flapper capable of free-flight is that of Tanaka et al. (2005), which is a butterfly-like flapper design as shown in Figure 2.41. Their design weighed merely 0.4 grams and had two wings which were flapped at a frequency of $10Hz$ via a rubber band driven crank-rocker mechanism. In addition, as seen in Figure 2.41 it had no tail, but could still fly freely for approximately $1.5m$. This flapper was used to study the stability of the leading-edge vortex on the wings

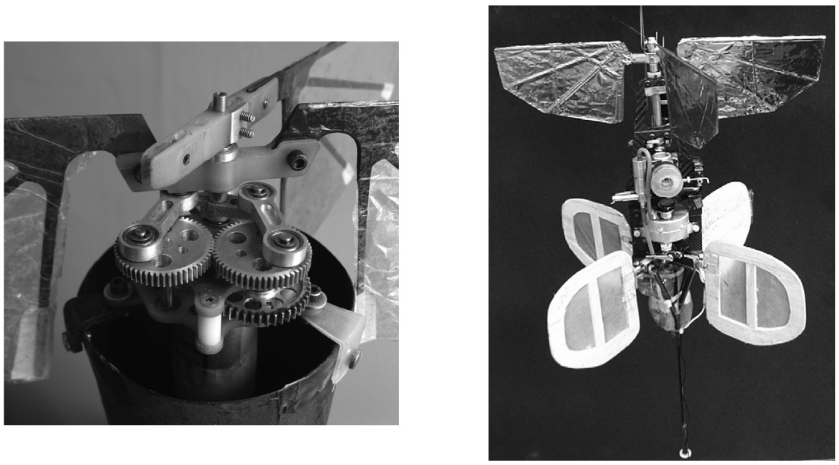

a) b)

Figure 2.40: Mentor MAV of Zdunich et al. (2007); a) flapping mechanism; b) working flapper

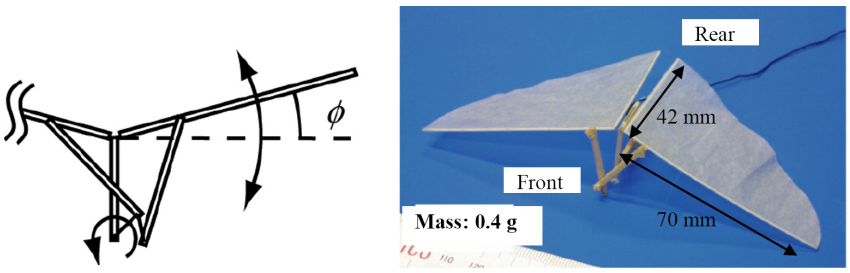

a) b)

Figure 2.41: Butterfly-like flapper of Tanaka et al. (2005); a) flapping mechanism; b) working flapper

for tethered and non-tethered flight by using flow visualisation with smoke in a wind tunnel.

The latest free-flying flapper and most successful at achieving propulsion and control with two wings just as insects do, is the Nano Hummingbird by AeroVironment Inc., discussed previously in § 1.4.3. Figure 2.42a shows the inner workings of the vehicle, along with the complete vehicle itself in Figure 2.42b. Reciprocating motion of the two wings originates from a crank-rocker mechanism which drives two wing spars forming the leading edges of each wing. Directional control is achieved via variable tensioning of the wing membrane by shifting the root spar (2161) relative to the main spar (2160), and by limiting the rotation of the root spar using stops, enabling angle of attack to be separately limited on upstrokes and downstrokes for each wing (Keennon et al., 2010). The vehicle

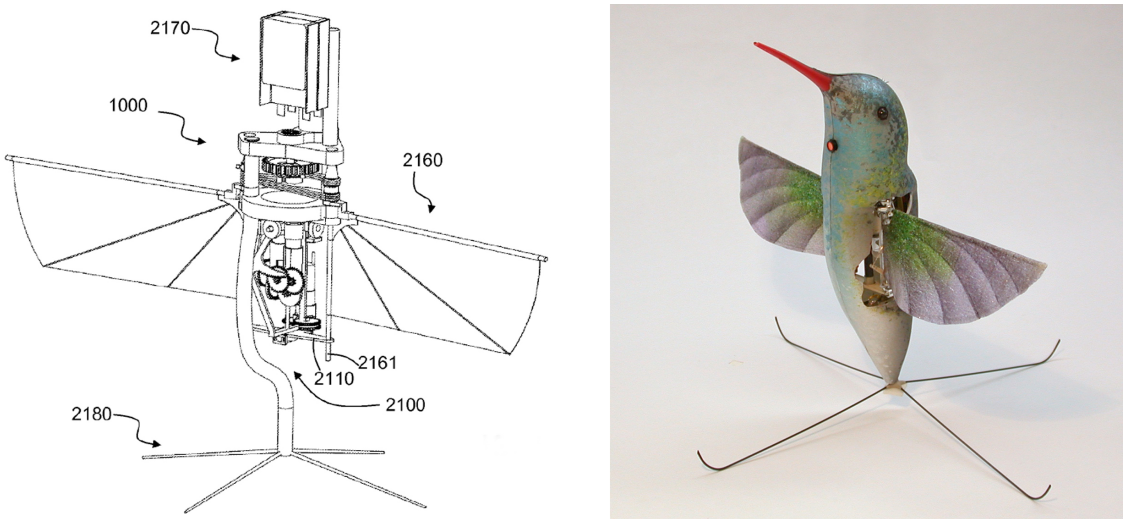

(a) (b)

Figure 2.42: Nano Hummingbird of AeroVironment Inc.; a) inner workings (Keennon et al., 2010); b) complete *FMAV* (AeroVironment, 2011a)

achieves 6 degrees-of-freedom, and thus is able to translate and rotate about all three axes.

2.5 Summary

An insect's wing motion is the composition of separate stroking, plunging and pitching motions, typically resulting in a figure-of-eight-like wing trajectory with pitch reversal at either end of the stroke. Insects experience a number of aerodynamic mechanisms and phenomena. Kelvin's circulation theorem assures that vorticity is shed whenever there is a change in wing-bound circulation, the Wagner effect limits the growth of lift at the start of a half-stroke, and the Kramer effect results in sudden rises in lift when the wing abruptly pitches up. Added mass subjects the wings to extra forces from accelerating (or decelerating) the fluid around it, and wake capture can enable the wing to re-encounter previously shed wake in a way that augments lift if the wing stroke is timed correctly. The clap-and-fling mechanism and different versions of it lead to further lift still as the proximity of the wings to each other diminishes the Wagner effect. One of the most important lift augmenting mechanisms, the *LEV*, takes the form of a spiralling vortex that grows towards the tip where it merges with the tip vortex.

In 2D the LEV always sheds, whereas in 3D, reports are mixed as conflicting findings of LEV stability arise above $Re = 10000$, which has been postulated to be a critical Reynolds number, above which the flow becomes turbulent and the LEV sheds. Vortex breakdown, resulting in a drop in axial vorticity and rise in vortex size, and affected by swirl level and axial pressure gradient, has been observed in the LEV at mid-span or more outboard at Reynolds numbers on the order of 10^3 and above.

Effects from Reynolds number are mixed as some reports show that lift coefficients continually rise, rise and then plateau, or rise and diminish as Reynolds number increases. As angle of attack increases, so does the size of the LEV, but even at a 90° angle of attack it is stable (seen at $Re \approx 8000$). Consistent reports show lift peaks between a $40 - 50°$ angle of attack, and that drag continually rises with it. It is generally seen that advancing pitch reversal by about 5% of the flapping cycle leads to peak lift, whereas any further advances or delays diminishes it. Increasing stroke amplitude with a fixed frequency leads to a rise in lift, drag, and lift coefficient, but a decline in drag coefficient. Keeping Reynolds number fixed and increasing stroke amplitude has been shown to decrease drag coefficients, but affect little change in lift coefficients. Employing figure-of-eight kinematics and increasing plunge amplitude has been mostly shown to decrease lift. A concave arc wingtip trajectory with higher plunge increases lift but increases drag much more leading to poor lift to drag ratios, whereas a convex arc slightly decreases lift but exhibits very good lift to drag ratios.

Experiments concerning insect-like flight using a liquid as the medium have been seen in two forms: two-dimensional, and three-dimensional experiments. Two-dimensional experiments started off studying mostly the 'clap-and-fling' manoeuvre using particle-streak photography, but eventually progressed to replicating complete flapping cycles with pure plunging and pitching with direct force measurement and flow field measurement with PIV. Similarly, three-dimensional experiments also started off focusing on the 'clap-and-fling' manoeuvre and measuring the induced flow velocities using particle-streak photography. Recent apparatuses of this kind typically employ separate sweep and pitch control with a force balance at the root. The most well known apparatus of this kind, Dickinson's Robofly, could replicate the full three degree-of-freedom motion of insect wings while simultaneously measuring forces and flow velocities with PIV. Experiments

with mechanical insect-like flappers in air have all been three-dimensional (with the exception of that of Bennett (1977)). Designs were originally quite simple (yet effective) using materials like rubber bands, music wire and cellophane tape, and aerodynamic forces were deduced by measuring induced velocities and using momentum theory. Recently, mechanical flappers of this kind have generally become more complex with multiple degrees of freedom and complex flapping mechanisms, and have been used for direct-force measurement in conjunction with PIV measurements. As for free-flying insect-like flappers, the first design consisted of a unique gas-driven spring oscillator driving a pair of wings, whereas today this type of flapper typically consists of a motor driving a crank-rocker coupled directly to a pair, or two pairs of wings and a conventional tail for control (except for the Nano Hummingbird which has no tail).

Chapter 3

Research Aims & Methodology

This chapter presents the aims of the present work, and outlines the method by which the aims will be achieved. The chapter starts with a discussion of some of the gaps in the present knowledge of insect-like flight relevant to *FMAVs*, which leads into the aims of the present study that intend to fill some of these gaps. Following this is a discussion and justification of the methodology that is employed in this study to meet the aims. The proposed method is to employ a flapping-wing mechanical model ('flapper') in a series of experiments. The necessary requirements for this 'flapper' to meet the research aims are also given. Before proceeding, it should be mentioned that this work focuses on flight in the hover condition, which is the most demanding phase in insect flight in terms of power, and it coincidentally simplifies the aerodynamics, and has been the focus of most past studies.

3.1 Aims

From the previous chapter it can be seen that there are a number of points of concern for *FMAV* development. The first of these is the stability of the preceding *LEV*. As mentioned in the preceding chapter, above Re = 10000 conflicting reports of *LEV* stability arise, and it has been postulated that the *LEV* becomes turbulent above this value and sheds. This is of particular interest to *FMAVs* as they will operate at Reynolds numbers on the order of 10^4, and an unstable *LEV* could potentially cause significant fluctuations in lift that would hamper operation and control. Furthermore, *LEV* shedding would lead to an increase in drag, particularly at outboard sections of the wing which would result in greater torque requirements to drive the wing, and hence lower efficiency (Ansari et al., 2008b). Therefore, one of the questions that will be addressed in this thesis is whether or not the *LEV* is stable at *FMAV*-scale Reynolds numbers.

Another point of concern to *FMAVs* is the fact that kinematic effects have not been adequately explored, as there are relatively few studies on the subject. Kinematic effects are of great interest to *FMAVs* because knowledge of how different

kinematic parameters impact the aerodynamic forces is a prerequisite to *FMAV* design. For example, when designing the flapping mechanism for an *FMAV*, the designer would need to know what flapping frequencies and stroke amplitudes the mechanism must be able to achieve to enable the vehicle to support its weight.

First of all, as discussed in the preceding chapter, effects of Reynolds number on force coefficients are unclear. Effects of Reynolds number on the flow structures, such as changes in *LEV* stability, structure and axial flow, have also not been adequately explored. Thus the question of how Reynolds number affects lift and the flow structures will be addressed in this thesis.

Effect of angle of attack on the flowfield, including the form and structure of the *LEV* has been investigated very little, especially above $Re = 10000$. Experiments addressing this, as well as angle-of-attack effects on the forces would be useful and thus will be investigated here.

Rotation phase effects have mostly only been explored at Reynolds numbers below 200, with the exception of Sunada et al. (2001) who looked at $Re = 1000$. However, this last work was performed with a $2D$ translating wing which does not completely replicate the flow on an insect wing, as $2D$ experiments lack the essential axial flow for stabilising the *LEV*. Thus, it currently remains unknown what the effects of rotation phase are on the forces and flow structures at the much higher Reynolds numbers (of the order 10^4) needed for *FMAVs*. An investigation that establishes these effects at this scale would be of interest as rotation phase has been shown to be quite effective at augmenting lift in the studies performed at much lower Reynolds numbers. Therefore, the effect of rotation phase at *FMAV* scale on the lift, as well as on the flow structures will be studied in this thesis.

Similar to rotation phase effects, the effect of stroke amplitude on forces has only been investigated below Reynolds numbers of 2000, and effects on the flow have been studied up to 8000. Thus, stroke amplitude effects on the forces and flow at *FMAV* scale have not been established, and will be addressed here.

Wingtip kinematics with varying plunge amplitude effects have also only been performed at lower Reynolds numbers, where the highest explored is $Re \approx 3700$, and most studies were done at Reynolds numbers on the order of 10^2. Hummingbirds which operate at the *FMAV* scale exhibit figure-of-eight wingtip kinematics, thus, an *FMAV* that makes use of this wingtip trajectory may exploit

some unknown benefit. This has yet to be answered, as studies on this subject have not been performed up to this scale. Therefore, this thesis will also investigate the effects on lift and the flow structures from employing figure-of-eight wingtip kinematics with varying plunge amplitude.

The aforementioned questions that will be addressed in this thesis can be summarised by two general questions:

- Is the *LEV* stable on an insect-like flapping-wing at *FMAV* scale?
- How are the lift and flow structures on an insect-like flapping-wing at *FMAV* scale affected by flapping kinematics?

Expanding on these general questions and adding other points of interest, the particular questions to be addressed are as follows:

- How do the flow structures generated by an insect-like wing at *FMAV* scale evolve over a half-stroke? This will answer the question of *LEV* stability, that is: is there evidence of *LEV* shedding throughout a half-stroke, or is there a single *LEV* present that stays relatively fixed with respect to the wing?
- Does vortex breakdown occur in the *LEV*? If it does, then why does it occur, where on the wing does it form, and how does it evolve?
- Is axial flow present through the *LEV* core at the *FMAV* scale?
- What is the contribution of the *LEV* to the mean lift generated?
- How do the kinematic parameters listed below affect the mean lift and flow structures, particularly the *LEV*, at *FMAV* scale? That is, when each one of these parameters is independently varied while all others are kept fixed, how are the mean lift and flowfield affected?
  - rotation phase
  - angle of attack
  - Reynolds number
  - stroke amplitude
  - figure-of-eight kinematics with varying plunge amplitude

- What is the effect of wing planform shape on the flow structures produced? This means, if flapping kinematics are held fixed and wing planform is varied, how does the flow change?

3.2 Methodology

To achieve the proposed research aims, the fundamental requirement is that an insect-like wing must be flapped with insect-like kinematics at the *FMAV* scale, while permitting separate control of the listed kinematic parameters to investigate their effects. This will be achieved experimentally, thus requiring the design and development of a flapping-wing mechanical model, a 'flapper'. One could argue that using live insects is another potential option as larger insects and hummingbirds operate at *FMAV* scale Reynolds numbers. However, using a live insect or hummingbird would give the experimenter no control over individual kinematic parameters, and it has been noted that tethered specimens behave differently than in free-flight (Willmott & Ellington (1997), Sane & Dickinson (2001)), thus complicating the ability to measure representative aerodynamic forces. Thus, a mechanical 'flapper' is the most appropriate option as it can enable control of flapping kinematics and parameters.

From the previous chapter, it can be seen that there are a number of flapper types to choose from, as either a $2D$ or $3D$ flapper operating in liquid or air, or a free-flying flapper can be employed. Using a free-flying mechanical flapper is the least useful option for studying insect flight as designs of this type are very limited in terms of what the wings can do. Even the Nano Hummingbird by AeroVironment Inc. has limited control over its wings, for instance stroke amplitude, rotation phase, wingtip kinematics and plunge amplitude cannot be varied. Thus, while the a free-flying flapper like the Nano Hummingbird is appropriate and very successful at achieving flight, it is not suitable for an experimental study as few parameters can be controlled. $2D$ experiments are also inappropriate to meet the research aims. As was mentioned before, $2D$ experiments do not completely replicate the flow on an insect wing, as the very important axial flow through the *LEV* core is lacking in such experiments. The remaining options are a $3D$ flapper that operates in either liquid or air. While experiments in a liquid have certain advantages, such as enabling the wing to be slowed down thereby simpli-

fying mechanism design and control, and ease of seeding the fluid, a flapper that operates in air has been chosen.

A flapper that operates in air on the *FMAV* scale would fully replicate the conditions of a real *FMAV*. Although experiments in liquid are dynamically scaled (preserving Reynolds number) to match the flow conditions of insects or *FMAVs*, such experiments may not replicate other aspects of *FMAV* conditions that are potentially important. For instance, flappers that operate in air experience much higher vibrations than those in a liquid, purely because they have to operate at much higher speeds. These vibrations may be significant enough to affect the wings and impact the aerodynamics. All air flappers that have been used above Re = 10000 have reported or speculated the presence of *LEV* shedding, which include those of Ellington & Usherwood (2001); Ramasamy et al. (2005); Ramasamy & Leishman (2006). On the other hand, above this Reynolds number, there have been reports of a stable *LEV* on a flapper that operates in liquid (Lentink & Dickinson, 2009). Thus, it could be possible that on an insect-like flapping wing above Re = 10000 the *LEV* is stable, but with the addition of vibrations from the *FMAV's* flapping mechanism, the *LEV* destabilises. With their 'flapper' that operated in air, Ellington and his colleagues reported potential reduced *LEV* stability caused by gearbox vibrations (van den Berg & Ellington, 1997a). If flapping mechanism vibrations do in fact impact the aerodynamics, then flapping-wing experiments would have to include a realistic level of vibration on the wings to replicate actual *FMAV* conditions, as *FMAVs* would exhibit a certain level of vibration. This is of course all speculation, however, the main point is that any unknown important aspects of *FMAV* operating conditions would be captured in such experiments that use a flapper that operates in air. Essentially, a flapper of this type would be an actual *FMAV*, and thus, there would be no question of the direct applicability of experimental findings to an *FMAV*.

Another reason for choosing a flapper of this type is that it serves as a stepping stone towards a working *FMAV*, a point also made by Mueller & DeLaurier (2001). For example, issues encountered and lessons learned would be applicable to *FMAV* design. In addition, a device of this kind could serve as a future test bed for *FMAV* wing designs, as wings could be tested for their performance under certain kinematics, and then installed directly on an *FMAV*.

Concerning the design of a flapper to be used in the present work, there are a

number of lessons to be learnt and points to be taken from past flappers. First of all, many flappers including those of Bennett (1966), Maxworthy (1979), Tarascio et al. (2005) and Syaifuddin et al. (2006) all use mechanical 'stops' to limit the wing's angle of attack. This method of controlling pitch is unattractive because each time the wing comes into contact with a hard stop, the wing is essentially impacted with an impulsive force that rapidly pitches the wing. An impulsive force is of a high frequency and thus is likely to excite unnecessarily large vibrations in the wing. From the point of view of studying attached vortices over a wing, this is undesirable because any unnecessary wing vibrations could potentially force *LEV* shedding. Thus, using this method of pitch reversal could potentially show flow features that are specific to a mechanism that uses this pitch reversal method.

Another lesson is that mechanical complexity and the use of backlash-prone components like gears and cams should be minimised. Bennett reported problems in his flapper with lost motion in the wing due to clearances between components such as the cam and the bobbin (Bennett, 1970). The flapper of Conn and his colleagues reported problems with friction in the gears and misaligned shafts, resulting in reduced flapping frequencies (Conn et al., 2007). In addition, the Mk2 flapper of Galiński, which had a complex drive train of gears, had problems with vibration as it would unintentionally resonate at a certain frequency (Galiński et al., 2007). Also, Ellington's flapper, which used a flapping mechanism consisting of a number of bevel gears, had to use anti-backlash springs to reduce backlash (van den Berg & Ellington, 1997b), but this added to the mechanical complexity. Thus, using such components should be avoided as they increase complexity and reduce the positional accuracy of the flapping wing.

Another point to be noted from past flappers is that most had wings with only two degrees of freedom, so they could only sweep back and forth, and pitch. This is especially true for flappers that operated in air, where only the flappers of van den Berg & Ellington (1997b), Żbikowski et al. (2005), Galiński & Żbikowski (2005) and Banala & Agrawal (2005) could achieve true insect-like wing motion with sweeping, plunging and pitching motions. Flappers with only two degrees of freedom are limiting because they cannot replicate the plunging motions that are clearly present in insect-like kinematics, as was seen in the previous chapter.

The last point that will be noted from previous mechanical flappers is that, with the exception of Ellington's flapper, none of the flappers that operated in air that

had wings with at least three degrees of freedom, had adjustable kinematics. Some flappers like that of Tarascio et al. (2005) and Conn et al. (2007), were adjustable in the sense that kinematics could be set before operation by reconfiguring parts; however, during operation the wing motion was fixed. This severely limits the number of kinematic parameters that can be altered, thus limiting the different kinematic effects that can be explored.

With the above points and the research aims in mind, the requirements for the flapper of the present study are listed as follows, where the flapper should:

- operate in air on the *FMAV* scale, that is, it should employ a wing that is of *FMAV* size ($\sim 150mm$ wingspan)
- permit separate control of stroke, plunge and pitch
- allow flapping kinematics (and thus kinematic parameters) to be altered without requiring mechanical parts to be changed or altered
- achieve a maximum stroke amplitude of at least $120°$
- achieve a maximum plunge amplitude of at least $20°$
- achieve pitch angles at least in the range of $45 - 135°$
- allow instantaneous flapping mechanism position to be measured; this is required to recover actual flapping mechanism kinematics
- enable instantaneous wing position to be measured; this is required to recover the actual wing flapping kinematics and kinematic parameters
- allow at least lift to be measured
- enable flowfield measurement via particle image velocimetry (PIV); this implies a level of optical access around the wing
- have a highly repeatable wing position, which implies a tight tolerance on flapping mechanism position; this is required to enable kinematic parameters to be held virtually fixed, and to give useful force and flowfield measurements
- achieve flapping frequencies up to $20Hz$

- have no mechanical hard stops
- avoid backlash-prone components, such as gears and cams
- have a minimal number of moving parts
- allow different wing designs to be mounted to the flapping mechanism

The design of a flapper to satisfy the requirements will now be addressed in the next chapter.

Chapter 4

Flapperatus

Recalling from Chapter 3, the proposed method to achieve the research goals is to conduct a series of experiments with a flapping-wing mechanical model (a 'flapper'). This chapter presents the design, development and performance of the developed mechanical flapper apparatus, termed the 'flapperatus'. First, the original system concept for the flapperatus is outlined. Following this are a number of sections outlining the flapping mechanism design and development. This starts with the evolution of the flapping mechanism conceptual design, followed by a presentation of the mechanism output coordinate systems that rotate with the wing. Details of the form and operation of the final flapping mechanism conceptual design are given next. After this, a kinematic analysis of the mechanism, as well as a description of a dynamic model, and the component designs are given. The stress analysis performed on the components to arrive at the final detailed design is then discussed. The final detailed design of the flapping mechanism is then presented.

The next section and subsections describe the form of the complete flapperatus system and its functional elements (other than the flapping mechanism). The main subsystems of the flapperatus are described. This begins with the flapping mechanism controller, which actuates the flapping mechanism, followed by the mechanism position measurement system, which measures the mechanism position and synchronises the wing with the measurement devices. Next, the flowfield / wing position measurement system which measures the flow over the wing and also the position of the wing itself is discussed. This includes a description of the *PIV* setup used in experiments. The force measurement system which measures lift on the wing is then described, and finally the wing designs for the flapperatus are presented.

The final section to this chapter illustrates the performance of the flapperatus by presenting results of high-speed photography which show the flapping kinematics achieved by the wing. In addition, the repeatability of the mechanism and wing position are discussed.

4.1 System Concept

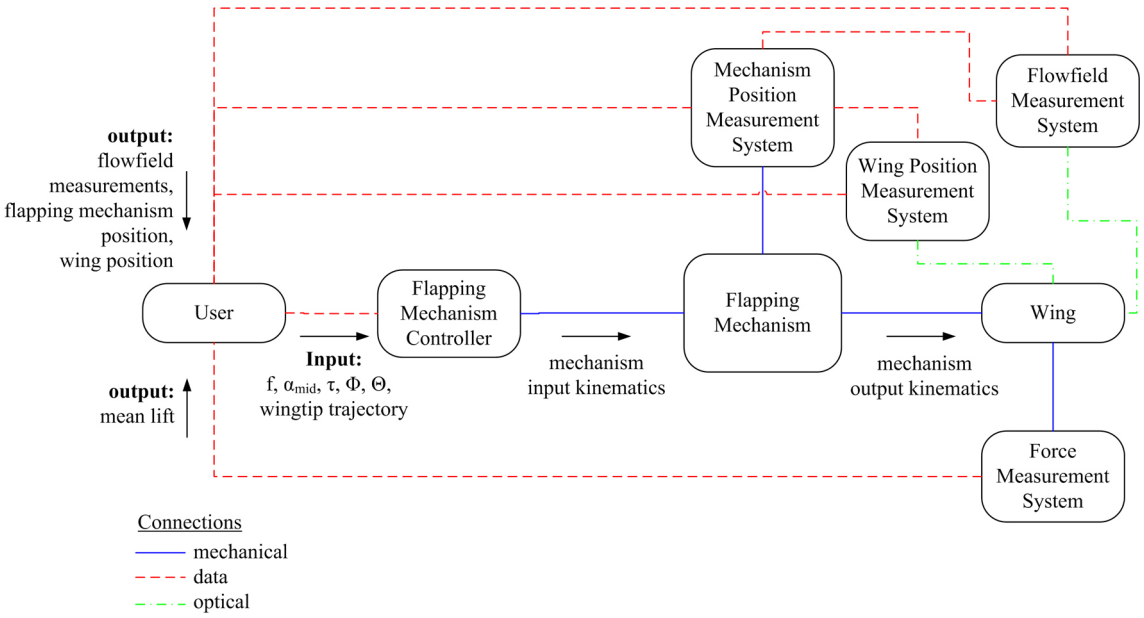

Figure 4.1: Flapperatus conceptual system block diagram

The system concept for the flapperatus outlined from the requirements at the end of Chapter 3, is given in the system block diagram in Figure 4.1 which illustrates all of the functional elements and the connections between them. At the start of the process, the user inputs the necessary kinematic parameters, as illustrated, to define the flapping kinematics of the wing using the expressions given in Appendix A. The flapping mechanism controller then outputs the necessary input kinematics for the flapping mechanism (the 'mechanism input kinematics'). Next, the flapping mechanism outputs kinematics (the 'mechanism output kinematics') to the wing, which are the kinematics that the flapping mechanism 'demands' that the wing follows. The actual kinematics that the wing produces, the flapping kinematics, will however differ from the mechanism output ('demanded') kinematics. This is because the wing will flex, and hence will not follow the mechanism output kinematics exactly. If the wing were infinitely rigid then the flapping kinematics would be the same as the mechanism output kinematics. Lift, flowfield measurements, and instantaneous wing position are taken from the wing via the force, flowfield and wing position measurement systems respectively. The mechanism position measurement system monitors the actual flapping mechanism position

to enable synchronous flowfield and wing position measurements. The flapping mechanism position can be correlated to the 'demanded' wing position, thus, for example, when the wing is at mid-stroke according to the 'demanded' kinematics (the mechanism output kinematics) flowfield and instantaneous wing position measurements can be taken at that point in time. End outputs to the user are the mean lift, flowfield measurements, and instantaneous flapping mechanism and wing position. With the history of flapping mechanism and wing position, the actual mechanism output kinematics, flapping kinematics, and actual kinematic parameters can be recovered.

4.2 Flapping Mechanism

From the system concept shown previously, the most important element is the flapping mechanism. This is also the most demanding element in terms of its required operation as it must have three degrees-of-freedom, operate at high speeds, and have a very repeatable motion. The design and development of the flapping mechanism will now be described.

4.2.1 Conceptual Design Evolution

As mentioned in Chapter 2, a very limited number of past flappers were capable of producing sweeping, plunging and pitching motions. That is, most could only perform sweeping and pitching motions. Of the flappers that were able to produce the three ranges of motion, the mechanism used in the design of the Mk2 flapper of Galiński & Żbikowski (2005) was initially selected for the present flapperatus' flapping mechanism. This mechanism was a double spherical Scotch yoke with a universal joint, and it was selected because it is capable of achieving a wide range of flapping kinematics. Other mechanisms in comparison would require linkage lengths to be varied in order to alter kinematics, whereas in the design of the flapping mechanism of the Mk2 flapper, only the input motion profiles of the scotch yokes and the actuated universal joint need to be altered. In this flapper these input motion profiles were fixed, however, they could be made variable when implemented into the flapperatus. Thus, the first design of the flapping mechanism for the flapperatus consisted of two spherical Scotch yokes

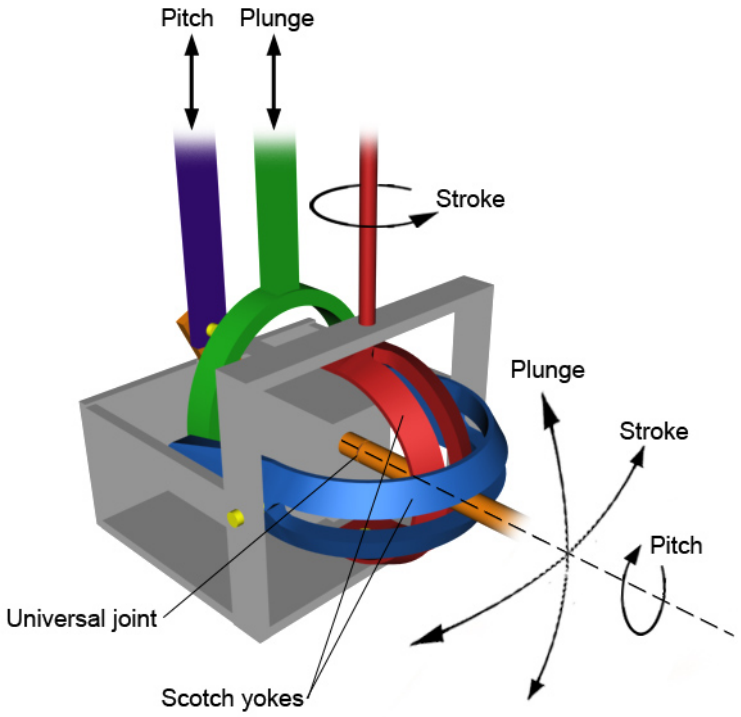

Figure 4.2: Flapping mechanism design 1: double spherical Scotch yoke with universal joint (after Galiński & Żbikowski (2005))

to produce the sweeping and plunging motions, and a universal joint to permit pitching motions. An illustration of this design is given in Figure 4.2.

It was soon discovered that this first design would only be able to achieve a maximum stroke amplitude of 90° because the maximum operational angle (maximum permissible misalignment between two shafts) of a single universal joint is 45°. This was a problem because one of the requirements laid out for the flapperatus was that it should achieve a maximum stroke amplitude of at least 120°, to be representative of typical insects. From this point, multiple methods of coupling a stationary rotating shaft to a moving rotating shaft with a varying misalignment were explored. Eventually a solution was found that permitted a maximum stroke amplitude of 120°, which was a telescopic double universal joint. This is merely two universal joints with a telescopic segment in between the two. With this type of coupler a maximum operation angle of 60° is permissible. Thus the single universal joint in the first design was exchanged for a telescopic double universal joint. In addition, the Scotch yoke that controlled stroke was exchanged for a ring with an attaching link that would passively follow the plunge movements of the remaining Scotch yoke, but still permit sweeping movements.

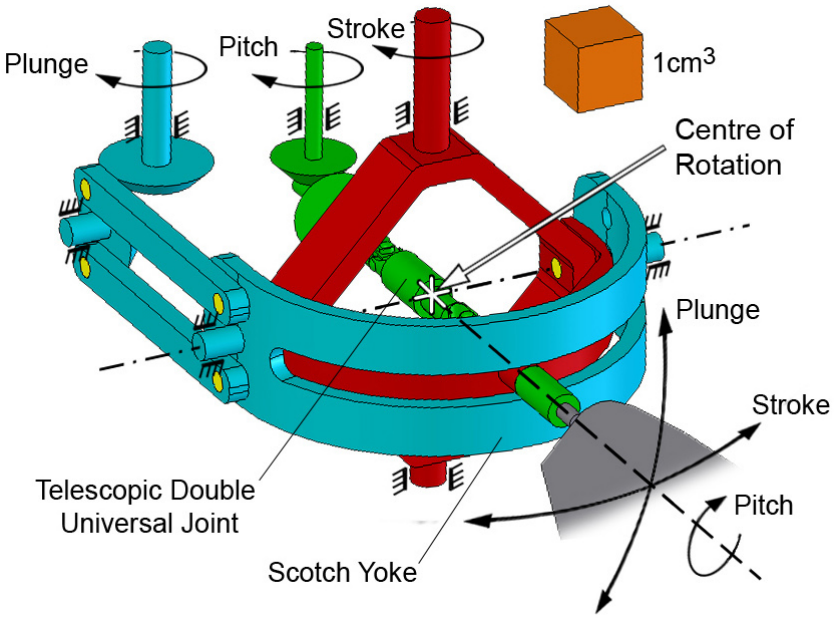

Figure 4.3: Flapping mechanism design 2: single spherical Scotch yoke with telescopic double universal joint

This modification was made to reduce backlash in the mechanism. Figure 4.3 illustrates the second design of the flapping mechanism for the flapperatus.

The next point of concern was the use of the Scotch yoke in the second design. First of all, the required clearances between the slot of the Scotch yoke and the sliding element that follows it would lead to undesirable levels of backlash in the plunge direction. Another problem was that as the stroke angle approaches +90° or −90°, the range of achievable plunge angles approaches zero. For example, if the slot of the Scotch yoke extended a full 180° and the wing was at a 90° stroke angle, then the wing could no longer be moved in the plunge direction. This is a problem because with a figure-of-eight wingtip trajectory, high plunge angles are required when the absolute stroke angle is also high. Thus, an alternative method of stroking and plunging the wing was sought.

For a new stroking and plunging mechanism, inspiration was drawn from the three degree-of-freedom 'Agile Eye' of Gosselin & Hamel (1994) and its simplified two degree-of-freedom version of Gosselin & Caron (1999), both from Université Laval. These are shown in Figure 4.4, where both are spherical mechanisms that employ linkages to rotate a camera about two or three axes. The three degree-of-freedom Agile eye offers a particular advantage as it employs parallel kinematics. This means that all motors work together to produce a panning (stroking), tilting

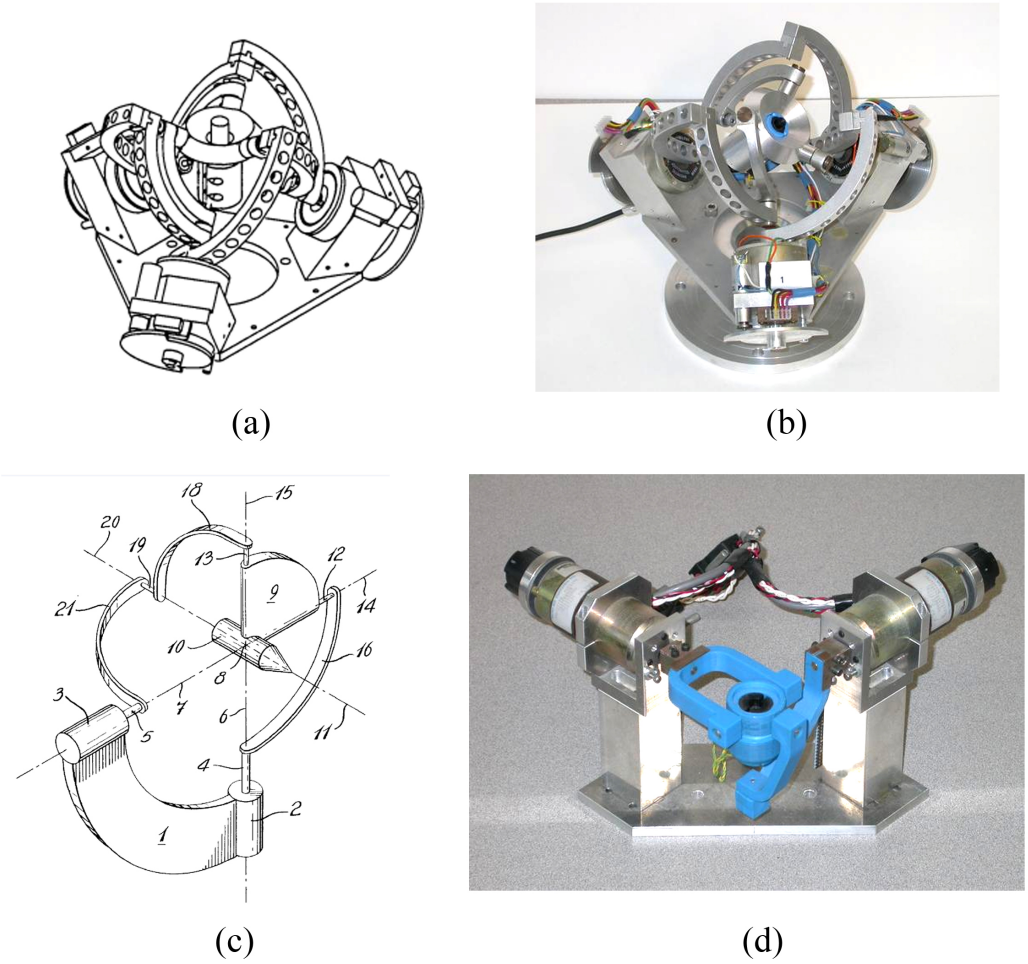

Figure 4.4: Versions of 'Agile Eye'; a) 3*DOF* Agile Eye schematic (Gosselin & Hamel, 1994); b) actual 3*DOF* Agile Eye embodiment (Laval, 2011); c) 2*DOF* Agile Eye schematic (Gosselin & Caron, 1999); d) 2*DOF* Agile Eye embodiment (Laval, 2011)

(plunging) or torsion (pitching) motion of the camera, rather than individual motors controlling each of these actions independently. The advantage of this is that with a given set of motors, much higher angular accelerations of the payload can be achieved. This enables the Agile eye to achieve angular accelerations of over 20000deg/s^2 (Laval, 2011). To produce an insect-like flapping wing trajectory, insect wings must undergo very high angular accelerations; thus, a flapping mechanism that uses parallel kinematics as the Agile eye does, would be ideal for this application.

Using the Agile eye for inspiration, a novel two degree of freedom parallel spherical mechanism was conceived that would perform the required stroking and plunging motions of the wing. This mechanism (Figure 4.5) consisted of

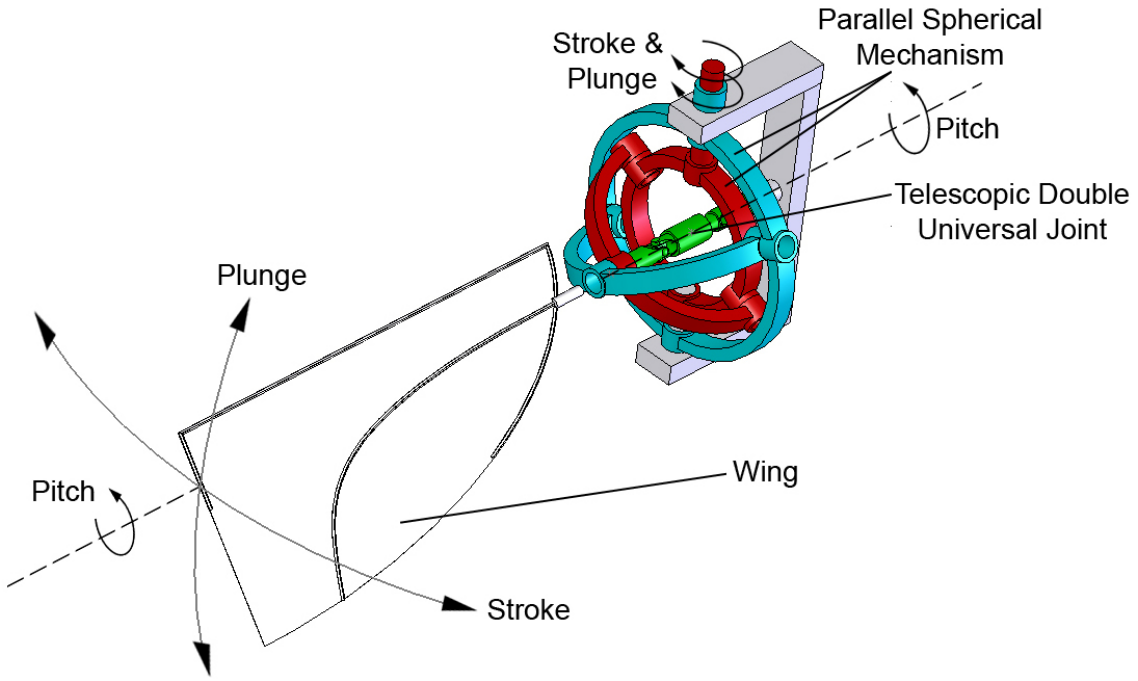

Figure 4.5: Flapping mechanism design 3: 2DOF parallel spherical mechanism with telescopic double universal joint

two concentric rings with two linkages to couple their motion. This mechanism design was conceived from a planar parallel mechanism consisting of two parallel sliders joined by a pair of links. Stroking and plunging motions were produced by this mechanism by rotating the concentric rings in the same and opposite directions respectively. The advantage of the new mechanism was that backlash in the system would be reduced drastically since all Scotch yokes (which are backlash-prone) were removed. In addition, the limitation on plunge angles at larger absolute stroke angles was eliminated. Thus, this new design was more successful at meeting the formulated requirements. Details on the operation of the mechanism will be given in greater detail in following section. The method of controlling pitch, however, remained the telescopic double universal joint.

The final design modification was the removal of the telescopic double universal joint which was replaced by a spherical slider-rocker mechanism. This reduced the part count and removed the constraint on maximum stroke amplitude imposed by the maximum operational angle of the telescopic double universal joint. With this design modification, the maximum stroke amplitude is infinite since all drive shafts become collinear as illustrated in Figure 4.6. In addition, all linkages could be made into full rings, which permits the centre of mass of

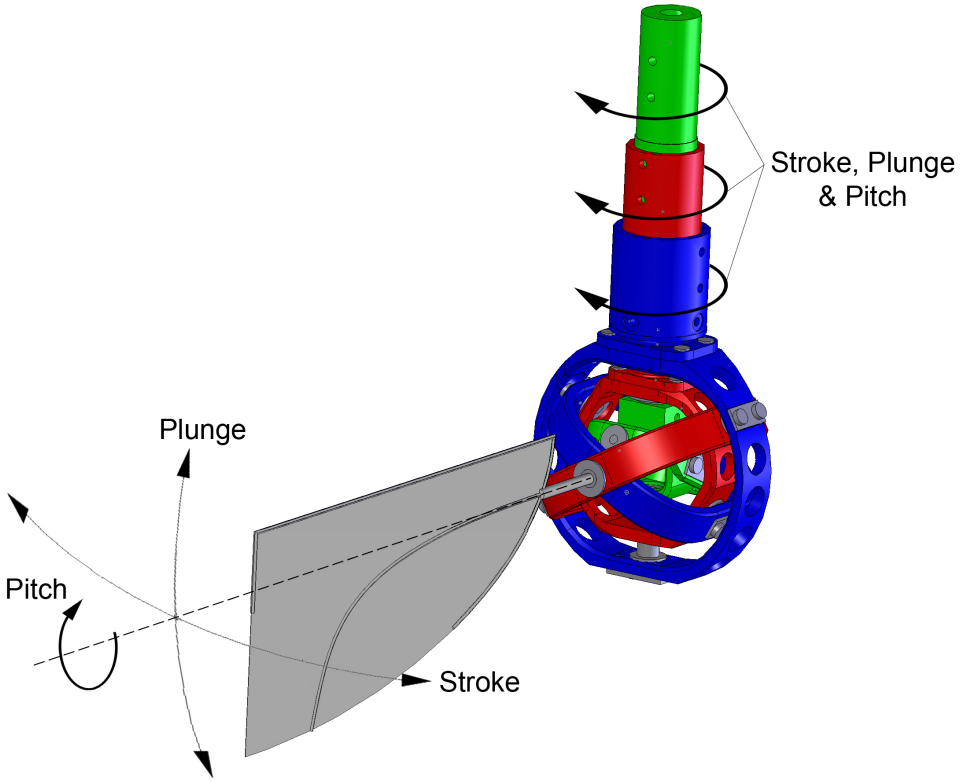

Figure 4.6: Flapping mechanism design 4: 3DOF parallel spherical mechanism

the mechanism to be located at the spherical centre of rotation. This would drastically reduce vibrations during operation. Thus, the final conceptual design of the flapping mechanism for the flapperatus is that shown in Figure 4.6, which is classified as a three degree-of-freedom 3-$\underline{\text{R}}$RR parallel spherical mechanism. The form and operation of this mechanism will be discussed in greater detail shortly.

4.2.2 Mechanism Output Coordinate Systems

Before proceeding, a description should be given of the mechanism output coordinate systems that rotate with the payload (wing). These are illustrated in Figure 4.7. The $x_{mec1}y_{mec1}z_{mec1}$ coordinate system is defined relative to the inertial axis, in the same manner that the xyz coordinate system fixed to the wing in Figure 2.4 (page 19) was defined. However, its orientation is defined by the mechanism stroke and plunge angles, ϕ_{mec} and θ_{mec} respectively. These are the stroke and plunge angles according to the mechanism output kinematics, thus, these are the 'demanded' stroke and plunge angles of the wing. In the same

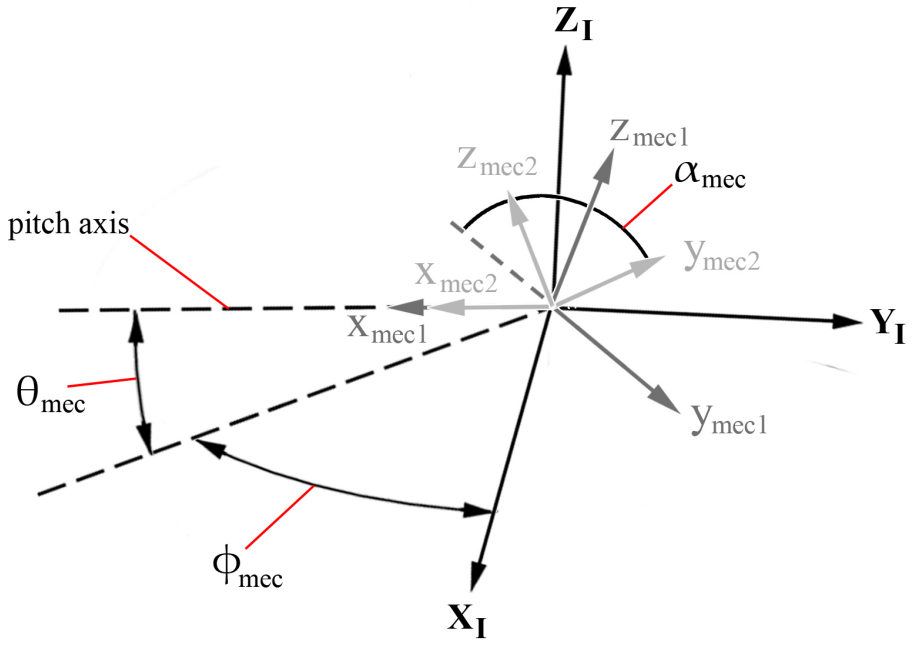

Figure 4.7: Mechanism output coordinate systems

fashion that the $x_w y_w z_w$ frame in Figure 2.4 is defined, the $x_{mec2} y_{mec2} z_{mec2}$ axis is defined relative to the $x_{mec1} y_{mec1} z_{mec1}$ axis by the mechanism pitch angle α_{mec}. This is the pitch angle according the mechanism output kinematics. Thus, ϕ_{mec}, θ_{mec}, and α_{mec} over time define the mechanism output kinematics. Mechanism output kinematic parameters including Φ_{mec}, Θ_{mec}, τ_{mec}, and $\alpha_{mid_{mec}}$ describe the mechanism output kinematics just as the kinematic parameters of the wing itself (Φ, Θ etc.) describe the flapping kinematics as discussed in § 2.1.3 (page 19). Thus, for example, Φ_{mec} is the stroke amplitude that the flapping mechanism commands the wing to perform.

As discussed in the first section of this chapter, with flexible wings the flapping kinematics (ϕ, θ, α), and thus, kinematic parameters (e.g. Φ) will differ from the mechanism output kinematics (ϕ_{mec}, θ_{mec}, α_{mec}) and mechanism output kinematic parameters (e.g. Φ_{mec}). If wing flexibility is ignored then the $x_{mec1} y_{mec1} z_{mec1}$ and xyz coordinate systems become the same, and similarly, the $x_{mec2} y_{mec2} z_{mec2}$ and $x_w y_w z_w$ coordinate systems become the same. Thus, mechanism output kinematics and flapping kinematics also become the same. For the remainder of this chapter up to (but not including) the last section, wing flexibility is irrelevant, thus, flapping kinematics are presented in place of mechanism output kinematics. For example, ϕ represents the stroke angle of the wing (ϕ) and the mechanism stroke angle

(ϕ_{mec}).

4.2.3 Form & Operation

The final flapping mechanism for the flapperatus described earlier will now be discussed in more detail. As mentioned, the mechanism that has been developed is a three degree-of-freedom 3-RRR parallel spherical mechanism. Here, 3-RRR is standard notation used to describe the architecture of parallel mechanisms. This indicates that there are three independent kinematic chains where each chain starts with a revolute input (denoted by the underline). Each input then connects to the end effector via a kinematic chain consisting of two revolute joints. In order to understand the operation of this mechanism, it must be described in parts.

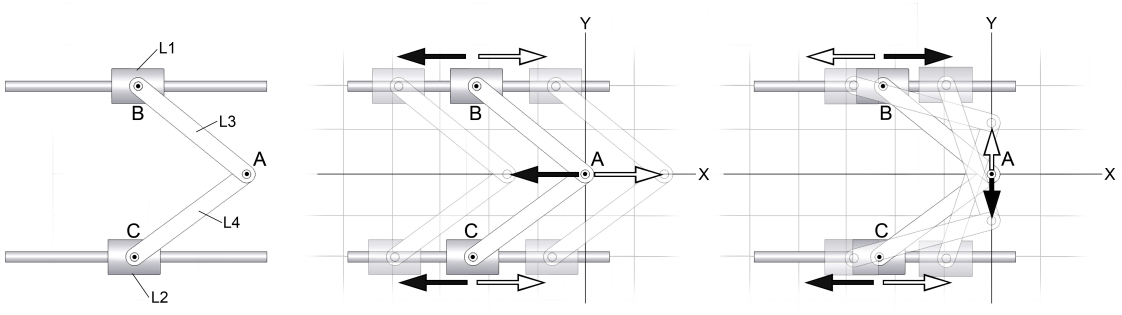

Figure 4.8: 2DOF planar parallel mechanism

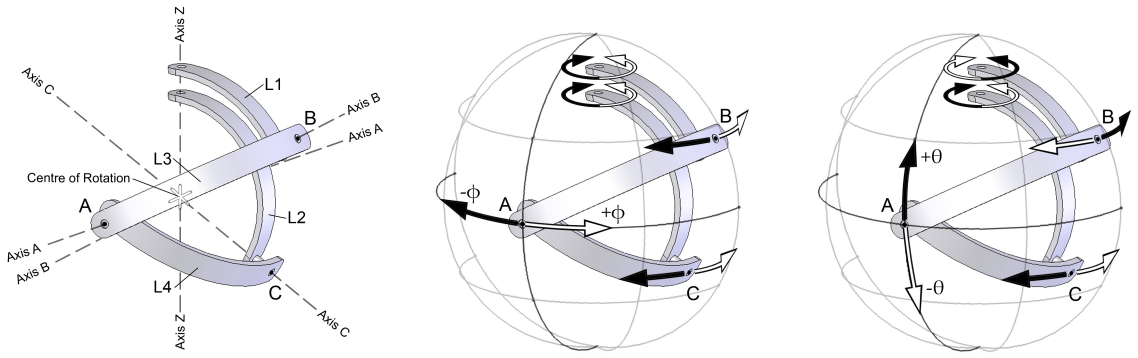

Figure 4.9: 2DOF parallel spherical mechanism

First, the manner in which the mechanism produces stroking and plunging motions will be described. To aid in this explanation, first consider a planar parallel mechanism consisting of two sliders joined by two links as shown in

Figure 4.8. From this figure, it can be seen that if both sliders (points B and C) translate together in the positive x direction by the same amount, then this will produce a translation of point A in the positive x direction, and vice versa for the negative x direction. A translation of point A in either the positive y or negative y direction may be achieved by moving each slider in opposite directions by the appropriate amount as illustrated. If this planar mechanism is converted to its spherical equivalent, then the x, y planar coordinate system will be replaced by a ϕ, θ spherical coordinate system. A radial 'r' coordinate in this case is not required since, for purposes of generality, spherical mechanisms are defined on the surface of a 'unit' sphere of radius one (Chiang, 1996). In this conversion from planar to spherical, lines of constant x become lines of longitude, and lines of constant y become lines of latitude. The equivalent spherical mechanism is illustrated in Figure 4.9, where links L1-L4 and points A, B, C correspond to the same links and points in the planar version in Figure 4.8. It can be seen that the sliders (L1 and L2) in the planar version take the form of links L1 and L2 in the spherical version, which both have the same axis of rotation (axis Z). One can see that these links are the spherical equivalent of the planar sliders by considering that if links L1 and L2 are rotated about their common axis of rotation then this will cause points B and C to translate along lines of constant θ (latitude lines). This is analogous to the planar case where points B and C translate along lines of constant y. Thus, analogous to the explanation given for the planar version, if links L1 and L2 are rotated in the same direction by the same degree then this will cause point A to translate along a line of constant latitude in the same direction. This is a stroking motion. If links L1 and L2 are rotated in opposite directions by the appropriate amount then this will cause point A to translate along a line of constant longitude, which is a plunging motion. It should be mentioned that the axis of rotation of all revolute joints must intersect the spherical centre of rotation for this mechanism to work as described. By fixing a wing through point A and the centre of rotation of the mechanism, the mechanism can orient the wing by specified ϕ and θ angles.

The remaining portion of the mechanism that adds the third degree of freedom to permit pitching will now be described. As before, first consider the planar mechanism from Figure 4.8 but redrawn in Figure 4.10 with an additional slider and links to give a third degree of freedom. These additional components form a

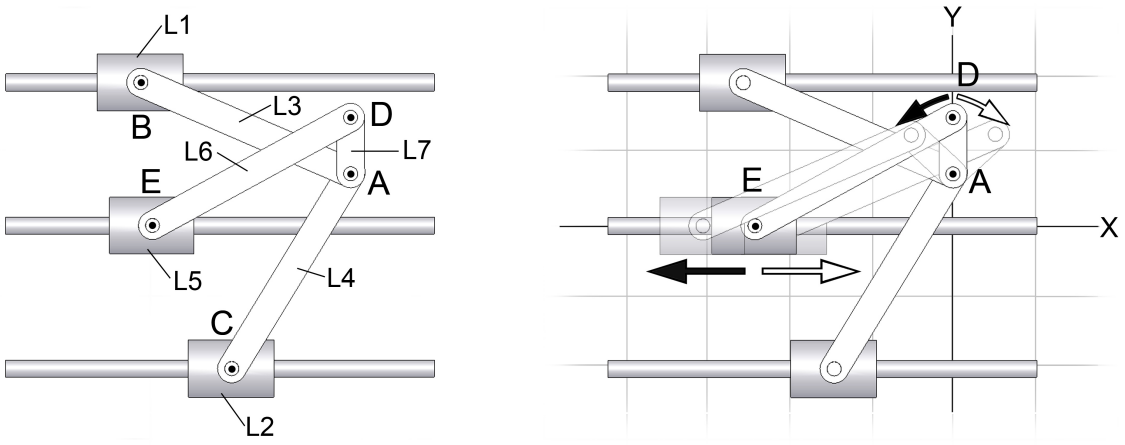

Figure 4.10: 3DOF planar parallel mechanism

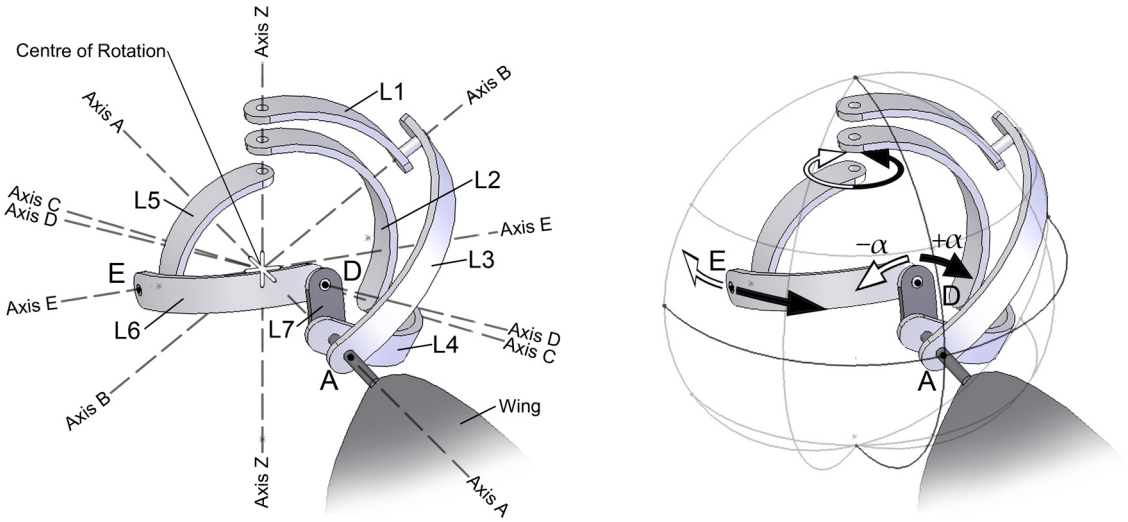

Figure 4.11: 3DOF parallel spherical mechanism

slider-rocker mechanism, with the rocker being link L7 pivoting about point A. It can be seen that varying the position of slider L5 for any given location of point A in the xy plane (which is dictated by the positions of sliders L1 and L2) will allow L7 to be rotated about point A.

Converting this additional slider-rocker mechanism to its spherical equivalent and adding it to the spherical mechanism described previously, results in the complete three-degree-of-freedom parallel spherical mechanism, which is illustrated in Figure 4.11. As before, the labeling of linkages and points on this mechanism corresponds to the same links and points on its planar counterpart in Figure 4.10. Similar to sliders L1 and L2 of the planar version, slider L5 becomes link L5 in

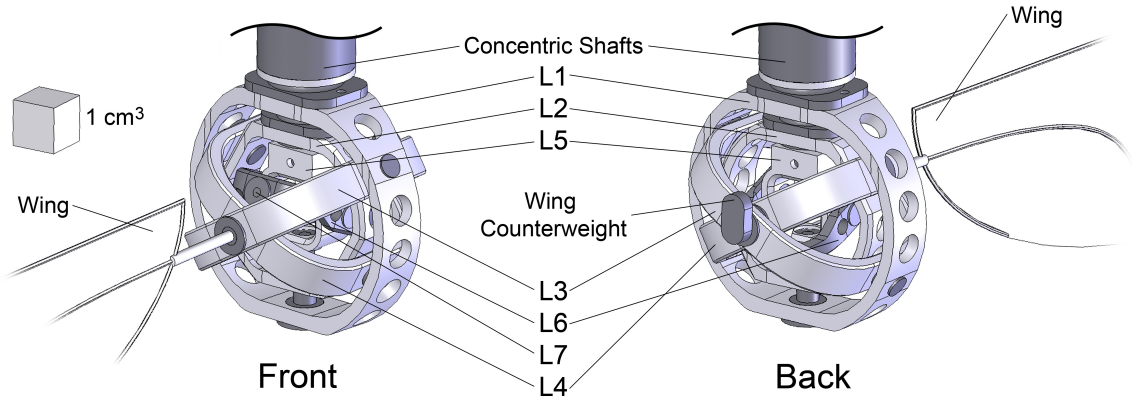

Figure 4.12: True embodiment of 3DOF parallel spherical mechanism

the spherical version which has the same axis of rotation (axis Z) as links L1 and L2. This results in point E translating along a line of constant θ (latitude) for a given rotation of link L5. Thus, similar to the planar version, for a given position of point A, a rotation of link L5 will push or pull the coupler link L6 which will cause link L7 (the rocker) to rotate about the common revolute joint between links L3, L4, and L7 at point A. As before, the axis of rotation of all revolute joints must intersect the spherical centre of rotation for the mechanism to function in this manner. If a wing is fixed to link L7, as illustrated, with its pitch axis of rotation coinciding with the axis of rotation (axis A) of the common revolute joint at point A, this complete mechanism will be capable of orienting a wing by specified ϕ, θ, and α angles. The input links to this mechanism are links L1, L2 and L5, thus mechanism input kinematics are imposed on these links, and the mechanism output kinematics are given to the wing fixed to link L7.

The form of the mechanism given in illustrations thus far in Figure 4.9 and Figure 4.11, would not be a practical embodiment due to play that would be encountered in the bearings, since the bearings would have to support large moments. This problem can be alleviated by turning all linkages into full rings and adding revolute joints that are collinear with the existing joints. Figure 4.12 illustrates the true embodiment of the three degree-of-freedom parallel spherical mechanism. Here, all linkages have been made into full rings, and revolute joints have been added collinearly with the existing ones, which can be seen in the front and back views of linkages L1 and L3. In this design, links L1, L2 and L5 subtend angles of 60°, 120°, and 25° respectively, and all other links subtend an angle of 90°. The method by which these numbers were arrived at will be given

in a later in § 4.2.6. With this configuration, the bearings will not be subjected to moments due to the additional joints, thus making the mechanism less prone to play and more stable. In addition, turning all linkages into full rings allows the mechanism centre of mass to be located at the spherical centre of rotation. The wing however, would displace the centre of mass, but this could be avoided by using a counterweight on the other side of the mechanism, as illustrated in Figure 4.12. Therefore, the entire mechanism's centre of mass can be located at the spherical centre of rotation, thereby minimising vibrations. This mechanism and its two degree-of-freedom version (which excludes the portion that enables pitching) are patent pending (Phillips, 2010).

4.2.4 Kinematic Analysis

Before proceeding, a description of the parallel kinematics of the three degree-of-freedom parallel spherical mechanism should be given. As can be seen by observing the planar version of the mechanism in Figure 4.10, the position of point A and the angle of the rocker link L7 are both functions of the positions of all three sliders. That is, the positions of all sliders together control all degrees-of-freedom, rather than each slider independently controlling a respective degree-of-freedom. The same is true for the spherical version of the mechanism, where the ϕ, θ, and α angles of an oriented wing are all a function of the positions of links L1, L2, and L5. This is the essence of parallel kinematics, in which a platform is manipulated by multiple independent kinematic chains (Bonev, 2007). In this case, link L7 (to which the wing is rigidly connected) is the platform which is manipulated by links 1 & 3, links 2 & 4 and links 5 & 6 which constitute three independent kinematic chains. The inverse kinematics of the mechanism will now be performed.

The portion of the mechanism that produces the stroking and plunging motions is illustrated in the left of Figure 4.13, whereas the portion that produces the pitching is shown to the right. Linkages and points labeled correspond to those shown previously. Before proceeding, recall that the wing spar passes through the centre of rotation and point A, and pitches with link L7. The positions of input links L1, L2 and L5 respectively denoted by ϕ_{L1}, ϕ_{L2} and ϕ_{L5}, for an arbitrary set of ϕ, θ, and α angles of the wing can be found using the spherical law of cosines to be:

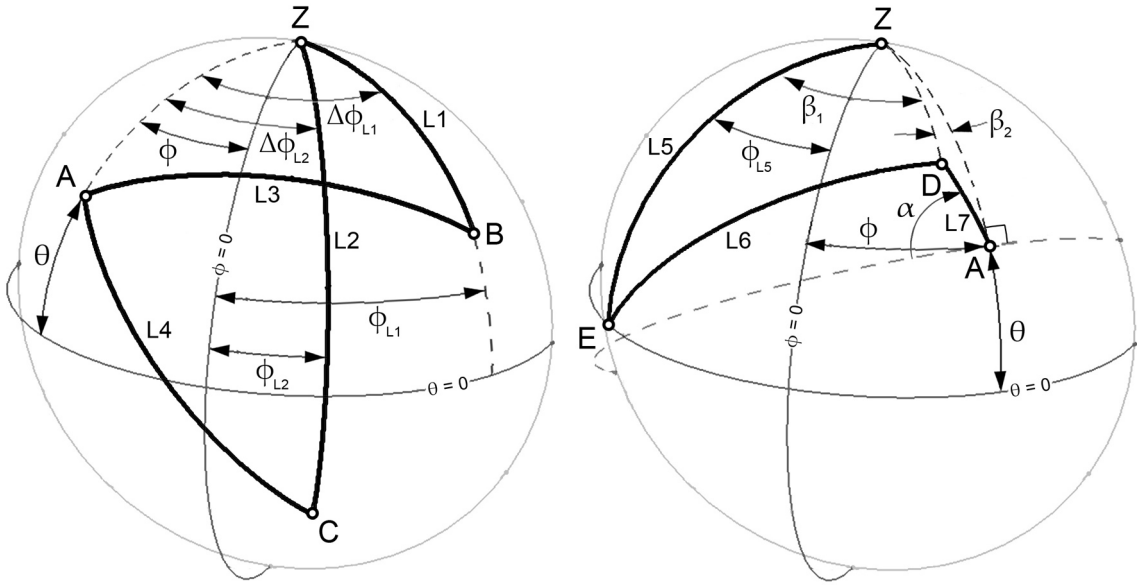

Figure 4.13: Position of Links L1-L4 for arbitrary location of point A (left); position of Links L5-L7 for arbitrary location of point A (right)

$$\phi_{L1} = \phi + cos^{-1}(\frac{cosL3 - cosL1\ sin\theta}{sinL1\ cos\theta}) \tag{4.1}$$

$$\phi_{L2} = \phi + cos^{-1}(\frac{cosL4 - cosL2\ sin\theta}{sinL2\ cos\theta}) \tag{4.2}$$

$$\phi_{L5} = \phi - \beta_1 + \frac{\alpha - \frac{\pi}{2}}{|\alpha - \frac{\pi}{2}|}\beta_2 \tag{4.3}$$

where:

$$\beta_1 = cos^{-1}(\frac{cosL6 - cosL5\ \sqrt{1 - (cosL7\ sin\theta + sinL7\ cos\theta\ sin\alpha)^2}}{sinL5\ \sqrt{1 - (cosL7\ sin\theta + sinL7\ cos\theta\ sin\alpha)^2}}) \tag{4.4}$$

$$\beta_2 = cos^{-1}(\frac{cosL7 - sin\theta\ (cosL7\ sin\theta + sinL7\ cos\theta\ sin\alpha)}{cos\theta\ \sqrt{1 - (cosL7\ sin\theta + sinL7\ cos\theta\ sin\alpha)^2}}) \tag{4.5}$$

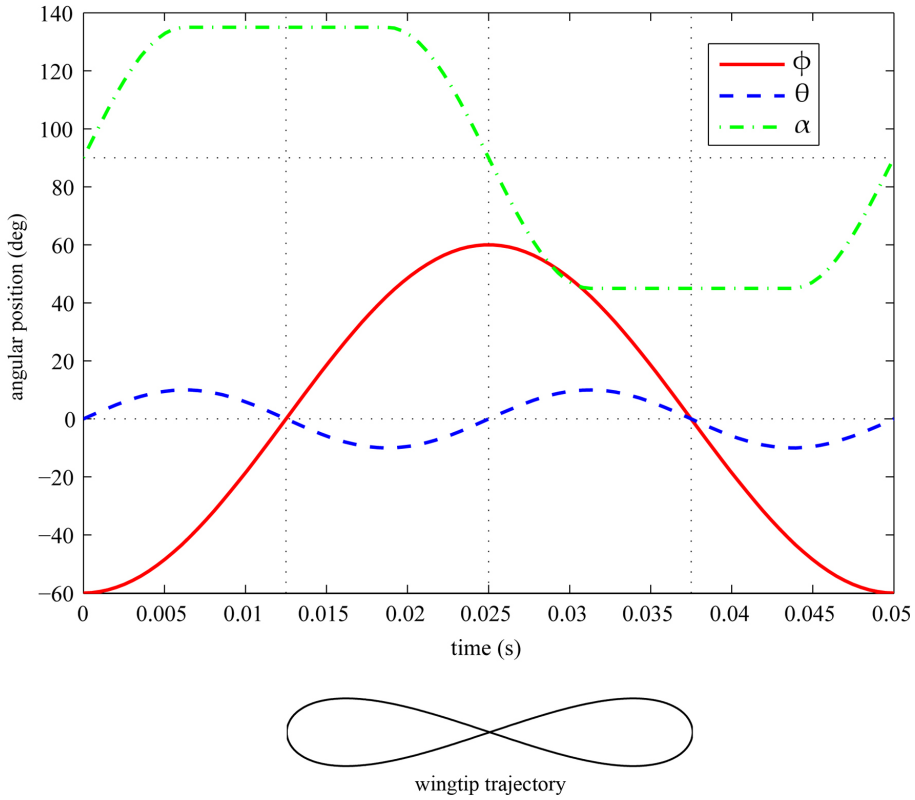

Figure 4.14: Example flapping kinematics and wingtip trajectory; $f = 20Hz$, $\alpha_{mid} = 45°$, $\tau = 0\%$, $\Phi = 120°$, $\Theta = 20°$, figure-of-eight wingtip trajectory

By observing Figure 4.13, it can be seen that when the pitch angle α (measured clockwise from the great circle perpendicular to the local line of longitude at point A) is less than 90° then $\phi_{L5} = \phi - \beta_1 - \beta_2$. On the other hand, when α is greater than 90° then $\phi_{L5} = \phi - \beta_1 + \beta_2$. Therefore, the expression in front of β_2 in Equation 4.3 is required to make β_2 of the appropriate sign. An alternative way of defining the angular positions of input links L1, L2, and L5 is to define them relative to their positions when the wing is at the 'neutral' position, which is when $\phi = 0°$, $\theta = 0°$, $\alpha = 90°$. In this manner, Equations 4.1-4.3 become:

$$\phi_{L1} = \phi + cos^{-1}\left(\frac{cosL3 - cosL1\ sin\theta}{sinL1\ cos\theta}\right) - cos^{-1}\left(\frac{cosL3}{sinL1}\right) \tag{4.6}$$

$$\phi_{L2} = \phi + cos^{-1}\left(\frac{cosL4 - cosL2\ sin\theta}{sinL2\ cos\theta}\right) - cos^{-1}\left(\frac{cosL4}{sinL2}\right) \tag{4.7}$$

$$\phi_{L5} = \phi - \beta_1 + \frac{\alpha - \frac{\pi}{2}}{abs(\alpha - \frac{\pi}{2})}\beta_2 + cos^{-1}\left(\frac{cosL6 - cosL5\ cosL7}{sinL5\ cosL7}\right) \tag{4.8}$$

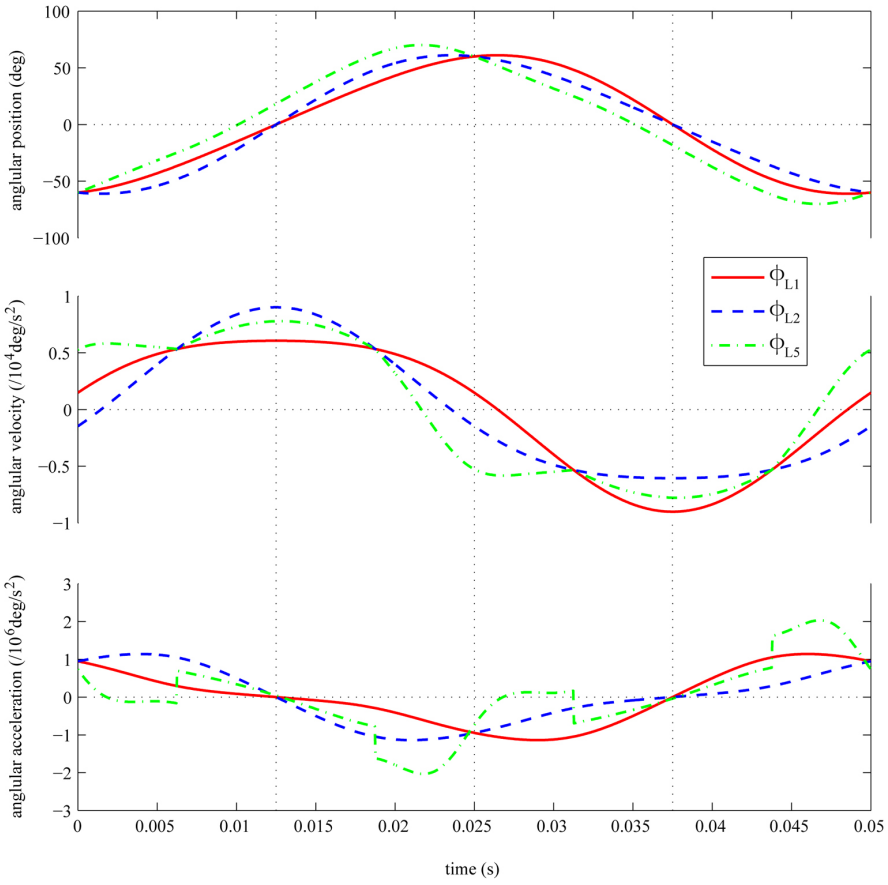

Figure 4.15: Example mechanism input kinematics required to produce flapping kinematics in Figure 4.14

With these new expressions, ϕ_{L1} through ϕ_{L5} become zero when $\phi = 0°$, $\theta = 0°$, and $\alpha = 90°$. Thus Equations 4.6-4.8 combined with Equations 4.5 and 4.4 provide the azimuthal positions of input links L1, L2 and L5, as a function of ϕ, θ, α and the link 'lengths' denoted by the same names of the links themselves. For example the 'length' of link L1 is 'L1'. The length of a given link is not an arc length, but rather an angle that the link subtends on a sphere. For example, a link which extends from the north to south pole on a sphere along a line of longitude would have a length of 180°. Therefore, with a given set of flapping kinematics, the angular position, velocity, and acceleration of links L1, L2, and L5 required to achieve the given kinematics, may be determined using these equations and their first and second time derivatives. These equations are derived in full along with their first and second time derivatives in Appendix B. In addition, this appendix also derives expressions for the ϕ, θ, and α angles of the wing and their first and second time derivatives as functions of the angular positions, velocities, and

accelerations of the input links L1, L2, and L5.

As an example, Figure 4.14 illustrates a set of flapping kinematics in which the wingtip traces a figure-of-eight, with f, α_{mid}, τ, Φ, and Θ of $20Hz$, 45°, 0%, 120°, and 20° respectively, and a constant pitch angle for 50% of the cycle. As mentioned, taking these kinematics and inputting them into Equations 4.6-4.8 and their first and second time derivatives yields the position, velocity and acceleration of links L1, L2 and L5, which are plotted in Figure 4.15. These are the mechanism input kinematics to the flapping mechanism. It should be noted that in this example, the angles that links L1, L2 and L7 subtend are 60°, 120°, and 25° respectively, and all remaining links subtend an angle of 90°.

4.2.5 Dynamic Modeling

To determine required forces and moments to drive the flapping mechanism under a given set of kinematics, as well as the loads that each component will be subjected to, a rigid-body dynamic model was formulated. This was evaluated using the matrix method, in which equations for the sum of forces and moments for all components are combined to give a system of n equations and n unknowns in matrix form. The resulting set of equations in the form $AX = B$ where A, X, and B are $n \times n$, $n \times 1$ and $n \times 1$ matrices respectively, were solved for the unknown X using Gaussian elimination. The number of components yielded 42 equations, with 42 unknowns and a sparse A matrix. Output from the model gave reaction forces at all of the joints, as well as required torques on the input links to drive the mechanism.

4.2.6 Component Design

Since its conception, the flapping mechanism was envisaged to be driven by three separate motors driving each of the input drive shafts (input links L1, L2, L5). Rather than having a complex drive train and additional mechanisms (e.g. planar crank-rockers) to convert continuous revolutions of the drive motors to reciprocating motions for the input links, the intention was to simply couple the motion of each motor directly to each of the input links of the flapping mechanism. For example, each motor would drive each input link via a 1 : 1 belt drive or

directly via a connecting shaft. The advantage of this drive method is that it minimises the number of moving parts and flapping kinematics are easily altered by simply changing the motion profiles of the motors.

The most challenging aspect of the proposed drive method is that the required input kinematics on the input links of the flapping mechanism must be within limits of what motors can achieve. These input kinematics (which the motors must achieve) will be similar to the flapping kinematics themselves. In insect-like kinematics, the wing exhibits high speeds and very high angular accelerations. For example, with the figure-of-eight kinematics at $20Hz$ in Figure 4.14, the stroking angular velocity and acceleration peak at $\sim 7500 deg/s$ and $9.5 \times 10^5 deg/s^2$ respectively. The required speeds can easily be achieved by most motors as, in the previous example, the peak velocity is equivalent to $\sim 1250 rpm$, which is well within the range of most motors. The limiting factor is the required angular accelerations, as their high values will limit what is achievable with a given motor, depending on the required mechanism input kinematics. Therefore, in optimising the design of the flapping mechanism, the lengths of the links must be chosen such that for a given set of flapping kinematics the required angular accelerations on the input links are minimised. This will enable the highest possible flapping frequencies and generally more demanding flapping kinematics to be achieved. In the following analysis employing the dynamic model, the lengths of links L1-L7 are optimised such that both the required input angular accelerations($\ddot{\phi}_{L1}$, $\ddot{\phi}_{L2}$, $\ddot{\phi}_{L5}$) and the required input torques (T_{L1}, T_{L2}, T_{L5}) on input links L1, L2, L5 are minimised. Here, it is also desired to minimise the input torque on these links required to overcome torques acting on the wing either due to aerodynamic or inertial forces. First, input links L1 and L2 are optimised, followed by the coupler links L3 and L4. Lastly, the links for the portion of the mechanism that enables pitching motions, links L6, L7 and L5, are then optimised. Before beginning, it should be noted that the lengths of links L1-L7 have no effect on the required input angular acceleration or torque required to output a desired angular acceleration or torque on the wing in the stroke direction.

Input Links L1 and L2

The design of links L1 and L2 have the greatest impact on the achievable plunge accelerations and output plunge torques (torque that drives the wing in the plunge

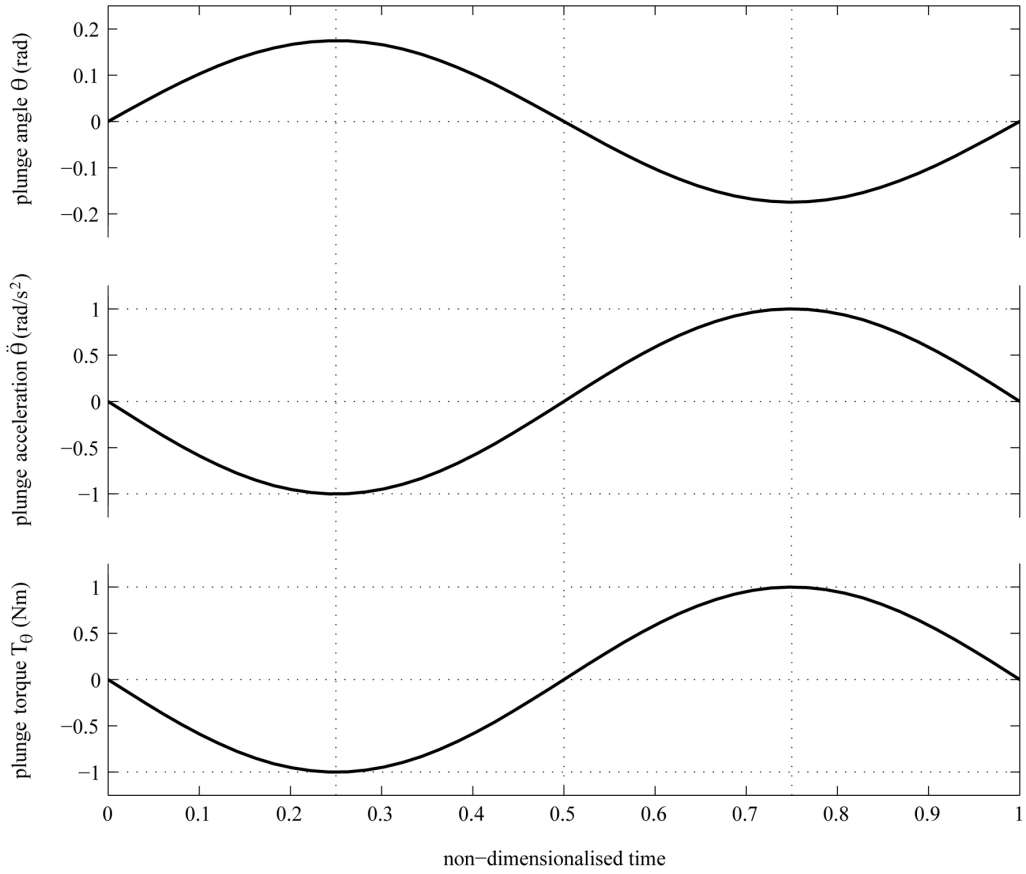

Figure 4.16: Pure plunging kinematics and required plunge torque; time is non-dimensionalised by the cycle period $T = 2.63s$

direction). Therefore, to choose appropriate lengths for these links a test case involving pure plunging of a payload with no stroke or pitch is employed. This test case is illustrated in Figure 4.16, where a payload with a unit moment of inertia in the plunging direction is plunged up and down with a peak angular acceleration of unity, and a peak required plunge torque also of unity, which is required to drive this motion. Thus, in this test case, the flapping mechanism must output a peak plunging acceleration and torque of one. In the following analysis, the lengths of links L1 and L2 are varied, and the required input kinematics and input torques on links L1 and L2 required to produce the desired motion with the specified payload, are computed with the dynamic model. This analysis uses massless links, and the lengths of links L3 and L4 are both taken as 90°. The portion of the mechanism for producing pitching motions is ignored in this analysis, because it has no influence during pure plunging motion with no pitch.

The effect of varying the lengths of links L1 and L2 on the maximum required

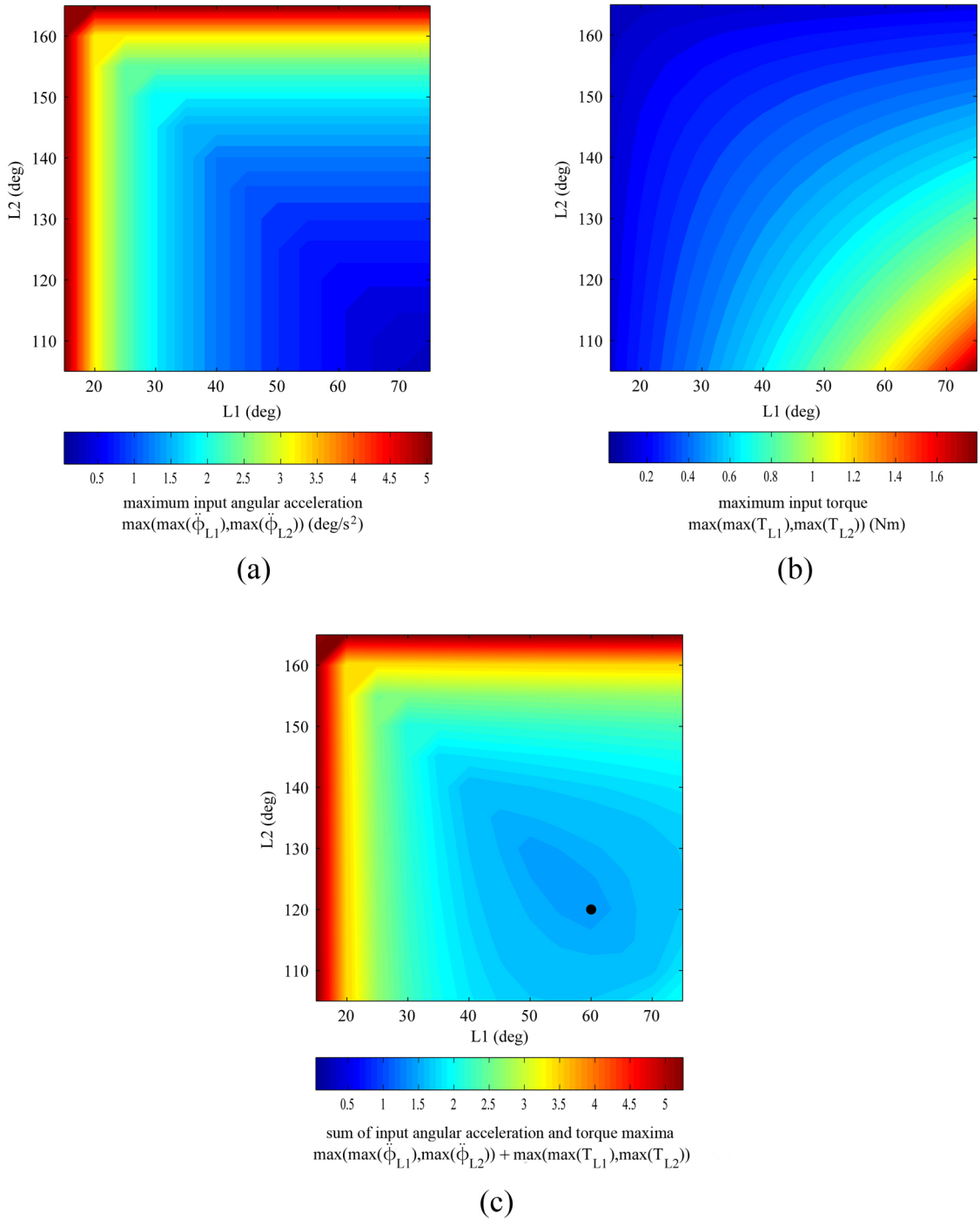

Figure 4.17: Effect of length of links L1 and L2 on (a) the maximum input acceleration (b) and torque required to output the kinematics and plunge torque in Figure 4.16, and (c) their sum; black dot in (c) shows an optimal point where the sum of maximum required input angular acceleration and torque is minimal

input accelerations and maximum required input torques on either of the two links, is shown in Figure 4.17a and b respectively. It can be seen that as L1 approaches 0° or L2 approaches 180°, then higher input accelerations are required

to produce a peak output plunging acceleration of unity. On the other hand, when L1 and L2 approach 90°, more input torque is required to produce a unit output plunge torque. This says that as the angle of separation (L2-L1) between the ends of links L1 and L2 increases, lower input torque on the links is required to achieve a desired output torque in the plunge direction, meanwhile, the links have to be accelerated at greater rates to achieve a required output angular acceleration in the plunge direction.

The goal of optimising the lengths of links L1 and L2 is to minimize both the required input angular accelerations and torques on these links needed to produce a desired motion. Thus, the sum of these two criteria must be minimised. Figure 4.17c shows the sum of the peak input angular accelerations and torques discussed previously. The black dot in this figure illustrates the chosen lengths for L1 and L2, which are 60° and 120° respectively, as they lie in the region where the sum is minimised. Therefore, with these values, the flapping mechanism will require lower input angular accelerations and torques to achieve a set of plunging kinematics and overcome torques on the wing in the plunge direction.

Coupler Links L3 and L4

Similar to input links L1 and L2, the lengths of coupler links L3 and L4 have the largest affect on the achievable plunge accelerations and output plunge torques. Thus, the test case used for input links L1 and L2 is used here, where the lengths of links L3 and L4 are varied and the required input kinematics and torques are calculated. As before, massless links are used, lengths of links L1 and L2 are taken as 60° and 120° respectively, and the portion of the mechanism for pitching is ignored.

As seen in Figure 4.18a, the optimum angle for both links is 90° to minimise the required input accelerations on the input links to produce a unit output plunge acceleration. The required input torque to produce an output plunge torque of unity is minimised as long as the lengths of links L3 and L4 are equal, as seen in Figure 4.18b. Therefore, without going further, the optimal lengths for links L3 and L4, to minimise the required input angular accelerations and torques, is 90° for both.

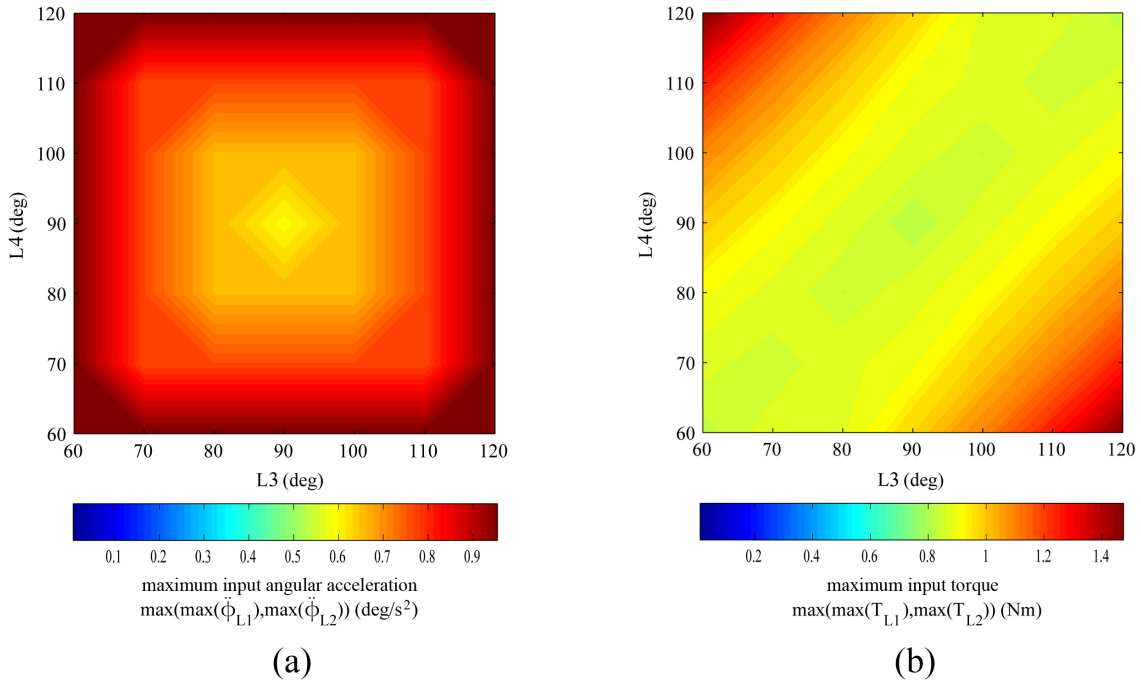

Figure 4.18: Effect of length of links L3 and L4 on (a) the maximum input acceleration and (b) torque on input links L1 and L2 required to output the kinematics and plunge torque in Figure 4.16

Coupler Link L6 and Rocker L7

The lengths of links L6 and L7 have the greatest influence on the output pitching accelerations and pitch torques on the wing. Thus, to optimise their performance, a test case involving pure pitching with no stroke or plunge is employed. This is illustrated in Figure 4.19, which depicts a payload with a unit moment of inertia in the pitch direction, being pitched with a peak angular acceleration of unity, and a peak required pitching torque of unity. As with the other links, the lengths of links L6 and L7 are varied while the peak required input acceleration and torque on the input link L5 (the input link to the pitching portion of the mechanism) are computed. Again, massless links are used, the length of link L5 is taken to be 90° and only the pitching portion of the mechanism is considered in this analysis.

Referring to Figure 4.20a, the optimal choice for link L6 can be seen to be is 90°. This is because, for any given length of link L7, the required angular acceleration on input link L5 to output a unit pitching acceleration is minimised when L6 is 90°. The effect of the length of link L6 on the required input torque is minimal, as seen in Figure 4.20b; thus the optimum choice for L6 is still taken to be 90°. For link L7, as its length increases, less input torque is required to produce a unit

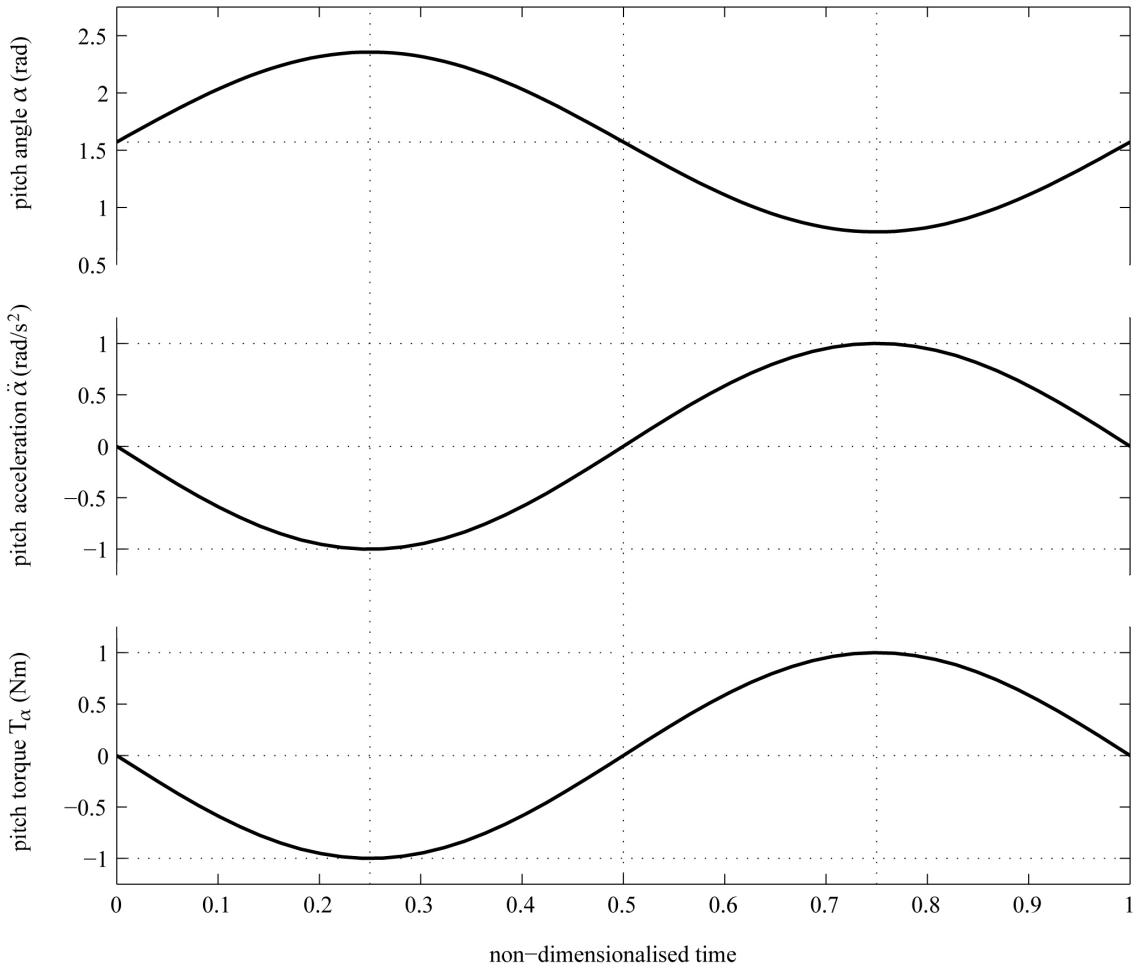

Figure 4.19: Pure pitching kinematics and required pitch torque; time is non-dimensionalised by the cycle period $T = 5.56s$

output pitch torque, however, a higher angular acceleration of the input link to achieve a unit pitching acceleration is required. As before, we want to design link L7 such that minimal input accelerations and torques are required, thus we want to minimise their sum, which is shown in Figure 4.20c. Here it can be seen that the optimal value for L7 is approximately 40°. However, more weight should be given to reducing required input accelerations, because in insect-like kinematics the pitching accelerations are by far the highest. For example, for the figure-of-eight kinematics in Figure 4.14, $max(\ddot{\phi}) \approx 9.5 \times 10^5 deg/s^2$ whereas $max(\ddot{\alpha}) \approx 2.8 \times 10^6 deg/s^2$. Thus, the choice of the length for L7 was reduced to 25°, which is at the lower end of the minimal region in Figure 4.20c. This leads to an approximately 50% rise in torque required compared to values when L7 = 40°, however, the required input acceleration on L5 is roughly halved. Another

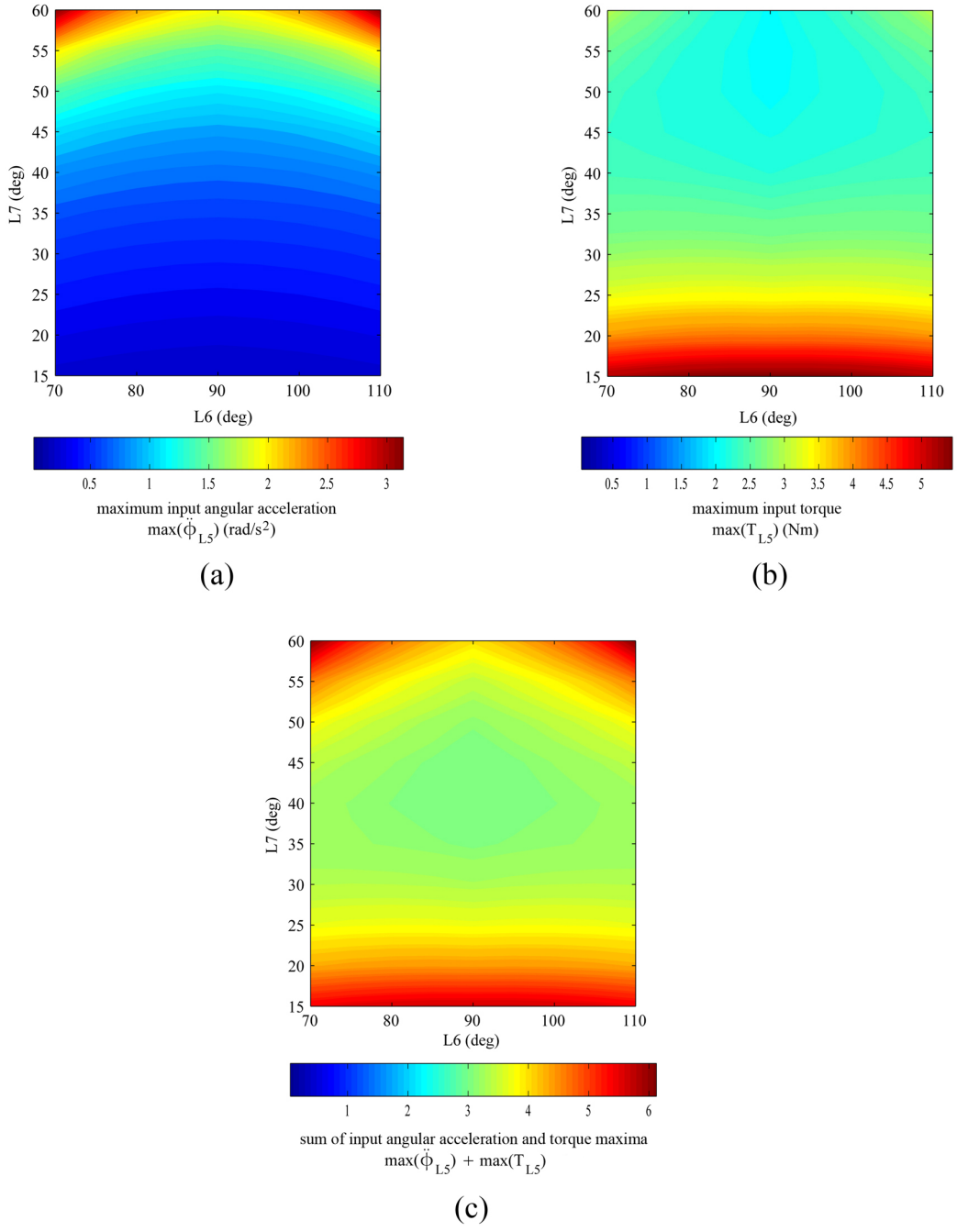

Figure 4.20: Effect of length of links L6 and L7 on (a) the maximum input acceleration and (b) torque required to output the kinematics and pitch torque in Figure 4.19, and (c) their sum

motivation for reducing link length L7 to 25°, is that it leads to a greater range of achievable plunge angles. The shorter this link is, the higher the wing can be plunged upwards before rocker link L7 collides with the top of link L1 or L2, which can be visualised with the aid of Figure 4.11.

Input Link L5

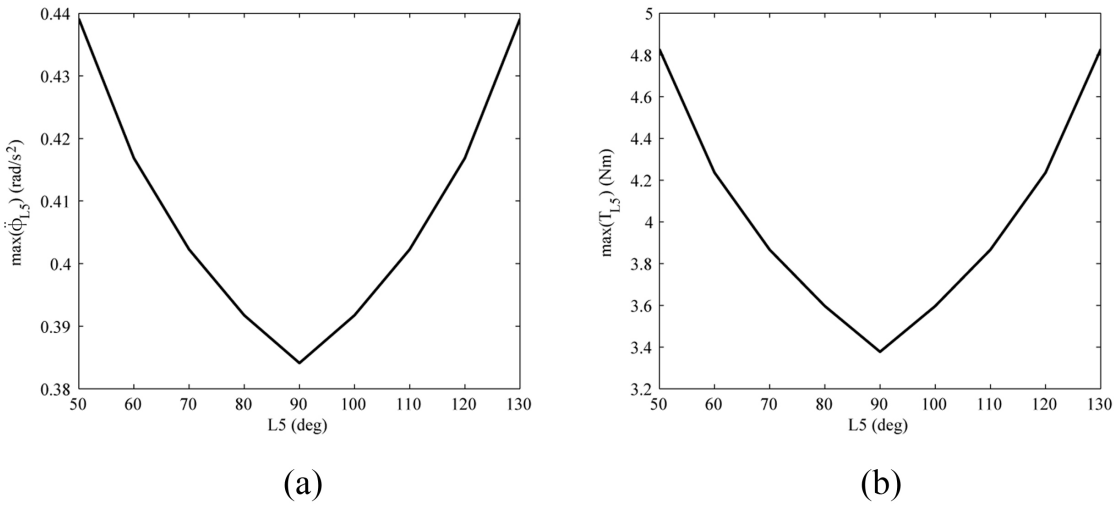

Figure 4.21: Effect of length of link L5 on the maximum input acceleration (a) and torque (b) required to output the kinematics and pitch torque in Figure 4.19

The input link L5 for the portion of the mechanism that enables pitching, also has the greatest effect on output pitching accelerations and torques delivered to the wing. The test case used to optimise the length of this link is the same as that used previously for links L6 and L7 with pure pitching. In the analysis for L5, the lengths of links L6 and L7 are taken to be 90° and 25° respectively, massless links are used, and only the pitching portion of the mechanism is considered. As seen in Figure 4.21, the optimal choice for the length of L5 is 90°, as it minimises both the required input angular acceleration, and torque required to output a unit pitch acceleration and unit pitch torque respectively.

4.2.7 Stress Analysis

Using the optimised lengths of links L1-L7 found previously, the final detailed design of the flapping mechanism was converged upon after performing a stress analysis of the components. Using the dynamic model on a given mechanism design, the reaction forces at the joints for each component were computed. This analysis included masses and moments of inertia of the links. With the computed reaction forces, stress analysis was performed on each part using SolidWorks. This was performed first using a coarse grid and then repeated with a fine grid to verify that the resulting factor of safety for each component was sufficiently high.

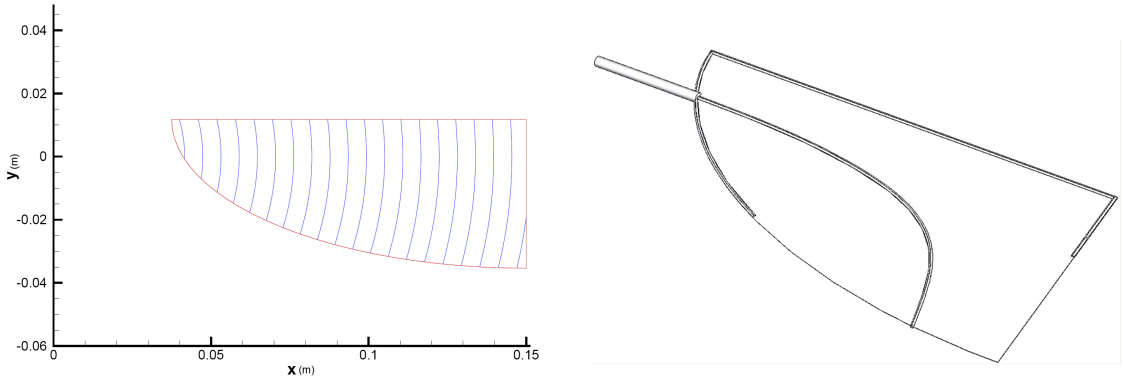

Figure 4.22: Wing design; a) planform for optimised FMAV from Ansari (2004) where 0,0 denotes the wing centre of rotation; b) isometric view of wing design used to compute loads for stress analysis

If parts failed then they were redesigned and the process was started over and repeated in an iterative loop until a successful design was achieved.

In this iterative process, a worst case scenario set of flapping kinematics, wing design, and expected aerodynamic forces were required in order to converge on a successful design. This was necessary to assure that the final design had an adequately high factor of safety to handle inertial forces from demanding flapping kinematics and aerodynamic forces. The flapping kinematics, wing geometry and aerodynamic forces used for this process will now be described. The flapping kinematics used in this iterative process were for a convex arc wing motion where the wingtip follows an inverted 'u'. The other kinematic parameters were a flapping frequency of $20Hz$, a respective stroke and plunge amplitude of 120° and 50°, angle of attack at mid-stroke of 30°, 0% rotation phase, and a constant angle of attack for 65% of the cycle. These kinematics were chosen because they were more demanding in comparison to other wingtip trajectories in terms of the maximum accelerations demanded by the mechanism.

The wing design used in this analysis was that identified by the unsteady aerodynamic model of Ansari (2004) for an optimized FMAV in air. This has a $12cm$ long wing with a reverse semi-ellipse planform shape and an aspect ratio of 6 which is illustrated in Figure 4.22a. Figure 4.22b is an isometric view of the actual wing design used in the analysis where the thickness of the spars was $0.9mm$, the membrane thickness was $0.1mm$ and the material was taken to be carbon fibre with a density of 0.002g/mm^3. The design of the wing spars was inspired by the wing design used on the Mk2 flapper of Galiński & Żbikowski (2005).

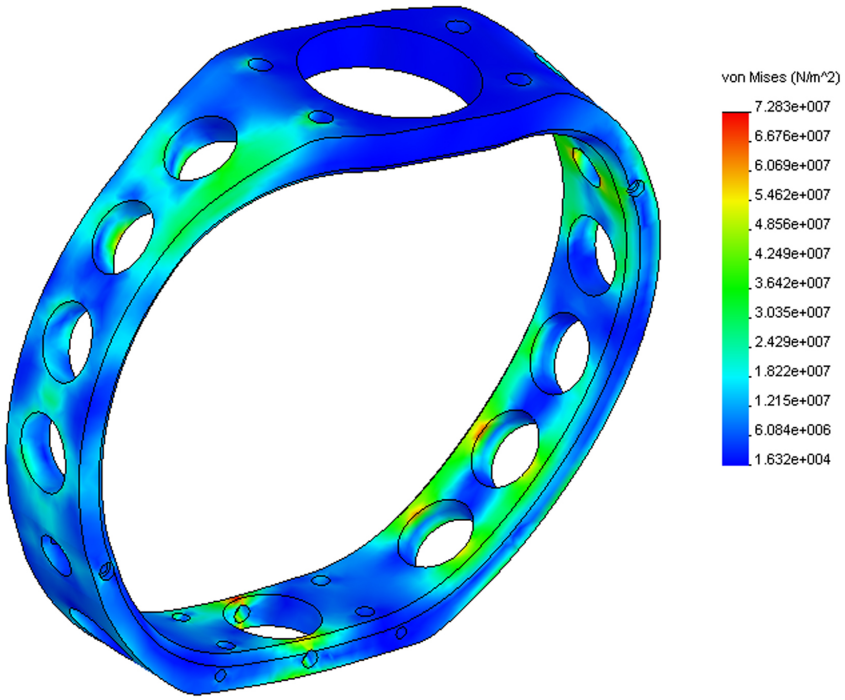

Figure 4.23: Stresses in input link L1 under worst case scenario flapping kinematics and aerodynamic forces

Aerodynamic forces on the wing were assumed to be a constant 2.5N for lift and 2.5N for drag acting at 73% span and 5.5mm back from the pitch axis. At this location, these forces create a stroke, plunge and pitch torque of 0.3Nm, 0.3Nm, and 0.194Nm respectively. These forces were chosen to act at this location because they closely approximate the peak values given from the unsteady aerodynamic model of Ansari (2004) for a 20Hz flapping frequency with a flat wingtip trajectory (wingtip follows a straight line) and using the same wing geometry described above. These values from Ansari's model are a peak lift, drag and stroke, plunge and pitch torque of 2.14N, 2.44N, 0.29Nm, 0.25Nm and 0.19Nm respectively. Although these values were obtained from a different set of kinematics than is used in this analysis, these forces and moments can be expected to be representative of the case here (Ansari, 2008). Furthermore, as these are peak values that are applied continuously throughout the flapping cycle, rather than mean values, a worst case scenario is employed, which in the end would yield a conservative factor of safety.

With these worst case scenario loads and flapping kinematics, a final design for the flapping mechanism was converged upon. The material used for the links

in this analysis was aluminium 6082 – $T6$, which has a yield strength of $255N/mm^2$ and a density of $0.0027g/mm^3$ (Harris, 1993). Drive shafts and pins were made from steel $EN3B$ which has approximately the same properties as steel $AISI1020$ (Goodland, 2008) which has a yield strength of $351.6N/mm^2$ and a density of $0.0079g/mm^3$. In the final design, the lowest factor of safety seen in any of the components was 1.28, and the average over all the components was 2.33. An example of the stresses in one for the components is shown in Figure 4.23, which illustrates the stresses in input link L1.

4.2.8 Final Detailed Design

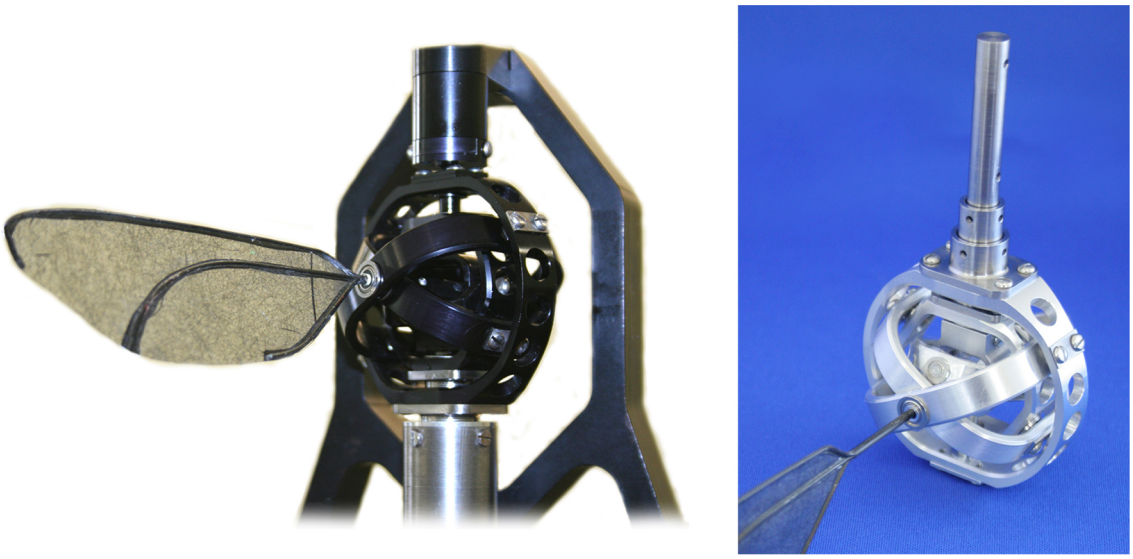

(a) (b)

Figure 4.24: Final flapping mechanism design; (a) mechanism anodised black and integrated into flapperatus; (b) mechanism on its own

Figure 4.24 illustrates the final design of the flapping mechanism, where it is shown on its own, and anodised black and integrated into the flapperatus. The overall diameter of the mechanism is $54.7mm$, and as used in the stress analysis, all linkages are made of aluminium 6082 – $T6$ and all pins and drive shafts are made from steel $EN3B$. As described in § 4.2.6, the lengths of links L1, L2, and L7 are 60°, 120° and 25°, while all other links (L3, L4, L5, and L6) subtend 90°. The range of motion of the mechanism enables plunge angles of ±25°, pitch angles from 30 – 150°, and stroke angles of $\pm\infty$ to be achieved. In practice, however, due

to the presence of other components such as a frame to mount the mechanism, a maximum range of stroke angles of ±90° is reasonable.

4.3 Complete System

The architecture of the complete flapperatus is illustrated in Figure 4.25. This shows the same systems discussed at the beginning of this chapter in the conceptual system design (Figure 4.1), however, Figure 4.25 illustrates the detailed system design and the components that make up each system. As before, the user inputs the desired kinematic parameters to define the flapping kinematics using the expressions given in Appendix A. Also, the user inputs the stroke angle ϕ_{cam}, which is the stroke angle in the flapping cycle at which it is desired to perform flowfield and instantaneous wing position measurements. Next, the flapping mechanism controller converts the flapping kinematics to input kinematics for the flapping mechanism using the expressions given in § B.1 in Appendix B. The controller then drives the flapping mechanism with these input kinematics, and the wing flaps. Meanwhile force measurements can be performed, as well as flowfield, and wing position measurements synchronised with mechanism position. As before, end outputs to the user are flowfield, mechanism and wing position, and mean lift measurements. Each one of the major systems including the flapping mechanism controller, mechanism position measurement system, flowfield / wing position measurement system, and the force measurement system will now be described in that order.

4.3.1 Flapping Mechanism Controller

The drive system of the flapperatus that controls the flapping mechanism is illustrated in Figure 4.26. Three concentric drive shafts connect to the input shafts (input links) of the flapping mechanism. Here, the outer, middle, and inner drive shafts connect to input links L1, L2 and L5 of the flapping mechanism respectively. Fixed at the end of each of the drive shafts is a 'drive pulley', each named appropriately. Each drive pulley is then coupled via a 1 : 1 cable drive to a 'motor pulley' fixed on the shaft of a servo motor. For each axis, the cable drive consists of two loops of cable that are turned through a set of smaller pulleys, and are

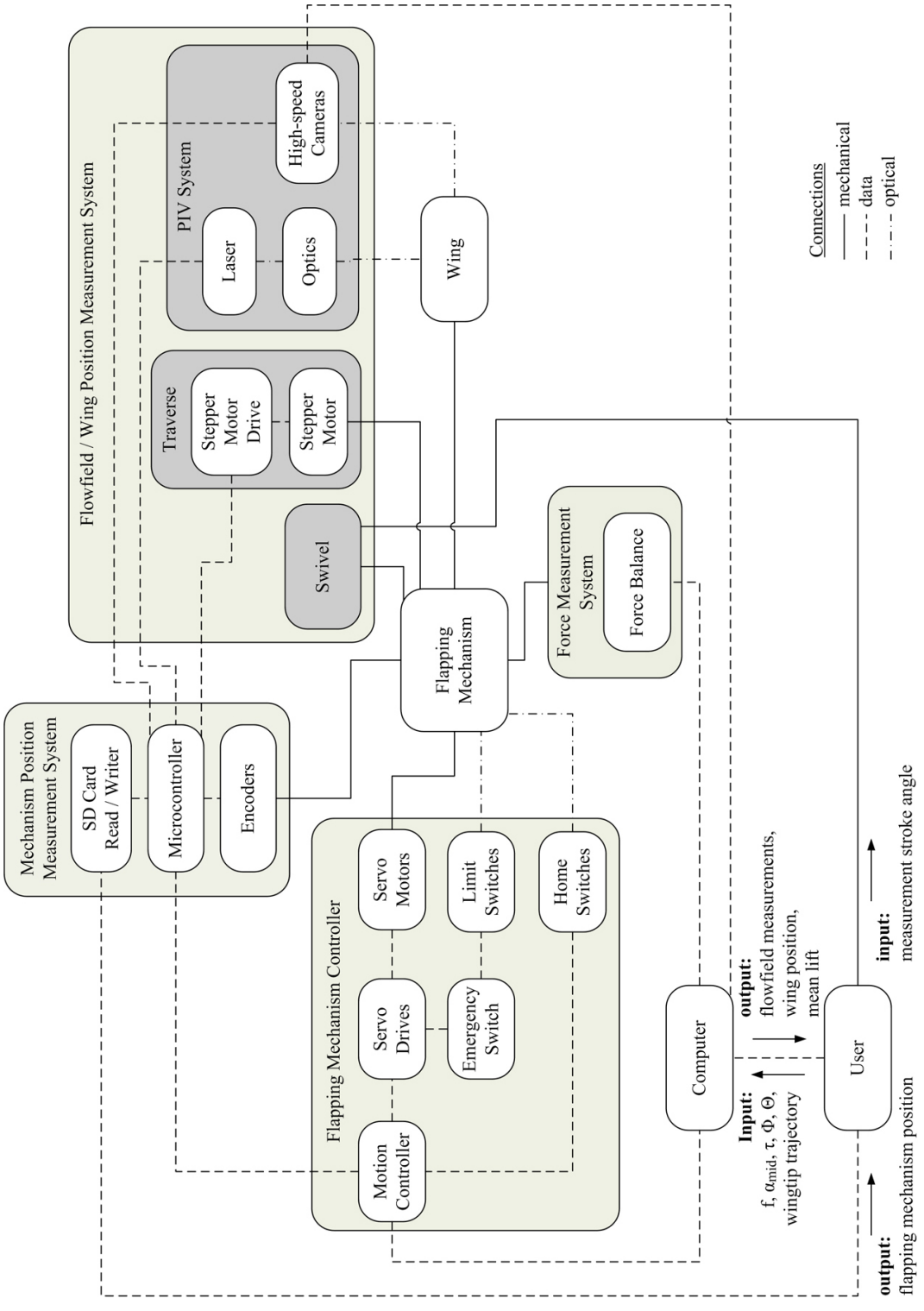

Figure 4.25: Flapperatus detailed system block diagram

fixed on opposite ends of the motor and drive pulleys. To prevent slippage, each loop of cable is clamped at both its drive and motor pulley ends. This is allowable because each drive shaft never rotates more that ±90°. An example set of these cable clamps for a single loop are labeled in Figure 4.26. The smaller pulleys that turn the cables at the servo motor end, are mounted to ball slides that allow these pulleys to be translated horizontally (via turning lead screws) to eliminate slack in the cables. The material used for the cables was Dyneema® thread.

The motors used were three 400*W SIGMAV* (*SGMAV*−04*ADA*61) servo motors from Omron, which have an instantaneous peak torque of 3.82*Nm* and a rated angular acceleration of $3.8 \times 10^6 deg/s^2$. Similar servo motors by Baldor were also considered, however, results from tests performed by the manufacturers showed that the motors from Omron had better performance when replicating insect-like kinematics. Each servo motor was driven by a SGDV (SGDV-2R8A11A) servo drive also by Omron, and all drives were controlled by a single Trajexia motion controller, by the same manufacturer.

As seen in the side view in Figure 4.26, home and limit switches are located behind the drive pulleys. Each switch consists of a slotted opto switch which breaks a circuit when the beam passing across the slot is cut. Notched disks are fixed to each one of the drive pulleys so that when a given drive shaft rotates to the appropriate degree, the notch on the attached disk will pass through the slot and trigger the switch. The home switches are connected to the motion controller (Figure 4.25), and they provide a positional reference for the system. When the system is started, the motion controller does not know the position of each of the drive shafts, so all shafts rotate in the positive stroke direction until each one of the axes triggers a home switch. At this point, the motion controller has established an absolute position for each one of the drive shafts. Each drive shaft is then rotated a known degree from the home switches until the wing reaches its neutral position (when $\phi = 0°$, $\theta = 0°$, $\alpha = 90°$). The limit switches serve a similar function. If one of the drive shafts rotates too far such that it approaches the limit of its range of motion, then its notched disk will trigger one of the limit switches. This then cuts a circuit connected through all the servo drives, and brings the motors to a halt. An emergency switch is also located in this circuit, so that the system can be stopped manually.

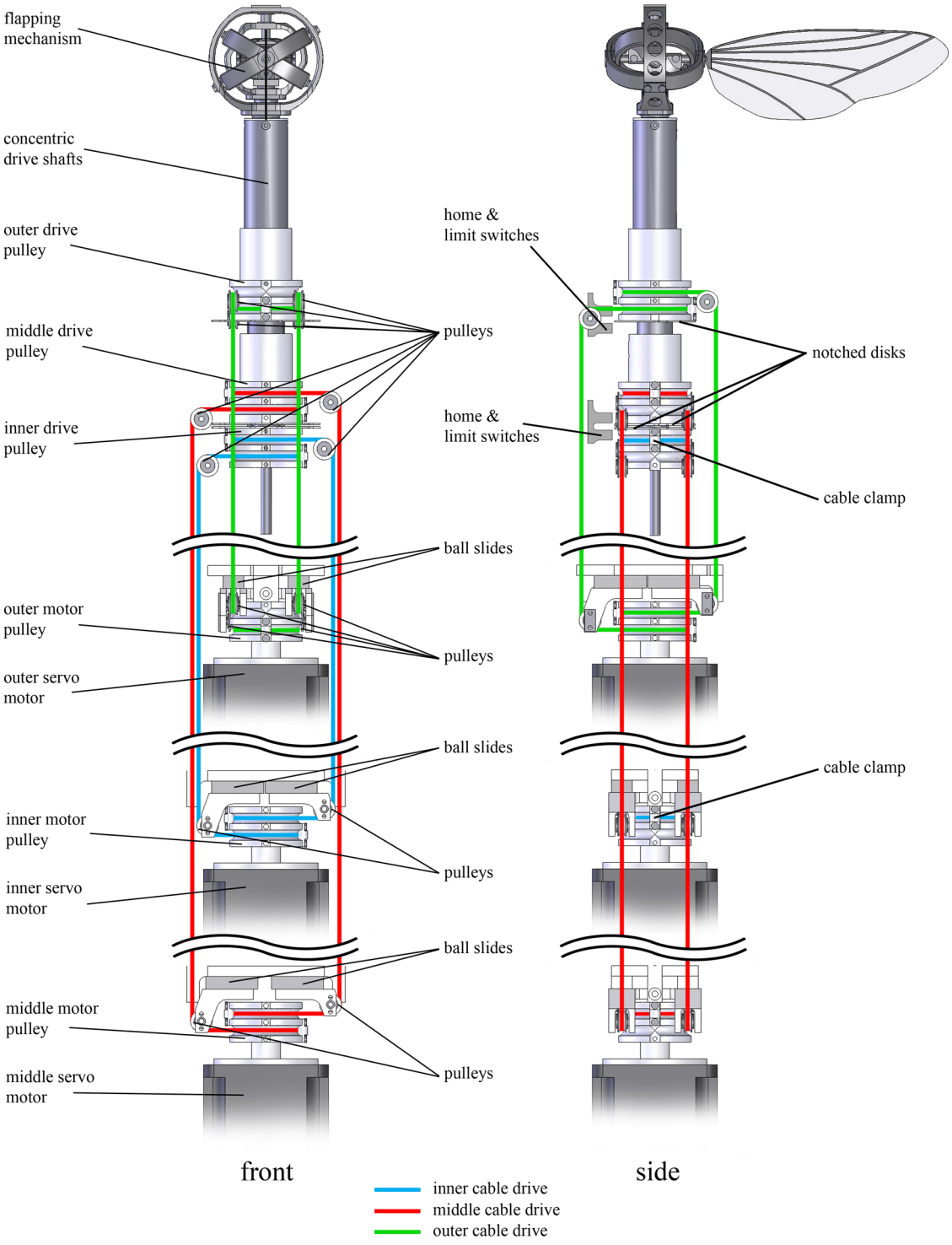

Figure 4.26: Flapperatus drive system

4.3.2 Mechanism Position Measurement System

The mechanism position is monitored via a set of encoders fixed to each one of the drive shafts. The encoder used on the outer and middle drive shafts was a 10000*PPR* (pulse per revolution) differential encoder by US Digital (model *E*6). On the innermost drive shaft a 4096*PPR* differential encoder also by US Digital (model *E*5) was used. A custom-made data acquisition system employing a 32-bit, 80*MHz*, 8-core microcontroller (Parallax Inc. protoboard no. 32212) which was custom programmed, was used to read the encoder positions and output the motion profiles to an SD card. As the microcontroller monitored the drive shaft angles, it also served the function of synchronising the mechanism position with flowfield and wing position measurements. Since the relation between the drive shaft angles and the output stroke, plunge and pitch angles of the flapping mechanism are known, data acquisition at a desired point in the flapping cycle can be triggered when the drive shafts reach the appropriate positions. For example, when it is desired to perform measurements at mid-stroke, the microcontroller triggers the flowfield and wing position measurement system when the drive shafts reach the positions that correspond to the mid-stroke point in the flapping cycle.

4.3.3 Flowfield / Wing Position Measurement System & PIV Setup

The flowfield and wing position measurement system is illustrated in Figure 4.27a, and it largely consisted of a stereoscopic *PIV* system comprised of two high-speed cameras and a laser-generated light sheet. See Appendix C for a description of the *PIV* flowfield measurement technique. The cameras used were PowerView^{TM} $HS-3000$ high-speed cameras (model 630064) with a resolution of $1024\times1024 px^2$, and were obtained from the EPSRC equipment loan pool. The laser was a New Wave Research Gemini Nd:YAG double pulsed laser with a wavelength of $532nm$, which was interfaced with a LaserPulse^{TM} light arm (model 610015) to convert the beam to a light sheet via a cylindrical and spherical lens at the exit of the light arm (see Figure 4.27b and c). As seen in Figure 4.27a, the PIV setup utilised an angular camera set-up. The right camera was aligned such that its axis was

normal to the light sheet, whereas the left camera's axis made a 48.5° angle with the right camera axis. In addition, the body of the left camera was rotated relative to the lens according to the Scheimpflug condition (described in Appendix C). The cameras were oriented to view a common area centred around the wing of approximately $95 \times 95mm^2$. A $60mm$ lens at an $f\#$ of 2.8, and a $105mm$ lens at an $f\#$ of 4 were used for the right and left cameras respectively.

Referring to Figure 4.27a, the flapping mechanism, drive shafts, cable drives and servo motors were mounted to a support frame. The wing was aligned such that it was 'edge-on' to the right camera when it was at the mid-stroke position (when $\phi = 0°$ and $\theta = 0°$) and the measurement stroke angle ϕ_{cam} (which will be explained shortly) set by the swivel position was zero. Recalling the coordinate systems from § 2.1.2 (page 17), the inertial $X_I Y_I Z_I$ frame is fixed to the support frame, and the xyz axis fixed to the wing rotates with respect to this inertial frame. The same $x_{cam}y_{cam}z_{cam}$ frame used in Appendix C is also employed here, which is the *PIV* measurement coordinate system and it is fixed in space. Again, the laser light sheet is coincident with the $y_{cam}z_{cam}$ plane, thus, measured velocity components are in the x_{cam}, y_{cam}, z_{cam} directions.

As seen in Figure 4.27a, the support frame was mounted on a swivel. This enables the inertial coordinate system, and hence, the wing to be rotated relative to the $x_{cam}y_{cam}z_{cam}$ measurement frame. The swivel position denoted by the measurement stroke angle ϕ_{cam}, is set with the aid of a protractor at the base of the support frame as seen in Figure 4.27a. This angle sets the point in the flapping cycle at which measurements are performed on the wing. For example, to perform measurements when the wing is at a stroke angle of $-60°$, the support frame is rotated 60° in the positive stroke direction, giving a measurement stroke angle of $-60°$. It should be noted that the measurement stroke angle is not always equal to the wing's stroke at the desired point in the flapping cycle due to wing flexion, which will be explained in more detail in § 5.2.

The support frame was also mounted on a traverse, which allowed the inertial axis and the wing to be translated relative to the measurement frame in the $\pm x_{cam}$ direction. This enabled flowfield measurements to be performed in a volume surrounding the wing, rather than just a single plane. In addition, raw images obtained in the *PIV* data acquisition provided a means to reconstruct the instantaneous wing position. By locating the position of the leading and trailing edges

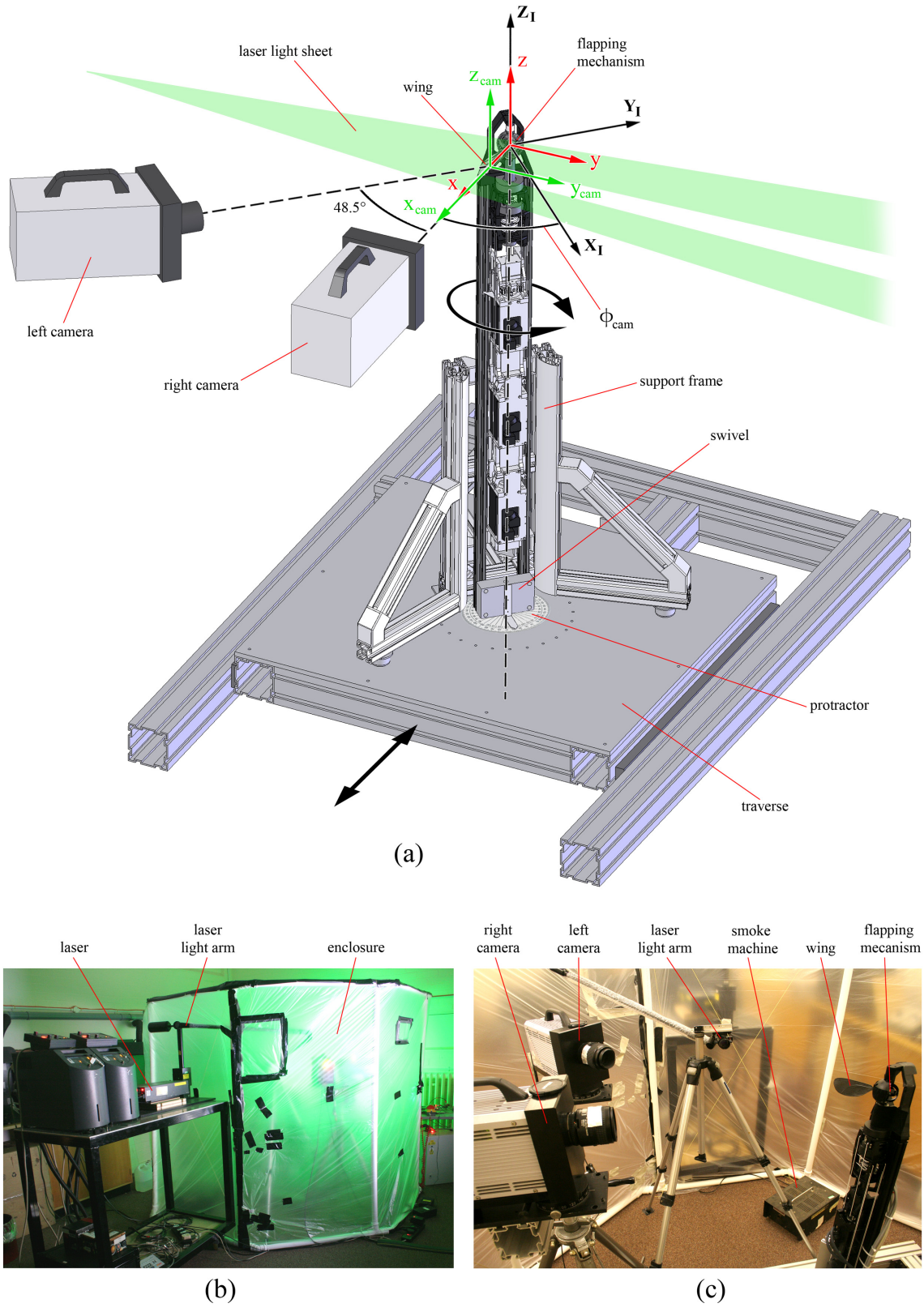

Figure 4.27: Flowfield / wing position measurement system & PIV setup; (a) schematic of hardware setup and coordinate systems; (b) photo of outside of setup illustrating enclosure; (c) photo inside enclosure illustrating hardware setup

in the many images taken along the span which essentially reveal local $2D$ slices along wing, the instantaneous wing position is reconstructed. Such a method was also employed by Poelma et al. (2006). This wing position reconstruction method is described in greater detail in § 5.2.

The flapperatus was placed inside an hexagonal enclosure (Figure 4.27b) which had a width of approximately $2.5m$ and a height of $1.8m$. This was designed to isolate the apparatus from outside disturbances and contain the seeding, whilst minimising wall interference effects. Inside the chamber the flapping wing was positioned over 15, 6 and 13 wing lengths from the walls, ceiling and floor respectively. The seeding used was smoke generated from a smoke machine (see Figure 4.27c) using global mix smoke fluid by Le Maitre.

It should be noted that the experiments which investigated wing planform shape effects used a different *PIV* system to that described previously, due to the limited availability of the previous system. These experiments used a spherical and cylindrical lens to generate the laser light sheet rather than a light arm. In addition, the cameras used were two FASTCAM-ultima APX high-speed cameras with the same resolution as the previous (PowerView^{TM}) cameras of $1024{\times}1024px^2$. These cameras were used in the same angular setup as shown in Figure 4.27a, however they were set up to view a larger common area of approximately $120 \times 120mm^2$, and the angle between the cameras was set to $45°$. The same laser, camera lenses and aperture settings were used.

4.3.4 Force Measurement System

The force measurement system consisted of a Nano 17 (FTD-Nano-17 SI-12-0.12) six-component force balance by ATI. Lift was measured using the vertical component which had an operational range of $\pm 17N$ and a resolution of $0.78mN$. The force balance was mounted to the support frame and the top of the flapping mechanism as illustrated in Figure 4.28a. Figure 4.28b depicts a free-body diagram of the mechanism and its drive shafts and pulleys. It can be seen that the tension forces from the cable drives exist only in the horizontal plane, thus the flapping mechanism and drive shafts are unrestrained in the vertical direction, except due to the connection to the support frame via the force balance. Thus vertical forces

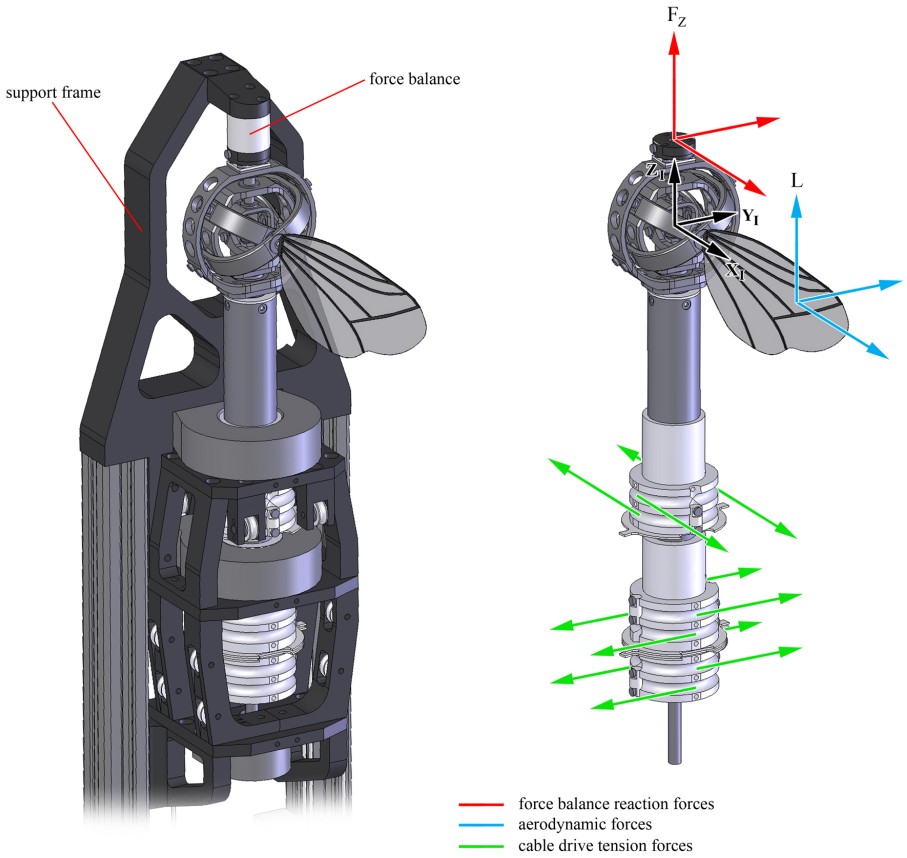

Figure 4.28: Force measurement system illustrating (a) connection of flapping mechanism to support frame through a force balance and (b) a free body diagram of the flapping mechanism and drive shafts and pulleys

(F_z) read by the force balance are lift forces. Raw voltages from the balance were acquired with an NI-PCI-6221 data acquisition board by National Instruments.

4.3.5 Wings

The wing used on the flapperatus for the majority of the experiments is illustrated in Figure 4.29b. This wing was designed and manufactured by Galiński & Żbikowski (2007), and its planform originated from the 'four-ellipse' shape of Pedersen (2003) (top of Figure 4.29a) which consisted of four elliptic arcs. However, due to mechanical limitations, portions of the original four-ellipse shape are truncated at the root end of the wing (Galiński & Żbikowski, 2007) resulting in the actual wing design as illustrated. This wing design will be referred to as the 'four-ellipse'.

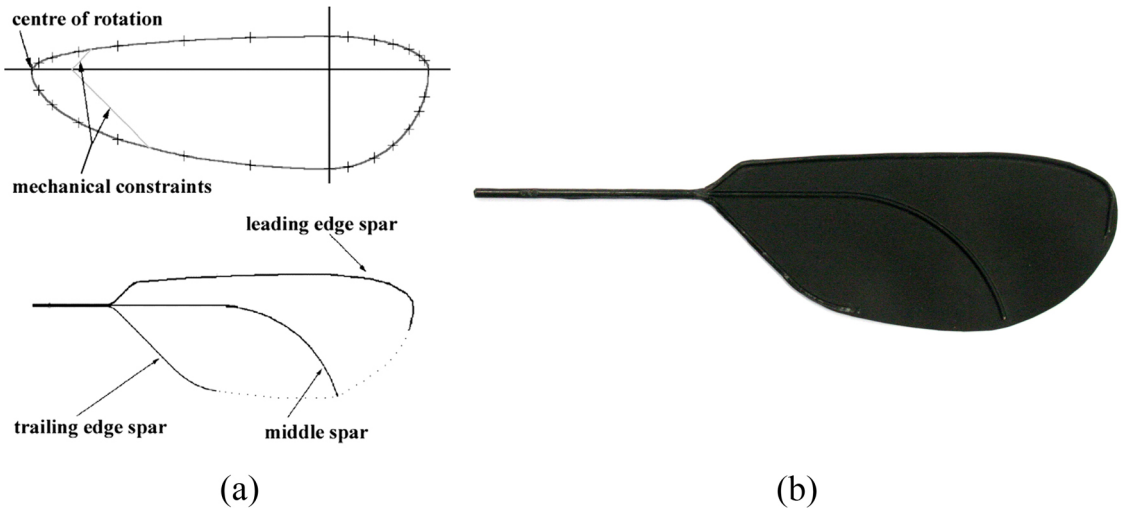

Figure 4.29: Four-ellipse wing design; (a) original four-ellipse shape after Pedersen (2003) with truncated areas due to mechanical constraints and wing structure (adapted from Galiński & Żbikowski (2007)); (b) actual manufactured wing used in experiments

As illustrated, the structure of the wing consisted of a 2*mm* diameter root spar which branches into three separate spars at the leading edge, middle, and trailing edge of the wing each with a 1*mm* diameter. This spar layout was inspired by entomological literature, which suggests that insect wings generally derive their strength from a main leading- and trailing-edge and middle spar (Galiński & Żbikowski, 2007). The root spar which forms the pitch axis, was located at approximately the quarter chord point of the maximum chord. Between the spars was a 0.1*mm* thick membrane. The wing was designed to be as rigid as possible so as to avoid effects due to wing flexibility, thus simplifying experiments. A carbon roving and epoxy composite was used to form the spars, while the membrane was made of a carbon tissue and epoxy composite. The entire wing was made in one step with a mould, thus creating a continuous composite structure. The wing length from root to tip was 82*mm*, and the wingtip measured 106*mm* from the centre of rotation when mounted on the flapping mechanism. In addition, the mean chord length was 27.7*mm*, the wing area was 2270mm^2, and the aspect ratio was 5.9.

Additional wing designs were made to study the effects of wing planform shape. These are illustrated in Figure 4.30, and include a 'reverse-ellipse', rectangle, four-ellipse, and ellipse planform shape. The reverse-ellipse, and ellipse planforms are simply made from half ellipses, but with opposite ends forming

the wingtip, and the four-ellipse is the same planform as described previously. Length, mean chord, aspect ratio and wing area for all shapes are given in Figure 4.30. All wings were designed to have a relatively constant mean chord, length and area giving a constant aspect ratio of about 6. It should be noted here that the reverse-ellipse planform had a slightly larger area due to the interface between the spar and the wing near the root section. In addition, for all planforms the pitch axis was placed at the quarter-chord of the maximum chord.

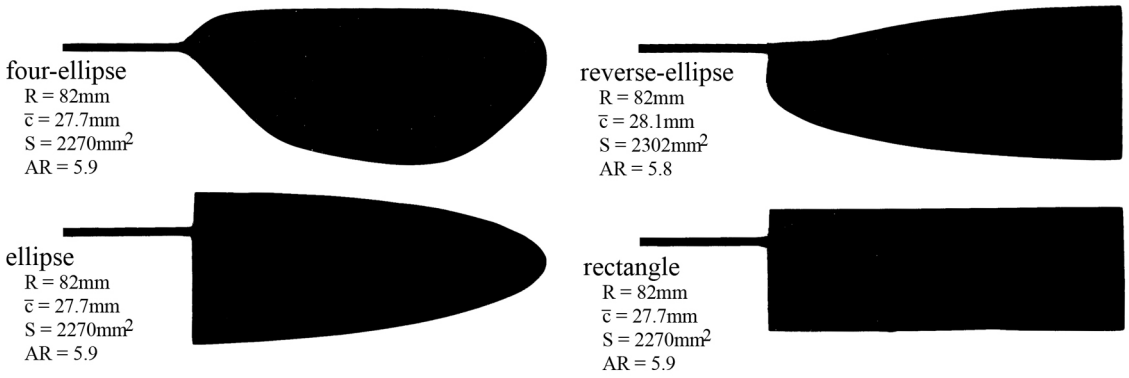

Figure 4.30: Additional wing planform shapes

The structure of the additional wing designs differed from the original four-ellipse wing design discussed at the beginning of this section, thus the four-ellipse wing was also made with this new structure to match the new wings. Again, to minimise effects due to flexibility, these additional wings were made as stiff as possible. This was accomplished by sandwiching a 2*mm* diameter carbon-fibre rod between two sheets of carbon-fibre cloth infused with epoxy resin, and cured in a mould. The resulting membrane thickness was 0.45*mm*. When mounted on the flapping mechanism, the wingtip of each wing design measured 106*mm* from the centre of rotation.

4.4 System Performance

This section discusses the performance of the flapperatus, starting with results from high-speed photography illustrating the kinematics achieved by the wing. Following this, the repeatability of the mechanism and wing position are discussed.

4.4.1 Kinematics

The flapping mechanism and flapperatus as a whole exhibited very good performance when executing the desired flapping kinematics. Figure 4.31 illustrates a reconstruction of the actual wingtip trajectory and angle of attack (from the camera's perspective) at 50% span for a number of cases at a $20Hz$ flapping frequency. This was obtained with high-speed photography filmed at $1200fps$. Markers were placed at the wingtip and leading and trailing edges at 50% span to make these points visible in individual frames, enabling the wingtip trajectory and angle of attack to be recovered. It should be noted that around mid-stroke the points marking the angle of attack were not visible, thus angle of attack is not shown around this point in the cycle. As seen in these figures, even at the high flapping frequency of $20Hz$, the motion of the wing is smooth and it successfully achieves insect-like flapping-wing kinematics.

4.4.2 Mechanism & Wing Position Repeatability

In addition to the motion of the flapping mechanism being very smooth, its position was also very repeatable. To quantify its positional repeatability, the flapping mechanism's drive shaft angles were measured (via the encoders) throughout $\sim$ 1000 flapping cycles. The flapping kinematics employed consisted of a flat wingtip trajectory, and with kinematic parameters (of the mechanism output kinematics) of $f = 20Hz$, $\Phi_{mec} = 131.7°$, $\Theta_{mec} = 1.2°$, $\alpha_{mid_{mec}} = 45.4°$, and $\tau_{mec} = 6.1\%$. By averaging the resulting wing positions, a time history of the mean wing position throughout a single flapping cycle, was obtained. This will be referred to as the 'average cycle'. The stroke, plunge and pitch angle over the average cycle is illustrated in Figure 4.32 (shown by markers) along with these angles over the 1000 flapping cycles measured (solid lines). The width of the solid lines provides an indication of the variability of each angle.

Over the many cycles measured, the difference of the stroke, plunge and pitch angles from those at the corresponding point in the average cycle were determined. Ultimately this revealed that the stroke, plunge and pitch angles had a standard deviation of 0.1°, 0.07° and 0.17° respectively. This analysis was repeated with a set of flapping kinematics defined by the same parameters used previously, however a more demanding figure-of-eight wingtip trajectory with

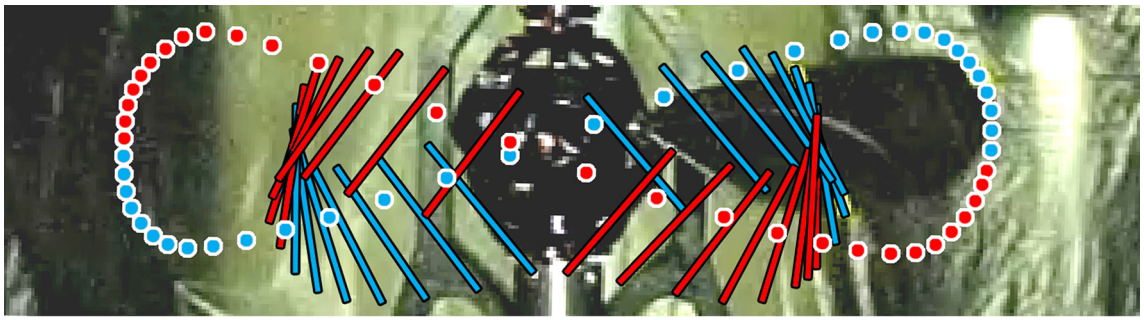

(a) figure-of-eight

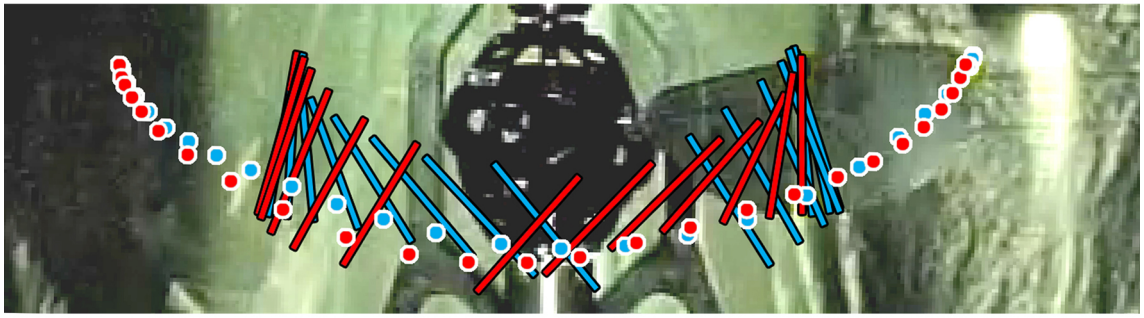

(b) concave arc

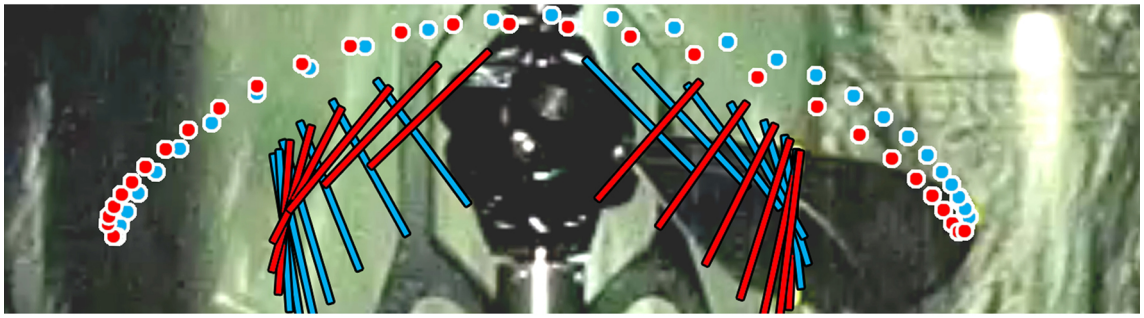

(c) convex arc

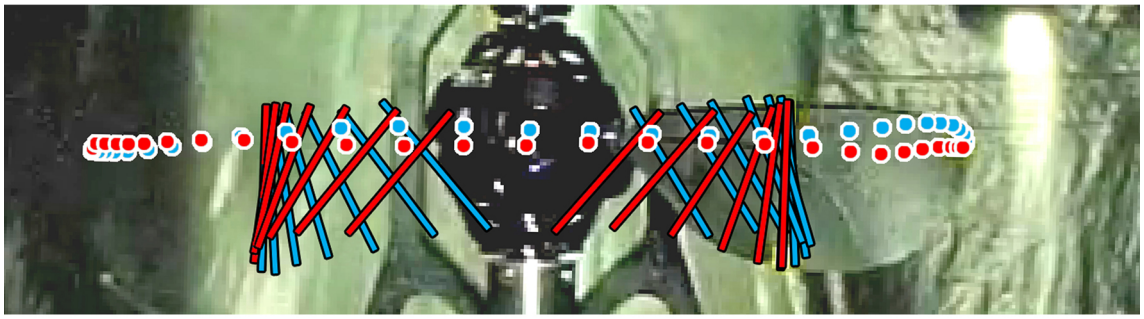

(d) flat

downstroke wingtip trajectory
upstroke wingtip trajectory
downstroke angle of attack at 50% span
upstroke angle of attack at 50% span

Figure 4.31: Wingtip trajectories executed at a 20Hz flapping frequency, and angle of attack recovered from high speed photography filmed at 1200fps for a (a) figure-of-eight trajectory, (b) concave arc trajectory, (c) convex arc trajectory, (d) flat trajectory; dots mark the position of the wingtip, while lines indicate angle of attack (as seen from the camera) at 50% span; red denotes downstroke (left to right) while blue denotes upstroke (right to left)

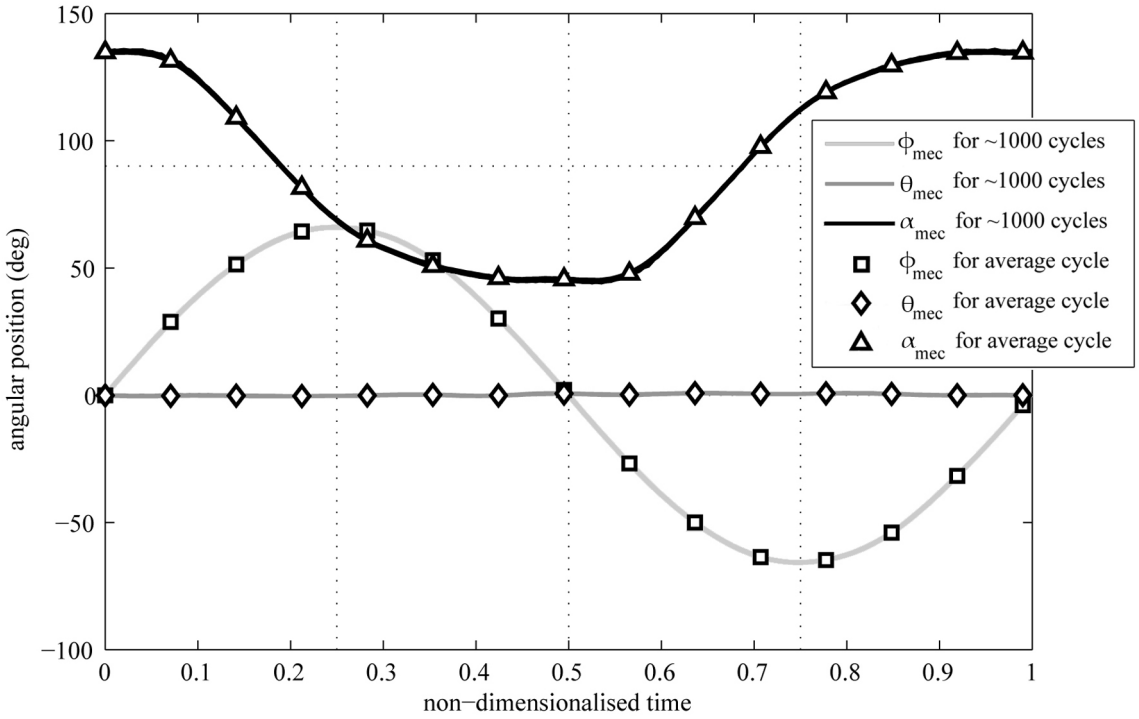

Figure 4.32: Repeatability of flapping mechanism output kinematics; solid lines show stroke, plunge and pitch angles over ~ 1000 flapping cycles, markers show these angles for the 'average cycle' (average of the ~ 1000 cycles); thickness of the solid lines provide an indication of variability of stroke, plunge and pitch; time is non-dimensionalised by the flapping period T = 0.05*s*

Θ_{mec} = 25.2° was employed instead of a flat one. The results from this test were very similar to those found with the flat wingtip trajectory, as a standard deviation of 0.04°, 0.06° and 0.17° were found for the stroke, plunge and pitch angle. Thus, taking the worst values, the repeatability of the stroke, plunge and pitch angle (from the mechanism output kinematics) are 0.1°, 0.07° and 0.17° respectively. This is a good result because it indicates that in addition to flapping kinematics, kinematic parameters can also be held virtually constant.

The repeatability of the flapping mechanism position and its output kinematics translated to a very repeatable wing position. This is illustrated with the aid of Figure 4.33, which depicts raw images at mid-stroke at ~ 90% span for a flat wingtip trajectory at 20*Hz*, as taken by the left camera. Figure 4.33a shows an image from one exposure (artificially made red), Figure 4.33b illustrates the sum of 15 exposures taken over 15 flapping cycles, and Figure 4.33c is the first figure (a) overlaid on top of the second figure (b). The solid band of light in all images is the intersection between the laser light sheet and the wing. Here the sum of many

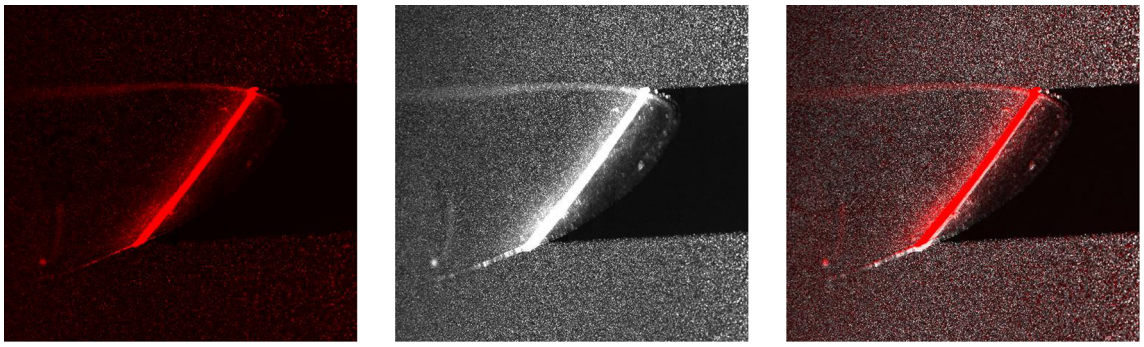

Figure 4.33: Wing position repeatability seen at mid-stroke at 90% span for flat wingtip trajectory at 20*Hz*; in all cases the solid band of light (red or white) is the intersection between the laser light sheet and the wing; (a) raw image from one exposure from left camera (colour is artificially made red); (b) sum of 15 exposures from left camera (taken over 15 flapping cycles); (c) single exposure overlaid over top of sum of 15 exposures, the comparison between these images provides an indication of wing position repeatability

exposures is computed for n images as $max(I_1, .., I_n)$, where for a given image, I is an array representing the intensity level at each pixel. Thus, for a given pixel in the 'summed' image, the sum is computed by taking the maximum intensity value at that pixel across the n separate exposures.

The summed image in Figure 4.33b provides an indication of the wing position repeatability. Across 15 flapping cycles, the intersection between the light sheet (which is fixed in space) and the wing falls at the same location in the image giving a band of light that is of similar height and thickness to a single exposure (Figure 4.33a). This is especially shown in Figure 4.33c, where the single and summed exposures are directly compared showing that the light sheet and wing intersection location is very repeatable, thus the wing position is also very repeatable. If the wing position were significantly variable then the white band of light in the summed image would be much wider and / or taller in comparison to a single exposure.

As will be seen later in Chapter 6, recovered flapping kinematics were very comparable to the mechanism output kinematics, indicating that the wing faithfully follows the flapping mechanism output. The actual degree to which the flapping kinematics differed from the mechanism output kinematics due to flexibility will be addressed later in § 5.4.

4.4.3 Summary & Conclusions

This chapter has outlined the design and development of the flapping-wing mechanical model, the 'flapperatus'. A novel flapping mechanism was conceived which gives separate control of each of the wing's three degrees of freedom (stroke, plunge, and pitch) and, hence, enables adjustable kinematics. After a kinematic analysis was performed, and a dynamic model was developed, the form of the flapping mechanism was arrived upon by optimising the design of each component such that required input torques and angular accelerations on the input links, are minimised for a given set of flapping kinematics. The final detailed design of the components was reached after performing a stress analysis with loads obtained from the dynamic model and assumed worst-case-scenario aerodynamic loads. The flapperatus contained all of the necessary hardware to drive the flapping mechanism, including cable drives and servo motors, and it interfaced with mechanism position, wing position, aerodynamic force, and flow-field measurement systems. The performance of the flapperatus was very good, as it was shown that desired insect-like flapping-wing motions were achieved smoothly, with a high degree of repeatability up to the maximum 20Hz flapping frequency.

Chapter 5

Experimentation

This chapter begins with a description of the experimental programme. Procedures used in conducting measurements are then outlined. Following this, a description of the *PIV* processing and analysis applied to the flowfield measurements is given. Finally, the chapter ends with an uncertainty analysis on the measurements performed in the study.

5.1 Experimental Programme

In this section, the experimental programme outlined to meet the research aims listed in Chapter 3 is described. This is divided into four main stages, beginning with the investigation of the effects of flapping kinematics on mean lift, followed by a study of the flow evolution throughout a half-stroke. Next is a stage investigating effects from flapping kinematics on the flow structures generated, followed by wing planform shape effects on the flows.

5.1.1 Kinematic Effects on Mean Lift

The experimental programme began with establishing the effects of flapping kinematics on the mean lift generated at the *FMAV* scale. This was performed by beginning with a baseline set of kinematics and then sequentially varying individual kinematic parameters while keeping all others relatively constant to observe the resulting change in mean lift. The baseline kinematics used are illustrated in Figure 5.1, and were based on the baseline kinematics used in the analytical parametric study of Ansari et al. (2008b). In addition, these were similar to the kinematics previously identified to be optimal for generating lift in Sane & Dickinson (2001). The kinematics identified by Sane & Dickinson (2001) were a flat wingtip trajectory, with $\Phi = 180°$, $\alpha_{mid} = 45°$, $\tau = +5\%$ and 'flip duration' of 10%. Here 'flip duration' is the time taken for pitch reversal to occur as a percentage of the flapping period T. For this investigation, this parameter was approximately 50%.

Although these results by Sane & Dickinson (2001) were obtained at a much lower Reynolds number, on the order of 10^2, it was felt that kinematics similar to theirs would likely be close to optimal at the *FMAV* scale. Thus, using such baseline kinematics would be an appropriate point from which to start a parametric study. Kinematic parameters that were investigated included flapping frequency, angle of attack at mid-stroke, rotation phase, stroke amplitude, and plunge amplitude with a figure-of-eight wingtip trajectory. The actual values tested for each test case, are listed later in Chapter 6. Test cases were performed at mean Reynolds numbers ranging form $\bar{Re} \approx 4000 - 21000$, where most were performed at the upper end of this range.

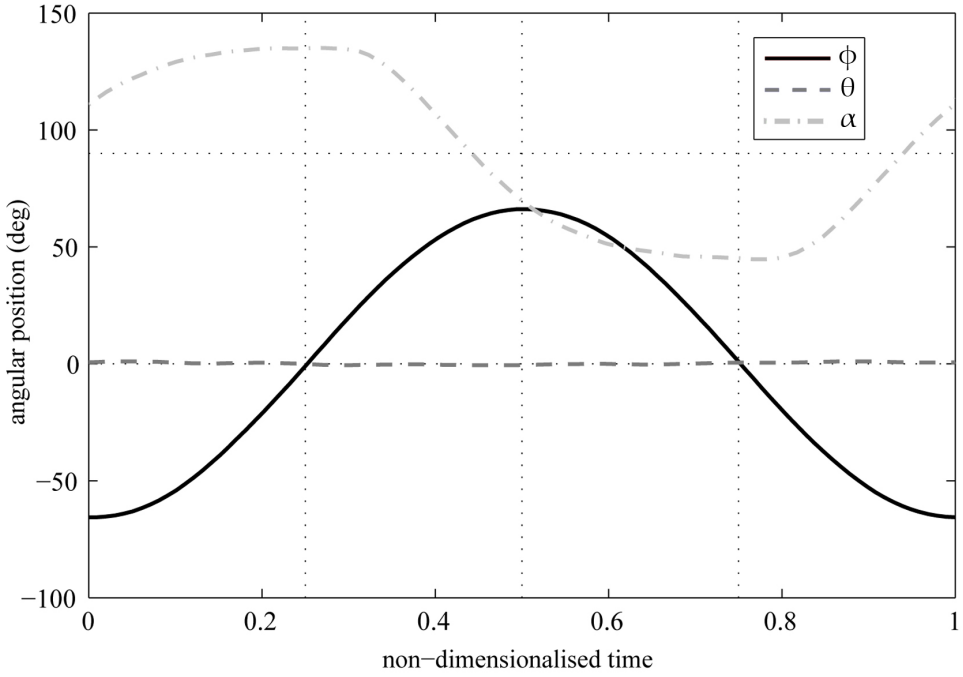

Figure 5.1: Baseline flapping kinematics; $f = 20Hz$, $\Phi_{mec} = 131.8°$, $\Theta_{mec} = 1.7°$, $\alpha_{mid_{mec}} = 45.7°$, $\tau_{mec} = 6.1\%$; time is non-dimensionalised by the flapping period $T = 0.05s$

It was originally envisaged that the flapperatus would be capable of synchronising lift measurements with wing position, which would provide a means to obtain plots of instantaneous lift forces over a flapping cycle. This would be achieved by first measuring pure inertial forces with a 'dummy' wing (e.g. a simple rod) with negligible aerodynamic lift force that has the same mass, centre of gravity and moment of inertia as the real wing. With synchronous force and wing position data, these inertial values could then be subtracted from raw force measurements with the real wing to obtain the instantaneous aerodynamic

forces, since the phase relationship is known. However, this capability was not implemented into the flapperatus. Thus, instantaneous plots of lift could not be obtained because the phase relationship between readings of pure inertial forces and those with inertial and aerodynamic forces, is unknown, and hence, they cannot be subtracted. Instead, in this study, mean lift values were simply obtained by averaging the lift readings. In doing so, inertial forces average out to zero when symmetric kinematics are employed, which was the case here.

Actual mechanism output kinematics for all the cases tested were recovered after mean lift measurements were performed. Although kinematic measurements were recovered in separate experimental runs to the lift measurements, the kinematics obtained still provide an accurate history of the kinematics during the force measurements owing to the high repeatability of the flapping mechanism and wing as described at the end of Chapter 4.

5.1.2 Flow Evolution

To address the topics of *LEV* stability, breakdown and axial flow at the *FMAV* scale, the next stage of the experimental programme conducted a detailed investigation of the flow evolution over the wing at $\bar{Re} \approx 15000$. This was performed by taking dense flowfield measurements along the wingspan at twelve instances evenly spaced in time over a half-stroke. The result of this was a spatially and temporally detailed picture of how the three-dimensional flow structures, such as the *LEV* and tip vortex, form and evolve over time as the wing executes a half-stroke. Thus, from this information, any potential *LEV* shedding, breakdown and axial flow can be observed and described. The flapping kinematics used for this investigation were the baseline kinematics shown previously, but with a smaller stroke amplitude of $\Phi = 120°$. A smaller stroke amplitude was used so that measurements throughout the half stroke would be closer temporally.

5.1.3 Kinematic Effects on Flow Structures

The next stage of the experimental programme was to determine how the observed trend of the flow evolution and the characteristics of the flow structures (found from the pervious stage) changed when flapping kinematics were altered. Of

greatest interest was the effects on the *LEV*. This investigation followed the same format to the study of flapping kinematics effects on lift, where the same baseline kinematics were used and kinematic parameters were sequentially varied in the same manner while others where held virtually constant at the baseline values. The same test cases were used so that flowfield measurements would complement the mean lift measurements, and provide further insight into the lift trends observed. Flowfield measurements along the wingspan providing a volume of velocity data were performed at mid-stroke for most of the test cases. Measurements were performed here because the flow typically reaches a quasi steady-state around mid-stroke, and most of the lift is produced during this phase of the cycle, so the flowfield at mid-stroke was felt to provide a good representation of the 'mean lift-generating' flow. However, for test cases varying rotation phase in particular, flowfield measurements were performed along the wingspan for six points in time throughout a half-stroke because this parameter was expected to have a significant impact on the flow evolution. It was desired to capture any such effect with numerous flowfield measurements.

5.1.4 Wing Planform Effects on Flow Structures

The end of the experimental programme addressed the effects of wing planform shape on the flows generated. As before, the same baseline kinematics were used, but with a lower flapping frequency of 15*Hz*. The wing planforms presented in § 4.3.5 were used, and flowfield measurements along the wingspan were performed at the mid-stroke position, as in the previous stage. As mentioned in § 4.3.3, this investigation used a different *PIV* system to that used in the other experiments.

5.2 Experimental Procedures

The procedures used in acquiring experimental data will be presented in this section. First, the procedure used when performing mean lift measurements will be outlined. This is followed by the procedure used for conducting flowfield measurements across the wingspan. Lastly, the method in which the instantaneous wing position and flexion is obtained from raw images is described.

5.2.1 Force Measurement

For each test case, vertical force was acquired from the force balance at a rate of $1200Hz$ over a period of more than 150 flapping cycles. This sampling rate was sixty times greater than the maximum flapping frequency, which is sufficiently high when compared to the cut-off frequencies used in similar experiments (Dickinson et al., 1999; Sane & Dickinson, 2001). Three minutes prior to and three minutes following each data acquisition, unloaded measurements were taken. This was done to detect any voltage drift in any of the force balance's channels and then correct the force measurements by interpolating between the unloaded readings before and after the data acquisition. Mean lift for each test case was obtained by simply averaging the acquired data. As mentioned before, when averaging the acquired force data, inertial forces from the wing and mechanism rapidly accelerating and decelerating will cancel since they are symmetric.

5.2.2 Flowfield Measurement

Before proceeding, a reader unfamiliar with the *PIV* flowfield measurement technique should review Appendix C. The first step in the experimental procedure for flowfield measurements was to rotate the flapperatus via the swivel to the appropriate measurement stroke angle so that the right camera would view the wing 'edge-on' at the desired point in the flapping cycle. The manner in which this was performed will be explained using Figure 5.2. This depicts the difference between the mechanism output $x_{mec1}y_{mec1}z_{mec1}$ coordinate system (recall from § 4.2.2 page 86) and the similar xyz coordinate system fixed to the wing, due to wing flexion. Recall that if the wing does not flex then these coordinate systems will coincide with each other. Point n_{cr} denotes the centre of rotation, and n_{flx} is the point on the root spar beyond which the wing flexes. This is the point where the root spar joins with the flapping mechanism. The location of the wing spar (pitch axis) if the wing had no flexion is shown by the 'no-flex' line, whereas the 'flex-line' shows its location for an arbitrary flexion of ϕ_{flx} and θ_{flx} in the stroke and plunge directions respectively from the 'no-flex' position. The stroke angle ϕ and mechanism stroke angle ϕ_{mec} are shown as defined in prior chapters. For the right camera to view the wing 'edge-on', the measurement coordinate system $x_{cam}y_{cam}z_{cam}$ must be oriented such that the x_{cam} axis is parallel to the line of in-

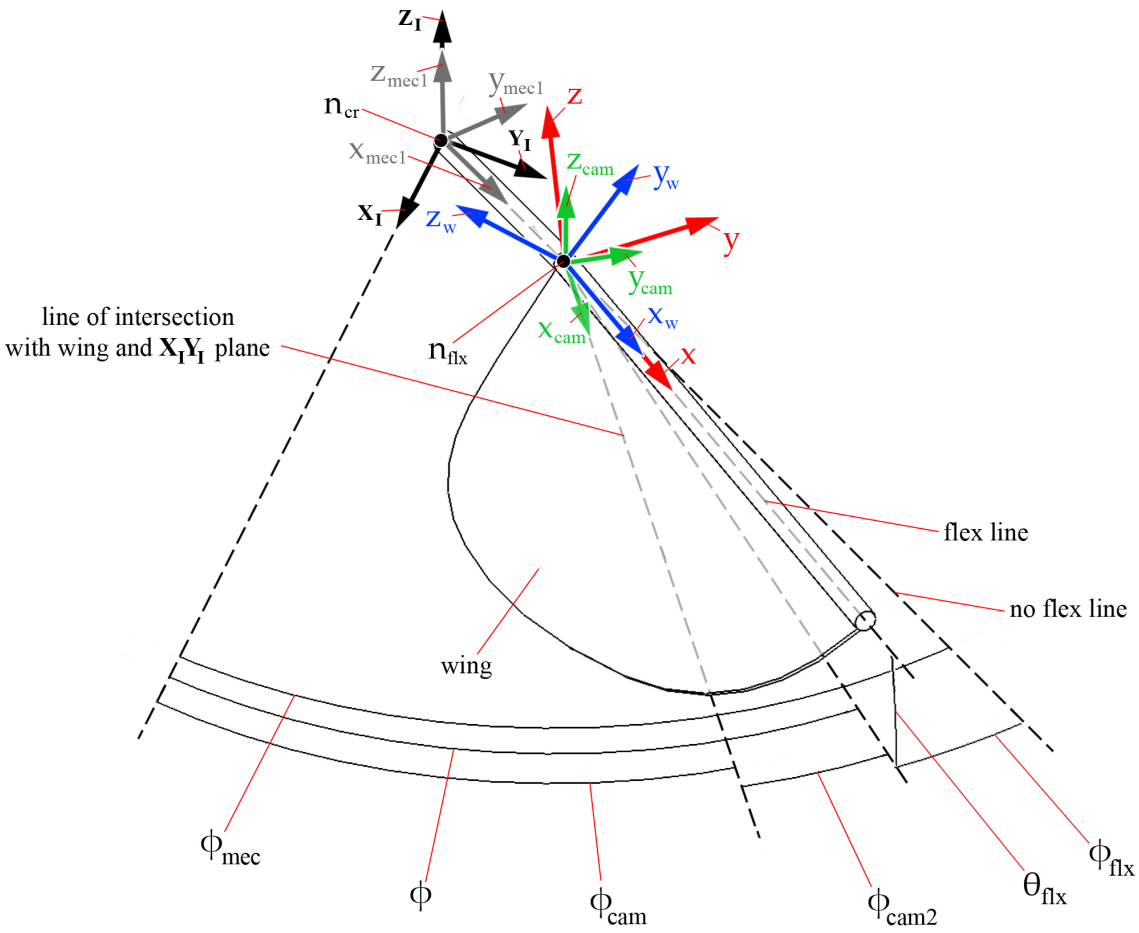

Figure 5.2: Difference between wing and mechanism output coordinate systems due to wing flexion

tersection of the wing with the $X_I Y_I$ plane. This way, even though the wing has plunged upwards due to flexion, the right camera can still view all the way across the wing by viewing in the $-x_{cam}$ direction. Otherwise, if for example the right camera viewed in the $-x_{mec1}$ direction, then only the underside of the wing would be visible and the topside would be obstructed. This condition was achieved through trial and error by running the flapperatus with the desired kinematics, capturing images at the desired point in the flapping cycle (set by ϕ_{mec}), and adjusting the measurement stroke angle ϕ_{cam} via the swivel and iteratively repeating this process until an edge-on condition was achieved.

Once the appropriate measurement stroke angle was set to achieve an 'edge-on' view of the wing, the next step was to release smoke into the test chamber and four minutes were allowed to elapse before beginning the experiment. As will be described in § 5.4, this 'settle time' was observed to be appropriate to allow

the seeder-induced flow to reduce to an acceptable level, and for the seeding density to become uniform. After this 'settle time', the flapperatus was ramped up to the desired flapping frequency with the specified flapping kinematics. Once the flapperatus reached its desired flapping frequency, 10 seconds (> 40 flapping cycles) were allowed to elapse, which was assumed to be sufficient to surpass any start-up effects. Next, starting from approximately 18% span where % span is defined from the root of the wing, 15 image pairs (for both cameras) were acquired for each of 81 spanwise locations extending up to 117% span, and spaced $1mm$ apart. As described in § 4.3.3, changing the spanwise measurement position is accomplished by traversing the flapperatus with respect to the measurement plane. Here the flapperatus was traversed in $1mm$ increments between measurements, where 40 flapping periods were allowed to elapse following the arrival at a new measurement position before acquiring image pairs. In acquiring the image pairs, for each test case a pulse separation was selected such that the maximum out-of-plane particle displacement would be less than one quarter of the thickness of the laser light sheet (given to be optimal in Keane & Adrian (1991)). Here the expected out-of-plane velocity was the mean wingtip speed, as the peak spanwise flow has consistently been reported to be comparable to this speed (Wilkins, 2008; Ellington et al., 1996; Ramasamy & Leishman, 2006; Ansari et al., 2009). However, in the present experiments, out-of-plane velocities of at most two times the mean wingtip speed were measured. In these cases, the maximum out-of-plane particle image displacement exceeded one quarter of the thickness of the laser light sheet, and would have been at most, half of the thickness of the light sheet. Given the number of samples obtained per measurement location (15) and the fact that out-of-plane particle displacements greater than one quarter and less than or equal to one half of the thickness of the laser light sheet still have a detection probability greater than 70% (Keane & Adrian, 1991), such velocities in this range could be measured with confidence.

For flowfield measurements over the wing, no velocity data is obtained under the wing due to the shadow cast by the wing. To obtain a complete picture of the flowfield around the entire wing, some test cases employed flowfield measurements underneath the wing to combine with the corresponding topside measurements. Here, flowfield measurements underneath the wing were performed at the same point in the cycle on the opposite stroke. For example, at mid-stroke

topside measurements are taken during the downstroke, and underside measurements are taken at mid-stroke on the upstroke. Such velocity measurements can be combined if the underside measurements are mirrored, because for symmetric kinematics (which was the case here) the flows generated during opposite half-strokes are mirror images of each other (Lu et al., 2006).

5.2.3 Wing Position Measurement

As mentioned in § 4.3.3, the instantaneous wing position is reconstructed by manually locating the leading- and trailing-edge positions in the raw images obtained during the *PIV* flowfield data acquisition. This process will now be described. For a given spanwise measurement location, the first exposure from the 15 image pairs for each camera were averaged, giving 'average' images for each. Here, a an 'average' image '$\bar{I}$' is computed from n images as $\bar{I} = I_1/n + I_2/n + ... + I_n/n$, where I_n is an array representing the intensity level at each pixel for a given image n. The average images from the left and right cameras were then combined into one image by dewarping the average image from the left camera and overlaying it over top of that from the right camera. Here, the left image is dewarped as described in Appendix C, which transforms the image so that it appears as it would be viewed if the camera axis were normal to the measurement plane (as the right camera's is), rather than angled to it. This way, the images can be directly combined since they are now from the same perspective, and the result is a clear indication of the intersection of the laser light sheet with the wing as shown in Figure 5.3a. As indicated, points in the $y_{cam}z_{cam}$ plane overlaid over the top of the image are then manually selected at the leading and trailing edges (red dots). This process is then repeated for every third spanwise measurement location, and the most tip-ward spanwise location that intersects the wingtip. The result is a collection of $3D$ points in the $x_{cam}y_{cam}z_{cam}$ coordinate system defining the instantaneous form and position of the wing as illustrated in Figure 5.3b. Leading- and trailing-edge points in between every third measurement location were inserted via interpolation.

With the $3D$ coordinates of the wing edge obtained using the above method, the instantaneous stroke, plunge and pitch angles of the wing can be recovered. As mentioned earlier, these coordinates are obtained in the $x_{cam}y_{cam}z_{cam}$ coordinate

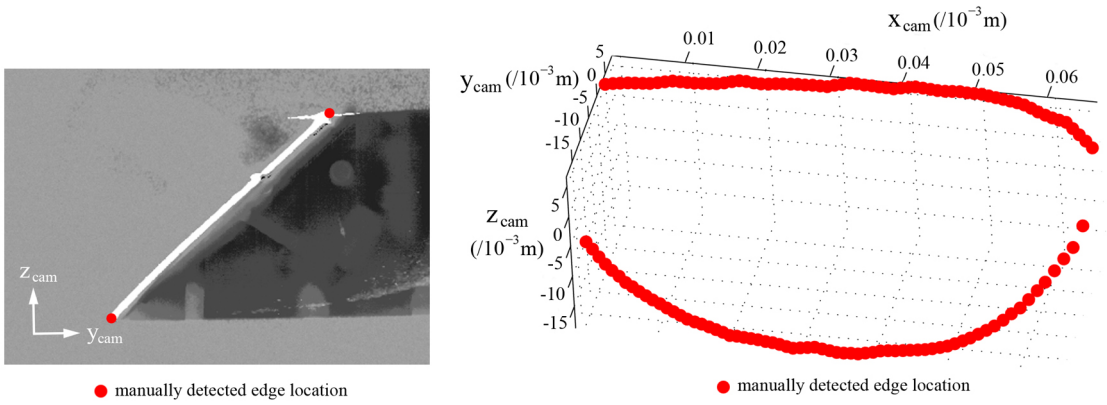

Figure 5.3: Recovery of instantaneous wing position and flexion from raw images; (a) average image from left camera view dewarped and overlaid over top of average image from right camera at 50% span, illustrating manual detection (red dots) of leading- and trailing edge; (b) manually detected edge locations (red dots) from all spanwise locations revealing instantaneous wing position and flexion

system. The pitch axis lies a known distance from the leading edge, thus a line forming the pitch axis can be constructed in this frame. The angle between the pitch axis and the $x_{cam}y_{cam}$ plane can then be found, which is the flex angle in the plunge direction θ_{flx} shown in Figure 5.2. However, all flowfield / instantaneous wing position measurements were performed when the wing was at a mechanism plunge angle (θ_{mec}) of zero, thus, the measured θ_{flx} angle in this manner, is the actual plunge angle θ of the wing. Next, the angle between the x_{cam} axis and the projection of the pitch axis onto the $x_{cam}y_{cam}$ plane can be found to give the angle ϕ_{cam2} shown in Figure 5.2. As seen in this figure, the stroke angle can then be found from $\phi = \phi_{cam} + \phi_{cam2}$. Here the measurement stroke angle ϕ_{cam} is known from the swivel setting mentioned in the prior section. The coordinates defining the wing edge can then be transformed from the $x_{cam}y_{cam}z_{cam}$ coordinate system to the xyz coordinate system since the angles between these coordinate systems are now known. The local angle of attack along the wingspan can then be computed with these transformed coordinates.

5.3 PIV Processing & Analysis

This section presents the method in which raw images captured during the *PIV* data acquisition were processed to produce volumes of velocity data. Following

this, the techniques used to analyse the data to visualise the flow and identify vortices are presented.

5.3.1 Processing

PIV data processing was performed with DaVis FlowMaster software by LaVision. The calibration for the processing was achieved with a calibration plate with dots spread across two planes. This was placed in the measurement plane in the area viewed by the two cameras. As discussed in Appendix C, with this calibration, a mapping function is generated that enables the two-component vector maps obtained from each camera to be dewarped and mapped onto a common orthogonal plane (the measurement plane) to obtain the three velocity components. Some degree of misalignment between the measurement plane (light sheet) and the calibration plate is however, unavoidable. This leads to errors in the reconstructed velocity components, and a registration error. The registration error is the more significant of the two (Scarano et al., 2005), and it results in the two-component vector maps from each camera not 'matching-up' correctly when dewarped and combined on the common orthogonal plane. This causes the wrong two-component vectors to be combined when obtaining the three components using Equations C.2-C.4 in Appendix C. In other words, the same two-component vector viewed at the same point in the measurement plane by the two cameras are not combined with each other to produce the three components, but rather, since the vector maps do not match-up, two-component vectors from slightly different points in the measurement plane are incorrectly combined.

Errors from this misalignment were corrected in the *PIV* processing using the approach based on a 'disparity map' (Willert, 1997; Scarano et al., 2005). In this approach, the same exposure (e.g. the first exposure) from the right and left cameras are dewarped and mapped onto the common orthogonal plane. These resulting images are then cross correlated with each other in the same manner that an image pair from a 2*D PIV* data acquisition are cross correlated to get a 2*D* vector map. If the calibration plate were perfectly aligned with the light sheet then the resulting vector map would have vectors with zero length everywhere since the particle images from each camera (which are taken at same

point in time, but from different perspectives) will perfectly match-up resulting in zero particle image displacements. However, as mentioned previously, with a degree of misalignment (which is unavoidable), the two dewarped views will not perfectly match-up, and the degree of mismatch is quantified by the vector map resulting from the cross correlation. This vector map is referred to as the 'disparity-map'. The disparity map is then used to correct the dewarping in the *PIV* processing, such that the correct points in the two vector maps match-up correctly to obtain the three components. After this correction is applied, and the same exposures from the two cameras are again dewarped and cross-correlated as done before, a 'residual' disparity map is obtained which provides an indication of the level of remaining registration error, and hence how well the two camera perspectives dewarp and match-up. The residual disparity can then be added to the first iteration disparity map to improve the correction. This process can be iterated until the desired level of registration error is achieved. Such a process was iterated three times, resulting in a residual disparity with a respective mean and maximum registration error of $0.3px$ and $0.8px$. For the different *PIV* setup used for the wing planform investigation (as noted in § 4.3.3), the mean and maximum residual registration error was $0.7px$ and $1.5px$ respectively. Errors on the reconstructed three velocity components due to calibration plate misalignment will be addressed later in § 5.4.5.

Before image pairs were cross-correlated, reflections on the wing and in the background were removed by averaging the multiple samples of images taken at a given spanwise location for each exposure, and then subtracting these averages from each sample at the same measurement location. The acquired image pairs were then cross-correlated with a standard cyclic fast Fourier transform-based algorithm which uses Equation C.1 (page 289). In the cross-correlation, a Gaussian peak fit was used to locate correlation peaks to within sub-pixel resolution. An initial interrogation window size of $32 \times 32\ px^2$ was employed, which progressed to a final interrogation window size of $16 \times 16\ px^2$ with two passes and a 50% overlap. This resulted in a spatial resolution for both *PIV* setups of $\sim 1mm^2$. Deformed interrogation windows were also used which increases the number of matched particles and the signal-to-noise ratio. Between passes from the initial to final interrogation window size, the median filter proposed by Westerweel (1994) was utilised to locate spurious vectors and replace them by interpolation.

The resulting vector maps for a given spanwise measurement location were averaged, and then assembled into a $3D$ matrix representing the flow velocities throughout the measurement volume surrounding the wing. As noted in § 4.3.3, the measured velocity components are in the $x_{cam}y_{cam}z_{cam}$ frame. These are then transformed to the xyz frame aligned with the wing using the known angles between these coordinate systems as discussed in § 5.2.3. Finally, the kinematic data obtained from the drive shaft encoders are used to determine the actual wing speeds at the measurement point, which are then used to convert measurements from vectors with respect to the ground to vectors with respect to the wing.

5.3.2 Analysis

Flow Visualisation

The flowfield in a given $2D$ plane in the measurement volume was visualised with the use of Line Integral Convolution (*LIC*), which was originally presented by Cabral & Leedom (1993). This technique visualises a vector field by taking an image of white noise with the same dimensions as the vector field, and stepping through each pixel and and integrating forwards and backwards a certain distance along the local streamline. As this happens, each pixel is assigned the mean intensity of the pixels underneath the streamline, and pixels that lie along the same streamlines are assigned similar intensities. Further details on the employed method may be found in Lawson et al. (2005). Essentially, this method smears points in the white noise image in the direction of the local velocity vector, and an example '*LIC*' image is shown in Figure 5.4. The result of this method is an image that resembles a streak photograph from a steady flow (recall from Chapter 2), in which a liquid flow is densely seeded with particles and a picture is taken with a prolonged exposure producing streaks defining the local streamlines. Thus, *LIC* provides a picture densely packed with streamlines, that has the advantage of identifying all of the flow features.

The *LIC* technique employed here is also known as steady flow *LIC*, as it uses an instantaneous, or time-averaged, vector field to produce the image. Another version known as unsteady flow *LIC*, or *UFLIC* (see e.g. Shen & Kao (1998)), also exists which produces the image using a time-dependent vector field. The

result of the latter technique is analogous to a streak photograph produced from an unsteady flow.

Vortex Identification

To identify vortical structures in the $3D$ flowfield, the velocity gradient tensor and its properties were examined. At a given point, the velocity gradient tensor is defined as:

$$\nabla v = \begin{pmatrix} \frac{\partial v_x}{\partial x} & \frac{\partial v_x}{\partial y} & \frac{\partial v_x}{\partial z} \\ \frac{\partial v_y}{\partial x} & \frac{\partial v_y}{\partial y} & \frac{\partial v_y}{\partial z} \\ \frac{\partial v_z}{\partial x} & \frac{\partial v_z}{\partial y} & \frac{\partial v_z}{\partial z} \end{pmatrix} \tag{5.1}$$

This can be split into a symmetric part S, and antisymmetric part Ω as follows (Mase, 1970):

$$\nabla v = S + \Omega \tag{5.2}$$

where

$$S = \frac{1}{2}\left(\nabla v + (\nabla v)^T\right) \tag{5.3}$$

$$\Omega = \frac{1}{2}\left(\nabla v - (\nabla v)^T\right) \tag{5.4}$$

Here ^{T} represents the transpose. S and Ω are also known as the rate of deformation tensor, and the spin tensor respectively (Mase, 1970). This decomposition can be thought of as separating the local fluid motion into strain and shear rates, which are lumped together in S, and rigid-body-like rotation rates which are grouped into Ω. The vortex identification criterion of Hunt et al. (1988), called the 'Q criterion', makes use of this decomposition to identify vortices, and is defined as:

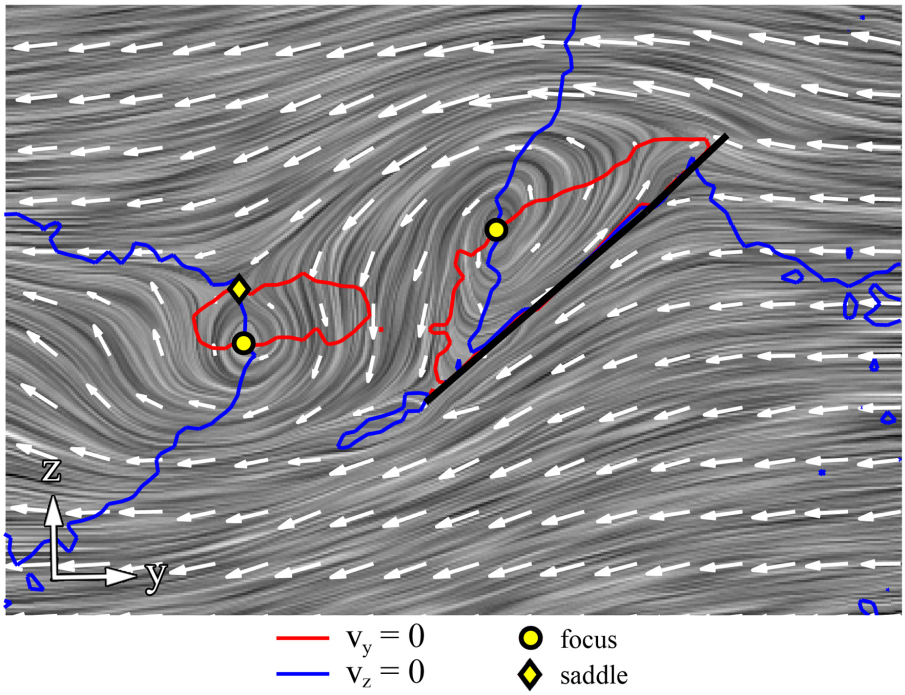

Figure 5.4: *yz* plane of vectors over top of a *LIC* image illustrating critical point identification method proposed by Knowles et al. (2006), where such points are identified where contours of $v_y = 0$ and $v_z = 0$ intersect; wing outline is indicated by the black line, where the right side is the leading edge

$$Q > 0 \tag{5.5}$$

where

$$Q = \frac{1}{2}\left(||\Omega||^2 - ||S||^2\right) \tag{5.6}$$

Here, $||\Omega|| = \sqrt{trace(\Omega\Omega^T)}$, and $||S|| = \sqrt{trace(SS^T)}$. This states that if at a given location Ω dominates over S (and thus $Q > 0$), then that region is a vortex since the local fluid motion will be dominated by rigid-body-like rotation. As we will see shortly, this criterion was used in the analysis to classify flow regions as vortices.

Vortex core locations were identified in the volumes of velocity data using the technique proposed by Knowles et al. (2006). This locates vortex cores and other features such as saddle points in $2D$ planes by finding intersections between contour lines of zero velocity for the two velocity components in that plane. For example, in the yz plane, intersections of contour lines of $v_y = 0$ and $v_z = 0$ mark

critical points as illustrated in Figure 5.4. An intersection point was automatically classified as a vortex if it passed the Q criterion mentioned previously, that is if $Q > 0$ at the intersection. Critical points identified in this manner can be automatically classified as other types, such as saddles, by using the same approach as Chong et al. (1990) and Peikert (undated). This approach uses the following properties of the velocity gradient tensor:

$$P = -trace(\nabla v) = -\left(\frac{\partial v_x}{\partial x} + \frac{\partial v_y}{\partial y} + \frac{\partial v_z}{\partial z}\right) \tag{5.7}$$

$$Q = (P^2 - trace((\nabla v)^2))/2 = \begin{vmatrix} \frac{\partial v_x}{\partial x} & \frac{\partial v_x}{\partial y} \\ \frac{\partial v_y}{\partial x} & \frac{\partial v_y}{\partial y} \end{vmatrix} + \begin{vmatrix} \frac{\partial v_x}{\partial x} & \frac{\partial v_x}{\partial z} \\ \frac{\partial v_z}{\partial x} & \frac{\partial v_z}{\partial z} \end{vmatrix} + \begin{vmatrix} \frac{\partial v_y}{\partial y} & \frac{\partial v_y}{\partial z} \\ \frac{\partial v_z}{\partial y} & \frac{\partial v_z}{\partial z} \end{vmatrix} \tag{5.8}$$

$$\mathfrak{R} = det(\nabla v) = \begin{vmatrix} \frac{\partial v_x}{\partial x} & \frac{\partial v_x}{\partial y} & \frac{\partial v_x}{\partial z} \\ \frac{\partial v_y}{\partial x} & \frac{\partial v_y}{\partial y} & \frac{\partial v_y}{\partial z} \\ \frac{\partial v_z}{\partial x} & \frac{\partial v_z}{\partial y} & \frac{\partial v_z}{\partial z} \end{vmatrix} \tag{5.9}$$

With just the calculated values of P,Q, and $\mathfrak{R}$, a given point can be classified as a certain critical point type according to the criteria outlined in Chong et al. and Peikert. For example, a point is a saddle if $Q < 0$, and a focus (vortex) if $Q > 0$. This is consistent with the Q criterion, as Q in Equation 5.8 is another form of Q in Equations 5.5 and 5.6. However, in the present analysis, only vortices were of interest, thus, as mentioned previously, intersection points were classified as vortices using the Q criterion.

The employed vortex core identification method was applied to every xy, yz, and xz plane in the measurement volume resulting in a collection of points in $3D$ each representing a vortex core location. These points revealed the form of vortex axes. Points along a vortex axis could be joined by a single line by using the fact that the $3D$ vorticity vector at a given point on the vortex axis points to the next point on the vortex axis. In other words, the vorticity vector along the vortex axis is tangent to the axis trajectory. A 'vortex point-joining algorithm' was therefore developed that exploited this fact to join collections of points with a line forming a vortex axis. Details of this algorithm are given in Appendix D.

With the vortex axes identified by $3D$ lines, numerous characteristics of a given vortex structure could then be obtained along its core including: tangential and axial velocity, helix angle, axial vorticity, vortex diameter, and circulation. Details of how these quantities are computed along a given vortex axis are presented in Appendix E. In addition, points along an identified vortex axis provided starting points from which to release instantaneous streamlines, making the vortex structure visible.

To provide a secondary indication of the presence of vortex structures, iso-surfaces of the Q criterion were also employed. A high enough threshold above zero had to be employed because simply plotting areas where $Q > 0$ saturated the measurement volume. A threshold of a certain multiple 'q' times the square of the mean wingtip speed was mostly employed, where $q \approx 8.5 \times 10^4 m^{-2}$ was found to be appropriate.

5.4 Uncertainty Analysis

This section presents an uncertainty analysis for the various measurements performed in this study. First, uncertainty on measured mean lift will be discussed, followed by uncertainty on the flapping mechanism output stroke, plunge and pitch angles. After this, the uncertainty on the optically measured (from raw images) wing position (wing stroke, plunge and pitch angle) will be discussed. In addition, the errors on the wing position when optical measurements are unavailable, and its position must be estimated from the flapping mechanism position, are given. Lastly, errors on the flowfield measurements are discussed.

5.4.1 Force Measurements

To verify that the procedure described in § 5.2.1 for measuring mean lift was reliable, a series of experiments were performed to quantify the error. In these experiments, the wing was removed and known masses were loaded onto the outermost drive shaft of the flapping mechanism. Mean vertical force was then measured using the same procedure outlined in § 5.2.1, and the result was compared to the weight of the known masses to compute the error. This was performed

using a number of masses ranging up to ~ 25 grams. Results revealed an error of $\pm 0.02N$ (95% confidence level) on the mean calculated vertical force. To verify that inertial forces from the wing in the vertical direction would in fact cancel and hence have no contribution to measured mean lift, a test was performed where a plain rod was put in place of the wing and vertical force was measured over a number of cases employing figure-of-eight kinematics at $20Hz$ with an increasing plunge amplitude. An increasing plunge amplitude leads to larger inertial forces in the vertical direction since plunging accelerations rise. It was found that in all cases, the measured vertical force was well within the error band centred at the expected value of zero, thus verifying that inertial forces average to zero.

5.4.2 Flapping Mechanism Position

Uncertainties in the computed mechanism output angles (ϕ_{mec}, θ_{mec}, α_{mec}) originate from physical backlash in the flapping mechanism, encoder resolution, and variability due to the degree of positional repeatability. These sources of error will be discussed, and their effects quantified.

Backlash Backlash only affected the mechanism plunge angle and was 0.3° in the plunge direction. This was measured by locking all of the drive shafts and measuring any remaining degree of wing movement.

Encoder Resolution Uncertainty on the drive shaft angles (ϕ_{L1}, ϕ_{L2}, ϕ_{L5}) originating from the resolution of the respective encoders, was 0.036° for the outer and middle shaft encoders and 0.088° for inner shaft encoder. Resulting error on the output stroke, plunge and pitch angles was found by running a simulation in Matlab in which 'actual' input kinematics are quantised to discrete values according to the encoder resolutions resulting in 'measured' input kinematics. Mechanism output kinematics were calculated with equations in Appendix B using both actual and measured input kinematics, and the resulting differences in the ϕ_{mec}, θ_{mec}, and α_{mec} angles between the two cases gave the error due to encoder resolution. This analysis was performed with all of the flapping kinematics used in experiments, and a maximum error on ϕ_{mec}, θ_{mec}, and α_{mec}, was found to be 0.04°, 0.03° and 0.4° respectively.

Position Variability The variability in the output stroke, plunge, and pitch angles due to the repeatability of the flapping mechanism position, was quantified in § 4.4.2. These values were found to be 0.1°, 0.07° and 0.17° for ϕ_{mec}, θ_{mec}, and α_{mec} respectively.

Combining all sources of error, the total error on the mechanism output stroke, plunge and pitch angles are:

$$\delta\phi_{mec} = \sqrt{0.04^{\circ 2} + 0.1^{\circ 2}} = \pm 0.1^{\circ} \tag{5.10}$$

$$\delta\theta_{mec} = \sqrt{0.3^{\circ 2} + 0.03^{\circ 2} + 0.07^{\circ 2}} = \pm 0.3^{\circ} \tag{5.11}$$

$$\delta\alpha_{mec} = \sqrt{0.4^{\circ 2} + 0.17^{\circ 2}} = \pm 0.4^{\circ} \tag{5.12}$$

5.4.3 Wing Position from Optical Measurements

Error in optically reconstructing the instantaneous wing position using the method outlined in § 5.2.3, arises from the uncertainty in locating the leading and trailing edge positions in the many raw images taken along the span. This uncertainty affects the calculated pitch angle α, as well as the ϕ_{cam2} and θ_{flx} angles described in § 5.2.3 (see Figure 5.2) which are used to obtain the stroke and plunge angles of the wing. The uncertainty in locating the leading and trailing edges both in the y_{cam} and z_{cam} directions was conservatively taken as half of the thickness of the perceived laser light sheet and wing intersection (e.g. half the thickness of the white line in Figure 5.3a), which was $0.47mm$. The impact of this uncertainty is a maximum error in α, ϕ_{cam2} and θ_{flx} of 2°, 1.2° and 1.2° respectively. Recalling from § 5.2.3 that $\phi = \phi_{cam} + \phi_{cam2}$, additional error in the wing's stroke angle arises from uncertainty in the measurement stroke angle ϕ_{cam}, which was 0.5°. Therefore, the total error in the stroke angle of the wing is:

$$\delta\phi = \sqrt{\delta\phi_{cam}^2 + \delta\phi_{cam2}^2} \tag{5.13}$$

$$\delta\phi = \sqrt{0.5^{\circ 2} + 1.2^{\circ 2}} \tag{5.14}$$

$$\delta\phi = \pm 1.3^{\circ} \tag{5.15}$$

Recalling from § 5.2.3 that in each measurement case, θ_{flx} is in fact the plunge angle of the wing, thus, the error in the wing's plunge angle is:

$$\delta\theta = \delta\theta_{flx} \tag{5.16}$$

$$\delta\theta = \pm 1.2^{\circ} \tag{5.17}$$

Lastly, the wing's pitch angle is directly found from the raw images, where the error has previously been stated to be:

$$\delta\alpha = \pm 2^{\circ} \tag{5.18}$$

It should be noted that the error in the local pitch angle will depend upon the local chord length, where the shorter the chord the higher the error since the leading and trailing edge location error of $0.47mm$ becomes comparatively bigger as the chord length decreases. However, error in α is previously quoted for the mean chord length and, thus, is the mean local error of α along the span.

5.4.4 Wing Position from Mechanism Position

As will be seen in Chapter 6, some experimental test cases only employed flowfield measurements at mid-stroke. In these cases, the actual wing position throughout the flapping cycle cannot be determined, simply because the wing position is only known at one point in the cycle. However, the actual wing position can be

described by the known mechanism output kinematics if effects due to flexibility are included. For example, the wing's stroke angle ϕ is equal to the mechanism output stroke angle ϕ_{mec} plus or minus some contributions to flexibility. Thus, contributions due to flexibility can be treated as a form of error in the mechanism output angles, when describing the angles of the wing. This 'flex' error can be determined by computing the difference between recovered flapping kinematics and mechanism output kinematics. As will be seen in Chapter 6, experimental test cases in which the flow evolution and rotation phase were investigated included simultaneous wing position and mechanism position measurement, thus providing data to compute differences between flapping and mechanism output kinematics due to flexion. After performing this computation it was revealed that the rms errors (differences) between the wing and mechanism output stroke, plunge, and pitch angles were 3.8°, 2.3°, and 4.5° respectively. Including the errors in the ϕ_{mec}, θ_{mec}, and α_{mec} angles found previously in § 5.4.2, and errors on the reconstructed wing position given in § 5.4.3 (which must be included since the computed difference between flapping and mechanism output kinematics is affected by this error), the errors in the wing stroke, plunge and pitch angles described by the mechanism output angles are as follows:

$$\delta\phi = \sqrt{0.11^{\circ 2} + 1.3^{\circ 2} + 3.8^{\circ 2}} = \pm 4^{\circ} \tag{5.19}$$

$$\delta\theta = \sqrt{0.31^{\circ 2} + 1.2^{\circ 2} + 2.3^{\circ 2}} = \pm 2.6^{\circ} \tag{5.20}$$

$$\delta\alpha = \sqrt{0.44^{\circ 2} + 2^{\circ 2} + 4.5^{\circ 2}} = \pm 4.9^{\circ} \tag{5.21}$$

5.4.5 Flowfield Measurements

Errors in flowfield measurements arise from a number of sources including: an inadequately large sample size, contaminating flows from the smoke machine, 'start-up' effects, potential flow recirculation, possible alteration of the flow from traversing the wing, calibration errors, and *PIV* processing error. These errors will now be discussed in order and, finally, the total error in the velocity measurements for the two *PIV* setups will be given.

Sample Size

As mentioned in § 5.3.1, for a given spanwise location in the measurement volume, multiple samples of *PIV* flowfield measurements were captured and then averaged. The act of averaging filters out noise in the velocity measurements, thus providing a picture of the 'true' flowfield. The question arises, however, of how sample size affects the averaged flowfield, and how close it is to the true mean. This section will address this question, and quantify how close velocity measurements were to the mean.

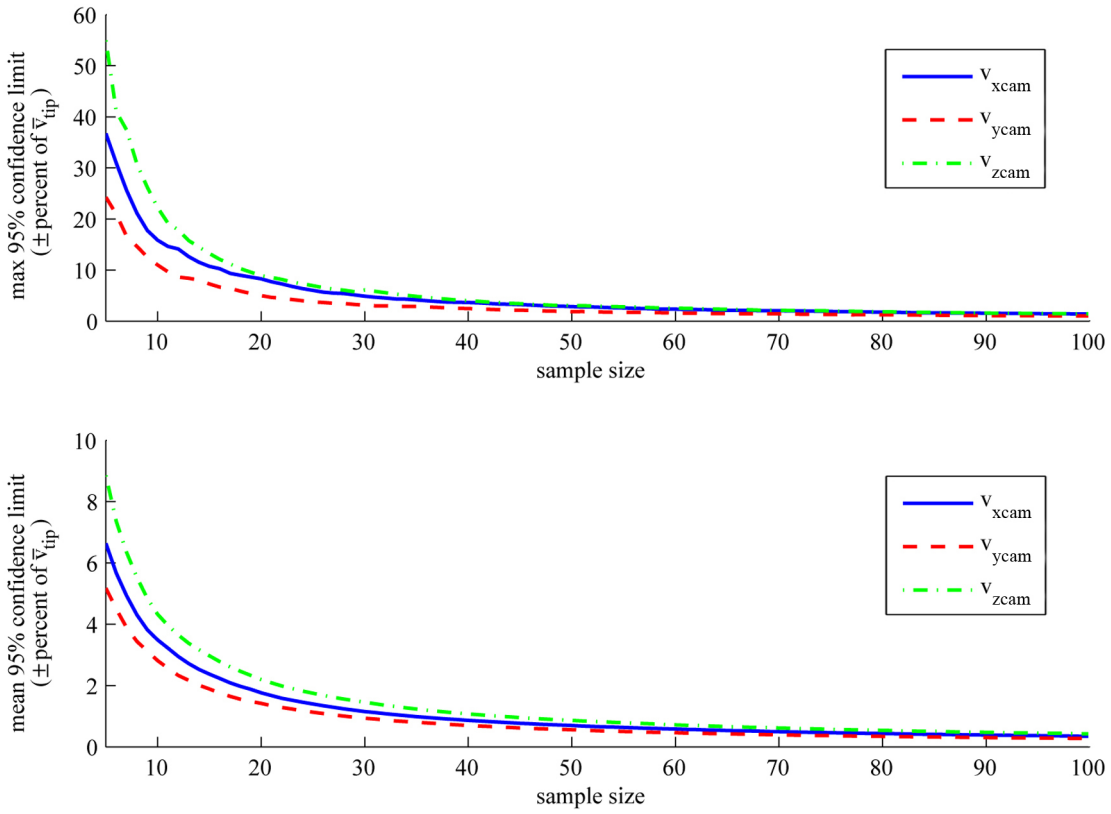

Figure 5.5: Maximum (top) and mean (bottom) of 95% confidence limits on velocity components in flowfield at 50% span versus sample size

One hundred instantaneous flowfield measurements (100 samples) at 50% span at mid-stroke with the baseline kinematics given in § 5.1.1 (but with $\Phi_{mec} \approx 120°$) were used for this analysis. For a given sample size n, each point in the measurement plane was stepped through and the sample of n v_{xcam}, v_{ycam}, and v_{zcam} velocity components at that point were used to compute a 95% confidence interval (CI) for each of the velocity components at that point using the following formula for a normal distribution:

$$CI = \pm 1.96\frac{\sigma}{n} \tag{5.22}$$

Where σ and n are the standard deviation and sample size respectively. The result for a given sample size is a 'map' of the 95% confidence limits at each point across the measurement plane. This was performed for sample sizes of $5 - 100$. Across this range the maximum and mean of the 95% confidence limits across the measurement plane, for a given sample size, are illustrated in Figure 5.5 as a percentage of the mean wingtip speed ($8.4m/s$). It can be seen that from the lowest sample size of 5, the confidence limits in the measurement plane rapidly narrow as sample size increases. Beyond a sample size of approximately 40, any further samples have very little impact on the proximity of flowfield velocities to the true mean. A sample size of this magnitude was however, deemed too large to be practical for the present experiments, as it would require large processing times for the desired level of spatial resolution in the measurement volume. Instead a sample size of 15 was chosen as an adequate compromise, as it lies approximately where the confidence limits in Figure 5.5 begin to level out after declining rapidly. At this sample size, all velocity components are within approximately 13% (maximum confidence limit) of the mean wingtip speed from the true mean; however, most are within 3% (mean confidence limit).

Settling Time

To ensure that measurements were not contaminated with flows generated in the act of filling the test chamber with smoke, an experiment was performed to determine the appropriate length of time to wait (the 'settle time') before beginning experiments. The experiment consisted of releasing seeding into the enclosure (using a fixed burst length of $\sim 3s$) and measuring the resulting flow every 5 seconds up to approximately 5 minutes, using a *PIV* laser pulse separation of $5ms$. The observed velocity levels over time are illustrated in Figure 5.6. Here the velocity level is measured by the mean of the velocity magnitudes in the measurement area, plus one standard deviation of the velocity magnitudes. It can be seen that flow velocities roughly level out just before 2 minutes. However, a settle time of 4 minutes was selected for experiments, as it gave more time to

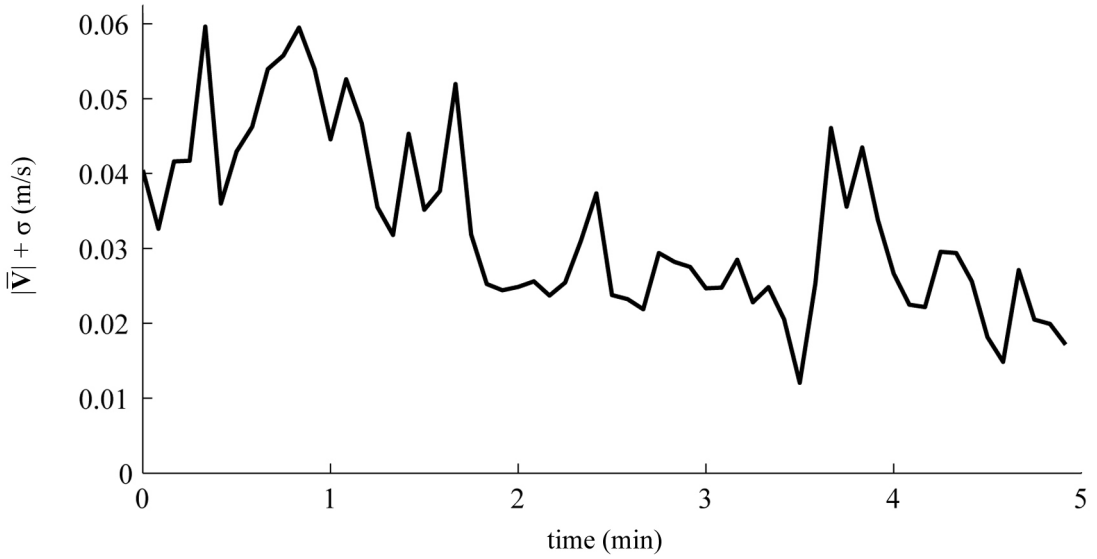

Figure 5.6: Flow velocity levels versus time since seeding burst; velocity level is shown by mean of velocity magnitudes over measurement area plus one standard deviation

allow the seeding density to become uniform. In addition, at this time, velocity levels drop below $0.03m/s$, which corresponded to a maximum level of around 1.4% of the mean wingtip speed (from the measurement test case with the lowest wingtip speed), where in most measurement test cases this value was in fact below 0.05%. This was deemed to be sufficiently low that subsequent experiments would not be contaminated.

Start-up Effects

As noted earlier in § 5.2.2, 10 seconds (> 40 flapping cycles) were allowed to elapse before measurements commenced. The purpose of this was to surpass any 'start-up' effects, and allow the flow to reach a quasi-steady state. In other words, to allow the flow to reach a state where the flowfield at the same point in the half-stroke between successive flapping cycles becomes virtually identical. To determine the number of flapping cycles required to surpass start-up effects, an experiment was conducted which involved $2D$ *PIV* measurements of the flowfield for a set of flat wingtip kinematics at a $5Hz$ flapping frequency and $\sim 132°$ stroke amplitude. The wing was allowed to flap from an originally quiescent flow, and once the desired flapping frequency was reached, flowfield measurements were taken every cycle at 50% span at mid-stroke, up to 100 cycles. This was repeated 5 times, and corresponding measurements were averaged. The results of this

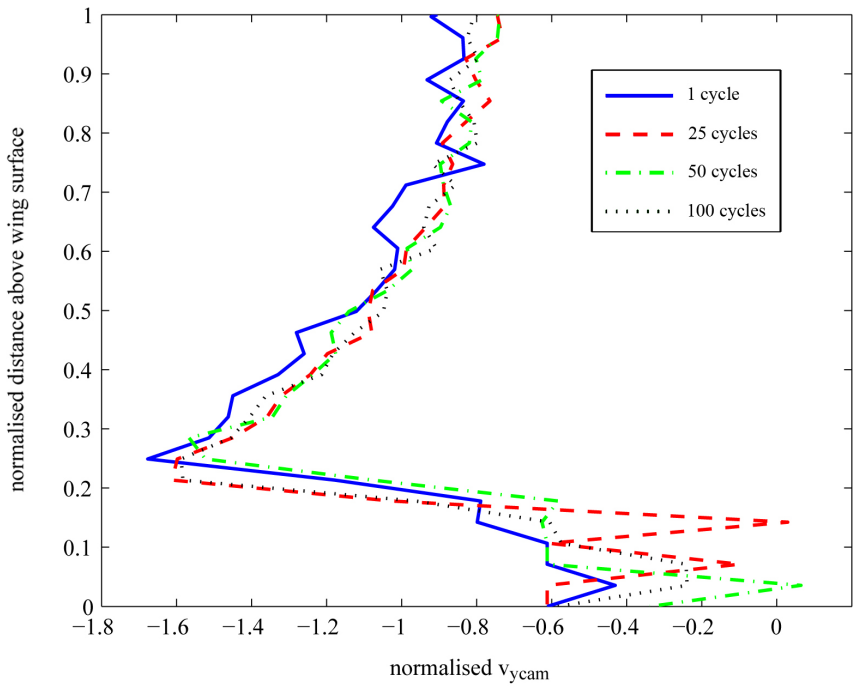

Figure 5.7: *LEV* tangential velocity profiles at mid-stroke, 50% span at 1, 25, 50 and 100 flapping cycles since start from rest; v_{xcam} components are approximately the axial velocities; velocities are normalised with respect to the mean wingtip speed ($2.4m/s$); distance above wing surface is normalised with respect to $\bar{c}$ ($27.7mm$)

experiment are illustrated in Figure 5.7, where v_{xcam} components (approximately *LEV* tangential velocity components) are shown plotted along a line in the z_{cam} direction rising from the wing surface at approximately the quarter-chord position. It can be seen that beyond 25 flapping cycles, the velocity profiles are similar, thus, any start-up effects are deemed to have been surpassed by this point. Therefore, the employed wait of 10 seconds, corresponding to 40 flapping cycles or more (depending on the flapping frequency), is sufficient. This aspect of flapping-wing experiments has been investigated before, where the study of Poelma et al. (2006) found that 3 flapping cycles were appropriate to surpass start-up effects.

Recirculation

As a result of operating the flapperatus in an enclosed volume for a prolonged period of time, there was the risk of recirculation forming if the enclosure were too small, which would influence results. To ensure that no recirculation was present, and hence ensure the enclosure was appropriately sized, the wing was flapped in an initially quiescent flow, and a sample size of 15 flowfield measurements

at 50% span were acquired and averaged every 300 flapping cycles over a total period of almost 9000 cycles. A given experimental run in the main experimental programme lasts approximately 6000 flapping cycles. The flapping kinematics used for this investigation were the same as those used in § 5.4.5. The means and maxima of the velocity components over this number of flapping cycles are plotted in Figure 5.8. If recirculation had formed then it would be expected that velocity components would have drifted over time, especially the mean and maximum v_{zcam} values (where this velocity is in the vertical direction). It can be seen that over time the means and maxima of the velocities do not drift and remain centred around the same value. Therefore, it was deemed that the enclosure was appropriately sized and no recirculation formed.

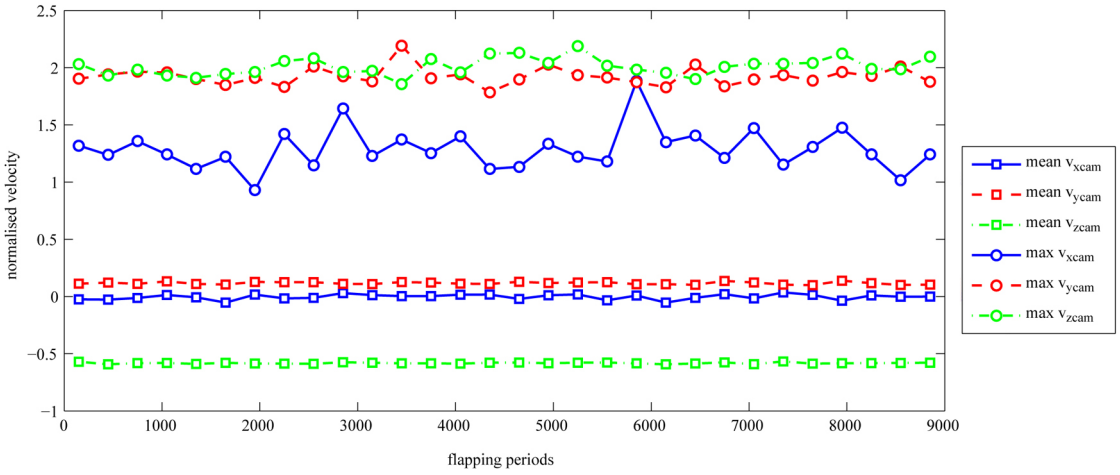

Figure 5.8: Mean and max of velocity components at 50% span versus number of flapping cycles; velocities are normalised with respect to the mean wingtip speed ($8.4m/s$)

Traversing Flow Error

Recall from § 5.2.2 that flowfield measurements throughout a volume surrounding the wing were accomplished by traversing the flapping-wing relative to the fixed measurement plane. It could be argued that the act of traversing the wing in this manner could have altered the flow and given results that are not characteristic of a flapping-wing in the hover condition. Although peak and average traversing speeds were well below 0.1% of the mean wingtip speed, any such effects from traversing the flapping wing were investigated, which will be described now.

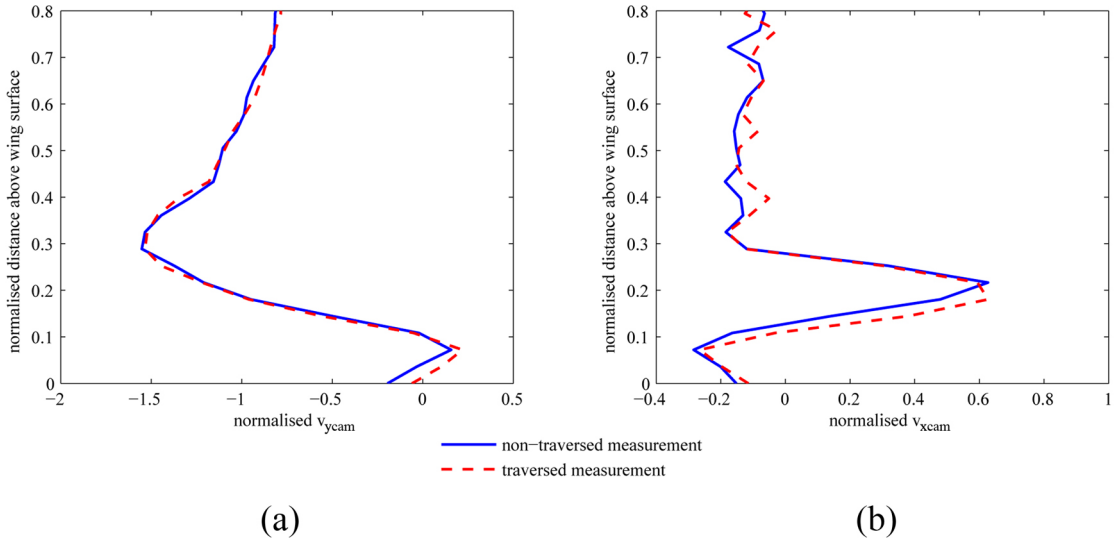

Figure 5.9: *LEV* velocity profiles for a traversed and non-traversed measurement at 50% span; (a) v_{ycam} components are approximately the *LEV* tangential velocities; (b) v_{xcam} components are approximately the axial velocities; velocities are normalised with respect to the mean wingtip speed ($8.4m/s$); distance above wing surface is normalised with respect to $\bar{c}$ ($27.7mm$)

As described in the measurement procedures, for each measurement location along the span, 40 flapping periods were allowed to elapse following the arrival at that measurement location before flowfield measurements commenced. This waiting time was imposed to surpass any potential effects on the flow from traversing the wing. To validate the use of this wait time, flowfield measurements along the entire span were captured using the aforementioned procedure, thus giving a 'traversed case'. For comparison, a 'non-traversed' case was employed where the measurement location was pre-set to 50% span, the wing was allowed to flap from a quiescent flow (which is also true for the traversed case) and measurements at just that spanwise location were taken thereafter with the same sample size (15). The same flapping kinematics used in the sample size study in § 5.4.5 were employed for this study. At the 50% span location for both traversed and non-traversed cases, the *LEV* core location was found using the technique outlined in § 5.3.2. In both cases, the *LEV* core was identified at approximately the same point, where the core location only differed by less than $0.5mm$ in the both horizontal (y_{cam}) and vertical (z_{cam}) directions. A vertical line in the z_{cam} direction was drawn upwards from the wing surface intersecting the *LEV* core location for both cases, and velocity components along this line for each case are plotting in Figure 5.9. Here v_{ycam} is approximately the *LEV* tangential velocity and v_{xcam} is approximately the axial velocity. It can be seen that the velocity profiles in

both cases are virtually identical; therefore, the employed method of traversing the wing was deemed to have no effect on the flow structures produced, and measurements represent a true hover condition.

Calibration Error

Calibration error occurs when the spatial measurement scales obtained using the calibration plate differ slightly from their true values. For both *PIV* setups, the calibration error resulted in a 0.2% error on measured displacements, thus, resulting in an error in velocity measurements also of 0.2%.

Calibration Plate Misalignment

Recall from § 5.3.1, that misalignment between the calibration plate and light sheet can lead to errors in the $3D$ velocity components. With this misalignment, the viewing angles (from the calibration plate) used in the three component reconstruction are not the true viewing angles with respect to the measurement plane in which the actual velocities are measured. Thus, error arises on the reconstructed $3D$ velocity components. The misalignment between the calibration plate and the light sheet can be computed from the disparity map mentioned in § 5.3.1. From the 'velocity' gradients in the disparity map, the misalignment can be computed with the expressions derived in Scarano et al. (2005). Using this approach, for the main *PIV* setup the calibration plate was found to be misaligned by 0.16° and -0.65° in the stroke and plunge directions respectively. For the second *PIV* setup used for the wing planform study (as noted in § 4.3.3), these misalignments were respectively 0.3° and 0.15° in the stroke and plunge directions.

With the determined misalignments, the errors in the reconstructed velocity components were determined numerically. Employing Equations C.2 - C.4 from Appendix C, a simulation was set up in Matlab which stepped through each point in the measurement area and computed the three velocity components from v^R_{ycam}, v^R_{zcam}, v^L_{ycam}, and v^L_{zcam}. At each point, these four components from the two cameras were each varied from $-10px$ to $10px$, which was the maximum range of particle image displacements in the experiments. Thus, at each point, the $3D$ velocity components were computed for every possible combination of

v^R_{ycam}, v^R_{zcam}, v^L_{ycam}, and v^L_{zcam} each ranging from $-10px$ to $10px$. This was performed for an array of points across the measurement area with viewing angles from the known geometry of the setup. The viewing angles were then perturbed according to the measured calibration plate misalignments, and the three velocity components at each point were recalculated with the same method mentioned previously. The resulting differences in the velocity components between the two cases provided the errors in the velocity components resulting from calibration plate misalignment. For the main *PIV* setup, this revealed an rms error in the in-plane components (norm of errors in y_{cam} and z_{cam} components) of $2.7\mu m$, and an rms error of $2.1\mu m$ in the out-of-plane components (error in x_{cam} components). This corresponds to a maximum in-plane and out-of-plane rms error in velocity components of 1.5%, and 1.2% of the mean wingtip speed respectively, resulting in a norm of 1.9%. For the *PIV* setup for the wing planform study, in-plane and out-of-plane rms errors were found respectively to be $5.3\mu m$ and $3.8\mu m$, translating to errors in velocity components of 2.4% and 1.7% of the mean wingtip speed for in-plane and out-of-plane respectively. These combine to a norm of 2.9% of the mean wingtip speed.

PIV Processing Error

Errors in PIV measurements can be divided into three forms: outliers, bias errors, and root mean square (rms) errors (Huang et al., 1997). Outliers were identified and removed using the median filter discussed in § 5.3.1. The other two forms of error will now be discussed and evaluated.

Bias error arises when a velocity gradient is present in the interrogation window. If the velocity gradient is large enough then the measured velocity in that interrogation window will be biased towards a lower value. This is because particles with higher velocities are more likely to leave the interrogation window between pulses, resulting in less detection of higher velocities in comparison to the lower velocities, for which the particles remain in the interrogation area. Bias error is directly proportional to the particle image displacement and the velocity gradient within an interrogation window; thus, if these are minimised then bias error may be made negligible (Keane & Adrian, 1990). If particle displacements are minimised, then the loss of particles with higher velocities from the interrogation window is reduced. As velocity gradients are minimised the velocity

across the interrogation area becomes more uniform, which results in a much higher correlation peak (ibid.) and better detection, and the measured velocity for that window is more representative of all the velocities in that window. In the present study particle image displacements were minimised through the use of an interrogation window offset, which moves the interrogation window with the particles between pulses, thus minimising loss of particles. In addition, deformed interrogation windows were also used, in which the interrogation window is deformed to prevent further loss of particle images from the interrogation area. Velocity gradients can be minimised by employing a progressively smaller interrogation window (Keane & Adrian, 1992), which was the technique employed here as described in § 5.3.1. It was felt that minimising these factors resulted in a negligible bias error from these sources.

The rms errors in the velocity field measurements were quantified using the approach described by Willert & Gharib (1991) and Willert (1997), in which error is measured by processing particle image pairs where the particles have displaced by an amount that is known reliably. Using this approach, the flow was measured four minutes after a seeding burst (at which it was known that the flow velocity was below $0.03m/s$) using a short pulse separation of $4\mu s$. This short pulse separation in conjunction with a low flow velocity meant that the actual displacement of the particles between pulses was virtually zero and, thus, any measured displacements would be pure error. The resulting vector map of particle image displacements then provides a large sample of errors, from which the rms error can be found. With this approach, for the main *PIV* setup, in-plane error on measured particle displacements was found to be $4\mu m$, whereas the out-of-plane error was $4.2\mu m$. This corresponds to a maximum rms error for in-plane and out-of-plane velocity measurements of 2.3% and 2.4% of the mean wingtip speed respectively, resulting in a norm of 3.3% of the mean wingtip speed. For the different *PIV* setup used for studying wing planform effects, in-plane and out-of-plane errors of $5.7\mu m$ and $7\mu m$ were found respectively. These translate to maximum rms in-plane and out-of-plane velocity errors of 2.6% and 3.1% of the mean wingtip speed respectively, giving a norm of 4%.

Total Error

Combining all of the errors discussed above, the total error on velocity measurements as a percentage of the mean wingtip speed, for the main *PIV* setup was:

$$\frac{\delta \mathbf{v}}{\bar{v}_{tip}} \times 100\% = \sqrt{3.3^2 + 1.4^2 + 0.2^2 + 1.9^2 + 3.3^2} = \pm 5\% \tag{5.23}$$

Similarly, for the second *PIV* setup for studying wing planform, the total error was:

$$\frac{\delta \mathbf{v}}{\bar{v}_{tip}} \times 100\% = \sqrt{3.3^2 + 1.4^2 + 0.2^2 + 2.9^2 + 4^2} = \pm 6\% \tag{5.24}$$

The results of the experimental programme described here, will now be presented and discussed in the next chapter.

Chapter 6

Results & Discussion

Following the experimental programme outlined in § 5.1, this chapter begins with a detailed investigation of the flow evolution throughout a single half-stroke in order to obtain a picture of how the flowfield generated by an insect-like flapping wing at FMAV scale is characterised. This is then followed by a parametric study in which various kinematic parameters and wing planform are altered, to observe how this flowfield changes as well as the mean lift generated. The effect of varying rotation phase is first investigated, followed by Reynolds number and stroke amplitude effects. Following this is a study of angle of attack effects, the effect of varying plunge amplitude with figure-of-eight kinematics, and finally wing planform shape effects are presented.

Before proceeding we must define a set of coordinate systems. Referring to Figure 6.1, the xyz coordinate system is the same as that presented in § 2.1.2

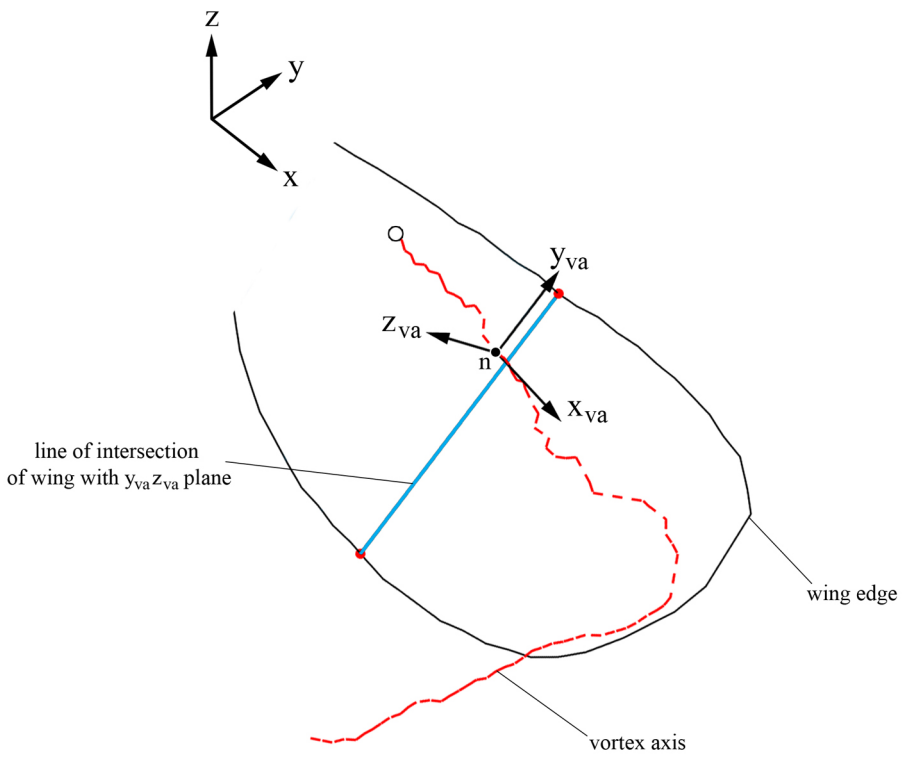

Figure 6.1: Wing fixed xyz (same as in § 2.1.2), and vortex axis fixed $x_{va}y_{va}z_{va}$ coordinate systems

(page 17). Here, the origin is placed at the root of the wing, which is located at the wing offset distance b (23.8mm) from the centre of rotation. The other x_{va}, y_{va}, z_{va} coordinate system, is a local coordinate system at a given point on a vortex axis. This is also illustrated in Figure 6.1 where this coordinate system is fixed at an arbitrary point n on the LEV/TPV vortex axis. It is oriented such that the x_{va} axis points in the local direction of the curve defining the axis, towards the end of the axis without a white dot. The y_{va}, z_{va} axes form a plane normal to the x_{va} axis, where the y_{va} axis is parallel to the line of intersection between this plane and the wing as illustrated. The z_{va} axis is then perpendicular to this line of intersection and x_{va}. If the $y_{va}z_{va}$ plane does not intersect the wing then z_{va} is oriented vertically such that the $x_{va}z_{va}$ plane is parallel to the z direction. Axial, and tangential directions along an axis are taken as the x_{va} and y_{va} directions respectively. For instance, a positive tangential velocity points in the y_{va} direction.

6.1 Flapping Half Stroke

The first investigation focuses on the development and evolution of the flow induced by an insect-like flapping-wing in hover throughout one half of a flapping cycle (a half-stroke), at a Reynolds number relevant to FMAVs (Re on the order of 10^4). Recall that a half-stroke lasts $T/2s$ and consists of the point when the wing is at rest and about to accelerate, followed by acceleration to a constant (or peak) velocity at mid-stroke, and then deceleration to rest with simultaneous pitch reversal. As described in § 5.1.2, numerous volumetric flowfield measurements were performed throughout a half-stroke and various flow structures were identified and analysed. First, the flapping kinematics used for this investigation including the measurement points will be presented, followed by a description of the flow evolution. Next discussions on other aspects relating to the observations will be given, including the presence of a secondary LEV, LEV breakdown, LEV circulation and lift, and LEV stability.

6.1.1 Flapping Kinematics & Measurement Points

The flapping kinematics used are illustrated in Figure 6.2 and the kinematic parameters are listed in Table 6.1. Mechanism output kinematics (the kinematics

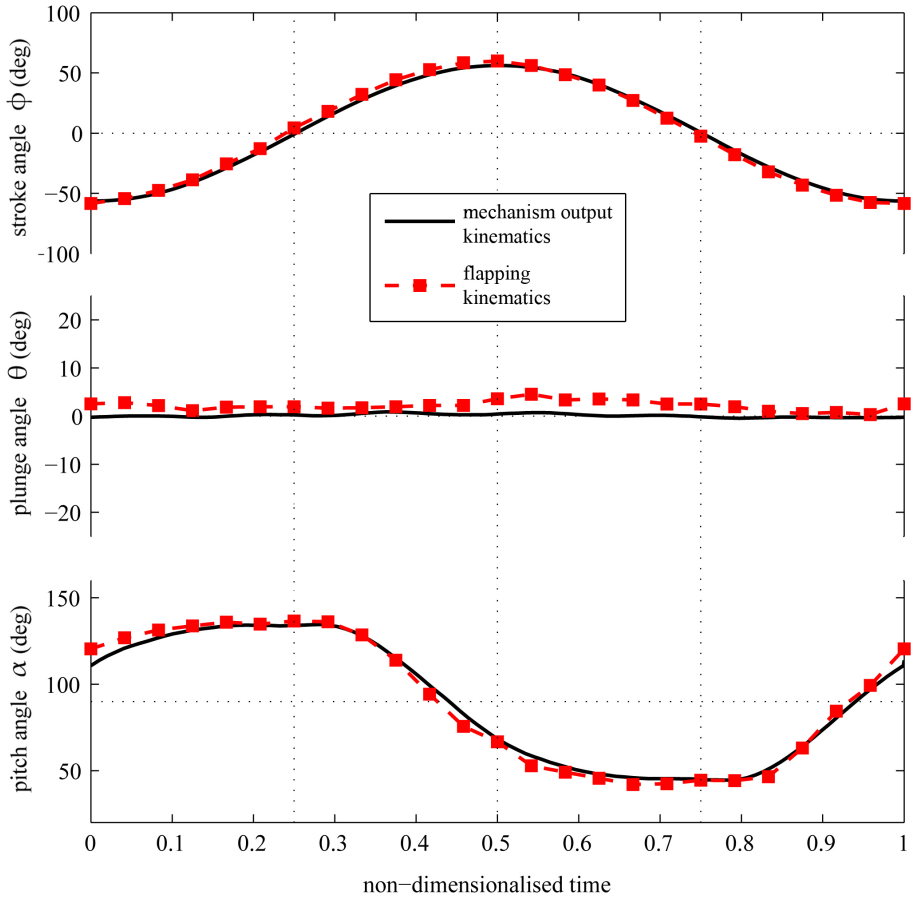

Figure 6.2: Mechanism output kinematics (black) and flapping kinematics (red) over a complete flapping cycle; time is non-dimensionalised with respect to the flapping period T (0.05s)

demanded by the flapping mechanism) are illustrated by the black lines in Figure 6.2; actual flapping kinematics (measured wing kinematics accounting for wing flexion) are shown by the red lines with symbols. If the wing were infinitely rigid then the mechanism flapping kinematics would be the same as the wing flapping kinematics. In addition, the pitching kinematics are re-plotted in Figure 6.3 with α_{min} and α_{max}, which refer to most horizontal and most vertical local pitch angles respectively along the wing at an instant. These angles give an indication of wing twist. Here, α_{max} occurs towards the root and α_{min} occurs towards the wingtip. The pitch angle α is simply the mean pitch angle along the span. For a full description of how all kinematic angles are defined, please see § 2.1.3 (page 19).

Twelve azimuthal positions evenly spaced in time throughout the flapping half cycle were chosen as the flowfield measurement positions. Again, the start

Table 6.1: Kinematic parameters

f	$20Hz$
$\bar{Re}$	15210
Φ	$118.3 \pm 2.6°$
Θ	$4.2 \pm 2.4°$
α_{mid}	$43.3 \pm 2°$
τ	$6.2 \pm 0.5\%$
Φ_{mec}	$112.7 \pm 0.2°$
Θ_{mec}	$1.3 \pm 0.6°$
$\alpha_{mec_{mid}}$	$45.6 \pm 0.4°$
τ_{mec}	$6.1 \pm 0.3\%$

of the half-stroke $0T$ was taken as the time when the wing is at rest and about to accelerate. The measurement positions start at $0.042T$ ($T/24$) and progress to $0.5T$ in increments of $T/24$. Measurements for only a half-stroke rather than a full cycle were performed because the flows generated by half-strokes in opposite directions have been reported to be mirror images of each other for symmetric kinematics (Lu et al., 2006). The flapping kinematics used here were virtually symmetric, thus only analysing a half-stroke was deemed sufficient to describe what occurs for a full flapping cycle. This also justified using mirrored flowfield

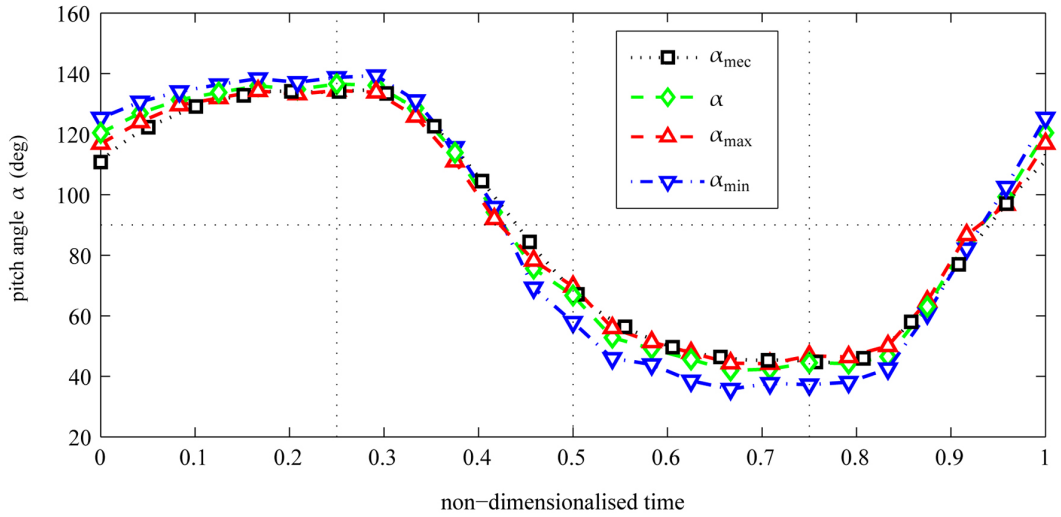

Figure 6.3: Comparison of mechanism output angle of attack (α_{mec}), mean (α), maximum (α_{max}) and minimum (α_{min}) angle of attack; time is non-dimensionalised with respect to the flapping period T (0.05s)

measurements under the wing from the return stroke to fill in masked areas in the measurement volume as described in § 5.2.

6.1.2 Flow Evolution

Figures 6.4 and 6.5 illustrate the flow evolution throughout the half-stroke viewed from the top ($-z$) and back (y) views respectively. The left column of each figure shows dark grey surfaces illustrating vortex core diameter overlaid with the vortex axis coloured with axial vorticity normalised by the mean wing angular velocity $\bar{\Omega}_{wng}$ ($79.7 rad/s$). Vortex axes become coloured dashed lines when behind other objects. Right columns show instantaneous streamlines released from vortex axes coloured with axial velocity normalised with respect to the mean wingtip speed $\bar{v}_{tip}$ ($8.4 m/s$). In addition, instantaneous black streamlines released along the wing edge are also shown, along with transparent grey isosurfaces of $Q = q\bar{v}_{tip}^2$ (where $q \approx 8.5 \times 10^4 m^{-2}$) to provide a secondary indication of the presence of vortical structures. For a given vortex axis, the positive axial direction points along the local direction of the axis (x_{va} direction) towards the end without a white dot. Figures F.1 - F.6 give these plots for all twelve measurement positions, whereas Figures 6.4 and 6.5 are condensed forms.

Immediately after the start of the half-stroke at $0.042T$ a starting vortex $STRV1$ is clearly visible at the outboard section of the trailing edge, along with a tip vortex $TPV1$ and a leading-edge vortex $LEV1$. Here, $STRV1$, $TPV1$ and $LEV1$ are one continuous vortical structure. The LEV from the previous half-stroke, $LEV0$ can also be seen at this time, particularly from the back view in Figure 6.5 underneath the wing towards the leading edge. This is highlighted by the fact that the black instantaneous streamlines released from the leading edge near the root curl underneath the wing in the same sense as the LEV from the previous half-stroke. In addition, the tip vortex $TPV0$ and root vortex $RTV0$ from the previous half stroke can be seen under the wing.

As the stroke progresses to $0.125T$, the starting vortex $STRV1$ is left behind in the wake, $TPV1$ grows in size. $LEV1$ develops more inboard where an increased level of axial vorticity is present and the vortex axis has shifted away from the leading edge. $LEV1$ and $TPV1$ remain as one continuous structure, but with an increased level of axial flow through the core. The presence of a secondary LEV

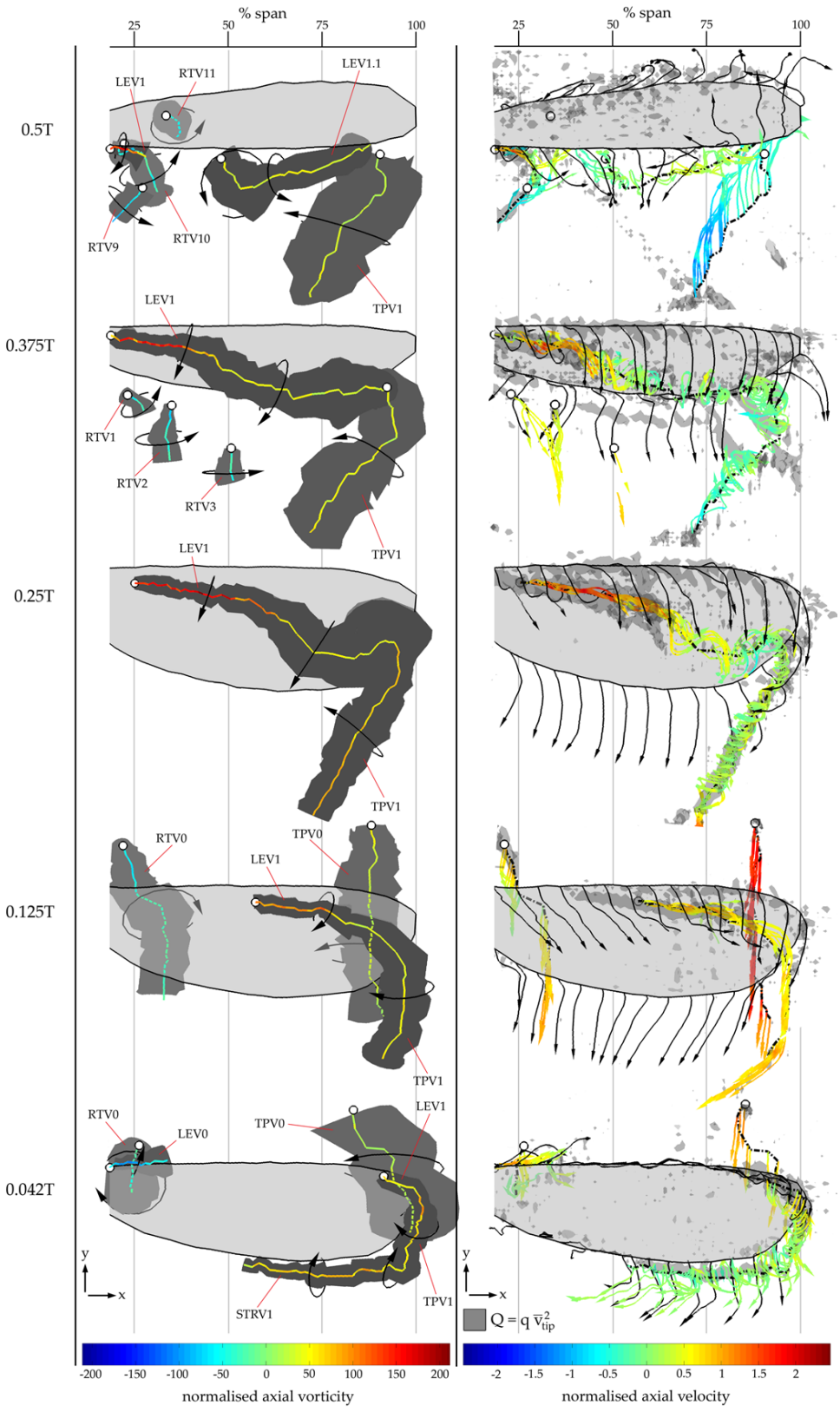

Figure 6.4: Top views illustrating flow formation over a flapping half cycle; left column shows vortex core diameter (dark grey surfaces) and vortex axes coloured with axial vorticity normalised with respect to $\bar{\Omega}_{wng}$ $(79.7 rad/s)$ (axes become dashed when behind other objects); right column shows instantaneous streamlines released from vortex axes coloured with axial flow normalised with respect to $\bar{v}_{tip}$ $(8.4 m/s)$, black streamlines released along the wing edge, and transparent grey isosurfaces of $Q = q\bar{v}^2_{tip}$ where $q \approx 8.5 \times 10^4 m^{-2}$; positive axial direction points along an axis towards the end without a white dot

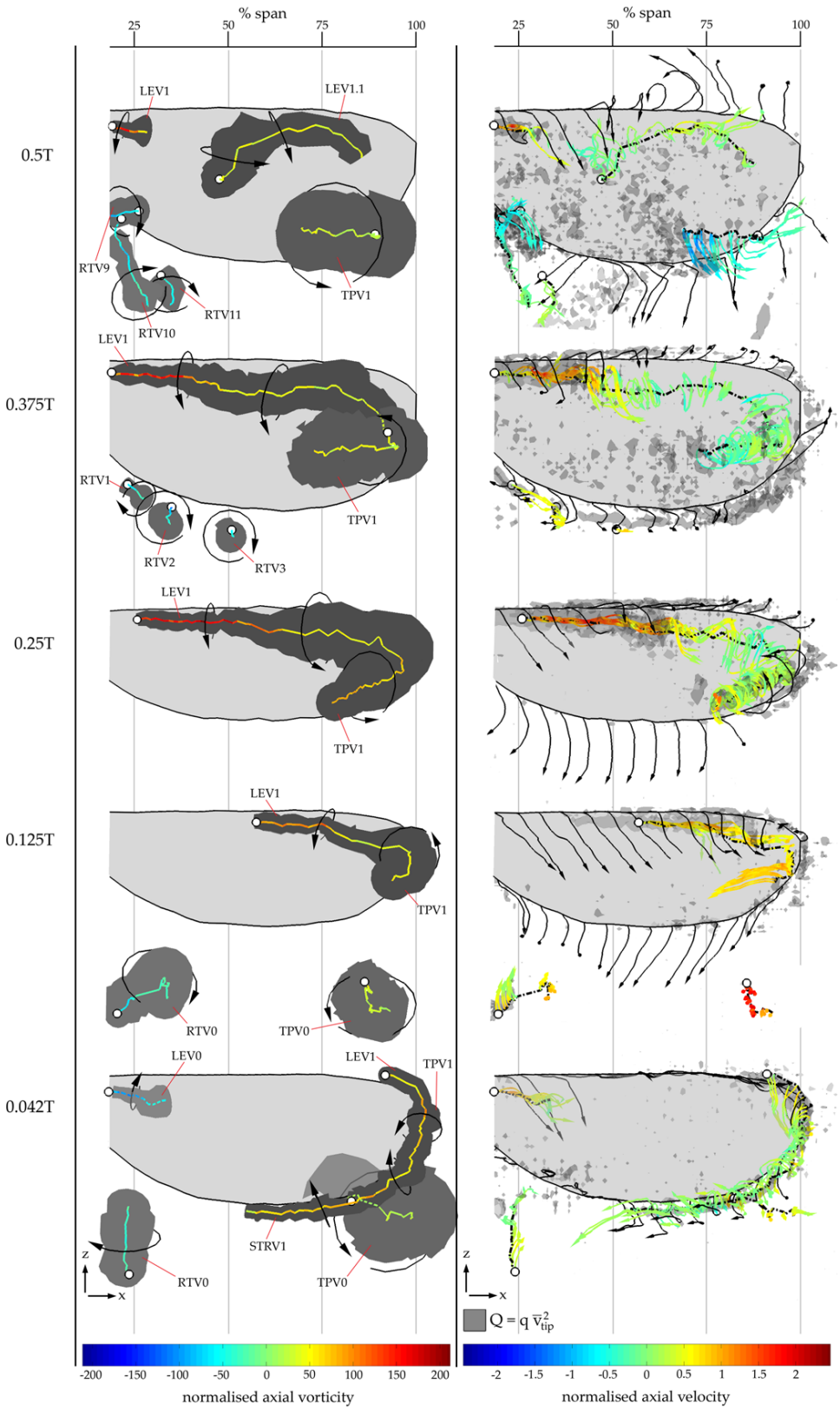

Figure 6.5: Back views illustrating flow formation over a flapping half cycle; left column shows vortex core diameter (dark grey surfaces) and vortex axes coloured with axial vorticity normalised with respect to $\bar{\Omega}_{wng}$ $(79.7 rad/s)$ (axes become dashed when behind other objects); right column shows instantaneous streamlines released from vortex axes coloured with axial flow normalised with respect to $\bar{v}_{tip}$ $(8.4 m/s)$, black streamlines released along the wing edge, and transparent grey isosurfaces of $Q = q\bar{v}_{tip}^2$ where $q \approx 8.5 \times 10^4 m^{-2}$; positive axial direction points along an axis towards the end without a white dot

right along the leading edge beyond 50% span is suggested by the Q criterion isosurfaces. $LEV0$ from the previous half stroke has disappeared at this time and is left behind in the wake. $TPV0$ and $RTV0$ are still present, but are further underneath the wing at this position in the cycle. Interestingly, the core axial velocity of $TPV0$ as seen by the wing is approximately two times the mean wingtip speed.

At the mid-stroke position $0.25T$ when the wing has reached its maximum speed, $LEV1$ has developed more towards the root with an even greater axial vorticity and axial velocity, which peaks at approximately two times the mean wingtip speed. Shortly after 50% span, a kink forms in the $LEV1$ axis. At this point the axial vorticity drops, which is accompanied by a dramatic increase in vortex diameter and a decrease in axial velocity. As $LEV1$ merges with $TPV1$, the axial vorticity rises slightly and the vortex diameter decreases. This inverse relationship between axial vorticity and vortex diameter is expected in order to obey the law of conservation of angular momentum. The observed sudden increase in vortex diameter and drop in axial velocity is an indication of vortex breakdown, which will be described in detail later on. At this point in the cycle, breakdown appears to occur around 65% span. As with the previous point in the cycle, a secondary LEV right along the leading edge extending from approximately 25% span to the wingtip is suggested by the Q criterion isosurfaces. $TPV0$ and $RTV0$ from the previous half-stroke have left the measurement domain at this point in the cycle.

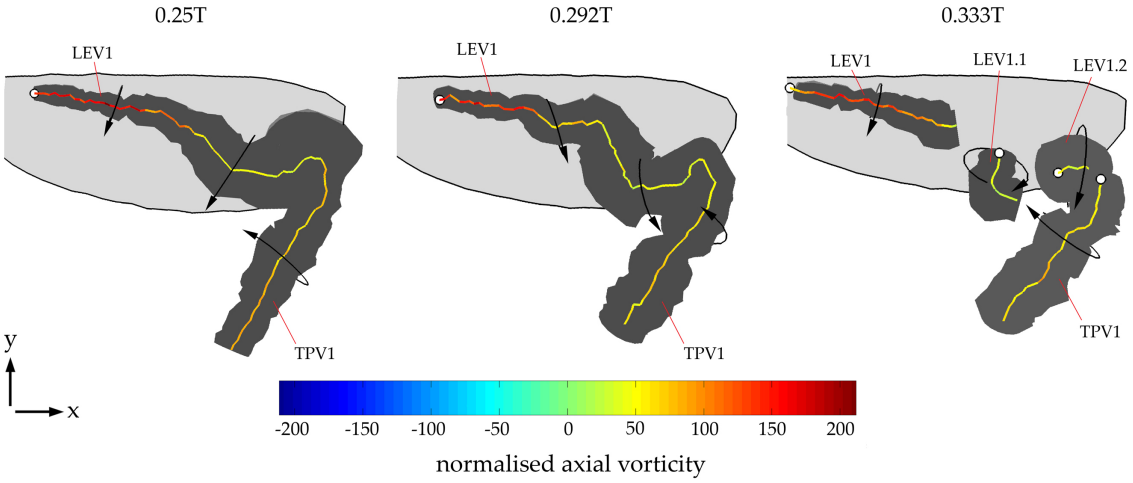

Figure 6.6: Top views of wing showing the kink in the vortex axis intensifying following mid-stroke; vortex core diameter (dark grey surfaces) is shown overlaid with vortex axes coloured with axial vorticity normalised with respect to $\bar{\Omega}_{wng}$ $(79.7 rad/s)$; positive axial direction points along an axis towards the end without a white dot

After mid-stroke, when the wing begins to decelerate, breakdown in *LEV*1 becomes intensified as the kink in the axis becomes more pronounced. This is illustrated in Figure 6.6. The portion of the vortex axis spanning approximately $70-75\%$ span turns such that the local axial direction approaches the y direction. Eventually at $0.333T$, which is shortly after pitch reversal has started, the kink in the axis has become so exaggerated that *LEV*1 outboard 'appears'[1] to break into separate structures *LEV*1.1 and *LEV*1.2. In addition, at this time the axial velocity of *TPV*1 has begun to reverse such that *TPV*1 starts to travel towards the wing rather than away from it. This occurs because as the wing decelerates it begins to see *TPV*1 as it would be viewed with respect to the ground. Here, an observer fixed to the ground sees *TPV*1 with an axial velocity directed towards the wing. As with previous points in the cycle, a secondary *LEV* right along the leading edge extending to the tip is present according to the Q criterion isosurfaces.

At this point it should be noted that structures beginning with the same number (e.g. *LEV*1, *LEV*1.1 & *LEV*1.2) are considered to be part of the same vortex structure, rather than being separate entities. These structures 'appear' separate in this analysis simply because of the vortex point-joining algorithm (described in Appendix D) being unable to join them. In reality, for most occurrences they are very likely one continuous vortex structure.

Returning to Figures 6.4 and 6.5, at $0.375T$, which is approximately one quarter into pitch reversal, the outboard section of the *LEV* has straightened. *TPV*1 has increased in diameter and its axial velocity has become even more negative as the wing decelerates. In general the axial velocity along the whole *LEV*1/*TPV*1 structure outboard of 50% span has decreased greatly at this point since the mid-stroke position. The sudden drop in axial velocity in *LEV*1 now occurs much closer to the root, implying a shift in the vortex breakdown location towards the root since mid-stroke. At this time a pitching vortex shed off the trailing edge can be seen in the Q criterion isosurfaces; this is a form of starting vortex, which occurs when the wing pitches up while still moving forward. A series of root vortices *RTV*$1-3$ is also present behind the root-ward end of the trailing edge. These root vortices appear to be the result of Kelvin-Helmholtz instability (*KHI*) in the shear layer between tip-ward flow induced by the tip vortex, and the root-ward

[1]The vortex point-joining algorithm in Appendix D, is unable to join structures *LEV*$1-$*LEV*1.2, thus they appear separate, when in reality they are probably one continuous structure

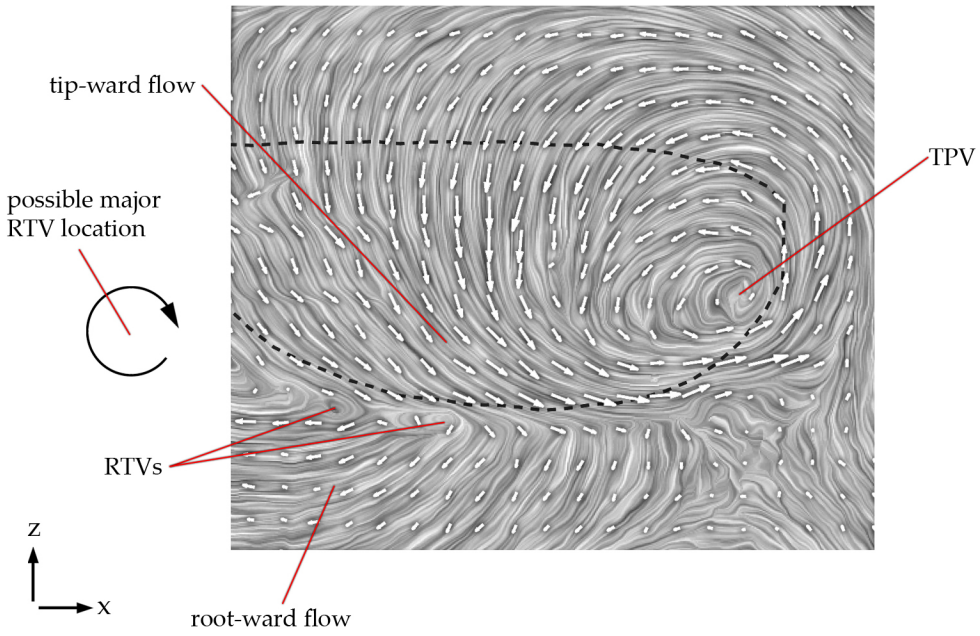

Figure 6.7: *xz* plane of vectors over top of a *LIC* image illustrating *RTV* formation at 0.375*T*; plane is approximately 20*mm* (0.72$\bar{c}$) downstream of the leading edge in the $-y$ direction; wing outline is indicated by the dashed black line

flow below as illustrated in Figure 6.7. This root-ward flow could be induced by a major root vortex outside of the measurement domain. *KHI* can occur in the shear layer between two parallel flows with different velocities, either as a result of the velocity gradient between the flows itself or due to different densities between the flows (Kundu & Cohen, 2008). In this case, the fluid density is constant everywhere (incompressible), thus it is the velocity gradient across the shear layer which leads to this instability causing the shear layer to roll up into a series of smaller vortices. It should be noted that the major *RTV* suggested earlier differs from the smaller ones as it is not created by *KHI* in a shear layer, but rather is created by the flow curling from underneath the wing at the root to the lower pressure upper side of the wing, just as the tip vortex is created.

Leading up to and at the end of the half-stroke at 0.5*T* when the wing has come to a rest, the portion of the *LEV* outboard of approximately 35% span, *LEV*1.1, contains a very low level of axial velocity. The inboard portion *LEV*1 still has a high axial vorticity and exhibits a dramatic increase in vortex diameter before the identified axis disappears. In addition, the point of decrease in axial velocity in *LEV*1 has shifted, along with the vortex breakdown location, even closer to the root since 0.375*T* and mid-stroke. As with 0.375*T*, numerous other root vortices

are observed leading up to, and at the end of the stroke. $TPV1$ has grown even larger in diameter and has separated from the LEV and is descending with the downwash, which begins around $0.417T$. The axial velocity of $TPV1$ at the end of stroke has become even more negative, where it is flowing towards the wingtip with a normalised velocity in places greater than the mean wingtip speed. This is because now that the wing has come to a rest, portions of $TPV1$ which were shed slightly earlier in the stroke are now catching up with the wing.

After the end of stroke position when the wing begins to accelerate into the next half-stroke, the process repeats and the flow returns to the beginning of the stroke as seen at $0.042T$. Since the end of stroke, the inboard portion of the LEV, $LEV1$ remains underneath the wing, becoming $LEV0$ while the outboard portion $LEV1.1$ rapidly disappears. $TPV1$ becomes $TPV0$ and continues to convect down into the downwash. The small root vortices have disappeared into the wake and a major root vortex $RTV0$ also is convected downwards with $TPV0$. At the end of stroke ($0.5T$) $RTV0$ was likely outside of the measurement domain towards the root.

Before proceeding it should be mentioned that in the previous discussion referencing Figures 6.4 and 6.5, vortex structures often start and end out of nowhere. In reality, vortex axes do not start or end in mid air, thus some of the observed structures seem impossible. In the present analysis, an identified vortex axis starts where a line of vortex points are observed and finishes when there are no more vortex points at the end of such a line as described in Appendix D. The employed method of Knowles et al. (2006) which identifies these vortex points (see § 5.3) possibly did not identify points beyond a certain extent for a given vortex axis, either because the vortex becomes too weak to identify a centre, or it has dissipated due to interference from other flows. For example, in yz planes at the start of the half-stroke the previous LEV under the wing, $LEV0$, is very visible inboard, but disappears outboard. This could occur simply because the wing speeds are higher towards the tip, where beyond a certain point moving outboard, $LEV0$ is dissipated by the stronger flow traveling underneath the wing. Thus, for such cases in which vortex structures suddenly end, it is possible that they are either very weak and continue beyond the identified 'end' or they dissipate shortly beyond this 'end'.

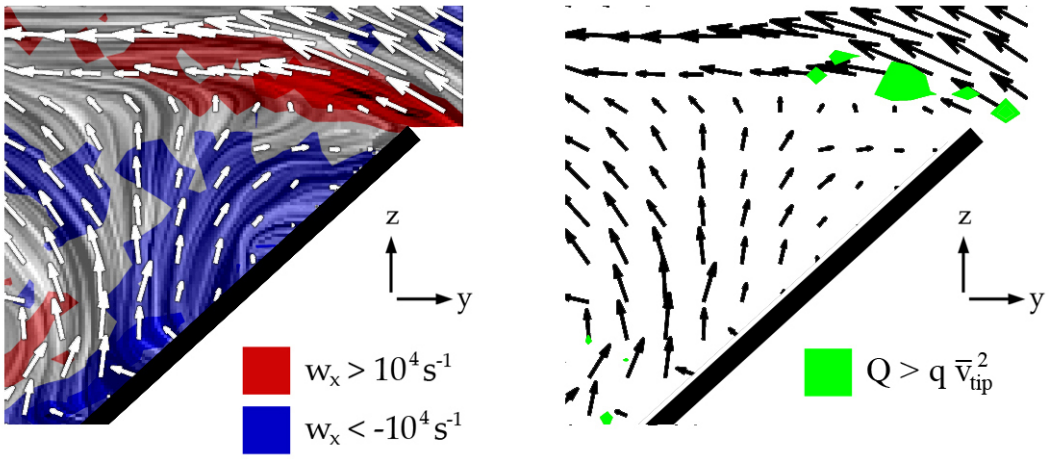

Figure 6.8: Closeup of leading edge showing secondary *LEV* and *KHVs* at 50% span at mid-stroke (primary *LEV* lies to the left outside the area viewed); velocity vectors illustrated over top of a line integral convolution (*LIC*) image and areas of highly positive (anticlockwise) and highly negative (clockwise) x-wise vorticity (left); velocity vectors and areas where $Q > q\bar{v}_{tip}^2$ ($q \approx 8.5 \times 10^4 m^{-2}$) (right)

6.1.3 Secondary LEV

As noted in the prior discussion, the presence of a secondary *LEV* right along the leading edge is suggested by the Q criterion isosurfaces. The presence and characteristics of this structure will now be investigated in more detail. Additional PIV flowfield measurements were taken at the mid-stroke position viewing a much smaller area centered at the leading edge. This gave a higher spatial resolution, revealing more details of the flow between the *LEV* and the leading edge.

Figure 6.8 illustrates a close up of the leading edge, showing approximately 20% of the local chord length at 50% span at mid-stroke. The left figure shows velocity vectors superimposed over a line integral convolution (*LIC*) image and areas of highly positive (anticlockwise) and highly negative (clockwise) x-wise vorticity. The right figure shows the same velocity vectors, together with areas with a Q value greater than $q\bar{v}_{tip}^2$ (where $q \approx 8.5 \times 10^4 m^{-2}$). For both subfigures the *LEV* lies just to the left, outside of the area viewed. It can be seen that between the *LEV* and the leading edge is a region of highly negative vorticity with a rotational sense opposite to that of the *LEV*. This is known as the secondary vortex on delta wings, as illustrated in Figure 6.9. Here, this structure will be referred to as the secondary *LEV*, while the other will be referred to as the primary. A secondary *LEV* between the primary *LEV* and leading edge has been observed at $Re >= 2500$

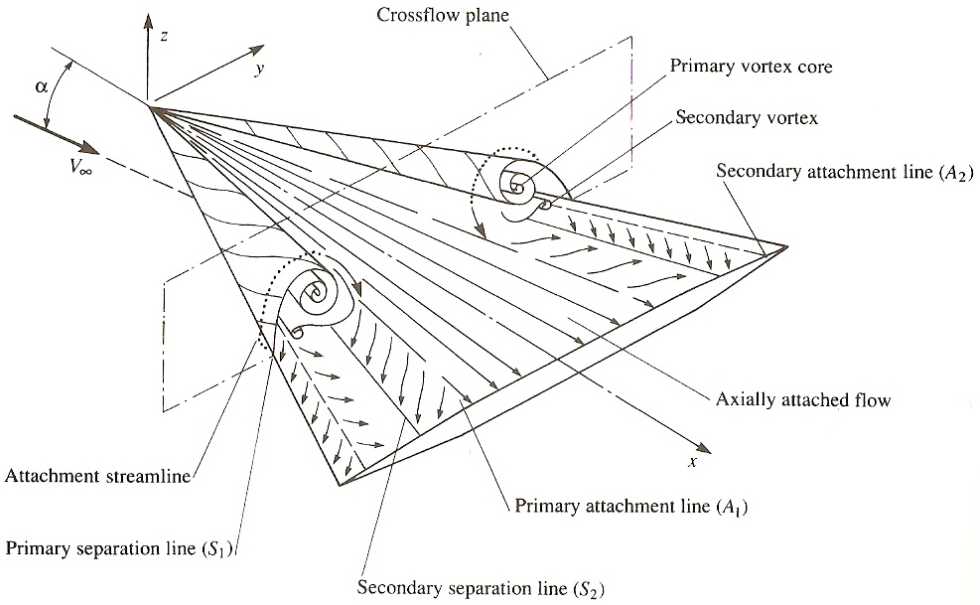

Figure 6.9: Subsonic flow over a sharp-edged delta wing (Anderson, 2001)

in CFD studies on insect-like flapping wings by Wilkins (2008)[2], and it was seen that this secondary *LEV* strengthens with increasing *Re*. Here, the secondary *LEV* extends from 33 – 95% span and grows in size towards the tip as the primary *LEV* does as shown in Figure 6.10. The secondary *LEV* was not identified by the employed vortex core identification scheme of Knowles et al. (2006) because the lower spatial resolution of the measurements (relative to those shown in Figure 6.8) combined with its position very close to the wing surface resulted in the secondary *LEV* often lacking a clearly defined centre.

The secondary *LEV* referred to above is, however, not the same structure highlighted at the leading edge by the *Q* criterion isosurfaces, which was also referred to as a secondary *LEV*. The right-hand part of Figure 6.8 shows these areas at the leading edge with the same *Q* value and above. This reveals a series of small vortices in the vortex sheet emanating from the leading edge, which resembles *KHI*. In the left-hand part of Figure 6.8 it can be seen that this area contains a high level of positive vorticity, indicating that these smaller vortices rotate in the same sense as the *LEV*. The vorticity in this region is so high due to

[2]Wilkins (2008) investigated insect-like wing geometries undergoing impulsive starts and steady rotation to simulate key elements of insect flapping aerodynamics

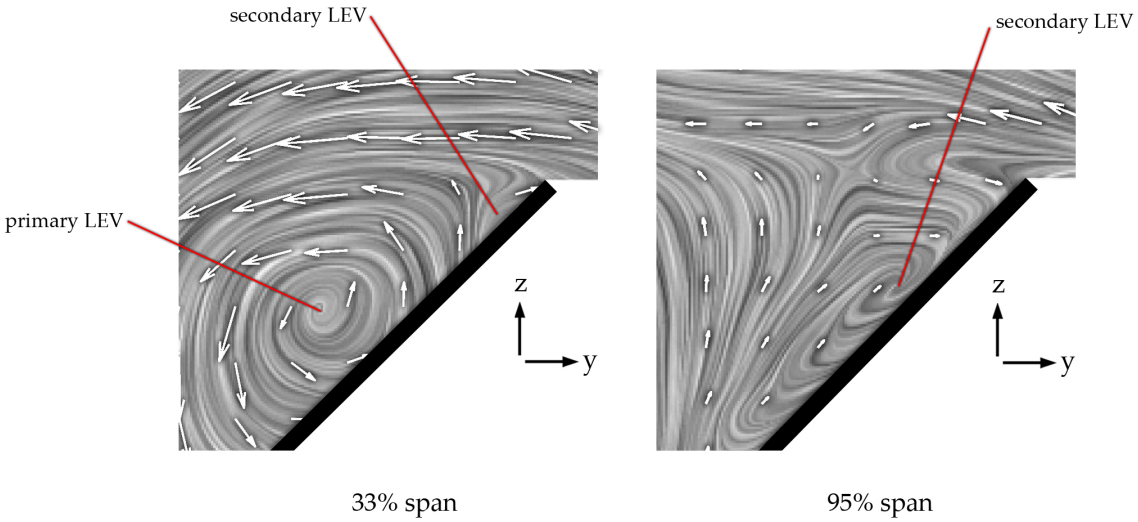

Figure 6.10: Closeup of leading-edge flowfield at mid-stroke at 33% span (left) and 95% span (right) illustrating secondary *LEV* growth; vectors are shown superimposed over *LIC* images of the measured flowfield; primary *LEV* lies to the left outside the area viewed in 95% span image

the shear between flow traveling in the $-y$ direction from the leading edge and the flow induced by the secondary *LEV* traveling in the opposite (positive y) direction. The velocity gradient is enough to lead to *KHI* in the vortex sheet leading to the formation of these smaller vortices, which will be referred to as Kelvin-Helmholtz vortices (*KHVs*). Such an instability in a vortex sheet has also been observed on delta wings as pictured in Figure 6.11c. In addition, the CFD studies of Wilkins have also reported the presence of *KHI* (termed 'breakdown' vortices) in the vortex sheet between the leading edge and the *LEV* core at $Re >= 2500$ (see Figure 6.11b). Wilkins reported that these 'breakdown' vortices in the vortex sheet were of the same sense as the primary *LEV*, as has been seen here.

From 30 – 95% span the same region of negative x-wise vorticity, highlighting the secondary *LEV*, is present along with a series of small vortices in the vortex sheet just behind the leading edge, shown by the Q criterion. Therefore, the additional vortex implied by the Q criterion isosurfaces along the leading edge in Figures 6.4 and 6.5 is not another *LEV*, but rather highlights *KHI* in the vortex sheet right at the leading edge along the span. As mentioned, this results from the level of shear between flow from the leading edge traveling towards the trailing edge, and the flow induced by the secondary *LEV* traveling in the opposite direction. Unlike that seen on delta wings, *KHVs* that form in the vortex sheet do not appear to propagate further downstream towards the primary vortex core, encircling it

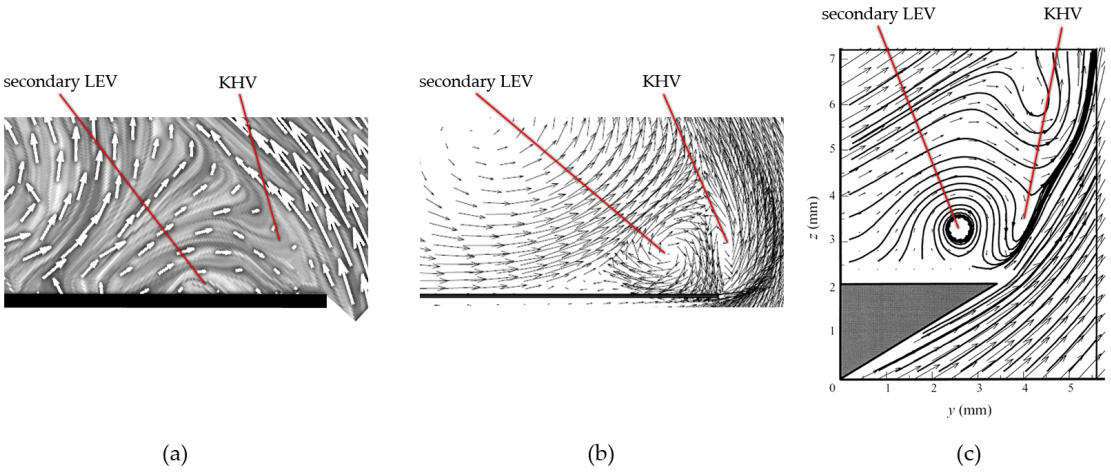

Figure 6.11: Comparison of flowfield at leading edge; (a) leading edge flowfield at 50% span at mid-stroke from the present study; (b) *CFD* results of the leading edge flow for an impulsively-started rotating (sweeping) wing at Re = 15000, α = 45° and 50% span from Wilkins (2008); (c) experimental leading edge flowfield data for a delta wing at Re = 121900, α = 12.5° from Riley & Lowson (1998); secondary vortex lies between the primary vortex and the leading edge and *KHV* results from *KHI*

and merging with it. Instead, this instability only occurs immediately above the secondary *LEV*, which suggests that the *KHVs* in the shear layer either maintain a stable position, or they dissipate or roll into the primary *LEV* as they flow past the secondary *LEV*. For convenience, from this point forward the primary *LEV* will simply be referred to as the *LEV*.

6.1.4 LEV Breakdown

At the mid-stroke position the *LEV* showed signs of breakdown. This breakdown will be investigated in greater detail. As mentioned in §2.2.8, vortex breakdown is characterised by the formation of a stagnation point on the vortex axis followed by a region of reversed axial flow (Leibovich, 1984), which is accompanied by a sudden increase in vortex size. For a detailed description of vortex breakdown and the factors affecting it, the reader is referred to §2.2.8 (page 31).

As illustrated in Figure 6.12, the trajectory of the *LEV* axis resembles the form of spiral-type breakdown given in Figure 2.10, where the sense of winding of the vortex axis is opposite to the sense of rotation of the vortex core. Figure 6.13 illustrates the axial and tangential velocity components normalised with respect to the mean wingtip speed $\bar{v}_{tip}$, vortex diameter normalised with respect to the

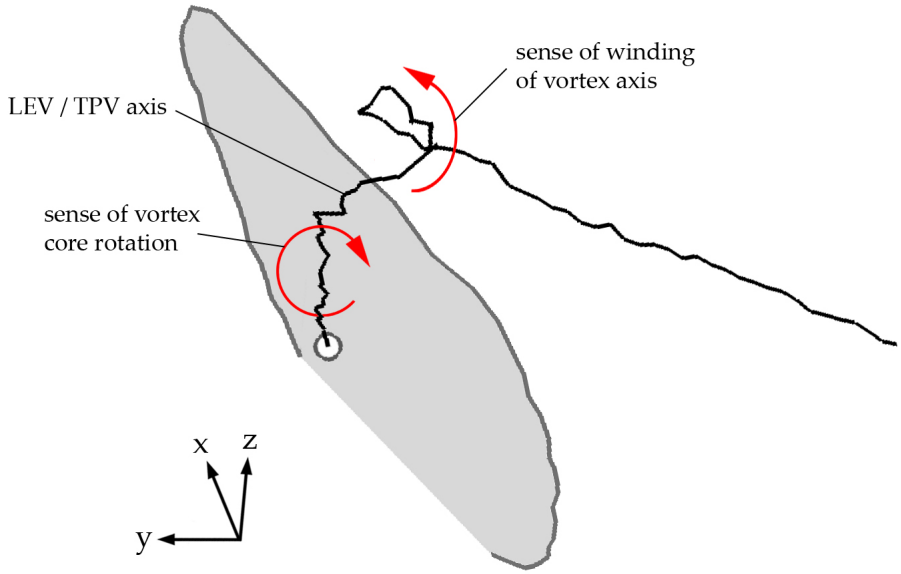

Figure 6.12: *LEV/TPV* vortex axis resembles a spiral, which is characteristic of spiral-type vortex breakdown; the sense of winding of *LEV/TPV* vortex axis is opposite to the sense of rotation of the vortex core

mean chord $\bar{c}$, and absolute helix angle along the vortex axis at mid-stroke. Here, helix angle is calculated at each axial position at approximately the centre of the vortex. For a detailed description of how helix angle is calculated, as well as the other quantities mentioned previously, see Appendix E. The identified vortex axis begins at approximately 25% span, and the axial position thereafter is normalised with respect to the wing length. Six points of interest ($n_1 - n_6$) are indicated in the graphs, and the corresponding points on the vortex axis coloured with axial vorticity, are shown in the bottom portion of Figure 6.13. In addition, Figure 6.14 illustrates the axial and tangential velocity profiles normalised with respect to $\bar{v}_{tip}$ for the same points highlighted.

Soon after the start of the vortex axis, point n_1, the axial velocity is at its peak of almost twice the mean wingtip speed, with a helix angle of approximately 30° and a jet-like axial velocity profile as seen in Figure 6.14. Further along the vortex at point n_2, which is approximately where the kink in the axis forms, the axial velocity has begun to decline, the helix angle stays at approximately 30° and the velocity profile remains jet-like. After this initial kink, the axial velocity continues to decline and the vortex diameter increases at a slightly higher rate. Eventually, at around point n_3, the helix angle surpasses the critical angle of 50° (ignoring the earlier localised spikes), which as stated in §2.2.8 is the helix angle at which

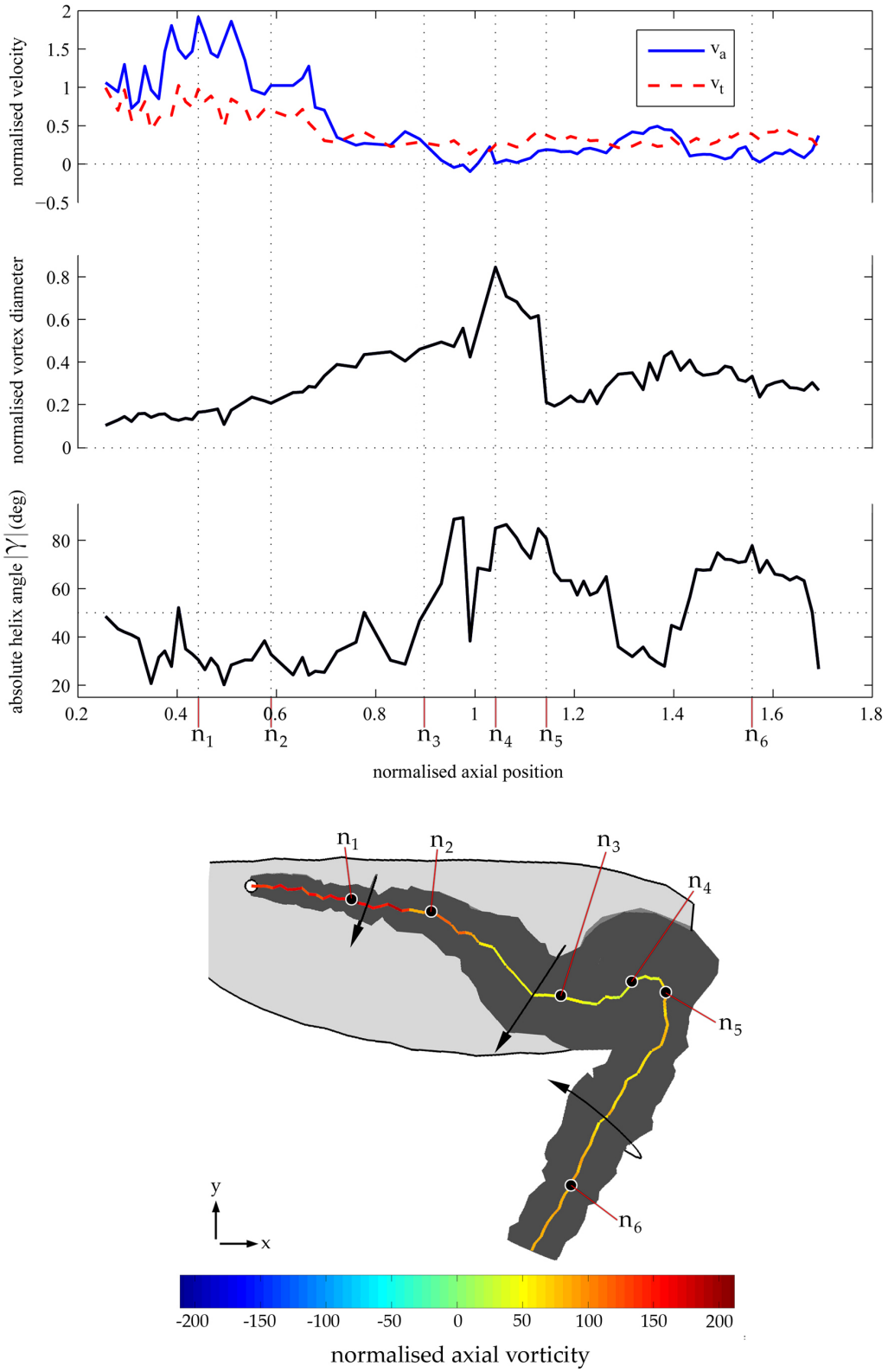

Figure 6.13: Vortex characteristics at $0.25T$; axial and tangential velocity normalised with respect to $\bar{v}_{tip}$, vortex diameter normalised with respect to $\bar{c}$, and absolute helix angle along vortex axis; vortex axis begins at approximately 25% span and axial position thereafter is normalised with respect to the wing length; points $n_1 - n_6$ mark points of interest, which correspond to points labeled on the vortex axis coloured with axial vorticity normalised with respect to $\bar{\Omega}_{wng}$ $(79.7 rad/s)$ (bottom)

breakdown occurs. In addition, at this point the axial velocity profile has changed to a wake-like velocity profile. A transition from a jet-like profile to a wake-like profile is typically observed across the breakdown location (Lucca-Negro & O'Doherty, 2001). Soon after the breakdown location, the vortex diameter rises more sharply and the axial velocity continues to decline until it eventually reaches zero, forming a stagnation point followed by region with a slightly negative axial flow. This is consistent with the definition of vortex breakdown noted at the start of this section. Also after breakdown, the magnitude of the tangential velocity has become much bigger in comparison to the axial velocity (recall that $\gamma = tan^{-1}(v_t/v_a)$), hence the helix angle has continued to rise sharply reaching almost 90°. Soon the peak vortex diameter is reached at point n_4, at which position the axial velocity is very close to zero. The axial flow is probably stagnant at this point because the axial velocity is of the same order of magnitude as the error on v_a (5% of $\bar{v}_{tip}$). Following point n_4, the vortex diameter rapidly declines to point n_5. As seen in Figure 6.14, the tangential velocity profile at this point resembles the summation of a tangential velocity profile of a larger vortex with that of a smaller vortex with the same sense. This is consistent with the *LEV* merging with the *TPV*, thus the tangential velocity profile of the *LEV* adds to that of the *TPV* resulting in the profile seen here, and reducing the vortex diameter to that of the newly added *TPV*. After this point the axial velocity profile continues to be wake-like, the vortex diameter stays relatively constant into the *TPV* and the helix angle drops below the critical value of 50° momentarily before rising above it again. This would indicate that the *TPV* is breaking down, since there the helix angle passes the critical value, which is accompanied by a slight decline in axial velocity. However, there is no accompanying increase in vortex diameter as seen at point n_6, thus either breakdown in the *TPV* is much less intense, or it is absent. As noted in §2.2.8, the level of swirl (helix angle) as well as the pressure gradient along the vortex axis affect breakdown, and independent changes in either of these can incite or suppress its occurrence. Thus, it is possible that in the *TPV* the axial pressure gradient is favourable enough to avoid breakdown despite having a helix angle above critical.

We have seen here, therefore that breakdown of the *LEV* at mid-stroke starts to occur at point n_3 which is at approximately 80% span, as at this point the helix angle reaches the critical value, and afterwards the axial flow stagnates soon and

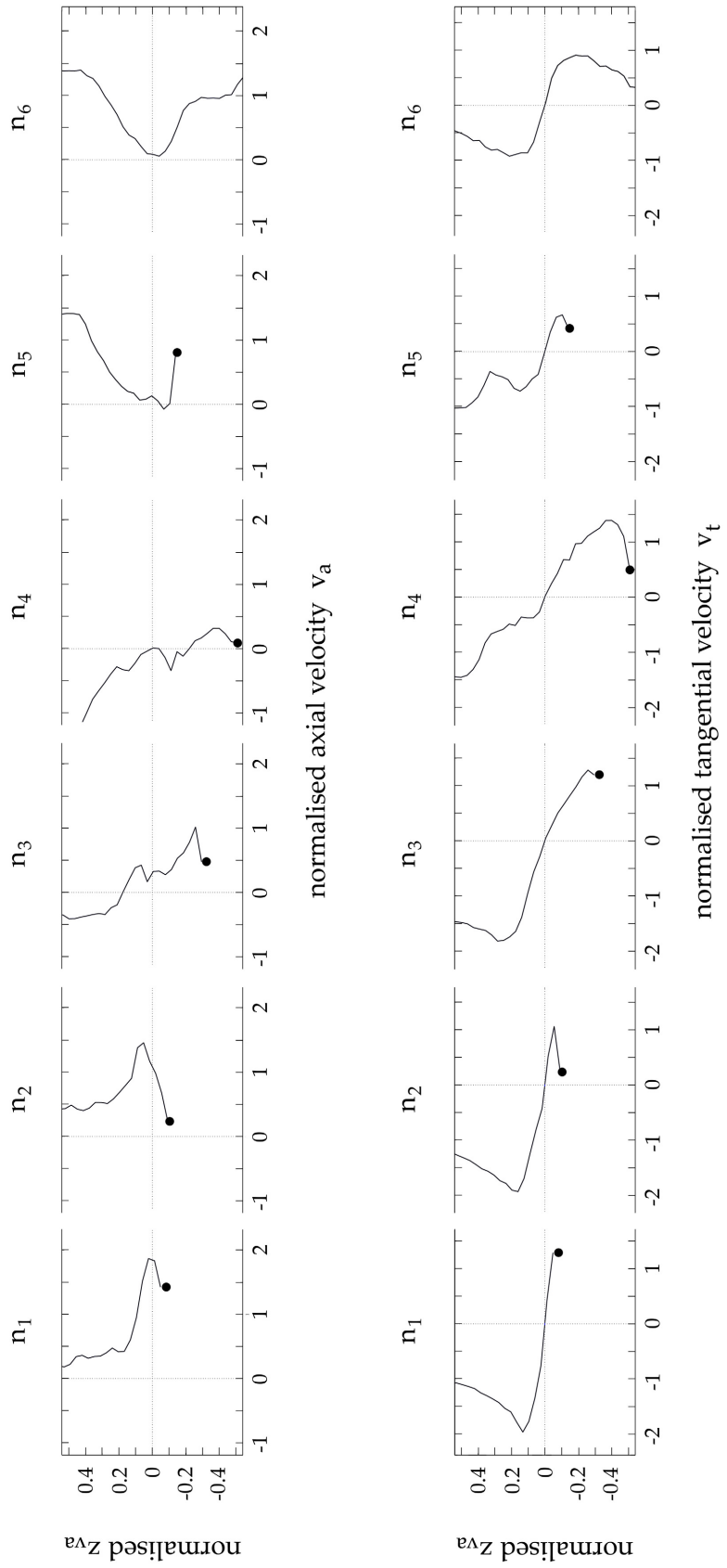

Figure 6.14: Axial (left) and tangential velocity (right) profiles normalised with respect to $\bar{v}_{tip}$ at points of interest ($n_1 - n_6$) along *LEV/TPV* axis labeled on Figure 6.13; z_{va} coordinate is normalised with respect to $\bar{c}$; black dots indicate location of wing surface

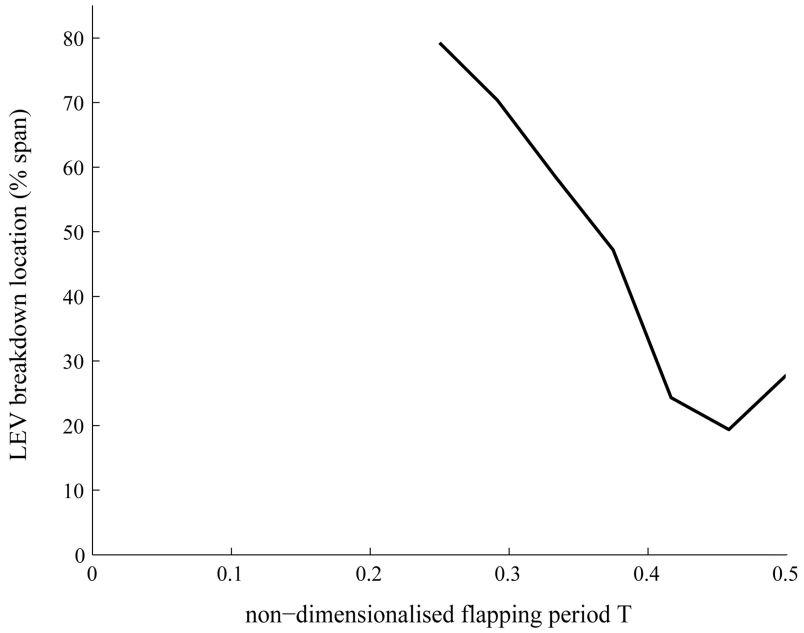

Figure 6.15: *LEV* breakdown location throughout half-stroke

the vortex diameter rises more sharply. This is much closer to the wingtip than previously estimated in §6.1.2, where the breakdown location at this point in the half-stroke was estimated to occur around 65% based on the position where the axial velocity declined rapidly and the kink formed in the axis. However, from the previous discussion it is evident that breakdown occurs beyond the kink in the axis much closer to the wingtip.

For the remainder of the half-stroke, the location of *LEV* breakdown is given in Figure 6.15. As before, the breakdown position was determined by locating the point on the *LEV* axis where the helix angle surpassed the critical value of 50°, combined with an increase in vortex diameter and a reversal in axial velocity. From Figure 6.15 it can be seen that *LEV* breakdown in fact does begin at mid-stroke, and the breakdown location generally moves inboard throughout the remainder of the half-stroke. It should be noted that at the first measurement position ($0.042T$) the helix angle did pass critical, but the vortex diameter along the entire axis was relatively constant, thus, breakdown was deemed to be absent at this point. In addition, for the prior two measurement points before mid-stroke ($0.167T$ and $0.208T$), the helix angle did pass critical at 98% span, however much less dramatic increases in vortex diameter were observed, and the axial velocity

did not reverse at any point, thus, breakdown was considered to be absent at these positions as well. However, this may suggest that the onset of *LEV* breakdown occurs shortly before mid-stroke at $0.167T$, and then becomes fully developed at mid-stroke.

It is interesting to note that the Q criterion isosurfaces around the *LEV* consistently disappear shortly before the *LEV* breakdown location as seen in Figures 6.4 and 6.5. Recalling the definition of Q from § 5.3, a sudden drop in Q level near the breakdown location implies that the vortex structure transitions from a rigid-body-like rotation to a state with comparatively higher strain rates. This makes sense in view of the fact that this vortex suddenly expands beyond the breakdown location, where by conservation of angular momentum the spiralling fluid with a tight radius from the root must decrease in angular velocity as the radius suddenly expands. Thus the rotation rates in the fluid go down with angular velocity and the strain rates become comparatively larger which means a lower Q value. For this reason, it is felt that a sudden drop in Q value is a good indication that *LEV* breakdown is present.

Cause of LEV Breakdown

Breakdown of the *LEV* probably occurs as a result of the presence of the *TPV*. Recall from §2.2.8 that downstream conditions (in the axial direction) affect the axial pressure gradient which in turn can trigger vortex breakdown. As also noted, experiments by Werlé (1960) illustrated this fact by triggering vortex breakdown in a *LEV* by blowing a jet of air in the axial direction opposite to the travel of the *LEV*. In the present investigation, the *TPV* is located a short distance away in the local *LEV* axial direction from the breakdown location. As in the experiments of Werlé (1960), the *TPV* creates an axial blowing effect by inducing a flow in the opposite direction to the axial flow of the *LEV*, which is illustrated in Figure 6.16. This occurs because the *TPV* axis is roughly perpendicular to the local axial direction (x_{va}) of the *LEV* axis at breakdown. The resulting pressure gradient is adverse enough to lead to formation of a stagnation point between these two competing flows. This can be seen in Figure 6.14 across points $n_2 - n_4$ as the axial velocity profile of the *LEV* becomes increasingly negative as it travels towards the tip. The end result is breakdown of the *LEV*. This cause of *LEV* breakdown has been postulated before by Liu et al. (1998).

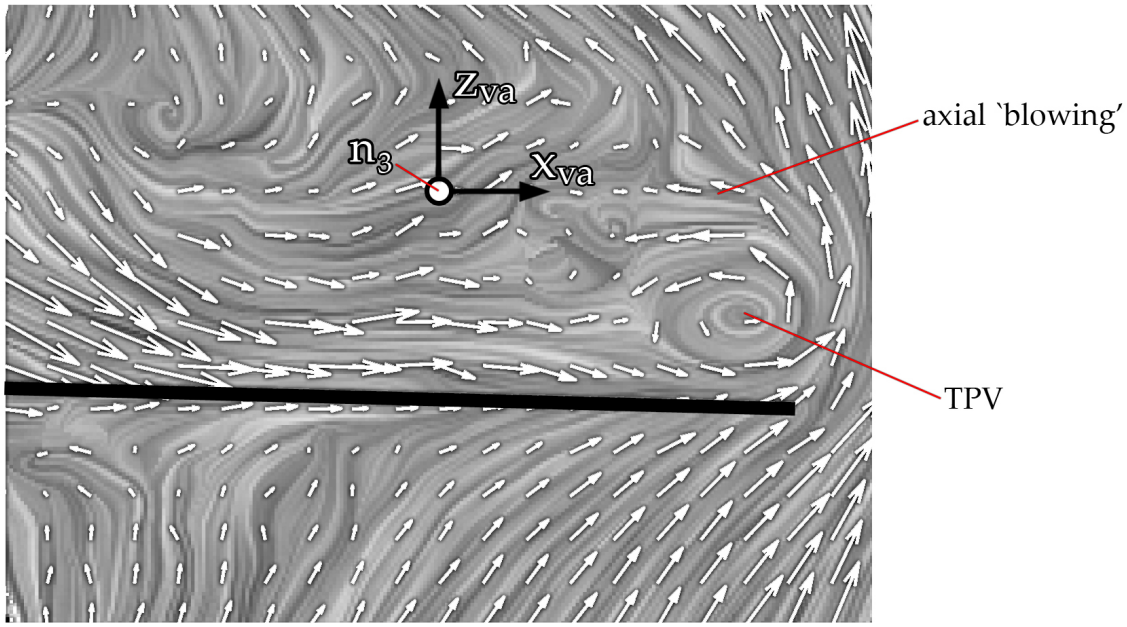

Figure 6.16: $x_{va}z_{va}$ plane at point n_3 (*LEV* breakdown location shown in Figure 6.13) on the *LEV* axis illustrating an axial 'blowing' effect originating form the *TPV*; x_{va} axis points in the local positive axial direction of the vortex axis

The observed shift in the *LEV* breakdown location inboard (Figure 6.15) also appears to be the result of an increasingly adverse axial pressure gradient, which would intensify breakdown as mentioned in §2.2.8. When examining Figure 6.4 it can be seen that following mid-stroke an increasingly greater portion of the *LEV*/*TPV* axis exhibits very low or negative axial velocities. This implies the presence of an adverse axial pressure gradient, which becomes more intense beyond mid-stroke to the point that it is strong enough to stagnate or reverse the majority of the flow along the vortex axis. The pressure gradient probably becomes more adverse in this phase of the flapping cycle because of a diminishing favourable pressure gradient, which results from a declining wing angular velocity (and, hence, declining centrifugal force) and increasing angle of attack (which we will see later in § 6.4.4 has a large effect on *LEV* breakdown).

TPV Stabilising Effect

As discussed previously, when the *LEV* merges with the *TPV*, the vortex diameter suddenly drops and soon after the helix angle falls below the critical level. This suggests that when the merger of the *LEV* with the *TPV* occurs, vortex breakdown is suppressed. Such a method for avoiding vortex breakdown using multiple

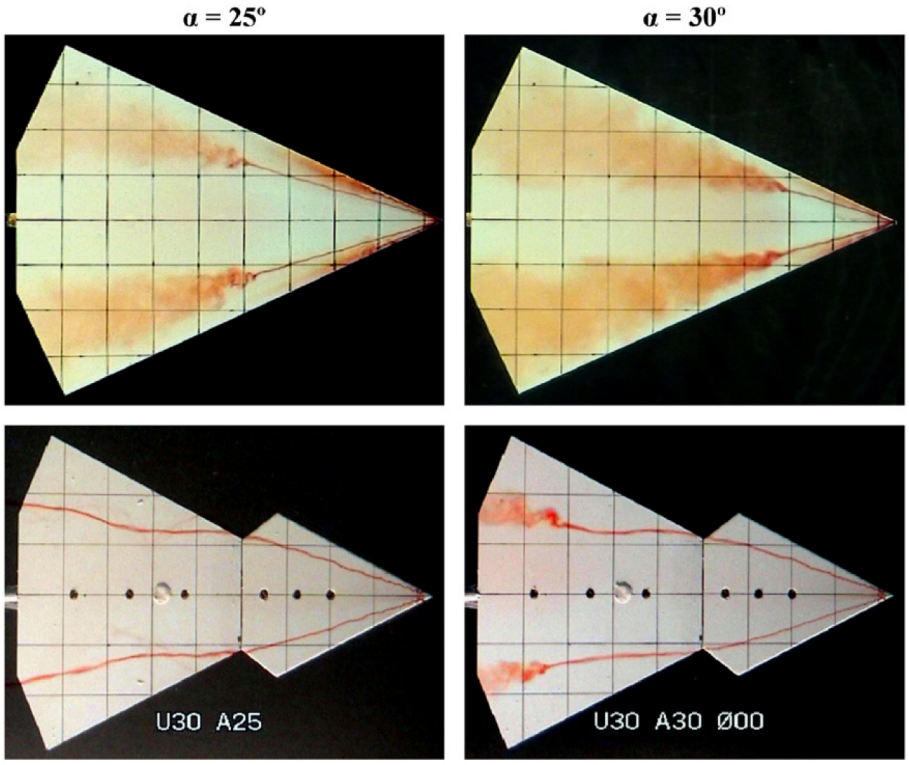

Figure 6.17: Dye visualisation of vortices over a delta wing (top) and double delta wing (bottom) at an angle of attack of 25° and 30° illustrating suppression of vortex breakdown using multiple vortices from Gursul et al. (2007)

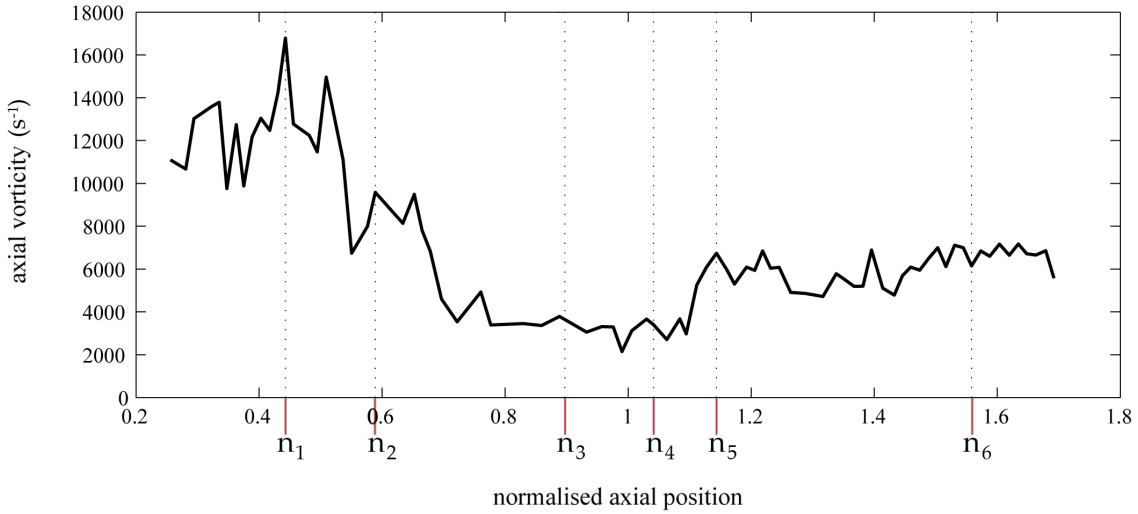

Figure 6.18: Axial vorticity along vortex axis at $0.25T$; vortex axis begins at approximately 25% span and axial position thereafter is normalised with respect to the wing length; points $n_1 - n_6$ mark points of interest along axis shown in Figure 6.13

vortices has been observed on delta wings. This is illustrated in Figure 6.17 which shows a delta wing and double delta wing at different angles of attack. On the standard delta wing the *LEVs* soon break down, however, on the double delta wing the *LEVs* from the forward delta wing are energised by the *LEVs* of the aft delta wing, which alters the pressure gradient favorably and delays or eliminates breakdown (Gursul et al., 2007). A similar mechanism takes place here. Although the *TPV* is responsible for breakdown at the identified breakdown point, when the *LEV* axis then twists following the breakdown location to join with the *TPV*, the *TPV* then suppresses breakdown by adding kinetic energy and re-energizing the vortex core. This is illustrated by Figure 6.18 which shows the axial vorticity along the vortex axis, where at the approximate point (n_5) when the *LEV* merges with the *TPV*, there is an increase in axial vorticity.

6.1.5 LEV Circulation

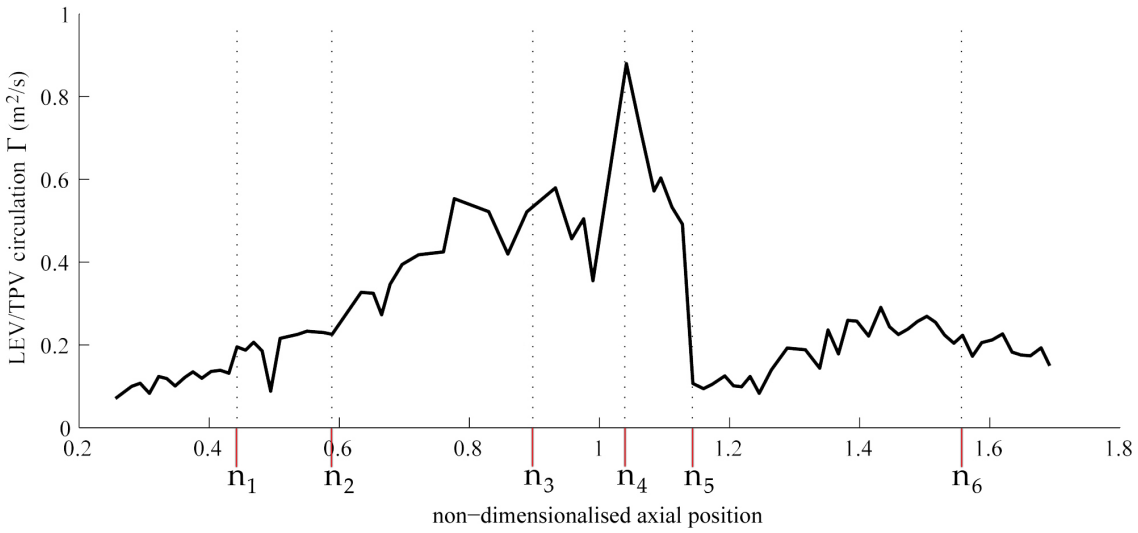

Figure 6.19: Circulation along *LEV*/*TPV* axis at 0.25*T*; vortex axis begins at approximately 25% span and axial position thereafter is normalised with respect to the wing length; points $n_1 - n_6$ mark points of interest along axis shown in Figure 6.13

The circulation along the *LEV* and *TPV* axis for a given point can be determined by using the computed vortex diameters and tangential velocity profiles according to:

$$\Gamma = \pi d v_t \tag{6.1}$$

Where d is the vortex diameter and v_t is the tangential velocity at a distance of $d/2$ from the vortex centre computed as described in Appendix E. The circulation along the *LEV*/*TPV* axis is given in Figure 6.19, where points $n_1 - n_6$ correspond to the same points of interest along the axis shown in Figure 6.13. It can be seen that the *LEV* circulation grows out towards the wingtip along with the vortex diameter growth seen in Figure 6.13. When the *LEV* merges with the *TPV* at approximately point n_5, the circulation drops with the diameter, but rises again shortly thereafter.

For the the entire half-stroke, the variation of the peak *LEV* circulation is given in Figure 6.20. It can be seen that peak circulation levels in the *LEV* rise up to the mid-stroke position, and then decline afterwards towards the end of the stroke. The variation in circulation is linked to the vortex diameter as, leading up to mid-stroke, the vortex diameter grows and then generally decreases after (see Figure 6.4). A similar trend has also been reported by van den Berg & Ellington (1997a), who observed on their 'flapper' that *LEV* circulation values on either side of the mid-stroke position were lower than at mid-stroke.

With the computed circulation, the sectional lift for a given point on the vortex axis can be computed using:

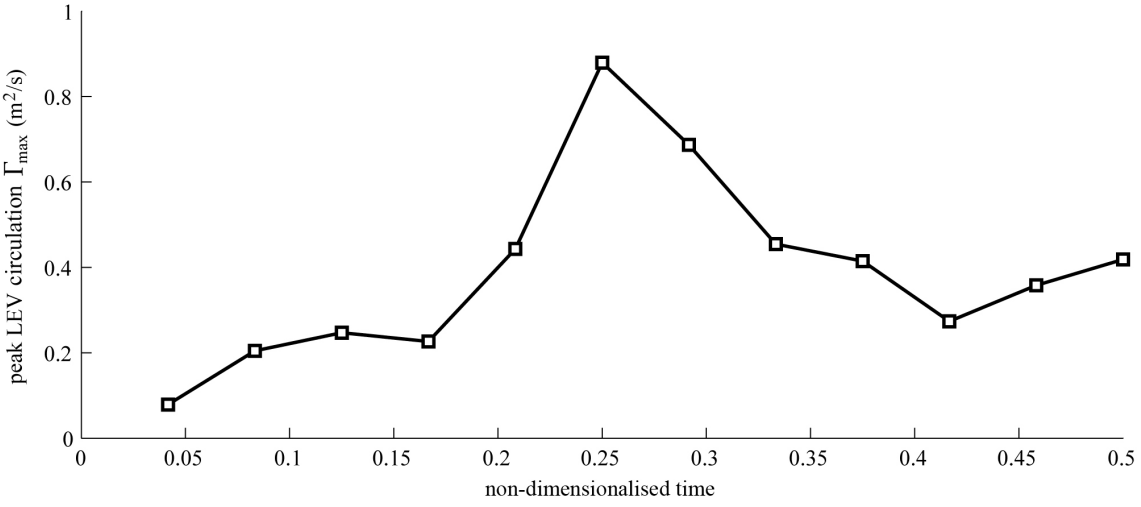

Figure 6.20: Peak *LEV* circulation throughout half-stroke; time is non-dimensionalised with respect to the flapping period T (0.05*s*)

$$L = \rho v_w \Gamma \tag{6.2}$$

Here v_w is the local wing velocity which varies along the span and throughout the half-stroke. Applying this equation to the computed circulation values and integrating the result for only the portion of the *LEV*/*TPV* that is above the wing surface provides a measure of the lift force due to the *LEV*. The identified *LEV* axis often does not start at the 'true' start of the vortex axis, thus circulation values were extrapolated inboard to the root using a power law fit through the data points up to the point of maximum circulation. The result of computing the *LEV* lift in this manner throughout the half-stroke including identified 'portions' of the *LEV* (e.g. *LEV*1 and *LEV*1.1 towards the end of stroke) is given in Figure 6.21. As with circulation, the lift on the *LEV* rises towards mid-stroke and then declines. It should be noted that the computed *LEV* lift at $0.333T$ is smaller than it should be because portions of the *LEV* between the separately identified segments of *LEV*1, *LEV*1.1 and *LEV*1.2 (see Figure 6.6) were not included in the lift calculation as these segments of the vortex axis were not identified. The same is true towards the end of the stroke from $0.417T - 0.5T$, where the computed lift would also be smaller than it truly is because the unidentified portion of the *LEV* axis between *LEV*1 and *LEV*1.1 (see Figure 6.4) could not be included in the calculation. However, the trend in Figure 6.21 provides a lower level estimate of the *LEV* lift throughout the half-stroke. Upon taking the mean of these values, it is revealed that the average *LEV* lift is $0.0734N$. In a later section, a mean lift measurement of $0.17 \pm 0.02N$ is given for a test case with a very similar set of mechanism output kinematics that only differs in the stroke amplitude, which is 1.5° larger. From these values it can be estimated that throughout a half-stroke, the *LEV* is responsible for at least 40% of the mean lift generation.

The same approach of determining the contribution of lift from the *LEV* was employed by van den Berg & Ellington (1997a). Using their 'flapper' they computed the *LEV* lift using the *LEV* diameter and tangential velocity for three points in a half-stroke, including a position before, at, and after mid-stroke. At these respective locations they quoted values of $5.27mN$, $5.45mN$ and $1.74mN$ of lift from the *LEV* and deduced using the weight of a hawkmoth (which their 'flapper' represented) that the mean lift would be $7.8mN$. Thus, they stated that the

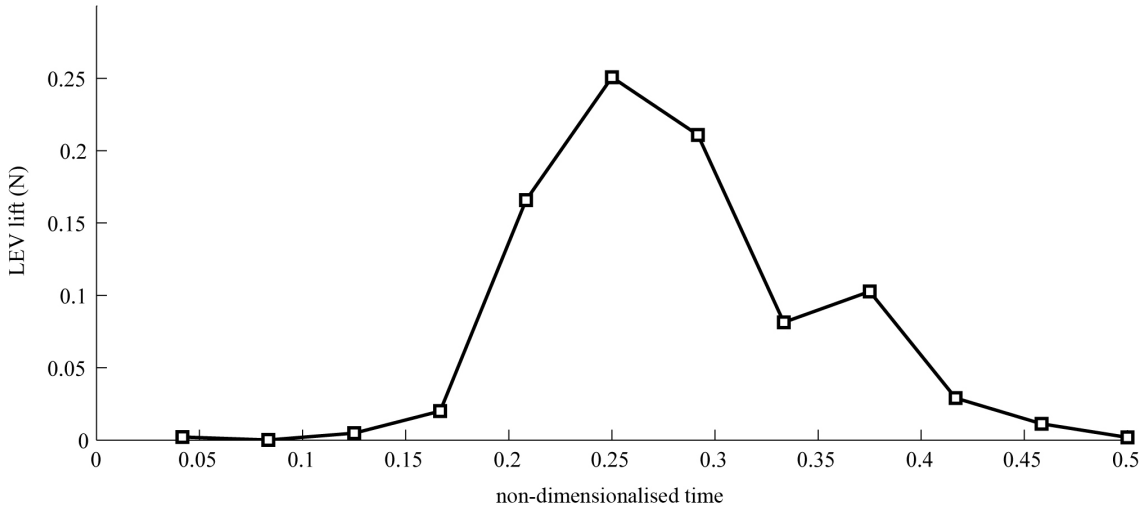

Figure 6.21: *LEV* lift throughout half-stroke; time is non-dimensionalised with respect to the flapping period T (0.05s)

LEV provides at most two-thirds of the lift generated. From the present results, it can be seen that this value is in fact much higher, as the peak *LEV* lift is larger than the estimated mean lift of $0.17 \pm 0.02N$, such that the *LEV* instantaneously generates at least 130% of the mean lift. When taking the mean of the *LEV* lift values from the study of van den Berg & Ellington (1997a), and comparing to their $7.8mN$ mean lift value, their results suggest that over a half-stroke the *LEV* contributes 53% of the generated lift. This is in closer agreement with the present result that the *LEV* generates at least 40% of the mean lift. At the upper bound of the mean force measurement ($0.19N$), the contribution of the *LEV* becomes 49%. Given this fact combined with the results of van den Berg & Ellington (1997a), it seems logical to conclude that the *LEV* contributes about half of the lift produced.

LEV Stability

From the discussion of the flow evolution throughout the half-stroke in § 6.1.2, it is apparent that the *LEV* at this FMAV scale Reynolds number is stable. Although the *LEV* becomes less coherent and 'appears' to break into separate structures in the latter half of the half-stroke (such as into *LEV*1, *LEV*1.1 and *LEV*1.2 at $0.333T$ in Figure 6.6), portions of the *LEV* are never seen to shed into the wake. As mentioned in the previous analysis when the *LEV* 'appears' to break into separate structures, this is simply a result of the vortex point-joining algorithm

being unable to join them, and in reality they are very likely one continuous vortex structure. It could be argued that shedding of the *LEV*, or portions of it, could have simply been missed between measurement points in the cycle. However, the measurement points in this investigation were close enough together that if portions of the *LEV* either inboard or outboard did shed for a given point in the cycle then they would have been observed within the measurement volume at the next measured point in the half-stroke. This can be proven by considering that even at the mid-stroke position where the wing velocity is the greatest, if the *LEV* did shed then it would only have a chance to travel at most one mean wing chord before the next measurement point in the cycle. This is based on the fact that at mid-stroke the maximum velocity along the wing at the tip was $13.2m/s$, and the time until the next measurement point was $0.0021s$ ($T/24$), thus any shed *LEV* would travel at most $(13.2m/s)(0.0021s) = 0.0275m$ (approximately equal to the mean chord length $\bar{c}$) downstream before the next measurement point. The measurement domain extends 2 mean chords downstream from the leading edge, thus any *LEV* shedding would have been observed. The mid-stroke position has the greatest risk of missing a shed *LEV*, because the wing velocity is the greatest, and thus any shed *LEV* will travel a greater distance downstream of the wing before the next measurement point. Since it has been demonstrated that even at mid-stroke any *LEV* shedding would have been detected, the possibility of missing a shed *LEV* elsewhere in the cycle can be ruled out. Therefore, despite the fact that it exhibits breakdown, the *LEV* is stable as it remains present on the upper side of the wing surface near the leading edge for the entire half-stroke, and even persists underneath the wing at the start of the subsequent half-stroke.

As mentioned in § 2.2.7 there is some controversy over the stability of the *LEV* for Reynolds numbers on the order of 10^3 and above. A possible explanation of why some researches have observed a stable *LEV* and others have not, is that *LEV* stability is very dependent on wing aspect ratio. This was concluded by Wilkins (2008) in his *CFD* studies, where he found that the *LEV* is stable up to $AR = 20$ (using the present definition of AR). He explained that the *LEV* will become unstable if it is allowed to grow to such a size that it forms a *TEV*, in which case the *TEV* will be pulled under the *LEV* toward the leading edge and the *LEV* will separate. If the aspect ratio of the wing is low enough such that the *LEV* merges with the *TPV*, before it grows too big and forms a *TEV*, then it will

be stable. This conclusion makes sense in view of the present results. It was seen in § 6.1.4 Figure 6.13, that the *LEV* continually grows in diameter towards the tip, approaching a size close to the mean chord length, before it merges with the *TPV* and the diameter suddenly drops. One can imagine that if the wing were any longer then the trend of vortex growth in Figure 6.13 would continue to rise beyond point $n4$ and ultimately the *LEV* would grow larger than the mean chord length. According to Wilkins (2008), a *TEV* would ultimately form and the *LEV* would shed. However, the aspect ratio of the wing of the present study ($AR = 6$), is low enough to prevent this.

Studies that have also observed a stable *LEV* have had a similar or lower aspect ratio to that of the present study. Investigations by Dickinson and his colleagues up to Reynolds numbers on the order of 10^4, using a fruit fly wing ($AR = 4.5$), have consistently reported a stable *LEV* (see e.g. Birch et al. (2004), Poelma et al. (2006), Lentink & Dickinson (2009)). Flow visualisation by Ellington and his co-workers on their flapper using a model hawkmoth wing ($AR = 4.2$) saw a stable *LEV* for the first half of a downstroke, but saw it shed after mid-stroke (Ellington et al., 1996; van den Berg & Ellington, 1997b,a). However, this shedding could have been a result of the operation of their flapper, as they report potential reduced *LEV* stability due to vibrations from the gearbox. A later study by the same research group using different versions of a hawkmoth wing ($AR = 5.66 - 6.33$) at $Re = 8071$ found that the *LEV* was stable on a continually revolving wing (Usherwood & Ellington, 2002a). However, in one of their prior studies using a hawkmoth and tapered wing ($AR = 5.6$ for both), they tentatively concluded that above $Re = 10000$, the *LEV* on a revolving wing lacks the axial flow required to stabilise it and it becomes turbulent and periodically grows and breaks away rather than remaining stable (Ellington & Usherwood, 2001). However, this conclusion was only drawn from force data and was not complemented with flowfield measurements or flow visualisation. From the present results we see that in fact axial flow in the *LEV* is clearly present above $Re = 10000$, and that the *LEV* does not repeatedly grow and shed. Experiments by Leishman and co-workers using their flapping wing model, in one study using a rectangular wing ($AR = 10$) (Tarascio et al., 2005), and in other studies with a fruit fly wing planform ($AR = 4.5$) (Ramasamy et al., 2005; Ramasamy & Leishman, 2006) over Reynolds numbers spanning 8000 to 19500, found shedding of the

LEV. However, this could have been a result of the wing pitching kinematics of their mechanical model, which upon examination show oscillations during the wing sweep. Pitching oscillations would lead to vortex shedding, which possibly explains their observations. Investigations by Lu & Shen studying a range of wings with aspect ratios ranging from $1.8 - 15.4$ over $Re = 160 - 3200$ reported the presence of dual *LEVs* for all wings tested. The primary *LEV* was reported to remain attached to the inboard portion of the wing and diffused out towards the tip, while the minor (secondary) *LEV* present along the leading edge, and of the same rotational sense as the primary *LEV* shed towards the wingtip (Lu et al., 2006). They noted that when compared to the dragonfly wing ($AR = 8$), the primary *LEV* of the fruit fly wing ($AR = 4.5$) only began to diffuse closer to the wingtip, and exhibited a more stable structure. In a later study performing more detailed flowfield measurements of the dragonfly wing ($AR = 8$), their observations of this wing were extended to include the presence of three minor *LEVs* in addition to the primary (Lu & Shen, 2008). These minor vortices were seen to shed at the tip-ward portion of the wing. For a similarly high aspect ratio wing, studies of Jones & Babinsky using a rotating wing model ($AR = 8$) observed continuous *LEV* shedding over the Reynolds numbers tested ($Re = 10000 - 60000$) (Jones & Babinsky, 2010, 2011). Therefore, there appears to be a trend where for aspect ratios up to approximately 6, the *LEV* is most often reported to be stable, which is consistent with the present results. As aspect ratio rises up to 8 stability of the *LEV* declines and shedding occurs. This is consistent with the findings of Wilkins (2008) that above a certain aspect ratio, the *LEV* will be unstable, however this 'critical' aspect ratio appears lower than he predicted, and appears to be somewhere between $AR = 6 - 8$.

6.2 Rotation Phase Effects

From the previous section we now have a detailed picture of how the flow develops throughout a typical flapping cycle. The next step is to see how this picture changes as kinematic parameters are altered. The first investigation of this type focuses on effects of varying rotation phase, which describes the phase relationship between the pitching kinematics and the stroke kinematics. Recall that a positive, zero, or negative rotation phase means that during pitch reversal the

wing reaches a 90° angle of attack before, at, or after the end of a half stroke respectively. Rotation phase is quantified in terms of a percentage of the flapping period (T). For example, at a 20Hz flapping frequency, a rotation phase of +5% means that the wing begins pitching early so that it reaches a 90° angle of attack 2.5ms before reaching the end of the stroke. Here the effects of changing rotation phase on the mean lift and flow structures generated throughout a stroke are investigated. The measurement cases will first be presented, followed by the mechanism output and flapping kinematics, mean lift measurements, and finally, the flowfield measurements.

Table 6.2: Kinematic parameters for test cases which vary rotation phase

case #	1.1	1.2	1.3	1.4	1.5	1.6	1.7	1.8
f	20Hz	20Hz	20Hz	20Hz	20Hz	20Hz	20Hz	20Hz
$\bar{Re}_1$	17760	17830	17800	17800	17840	18120	17870	17590
$\bar{Re}_2$	–	–	17430	17420	17490	–	17570	–
Φ	129.2 ±8°	129.8 ±8°	140.9 ±2.6°	137.5 ±2.6°	135.7 ±2.6°	131.8 ±8°	136.9 ±2.6°	127.9 ±8°
Θ	1.2 ±5.2°	1.7 ±5.2°	3.7 ±2.4°	3.8 ±2.4°	3.2 ±2.4°	1.7 ±5.2°	5.8 ±2.4°	1.8 ±5.2°
α_{mid}	43.9 ±4.9°	43 ±4.9°	45.3 ±2°	44.7 ±2°	46.2 ±2°	43.2 ±2°	47.3 ±2°	47.1 ±4.9°
τ	−14.7 ±1.4%	−10.1 ±1.4%	−3.7 ±0.5%	+1.6 ±0.5%	+5.5 ±0.5%	+6.1 ±1.4%	+10.1 ±0.5%	+15.2 ±1.4%
Φ_{mec}	129.2 ±0.2°	129.8 ±0.2°	129.5 ±0.2°	129.5 ±0.2°	129.7 ±0.2°	131.8 ±0.2°	130.1 ±0.2°	127.9 ±0.2°
Θ_{mec}	1.2 ±0.6°	1.7 ±0.6°	1.6 ±0.6°	1.4 ±0.6°	1.7 ±0.6°	1.7 ±0.6°	1.7 ±0.6°	1.8 ±0.6°
$\alpha_{mec_{mid}}$	43.9 ±0.4°	43 ±0.4°	44.4 ±0.4°	45.5 ±0.4°	45.3 ±0.4°	45.7 ±0.4°	46.8 ±0.4°	47.1 ±0.4°
τ_{mec}	−14.7 ±0.3%	−10.1 ±0.3%	−5 ±0.3%	+0.2 ±0.3%	+4.9 ±0.3%	+6.1 ±0.3%	+10.2 ±0.3%	+15.2 ±0.3%

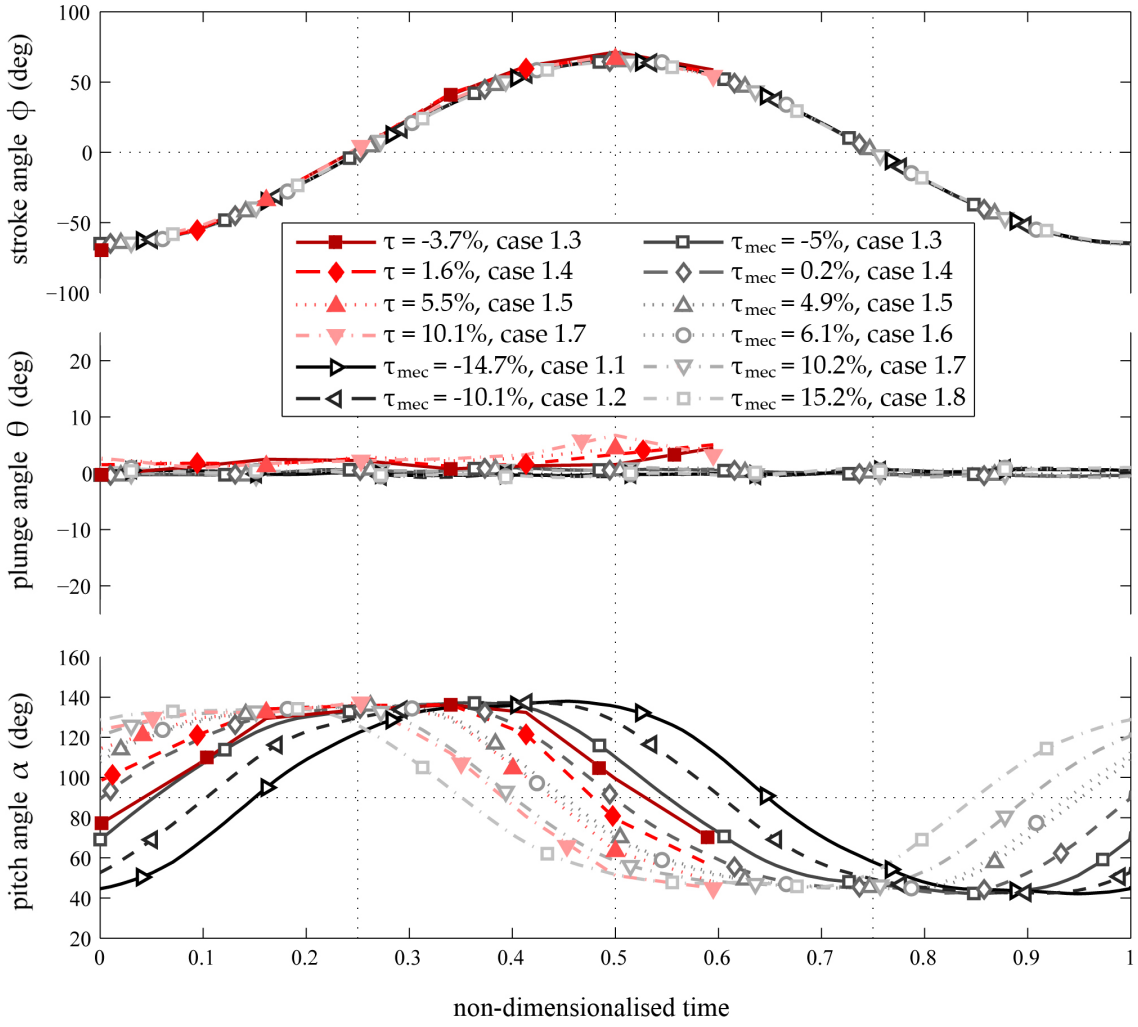

Figure 6.22: Mechanism output kinematics (black) and flapping kinematics (red) for test cases that vary rotation phase; time is non-dimensionalised with respect to the flapping period T (0.05s)

6.2.1 Flapping Kinematics & Measurement Cases

Starting from the 'baseline' set of kinematics presented in § 5.1, rotation phase was varied while all other parameters were held virtually constant. Eight rotation phases ranging from very negative to very positive values were tested giving the eight test cases listed in Table 6.2. For all test cases, mean lift measurements were performed. Flowfield measurements and the accompanying instantaneous wing position measurements were performed only for cases 1.3 – 1.5&1.7. These cases have smaller errors on their kinematics parameters as the flapping kinematics were measured directly via the instantaneous wing position measurement procedure outlined in § 5.2.3 (page 132) rather than estimating flapping kinematics

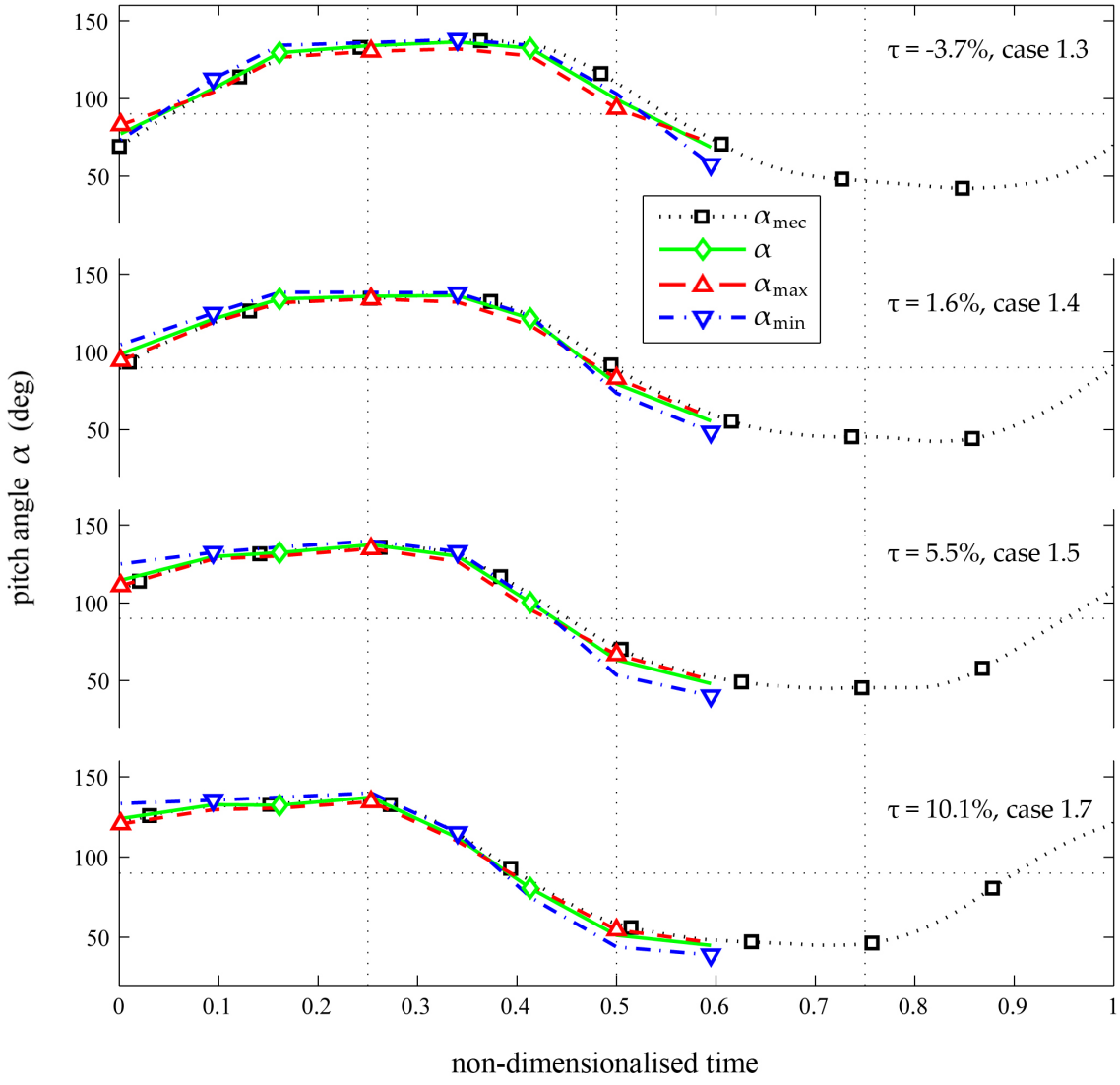

Figure 6.23: Comparison of mechanism output angle of attack (α_{mec}), mean (α), maximum (α_{max}) and minimum (α_{min}) angle of attack for rotation phase test cases involving flowfield measurements; time is non-dimensionalised with respect to the flapping period T (0.05s)

from the mechanism output kinematics as described in § 5.4.4 (page 143). Flowfield measurements were only performed on these cases because they adequately encompassed the peaks in the mean lift and mean lift coefficient versus rotation phase trends as will be shown later. Re_1 and Re_2 indicate the Reynolds numbers during the mean lift, and flowfield measurements respectively. These differ slightly because of varying air pressure on the day of measurement.

For each test case involving flowfield measurements, six measurement points throughout a half-stroke were chosen for flowfield measurement including: $0.09T$,

$0.16T$, $0.25T$, $0.34T$, $0.41T$, $0.5T$. Again, the beginning of the half-stroke $0T$ is the time when the wing is at rest and about to accelerate into a half-stroke. As with §6.1, only a flapping half cycle was examined as the flowfield generated by half strokes in opposite directions would be the same (but mirrored), due to the symmetric kinematics used. With this in mind, flowfield measurements were also performed under the wing at $0.59T$ and $0T$ to fill in the masked areas in the measurement volume at $0.09T$ and $0.5T$ respectively. Only under-the-wing measurements were performed at these times since these are the points when the *LEV* from the previous stroke is likely to be under the wing.

The mechanism output and flapping kinematics for each of the test cases are given in Figure 6.22. In addition, plots of α_{mec}, α, α_{max} and α_{min} (recall that α_{max} & α_{min} represent the most vertical and horizontal pitch angles respectively) throughout the flapping cycle for the test cases involving flowfield measurements are shown in Figure 6.23, giving an indication of wing twist. For both figures, the flapping kinematics (red) only extend to $0.59T$ since flowfield measurements were only performed up until this point, as mentioned previously.

6.2.2 Effect on Mean Lift

The effect of varying rotation phase on mean lift is illustrated in Figure 6.24. It can be seen that mean lift and mean lift coefficient peak at a rotation phase of +5.5%, beyond which any positive effects from pitching the wing early are diminished. In addition, it can be seen that negative rotation phases are especially detrimental to lift production.

It has been noted by Ansari et al. (2008b) that the benefits of an advanced pitch reversal and the detriments of negative ones are a consequence of the Kramer effect (see Chapter 2 for a description of the Kramer effect). Here, for an advanced pitch reversal (positive rotation phase) the wing begins to pitch up sooner than it would with a 0% rotation phase. According to the Kramer effect, the rapid change in pitch will be accompanied by an increase in lift. Since pitch reversal is advanced, the wing will have a higher speed while it is pitching and hence more lift compared with a 0% rotation phase.

As rotation phase is further increased, however, the segment where the wing travels with a negative angle of attack before coming to the end of the stroke

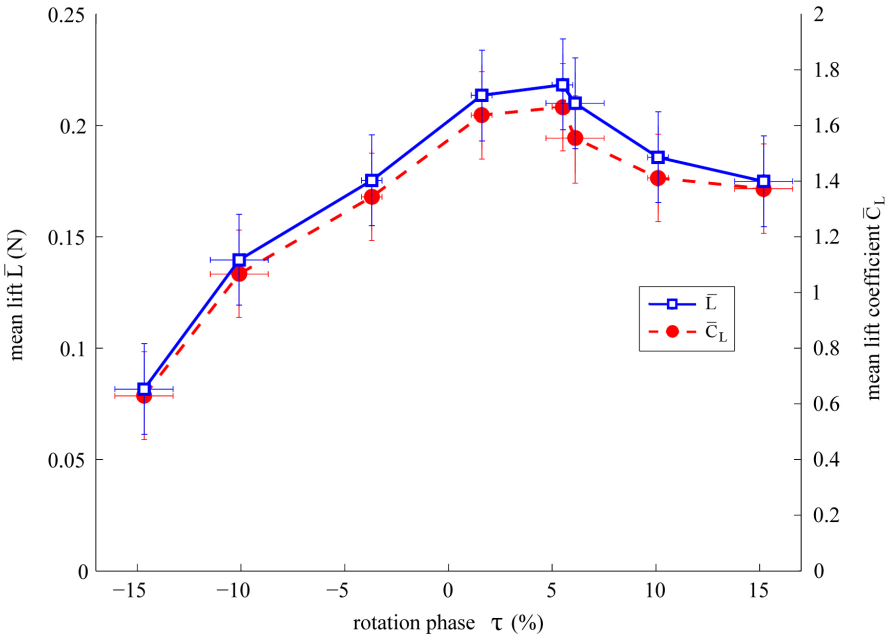

Figure 6.24: Effect of rotation phase on mean lift and mean lift coefficient

gets longer. Beyond a +5.5% rotation phase, the length of this segment and the negative lift it produces appears to negate the lift-enhancing benefits of pitching the wing early. As rotation phase decreases below zero, lift drops dramatically. This is because, as the wing begins to pitch later and later, the wing starts the subsequent half-stroke with an increasingly negative angle of attack. When the wing starts a half stroke with a negative angle of attack, it suffers a negative Kramer effect, where the wing rapidly pitches down, resulting in a sharp increase in negative lift.

The theoretical results of Ansari et al. (2008b) determined a similar rotation phase of +5% to be optimal for creating lift, and the trend of mean lift versus rotation phase observed was very similar to that illustrated in Figure 6.24. It appears that the only previous experiments that have investigated rotation phase effects are those by Dickinson et al. (1999) and later by the same research group in the study of Sane & Dickinson (2001). The earlier study investigated delayed, symmetric and advanced pitch reversals, where they found that advancing pitch reversal led to higher mean lift. In their later study various kinematic parameters were altered including rotation phase to observe the effects on forces. Similar to the present results, they found that a rotation phase of +5% maximised lift along

with a stroke amplitude, angle of attack at mid-stroke, and 'flip duration' of 180°, 45°, and 10% respectively. Here 'flip duration' is the time taken for pitch reversal to occur as a percentage of the flapping period T. For the present experiments, this parameter was approximately 50%. Both of Dickinson's experimental studies were performed at much lower Reynolds numbers (Re on the order of 10^2), thus results presented here show that the benefits of pitching the wing early by approximately +5.5% of the flapping cycle extend to the FMAV scale.

6.2.3 Effect on Flow Evolution

The effect of varying rotation phase on the evolution of the flow throughout a half-stroke will now be presented, which should also give further insight into the mean lift and lift coefficient versus rotation phase trend shown previously. Figures 6.25 - 6.27 illustrate the flow evolution throughout the flapping half cycle for the four rotation phases $\tau = -3.7\%, 1.6\%, 5.5\%, 10.1\%$ from test cases 1.3 – 1.5&1.7 respectively. As mentioned previously, it can be seen that these rotation phases investigated span across the mean lift and mean lift coefficient peaks in Figure 6.24. Top ($-z$) and back (y) views of the wing are respectively shown by Figures 6.25 and 6.26, which illustrate vortex diameter with dark grey surfaces overlaid with vortex axes coloured with axial vorticity (normalised by the mean wing angular velocity). Figure 6.27 shows the top views of the wing with instantaneous streamlines released from vortex axes coloured with axial velocity (normalised with respect to the mean wingtip speed). In addition, instantaneous black streamlines released along the wing edges are also shown, along with transparent grey isosurfaces of $Q = q\bar{v}_{tip}^2$ (where $q \approx 8.5 \times 10^4 m^{-2}$). As with the similar figures in § 6.1.2, the positive axial direction points along the local direction of a given axis towards the end without a white dot. Figures F.7 - F.14 (see Appendix F) present these top and back view plots for all six measurement positions, whereas Figures 6.25 - 6.27 are condensed forms.

From Figures 6.25 - 6.27 it can be seen that the general trend of flow evolution from $\tau = -3.7\%$ to 10.1% is the same as that presented in § 6.1.2. That is, at the start of the stroke a starting vortex ($STRV1$) is shed and the primary LEV ($LEV1$) and the tip vortex ($TPV1$) form, while the LEV, tip vortex and root vortex from the previous stroke ($LEV0$, $TPV0$, $RTV0$) still persist under the wing. $LEV0$,

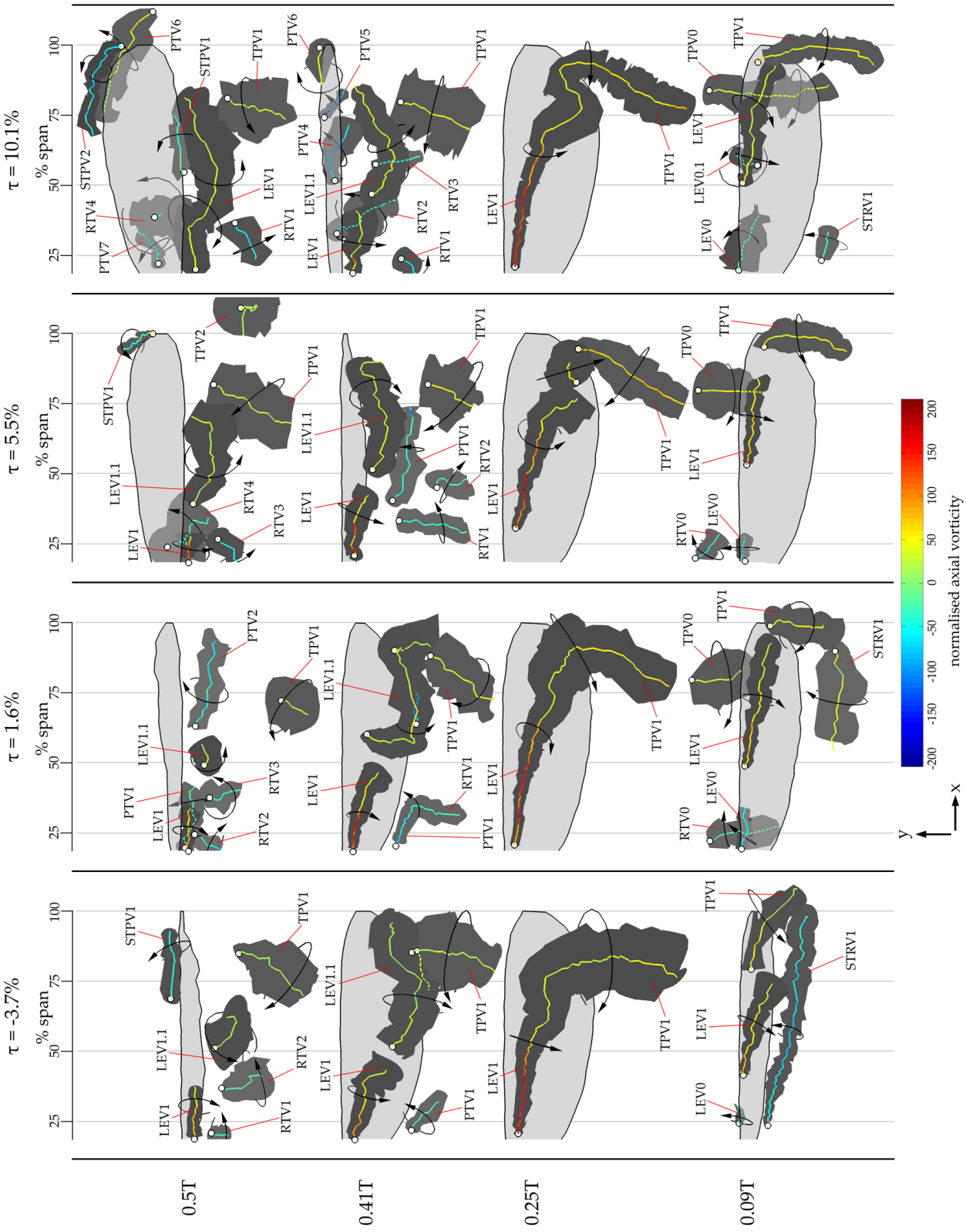

Figure 6.25: Top views illustrating flow formation over a flapping half cycle for four rotation phases: τ = −3.7%, 1.6%, 5.5%, 10.1%; vortex core diameter (dark grey surfaces) shown with vortex axes coloured with axial vorticity normalised with respect to $\bar{\Omega}_{wng}$ (91.7rad/s) (axes are dashed lines behind objects); positive axial direction points along an axis towards the end without a white dot

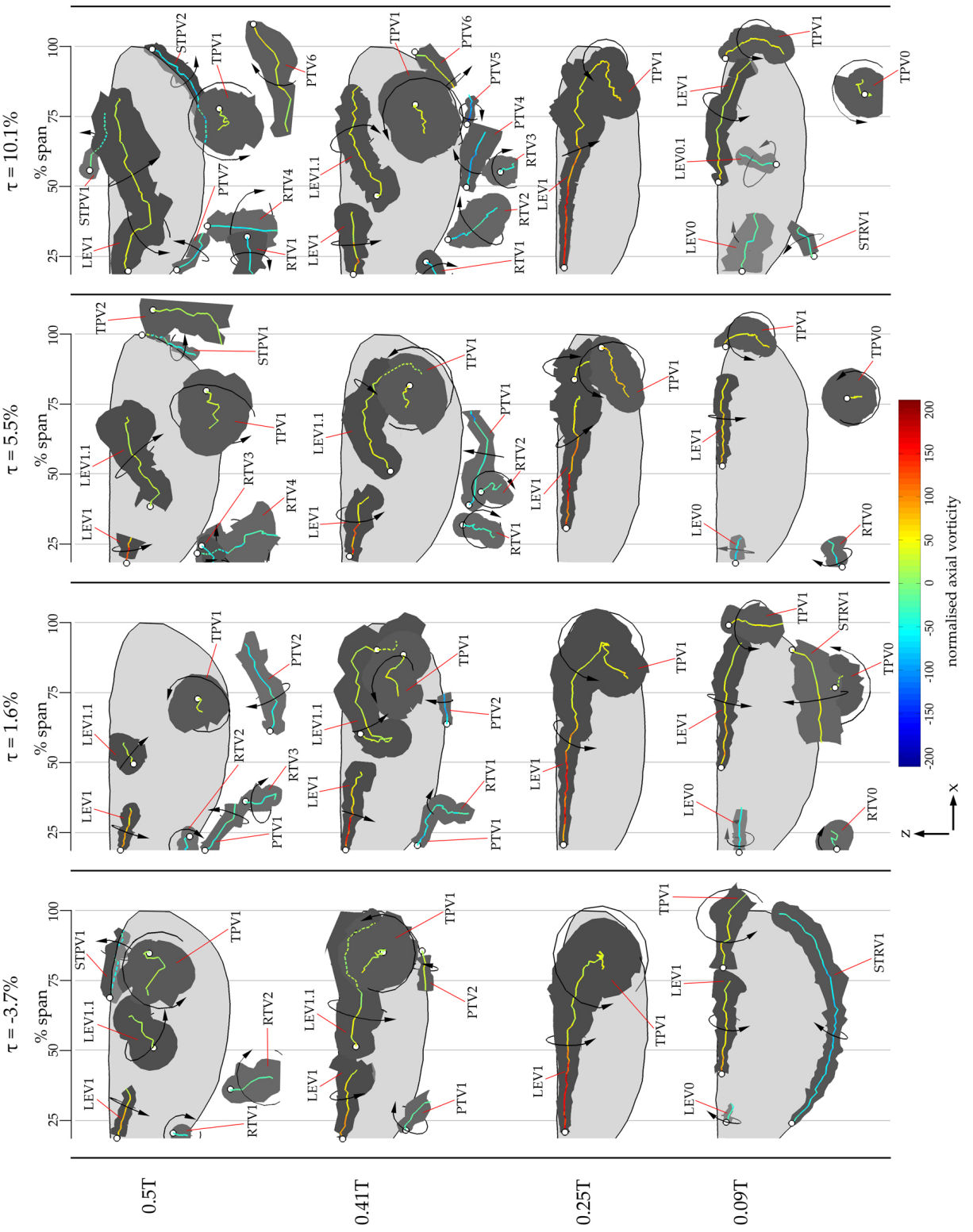

Figure 6.26: Back views illustrating flow formation over a flapping half cycle for four rotation phases: τ = −3.7%, 1.6%, 5.5%, 10.1%; vortex core diameter (dark grey surfaces) shown with vortex axes coloured with axial vorticity normalised with respect to $\bar{\Omega}_{wng}$ (91.7rad/s) (axes are dashed lines behind objects); positive axial direction points along an axis towards the end without a white dot

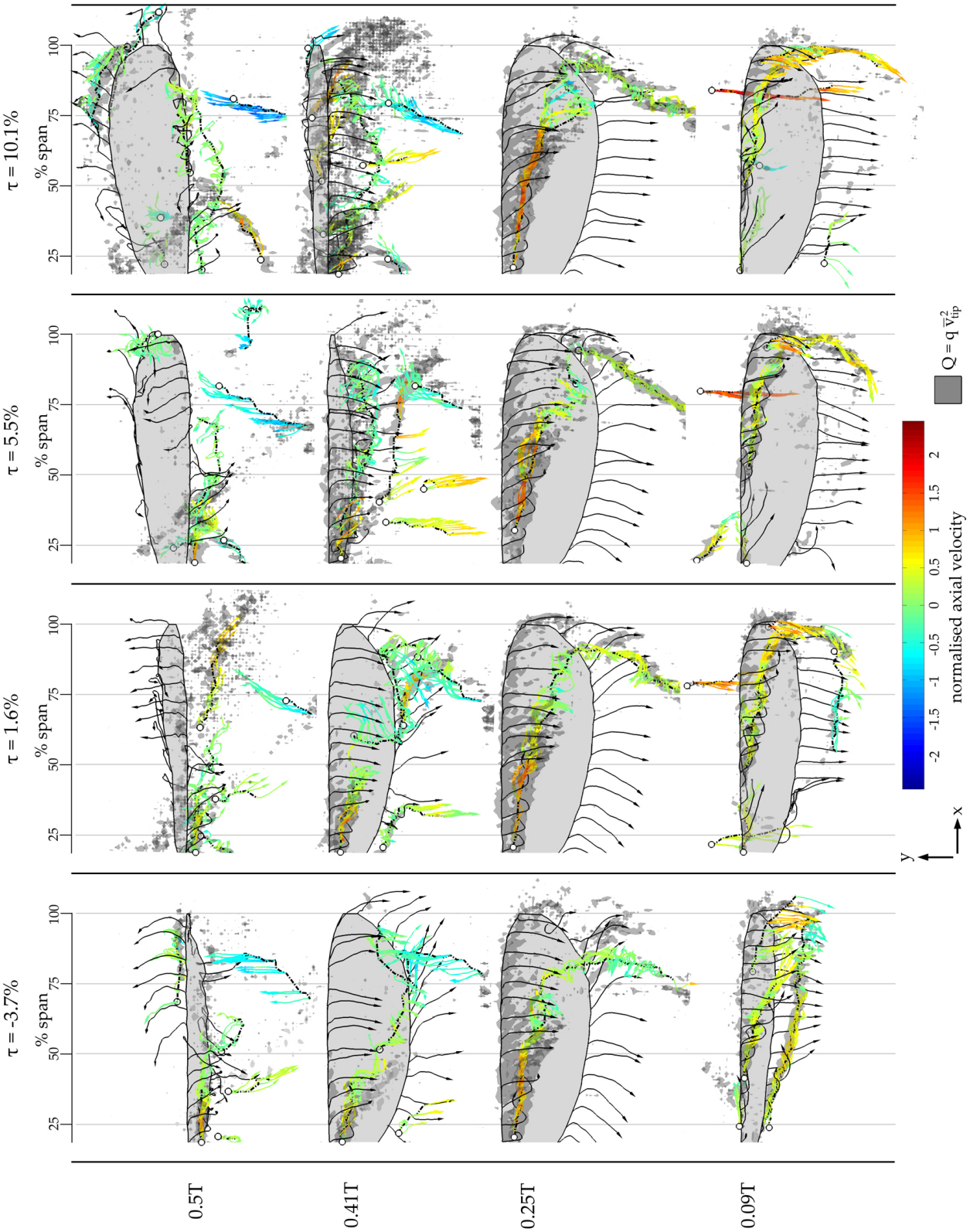

Figure 6.27: Top views illustrating flow formation over a flapping half cycle for four rotation phases: τ = −3.7%, 1.6%, 5.5%, 10.1%; instantaneous streamlines released from vortex axes coloured with axial velocity normalised with respect to the mean wingtip speed ($9.7m/s$); black streamlines are released along wing edge; transparent grey isosurfaces indicate areas where $Q = q\bar{v}_{tip}^2$ where $q \approx 8.5 \times 10^4 m^{-2}$; positive axial direction points along an axis towards the end without a white dot

*TPV*0, and *RTV*0 are then convected away into the downwash and *LEV*1 develops more inboard with an increasing level of axial vorticity and axial velocity peaking at mid-stroke where a sudden increase in vortex diameter is present, indicating breakdown. Following mid-stroke, the *LEV*1 axis becomes more distorted, the breakdown location moves inboard resulting in a drop in axial velocity level in *LEV*1 closer to the root, and the axial velocity of *TPV*1 reverses. When pitch reversal occurs towards the end of the stroke, pitching vortices (*PTVs*) are shed off the trailing edge. Leading to the end of the stroke, the *LEV* persists over the wing, and root vortices (*RTVs*) form and *TPV*1 breaks away and begins descending with the downwash. It should be noted that the stroke amplitude used in the measurement cases for this section is larger than the stroke amplitude used in the kinematics in § 6.1.2. Thus, the mean wing speeds for these cases are higher, which has resulted in the presence of other flow structures that were not identified in § 6.1.2. These include more pitching vortices (PTVs), stopping vortices (STPVs) seen at 0.5*T*, and a second tip vortex, *TPV*2, at 0.5*T* for τ = +5.5%, which forms and sheds very shortly before the end of the half stroke. The investigation in § 6.1.2 likely did not pick up these additional structures because they were too weak to identify owing to the lower mean wing speed, or they simply were not present.

Although the general flow evolution for all rotation phases tested is the same, there are noticeable effects due to the varying rotation phase. First of all, aspects of the pattern of flow evolution are linked to the pitching kinematics. Changing the rotation phase alters the phase relationship between the stroke kinematics and the flow evolution pattern, just as it does to the phase relationship between stroke kinematics and the pitching kinematics. For instance, starting vortices are shed later in the cycle if pitch reversal is delayed, and vice versa if pitch reversal is advanced. This can be seen at 0.09*T* in Figure 6.25 where the starting vortex, *STRV*1 is closer to the trailing edge for more negative rotation phases, indicating that it is shed later. In addition, at 0.5*T* for τ = +10.1%, there is a stopping vortex *STPV*2, which is the starting vortex for the next cycle, that has already been shed because of a more advanced pitch reversal. Similarly, pitching vortices form sooner, and the tip vortex (*TPV*1) breaks away from the wing and descends into the wake sooner if pitch reversal is advanced. This can clearly be seen at 0.5*T* in the back views in Figure 6.26.

The trends observed here provide further explanation of the mean lift and lift coefficient versus rotation phase trends presented in Figure 6.24. Recall from Chapter 2 that when a wing starts from rest and sheds a starting vortex the effect of the starting vortex is to reduce the bound circulation on the wing and slow its growth, as it is in the opposite sense to the wing bound circulation. This is the Wagner effect (Wagner, 1925). As seen previously, for more negative rotation phases the wing sheds a starting vortex later in the cycle, therefore, the negative effects of the Wagner effect extend further into the half-stroke. This is especially detrimental to lift because further into the half-stroke the wing velocities are higher and, thus, it is where the wing has the most opportunity for producing lift. Starting vortices shed later in the cycle will also be stronger owing to the higher wing velocity, which combined with their negative impact during a significant lift-producing phase of the cycle results in decreased lift for more negative rotation phases. In addition, as mentioned previously, for a more delayed pitch reversal (more negative rotation phase), the wing travels with a negative angle of attack for a longer period of time into the half-stroke and suffers from a negative Kramer effect, which also leads to lift reduction. Therefore, the influence of an increasingly significant Wagner effect combined with an increasingly negative angle of attack at the start of the stroke and negative Kramer effect, results in a drastic decline in lift below a rotation phase of about 0%.

As rotation phase is increased, the starting vortex is shed sooner in the cycle when the wing velocity is relatively low. When the wing reaches higher velocities in the half-stroke it is distanced much further from the starting vortex, and the wing bound circulation has had more opportunity to grow, thus lift values are higher. Furthermore, as mentioned previously, when pitch reversal occurs sooner, the wing exploits a Kramer effect when the wing velocities are higher, leading to an increase in lift. Kramer attributed the increase in lift resulting from a rapid increase in incidence, to a lag in flow separation, as it was observed that the flow did not separate right away and all at once (Kramer, 1932). A similar story can be seen in the present results in Figure 6.25 and Figure 6.26, where it can be seen that when the wing pitches early, the *LEV* (*LEV*1 & *LEV*1.1) does not shed. As rotation phase increases, however, the wing travels with a negative angle of attack for a longer period of time towards the end of the half-stroke, leading to a decline in lift beyond a rotation phase of about 6%. Therefore, higher rotation phases benefit

from a decreased Wagner effect and a positive Kramer effect, but eventually suffer from an increasingly negative angle of attack before the end of stroke.

It is interesting to note that across the rotation phases here ($\tau = -3.7\%$ to 10.1%), the *LEV* appears stable as it did in § 6.1.2, even in the case of the most advanced rotation phase of 10.1% where the wing travels with a negative angle of attack for a significant period of time. As in § 6.1.2, although the *LEV* shows signs of breakdown and becomes distorted after mid-stroke, the *LEV*, and any other portions of the *LEV* identified separately by the vortex point-joining algorithm (e.g. *LEV*1.1), remain present over the wing surface even up until the end of the stroke.

6.3 Reynolds Number & Stroke Amplitude Effects

The next investigation focuses on Reynolds number and stroke amplitude effects, that is, effects of varying the mean wing speed and the distance traveled respectively. For a constant mean wing chord, mean Reynolds number may be altered in one of two ways by either increasing flapping frequency and keeping the distance traveled constant (constant stroke amplitude in this case), or by increasing the distance traveled (increasing stroke amplitude) and keeping flapping frequency constant. In the latter case, mean Reynolds number simultaneously increases with stroke amplitude because the wing is required to travel over greater distances in the same period of time, thus increasing the mean wing speed. Stroke amplitude, however, may be independently increased while holding mean Reynolds number constant by proportionately decreasing flapping frequency for an increasing stroke amplitude to achieve a constant mean wing speed. This section investigates Reynolds number and stroke amplitude effects on the mean lift generated and on the *LEV*, by examining these three cases of varying $\bar{Re}$ with a constant Φ, varying $\bar{Re}$ and Φ with a constant f, and varying Φ with a constant $\bar{Re}$. First, the measurement cases will be presented, followed by the mechanism output and flapping kinematics, mean lift measurements, and flowfield measurements. In addition, the effects of Reynolds number and stroke amplitude on *LEV* breakdown and axial flow are discussed.

Table 6.3: Kinematic parameters for test cases which vary $\bar{Re}$ with a constant Φ

case #	2.1	2.2	2.3	2.4
f	$5Hz$	$10Hz$	$15Hz$	$20Hz$
$\bar{Re}_1$	4590	9200	13810	18320
$\bar{Re}_2$	4390	8790	13240	17760
Φ	131.7 ± 8°	131.5 ± 8°	131.7 ± 8°	131.8 ± 8°
Θ	0.7 ± 5.2°	0.8 ± 5.2°	1.1 ± 5.2°	1.7 ± 5.2°
α_{mid}	46.7 ± 2°	45.8 ± 2°	45.4 ± 2°	43.2 ± 2°
τ	6.1 ± 1.4%	5.7 ± 1.4%	6 ± 1.4%	6.1 ± 1.4%
Φ_{mec}	131.7 ± 0.2°	131.5 ± 0.2°	131.7 ± 0.2°	131.8 ± 0.2°
Θ_{mec}	0.7 ± 0.6°	0.8 ± 0.6°	1.1 ± 0.6°	1.7 ± 0.6°
$\alpha_{mec_{mid}}$	45.2 ± 0.4°	45.3 ± 0.4°	45 ± 0.4°	45.1 ± 0.4°
τ_{mec}	6.1 ± 0.3%	5.7 ± 0.3%	6 ± 0.3%	6.1 ± 0.3%

Table 6.4: Kinematic parameters for test cases which vary $\bar{Re}$ and Φ with a constant f

case #	3.1	3.2	3.3	3.4	3.5
f	$20Hz$	$20Hz$	$20Hz$	$20Hz$	$20Hz$
$\bar{Re}_1$	3870	7790	11670	15690	18120
$\bar{Re}_2$	3790	7630	11430	15190	17760
Φ	28.1 ± 8°	56.6 ± 8°	84.9 ± 8°	112.7 ± 8°	131.8 ± 8°
Θ	0.5 ± 5.2°	0.7 ± 5.2°	1 ± 5.2°	1.3 ± 5.2°	1.7 ± 5.2°
α_{mid}	46.4 ± 2°	45.4 ± 2°	44.6 ± 2°	43.6 ± 2°	43.2 ± 2°
τ	6.8 ± 1.4%	6.2 ± 1.4%	6.2 ± 1.4%	6.1 ± 1.4%	6.1 ± 1.4%
Φ_{mec}	28.1 ± 0.2°	56.6 ± 0.2°	84.9 ± 0.2°	112.7 ± 0.2°	131.8 ± 0.2°
Θ_{mec}	0.5 ± 0.6°	0.7 ± 0.6°	1 ± 0.6°	1.3 ± 0.6°	1.7 ± 0.6°
$\alpha_{mec_{mid}}$	44.8 ± 0.4°	45.1 ± 0.4°	45.3 ± 0.4°	45.6 ± 0.4°	45.1 ± 0.4°
τ_{mec}	6.8 ± 0.3%	6.2 ± 0.3%	6.2 ± 0.3%	6.1 ± 0.3%	6.1 ± 0.3%

Table 6.5: Kinematic parameters for test cases which vary Φ with a constant $\bar{Re}$

case #	4.1	4.2	4.3	4.4	4.5
f	$20Hz$	$9.93Hz$	$6.63Hz$	$4.92Hz$	$4.27Hz$
$\bar{Re}_2$	3790	3770	3780	3780	3770
Φ	$28.1 \pm 8°$	$56.4 \pm 8°$	$85 \pm 8°$	$114.3 \pm 8°$	$131.9 \pm 8°$
Θ	$0.5 \pm 5.2°$	$0.4 \pm 5.2°$	$0.5 \pm 5.2°$	$0.6 \pm 5.2°$	$0.7 \pm 5.2°$
α_{mid}	$46.4 \pm 2°$	$45.6 \pm 2°$	$45.3 \pm 2°$	$45 \pm 2°$	$44.9 \pm 2°$
τ	$6.8 \pm 1.4\%$	$6.3 \pm 1.4\%$	$6 \pm 1.4\%$	$6 \pm 1.4\%$	$6 \pm 1.4\%$
Φ_{mec}	$28.1 \pm 0.2°$	$56.4 \pm 0.2°$	$85 \pm 0.2°$	$114.3 \pm 0.2°$	$131.9 \pm 0.2°$
Θ_{mec}	$0.5 \pm 0.6°$	$0.4 \pm 0.6°$	$0.5 \pm 0.6°$	$0.6 \pm 0.6°$	$0.7 \pm 0.6°$
$\alpha_{mec_{mid}}$	$44.8 \pm 0.4°$	$44.6 \pm 0.4°$	$44.4 \pm 0.4°$	$44.5 \pm 0.4°$	$44.6 \pm 0.4°$
τ_{mec}	$6.8 \pm 0.3\%$	$6.3 \pm 0.3\%$	$6 \pm 0.3\%$	$6 \pm 0.3\%$	$6 \pm 0.3\%$

6.3.1 Flapping Kinematics & Measurement Cases

Again, starting from the 'baseline' set of kinematics presented in § 5.1, flapping frequency and stroke amplitude were varied to give the three following sets of cases: varying $\bar{Re}$ with a constant Φ (cases $2.x$)[3], varying $\bar{Re}$ and Φ with a constant f (cases $3.x$), and varying Φ with a constant $\bar{Re}$ (cases $4.x$). The kinematic parameters for each set of cases are listed in Tables 6.3 - 6.5. Mean lift measurements were obtained for cases 2.1 – 2.4, 3.1 – 3.5, 4.1 and 4.5. It should be noted that the mean lift for case 4.5 was not measured directly, but rather was obtained by the identified mean lift trend from cases 2.1 – 2.4. Also, the flapping kinematics during the mean lift measurements for case 3.4 differed slightly from those during the flowfield measurements, with only a small difference in the stroke amplitude of 1.5°. This difference was deemed small enough such that the flowfield measurements adequately represented the flow generated during the mean lift measurements.

For every case, flowfield measurements and the accompanying instantaneous wing position measurements were performed only at the mid-stroke position. As has been shown previously, the flow is quasi-steady on either side of mid-stroke where the wing is translating with a relatively constant velocity. In addition, the aerodynamic forces over this phase of the flapping cycle are typically seen to be quasi steady (see e.g. Dickinson et al. (1999)), and it is the phase where most

[3]shorthand for cases 2.1 – 2.4 etc.

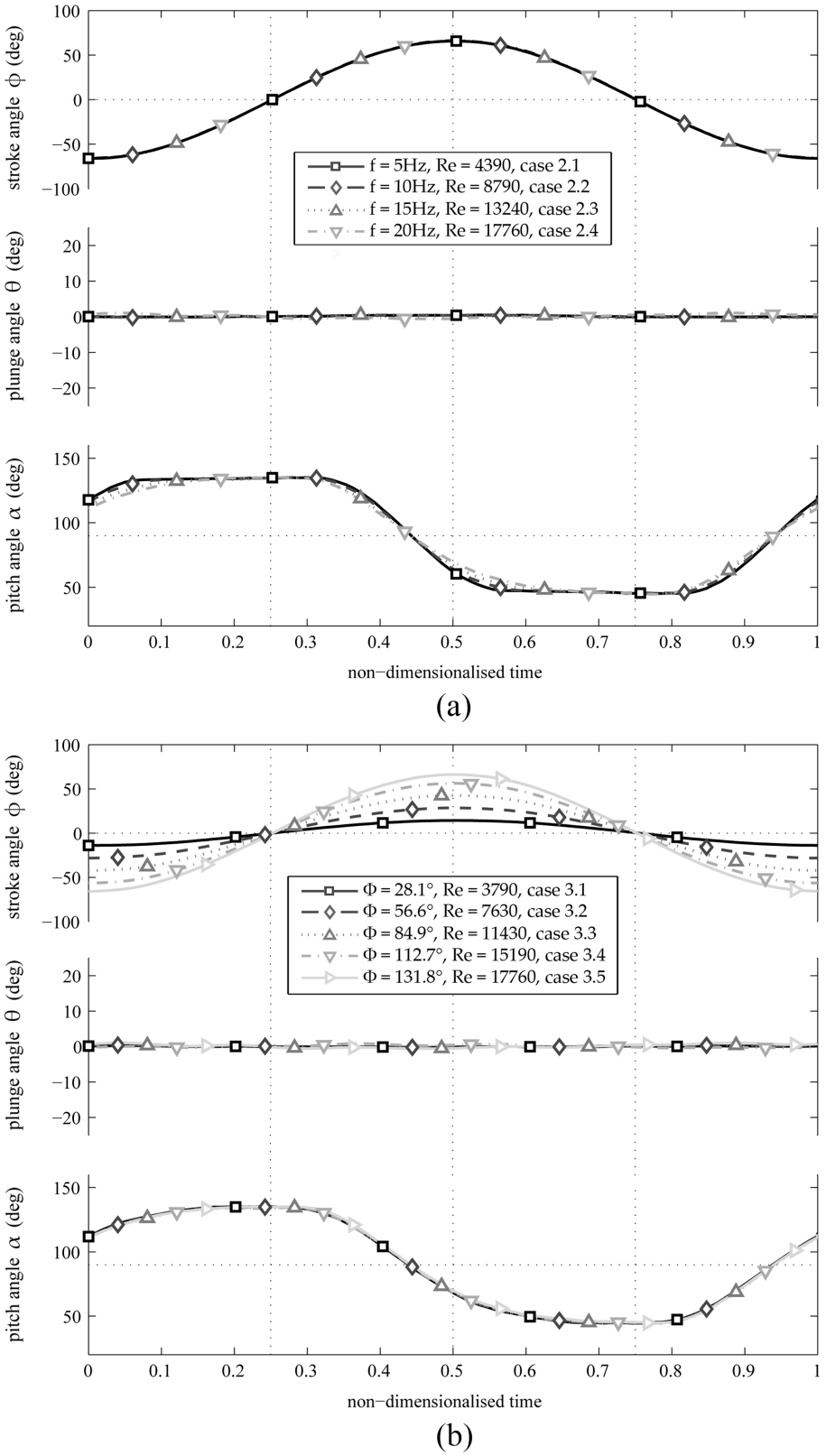

Figure 6.28: (a) mechanism output kinematics for test cases which vary $\bar{Re}$ and f with a constant Φ; (b) mechanism output kinematics for test cases that vary $\bar{Re}$ and Φ with a constant f

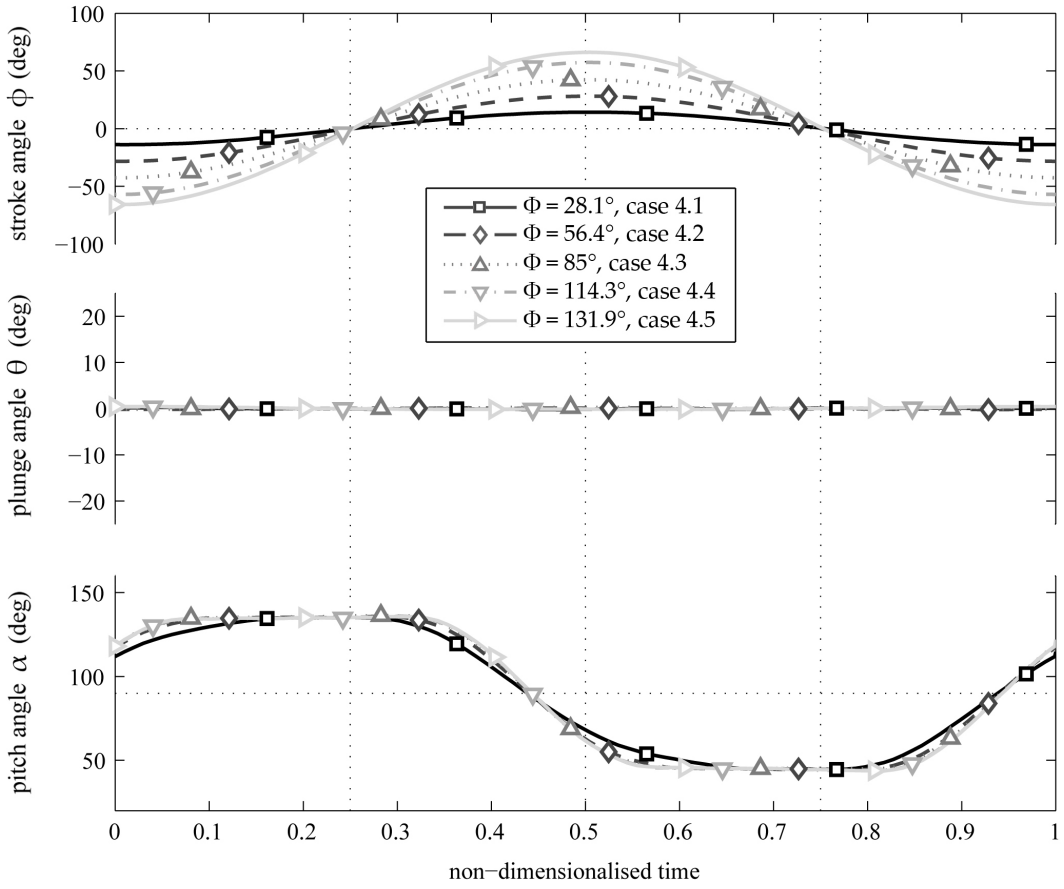

Figure 6.29: Mechanism output kinematics for test cases that vary Φ with a constant $\bar{Re}$

of the lift is generated. Thus, looking at the flowfield at mid-stroke provides a good representation of the mean lift-producing flow. Mechanism output and kinematics for each test case are given in Figures 6.28 - 6.29.

6.3.2 Effect on Mean Lift

Starting with cases 2.*x*, the effect of increasing mean Reynolds number (by increasing flapping frequency) with a constant stroke amplitude is illustrated in Figure 6.30. The effect is an increase in mean lift with increasing $\bar{Re}$, and results in a decrease in mean lift coefficient. The lift coefficient decreases in this case because the ratio of mean lift to average wingtip speed decreases as flapping frequency increases. This observed trend is to be expected since increasing flapping frequency proportionately increases the average wing speed which results in higher

lift. Fitting a power law to the data reveals that mean lift varies directly with $\bar{v}_{tip}^{1.5}$, which is lower than expected since, conventionally, lift varies with the square of velocity. Although $\bar{v}_{tip}$ to a power as high as 2.1 can fit within the error bars, an exponent of less than 2 makes sense physically because throughout a flapping cycle there are periods where the wing sheds its wake and loses lift, which brings down the average lift. This was a note made by Ansari et al. (2008b) who in their analytical parametric study saw that lift varied with f to a power slightly less than 2. In their study, a rigid wing was used, whereas the present experiments used a stiff but non-rigid wing which would have dampened the sudden spikes in instantaneous lift resulting in smaller values of mean lift (in comparison to analytical predictions with an infinitely rigid wing) sensed at the root.

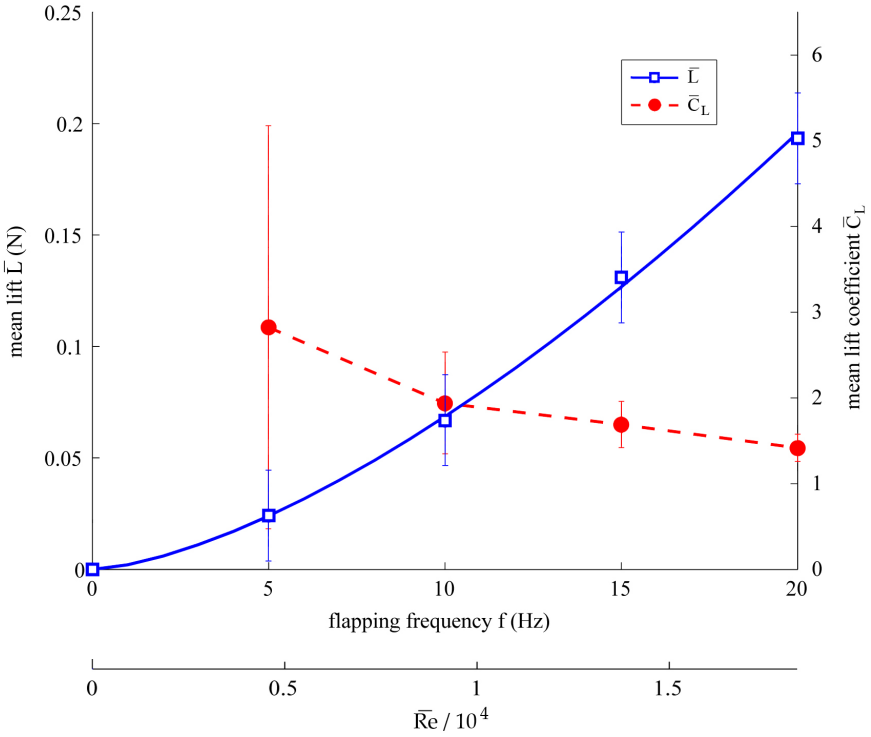

Figure 6.30: Effect of flapping frequency ($\bar{Re}$) on mean lift and mean lift coefficient

As shown in Figure 6.31 for cases 3.x, the effect of increasing mean Reynolds number and stroke amplitude while holding flapping frequency constant is also an increase in mean lift. Again, this trend is expected because the mean wingtip speed is increasing. The mean lift coefficient declines in this case because the ratio of mean lift to mean wingtip speed squared ($L/\bar{v}_{tip}^2$ term in the coefficient of lift

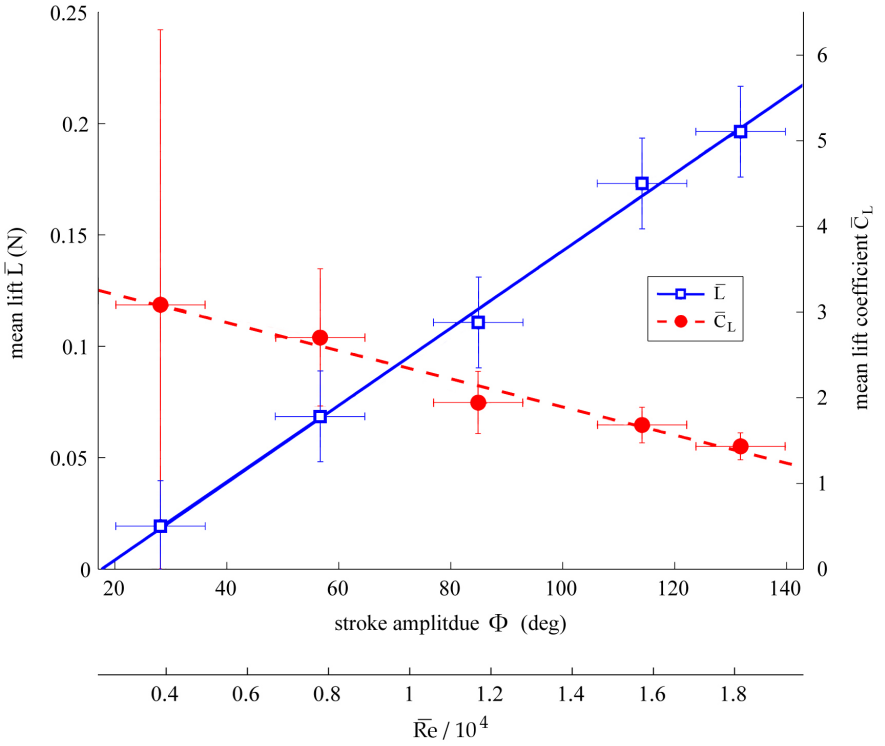

Figure 6.31: Effect of stroke amplitude with constant flapping frequency on mean lift and mean lift coefficient

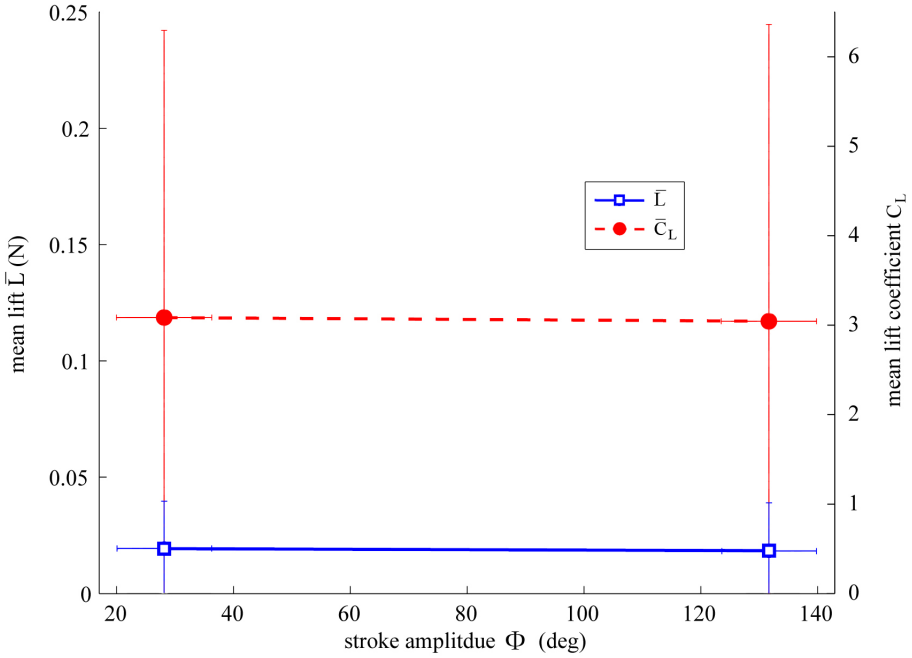

Figure 6.32: Effect of stroke amplitude with constant mean Reynolds number on mean lift and mean lift coefficient

equation) decreases with increasing mean Reynolds number and stroke amplitude for a constant flapping frequency. As with the previous case, a non-linear relationship would be expected because $\bar{v}_{tip}$ is increasing and lift conventionally scales with the square of velocity. However, the relationship presented here is a linear one, where doubling the mean Reynolds number and stroke amplitude for a constant flapping frequency roughly doubles the lift. Interestingly the study of Ansari et al. (2008b) also saw a linear relation between stroke amplitude and mean lift. As will be seen later, this relationship probably results from *LEV* breakdown which becomes more intense with increasing stroke amplitude.

Increasing stroke amplitude while holding mean Reynolds number constant (cases 4.x) is seen to have no effect on mean lift as seen in Figure 6.32. This makes sense because the mean wing speed is remaining constant, and hence lift should remain constant. It should be noted that the second point on this graph at $\Phi = 132°$ was not measured directly, but rather, was obtained from the mean lift versus mean Reynolds number trend for a constant stroke amplitude ($\Phi = 132°$) illustrated in Figure 6.30.

6.3.3 Effect on Flowfield

Figures 6.33 - 6.35 illustrate the flow formation at mid-stroke for cases 2.x-4.x respectively. These are the same style of plots presented in § 6.1 illustrating vortex diameter, axial vorticity, and instantaneous streamlines with axial velocity. The same plots, but showing back views rather than top views are shown in Appendix F Figures F.15 - F.16.

For an increasing mean Reynolds number with a constant stroke amplitude, it can be seen in Figure 6.33 that the general flow structure of the *LEV* remains relatively unchanged. The LEV starts off closer to the leading edge towards the root and travels outboard and aft to where it merges with the tip vortex, and the general trajectory of the vortex axis is the same. In all cases, the axial velocity of the vortex peaks around mid-span, after which the axial velocity in the *LEV* rapidly drops to a level below a normalised velocity of 0.5. This drop is accompanied by a sudden increase in the diameter of the *LEV* indicating *LEV* breakdown.

If mean Reynolds number and stroke amplitude are simultaneously increased by holding flapping frequency constant, then quite a different result is obtained

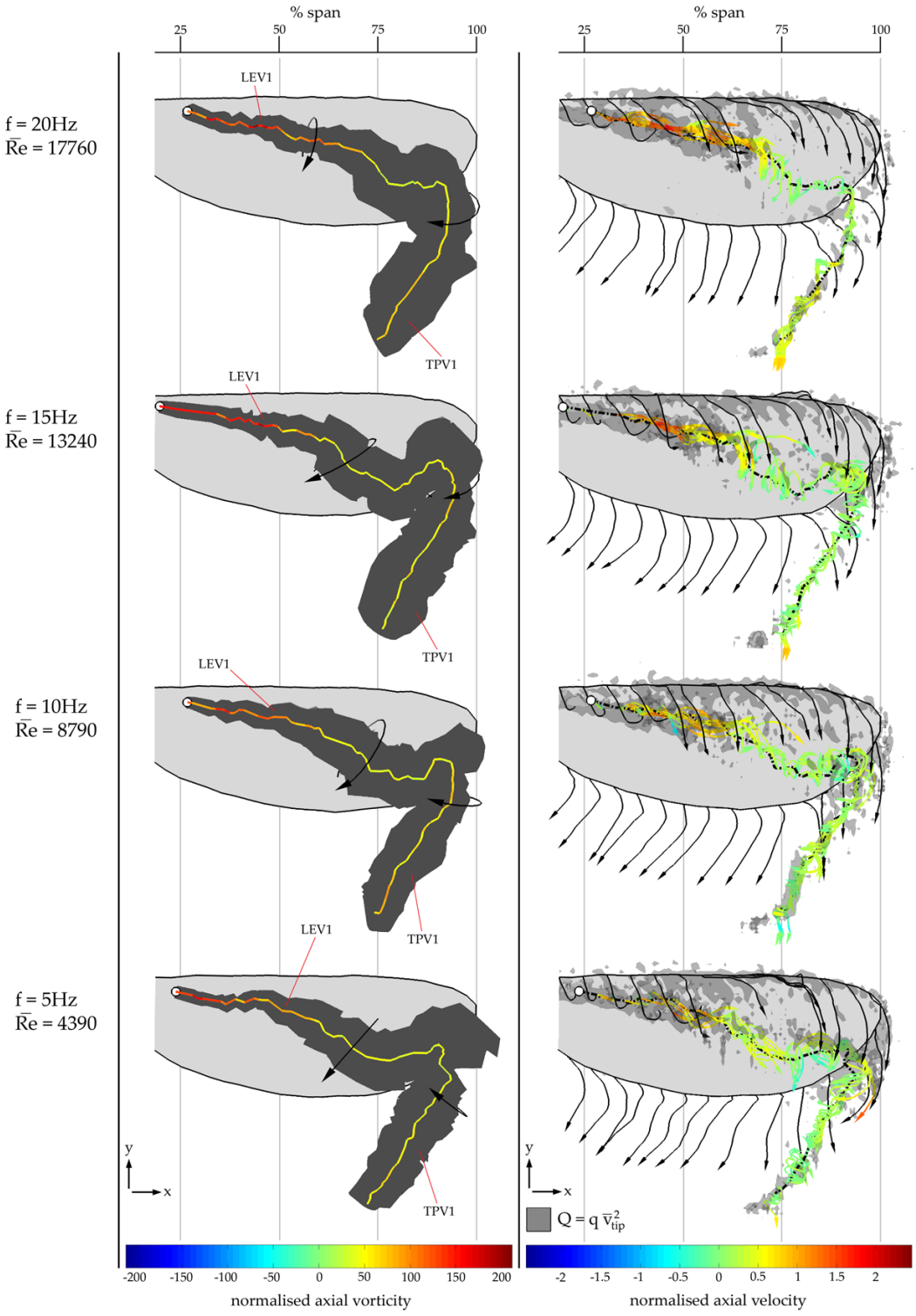

Figure 6.33: Top views illustrating flow formation at mid-stroke for test cases with varying f ($\bar{Re}$); left column shows vortex core diameter (dark grey surfaces) and vortex axes coloured with axial vorticity normalised with respect to the mean wing angular velocity $\bar{\Omega}_{wng}$ (23.1, 46.2, 69.6, 93.2rad/s); vortex axes become dashed when behind other objects; right column shows instantaneous streamlines released from vortex axes coloured with axial velocity normalised with respect to $\bar{v}_{tip}$ (2.4, 4.9, 7.4, 9.9m/s), black streamlines released along the wing edge, and transparent grey isosurfaces of $Q = q\bar{v}_{tip}^2$ where $q \approx 8.5 \times 10^4 m^{-2}$; positive axial direction points along an axis towards the end without a white dot

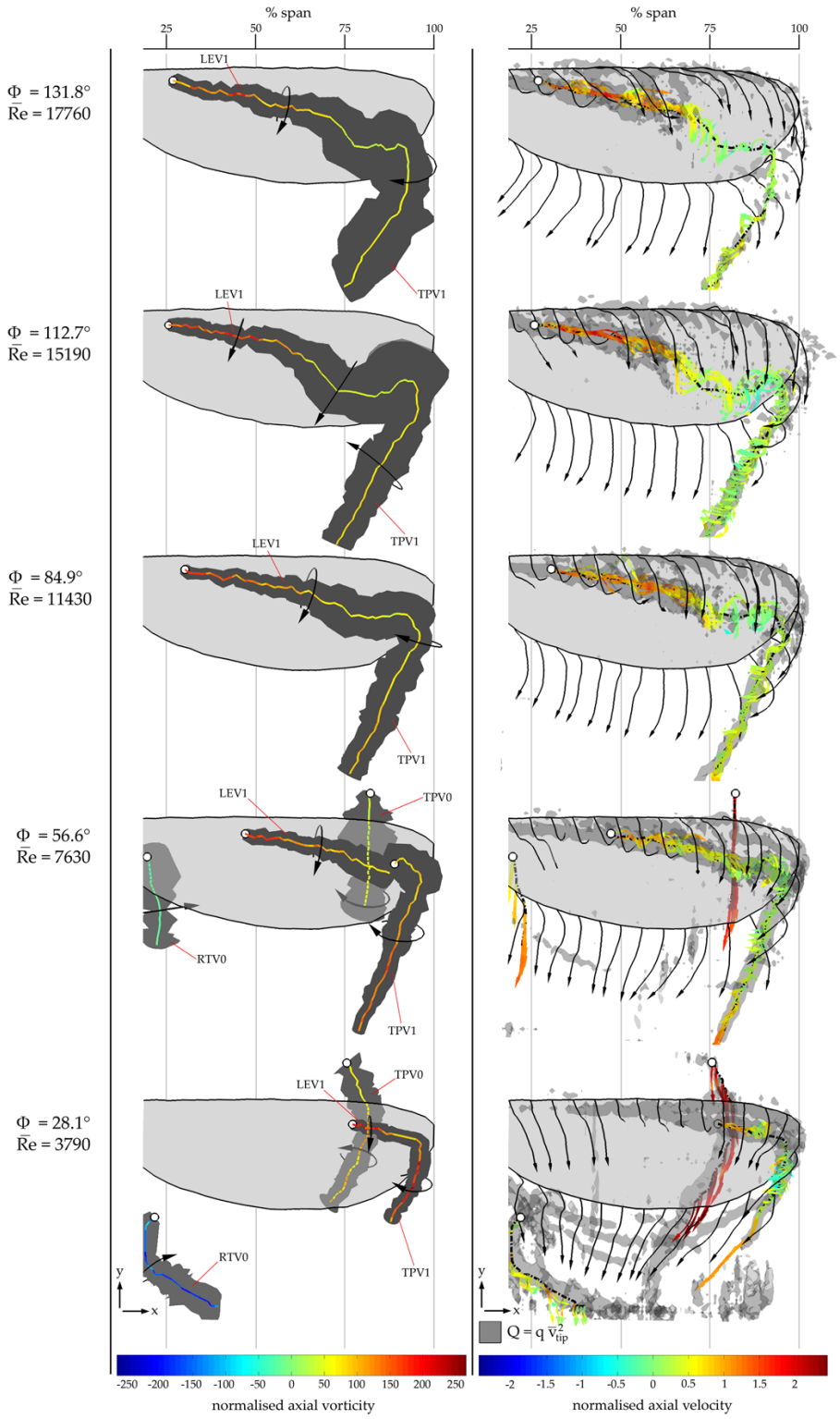

Figure 6.34: Top views illustrating flow formation at mid-stroke for test cases with varying Φ and constant $f = 20Hz$; left column shows vortex core diameter (dark grey surfaces) and vortex axes coloured with axial vorticity normalised with respect to $\bar{\Omega}_{wng}$ (19.8, 40, 60, 79.7, 93.2rad/s); vortex axes become dashed behind other objects; right column shows instantaneous streamlines released from vortex axes coloured with axial velocity normalised with respect to $\bar{v}_{tip}$ (2.1, 4.2, 6.4, 8.4, 9.9m/s), black streamlines released along the wing edge, and transparent grey isosurfaces of $Q = q\bar{v}_{tip}^2$ where $q \approx 8.5 \times 10^4 m^{-2}$; positive axial direction points along an axis towards the end without a white dot

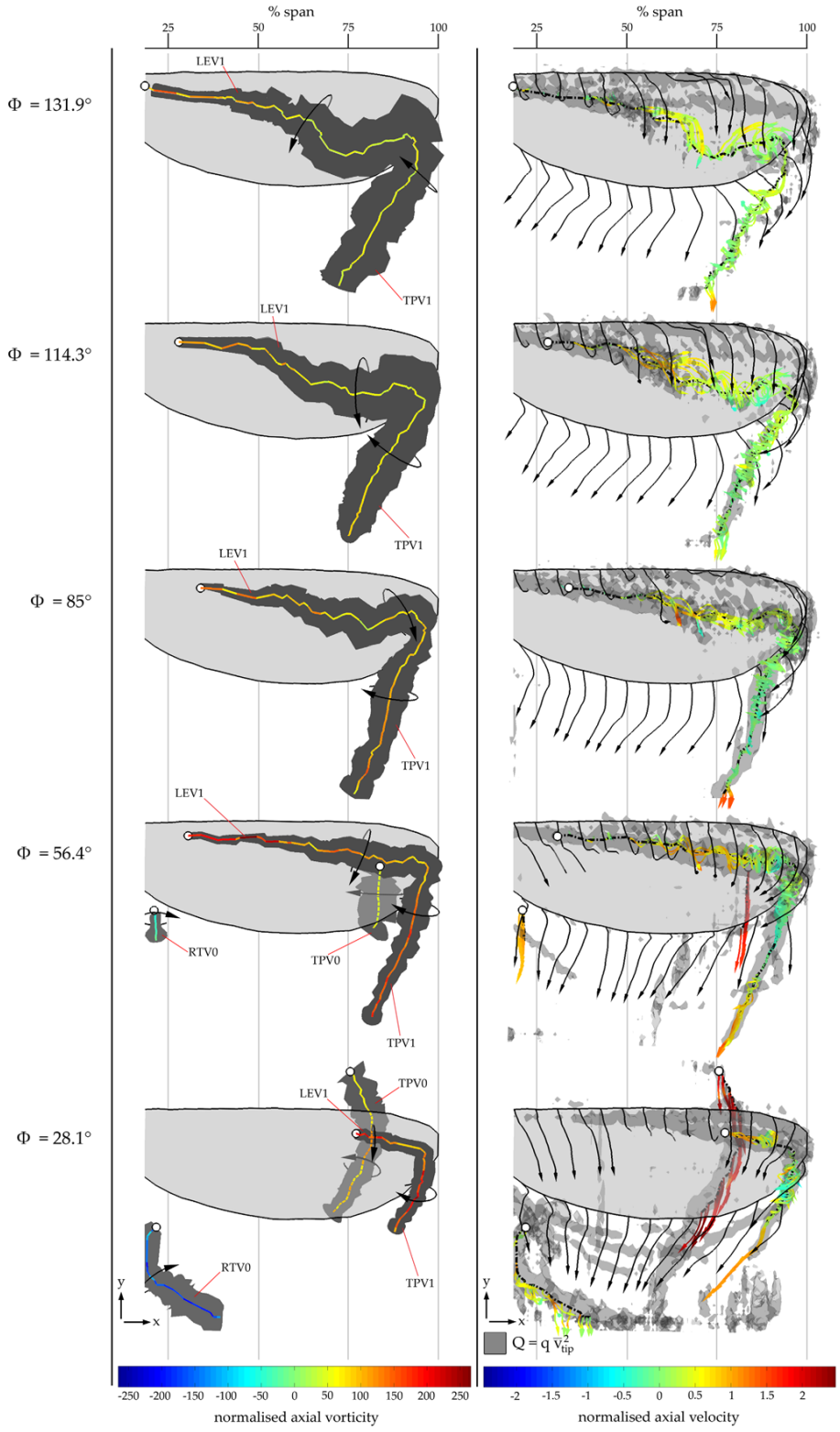

Figure 6.35: Top views illustrating flow formation at mid-stroke for test cases with varying Φ and constant $\bar{R}e \approx 3780$; left column shows vortex core diameter (dark grey surfaces) and vortex axes coloured with axial vorticity normalised with respect to $\bar{\Omega}_{wng}$ $(19.8 rad/s)$; vortex axes become dashed when behind other objects; right column shows instantaneous streamlines released from vortex axes coloured with axial velocity normalised with respect to $\bar{v}_{tip}$ $(2.1 m/s)$, black streamlines released along the wing edge, and transparent grey isosurfaces of $Q = q\bar{v}^2_{tip}$ where $q \approx 8.5 \times 10^4 m^{-2}$; positive axial direction points along an axis towards the end without a white dot

as seen in Figure 6.34. At lower stroke amplitudes ($\Phi = 28.1°\&56.6°$) the *LEV* axis is relatively straight with a smaller vortex diameter, and breakdown appears to be either absent or much less intense as there is no dramatic increase in vortex size. Lower amplitudes are more prone to *TEV* shedding off the trailing edge, as seen in the Q criterion isosurfaces, which are probably due to *KHI* in the shear layer between fluid originating from above and below the wing. The tip and root vortices from the previous half stroke (*RTV*0 and *TPV*0) are closer to the under side of the wing at mid-stroke for smaller stroke amplitudes owing to the fact that the wing reverses into its own wake sooner for a smaller stroke amplitude. As stroke amplitude increases, the *LEV* is more developed and is larger in size. The outboard section of the *LEV* axis at higher stroke amplitudes moves aft and becomes more distorted and indications of *LEV* breakdown arise as a sudden increase in vortex diameter occurs. If stroke amplitude is varied at a fixed mean Reynolds number, the very same trend is observed as seen in Figure 6.35, although normalised axial velocity levels in the *LEV* are noticeably lower.

The change in the flowfield at mid-stroke seen as stroke amplitude is increased resembles the flow evolution that occurs between the start of a half-stroke and the mid-stroke position presented in § 6.1. This indicates that the extent of *LEV* development is a function of the number of mean chords traveled, where the larger the stroke amplitude (more mean chords traveled) the more the *LEV* grows.

6.3.4 LEV Breakdown

The presence of *LEV* breakdown mentioned previously will now be examined in more detail. If the helix angle is computed along the *LEV* it is found that in all cases the critical helix angle of 50° (see § 2.2.8) is eventually passed. For cases 2.x, it is found that as mean Reynolds number increases for a fixed stroke amplitude, the breakdown location at mid-stroke remains relatively fixed between $60-70\%$ span. As stroke amplitude is increased with either a fixed flapping frequency (cases 3.x) or a fixed mean Reynolds number (cases 4.x), the point where the critical helix angle is passed is variable and occurs between $65-90\%$ span. Thus, for the range of Reynolds numbers and stroke amplitudes tested here, *LEV* breakdown appears to be present based upon the computed helix angles. However, as mentioned previously, for smaller stroke amplitudes the *LEV* diameter is much smaller at

mid-stroke and sudden increases in vortex diameter are absent. This is illustrated in Figure 6.36, which shows the degree of *LEV* diameter increase along axis versus stroke amplitude for all cases. The degree of increase is measured by the ratio of maximum *LEV* diameter to the diameter at the start of the axis towards the root. Again, with a smaller stroke amplitude the percent increase in vortex size is less, and as stroke amplitude is increased, much more dramatic increases in vortex diameter are observed. Including vortex diameter increase when assessing the presence of vortex breakdown (as has been done previously) suggests that *LEV* breakdown is absent at $\Phi = 28.1°$ and &56.6°. In Figure 6.34 and Figure 6.35, the vortex diameter grows very little in these cases. Recall from §2.2.8 that in addition to the swirl level, the pressure gradient along the vortex axis also affects breakdown, and that independent changes in either of these can incite or suppress its occurrence. Given this fact combined with the lack of vortex diameter increase at lower stroke amplitudes, *LEV* breakdown is probably suppressed thanks to a favourable pressure gradient preventing breakdown even though the critical helix angle is surpassed. Regardless of whether breakdown is absent, or is present but more suppressed, what is certain is that the extent of *LEV* breakdown at mid-stroke is very dependent on stroke amplitude, and that mean Reynolds number has no noticeable effect on breakdown within the range tested.

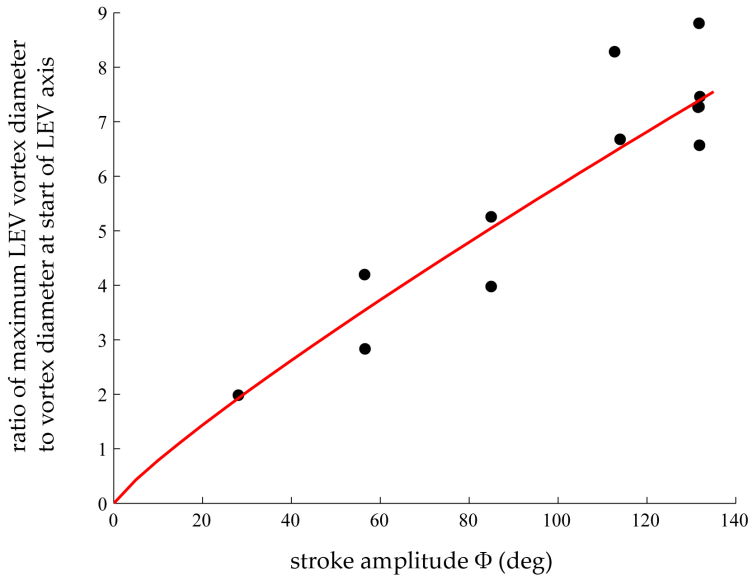

Figure 6.36: Degree of *LEV* diameter increase along axis (shown by ratio of maximum *LEV* diameter to the diameter at the start of the axis) at mid-stroke versus stroke amplitude; red line is a power fit to the data points

If *LEV* breakdown were absent at lower stroke amplitudes it would explain the stroke amplitude versus mean lift trend in Figure 6.31 for a constant flapping frequency. On delta wings, the result of vortex breakdown is a decrease in lift (Escudier, 1988). Assuming that the same is true for flapping wings, then as stroke amplitude increases, the *LEV* is more prone to breakdown, which would then lead to a shallower rate of lift increase with increasing stroke amplitude. However, if this were true then it would be expected that the mean lift at $\Phi = 131.9°$ in Figure 6.32 would be lower than that at $\Phi = 28.1°$. However, these values are virtually the same, thus something must be decreasing the lift at low stroke amplitudes as well. This could be explained by the fact that with lower stroke amplitudes, the root vortex and tip vortex shed from the previous half-stroke are closer to the wing underside during the middle portion of the stroke when most of the lift is generated. This is clearly seen in Figure 6.34 and Figure 6.35. The effect of these previous shed vortices is to induce a downwash, thus decreasing lift. With larger stroke amplitudes this negative effect declines, as the previously shed wake has a longer time to descend before the wing re-encounters it. Therefore, provided that vortex breakdown results in decreased lift, there are two competing effects. Lower stroke amplitudes suffer from decreased lift due to proximity to shed wake, which declines in effect with increasing stroke amplitude, but is met with another effect of decreased lift due to more intense *LEV* breakdown at higher stroke amplitudes. This could account for the linear trend as seen in Figure 6.32.

6.3.5 LEV Axial Flow

Observed dependencies of the axial flow level in the *LEV* on stroke amplitude and mean Reynolds number will now be presented. Figure 6.37a illustrates the stroke amplitude versus peak *LEV* axial velocity for cases 2.x, 3.x and 4.x. It can be seen from cases 4.x that an increase in stroke amplitude while mean Reynolds number is held constant has no effect on *LEV* axial velocity, and that it is only affected if mean Reynolds number is varied. Axial velocity, therefore, is a function of Reynolds number. Plotting the same data, but with mean Reynolds number on the horizontal axis, reveals the peak *LEV* axial velocity versus mean Reynolds number trend, shown in Figure 6.37b. A linear and power fit of the data are shown, where the power equation fits the data much better as it has a lower

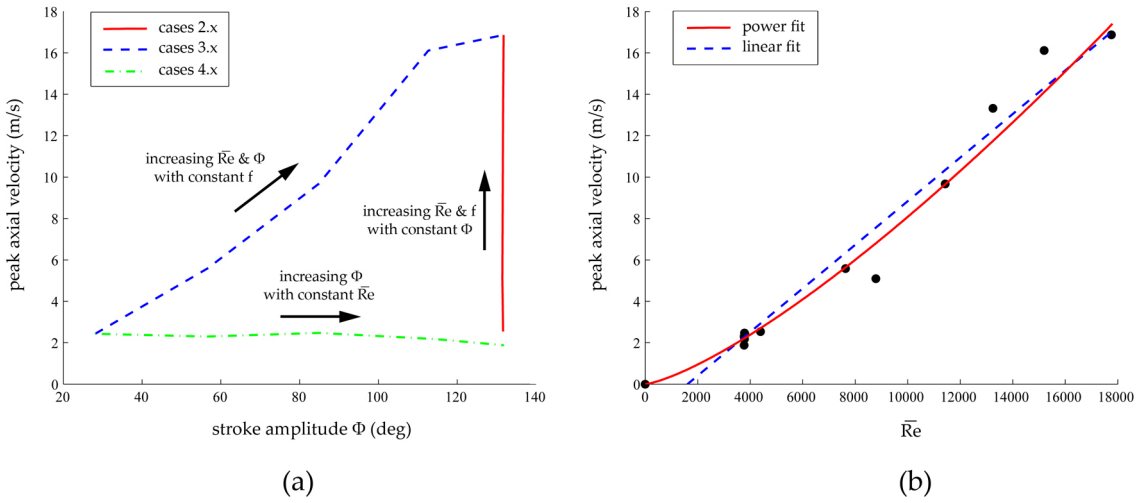

Figure 6.37: Peak *LEV* axial velocity at mid-stroke versus (a) stroke amplitude and (b) mean Reynolds number

standard error ($0.9m/s$ compared to $1.1m/s$), and passes through $0, 0$ as it should. This reveals that peak axial velocity in the *LEV* is a function of $\bar{Re}^{1.3}$.

A non-linear relationship between *LEV* axial velocity and mean Reynolds number could be explained by centrifugal forces. Centrifugal force is proportional to v^2, and since mean Reynolds number is proportional to the mean wingtip speed, it follows that centrifugal force will vary with $\bar{Re}^2$. Thus, doubling the mean Reynolds number will quadruple centrifugal forces, causing higher accelerations in the fluid and leading to higher axial velocities. The accelerations due to viscous, Euler, Coriolis and centrifugal forces in the axial direction along the vortex axis for case 2.4 are shown in Figure 6.38. For a description of these accelerations and how they are computed, please see Appendix G. It can be seen that centrifugal forces dominate in the axial direction. Given this dominance and the fact that both centrifugal force and *LEV* axial velocity follow a non-linear relationship with mean wing speed ($\bar{Re}$), it seems plausible that *LEV* axial velocity originates partially from centrifugal force, which has been postulated before by van den Berg & Ellington (1997a). This would explain why in cases $3.x$ axial velocity remains constant as stroke amplitude is varied and mean Reynolds number is held constant. Here, the mean wing speed is fixed, thus the centrifugal forces remain constant and the result is a constant axial velocity. It must be noted, however, that contributions from the axial pressure gradient along the vortex axis are unknown since there is no pressure data. Axial flow through the *LEV* has been

shown to be the result of an axial pressure gradient along the *LEV*. It is likely that both centrifugal and pressure forces dominate in the axial direction in the *LEV*, and the combined effect results in axial flow, and the trend shown in Figure 6.37b as $\bar{Re}$ is increased. This could explain why axial velocity varies with $\bar{Re}^{1.3}$, rather than $\bar{Re}^2$. If axial velocity were purely the result of centrifugal force then it would vary with $\bar{Re}^2$, however, with contributions from other forces, mainly pressure, the result is an increase with $\bar{Re}^{1.3}$.

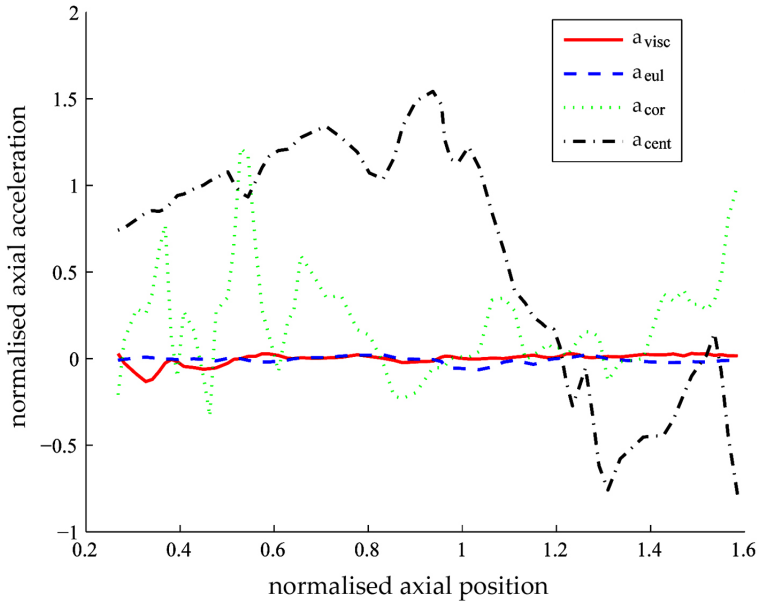

Figure 6.38: Axial accelerations along vortex axis due to viscous (a_{visc}), euler (a_{eul}), coriolis (a_{cor}), and centrifugal (a_{cent}) forces for case 2.4; accelerations are normalised with respect to the mean wingtip acceleration ($1230 m/s^2$); vortex axis begins at approximately 27% span and axial position thereafter is normalised with respect to the wing length

6.4 Angle of Attack Effects

The effects of varying the angle of attack at mid-stroke on the flow formation and mean lift will now be investigated. Measurement cases will first be presented, followed by the mechanism output and flapping kinematics, mean lift measurements, and then flowfield measurements. Also, a discussion of how angle of attack affects *LEV* breakdown will be given.

Table 6.6: Kinematic parameters for test cases which vary angle of attack

case #	5.1	5.2	5.3	5.4	5.5
f	20Hz	20Hz	20Hz	20Hz	20Hz
$\bar{Re}_1$	17850	18120	18090	18110	18110
$\bar{Re}_2$	17630	17760	17830	17850	17890
Φ	129.9 ± 8°	131.8 ± 8°	131.6 ± 8°	131.8 ± 8°	131.8 ± 8°
Θ	1.4 ± 5.2°	1.7 ± 5.2°	1.6 ± 5.2°	1.6 ± 5.2°	1.5 ± 5.2°
α_{mid}	35.5 ± 2°	43.2 ± 2°	53.6 ± 2°	64.1 ± 2°	74 ± 2°
τ	6.2 ± 1.4%	6.1 ± 1.4%	5.9 ± 1.4%	5.6 ± 1.4%	5 ± 1.4%
Φ_{mec}	129.9 ± 0.2°	131.8 ± 0.2°	131.6 ± 0.2°	131.8 ± 0.2°	131.8 ± 0.2°
Θ_{mec}	1.4 ± 0.6°	1.7 ± 0.6°	1.6 ± 0.6°	1.6 ± 0.6°	1.5 ± 0.6°
$\alpha_{mec_{mid}}$	35.8 ± 0.4°	45.1 ± 0.4°	55 ± 0.4°	65.3 ± 0.4°	75.5 ± 0.4°
τ_{mec}	6.2 ± 0.3%	6.1 ± 0.3%	5.9 ± 0.3%	5.6 ± 0.3%	5 ± 0.3%

6.4.1 Flapping Kinematics & Measurement Cases

As with the other cases, starting from the 'baseline' kinematics given in § 5.1, α_{mid} was varied while all other parameters were held virtually constant to give the five test cases listed in Table 6.6. Mean lift measurements were obtained for all cases, in addition to flowfield measurements at the mid-stroke position. Mechanism output kinematics for each test case are shown in Figure 6.39.

6.4.2 Effect on Mean Lift

The effect of varying α_{mid} on mean lift and mean lift coefficient is given in Figure 6.40. It can be seen that mean lift and the mean lift coefficient peak at an angle of attack of around 45°, declining either side of this value. An explanation for this is provided by Wilkins (2008), who in a CFD study observed the same trend illustrated in Figure 6.40 with peak mean lift also occurring at an angle of attack around 45°. He observed that increasing angle of attack increased the stable size of the leading-edge vortex, which had the effect of increasing the wing-normal force. From 0° to 45° angle of attack he found that the increase in normal force was great enough that its vertical component (lift) would increase despite the fact that the normal force points in an increasingly horizontal direction. Beyond an angle

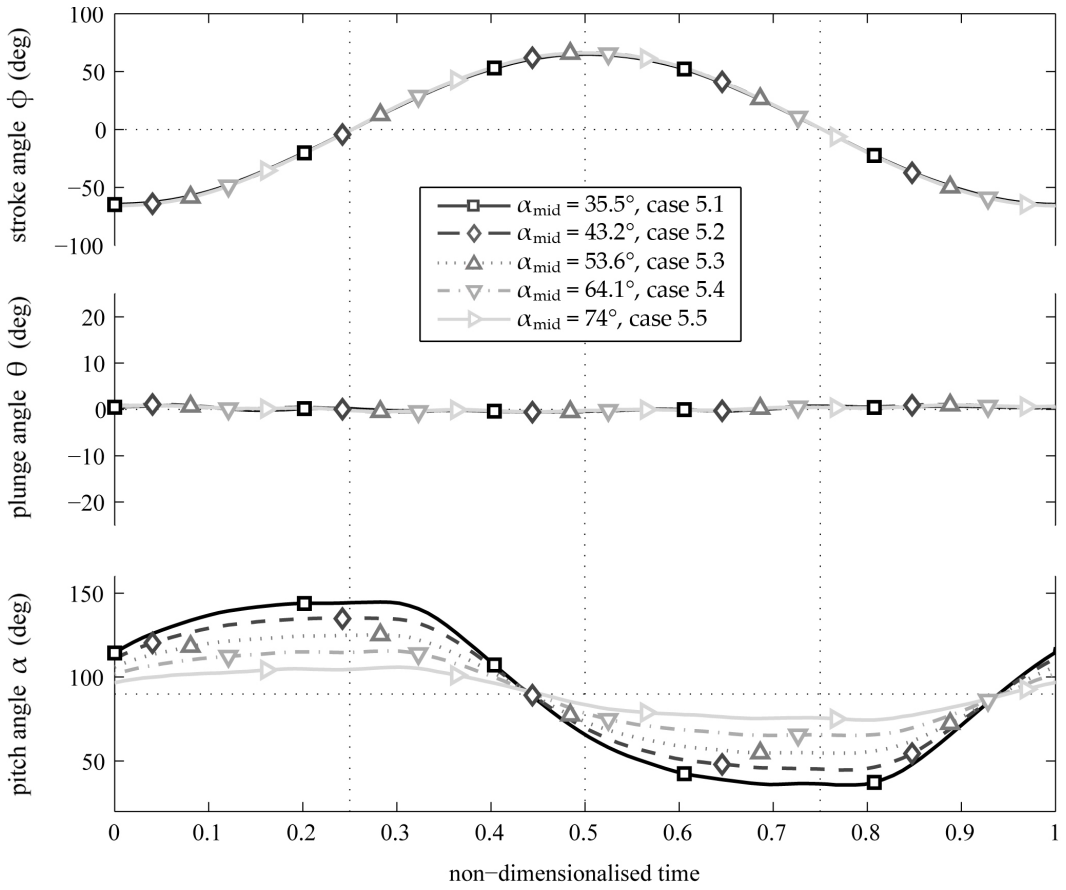

Figure 6.39: Mechanism output kinematics for test cases that vary angle of attack at mid-stroke

of attack of 45°, the increase in normal force became less steep, which combined with an increasingly horizontal normal force resulted in lift decreasing. The net aerodynamic force acting on an insect-like flapping wing has been shown experimentally to act nearly normal to the wing surface (see, e.g. Sane & Dickinson (2001)), thus this explanation seems appropriate to explain the trend presented here. It is also interesting to note that experiments by Sane & Dickinson (2001) and Usherwood & Ellington (2002a), which were performed at Reynolds numbers on the order of 10^2 and 10^3 respectively, found that the mean lift coefficient reaches a maximum between 40° and 50° angle of attack. Therefore, results presented here show this trend extends to FMAV scale Reynolds numbers on the order of 10^4.

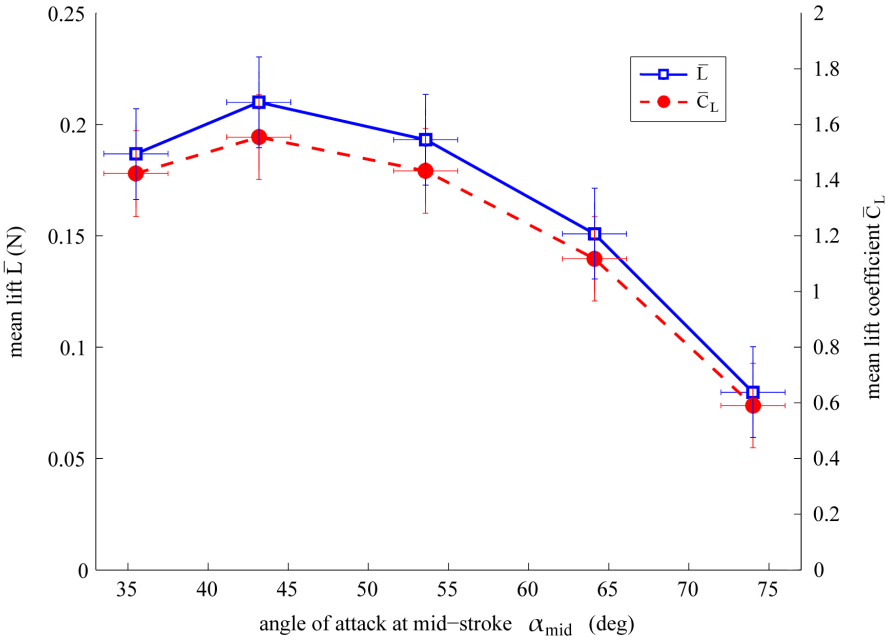

Figure 6.40: Effect of angle of attack at mid-stroke on mean lift and mean lift coefficient

6.4.3 Effect on Flowfield

Figure 6.41 illustrates plots of the same style seen previously, with top views of the wing revealing the effect on the flow structures of increasing α_{mid}. A back view of the wing for the same cases may be found in Figure F.18 of Appendix F. It can be seen that the effect is an increase in *LEV* and *TPV* diameter as α_{mid} is increased, which is consistent with observations by Wilkins (2008). This is also illustrated in Figure 6.42a which shows the vortex diameter normalised with respect to the mean chord at 40%, 50%, and 60% span versus α_{mid}, where the identified trends indicate that the *LEV* should disappear below an angle of attack of about 20°. Returning to Figure 6.41, as α_{mid} is increased beyond 45°, the *LEV* axial velocity drops quite drastically. Comparing flows for α_{mid} = 35.5° and α_{mid} = 74° shows that axial flow changes from quite positive values to mostly negative values. Figure 6.42b also illustrates this with plots of minimum and maximum *LEV* axial velocity versus α_{mid}, where there is a clear link between angle of attack and axial velocity level. Thus, the previous conclusion that *LEV* axial velocity is a function of mean Reynolds number, must be extended by noting that axial velocity is also a function of angle of attack.

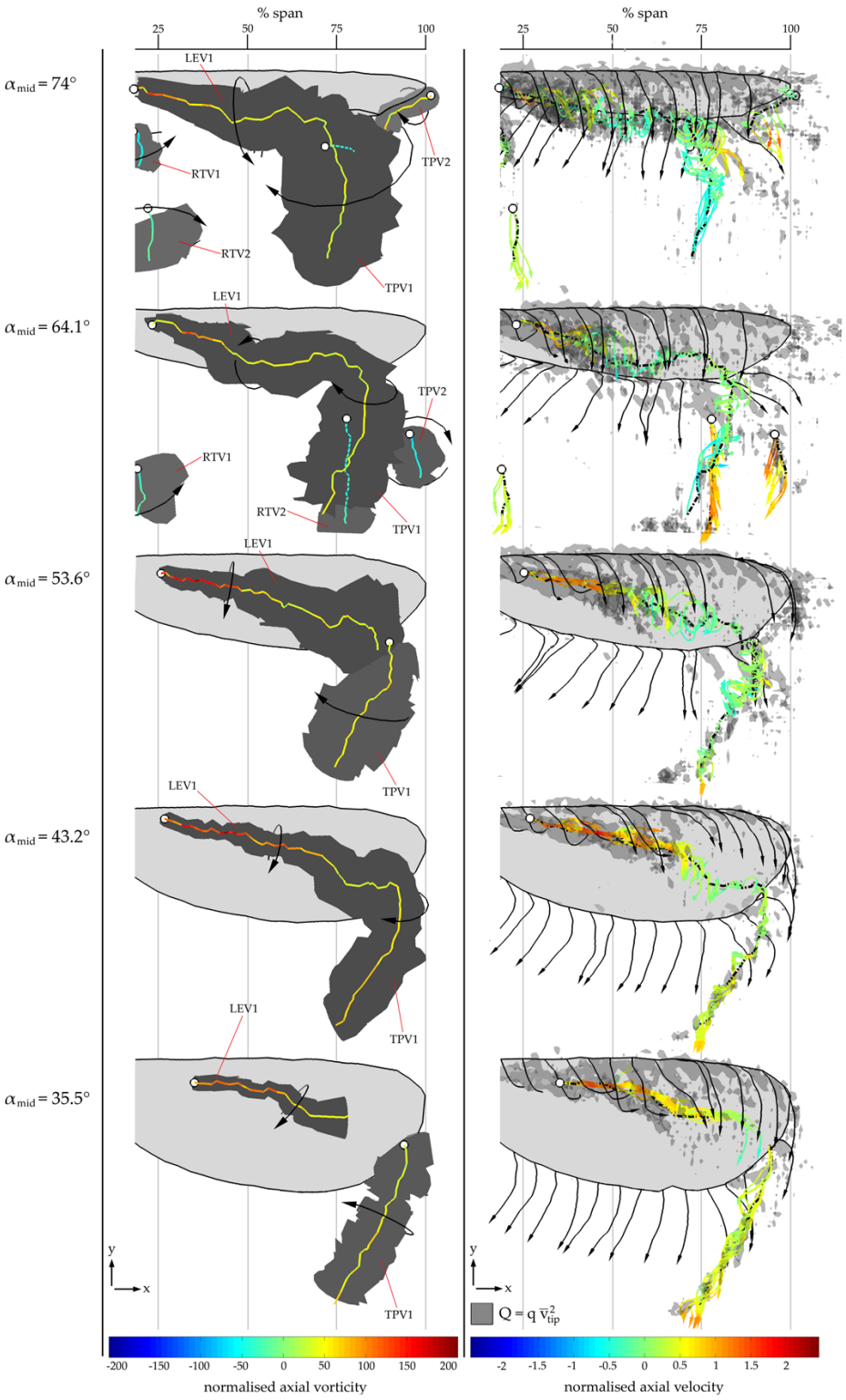

Figure 6.41: Top views illustrating flow formation at mid-stroke for test cases with varying α_{mid}; left column shows vortex core diameter (dark grey surfaces) and vortex axes coloured with axial vorticity normalised with respect to $\bar{\Omega}_{wng}$ ($92.9 rad/s$); vortex axes become dashed behind other objects; right column shows instantaneous streamlines released from vortex axes coloured with axial velocity normalised with respect to $\bar{v}_{tip}$ ($9.7 m/s$), black streamlines released along the wing edge, and transparent grey isosurfaces of $Q = q\bar{v}_{tip}^2$ where $q \approx 8.5 \times 10^4 m^{-2}$; positive axial direction points along an axis towards the end without a white dot

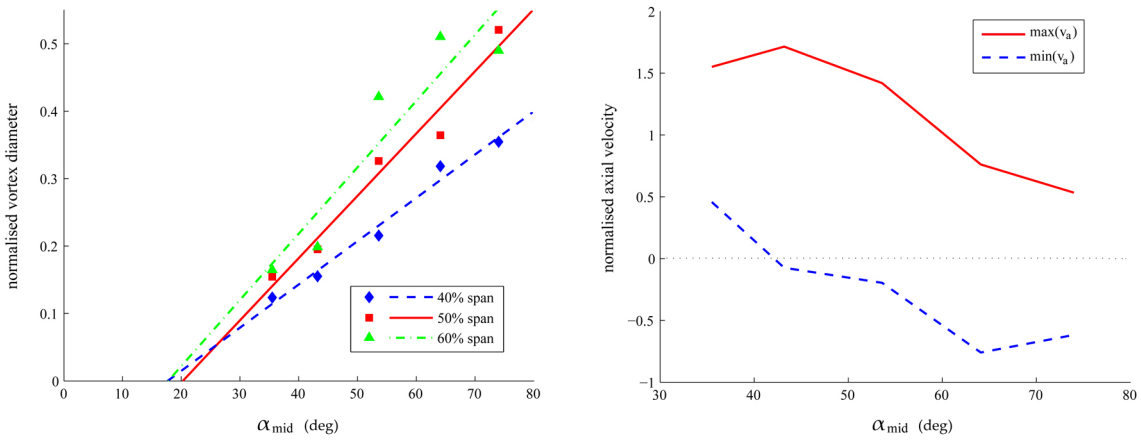

(a) (b)

Figure 6.42: (a) *LEV* diameter normalised with respect to $\bar{c}$ (27.7mm) versus α_{mid} at 40%, 50%, & 60% span; (b) minimum and maximum *LEV* axial velocity normalised with respect to $\bar{v}_{tip}$ (9.9m/s) versus α_{mid}

Interestingly the axial velocity of the tip vortex switches from positive to negative as α_{mid} rises. This switch appears to occur somewhere around 55°. The same phenomenon was observed in § 6.1.2 when the wing came to the end of the half-stroke and pitch reversal was underway (see Figure 6.4). There the switch in the axial direction of the *TPV* was attributed to the fact that since the wing was decelerating it was beginning to view the *TPV* as it would be seen by an observer fixed to the ground. However, the results presented here show that this is not the whole story, as at the mid-stroke measurement position the wing is not decelerating, but rather has reached peak angular velocity, and still a switch in *TPV* axial velocity is observed. This switch is possibly the result of an increasingly lower pressure region on the upper surface of the wing. As mentioned, *CFD* studies of Wilkins (2008) found that the wing normal force continually rose as angle of attack was increased, which implies an increasingly negative pressure region above the wing compared to the free stream. If the angle of attack is sufficiently high then this region is a low enough pressure such that pressure forces are able to overcome the momentum of the free stream flow and reverse its direction. Therefore, a reverse in *TPV* axial direction can also result from instantaneous wing angle of attack, in addition to wing deceleration.

It can also be seen that as α_{mid} increases, root vortices form, which have been attributed to *KHI* in the shear layer between a tip-ward flow above the wing and root-ward flow below the wing as discussed in § 6.1.2 and seen in Figure 6.7. As

α_{mid} rises, the region of fluid aft of the *LEV* develops a stronger tip-ward flow due to the increased size of the tip vortex, which eventually leads to a sufficiently high velocity gradient between the root-ward flow below the wing, causing *KHI*. Also as seen in Figure 6.41, if α_{mid} is high enough then a secondary tip vortex (*TPV*2) forms.

6.4.4 LEV Breakdown

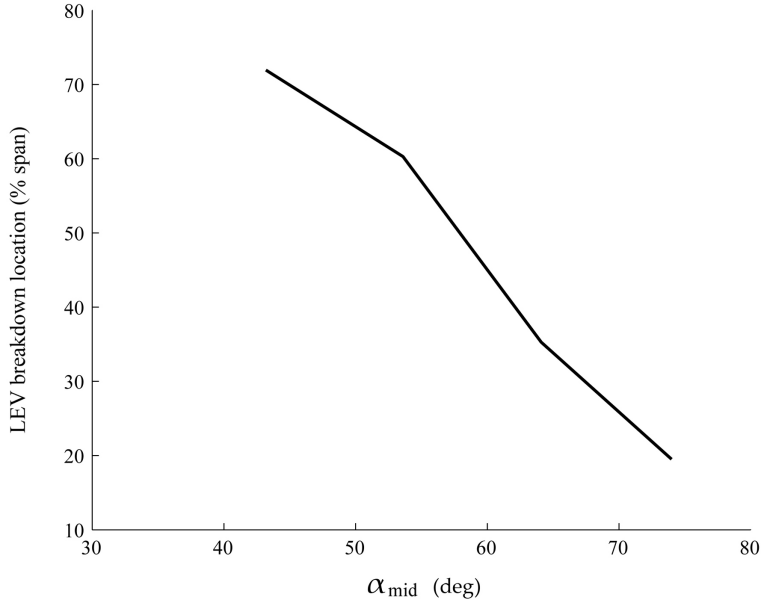

Figure 6.43: *LEV* breakdown location versus α_{mid}

The effect of α_{mid} on the vortex breakdown location is illustrated in Figure 6.43. Again, breakdown was identified as the point at which the helix angle passed 50°, accompanied by an increase in vortex diameter and a reversal in axial velocity. For case 5.1, for α_{mid} = 35.5°, the helix angle was always below critical, thus no breakdown location for this case was identified. However, breakdown could have been present between the end of the identified *LEV* axis and the start of the *TPV* axis, which the vortex point-joining algorithm was unable to connect. As seen in Figure 6.43, α_{mid} has a clear impact on the vortex breakdown location, as it shifts towards the root for higher α_{mid} values. The same effect was seen in § 6.1.2, when the *LEV* breakdown location was also reported to move inboard as pitch reversal occurred towards the end of stroke. This suggests that in addition to

being dependent on stroke amplitude as discussed in § 6.3.4, the extent of *LEV* breakdown is strongly dependent on angle of attack. The same is true for delta wings, where the vortex breakdown locations in the *LEVs* over the wing move upstream as angle of attack increases (Gursul et al., 2007).

6.4.5 General Effect of Angle of Attack

Comparing Figure 6.41 to Figure 6.4 in § 6.1.2, shows that the flowfield at mid-stroke for larger α_{mid} values strongly resembles the flowfield seen towards the end of a half-stroke when pitch reversal is occurring. For example comparing the flow at $\alpha_{mid} = 64.1°$ in Figure 6.41 to the flow at $0.375T$ in Figure 6.4, shows a very similar picture. Many of the effects of varying α_{mid} noted previously are also observed to occur towards the end of a half-stroke during pitch reversal, including a shift in *LEV* breakdown location inboard, a drastic drop in axial velocity levels, *LEV* and tip vortex diameter increase, and axial reversal of the tip vortex. The mid-stroke and end of stroke position are very different in the sense that at mid-stroke the wing is at peak velocity and has no acceleration, whereas towards the end of stroke the wing is at a reduced velocity and is decelerating and pitching rapidly. The fact that the flowfield and flow phenomena seen at mid-stroke for high α values also occur towards the end of stroke when the wing is at a similar angle of attack, suggests that the effects of *LEV* breakdown intensification, axial velocity drop, *LEV* and tip vortex size increase, and axial flow reversal of the tip vortex, are largely the result of instantaneous angle of attack, and less the result of wing deceleration.

6.5 Effect of Figure-of-Eight Kinematics

The effects of using figure-of-eight wingtip kinematics will now be investigated. This is performed by starting with the baseline 'flat' wingtip kinematics and progressing to figure-of-eight kinematics with an increasing plunge amplitude while observing the resulting effects on mean lift and flowfield. First, measurement cases will be presented, followed by the mechanism output and flapping kinematics, mean lift measurements, and lastly, the flowfield measurements.

6.5.1 Flapping Kinematics & Measurement Cases

Beginning with the 'baseline' kinematics presented in § 5.1, Θ was varied using figure-of-eight wingtip kinematics while all other parameters were held virtually constant, giving the seven test cases in Table 6.7. For all cases, mean lift was measured, whereas flowfield measurements at the mid-stroke position were only performed for cases 6.1 – 6.5. The mechanism output kinematics for each test case are given in Figure 6.44.

Table 6.7: Kinematic parameters for test cases which vary plunge amplitude

case #	6.1	6.2	6.3	6.4	6.5	6.6	6.7
f	20Hz	20Hz	20Hz	20Hz	20Hz	20Hz	20Hz
$\bar{Re}_1$	18570	18720	18970	19320	19730	20140	20720
$\bar{Re}_2$	17760	17860	18100	18430	18820	20160	20760
Φ	131.8 ±8°	131.9 ±8°	131.9 ±8°	132.1 ±8°	132.1 ±8°	131.9 ±8°	132 ±8°
Θ	1.7 ±5.2°	4.8 ±5.2°	8.6 ±5.2°	12.7 ±5.2°	16.9 ±5.2°	21 ±5.2°	25.2 ±5.2°
α_{mid}	43.2 ±2°	42.3 ±2°	43 ±2°	42.7 ±2°	43.3 ±2°	44.4 ±4.9°	44 ±4.9°
τ	6.1 ±1.4%	6 ±1.4%	6.1 ±1.4%	6 ±1.4%	6 ±1.4%	6 ±1.4%	5.9 ±1.4%
Φ_{mec}	131.8 ±0.2°	131.9 ±0.2°	131.9 ±0.2°	132.1 ±0.2°	132.1 ±0.2°	131.9 ±0.2°	132 ±0.2°
Θ_{mec}	1.7 ±0.6°	4.8 ±0.6°	8.6 ±0.6°	12.7 ±0.6°	16.9 ±0.6°	21 ±0.6°	25.2 ±0.6°
$\alpha_{mec_{mid}}$	45.1° ±0.4°	44.6° ±0.4°	44.6° ±0.4°	44.6° ±0.4°	44.3° ±0.4°	44.4° ±0.4°	44° ±0.4°
τ_{mec}	6.1 ±0.3%	6 ±0.3%	6.1 ±0.3%	6 ±0.3%	6 ±0.3%	6 ±0.3%	5.9 ±0.3%

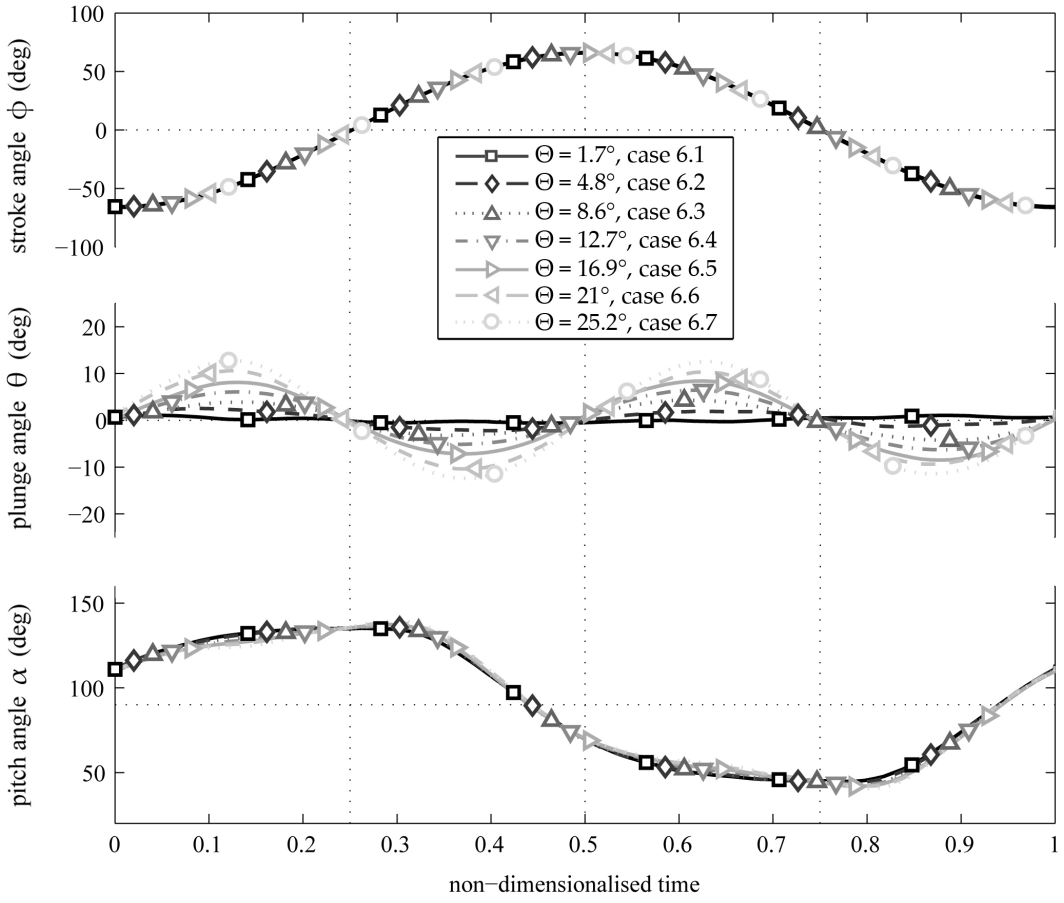

Figure 6.44: Mechanism output kinematics for test cases that vary plunge amplitude with figure-of-eight kinematics

6.5.2 Effect on Mean Lift

The effect on mean lift and mean lift coefficient from varying Θ using figure-of-eight kinematics is given in Figure 6.45. Increasing plunge amplitude has only a small effect on mean lift and mean lift coefficient. As plunge amplitude increases, the mean lift increases slightly and reaches a maximum at 8.6°, whereas mean lift coefficient reaches a maximum at 4.8°. Here, the peak in mean lift coefficient occurs at a different angle than the peak in mean lift because the ratio of mean lift to mean wingtip speed is greater at a plunge amplitude of 4.8° than at 8.6°. Beyond these angles, further increases in plunge amplitude reduce both mean lift and mean lift coefficient.

A possible explanation for the observed trend is that, as with increasing stroke amplitude, increasing the plunge amplitude also increases the distance that the

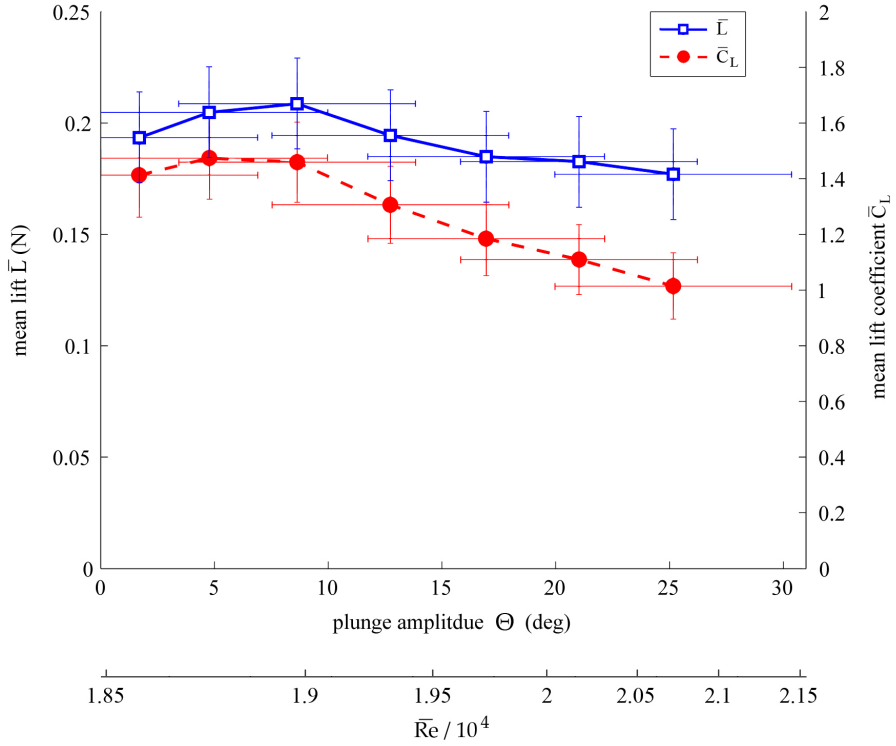

Figure 6.45: Effect of plunge amplitude with figure-of-eight kinematics on mean lift and mean lift coefficient

wing must travel in the same period of time. Thus, for a fixed stroke amplitude and flapping frequency, this will bring an increase in the mean wing speed (and thus, an increase in $\bar{Re}$) and should increase lift. The change in mean wing speed for a given change in plunge amplitude is, however, quite small. Increasing the plunge amplitude from 1.7° to 8.6° increases the mean wing speed by about 2%. This would be accompanied by a 4% increase in mean lift, if mean lift scales with v^2, or a 3% increase if it scales with $v^{1.5}$ as seen in § 6.3.2. The increase in lift from Θ = 1.7° to 8.6° is 8%, which is larger than either of these. However, considering the level of error, this increase could in fact be closer to 3% or 4%, in which case, the peak in mean lift at 8.6° can be explained simply by an increase in wing speed.

The decreasing mean lift seen beyond Θ = 8.6° could be attributed to an increase in effective angle of attack. This increases for greater plunge amplitudes since the wing's velocity has a downward component. The angle of attack at mid-stroke for these experiments was set approximately to 45°; thus, as the plunge amplitude was increased, effective angle of attack would have risen beyond 45°. According to Figure 6.40, beyond 45° mean lift falls. Increasing the plunge ampli-

tude in this case up to 8.6° would have increased the effective angle of attack by 7.4°, bringing it up to around 52.4°. This is still in the 'plateau' region in Figure 6.40 where changes in angle of attack give only small changes in mean lift. Thus, up to a plunge amplitude of 8.6°, the positive effects of increased mean wing speed possibly dominate over the negative effects of increased effective angle of attack. Beyond an effective angle of attack of 55°, however, lift falls more sharply. Hence, above a plunge amplitude of around 8.6° the negative effects of increased effective angle of attack appear to dominate over the positive effects from increased mean wing speed.

All of the measurements in Figure 6.45 are roughly in the same error band, and so it is possible that the trend observed here is simply due to measurement error. For instance, the true trend could simply be a positive or negative sloping line, both of which can fit within all the error bars. To test if the trend observed here was genuine, the experiment was repeated and it was again revealed that mean lift peaks at a plunge amplitude of 8.6°, after which, it declines as plunge amplitude increases further.

6.5.3 Effect on Flowfield

The effect of varying Θ on the flowfield at mid-stroke is shown in Figure 6.46, which shows the same style of plot shown previously illustrating vortex diameter, vortex axes, axial vorticity, and instantaneous streamlines with axial velocity for each test case. A similar plot showing back views of the wing is given in Figure F.19 of Appendix F. It can be seen that the effect of varying the wingtip kinematics from an almost flat wingtip trajectory to a figure-of-eight wingtip trajectory with an increasing plunge angle, are very slight. Generally, the effects of increasing Θ are similar to those seen previously from increasing α_{mid}, such as an increase in *LEV* diameter (Figure 6.47a), reversal of the axial velocity of the *TPV* and a shift in the *LEV* breakdown location inboard (Figure 6.47b). A similarity between plunge amplitude and angle of attack effects would be expected because as Θ increases, so does the effective angle of attack. However, there are notable differences, including a relatively constant peak axial velocity with increasing Θ seen in Figure 6.47c, as well as a noticeable shift in the outboard portion of the *LEV* axis away from the wing surface as illustrated in Figure 6.48. In addition,

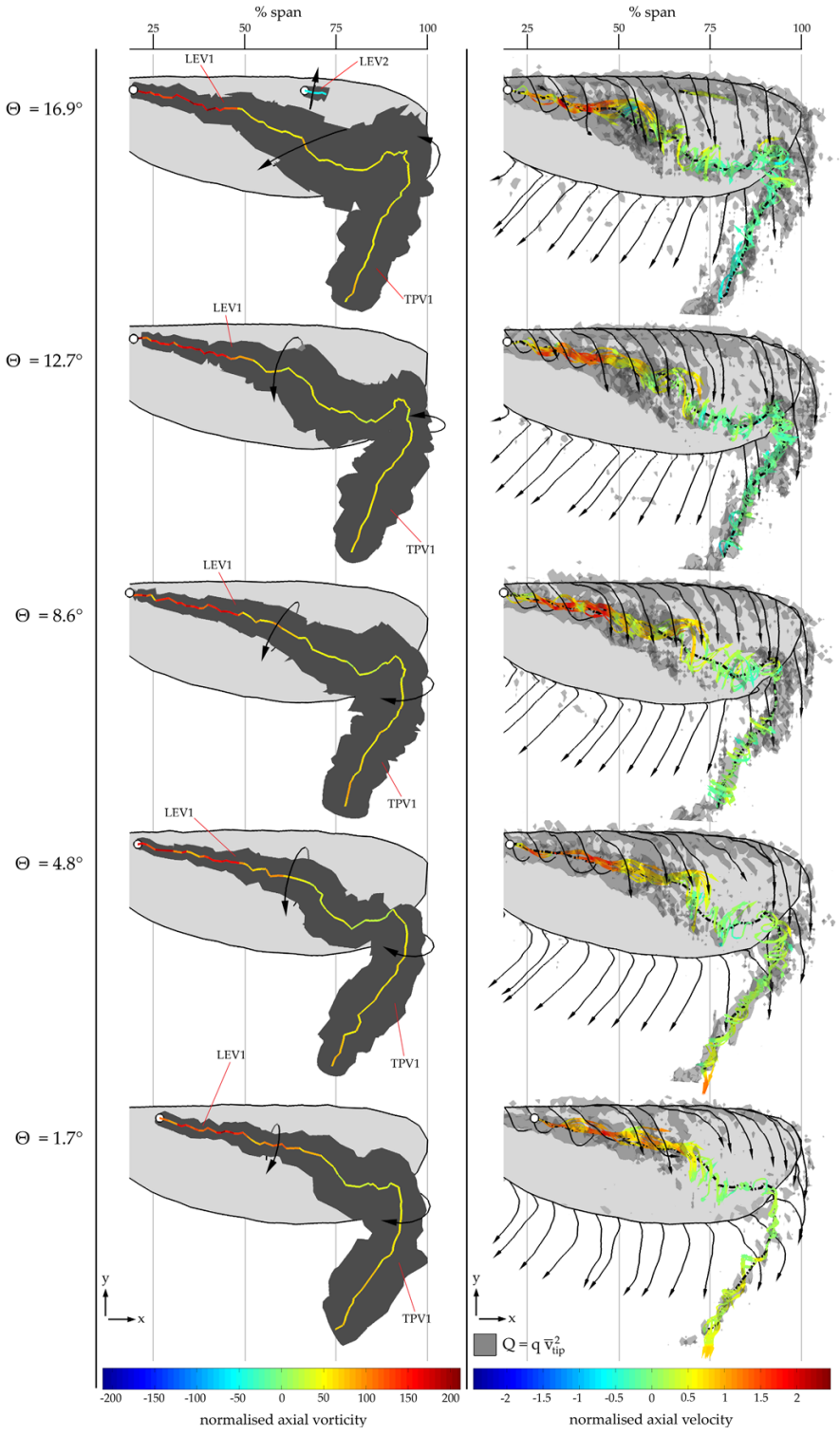

Figure 6.46: Top views illustrating flow formation at mid-stroke for test cases with varying Θ with figure-of-eight kinematics; left column shows vortex core diameter (dark grey surfaces) and vortex axes coloured with axial vorticity normalised with respect to $\bar{\Omega}_{wng}$ (93.2, 94, 95.2, 97, 99rad/s); vortex axes become dashed behind other objects; right column shows instantaneous streamlines released from vortex axes coloured with axial velocity normalised with respect to $\bar{v}_{tip}$ (9.9, 9.9, 10.1, 10.3, 10.5m/s), black streamlines released along the wing edge, and transparent grey isosurfaces of $Q = q\bar{v}_{tip}^2$ where $q \approx 8.5 \times 10^4 m^{-2}$; positive axial direction points along an axis towards the end without a white dot

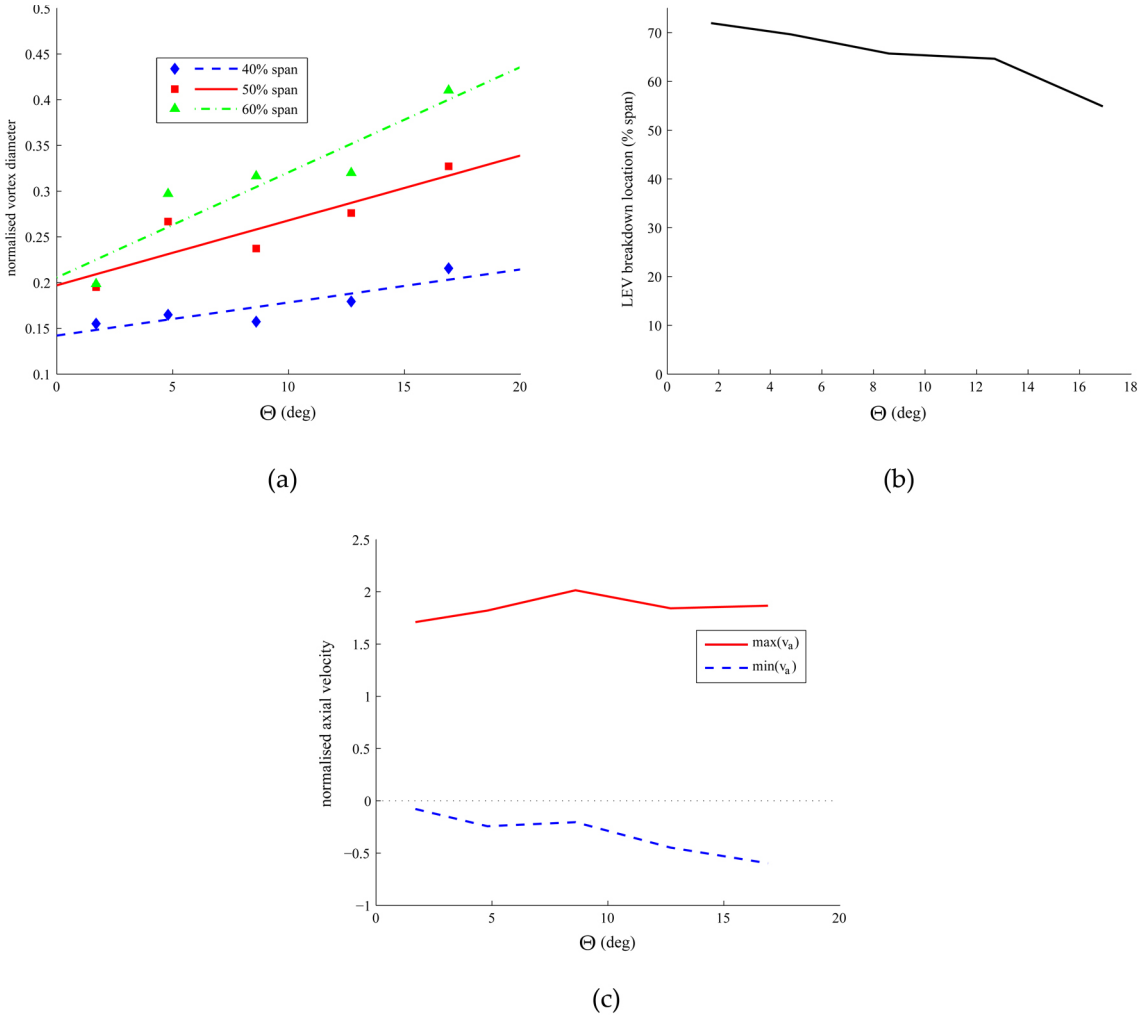

Figure 6.47: (a) *LEV* diameter normalised with respect to $\bar{c}$ (27.7*mm*) at 40%, 50%, & 60% span, (b) *LEV* breakdown location, and (c) minimum and maximum *LEV* axial velocity normalised with respect to $\bar{v}_{tip}$ versus Θ

the secondary *LEV* becomes more visible at $\Theta = 16.9°$, seen in Figure 6.46 (*LEV*2), as it is identified by the employed vortex identification scheme.

6.6 Planform Shape Effects

We now shift from investigating kinematic effects to wing planform shape effects. In this study, four planforms varying in shape, but with a relatively constant wing length, area, mean chord and aspect ratio are tested to investigate the effects on the flowfield. First the measurement cases and details of the wing geometries will be presented, followed by the mechanism output and flapping kinematics, and the

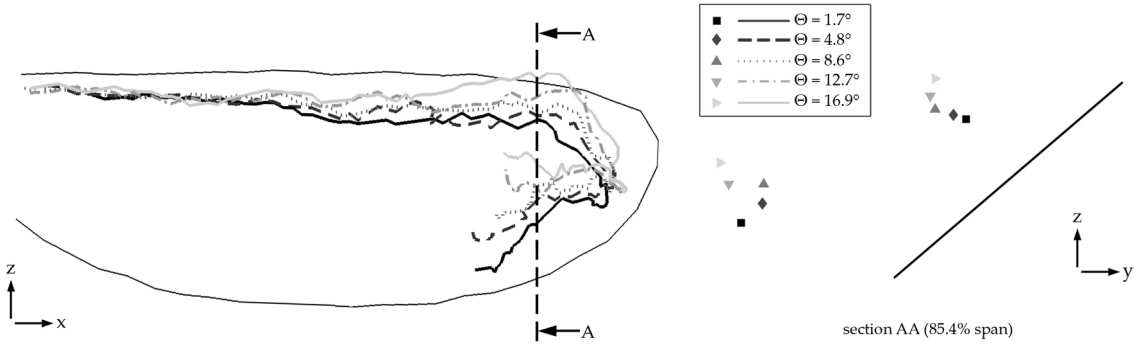

Figure 6.48: Back view of wing (left) and sectional chordwise view at 85.4% span (right) illustrating shift in outboard portion of *LEV* axis away from the wing surface with increasing Θ

flowfield measurements. Also, discussions on *LEV* breakdown, and leading-edge sweep effects will also be given.

6.6.1 Flapping Kinematics & Wing Planforms

The flapping kinematics used for this investigation were the same as the 'baseline' kinematics presented in § 5.1, but at a lower flapping frequency of 15Hz. The kinematic parameters are listed in Table 6.8, and the flapping mechanism output kinematics are shown in Figure 6.49.

The wing planforms investigated included a 'reverse-ellipse', rectangle, 'four-ellipse', and ellipse shape as presented in § 4.3.5 in Figure 4.30 (page 116). As

Table 6.8: Kinematic parameters

f	15Hz
$\bar{Re}$	13830
Φ	131.7 ± 8°
Θ	1.2 ± 5.2°
α_{mid}	46.4 ± 4.9°
τ	6 ± 1.6%
Φ_{mec}	131.7 ± 0.2°
Θ_{mec}	1.2 ± 0.6°
$\alpha_{mec_{mid}}$	46.4 ± 0.4°
τ_{mec}	6 ± 0.3%

with the wing design used in the preceding discussion (the 'four-ellipse'), all wing geometries tested here had the same mean chord length of approximately 28*mm* and a constant aspect ratio of about 6. It should be noted here that the reverse-ellipse planform had a slightly larger area due to the interface between the spar and the wing near the root section. In addition, for all planforms the pitch axis is located at the quarter-chord of the maximum chord. Overall, these shapes encompass a number of geometric variations including area distribution, leading and trailing edge sweep, and tip chord length.

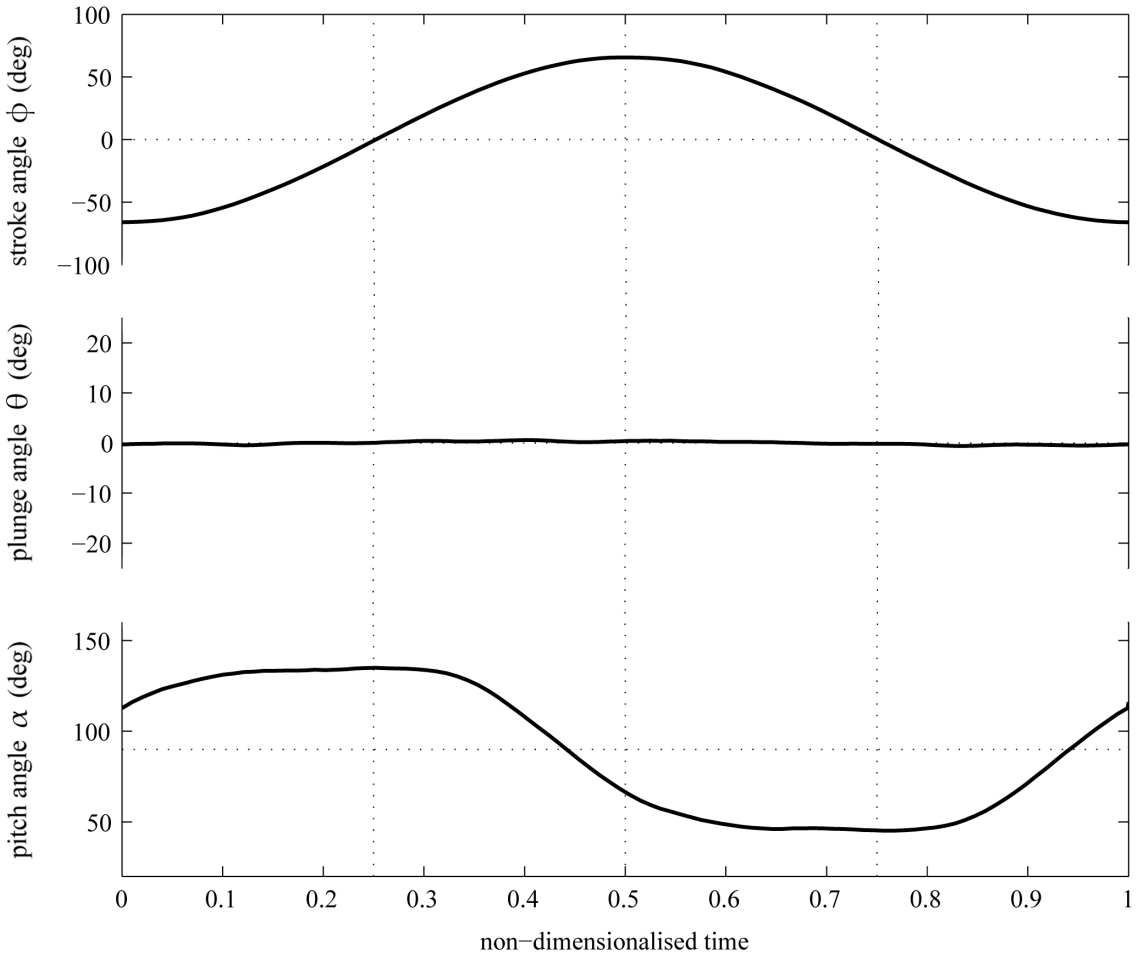

Figure 6.49: Mechanism output kinematics for test cases that vary planform shape; time is non-dimensionalised by the flapping period T (0.067*s*)

6.6.2 General Flow Structure

The form of the major flow structures for each of the wing geometries at mid-stroke is illustrated in Figure 6.50 which depicts the top, back and root views which look in the $-z$, y, and x directions respectively. Vortical structures are highlighted with transparent isosurfaces of Q normalised with respect to the maximum Q value. These are plotted for three different 'normalised Q' values: purple = 0.2, orange = 0.1, yellow = 0.05. In addition, the structure of the flow around these major vortices is illustrated with vectors in wing coordinates plotted on an isosurface of velocity magnitude (in laboratory coordinates) equal to the mean wingtip speed ($7.4m/s$). It should be noted that the employed vortex identification scheme of Knowles et al. (2006) did not reveal clear vortex axes for these measurements, and thus, vortex axes and vortex diameters were not identified as they have been in previous sections. This is possibly because a different *PIV* measurement system was used for these measurements.

Recall that Q provides a measure of the dominance of rotation rates over strain rates at a point in the fluid, where the more positive Q is the more rigid-body motions dominate, and the more negative Q is the more shearing motions dominate. Since vortex cores exhibit nearly rigid-body rotation, Q values will be largest in such regions because shear is virtually nonexistent. Thus, higher normalised Q values indicate regions where vortex cores are present.

It can be seen from the isosurfaces of normalised $Q = 0.2$ for all wing geometries, that two vortex core structures appear to be present along the leading edge. The more aft of these structures is the *LEV*, and the more forward structure highlights *KHVs* resulting from *KHI* in the vortex sheet emanating from the leading edge as described in § 6.1.3. To provide a comparison of the strength of the *LEV* across the planforms, the upper portion of Figure 6.51 illustrates the normalised $Q = 0.2$ isosurfaces coloured with x-wise vorticity for the top views. As reported before in § 6.1.3, it can be seen that both of the *KHVs* at the primary *LEVs* rotate in the same sense. Also, it can be seen by the vorticity values that the strength of the *LEV* across all planforms is very similar. Returning again to Figure 6.50, at the isosurfaces for the lower two normalised Q values, more of the vortex structures become visible. The moderate normalised Q level (0.1) is concentrated around the *LEV* and *KHVs*, and with addition of the low normalised Q level (0.05) the tip

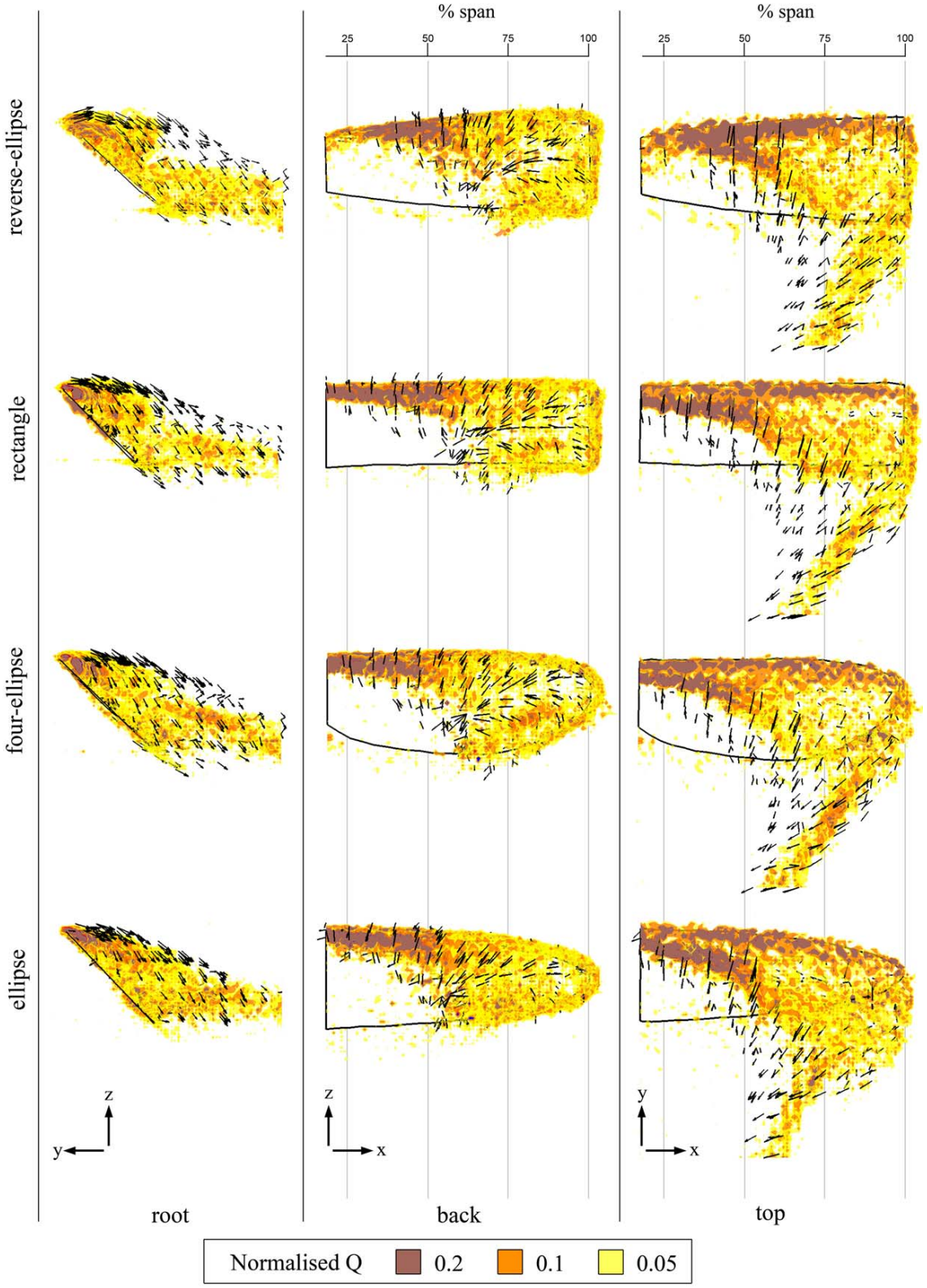

Figure 6.50: 3–view of flow around each planform shape at mid-stroke; isosurfaces are of constant Q normalised with respect to the maximum

vortex for each wing planform becomes clear. A conical region of vortical flow extending outboard from the *LEV* is also made visible on all wing planforms by the lower two normalised Q isosurfaces.

6.6.3 LEV Breakdown

In all cases, the *LEV* starts off with a smaller diameter and with a higher Q value at the root. Progressing towards the tip it stays somewhat the same size as indicated by the highest level Q isosurface, which then spontaneously ends around mid-span. Recall from § 6.1.4 that high Q level isosurfaces were observed to consistently disappear shortly before the vortex breakdown location, thus, a sudden drop in Q value is an indication of *LEV* breakdown. Therefore, *LEV* breakdown is present for all planforms, which according to previous observations in past sections, must occur shortly after the sudden drop in Q. The lower normalised Q isosurfaces beyond approximately mid-span, suggest an expanding vortical region, or in other words, an increase in vortex diameter, which is consistent with the occurrence of breakdown.

An unexpected consequence of averaging multiple images obtained at a given measurement location is that the core of the primary LEV becomes visible. This is because the seeding particles (smoke) are slightly more dense than the fluid (air). In a vortical flow this means that in comparison to a fluid element, the smoke particles will have a larger centrifugal force (pulling the particle away from the centre of rotation) compared to the radial pressure gradient (pulling the particle towards the centre of rotation). The result is that the seeding density in the core of the LEV is less than elsewhere in the fluid. In a single exposure this lower level of seeding density in such a region is invisible, however, when multiple images for the same measurement location are averaged it becomes quite clear.

Figure 6.51 shows images averaged in the manner mentioned previously. These images were generated from averaging 15 samples of the first exposure at each of four spanwise locations (30.5%, 42.7%, 54.9%, 67.1%) straddling the region where the Q level suddenly drops in the *LEV* for each wing planform. For comparison, the same spanwise locations are also labeled on the isosurfaces of normalised $Q = 0.2$ coloured with x-wise vorticity. It can be seen for the rectangle, four-ellipse and ellipse planforms that more inboard, the *LEV* is quite

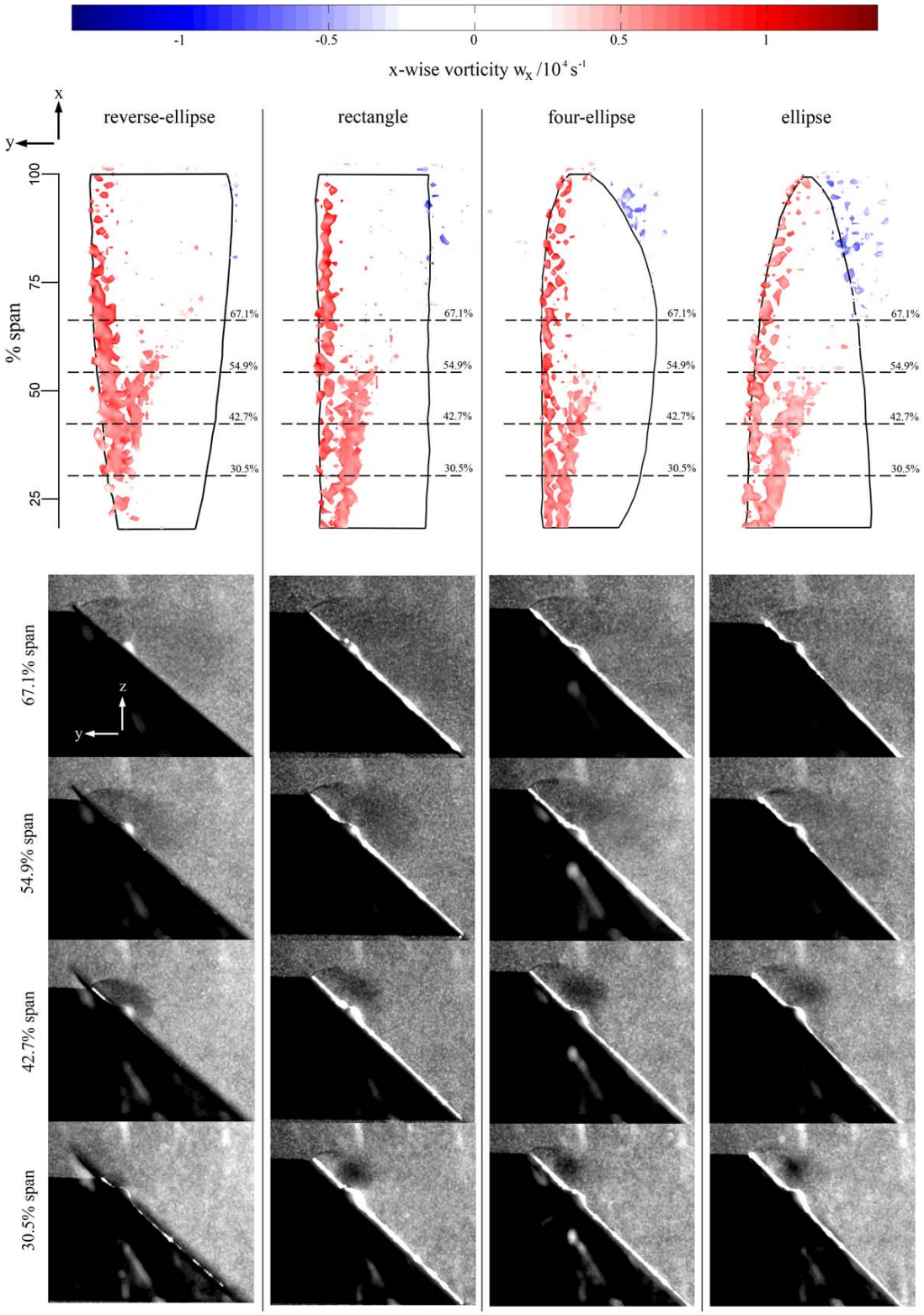

Figure 6.51: Isosurfaces of normalised Q = 0.2 coloured with $x-$wise vorticity for each planform at mid-stroke (top); average of multiple image samples at various spanwise locations revealing a dark spot, which is the core of the *LEV* (bottom)

concentrated and grows only slightly from 30.5% to 42.7% span. The reverse-ellipse differs from this, where at 30.5% span the *LEV* is barely visible, however at 42.7% span it grows to a size comparable to that seen at the same spanwise location for the other planforms. At 54.9% span and beyond to 67.1% span, the core structures for all planforms are similar and appear to suddenly expand and become less distinct. This is in agreement with the conical vortex structures observed in the moderate and low normalised Q isosurfaces in Figure 6.50.

6.6.4 Leading-Edge Sweep Effects

The observations in Figure 6.51 suggest that a forward-swept leading edge suppresses the formation of the *LEV*. Given that the normalised $Q = 0.2$ isosurface for this planform does not appear close to the root and the *LEV*'s small structure seen in the averaged image at 30.5% span, it seems as though the *LEV* does not form until close to 30.5% span. In contrast, the *LEV* is quite visible inboard of 30.5% span for the other planform shapes. The forward-sweep on the leading edge of the reverse-ellipse planform varies in this case from root to tip. Towards the root, where the forward-sweep is greatest, the *LEV* is more affected and is even absent. The leading edge for this planform approaches a straight leading edge geometry towards the tip, and it appears as a consequence of this that the vortex structures towards the tip more resemble those seen on planforms with straight leading edges (rectangle and four-ellipse), where highest Q isosurface for the *LEV* disappears around the same location, implying a similar point of breakdown. However, it appears as though the breakdown location on the reverse-ellipse is slightly further outboard than the rest, as the high Q isosurface extends slightly further. This suggests that a forward-swept leading edge also shifts the *LEV* breakdown location outboard.

An aft-swept leading edge (ellipse planform) appears to have no noticeable effect on the vortex structures when compared to the straight leading edge planforms. The vortex cores are of similar size across 30.5%-42.7% span as depicted in the averaged images in Figure 6.51, and the point when the high Q isosurface disappears is the same, implying a similar breakdown location.

6.6.5 Overall Planform Effect

It is apparent that, overall, the flow structures on all four planform shapes are very similar, despite the drastic differences in geometry. This implies that planform shape generally has little effect on the flow structure over the wing. This view has been supported elsewhere. Experiments of Lu et al. (2006) who looked at the Reynolds number range $160-3200$, postulated that the effect of geometry was only slight. CFD studies of Wilkins (2008) who tested the same ellipse, rectangle, and reverse-ellipse planforms (but with a smaller aspect ratio) reported little impact on the flow phenomenology for a constant aspect ratio. From the present results these conclusions have now been extended to *FMAV* scale Reynolds numbers.

It is worth noting that although planform shape has little effect on the general flow structures, it has been seen computationally and analytically that it significantly impacts aerodynamic forces. Wilkins (2008), who as previously mentioned computationally studied similar wing geometries, found lift coefficients between these planform shapes to be quite different. Here, the reverse-ellipse performed the best, followed by the rectangle and then the ellipse planform which performed the worst. Similarly, results from Ansari et al. (2008a), who analytically studied wing geometry effects (on the same wing geometries presented here), indicate that the reverse and four-ellipse planform shapes are best and will produce comparable values of lift. This is followed by the rectangle and ellipse planform shapes which would perform the worst in terms of lift production. It should be noted, however, that Ansari's model was based on a blade element approach using radial chords. Due to its only quasi-3*D* nature, it did not capture the tip vortex, spanwise flow, or vortex breakdown, and did not reveal a stable *LEV*.

Chapter 7

Conclusions & Recommendations

This chapter summarises the findings and achievements of the thesis. Based upon key results, recommendations for future *FMAV* design are then given. This is followed by a discussion of potential future work.

Flapping Mechanism Design & Development

A novel flapping mechanism was conceived and created which permits separate control of a flapping wing's sweeping, plunging and pitching motions. This separate control enables flapping kinematics to be altered so that a wide range of insect-like kinematics can be achieved. These capabilities of separate stroke, plunge and pitch control, and the ability to alter kinematics, are features which have rarely been seen in devices of this kind developed by previous research groups. Kinematic analysis was performed on the mechanism so that desired output kinematics to the wing could be related to the input kinematics of the input links of the mechanism. A dynamic model of the mechanism was created, which enabled the design of the mechanism's links to be chosen such that required input torques and accelerations of the input links to produce a desired set of kinematics would be minimised; thus, enabling high flapping frequencies and complicated kinematics to be achieved. A final detailed design of the mechanism was converged upon by performing a stress analysis with loads obtained from the dynamic model, which resulted from a worst-case-scenario set of flapping kinematics and aerodynamic loads.

Flapping-wing Apparatus Design & Performance

The final flapping mechanism design formed the heart of the greater experimental flapping-wing apparatus, the 'flapperatus'. This contained all of the necessary hardware to drive the flapping mechanism, including servo motors and cable drives. In addition, the flapperatus interfaced with aerodynamic force, flowfield, and wing position measurement devices, to enable such measurements. When fitted with a wing, the performance of the flapperatus was proved to be very good. The flapping mechanism successfully

achieved variable insect-like kinematics smoothly, even up to the maximum 20Hz flapping frequency. Even at this high frequency, the repeatability of the mechanism's output kinematics was very good. Although the flapping wing was slightly flexible, it faithfully followed the mechanism output kinematics, and the wing position was very repeatable. This was a result of the excellent repeatability of the flapping mechanism position. The flapperatus is the first of its kind in its abilities to mimic insect-like flapping-wing kinematics smoothly with a high degree of repeatability up to a 20Hz flapping frequency in air (thus, true *FMAV* conditions), with separate stroke, plunge and pitch control and variable kinematics.

Flow Evolution Throughout Half-Stroke at FMAV Scale

The first experimental investigation utilising the flapperatus focused on the flow formation throughout a half-stroke at an FMAV scale Reynolds number of approximately 15000. It was revealed that the flow evolution is characterised by the formation of a starting vortex soon after the start of the half-stroke, with the beginnings of a *LEV* forming outboard and a *TPV*. In addition, at the start of the half-stroke the *LEV*, *TPV* and major *RTV* from the previous stroke still persisted underneath the wing. As the stroke progressed these structures were left behind in the wake and the current *LEV* grew in size with an increasing level of axial vorticity and velocity towards the mid-stroke position where the *LEV* broke down. Beyond mid-stroke the *LEV* became more distorted and axial velocity levels dropped in the core as the breakdown location moved inboard. The axial direction of the *TPV* reversed as the wing decelerated because the wing began to view the *TPV* as it would be seen by an observer fixed to the ground. Towards the end of the stroke when pitch reversal occurred, pitching vortices were shed off the trailing edge and the *TPV* began descending with the downwash. In addition, a series of *RTVs* formed due to *KHI* in the shear layer between a tip-ward flow above the wing and a root-ward flow below the wing.

LEV Stability at FMAV Scale

Throughout the entire half-stroke even up until the end of stroke at the *FMAV* scale Reynolds number tested ($Re \approx 15000$), the *LEV* was stable and was not observed to shed into the wake. A possible explanation for why

this study revealed a stable *LEV* at this scale and others have not was that, after Wilkins (2008), the *LEV* becomes unstable beyond a certain aspect ratio. Examination of past studies showed more reports of a stable *LEV* at aspect ratios of around 6 or below (where $AR = 6$ for the present study), and more reports of an unstable *LEV* towards $AR = 8$, suggesting a critical aspect ratio somewhere between 6 and 8.

Secondary LEV

The presence of a secondary *LEV* between the (primary) *LEV* and the leading edge, as has been observed on delta wings, was revealed. This rotated in the opposite sense to the *LEV*, and grew in size towards the tip. *KHI* in the vortex sheet emanating from the leading edge was present immediately above the secondary *LEV*. This was due to the level of shear between the flow originating from the free-stream traveling towards the trailing edge and flow traveling towards the leading edge induced by the secondary *LEV*. In plots of Q criterion isosurfaces, the resulting *KHVs* in the shear layer resemble an addition *LEV* which is present along the leading edge and has the same sense of rotation as the (primary) *LEV*.

Vortex Breakdown in LEV

Details of *LEV* breakdown revealed that it exhibited the spiral type of breakdown. Upon examining the mid-stroke position (for $Re \approx 15000$, stroke amplitude $\Phi \approx 120°$), it was seen that the helix angle of the *LEV* surpassed the critical value of 50° around 80% span, which was followed by a steeper increase in vortex size and a drop in axial velocity levels to negative values. This breakdown appeared to be caused by an axial 'blowing' effect from the *TPV*, which induces a flow in the opposite direction to the vortex axial flow. After breakdown the *LEV* soon merged with the *TPV* which reduced the vortex diameter and added energy resulting in an axial vorticity increase and a suppression of vortex breakdown as the helix angle dropped below critical. Beyond mid-stroke, the intensification of breakdown was blamed on an increasingly adverse pressure gradient, which caused the breakdown location to move steadily inboard ultimately to approximately 20% span at the end of stroke.

LEV Circulation & LEV Lift Contribution

Examining *LEV* circulation showed that circulation increases towards the tip along with the vortex diameter. Throughout a half-stroke the level of *LEV* circulation increases to a peak at mid-stroke and then declines thereafter. It was discussed that the *LEV* can instantaneously produce 130% of the mean lift value, which occurs at mid-stroke and is a much higher value than has been previously reported. After averaging the *LEV* lift values over a half-stroke and examining previously-reported values of *LEV* lift, it is apparent that the *LEV* is responsible for about half of the mean lift produced.

Effect of Rotation Phase on Mean Lift & Flow Structures

If the timing of pitch reversal with stroke reversal (rotation phase) is varied, the pattern of flow evolution does not change greatly. However, a noticeable effect was that the phase relationship between the pattern of flow evolution and stroke kinematics was altered with rotation phase. For a more delayed pitch reversal (more negative rotation phase), a starting vortex is shed later in the stroke, and the *TPV* begins descending into the downwash later. Starting from a negative value, as rotation phase is increased, mean lift rises and peaks around a rotation phase of about +5.5%, after which it declines. More negative rotation phases suffer from low lift due to a more pronounced Wagner effect, as a starting vortex is shed further into the half-stroke. They also suffer from a negative Kramer effect as the wing starts with a negative angle of attack and rapidly pitches down at the start of a half-stroke. More positive rotation phases benefit from a more enhanced Kramer effect when the wing pitches up earlier when the wing has a higher velocity. However, they eventually suffer from negative lift as the wing translates a further distance with a negative effective angle of attack towards the end of stroke as rotation phase increases beyond the optimal value.

Reynolds Number & Stroke Amplitude Effects on Mean Lift & Flow Structures

Increasing mean Reynolds number by increasing flapping frequency and holding stroke amplitude constant led to an increase in lift proportional to $v^{1.5}$, whereas increasing mean Reynolds number via stroke amplitude increase and constant flapping frequency led to a linear relation between mean lift and wing speed. Keeping Reynolds number constant and increasing the

stroke amplitude had no effect on the mean lift produced. In the range tested ($Re \approx 4000 - 18000$) a mean Reynolds number increase with constant stroke amplitude had little effect on the flow at mid-stroke and *LEV* breakdown occurred between 60 – 70% span. Increasing stroke amplitude either with a fixed mean Reynolds number or fixed flapping frequency produced a similar flowfield at mid-stroke. In general, for larger stroke amplitudes the *LEV* is larger, and *LEV* breakdown is more developed. It is postulated that the greater extent of *LEV* breakdown at larger stroke amplitudes, and the closer proximity of the wing underside to the *TPV* and *RTV* from the previous half-stroke for small stroke amplitudes, led to decreased lift at a high and low stroke amplitude respectively, resulting in the observed linear trend. The axial flow level in the core of the *LEV* was shown to be independent of stroke amplitude, and dependent on mean Reynolds number, where peak axial velocity varied with $\bar{Re}^{1.3}$. It was shown that in the axial direction, centrifugal forces dominate over viscous, Euler, and Coriolis forces, which possibly explains the non-linear trend between vortex axial velocity and wing speed ($\bar{Re}$), as the relation between centrifugal force and wing speed (which is a function of wing angular velocity) is also non-linear.

Effect of Angle of Attack on Mean Lift & Flow Structures

The optimal angle of attack at mid-stroke occurs around 45° and lift declines on either side of this value. As angle of attack increases, the *LEV* becomes larger and vortex axial velocity levels drop, eventually to the point where the axial direction of the *TPV* reverses. *LEV* breakdown is also a function of angle of attack, as the breakdown location is more inboard for higher angle of attack values. This was blamed on an increasingly adverse axial pressure gradient. Similarities in the flowfield seen at mid-stroke for high angle of attack, and the end-of-stroke position in other measurements when the angle of attack is similarly high, suggests that effects such as a shift in breakdown location inboard, axial reversal of the *TPV*, and *LEV* and *TPV* diameter increase are largely the result of instantaneous angle of attack.

Effect of Figure-of-Eight Kinematics on Mean Lift & Flow Structures

Transitioning to figure-of-eight kinematics, and increasing plunge amplitude to approximately 9° results in a slight increase in lift. This could be

explained by an increase in wing speed, which must increase with plunge amplitude as flapping frequency is held constant. Beyond a plunge amplitude of 9°, lift steadily declines, probably due to an increasing effective angle of attack. The effects on the flowfield at mid-stroke are only slight, as the *LEV* exhibits a similar structure as plunge amplitude increases. However, vortex diameter increases slightly, the *LEV* breakdown location gradually moves inboard, and the portion of the *LEV* axis towards the tip lifts further away from the wing surface.

Effect of Wing Planform Shape on Flow Structures

For a constant aspect ratio, and mean chord length, varying wing planform shape was seen to have very little effect on the flow structures produced. Even with drastic differences in wing geometry, a *LEV* of similar size and strength forms, *KHVs* are present along the leading edge, and *LEV* breakdown occurs in a similar location. However, one noticeable effect was that a forward-swept leading edge suppresses the formation of the *LEV* inboard and possibly shifts the *LEV* breakdown location towards the tip.

Main Findings of Thesis

There are two main findings that the reader should take from this thesis. The first is that despite the fact that it breaks down, the *LEV* on an insect-like wing in actual *FMAV* conditions remains attached to the wing and continues to augment lift as Reynolds number is increased. This confirms that *FMAVs* can exploit the lifting mechanism of the *LEV*, which supplies about half of the generated lift. The second finding is the identification of the mean lift versus kinematics trends themselves at *FMAV* scale which, as will be discussed next, can inform *FMAV* design.

7.1 Recommendations for FMAV Design

The identified trends showed that using figure-of-eight kinematics instead of flat wingtip kinematics gave very little benefit, as it only increased mean lift slightly for a small plunge amplitude ($\Theta \approx 9°$). Implementing plunge control into a flapping mechanism, greatly complicates its design and control. This small

benefit from figure-of-eight kinematics does not justify the added complications in mechanism design required to achieve these kinematics. A flapping mechanism with only stroke and pitch control, would achieve a slightly lower peak lift (0.015N less), however the design would be greatly simplified as it would be less complex, with fewer moving parts, and simpler control, which leads to lighter weight and better reliability. However, it should be noted that to transition from hover to forward flight and back, the flapping mechanism must be capable of tilting the stroke plane.

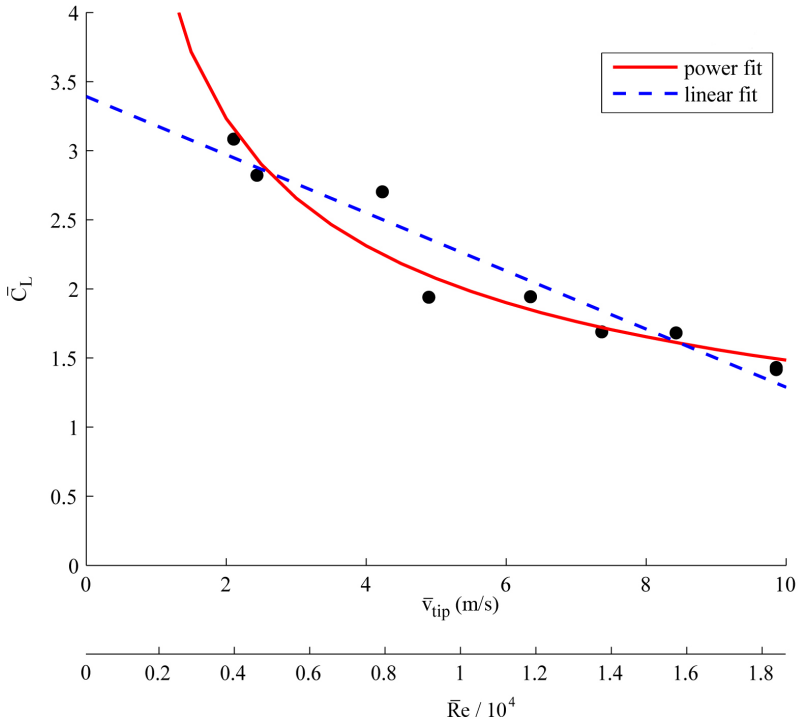

Figure 7.1: Mean wingtip speed and Reynolds number versus mean lift coefficient showing power and linear fit

The mid-stroke angle of attack (α_{mid}) and the end-of-stroke pitch phase advance (τ) should be set to the optimal values of approximately 45° and +5.5% respectively to obtain peak lift. As noted previously, figure-of-eight kinematics do not yield a sufficient benefit, thus plunge amplitude $\Theta = 0°$. The selection of the remaining parameters of f and Φ is somewhat arbitrary, as increasing either of these results in an increase in lift, thus there is no 'optimal' value. The choice of f and Φ will depend upon the application. For example, some applications may constrain the maximum value of f to less than 20Hz so that the vehicle is as silent as possible. Meanwhile, others may not place a restriction on f, but restrict Φ due to size

constraints where, for a larger Φ, the wings sweep over a larger area, thus the 'effective' size of the vehicle is larger.

For a given situation, the choice of f and Φ can be aided with an expression for mean lift as a function of f and Φ. Such an expression will be derived now. It was seen that changing stroke amplitude while holding the mean wingtip speed (Reynolds number) constant, did not affect lift production (see Figure 6.32). Increasing mean wingtip speed either via an increase in f with constant Φ or increase in Φ with constant f, resulted in increased lift. Thus, lift is a function of mean wingtip speed. Plotting the mean lift coefficient versus mean wingtip speed from these measurements, as seen in Figure 7.1, reveals that:

$$\bar{C}_L = 4.52\bar{v}_{tip}^{-0.5} \tag{7.1}$$

This was obtained from the power fit of the data points which, in comparison to the linear fit shown, yields a smaller standard error and better fits the data points at higher $\bar{v}_{tip}$ values which have smaller error. Now, substituting Equation 7.1 into the mean lift equation:

$$\bar{L} = 1/2\rho\bar{C}_L\bar{v}_{tip}^2 S \tag{7.2}$$

leads to:

$$\bar{L} = 2.26\rho\bar{v}_{tip}^{1.5} S \tag{7.3}$$

As in § 6.3.2, we see that mean lift scales with $v^{1.5}$. Now we want to find $\bar{v}_{tip}$ as a function of f and Φ. By definition:

$$\bar{v}_{tip} = l\bar{\Omega}_{wng} \tag{7.4}$$

Where l is the distance from the centre of rotation to the wingtip, and Ω_{wng} is the angular velocity of the wing. For flat wingtip kinematics (i.e. no plunge)

$\Omega_{wng} = \dot{\phi} = \Phi\pi f sin(2\pi ft - 2\pi\tau/100)$ (from Appendix A). In general, for a sine wave with amplitude 'A', the mean of the absolute value of the sine wave for one cycle is $\sim 0.637A$. Noting this, and the fact that $0.637\pi \approx 2$, gives:

$$\bar{\Omega}_{wng} = 2\Phi f \tag{7.5}$$

Substituting Equation 7.5 into Equation 7.4, and then inserting into Equation 7.3 gives:

$$\bar{L} = 6.39\rho(\Phi fl)^{1.5}S \tag{7.6}$$

The data used to obtain this expression are for a wing of aspect ratio 6, which must be reflected in this expression. Noting that $AR = 2R^2/S$, thus $S = R^2/3$ (for $AR = 6$), $l = b + R$, and multiplying by two, so that we have an expression for mean lift from two wings, we obtain the final expression:

$$\bar{L} = 4.26\rho R^2[\Phi f(b + R)]^{1.5} \tag{7.7}$$

Thus, with flat wingtip kinematics, a wing of aspect ratio 6, and α_{mid} and τ set to 45° and +5.5% respectively, Equation 7.7 may be used to select f and Φ for a given wing length R and wing offset b. For example, if an application constrains R to $100mm$, the wing offset is $10mm$, the $FMAV$ mass is $75g$ and the flapping frequency must be at most $20Hz$, then the required stroke amplitude to achieve the required lift at standard sea-level conditions is approximately 150°. It must be noted that this relation is not necessarily true for other wing planform shapes aside from the 'four-ellipse' used, and it only applies to a wing of aspect ratio 6. Therefore, this expression must be used for obtaining rough estimates of unknown quantities given known parameters and constraints.

7.2 Recommendations for Future Work

Although this thesis has answered a number of questions on the subject of insect-like flight in relation to $FMAVs$, many questions still remain. At present, this field

is quite young and the number of aspects related to insect-like flight that require further research and experimentation, is great. This section discusses a few areas of future research which can extend from the present work.

Synchronised Force, Torque and Wing Position Measurements

One of the capabilities envisaged for the flapperatus was the ability to simultaneously measure all three instantaneous force and torque components on the flapping-wing in addition to instantaneous wing position. Only lift measurements were implemented for the present work, with which position measurements were not synchronized. It was for this reason that instantaneous lift plots could not be produced as discussed in § 5.1. With synchronised force, torque and wing position measurement, pure inertial forces and torques can be measured using a 'dummy' wing (e.g. a simple rod) with negligible aerodynamic force that has the same mass, centre of gravity location and moment of inertia as the real wing. These inertial readings can then be appropriately subtracted from those with the real wing to obtain the instantaneous aerodynamic forces and moments, because the phase relationship between the measurements is known. Since wing position was not simultaneously measured in the present work, this subtraction could not be performed. Thus, inertial forces could only be eliminated by averaging the readings (inertial forces are symmetric, and thus average to zero) to obtain a mean lift value.

With all three instantaneous force and torque components on the flapping-wing, a lot of useful information can be obtained. For instance, force and torque values can be used to determine the centre of pressure for a given wing design. This would be useful in the structural design of wings, as it would be known where all loads on the wing are applied. In addition, with torque measurements the power required to drive the wing can be determined. In conjunction with the lift produced, this would provide a measure of efficiency. Furthermore, with instantaneous values of all force and torque components, further insight into the link between the instantaneous flowfield and the forces can be obtained.

Manoeuvres

With instantaneous force and torque measurements as discussed previously, kinematics which are suitable for performing manoeuvres can be explored. Forces and torques acting on the wing can be transformed to *FMAV* body forces if the wing position is simultaneously known. With a pair of wings, and by testing a range of different flapping kinematics, particulary asymmetric ones, kinematics that are suitable for achieving roll, pitch and yaw control of the *FMAV* body can be determined. Furthermore, with force and torque values known, one can determine which methods of achieving this control are most efficient.

Wing Flexibility

Another area of interest is wing flexibility. The present work used wings that were made as rigid as they could be so that experiments and analysis could be simplified by excluding effects due to flexibility as much as possible. A logical next step is to investigate wing flexibility, as in nature insects possess very flexible wings. Experiments on this aspect are few, but those that have been performed have shown clear benefits of flexibility. The experiments of Heathcote et al. (2004); Heathcote (2007), showed that flexibility can improve lift and efficiency. In addition, in the study of Young et al. (2009), which employed wing flexibility measurements from live insects combined with *CFD*, it was found that flexible wings give better power efficiency. Further research on the effects of flexibility on aerodynamic forces and flow structures would be useful. Ultimately it should be known how flexible a wing should be, and how wing stiffness should be distributed (e.g. stiff towards base, but flexible towards wingtip) to achieve optimal performance.

Wing Aspect Ratio

It was discussed in § 6.1.5 that differing reports of *LEV* stability could be the result of an aspect ratio effect, as at aspect ratios of 6 or below, the *LEV* is often reported to be stable, whereas up towards a value of 8 it appears to be unstable and sheds. As noted, such a dependency of *LEV* stability on aspect ratio was found in *CFD* studies by Wilkins (2008). It would be useful for future work to confirm this

effect by gradually varying aspect ratio and measuring the flowfield to determine if there is a 'critical' aspect ratio beyond which the *LEV* becomes unstable and sheds. In addition, it would be of interest to determine how the aerodynamic performance of a wing with a *LEV* that is stable, differs from one with an *LEV* that is unstable.

References

References

Adkins, C. (2008). (private communication).

Adrian, R. J. (1988). Statistical Properties of Particle Image Velocimetry Measurements in Turbulent Flow. *Laser Anemometry in Fluid Mechanics III*, 115–129. Springer-Verlag, Berlin Heidelberg.

AeroVironment, I. (2011a). AeroVironment Develops World's First Fully Operational Life-Size Hummingbird-Like Unmanned Aircraft for DARPA. AeroVironment News Release. February 17.

AeroVironment, I. (2011b). Nano Hummingbird. www.avinc.com/nano. accessed: 10/02/2011.

AeroVironment, I. (2011c). UAS Advanced Development Black Widow. www.avinc.com/uas/adc/black_widow. accessed: 10/02/2011.

Anderson, J. D. (2001). *Fundamentals of Aerodynamics* (3rd ed.). Mc-Graw Hill.

Ania, A., Poirel, D., & Potvin, M. J. (2011). Kinematics and Experimental Characterisation of the RotaFlap - a Novel Flapping Wing Mechanism. *Aeronautical Journal*, *115*(1163), 1–13.

Ansari, S. A. (2004). *A Nonlinear, Uunsteady, Aerodynamic Model for Insect-like Flapping Wings in the Hover with Micro Air Vehicle Applications*. PhD thesis, Cranfield University (Shrivenham).

Ansari, S. A. (2008). Cranfield University (Shrivenham). (private communication).

Ansari, S. A., Knowles, K., & Żbikowski, R. (2008a). Design Study of Insect-like Flapping Wings in the Hover. Part II: Effect of Wing Geometry, 1976–1990.

Ansari, S. A., Knowles, K., & Żbikowski, R. (2008b). Insectlike Flapping Wings in the Hover. Part I: Effect of Wing Kinematics. *Journal of Aircraft*, *45*(6), 1945–1954.

Ansari, S. A., Phillips, N., Stabler, G., Wilkins, P. C., Żbikowski, R., & Knowles, K. (2009). Experimental Investigation of some Aspects of Insect-like Flapping Flight Aerodynamics for Application to Micro Air Vehicles. *Experiments in*

Fluids, Special Issue: Animal Locomotion-The Physics of Flying, *46*(5), 777–798. (invited paper).

Aono, H. & Liu, H. (2006). Vortical Structure and Aerodynamics of Hawkmoth Hovering. *Journal of Biomechanical Science and Engineering*, *1*, 234–245.

AscTech (2010). New World Record. AscTech News Release. www.asctec.de/update-new-world-record. accessed: 10/02/2011.

AscTech (2011). Ascending Technologies. www.asctec.de. accessed: 10/02/2011.

Azuma, A. (2006). *The Biokinetics of Flying and Swimming*. AIAA Education Series. Reston, VA: American Institute of Aeronautics and Astronautics.

Banala, S. K. & Agrawal, S. K. (2005). Design and Optimization of a Mechanism for Out-of-Plane Insect Winglike Motion with Twist. *Journal of Mechanical Design*, *127*, 841–844.

Beckwith, R. M. H. & Babinsky, H. (2009). Impulsively Started Flat Plate Flow. *Journal of Aircraft*, *46*(6), 2186–2188.

Benjamin, T. B. (1962). Theory of the Vortex Breakdown Phenomenon. *Journal of Fluid Mechanics*, *14*, 593 – 629.

Bennett, L. (1966). Insect Aerodynamics: Vertical Sustaining Force in Near-Hovering Flight. *Science*, *152(3726)*, 1263–1266.

Bennett, L. (1970). Insect Flight: Lift and Rate of Change of Incidence. *Science*, *167(3915)*, 177–179.

Bennett, L. (1977). Clap and Fling Aerodynamics – an Experimental Evaluation. *Journal of Experimental Biology*, *69*, 261–272.

Berman, G. J. & Wang, Z. J. (2007). Energy-Minimizing Kinematics in Hovering Insect Flight. *Journal of Fluid Mechanics*, *582*, 153–168.

Birch, J. M. & Dickinson, M. H. (2001). Spanwise flow and the attachment of the leading-edge vortex on insect wings. *Nature*, *412*(6848), 729–733.

Birch, J. M. & Dickinson, M. H. (2003). The Influence of Wing-Wake Interactions on the Production of Aerodynamic Forces in Flapping Flight. *Journal of Experimental Biology*, *206*(13), 2257–2272.

Birch, J. M., Dickson, W. B., & Dickinson, M. H. (2004). Force Production and Flow Structure of the Leading Edge Vortex on Flapping Wings at High and Low Reynolds Numbers. *Journal of Experimental Biology*, *207*, 1063–1072.

Bonev, I. (2007). General Terminology related to Parallel Mechanisms. http://www.parallemic.org/Terminology/General.html. accessed: 27/04/2008.

Brackenbury, J. H. (1995). *Insects in Flight*. Blandford.

Brücker, C. (1993). Study of Vortex Breakdown by Particle Tracking Velocimetry (PTV) Part 2: Spiral-type Vortex Breakdown. *Experiments in Fluids*, *14*, 133–139.

Cabral, B. & Leedom, L. C. (1993). Imaging Vector Fields Using Line Integral Convolution. In *SIGGRAPH 93*, Anaheim, US.

Chiang, C. H. (1996). *Kinematics of Spherical Mechanisms*. Malabar, Florida: Krieger Publishing Company.

Chong, M. S., Perry, A. E., & Cantwell, B. J. (1990). A General Classification of Three-Dimensional Flow Fields. *Physics of Fluids*, *2*(5), 765–777.

Conn, A. T., Burgess, S. C., & Ling, C. S. (2007). Design of a Parallel Crank-Rocker Flapping Mechanism for Insect-inspired Micro Air Vehicles. *Proc. IMechE, Part C: Journal of Mechanical Engineering Science*, *221*, 1211–1222.

Conn, A. T., Burgess, S. C., Ling, C. S., & Hyde, R. A. (2006). An insect-inspired MAV flapping mechanism based on parallel crank-rockers with phase control, 25-26 July. In *Proceedings of European Micro Air Vehicle Conference*, 25-26 July, Braunschweig, Germany.

Conn, A. T., Burgess, S. C., Ling, C. S., & Vaidyanathan, R. (2008). The Design Optimisation of an Insect-inspired Micro Air Vehicle. *International Journal of Design & Nature*, *3*, 1–16.

Dantec (2011). Particle Image Velocimetry Measurement Principles. www.dantecdynamics.com/Default.aspx?ID=1049. accessed: 25/03/2011.

Davis, W. R. J., Kosicki, B. B., Boroson, D. M., & Kostishack, D. F. (1996). Micro Air Vehicles for Optical Surveillance. *The Lincoln Laboratory Journal*, *9*(2), 197–214.

Délery, J. M. (1994). Aspects of Vortex Breakdown. *Progress in Aerospace Sciences*, *30*, 1–59.

Dickinson, M., Lehmann, F. O., & Götz, K. G. (1993). The Active Control of Wing Rotation by Drosophila. *Journal of Experimental Biology*, *182*, 173–189.

Dickinson, M. H. & Götz, K. G. (1993). Unsteady Aerodynamic Performance of Model Wings at Low Reynolds Numbers. *Journal of Experimental Biology*, *174*(1), 45–64.

Dickinson, M. H., Lehmann, F.-O., & Sane, S. P. (1999). Wing Rotation and the Aerodynamic Basis of Insect Flight. *Science*, *284*(5422), 1954–1960.

Dudley, R. (2000). *The Biomechanics of Insect Flight: Form, Function, Evolution*. Princeton: Princeton University Press.

Ellington, C. P. (1984a). The Aerodynamics of Hovering Insect Flight: II Morphological Parameters. *Philosophical Transactions of the Royal Society of London Series B*, *305*, 17–40.

Ellington, C. P. (1984b). The Aerodynamics of Hovering Insect Flight: III Kinematics. *Philosophical Transactions of the Royal Society of London Series B*, *305*, 41–78.

Ellington, C. P. (1984c). The Aerodynamics of Hovering Insect Flight: IV Aerodynamic Mechanisms. *Philosophical Transactions of the Royal Society of London Series B*, *305*, 79–113.

Ellington, C. P. (1984d). The Aerodynamics of Hovering Insect Flight: VI Lift and Power Requirements. *Philosophical Transactions of the Royal Society of London Series B*, *305*, 145–181.

Ellington, C. P. (2006). Insects Versus Birds: The Great Divide, 10–13 January. In *44th AIAA Aerospace Sciences Meeting and Exhibit*, 10–13 January, Reno, NV. AIAA. AIAA-2006-0035.

Ellington, C. P. & Usherwood, J. R. (2001). Lift and Drag Characteristics of Rotary and Flapping Wings. *In Fixed and Flapping Wing Aerodynamics for Micro Air Vehicle Applications*, *AIAA books*, 231–248.

Ellington, C. P., van den Berg, C., Willmott, A. P., & Thomas, A. L. R. (1996). Leading-edge vortices in insect flight. *Nature*, *384*, 626–630.

Escudier, M. (1988). Vortex Breakdown: Observations and Explanations. *Progress in Aeronautical Science*, *25*, 189 – 229.

Galiński, C., Ansari, S. A., & Żbikowski, R. (2007). Progress in Design and Testing of an Insect-like Flapping-wing Mechanism and Conceptual re-design for Resonance. *Unpublished*.

Galiński, C., Mieloszyk, J., & Piechna, J. (2010). Progress in the Gust Resistant MAV Programme, 19-24 September. In *27th International Congress of the Aeronautical Sciences (ICAS)*, 19-24 September, Nice, France.

Galiński, C. & Żbikowski, R. (2005). Insect-like Flapping Wing Mechanism based on a Double Spherical Scotch Yoke. *Journal of the Royal Society: Interface*, *2*, 223–235.

Galiński, C. & Żbikowski, R. (2007). Materials Challenges in the Design of an Insect-like Flapping Wing Mechanism based on a Four-bar Linkage. *Materials & Design*, *28*(3), 783–796.

Gautier, G. & Riethmuller, M. (1988). Application of PIDV to Complex Flows: Measurement of the Third Component. *VKI Lecture Series*, *1988-06*.

Giordano, R. & Astarita, T. (2009). Spatial Resolution of the Stereo PIV Technique. *Experiments in Fluids*, *46*, 643–658.

Goodland, M. (2008). Machine shop, Cranfield University (Shrivenham). private communication.

Gosselin, C. M. & Caron, F. (1999). Two Degree-of-Freedom Spherical Orienting Device. United States Patent 5966991.

Gosselin, C. M. & Hamel, J. (1994). The Agile Eye: a High Performance Three Degree-of-Freedom Camera-Orienting Device, 8-13 May. In *IEEE International Conference on Robotics and Automation*, volume 1050-4729, (pp. 781–786)., 8-13 May, San Diego, USA.

Gursul, I., Wang, Z., & Vardaki, E. (2007). Review of Flow Control Mechanisms of Leading-edge Vortices. *Progress in Aeronautical Science*, *43*, 246–270.

Hall, M. G. (1972). Vortex Breakdown. *Annual Review of Fluid Mechanics*, *4*, 195–218.

Harris, D. A. (1993). *The Properties of Aluminium and Its Alloys*. Alfed Limited.

Heathcote, S.and Gursul, I. (2007). Flexible Flapping Airfoil Propulsion at Low Reynolds Numbers. *AIAA Journal*, *45*, 1066–1078.

Heathcote, S., Martin, D., & Gursul, I. (2004). Flexible Flapping Airfoil Propulsion at Zero Freestream Velocity. *AIAA*, *42*(11), 2196–2205.

Huang, H., Dabiri, D., & Gharib, M. (1997). On Errors of Digital Particle Image Velocimetry. *Measurement Science and Technology*, *8*(12), 1427–1440.

Hunt, J. C. R., Wray, A. A., & Moin, P. (1988). Eddies, Stream, and Convergence Zones in Turbulent Flows. *Center for Turbulence Research*, *Report CTR-S88*, 193–208. Report CTR-S88.

Jones, A. & Babinsky, H. (2010). Unsteady Lift Generation on Rotating Wings at Low Reynolds Numbers. *Journal of Aircraft*, *47*(3), 1013–1021.

Jones, A. & Babinsky, H. (2011). Reynolds Number Effects on Leading edge Vortex development on a Waving Wing. *Experiments in Fluids*, 1–14. 10.1007/s00348-010-1037-3.

Jones, K. D., Bradshaw, C. J., Papadopoulos, J., & Platzer, M. F. (2004). Improved Performance and Control of Flapping-wing Propelled Micro Air Vehicles, 5-8 January. In *42nd AIAA Aerospace Sciences Meeting and Exhibit*, 5-8 January, Reno, USA.

Keane, R. & Adrian, R. J. (1992). Theory of Cross-Correlation Analysis of PIV Images. *Applied Scientific Research*, *49*(3), 191–215.

Keane, R. D. & Adrian, R. J. (1990). Optimization of Particle Image Velocimeters. Part I: Double Pulsed Systems. *Measurement Science and Technology*, *1*(11), 1202–1215.

Keane, R. D. & Adrian, R. J. (1991). Optimization of Particle Image Velocimeters. Part II: Multiple Pulsed Systems. *Measurement Science and Technology*, *2*, 963–974.

Keennon, M. T. & Grasmeyer, J. M. (2003). Development of the Black Widow and Microbat MAVs and a Vision of the Future of MAV Design, 14-17 July. In *2003 AIAA/ICAS International Air and Space Symposium and Exposition: The Next 100 Years, Dayton, OH*, 14-17 July, Dayton, USA.

Keennon, M. T., Klingebiel, K. R., Andryukov, A., & Hibbs, B. D. (2010). Air Vehicle Flight Mechanism and Control Method. International Patent WO 2010/141916 A1.

Kellogg, J., Bovais, C., Dahlburg, J., Foch, R., Gardner, J., Gordon, D., Hartley, R., Kamgar-Parsi, B., McFarlane, H., Pipitone, F., Ramamurti, R., Sciambi, A., Spears, W., Srull, D., & Sullivan, C. (2001). The NRL Mite Air Vehicle. In *16th Inernational Conference on Unmanned Air Vehicle Systems*, Bristol, UK.

Kieser, F. (1985). Canard Biplane. http://www.ornithopter.org/plans/canardbiplane.gif. accessed 05/09/2008.

Knowles, R. D., Finnis, M. V., Saddington, A. J., & Knowles, K. (2006). Planar visualization of vortical flows. *Proceedings of the Institution of Mechanical Engineering, Part G: Journal of Aerospace Engineering*, *220*(6), 619–627.

Kramer, M. (1932). Die Zunahme des Maximalauftriebes von Tragflügeln bei plötzlicher Anstellwinkelvergrösserung (Böeneffekt). *Zeitschrift für Flugtechnik und Motorluftschiffahrt*, *23*(7), 185–189. (also appeared as *Increase in the Maximum Lift of an Airfoil due to a Sudden Increase in its Effective Angle of Attack Resulting from a Gust*, NACA TM-678).

Kundu, P. K. & Cohen, I. M. (2008). *Fluid Mechanics*. Academic Press.

Lambourne, N. C. & Bryer, D. W. (1961). The Bursting of Leading-edge Vortices. *Aeronautical Research Council*, *R and M 3282*.

Laval, U. (2011). The Agile Eye. robot.gmc.ulaval.ca/en/research/theme103.html. accessed: 10/03/2011.

Lawson, N. J., Finnis, M. V., Tatum, J. A., & Harrison, G. M. (2005). Combined Stereoscopic Particle Image Velocimetry and Line Integral Convolution Methods: Applications fo a Sphere Sedimenting Near a Wall in a Non-Newtonian Fluid. *Journal of Visualization*, *8*(3), 261–268.

Lawson., N. J. & Wu, J. (1997). Three-Dimensional Particle Image Velocimetry: Error Analysis of Stereoscopic Techniques. *Measurement Science and Technology*, *8*, 894–900.

Leibovich, S. (1978). The Structure of Vortex Breakdown. *Annual Review of Fluid Mechanics*, *10*, 221–246.

Leibovich, S. (1984). Vortex Stability and Breakdown: Survey and Extension. *AIAA Journal*, *22*(9), 1192–1206.

Lentink, D. & Dickinson, M. H. (2009). Rotational Accelerations Stabilize Leading Edge Vortices on Revolving Fly Wings. *Journal of Experimental Biology*, *212*, 2705–2719.

Lighthill, M. J. (1973). On the Weis-Fogh Mechanism of Lift Generation. *Journal of Fluid Mechanics*, *60*(1), 1–17.

Liu, H., Ellington, C. P., Kawachi, K., van den Berg, C., & Willmott, A. P. (1998). A Computational Fluid Dynamic Study of Hawkmoth Hovering. *Journal of Experimental Biology*, *201*, 461–477.

Lu, Y. & Shen, G. X. (2008). Three-Dimensional Flow Structures and Evolution of the Leading-edge Vortices on a Flapping Wing. *Journal of Experimental Biology*, *211*(8), 1221–1230.

Lu, Y., Shen, G. X., & Lai, G. J. (2006). Dual Leading-edge Vortices on Flapping Wings. *Journal of Experimental Biology*, *209*, 5005–5016.

Lu, Y., Shen, G. X., & Su, W. H. (2007). Flow Visualization of Dragonfly Hovering via an Electromechanical Model. *AIAA Journal*, *45*, 615–623.

Lua, K. B., Lim, T. T., & Yeo, K. S. (2011). Effect of Wing-Wake Interaction on Aerodynamic Force Generation on a 2D Flapping Wing. *Experiments in Fluids*, 1–19. 10.1007/s00348-010-1032-8.

Luc-Bouhali, A. (2006). Progress of the REMANTA Project on MAV with Flapping Wings, 25-26 July. In *Proceeding of the 2nd European Micro Air Vehicle Conference*, 25-26 July, Braunschweig, Germany.

Lucca-Negro, O. & O'Doherty, T. (2001). Vortex Breakdown: a Review. *Progress in Energy and Combustion Science*, *27*, 431–481.

Marks, P. (2009). Robotic Insect Flight could just be Good Vibrations. *The New Scientist*, *203*(2718), 22.

Mase, G. E. (1970). *Schaum's outline of theory and problems of Continuum Mechanics*. New York: McGraw-Hill.

Maxworthy, T. (1979). Experiments on the Weis-Fogh Mechanism of Lift Generation by Insects in Hovering Flight. Part 1: Dynamics of the 'Fling'. *Journal of Fluid Mechanics*, *93*, 47–63.

Maybury, W. J. & Lehmann, F.-O. (2004). The Fluid Dynamics of Flight Control by Kinematic Phase Lag Variation between two Robotic Insect Wings. *Journal of Experimental Biology*, *207*, 4707–4726.

McIntosh, S. H., Agrawal, S. K., & Khan, Z. (2006). Design of a Mechanism for Biaxial Rotation of a Wing for a Hovering Vehicle. *IEEE/ASME Transactions on Mechatronics*, *11(2)*, 145–153.

McMichael, J. M. & Francis, M. S. (1997). Micro Air Vehicles – Toward a New Dimension in Flight. *Unmanned Systems*, *15*(3), 10–15. Asssociation for Unmanned Vehicle Systems International (AUVSI).

Meng, X. G., Xu, L., & Sun, M. (2010). Aerodynamic Effects of Corrugation in Flapping Insect Wings in Hovering Flight. *Journal of Experimental Biology*, *214*, 432–444.

Mitchell, A. M. & Délery, J. M. (2001). Research into Vortex Breakdown Control. *Progress in Aerospace Sciences*, *37*, 385–418.

Mols, B. (2005). Flapping micro plane watches where it goes. *Delft Outlook*, *22(4)*, 3–7.

Mueller, T. J. (2009). On the Birth of Micro Air Vehicles. *International Journal of Micro Air Vehicles*, *1*(1), 1–12.

Mueller, T. J. & DeLaurier, J. D. (2001). An Overview of Micro Air Vehicle Aerodynamics. *In Fixed and Flapping Wing Aerodynamics for Micro Air Vehicle Applications*, *AIAA books*, 1–10.

Mueller, T. J. & DeLaurier, J. D. (2003). Aerodynamics of Small Vehicles. *Annual Review of Fluid Mechanics*, *35*, 89–111.

Muren, P. (2008). Passively Stable Rotor System for Indoor Hovering UAS, 22-24 July. In *International Powered Lift Conference (IPLC)*, 22-24 July, London, UK. Royal Aeronautical Society.

Nachtigall, W. (1977). Zur Bedeutung der Reynoldszahl und der damit zusammenhiängenden striömungsmechanischen Phiänomene in der Schwimmphysiologie und Flugbiophysik. *Fortschritt der Zoologie*, *24*(2-3), 13–59.

Nagai, H. & Hayase, T. (2009). Experimental and Numerical Study of Forward Flight Aerodynamics of Insect Flapping Wing. *AIAA Journal*, *47*(3), 730–742.

Nguyen, V., Syaifuddin, M., Park, H. C., Byun, D. Y., Goo, N. S., & Yoon, K. J. (2008). Characterisitics of an Insect-mimicking Flapping System Actuated by a Unimorph Piezoceramic Actuator. *Journal of Intelligent Material Systems and Structures*, *19*, 1185 – 1193.

Parrot (2011). AR Drone. ardrone.parrot.com/parrot-ar-drone/uk. accessed: 10/02/2011.

Peckham, D. H. & Atkinson, S. A. (1957). Preliminary Results of Low Speed Wind Tunnel Tests on a Gothic Wing of Aspect Ratio 1.0. *British Aeronautical Research Council*, *CP 508*.

Pedersen, C. B. (2003). *An indicial-Polhamus model of aerodynamics of insect-like flapping wings in hover*. PhD thesis, Cranfield University (Shrivenham).

Phillips, N. (2010). Three Degree-of-Freedom Parallel Spherical Mechanism for Payload Orienting Applications. UK Patent GB2464147 (pending).

Poelma, C., Dickson, W. B., & Dickinson, M. H. (2006). Time-Resolved Reconstruction of the Full Velocity Field around a Dynamically-Scaled Flapping Wing. *Experiments in Fluids*, *41*, 213–225.

Pornsin-Sirirak, T. N., Tai, Y. C., Ho, C. M., & Keennon, M. (2001). Microbat: A Palm-Sized Electrically Powered Ornithopter. In *Proceedings of NASA/JPL Workshop on Biomorphic Robotics*.

Prasad, A. K. (2000). Stereoscopic Particle Image Velocimetry. *Experiments in Fluids*, *29*, 103–116.

Prasad, A. K. & Jensen, K. (1995). Scheimpflug Stereocamera for Particl Image Velocimetry to Liquid Flows. *Applied Optics*, *34*(30), 7092–7099.

ProxDynamics (2011). Pd-100 Black Hornet. www.proxdynamics.com/products/pd_100_black_hornet. accessed: 10/02/2011.

Raffel, M., Willert, C., & Kompenhans, J. (1998). *Particle Image Velocimetry: A Practical Guide*. Springer.

Ramamurti, R. & Sandberg, W. C. (2002). A Three-Dimensional Computational Study of the Aerodynamic Mechanisms of Insect Flight. *Journal of Experimental Biology*, *205*(10), 1507–1518.

Ramasamy, M. & Leishman, J. G. (2006). Phase-Locked Particle Image Velocimetry Measurements of a Flapping Wing. *Journal of Aircraft*, *43*(6), 1867–1875.

Ramasamy, M., Leishman, J. G., & Singh, B. (2005). Wake Structure Diagnostics of a Flapping Wing MAV, 3–6 October. In *SAE International Powered Lift Conference*, number IPLC 2005-01-3198, (pp. 1–13)., 3–6 October, Texas.

Riley, A. J. & Lowson, M. V. (1998). Development of a Three-Dimensional Free Shear Layer. *Journal of Fluid Mechanics*, *369*, 49–89.

Saharon, D. & Luttges, M. (1987). Three-Dimensional Flow produced by a Pitching-Plunging Model Dragonfly Wing. *AIAA*, *AIAA Paper 87-0121*.

Saharon, D. & Luttges, M. (1988). Visualization of Unsteady Separated Flow produced by Mechanically Driven Dragonfly Wing Kinematics Model. *AIAA Paper 88-0569*.

Sane, S. P. & Dickinson, M. H. (2001). The Control of Flight Force by a Flapping Wing: Lift and Drag Production. *Journal of Experimental Biology*, *204*, 2607–2626.

Sarpkaya, T. (1971). On Stationary and Travelling Vortex Breakdowns. *Journal of Fluid Mechanics*, *45*(3), 545–559.

Savage, S. B., Newman, B. G., & Wong, D. T. M. (1979). The Role of Vortices and Unsteady Effects during the Hovering Flight of Dragonflies. *Journal of Experimental Biology*, *83*, 59–77.

Scarano, F., David, L., Bsibsi, M., & Calluaud, D. (2005). S-PIV Comparative Assessment: Iimage Dewarping+Misalignment Correction and Pinhole+Geometric Back Projection. *Experiments in Fluids*, *39*, 257–266.

Shen, H.-W. & Kao, D. L. (1998). A New Line Integral Convolution Algorithm for Visualizing Time-Varying Flow Fields, April-June. In *IEEE Transactions on Visualization and Computer Graphics*, volume 4, (pp. 98–108)., April-June.

Singer, B. & Banks, D. (1994). A Predictor-Corrector Scheme for Vortex Identification. Technical Report NASA Contractor Report 194882, ICASE Report No. 94-11, NASA Langley.

Soloff, S. M., Adrian, R. J., & Liu, Z. C. (1997). Distortion Compensation for Generalized Stereoscopic Particle Image Velocimetry. *Measurement Science and Technology*, *8*, 1441–1454.

Spedding, G. R. & Maxworthy, T. (1986). The generation of circulation and lift in a rigid two-dimensional fling. *Journal of Fluid Mechanics*, *165*, 247–272.

Steltz, E., Avadhanula, S., & Fearing, R. (2007). High Lift Force with 275Hz Wing Beat in MFI, 29 October - 2 November. In *IEEE/RSJ International Conference on Intelligent Robots and Systems*, 29 October - 2 November, San Diego, USA.

Sun, M. (2005). High-Lift Generation and Power Requirements of Insect Flight. *Fluid Dynamics Research*, *37*, 21–39.

Sun, M. & Tang, J. (2002a). Lift and Power Requirements of Hovering Flight in *Drosophila virilis*. *Journal of Experimental Biology*, *205*(16), 2413–2427.

Sun, M. & Tang, J. (2002b). Unsteady Aerodynamic Force Generation by a Model Fruit Fly Wing in Flapping Motion. *Journal of Experimental Biology*, *205*, 55–70.

Sunada, S., Kawachi, K., Matsumoto, A., & Sakaguchi, A. (2001). Unsteady Forces on a Two-Dimensional Wing in Plunging and Pitching Motions. *AIAA Journal*, *39*(7), 1230–1239.

Syaifuddin, M., Park, H. C., & Goo, N. (2006). Design and Evaluation of a LIPCA-Actuated Flapping Device. *Journal of Smart Materials & Structures*, *15(5)*, 1225–1230.

Tanaka, H., Hoshino, K., Matsumoto, K., & Shimoyama, I. (2005). Flight dynamics of a butterfliy-type ornithopter, 2-6 August. In *IEEE/RSJ International Conference on Intelligent Robots and Systems*, 2-6 August.

Tarascio, M. J., Ramasamy, M., Chopra, I., & Leishman, J. G. (2005). Flow Visualization of Micro Air Vehicle Scaled Insect-Based Flapping Wings. *Journal of Aircraft*, *42*(2), 385–390.

Uchida, S., Nakamura, Y., & Oshawa, M. (1985). Experiments on the Axisymmetric Vortex Breakdown in a Swirling Air Flow. *Transactions of the Japan Society for Aeronautical and Space Sciences*, *27*(78), 206–216.

Usherwood, J. R. (2009). The Aerodynamic Forces and Pressure Distribution of a Revolving Pigeon Wing. *Experiments in Fluids*, *46*(5), 991–1003.

Usherwood, J. R. & Ellington, C. P. (2002a). The Aerodynamics of Revolving Wings I. Model Hawkmoth Wings. *Journal of Experimental Biology*, *205*, 1547–1564.

Usherwood, J. R. & Ellington, C. P. (2002b). The Aerodynamics of Revolving Wings II. Propeller Force Coefficients from Mayfly to Quail. *Journal of Experimental Biology*, *205*, 1565–1576.

van den Berg, C. & Ellington, C. P. (1997a). The Three-Dimensional Leading-Edge Vortex of a "Hovering" Model Hawkmoth. *Philosophical Transactions of the Royal Society of London Series B*, *352*(1351), 329–340.

van den Berg, C. & Ellington, C. P. (1997b). The Vortex Wake of a "Hovering" Model Hawkmoth. *Philosophical Transactions of the Royal Society of London Series B*, *352*(1351), 317–328.

Wagner, H. (1925). Über die Entstehung des Dynamischen Aufftriebes von Tragflügeln. *Zeitschrift für Angewandie Mathematik und Mechanik*, *5*(1), 17–35. (On the Occurrence of Dynamic Lift of Wings).

Warkentin, J. & DeLaurier, J. (2007). Experimental Aerodynamic Study of Tandem Flapping Membrane Wings. *Journal of Aircraft*, *44(5)*, 1653–1661.

Weis-Fogh, T. (1973). Quick Estimates of Flight Fitness in Hovering Animals, Including Novel Mechanisms for Lift Production. *Journal of Experimental Biology*, *59*, 169–230.

Werlé, H. (1960). Sur l'éclatement des Tourbillons d'Apex d'une Aile Delta aux Faibles Vitesses. *La Recherche Aéronautique (ONERA)*, *74*, 25–30. (On the turbulent bursting of leading edge vortices on a delta wing at low speeds).

Westerweel, J. (1994). Efficient detection of spurious vectors in particle image velocimetry data. *Experiments in Fluids*, *16*, 236–247.

Wilkins, P. C. (2008). *Some Unsteady Aerodynamics Relevant to Insect-Inspired Flapping-Wing Micro Air Vehicles*. PhD thesis, Cranfield University (Shrivenham). http://hdl.handle.net/1826/2913.

Wilkins, P. C. & Knowles, K. (2009). The Leading-Edge Vortex and Aerodynamics of Insect-Based Flapping-Wing Micro Air Vehicles. *Aeronautical Journal*, *113*(1143), 253–262.

Willert, C. E. (1997). Stereoscopic digital particle image velocimetry for application in wind tunnel flows. *Measurement Science and Technology*, *8*, 1465–1479.

Willert, C. E. & Gharib, M. (1991). Digital Particle Image Velocimetry. *Experiments in Fluids*, *10*, 181–193.

Willmott, A. P. & Ellington, C. P. (1997). The mechanics of flight in the hawkmoth manduca sexta: I. kinematics of hovering and forward flight. *Journal of Experimental Biology*, *200*, 2705–2722.

Willmott, A. P., Ellington, C. P., & Thomas, A. L. R. (1997). Flow Visualization and Unsteady Aerodynamics in the Flight of the Hawkmoth, *Manduca sexta*. *Philosophical Transactions of the Royal Society of London Series B*, *352*, 303–316.

Wood, R. (2008). Fly, Robot Fly. *IEEE Spectrum*, 25–29.

Woods, M. I., Henderson, J. F., & Lock, G. D. (2001). Energy Requirements for the Flight of Micro Air Vehicles. *The Aeronautical Journal*, *105*(1043), 135–149.

Yamamoto, M. & Isogai, K. (2005). Measurement of Unsteady Fluid Dynamic Forces for a Mechanical Dragonfly Model. *AIAA Journal*, *43*(12), 2475–2480.

Yan, J., Wood, R. J., Avadhanula, S., Sitti, M., & Fearing, R. S. (2001). Towards Flapping Wing Control for a Micromechanical Flying Insect. In *Proceedings of the IEEE Inernational Conference on Robotics & Automation*, Seoul, South Korea.

Young, J., Walker, S. M., Bomphrey, R. J., Taylor, G. K., & Thomas, A. L. R. (2009). Details of Insect Wing Design and Deformation Enhance Aerodynamic Function and Flight Efficiency. *Science*, *325*, 1549–1552.

Żbikowski, R. (2002). On aerodynamic modelling of an insect-like flapping wing in hover for micro air vehicles. *Philosophical Transactions of the Royal Society of London Series A*, *360*, 273–290.

Żbikowski, R., Galiński, C., & Pedersen, C. B. (2005). A Four-Bar Linkage Mechanism for Insect-like Flapping Wings in Hover: Concept and an Outline of its Realisation. *Transactions of the ASME: Journal of Mechanical Design*, *127*(4), 817–824.

Zdunich, P., Bilyk, D., MacMaster, M., Loewen, D., DeLaurier, J., Kornbluh, R., Low, T., Stanford, S., & Holeman, D. (2007). Development and Testing the Mentor Flapping-wing Micro Air Vehicle. *Journal of Aircraft*, *44(5)*, 1701–1711.

Appendices

Appendix A

Flapping Kinematics Functions

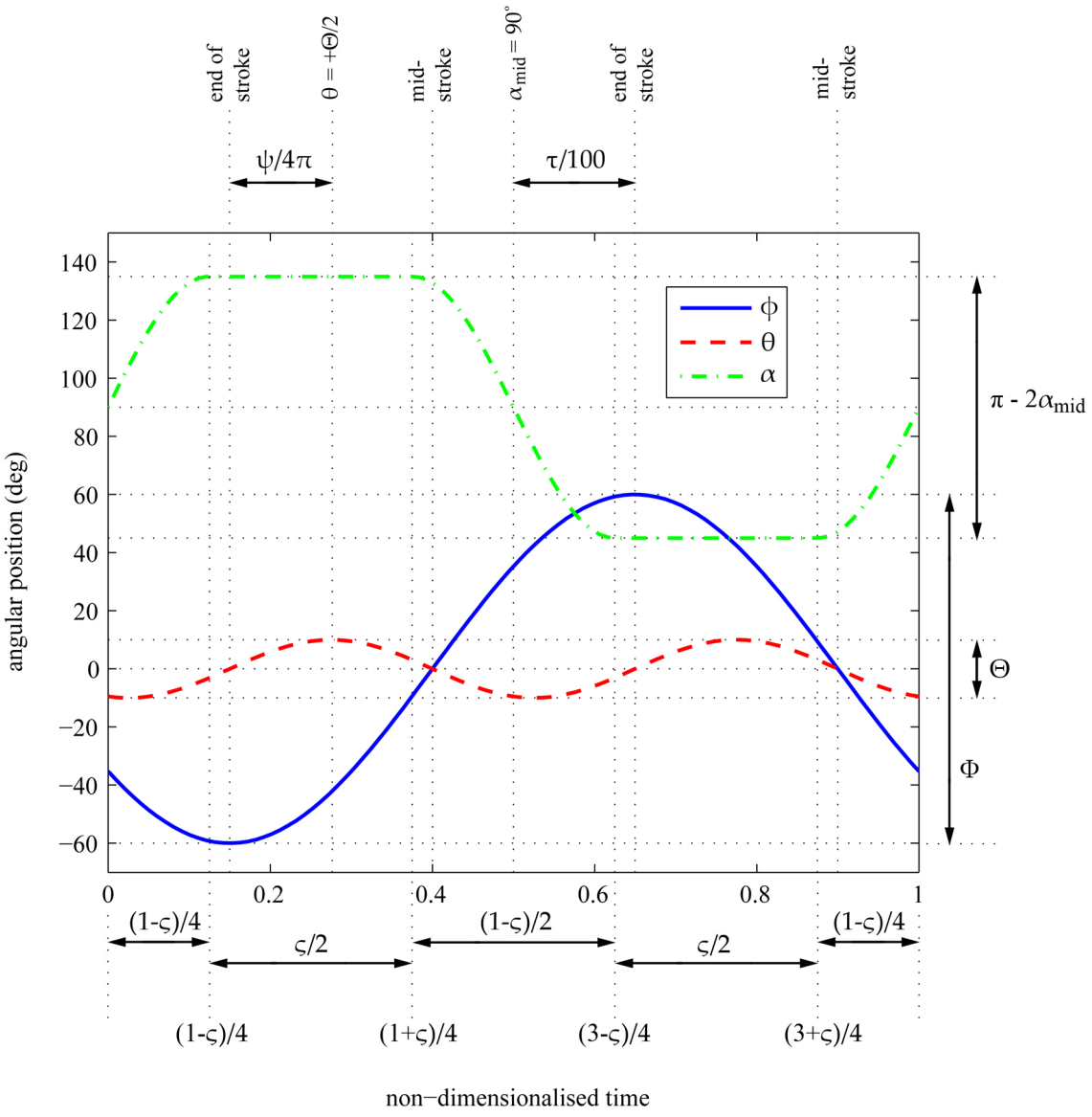

Figure A.1: Definitions of flapping kinematic parameters; time is non-dimensionalised by the flapping period T

This appendix presents expressions for flapping kinematics (ϕ, $\dot{\phi}$, $\ddot{\phi}$, θ, $\dot{\theta}$, $\ddot{\theta}$, α, $\dot{\alpha}$, $\ddot{\alpha}$) as functions of kinematic parameters f, Φ, Θ, α_{mid}, and τ. for a description of how these parameters are defined, the reader is referred to § 2.1.3 page 19. Figure A.1 illustrates how each parameter is defined, and complements the following definitions.

The stroke and plunge angles and their first time derivatives (stroke and plunge velocities) and second time derivatives (stroke and plunge accelerations) are defined as follows:

$$\phi = -\frac{\Phi}{2}cos\left(2\pi ft - \frac{2\pi\tau}{100}\right) \tag{A.1}$$

$$\dot{\phi} = \Phi\pi f sin\left(2\pi ft - \frac{2\pi\tau}{100}\right) \tag{A.2}$$

$$\ddot{\phi} = 2\Phi\pi^2 f^2 cos\left(2\pi ft - \frac{2\pi\tau}{100}\right) \tag{A.3}$$

$$\theta = \frac{\Theta}{2}cos\left(4\pi ft - \frac{4\pi\tau}{100} - \psi\right) \tag{A.4}$$

$$\dot{\theta} = -2\Theta\pi f sin\left(4\pi ft - \frac{4\pi\tau}{100} - \psi\right) \tag{A.5}$$

$$\ddot{\theta} = -8\Theta\pi^2 f^2 cos\left(4\pi ft - \frac{4\pi\tau}{100} - \psi\right) \tag{A.6}$$

Here, ψ is the phase angle between the plunging and stroking kinematics where:

$\psi = 0$ for concave arc ('u' shape)
$\psi = \pi/2$ for figure-of-eight
$\psi = \pi$ for convex arc (inverted 'u' shape)

The pitching kinematics are described by a number of functions to separately define the segments where there pitch angle is varying, and remains constant. Let ς represent the fraction of the flapping period T (where $T = 1/f$) where the pitch angle is constant. Therefore the pitch angle is fixed, and varies for ςT and $T(1-\varsigma)$

of the flapping period respectively. In this thesis, ς is always approximately 0.5. The pitch angle is defined as follows:

$$\alpha = \Big(\frac{\pi}{2} - \alpha_{mid}\Big) sin\Big(\frac{2\pi t}{T(1-\varsigma)}\Big) + \frac{\pi}{2}, \qquad 0 \le t \le \frac{T(1-\varsigma)}{4} \quad \text{(A.7)}$$

$$\alpha = \pi - \alpha_{mid}, \qquad \frac{T(1-\varsigma)}{4} < t < \frac{T(1+\varsigma)}{4} \quad \text{(A.8)}$$

$$\alpha = \Big(\frac{\pi}{2} - \alpha_{mid}\Big) sin\Big(\frac{\pi(2t-\varsigma T)}{T(1-\varsigma)}\Big) + \frac{\pi}{2}, \qquad \frac{T(1+\varsigma)}{4} \le t \le \frac{T(3-\varsigma)}{4} \quad \text{(A.9)}$$

$$\alpha = \alpha_{mid}, \qquad \frac{T(3-\varsigma)}{4} < t < \frac{T(3+\varsigma)}{4} \quad \text{(A.10)}$$

$$\alpha = \Big(\frac{\pi}{2} - \alpha_{mid}\Big) sin\Big(\frac{\pi(2t-\varsigma T-T)}{T(1-\varsigma)}\Big) + \frac{\pi}{2}, \qquad \frac{T(3+\varsigma)}{4} \le t \le T \quad \text{(A.11)}$$

the first time derivatives (pitch velocities) are:

$$\dot{\alpha} = \Big(\frac{\pi}{2} - \alpha_{mid}\Big)\Big(\frac{2\pi}{T(1-\varsigma)}\Big) cos\Big(\frac{2\pi t}{T(1-\varsigma)}\Big), \qquad 0 \le t \le \frac{T(1-\varsigma)}{4} \quad \text{(A.12)}$$

$$\dot{\alpha} = 0, \qquad \frac{T(1-\varsigma)}{4} < t < \frac{T(1+\varsigma)}{4} \quad \text{(A.13)}$$

$$\dot{\alpha} = \Big(\frac{\pi}{2} - \alpha_{mid}\Big)\Big(\frac{2\pi}{T(1-\varsigma)}\Big) cos\Big(\frac{\pi(2t-\varsigma T)}{T(1-\varsigma)}\Big), \qquad \frac{T(1+\varsigma)}{4} \le t \le \frac{T(3-\varsigma)}{4} \quad \text{(A.14)}$$

$$\dot{\alpha} = 0, \qquad \frac{T(3-\varsigma)}{4} < t < \frac{T(3+\varsigma)}{4} \quad \text{(A.15)}$$

$$\dot{\alpha} = \left(\frac{\pi}{2} - \alpha_{mid}\right)\left(\frac{2\pi}{T(1-\varsigma)}\right)cos\left(\frac{\pi(2t - \varsigma T - T)}{T(1-\varsigma)}\right), \qquad \frac{T(3+\varsigma)}{4} \leq t \leq T \quad \text{(A.16)}$$

the second time derivatives (pitch accelerations) are:

$$\ddot{\alpha} = -\left(\frac{\pi}{2} - \alpha_{mid}\right)\left(\frac{2\pi}{T(1-\varsigma)}\right)^2 sin\left(\frac{2\pi t}{T(1-\varsigma)}\right), \qquad 0 \leq t \leq \frac{T(1-\varsigma)}{4} \quad \text{(A.17)}$$

$$\ddot{\alpha} = 0, \qquad \frac{T(1-\varsigma)}{4} < t < \frac{T(1+\varsigma)}{4} \quad \text{(A.18)}$$

$$\ddot{\alpha} = -\left(\frac{\pi}{2} - \alpha_{mid}\right)\left(\frac{2\pi}{T(1-\varsigma)}\right)^2 sin\left(\frac{\pi(2t - \varsigma T)}{T(1-\varsigma)}\right), \qquad \frac{T(1+\varsigma)}{4} \leq t \leq \frac{T(3-\varsigma)}{4} \quad \text{(A.19)}$$

$$\ddot{\alpha} = 0, \qquad \frac{T(3-\varsigma)}{4} < t < \frac{T(3+\varsigma)}{4} \quad \text{(A.20)}$$

$$\ddot{\alpha} = -\left(\frac{\pi}{2} - \alpha_{mid}\right)\left(\frac{2\pi}{T(1-\varsigma)}\right)^2 sin\left(\frac{\pi(2t - \varsigma T - T)}{T(1-\varsigma)}\right), \qquad \frac{T(3+\varsigma)}{4} \leq t \leq T \quad \text{(A.21)}$$

Appendix B

Derivation of Flapping Mechanism Kinematics

In this appendix, expressions describing the the mechanism kinematics as functions of flapping kinematics will be derived, followed by a derivation of flapping kinematics as functions of the mechanism kinematics. A summary is given at the end, which presents tables listing the appropriate equations to use to calculate a desired variable.

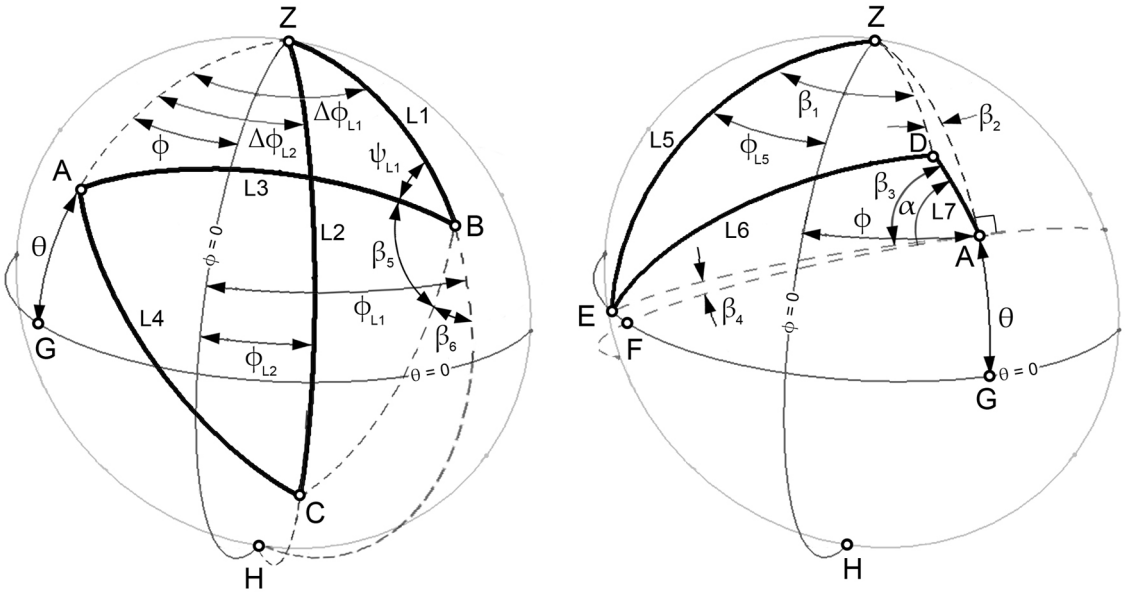

Figure B.1: Position of Links L1-L7 for arbitrary location of point A for defining flapping kinematics a function of mechanism kinematics, and mechanism kinematics as a function of flapping kinematics; positions of links L1-L4 (left); position of Links L5-L7 (right)

B.1 Mechanism Kinematics as Functions of Flapping Kinematics

First, expressions describing the flapping mechanism kinematics will be derived. The positions (ϕ_{L1}, ϕ_{L2}, ϕ_{L5}), velocities ($\dot{\phi}_{L1}$, $\dot{\phi}_{L2}$, $\dot{\phi}_{L5}$), and accelerations ($\ddot{\phi}_{L1}$, $\ddot{\phi}_{L2}$,

$\ddot{\phi}_{L5}$) of input the links (L1, L2, L5), all as functions of the flapping kinematics (ϕ, $\dot{\phi}$, $\ddot{\phi}$, θ, $\dot{\theta}$, $\ddot{\theta}$, α, $\dot{\alpha}$, $\ddot{\alpha}$), and the link 'lengths' (angles subtended by each link on the surface of a sphere) will be derived in that order.

B.1.1 Link Positions

First, expressions for the positions of links L1 and L2, denoted by ϕ_{L1} and ϕ_{L2} respectively, will be derived. Applying the spherical law of cosines to triangle ABZ illustrated in Figure B.1:

$$cosL3 = cosL1\ cos(\frac{\pi}{2} - \theta) + sinL1\ sin(\frac{\pi}{2} - \theta)\ cos(\Delta\phi_{L1}) \tag{B.1}$$

$$\Delta\phi_{L1} = cos^{-1}(\frac{cosL3 - cosL1\ sin\theta}{sinL1\ cos\theta}) \tag{B.2}$$

since $\phi_{L1} = \Delta\phi_{L1} + \phi$:

$$\phi_{L1} = \phi + cos^{-1}(\frac{cosL3 - cosL1\ sin\theta}{sinL1\ cos\theta}) \tag{B.3}$$

Applying the same procedure to triangle ACZ gives:

$$\phi_{L2} = \phi + cos^{-1}(\frac{cosL4 - cosL2\ sin\theta}{sinL2\ cos\theta}) \tag{B.4}$$

Now, the expression for the position of link L5, denoted by ϕ_{L5} will be derived. First, an expression for the angle that the segment of the great circle joining points D and Z subtends, which will be referred to as 'DZ', must be found. Applying the spherical law of cosines to triangle ADZ illustrated in Figure B.1:

$$cosDZ = cosL7\ cos(\frac{\pi}{2} - \theta) + sinL7\ sin(\frac{\pi}{2} - \theta)\ cos(\frac{\pi}{2} - \alpha) \tag{B.5}$$

$$DZ = cos^{-1}(cosL7\ sin\theta + sinL7\ cos\theta\ sin\alpha) \tag{B.6}$$

Again, applying the spherical law of cosines to triangle ADZ, an expression for β_2 may be found:

$$cosL7 = cosDZ\ cos(\frac{\pi}{2} - \theta) + sinDZ\ sin(\frac{\pi}{2} - \theta)\ cos\beta_2 \tag{B.7}$$

$$\beta_2 = cos^{-1}(\frac{cosL7 - cosDZ\ sin\theta}{sinDZ\ cos\theta}) \tag{B.8}$$

Applying the same procedure to triangle EDZ gives and expression for β_1:

$$\beta_1 = cos^{-1}(\frac{cosL6 - cosL5\ sinDZ}{sinL5\ sinDZ}) \tag{B.9}$$

Finally, substituting Equation B.6, Equation B.8 & Equation B.9 into the following expression will give the final expression for the position of link L5:

$$\phi_{L5} = \phi - \beta_1 + \frac{\alpha - \frac{\pi}{2}}{|\alpha - \frac{\pi}{2}|}\beta_2 \tag{B.10}$$

By observing Figure B.1, it can be seen that when the pitch angle α (measured clockwise from the great circle perpendicular to the local line of longitude) is greater than 90° then $\phi_{L5} = \phi - \beta_1 + \beta_2$. On the other hand, when α is less than 90° then $\phi_{L5} = \phi - \beta_1 - \beta_2$. Therefore, the expression in the brackets in front of β_2 in Equation B.10 is required to make β_2 the appropriate sign.

A more convenient way of defining the angular positions of input links L1, L2, and L5 (Equation B.3,B.4,B.10) is to define them relative to their positions when the wing is at the 'neutral' position, which is when $\phi = 0°$, $\theta = 0°$, $\alpha = 90°$. In this manner, Equation B.3,B.4 & B.10 become:

$$\phi_{L1} = \phi + cos^{-1}(\frac{cosL3 - cosL1\ sin\theta}{sinL1\ cos\theta}) - cos^{-1}(\frac{cosL3}{sinL1}) \tag{B.11}$$

$$\phi_{L2} = \phi + cos^{-1}(\frac{cosL4 - cosL2\ sin\theta}{sinL2\ cos\theta}) - cos^{-1}(\frac{cosL4}{sinL2}) \tag{B.12}$$

$$\phi_{L5} = \phi - \beta_1 + \frac{\alpha - \frac{\pi}{2}}{|\alpha - \frac{\pi}{2}|}\beta_2 + cos^{-1}(\frac{cosL6 - cosL5\ cosL7}{sinL5\ cosL7}) \tag{B.13}$$

This way, ϕ_{L1}, ϕ_{L2} & ϕ_{L5} become zero when $\phi = 0°$, $\theta = 0°$, and $\alpha = 90°$. Thus Equation B.11, B.12 and B.13 combined with Equation B.6, B.8 and B.9 provide the azimuthal positions of input links L1, L2 and L5, as a function of ϕ, θ, α and the link 'lengths' (angle subtended on the surface of a sphere) denoted by the same names of the links themselves.

B.1.2 Link Velocities

Taking the first time derivative of Equation B.11 - B.13, we obtain the velocities $\dot{\phi}_{L1}$, $\dot{\phi}_{L2}$, $\dot{\phi}_{L5}$ of the input links:

$$\dot{\phi}_{L1} = \dot{\phi} - \dot{\theta}\left(\frac{sin\theta cosL3 - cosL1}{cos\theta\sqrt{(sinL1cos\theta)^2 - (cosL3 - cosL1sin\theta)^2}}\right) \tag{B.14}$$

$$\dot{\phi}_{L2} = \dot{\phi} - \dot{\theta}\left(\frac{sin\theta cosL4 - cosL2}{cos\theta\sqrt{(sinL2cos\theta)^2 - (cosL4 - cosL2sin\theta)^2}}\right) \tag{B.15}$$

$$\dot{\phi}_{L5} = \dot{\phi} - \dot{\beta}_1 + \frac{\alpha - \frac{\pi}{2}}{|\alpha - \frac{\pi}{2}|}\dot{\beta}_2 \tag{B.16}$$

where:

$$\dot{\beta}_1 = \frac{(\dot{C}S - \dot{S}C)cosL5sinL5 + \dot{S}sinL5cosL6}{SsinL5\sqrt{(SsinL5)^2 - (cosL6 - CcosL5)^2}} \tag{B.17}$$

$$\dot{\beta}_2 = \frac{(\dot{C}S - \dot{S}C)cos\theta sin\theta + (\dot{S}cos\theta - \dot{\theta}Ssin\theta)cosL7 + \dot{\theta}CS}{Scos\theta\sqrt{(Scos\theta)^2 - (cosL7 - Csin\theta)^2}} \tag{B.18}$$

$$C = cosDZ = cosL7\ sin\theta + sinL7\ cos\theta\ sin\alpha \tag{B.19}$$

$$S = sinDZ = \sqrt{1 - C^2} \tag{B.20}$$

$$\dot{C} = \dot{\theta}cosL7cos\theta - \dot{\theta}sinL7sin\theta sin\alpha + \dot{\alpha}sinL7cos\theta cos\alpha \tag{B.21}$$

$$\dot{S} = \frac{-C\dot{C}}{\sqrt{1 - C^2}} \tag{B.22}$$

B.1.3 Link Accelerations

Taking the second time derivative of Equation B.11 - B.13, the accelerations $\ddot{\phi}_{L1}$, $\ddot{\phi}_{L2}$, $\ddot{\phi}_{L5}$ of the input links are obtained:

$$\ddot{\phi}_{L1} = \ddot{\phi} - \frac{1}{\sqrt{(sinL1cos\theta)^2 - (cosL3 - cosL1sin\theta)^2}}\left(\ddot{\theta}\left(\frac{sin\theta cosL3 - cosL1}{cos\theta}\right) + \right.$$
$$\left. + \dot{\theta}^2\left(cosL3 - \frac{sin\theta cos^2 L3 cosL1 - sin^2\theta cosL3 - 2cos^2 L1 cosL3 + 2cosL1 sin\theta}{(sinL1cos\theta)^2 - (cosL3 - cosL1sin\theta)^2} - \frac{sin\theta cosL1 - sin^2\theta cosL3}{cos^2\theta}\right)\right) \tag{B.23}$$

$$\ddot{\phi}_{L2} = \ddot{\phi} - \frac{1}{\sqrt{(sinL2cos\theta)^2 - (cosL4 - cosL2sin\theta)^2}}\left(\ddot{\theta}\left(\frac{sin\theta cosL4 - cosL2}{cos\theta}\right) + \right.$$
$$\left. + \dot{\theta}^2\left(cosL4 - \frac{sin\theta cos^2 L4 cosL2 - sin^2\theta cosL4 - 2cos^2 L2 cosL4 + 2cosL2 sin\theta}{(sinL2cos\theta)^2 - (cosL4 - cosL2sin\theta)^2} - \frac{sin\theta cosL2 - sin^2\theta cosL4}{cos^2\theta}\right)\right) \tag{B.24}$$

$$\ddot{\phi}_{L5} = \ddot{\phi} - \ddot{\beta}_1 + \frac{\alpha - \frac{\pi}{2}}{|\alpha - \frac{\pi}{2}|}\ddot{\beta}_2 \tag{B.25}$$

where:

$$\ddot{\beta}_1 = \frac{\dot{N}1D1 - \dot{D}1N1}{D1^2} \tag{B.26}$$

$$\ddot{\beta}_2 = \frac{\dot{N}2D2 - \dot{D}2N2}{D2^2} \tag{B.27}$$

$$\begin{aligned}\ddot{C} = \ddot{\theta}cosL7cos\theta - \dot{\theta}^2 cosL7sin\theta - \ddot{\theta}sinL7sin\theta sin\alpha + \\ -(\dot{\theta}^2 + \dot{\alpha}^2)sinL7cos\theta sin\alpha - 2\dot{\theta}\dot{\alpha}sinL7sin\theta cos\alpha + \ddot{\alpha}sinL7cos\theta cos\alpha\end{aligned} \tag{B.28}$$

$$\ddot{S} = -\frac{\dot{C}^2 + C\ddot{C} - C^3\ddot{C}}{(1-C^2)^{3/2}} \tag{B.29}$$

$$N1 = (\dot{C}S - \dot{S}C)cosL5sinL5 + \dot{S}sinL5cosL6 \tag{B.30}$$

$$\dot{N}1 = (\ddot{C}S - C\ddot{S})cosL5sinL5 + \ddot{S}sinL5cosL6 \tag{B.31}$$

$$D1 = SsinL5\sqrt{(SsinL5)^2 - (cosL6 - CcosL5)^2} \tag{B.32}$$

$$\begin{aligned}\dot{D}1 = \Big(2\dot{S}S^2 sin^3 L5 - \dot{S}sinL5cos^2 L6 + (2\dot{S}C + \dot{C}S)cosL5sinL5cosL6 + \\ -(\dot{S}C^2 + \dot{C}SC)cos^2 L5sinL5\Big) / \sqrt{(SsinL5)^2 - (cosL6 - CcosL5)^2}\end{aligned} \tag{B.33}$$

$$N2 = (\dot{C}S - \dot{S}C)cos\theta sin\theta + (\dot{S}cos\theta - \dot{\theta}Ssin\theta)cosL7 + \dot{\theta}CS \tag{B.34}$$

$$\begin{aligned}\dot{N}2 = (\ddot{C}S - C\ddot{S})sin\theta cos\theta + (C\dot{S} - \dot{C}S)\dot{\theta}sin^2\theta + (\dot{C}S - C\dot{S})\dot{\theta}cos^2\theta + \\ +(\ddot{S} - \dot{\theta}^2 S)cos\theta cosL7 - (2\dot{S}\dot{\theta} + S\ddot{\theta})sin\theta cosL7 + \ddot{\theta}CS + \dot{\theta}\dot{C}S + \dot{\theta}\dot{S}C\end{aligned} \tag{B.35}$$

$$D2 = Scos\theta\sqrt{(Scos\theta)^2 - (cosL7 - Csin\theta)^2} \tag{B.36}$$

$$\begin{aligned}\dot{D}2 = \Big(2\dot{S}S^2 cos^3\theta - (C^2\dot{\theta} + 2S^3\dot{\theta})cos\theta sin\theta - (\dot{C}CS + C^2\dot{S})cos\theta sin^2\theta + (\dot{C}S + \\ +2C\dot{S})cos\theta sin\theta cosL7 + CS\dot{\theta}cos^2\theta cosL7 - \dot{S}cos\theta cos^2 L7 + S\dot{\theta}sin\theta cos^2 L7 + \\ -2CS\dot{\theta}sin^2\theta cosL7 + C^2 S\dot{\theta}sin^3\theta\Big) / \sqrt{(Scos\theta)^2 - (cosL7 - Csin\theta)^2}\end{aligned} \tag{B.37}$$

B.2 Flapping Kinematics as Functions of Mechanism Kinematics

Now, the flapping kinematics (ϕ, $\dot{\phi}$, $\ddot{\phi}$, θ, $\dot{\theta}$, $\ddot{\theta}$, α, $\dot{\alpha}$, $\ddot{\alpha}$) will be derived as functions of the positions (ϕ_{L1}, ϕ_{L2}, ϕ_{L5}), velocities ($\dot{\phi}_{L1}$, $\dot{\phi}_{L2}$, $\dot{\phi}_{L5}$), and accelerations ($\ddot{\phi}_{L1}$, $\ddot{\phi}_{L2}$, $\ddot{\phi}_{L5}$) of input the links (L1, L2, L5), and the link 'lengths'.

B.2.1 Wing Position

First, expressions for ϕ, θ, as functions of the link positions ϕ_{L1} and ϕ_{L2} will be derived. Applying the spherical law of cosines to triangle BCZ illustrated in Figure B.1, and letting 'BC' represent the angle subtended by the segment of the great circle joining points B and C:

$$cosBC = cosL1\ cosL2 + sinL1\ sinL2\ cos(\phi_{L1} - \phi_{L2}) \tag{B.38}$$

Now apply the spherical law of cosines to triangle ABC:

$$cosL4 = cosL3\ cosBC + sinL3\ sinBC\ cos\beta_5 \tag{B.39}$$

$$cos\beta_5 = \frac{cosL4 - cosL3\ cosBC}{sinL3\ sinBC} \tag{B.40}$$

Now apply the spherical law of cosines to triangle BCH:

$$cos(\pi - L2) = cos(\pi - L1)\ cosBC + sin(\pi - L1)\ sinBC\ cos\beta_6 \tag{B.41}$$

$$cos\beta_6 = \frac{cosL1\ cosBC - cosL2}{sinL1\ sinBC} \tag{B.42}$$

Substituting Equation B.38 into Equations B.40 & B.42 and noting that $sinBC = \sqrt{1 - cos^2 BC}$:

$$cos\beta_5 = \frac{cosL4 - cosL3\left(cosL1\ cosL2 + sinL1\ sinL2\ cos(\phi_{L1} - \phi_{L2})\right)}{sinL3\sqrt{1 - \left(cosL1\ cosL2 + sinL1\ sinL2\ cos(\phi_{L1} - \phi_{L2})\right)^2}} \tag{B.43}$$

$$cos\beta_6 = \frac{cosL1\left(cosL1\ cosL2 + sinL1\ sinL2\ cos(\phi_{L1} - \phi_{L2})\right) - cosL2}{sinL1\sqrt{1 - \left(cosL1\ cosL2 + sinL1\ sinL2\ cos(\phi_{L1} - \phi_{L2})\right)^2}} \tag{B.44}$$

Since $\psi_{L1} + \beta_5 + \beta_6 = \pi$, we can now obtain an expression for ψ_{L1} by substituting in Equations B.43 & B.44:

$$\begin{aligned}\psi_{L1} = \pi - cos^{-1}\left(\frac{cosL4 - cosL3\left(cosL1\ cosL2 + sinL1\ sinL2\ cos(\phi_{L1} - \phi_{L2})\right)}{sinL3\sqrt{1 - \left(cosL1\ cosL2 + sinL1\ sinL2\ cos(\phi_{L1} - \phi_{L2})\right)^2}}\right) + \\ -cos^{-1}\left(\frac{cosL1\left(cosL1\ cosL2 + sinL1\ sinL2\ cos(\phi_{L1} - \phi_{L2})\right) - cosL2}{sinL1\sqrt{1 - \left(cosL1\ cosL2 + sinL1\ sinL2\ cos(\phi_{L1} - \phi_{L2})\right)^2}}\right)\end{aligned} \tag{B.45}$$

We can finally obtain an expression for θ by applying the spherical law of cosines to triangle ABZ:

$$\theta = \frac{\phi_{L1} - \phi_{L2}}{|\phi_{L1} - \phi_{L2}|} sin^{-1}\left(cosL1\ cosL3 + sinL1\ sinL3\ cos\psi_{L1}\right) \tag{B.46}$$

The fraction in front is required to make θ the appropriate sign. Thus, substituting Equation B.45 into Equation B.46 gives the final expression for θ as a function of ϕ_{L1}, ϕ_{L2} and the link 'lengths'. This expression applies in either case when ϕ_{L1}, ϕ_{L2} are defined relative to the $\phi = 0$ longitude line, or when they are defined relative to their positions when the wing is at the neutral position (when $\phi = 0°$, $\theta = 0°$, $\alpha = 90°$).

Now that θ is known, we can find ϕ as a function of ϕ_{L1}, ϕ_{L2}. Again, applying the spherical law of cosines to triangle ABZ:

$$cosL3 = cosL1\ cos(\pi/2 - \theta) + sinL1\ sin(\pi/2 - \theta)\ cos\Delta\phi_{L1} \tag{B.47}$$

$$\Delta\phi_{L1} = cos^{-1}\left(\frac{cosL3 - cosL1\ sin\theta}{sinL1\ cos\theta}\right) \tag{B.48}$$

Noting that $\phi = \phi_{L1} - \Delta\phi_{L1}$, and substituting in Equation B.48, we can obtain an expression for ϕ:

$$\phi = \phi_{L1} - cos^{-1}\left(\frac{cosL3 - cosL1\ sin\theta}{sinL1\ cos\theta}\right) \tag{B.49}$$

However, if ϕ_{L1} is defined relative to its position when the wing is at the neutral position, then we must add an extra term:

$$\phi = \phi_{L1} - cos^{-1}\left(\frac{cosL3 - cosL1\ sin\theta}{sinL1\ cos\theta}\right) + cos^{-1}(\frac{cosL3}{sinL1}) \tag{B.50}$$

Therefore, Equation B.49 combined with Equations B.45 & B.46 gives ϕ as a function of ϕ_{L1}, ϕ_{L2} and the link 'lengths'. If ϕ_{L1}, ϕ_{L2} & ϕ_{L5} are defined relative to their positions when the wing is at the neutral position, then Equation B.50 is used instead of Equation B.49.

Now find an expression for α as a function of ϕ_{L1}, ϕ_{L2} & ϕ_{L5}. Applying the spherical law of cosines to triangle AEZ and letting 'AE' represent the angle subtended by the segment of the great circle joining points A and E:

$$cosAE = cosL5\ sin\theta + sinL5\ cos\theta\ cos(\phi - \phi_{L5}) \tag{B.51}$$

Again, apply the spherical law of cosines to triangle AEZ:

$$cosL6 = cosAE\ cosL7 + sinAE\ sinL7\ cos\beta_3 \tag{B.52}$$

$$cos\beta_3 = \frac{cosL6 - cosAE\ cosL7}{sinAE\ sinL7} \tag{B.53}$$

Now apply the spherical law of cosines to triangle AEF, noting that the angle subtended between points A and F is 90°, and letting 'EF' represent the angle subtended by the segment of the great circle joining points E and F:

$$cosEF = cosAE\ cos(\pi/2) + sinAE\ sin(\pi/2)\ cos\beta_4 \tag{B.54}$$

$$cos\beta_4 = \frac{cosEF}{sinAE} \tag{B.55}$$

Noting that the angle subtended between points F and G is 90°, thus $EF = \phi - \phi_{L5} - \pi/2$ Equation B.55 becomes:

$$cos\beta_4 = \frac{sin(\phi - \phi_{L5})}{sinAE} \tag{B.56}$$

Substituting Equation B.51 into Equations B.53 & B.56 and noting that $sinAE = \sqrt{1 - cos^2 AE}$:

$$\beta_3 = cos^{-1}\left(\frac{cosL6 - \Big(cosL5\ sin\theta + sinL5\ cos\theta\ cos(\phi - \phi_{L5})\Big)\ cosL7}{sinL7\ \sqrt{1 - \Big(cosL5\ sin\theta + sinL5\ cos\theta\ cos(\phi - \phi_{L5})\Big)^2}}\right) \tag{B.57}$$

$$\beta_4 = cos^{-1}\left(\frac{sin(\phi - \phi_{L5})}{\sqrt{1 - \Big(cosL5\ sin\theta + sinL5\ cos\theta\ cos(\phi - \phi_{L5})\Big)^2}}\right) \tag{B.58}$$

Noting that $\alpha = \beta_3 + \beta_4$ and substituting in Equations B.57 & B.58, we obtain:

$$\begin{aligned}\alpha = {} & cos^{-1}\left(\frac{cosL6 - \Big(cosL5\ sin\theta + sinL5\ cos\theta\ cos(\phi - \phi_{L5})\Big)\ cosL7}{sinL7\ \sqrt{1 - \Big(cosL5\ sin\theta + sinL5\ cos\theta\ cos(\phi - \phi_{L5})\Big)^2}}\right) + \\ & + \frac{\theta}{|\theta|}\frac{\phi - \phi_{L5} - cos^{-1}\left(\frac{cosL6 - cosL5\ cosL7}{sinL5\ cosL7}\right)}{\left|\phi - \phi_{L5} - cos^{-1}\left(\frac{cosL6 - cosL5\ cosL7}{sinL5\ cosL7}\right)\right|} cos^{-1}\left(\frac{sin(\phi - \phi_{L5})}{\sqrt{1 - \Big(cosL5\ sin\theta + sinL5\ cos\theta\ cos(\phi - \phi_{L5})\Big)^2}}\right)\end{aligned} \tag{B.59}$$

If ϕ_{L1}, ϕ_{L2} & ϕ_{L5} are defined relative to their positions when the wing is at the neutral position, then EquationB.59 is rewritten as:

$$\alpha = cos^{-1}\left(\frac{cosL6-\left(cosL5\ sin\theta+sinL5\ cos\theta\ cos(\phi-\phi_{L5}+cos^{-1}(\frac{cosL6-cosL5\ cosL7}{sinL5\ cosL7}))\right)cosL7}{sinL7\sqrt{1-\left(cosL5\ sin\theta+sinL5\ cos\theta\ cos(\phi-\phi_{L5}+cos^{-1}(\frac{cosL6-cosL5\ cosL7}{sinL5\ cosL7}))\right)^2}}\right)+ \\ +\frac{\theta}{|\theta|}\frac{\phi-\phi_{L5}}{|\phi-\phi_{L5}|}cos^{-1}\left(\frac{sin(\phi-\phi_{L5}+cos^{-1}(\frac{cosL6-cosL5\ cosL7}{sinL5\ cosL7}))}{\sqrt{1-\left(cosL5\ sin\theta+sinL5\ cos\theta\ cos(\phi-\phi_{L5}+cos^{-1}(\frac{cosL6-cosL5\ cosL7}{sinL5\ cosL7}))\right)^2}}\right) \tag{B.60}$$

In Equations B.59 & B.60, the fractions in front of the second term are required to make it of the appropriate sign. Therefore, Equation B.59 combined with Equations B.45, B.46 & B.49 provides an expression for α as a function of ϕ_{L1}, ϕ_{L2} & ϕ_{L5}, and the link lengths. If ϕ_{L1}, ϕ_{L2} & ϕ_{L5} are defined relative to their positions when the wing is at the neutral position, then Equation B.60 is used instead, along with Equations B.45, B.46 & B.50.

B.2.2 Wing Velocity

Taking the first time derivative of Equation B.46, we obtain an expression for the wing's plunge velocity:

$$\dot{\theta} = -\frac{\phi_{L1}-\phi_{L2}}{|\phi_{L1}-\phi_{L2}|}\left(\frac{\dot{\psi_{L1}}sinL1sinL3sin\psi_{L1}}{\sqrt{1-(cosL1cosL3+sinL1sinL3cos\psi_{L1})^2}}\right) \tag{B.61}$$

where

$$\dot{\psi_{L1}} = \frac{F\ \dot{F}\ cosL4-\dot{F}cosL3}{(1-F^2)\sqrt{sin^2L3-F^2-cos^2L4+2FcosL3cosL4}}+ \\ -\frac{F\ \dot{F}\ cosL2-\dot{F}cosL1}{(1-F^2)\sqrt{sin^2L1-F^2-cos^2L2+2FcosL1cosL2}} \tag{B.62}$$

$$F = cosBC = cosL1\ cosL2 + sinL1\ sinL2\ cos(\phi_{L1}-\phi_{L2}) \tag{B.63}$$

$$\dot{F} = -(\dot{\phi}_{L1}-\dot{\phi}_{L2})sinL1\ sinL2\ sin(\phi_{L1}-\phi_{L2}) \tag{B.64}$$

Again, the fraction at the front of Equation B.61 is required to make it the appropriate sign. Thus, Equation B.61 combined with Equations B.45, B.62 - B.64 provides an expression for the wing's plunge velocity as a function of the positions and velocities of links L1, and L2, and the link lengths. These expressions hold if the positions of the links are defined relative to their neutral position, or if they are defined with respect to the $\phi = 0°$ longitude line.

Now, taking the first time derivative of Equation B.50, we obtain an expression for the wing's stroke velocity:

$$\dot{\phi} = \dot{\phi}_{L1} - \frac{\dot{\theta} cosL1 - \dot{\theta} sin\theta cosL3}{cos\theta \sqrt{cos^2\theta - cos^2L1 - cos^2L3 + 2cosL1 cosL3 sin\theta}} \tag{B.65}$$

When combined with Equations B.46 & B.61, Equation B.65 provides an expression for the stroke velocity as a function of the link positions, velocities, and lengths. Again, this holds if the input link positions are defined relative to the $\phi = 0$ longitude line, or if they are defined relative to their position when the wing is at the neutral position.

Lastly, taking the first time derivative of Equation B.59, we obtain the pitch velocity:

$$\dot{\alpha} = \frac{\dot{E} cosL7 - E\dot{E} cosL6}{(1-E^2)\sqrt{sin^2L7 - E^2 - cos^2L6 + 2E cosL7 cosL6}} + \\ -\frac{\theta}{|\theta|} \frac{\phi - \phi_{L5} - cos^{-1}\left(\frac{cosL6 - cosL5\ cosL7}{sinL5\ cosL7}\right)}{\left|\phi - \phi_{L5} - cos^{-1}\left(\frac{cosL6 - cosL5\ cosL7}{sinL5\ cosL7}\right)\right|} \left(\frac{(\dot{\phi} - \dot{\phi}_{L5})(1-E^2)cos(\phi - \phi_{L5}) + E\dot{E} sin(\phi - \phi_{L5})}{(1-E^2)\sqrt{1 - E^2 - sin^2(\phi - \phi_{L5})}} \right) \tag{B.66}$$

where

$$E = cosAE = cosL5\ sin\theta + sinL5\ cos\theta\ cos(\phi - \phi_{L5}) \tag{B.67}$$

$$\dot{E} = \dot{\theta} cosL5\ cos\theta - \dot{\theta} sinL5\ sin\theta\ cos(\phi - \phi_{L5}) - (\dot{\phi} - \dot{\phi}_{L5}) sinL5 cos\theta sin(\phi - \phi_{L5}) \tag{B.68}$$

Again, the fractions in front of the second term in Equation B.66 are required to make it the appropriate sign. Equation B.66 in conjunction with Equations B.46,

B.49, B.61, B.65, B.67, & B.68 provide an expression for the pitch velocity as a function of the link positions, and velocities, and lengths. Equations B.66 - B.68 apply if the link positions are defined relative to the $\phi = 0°$ longitude line. If, however, ϕ_{L1}, ϕ_{L2} & ϕ_{L5} are defined relative to their positions when the wing is at the neutral position, then Equations B.66 - B.68 are rewritten as:

$$\dot{\alpha} = \frac{\dot{E}cosL7 - E\dot{E}cosL6}{(1-E^2)\sqrt{sin^2L7 - E^2 - cos^2L6 + 2EcosL7cosL6}} + \\ -\frac{\theta}{|\theta|}\frac{\phi-\phi_{L5}}{|\phi-\phi_{L5}|}\left(\frac{(\dot{\phi}-\dot{\phi}_{L5})(1-E^2)cos\left(\phi-\phi_{L5}+cos^{-1}(\frac{cosL6-cosL5\ cosL7}{sinL5\ cosL7})\right)+E\dot{E}sin\left(\phi-\phi_{L5}+cos^{-1}(\frac{cosL6-cosL5\ cosL7}{sinL5\ cosL7})\right)}{(1-E^2)\sqrt{1-E^2-sin^2\left(\phi-\phi_{L5}+cos^{-1}(\frac{cosL6-cosL5\ cosL7}{sinL5\ cosL7})\right)}}\right) \quad \text{(B.69)}$$

$$E = cosAE = cosL5\,sin\theta + sinL5\,cos\theta\,cos\left(\phi - \phi_{L5} + cos^{-1}(\frac{cosL6 - cosL5\ cosL7}{sinL5\ cosL7})\right) \quad \text{(B.70)}$$

$$\dot{E} = \dot{\theta}cosL5\ cos\theta - \dot{\theta}sinL5\ sin\theta\ cos\left(\phi - \phi_{L5} + cos^{-1}(\frac{cosL6-cosL5\ cosL7}{sinL5\ cosL7})\right) + \\ -(\dot{\phi} - \dot{\phi}_{L5})sinL5cos\theta sin\left(\phi - \phi_{L5} + cos^{-1}(\frac{cosL6-cosL5\ cosL7}{sinL5\ cosL7})\right) \quad \text{(B.71)}$$

B.2.3 Wing Acceleration

Taking the second time derivative of Equation B.46, we obtain an expression for the wing's plunge acceleration:

$$\ddot{\theta} = -\frac{\phi_{L1}-\phi_{L2}}{|\phi_{L1}-\phi_{L2}|}\Bigg(\Big(\ddot{\psi}_{L1}sinL1sinL3sin\psi_{L1} + \dot{\psi}^2_{L1}sinL1sinL3cos\psi_{L1}\Big)\Big(1 - (cosL1cosL3 + \\ +sinL1sinL3cos\psi_{L1})^2\Big) - \dot{\psi}^2_{L1}sin^2L1sin^2L3sin^2\psi_{L1}\Big(cosL1cosL3 + \\ +sinL1sinL3cos\psi_{L1}\Big)\Bigg)/\Big(1 - (cosL1cosL3 + sinL1sinL3cos\psi_{L1})^2\Big)^{\frac{3}{2}} \quad \text{(B.72)}$$

where:

$$\ddot{\psi}_{L1} = \Big((\dot{F}^2 cosL4 + \ddot{F}FcosL4 - \ddot{F}cosL3)(1-F^2)(sin^2L3 - F^2 - cos^2L4 + 2FcosL3cosL4) + \\ -\dot{F}^2(3F^3 - 2Fsin^2L3 + 2Fcos^2L4 - 5F^2cosL3cosL4 - F + \\ +cosL3cosL4)(FcosL4 - cosL3)\Big)/(1-F^2)^2(sin^2L3 - F^2 - cos^2L4 + 2FcosL3cosL4)^{\frac{3}{2}} + \\ -\Big((\dot{F}^2 cosL2 + \ddot{F}FcosL2 - \ddot{F}cosL1)(1-F^2)(sin^2L1 - F^2 - cos^2L2 + 2FcosL3cosL2) + \\ -\dot{F}^2(3F^3 - 2Fsin^2L1 + 2Fcos^2L2 - 5F^2cosL3cosL2 - F + \\ +cosL1cosL2)(FcosL2 - cosL1)\Big)/(1-F^2)^2(sin^2L1 - F^2 - cos^2L2 + 2FcosL1cosL2)^{\frac{3}{2}} \tag{B.73}$$

$$\ddot{F} = -(\ddot{\phi}_{L1} - \ddot{\phi}_{L2})sinL1sinL2sin(\phi_{L1} - \phi_{L2}) - (\dot{\phi}_{L1} - \dot{\phi}_{L2})^2 sinL1sinL2cos(\phi_{L1} - \phi_{L2}) \tag{B.74}$$

The fraction at the front of Equation B.72 is required to make it the appropriate sign. These expressions apply when the positions of the input links are defined in either manner mentioned previously.

Now, taking the second time derivative of Equation B.50, we obtain an expression for the wing's stroke acceleration:

$$\ddot{\phi} = \ddot{\phi}_{L1} - \Big(\Big(\ddot{\theta}cosL1 - \ddot{\theta}sin\theta cosL3 - \dot{\theta}^2 cos\theta cosL3\Big)cos\theta\Big(cos^2\theta - cos^2L1 - cos^2L3 + \\ +2cosL1cosL3sin\theta\Big) - \dot{\theta}^2\Big(cosL1 - sin\theta cosL3\Big)\Big(sin\theta cos^2L1 - 2sin\theta cos^2\theta + sin\theta cos^2L3 + \\ -3sin^2\theta cosL1cosL3 + cosL1cosL3\Big)\Big)/cos^2\theta(cos^2\theta - cos^2L1 - cos^2L3 + 2cosL1cosL3sin\theta)^{\frac{3}{2}} \tag{B.75}$$

Finally, taking the second time derivative of Equation B.59, we obtain the pitch acceleration:

$$\ddot{\alpha} = -\Big((\dot{E}^2 cosL6 + \ddot{E}EcosL6 - \ddot{E}cosL7)(1-E^2)(sin^2L7 - E^2 - cos^2L6 + 2EcosL7cosL6) + \\ -\dot{E}^2(3E^3 - 2Esin^2L7 + 2Ecos^2L6 - 5E^2cosL7cosL6 - E + \\ +cosL7cosL6)(EcosL6 - cosL7)\Big)/(1-E^2)^2(sin^2L7 - E^2 - cos^2L6 + 2EcosL7cosL6)^{\frac{3}{2}} + \\ -\frac{\theta}{|\theta|}\frac{\phi-\phi_{L5}-cos^{-1}(\frac{cosL6-cosL5\ cosL7}{sinL5\ cosL7})}{|\phi-\phi_{L5}-cos^{-1}(\frac{cosL6-cosL5\ cosL7}{sinL5\ cosL7})|}\Big((1-E^2)(1-E^2-sin^2(\phi-\phi_{L5}))\Big((\ddot{\phi}-\ddot{\phi}_{L5})cos(\phi-\phi_{L5})(1-E^2) + \\ -(\dot{\phi}-\dot{\phi}_{L5})^2 sin(\phi-\phi_{L5})(1-E^2) - E\dot{E}(\dot{\phi}-\dot{\phi}_{L5})cos(\phi-\phi_{L5}) + E\ddot{E}sin(\phi-\phi_{L5}) + \\ +\dot{E}^2 sin(\phi-\phi_{L5})\Big) - \Big((\dot{\phi}-\dot{\phi}_{L5})cos(\phi-\phi_{L5})(1-E^2) + \\ +E\dot{E}sin(\phi-\phi_{L5})\Big)\Big(3E^3\dot{E} - 3E\dot{E} + 2E\dot{E}sin^2(\phi-\phi_{L5}) + \\ -(1-E^2)(\dot{\phi}-\dot{\phi}_{L5})cos(\phi-\phi_{L5})sin(\phi-\phi_{L5})\Big)\Big)/(1-E^2)^2(1-E^2-sin^2(\phi-\phi_{L5}))^{\frac{3}{2}} \tag{B.76}$$

where:

$$\ddot{E} = \ddot{\theta}cosL5cos\theta - \dot{\theta}^2 cosL5sin\theta - \ddot{\theta}sinL5sin\theta cos(\phi-\phi_{L5}) + \\ -sinL5cos\theta cos(\phi-\phi_{L5})\Big(\dot{\theta}^2 + (\dot{\phi}-\dot{\phi}_{L5})^2\Big) + \\ +sinL5sin(\phi-\phi_{L5})\Big(2\dot{\theta}(\dot{\phi}-\dot{\phi}_{L5})sin\theta - (\ddot{\phi}-\ddot{\phi}_{L5})cos\theta\Big) \tag{B.77}$$

As before, the fractions in front of the second term in Equation B.76 are required to make it the appropriate sign. These expressions apply when the link positions are defined relative to the $\phi = 0^\circ$ longitude line. When ϕ_{L1}, ϕ_{L2} & ϕ_{L5} are defined relative to their positions when the wing is at the neutral position, then Equations B.76 - B.77 become:

$$\ddot{\alpha} = -\Big((\dot{E}^2 cosL6 + \ddot{E}EcosL6 - \ddot{E}cosL7)(1-E^2)(sin^2L7 - E^2 - cos^2L6 + 2EcosL7cosL6) +$$
$$-\dot{E}^2(3E^3 - 2Esin^2L7 + 2Ecos^2L6 - 5E^2cosL7cosL6 - E +$$
$$+cosL7cosL6)(EcosL6 - cosL7)\Big)/(1-E^2)^2(sin^2L7 - E^2 - cos^2L6 + 2EcosL7cosL6)^{\frac{3}{2}} +$$
$$-\tfrac{\theta}{|\theta|}\tfrac{\phi-\phi_{L5}}{|\phi-\phi_{L5}|}\Big((1-E^2)(1-E^2-sin^2(\phi-\phi_{L5}+cos^{-1}(\tfrac{cosL6-cosL5\ cosL7}{sinL5\ cosL7})))\Big((\ddot{\phi}+$$
$$-\ddot{\phi}_{L5})cos(\phi-\phi_{L5}+cos^{-1}(\tfrac{cosL6-cosL5\ cosL7}{sinL5\ cosL7}))(1-E^2) - (\dot{\phi}-\dot{\phi}_{L5})^2 sin(\phi-\phi_{L5}+$$
$$+cos^{-1}(\tfrac{cosL6-cosL5\ cosL7}{sinL5\ cosL7}))(1-E^2) - E\dot{E}(\dot{\phi}-\dot{\phi}_{L5})cos(\phi-\phi_{L5}+cos^{-1}(\tfrac{cosL6-cosL5\ cosL7}{sinL5\ cosL7})) +$$
$$+E\ddot{E}sin(\phi-\phi_{L5}+cos^{-1}(\tfrac{cosL6-cosL5\ cosL7}{sinL5\ cosL7})) +$$
$$+\dot{E}^2 sin(\phi-\phi_{L5}+cos^{-1}(\tfrac{cosL6-cosL5\ cosL7}{sinL5\ cosL7}))\Big) - \Big((\dot{\phi}-\dot{\phi}_{L5})cos(\phi-\phi_{L5}+$$
$$+cos^{-1}(\tfrac{cosL6-cosL5\ cosL7}{sinL5\ cosL7}))(1-E^2) + E\dot{E}sin(\phi-\phi_{L5}+cos^{-1}(\tfrac{cosL6-cosL5\ cosL7}{sinL5\ cosL7}))\Big)\Big(3E^3\dot{E} +$$
$$-3E\dot{E} + 2E\dot{E}sin^2(\phi-\phi_{L5}+cos^{-1}(\tfrac{cosL6-cosL5\ cosL7}{sinL5\ cosL7})) +$$
$$-(1-E^2)(\dot{\phi}-\dot{\phi}_{L5})cos(\phi-\phi_{L5}+cos^{-1}(\tfrac{cosL6-cosL5\ cosL7}{sinL5\ cosL7}))sin(\phi-\phi_{L5}+$$
$$+cos^{-1}(\tfrac{cosL6-cosL5\ cosL7}{sinL5\ cosL7}))\Big)\Big)/(1-E^2)^2(1-E^2-sin^2(\phi-\phi_{L5}+cos^{-1}(\tfrac{cosL6-cosL5\ cosL7}))^{\frac{3}{2}} \tag{B.78}$$

$$\ddot{E} = \ddot{\theta}cosL5cos\theta - \dot{\theta}^2 cosL5sin\theta - \ddot{\theta}sinL5sin\theta cos(\phi-\phi_{L5}+cos^{-1}(\tfrac{cosL6-cosL5\ cosL7}{sinL5\ cosL7})) +$$
$$-sinL5cos\theta cos(\phi-\phi_{L5}+cos^{-1}(\tfrac{cosL6-cosL5\ cosL7}{sinL5\ cosL7}))\Big(\dot{\theta}^2 + (\dot{\phi}-\dot{\phi}_{L5})^2\Big) +$$
$$+sinL5sin(\phi-\phi_{L5}+cos^{-1}(\tfrac{cosL6-cosL5\ cosL7}{sinL5\ cosL7}))\Big(2\dot{\theta}(\dot{\phi}-\dot{\phi}_{L5})sin\theta - (\ddot{\phi}-\ddot{\phi}_{L5})cos\theta\Big) \tag{B.79}$$

B.3 Summary

A summary of the expressions obtained are listed in Table B.1 for mechanism kinematics (ϕ_{L1}, $\dot{\phi}_{L1}$, $\ddot{\phi}_{L1}$, ϕ_{L2}, $\dot{\phi}_{L2}$, $\ddot{\phi}_{L2}$, ϕ_{L5}, $\dot{\phi}_{L5}$, $\ddot{\phi}_{L5}$) as functions of the flapping kinematics (ϕ, $\dot{\phi}$, $\ddot{\phi}$, θ, $\dot{\theta}$, $\ddot{\theta}$, α, $\dot{\alpha}$, $\ddot{\alpha}$) and link lengths (L1-L7). Conversely, Table B.2 lists the expressions for flapping kinematics as functions of the mechanism kinematics and link lengths. In both tables the first column applies when the positions of the input links ϕ_{L1}, ϕ_{L2}, & ϕ_{L5} are defined relative to the $\phi = 0°$ longitude line (as shown in Figure B.1). The second column applies when ϕ_{L1}, ϕ_{L2}, & ϕ_{L5} are defined relative to the input link positions when the wing is at the 'neutral' position

(when $\phi = 0°$, $\theta = 0°$, & $\alpha = 90°$). For each variable, the main equation is listed first, followed by additional equations which must be used in conjunction with the main equation in order to calculate the desired variable. For example, the first row, first column of Table B.2 states that to calculate ϕ, Equation B.49 is used in conjunction with Equations B.45 & B.46.

Table B.1: Summary of equations defining mechanism kinematics as functions of flapping kinematics and link 'lengths'; for each variable, the main equation equation is listed first, followed by additional equations which must be used in conjunction with the main equation in order to calculate the desired variable

	if link positions defined relative to $\phi = 0$ longitude line	if link positions defined relative to 'neutral' position
ϕ_{L1}	B.3	B.11
$\dot{\phi}_{L1}$	B.14	B.14
$\ddot{\phi}_{L1}$	B.23	B.23
ϕ_{L2}	B.4	B.12
$\dot{\phi}_{L2}$	B.15	B.15
$\ddot{\phi}_{L2}$	B.24	B.24
ϕ_{L5}	B.10 with B.6, B.8, B.9	B.13 with B.6, B.8, B.9
$\dot{\phi}_{L5}$	B.16 with B.17 - B.22	B.16 with B.17 - B.22
$\ddot{\phi}_{L5}$	B.25 with B.19 - B.22,B.26 - B.37	B.25 with B.19 - B.22,B.26 - B.37

Table B.2: Summary of equations defining flapping kinematics as functions of mechanism kinematics and link 'lengths'; for each variable, the main equation equation is listed first, followed by additional equations which must be used in conjunction with the main equation in order to calculate the desired variable

	if link positions defined relative to $\phi = 0$ longitude line	if link positions defined relative to 'neutral' position
ϕ	B.49 with B.45, B.46	B.50 with B.45, B.46
$\dot{\phi}$	B.65 with B.45, B.46, B.61 - B.64	B.65 with B.45, B.46, B.61 - B.64
$\ddot{\phi}$	B.75 with B.45, B.46, B.61 - B.64, B.72 - B.74	B.75 with B.45, B.46, B.61 - B.64, B.72 - B.74
θ	B.46 with B.45	B.46 with B.45
$\dot{\theta}$	B.61 with B.45, B.62 - B.64	B.61 with B.45, B.62 - B.64
$\ddot{\theta}$	B.72 with B.45, B.62 - B.64, B.73, B.74	B.72 with B.45, B.62 - B.64, B.73, B.74
α	B.59 with B.45, B.46, B.49	B.60 with B.45, B.46, B.50
$\dot{\alpha}$	B.66 with B.45, B.46, B.49, B.61 - B.64, B.65, B.67, B.68	B.69 with B.45, B.46, B.50, B.61 - B.64, B.65, B.70, B.71
$\ddot{\alpha}$	B.76 with B.45, B.46, B.49, B.61 - B.65, B.67, B.68, B.72 - B.75, B.77	B.78 with B.45, B.46, B.50, B.61 - B.65, B.70, B.71 - B.75, B.79

Appendix C

Particle Image Velocimetry

In this Appendix, the non-intrusive flowfield measurement technique of Particle Image Velocimetry, or *PIV*, will be described. First, the standard *PIV* technique that gives 2*D* vectors will be described, followed by the stereoscopic *PIV* technique which allows 3*D* velocity vectors to be measured.

PIV is a flowfield measurement technique similar to the 'streak photograph' technique mentioned in Chapter 2. Recall that in this technique, a plane is illuminated with a light sheet and a photograph with a prolonged exposure is taken of a seeded flow, revealing streaks of light representing local particle paths, or instantaneous streamlines. With the lengths of the streaks, and known exposure time, the local velocities throughout the measurement plane can be computed. The modern technique of *PIV* uses a very similar principal to measure fluid velocities in a measurement plane. As illustrated in Figure C.1, a laser light sheet is used to illuminate a plane, and two short exposures of the seeded flow are taken at a known time separation. This gives a snapshot of particle positions at two separate times. Therefore, the magnitude and direction of local particle displacements during the time between exposures is known, and local fluid velocities can be determined. This technique will be described in more detail shortly.

The theory for this technique was first outlined by Adrian (1988), and it originally employed a film camera in which the film was continually exposed while a light sheet was pulsed twice in quick succession, resulting in particle positions at two separate times on the same image. From these images, velocity vectors were recovered with an auto-correlation function. With the advent of high-speed digital video recording, it became possible to employ double image recordings and determine velocity vectors from particle images between the successive images using a cross-correlation analysis (Keane & Adrian, 1992). Here, instead of recording particles on the same image, particle positions from the first and second laser pulses are captured on two separate images. This technique is generally preferred because it does not suffer from some of the problems associated with the double-exposed single image technique. These issues include the need for a prior knowledge of fluid velocity, since it is otherwise unknown which particle

images originate from which exposure, difficulty in measuring velocities close to zero since particle images overlap, and noise levels which are close to the signal level (Raffel et al., 1998). Thus, the standard *PIV* technique used today employs single exposed double images.

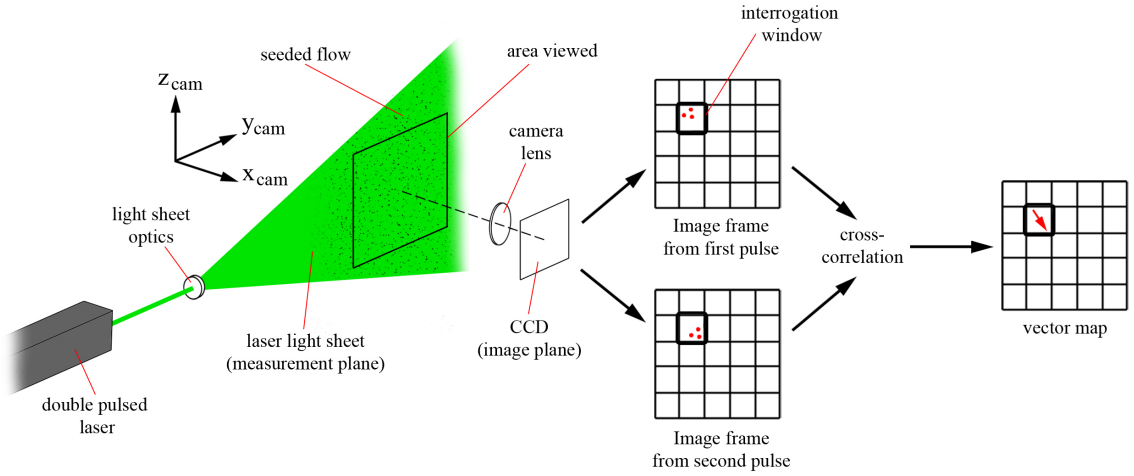

Figure C.1: Standard *PIV* technique (adapted from Dantec (2011))

Further details of *PIV* will now be given. Figure C.1 illustrates the workings of this technique, where a laser beam is converted to a light sheet via a set of optics, and is used to illuminate the measurement plane. The measurement coordinate system $x_{cam}y_{cam}z_{cam}$ is oriented such that the $y_{cam}z_{cam}$ plane coincides with the measurement plane, y_{cam} is horizontal, and z_{cam} is vertical. Thus, measured in-plane velocities are in the y_{cam} and z_{cam} directions. It should be noted that in the literature, the in-plane axes are often denoted by x (horizontal) and y (vertical), however, for the sake of continuity with the rest of this thesis, the in-plane axes are taken as y_{cam} and z_{cam}. The flow is seeded with particles, and the laser is pulsed twice in quick succession, where the pulses are separated by time Δt. With each laser pulse, an image of the particle positions is taken with a high-speed camera (lens and *CCD* in Figure C.1), giving two images (an 'image pair') with particle positions at two separate times. Each image is then broken into a grid of 'interrogation windows'. Corresponding interrogation windows between the two images are stepped through and cross-correlated using a function typically of the form:

$$C(dy_{cam}, dz_{cam}) = \sum_{y_{cam}=0, z_{cam}=0}^{y_{cam}<n, z_{cam}<n} I_1(y_{cam}, z_{cam}) I_2(y_{cam}+dy_{cam}, z+dz_{cam}), \qquad -\frac{n}{2} < dy_{cam},\, dz_{cam} < \frac{n}{2} \tag{C.1}$$

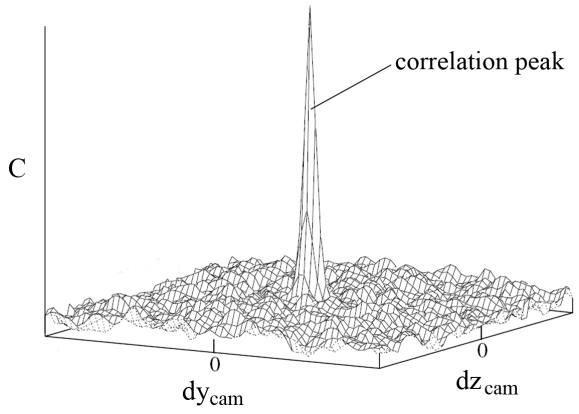

Figure C.2: Correlation map (adapted from Raffel et al. (1998))

Here, I_1 and I_2 are arrays of pixel intensities in the interrogation window for the first and second images, respectively, n is the interrogation window size (in pixels), and dy_{cam} and dz_{cam} are the particle image displacements in the y_{cam} and z_{cam} directions, respectively. Essentially, this function works by multiplying the pixel intensities at each point in the first image with intensities at the corresponding points in the second image, but shifted by dy_{cam} and dz_{cam}, and then these products are summed to give a correlation value C. This is performed over a range of dy_{cam} and dz_{cam} values, thus creating a $3D$ 'correlation map' which represents the computed C value versus dy_{cam} and dz_{cam} as shown in Figure C.2. When dy_{cam} and dz_{cam} are the values of the actual particle image displacements, C peaks as seen in the correlation map (Figure C.2), which is called the correlation peak. This peak occurs because when the 'shifts' dy_{cam} and dz_{cam} are the particle displacements, the arrays of pixel intensities (the particle images themselves) between the two exposures 'match-up'. Thus, pixels with high intensity levels, which occur where particle images are present in the first image, are directly compared with the pixels in the second image where the particle images have displaced to, which also have high intensity levels. This gives especially large products when the intensities are multiplied, and hence a large C value. Therefore, in each interrogation window in the measurement area, the displacement components dy_{cam} and dz_{cam} representing

the fluid displacement between images, are found by obtaining the dy_{cam} and dz_{cam} values at the peak C in the correlation map. With the known time between pulses Δt, the displacement vectors can be converted to velocity vectors.

A limitation of the standard *PIV* technique is that it can only measure fluid velocities within the measurement plane, that is, out-of-plane velocities cannot be measured. An extension to this technique was first revealed by Gautier & Riethmuller (1988), in which a pair of cameras in a stereoscopic arrangement view the same measurement area, instead of just one. This is called stereoscopic *PIV*, and it enables the third velocity component to be deduced from the in-plane velocity components seen in the two camera perspectives. As illustrated in Figure C.3a and b, a stereoscopic *PIV* setup is comprised of two cameras (lens and *CCD*) angled to the measurement plane, which is called an angular setup. Again the $x_{cam}y_{cam}z_{cam}$ frame is fixed to the measurement plane, and new frames $x_{imgR}y_{imgR}z_{imgR}$ and $x_{imgL}y_{imgL}z_{imgL}$ fixed to the image plane (*CCD*) of the right and left cameras respectively, are introduced. Figure C.3a shows a view of the $x_{cam}y_{cam}$ plane (parallel to the earth's surface), where for a given point 'n' in the measurement plane, a ray through the lens to the image plane makes an angle of λ with the normal (x_{cam} direction) for the left 'L' and right 'R' cameras denoted by the superscripts. Similarly, Figure C.3b depicts a $x_{cam}z_{cam}$ plane, where for point n, a ray to the image plane makes an angle of ζ with the normal for each camera. The ζ angle for each camera in almost all applications is zero. The cameras can also be oriented perpendicularly to the measurement plane (such that $\lambda^R, \lambda^L, \zeta^R, \zeta^L = 0°$), which is called a translational setup, however, the angular setup has greater out-of-plane accuracy (Lawson. & Wu, 1997; Prasad, 2000), and thus is the most widely used. However, as a consequence of angling a given camera in this manner, the lens plane for a given camera is no longer parallel to the measurement plane, and thus, only a portion of the area viewed in this plane will be in focus due to the finite depth of field. This can be avoided by angling the camera's *CCD* (the image plane) relative to the lens according to the Scheimpflug condition which is achieved when the measurement, lens and image planes intersect at a common line for a given camera (Prasad & Jensen, 1995). This is illustrated in Figure C.3a, but not in the other plane in Figure C.3b because the ζ angles are often close to zero, thus, there is no need to angle the image plane in this direction. When the Scheimpflug condition is achieved, the area viewed in

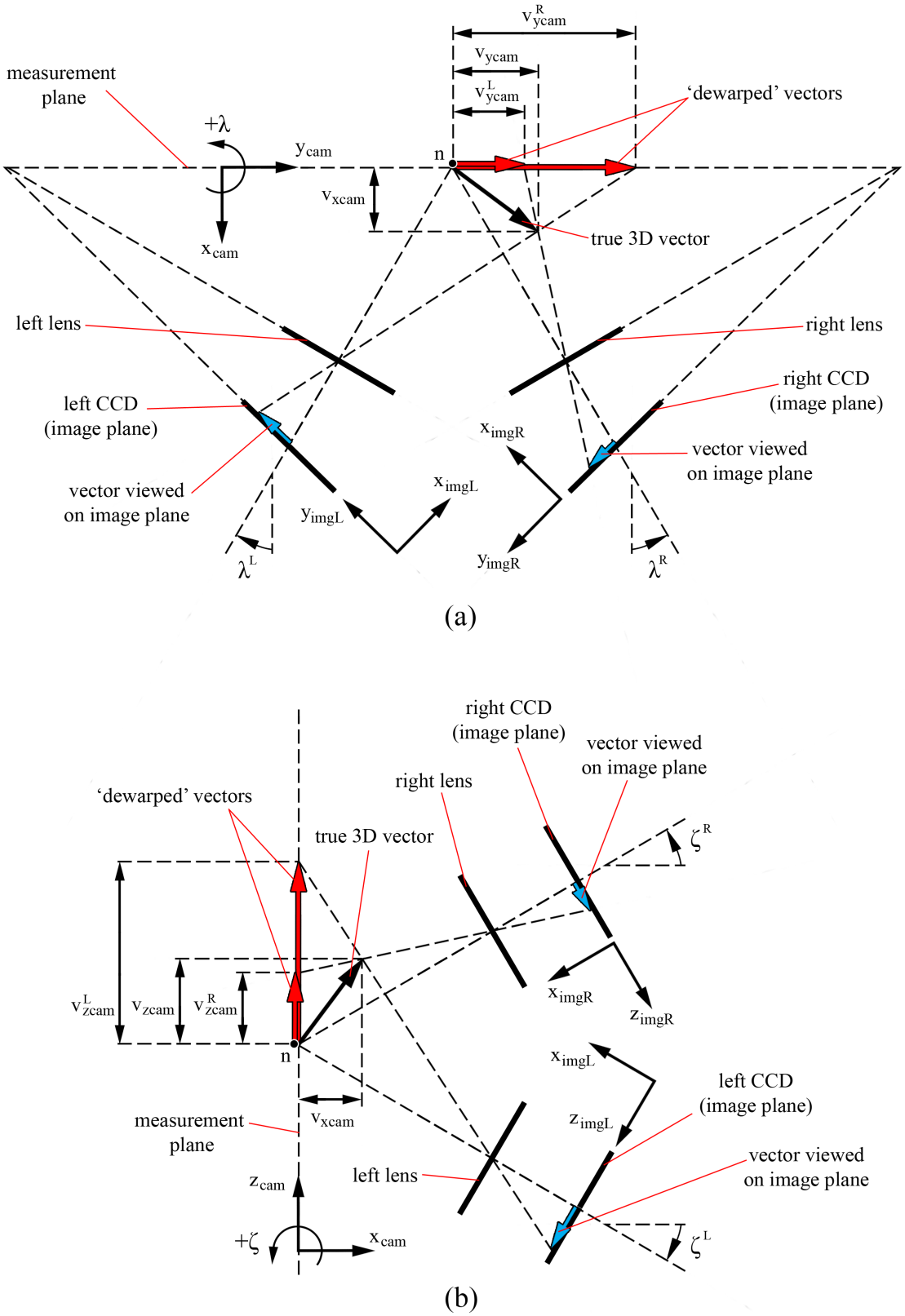

Figure C.3: 3D vector reconstruction by Willert (1997) for (a) $x_{cam}y_{cam}$ plane and (b) $x_{cam}z_{cam}$ plane (adapted from Giordano & Astarita (2009))

the measurement plane angled to the lens will all be in focus.

Once the cameras are setup and focused on a common area in the measurement plane, as described previously, a calibration must be performed so that the two camera views can be related. After Soloff et al. (1997), the calibration method consists of placing a calibration plate parallel to the light sheet and in the area viewed by the two cameras. The calibration plate typically consists of an array of dots a known distance apart. After both cameras image the calibration plate, a mapping function is formulated for each camera by matching the same dots between the two camera perspectives. These functions allow coordinates in the image plane of each camera (in the $x_{imgR}y_{imgR}z_{imgR}$ & $x_{imgL}y_{imgL}z_{imgL}$ frames) to be transformed to common coordinates in the measurement plane (the $x_{cam}y_{cam}z_{cam}$ frame). Calibration plates used for this purpose are either dual plane plates, or single plane plates that can be translated perpendicular to the measurement plane. Dual plane plates consist of dots distributed across two planes a known distance apart. In either case, an additional plane of dots is provided, from which another mapping function is created for each camera. For a given camera, the additional mapping function for the second plane combined with the first mapping function, enables the viewing angles of the camera relative to the measurement plane (the λ and ζ angles) to be recovered. Therefore, the calibration simultaneously establishes the relation between the image planes of the two cameras and measurement plane, and the geometric relation of the cameras to the measurement plane.

With the calibration between the two camera views established, $3D$ flowfield measurements can be performed. The laser light sheet is pulsed twice and each camera captures an image pair. Image pairs from each of the camera views are then cross correlated using the same method described earlier for a single *PIV* camera setup. This creates a vector map in each of the image planes. The interrogation windows used in the cross-correlation form an irregular grid resulting from the camera perspective, as illustrated in Figure C.4. This way, corresponding interrogation windows between the two camera views still represent the same area (and hence the same particles) in the measurement plane, despite the different perspectives. These grids are formulated from the previously discussed calibrations. The $2D$ vectors in the the irregular grids, and the grids themselves for each camera view are then 'dewarped' and mapped onto a common orthogonal plane (the measurement plane) using the aforementioned mapping functions. In other

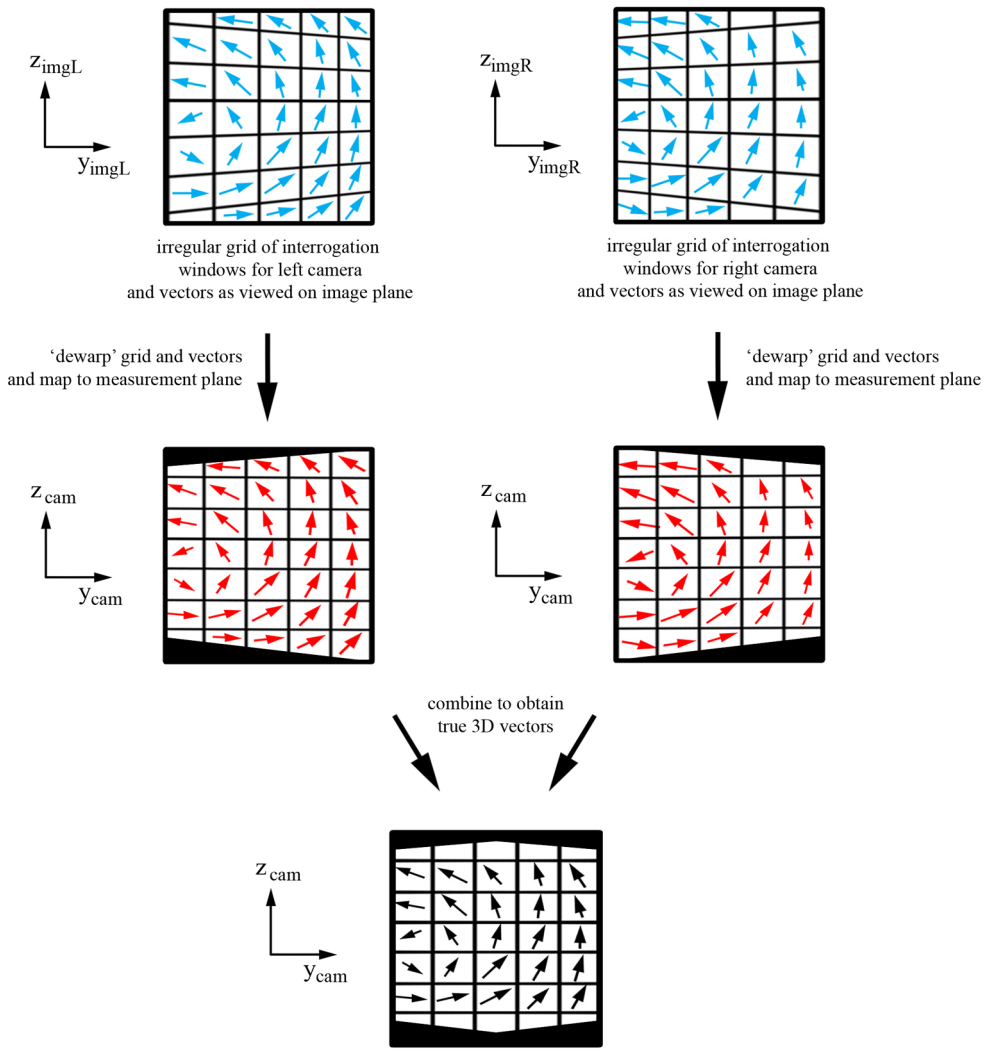

Figure C.4: Reconstruction of 3*D* vectors

words, vectors from the $x_{imgR}y_{imgR}z_{imgR}$ and $x_{imgL}y_{imgL}z_{imgL}$ frames are transformed to the $x_{cam}y_{cam}z_{cam}$ frame. Thus at each point in the orthogonal plane ($x_{cam}y_{cam}z_{cam}$ frame), there is a pair of v_{ycam} and v_{zcam} velocity components from the left and right cameras denoted by the superscripts (see Figure C.3a & b). These are then used in the following formulae to reconstruct the true 3*D* velocity components (from Willert (1997) and adapted by Giordano & Astarita (2009)):

$$v_{xcam} = \frac{v^L_{ycam} - v^R_{ycam}}{tan\lambda^R - tan\lambda^L} \tag{C.2}$$

$$v_{ycam} = \frac{v^L_{ycam} tan\lambda^R - v^R_{ycam} tan\lambda^L}{tan\lambda^R - tan\lambda^L} \tag{C.3}$$

$$v_{zcam} = \frac{v^L_{zcam} tan\zeta^R - v^R_{zcam} tan\zeta^L}{tan\zeta^R - tan\zeta^L} = \frac{v^L_{zcam} + v^R_{zcam}}{2} + \frac{v_{xcam}}{2}(tan\zeta^L + tan\zeta^R) \tag{C.4}$$

Appendix D

Vortex Axis Identification Procedure & Vortex Point-Joining Algorithm

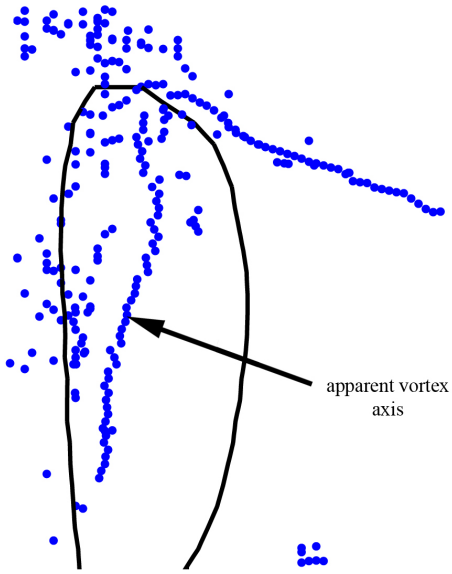

Figure D.1: Example result of the vortex identification method of Knowles et al. (2006) applied to volumetric flowfield data; blue dots indicate identified vortex core locations; wing outline is indicated by the solid black line

This appendix presents the procedure and algorithms developed to reconstruct vortex axes in the collection of 'vortex points' returned by the vortex identification method of Knowles et al. (2006) discussed in § 5.3.2 (page 137). First, the method in which groups of vortex points belonging to a common axis were identified will be presented. This is followed by a description of the algorithm developed to join vortex points with a line representing the vortex axis.

A shortcoming of the vortex identification method of Knowles et al. (2006), is that it is sensitive to noise and returns false vortex core locations. When this method is applied to every xy, yz, and xz plane, the result is a collection of points ('vortex points') in a $3D$ volume as pictured in Figure D.1, where some points are true vortex cores and others are spurious. The problem then is how to pick out groups of true vortex core points that mark the vortex axis of a common vortex structure. Although an obvious vortex axis can be seen right away in the group of

points that form an organised line as pointed out in Figure D.1, a less subjective and more automated method of finding vortex axes is required.

The method developed to identify groups of points that belong to a common axis relies on the following two facts: the vorticity vectors at points close together on a vortex axis point in roughly the same direction, and the vorticity vector at any point on a vortex axis will be a tangent to the curve defining the vortex axis at that point. Thus, if a given point is a true vortex and is on the same vortex axis as its neighbours, then it will meet the following criteria:

1. the vorticity vector points in the same direction as the vorticity vectors of its neighbouring points;
2. the path from the given point to neighbouring points is roughly tangential to the vorticity vectors at the current and neighbouring points.

These are the criteria used in locating groups of such points, which will be illustrated now with an example. Consider a group of m points and their vorticity vectors illustrated in Figure D.2. Points $n_5 - n_{10}$ define the true vortex axis and the other points are spurious. For a given point n_i the following quantity K is computed:

$$K_i = \sum_{j=1}^{j=m} \frac{\pi}{2} - |\beta_{r_{j/i},w_j} - \frac{\pi}{2}| + \beta_{w_i,w_j} \tag{D.1}$$

Here $\beta_{r_{j/i},w_j}$ is the angle between the vector $\mathbf{r}_{j/i}$ (position vector of point n_j relative to n_i) and the vorticity vector $\mathbf{w}_j$, and β_{w_i,w_j} is the angle between vorticity vectors $\mathbf{w}_i$ and $\mathbf{w}_j$. These angles are illustrated in Figure D.2 for $i = 1$ and $j = 2$, and they are always positive and less than or equal to 180°. The term β_{w_i,w_j} in the above equation quantifies how much the point n_i meets criterion 1 with its neighbouring point n_j. The $\frac{\pi}{2} - |\beta_{r_{j/i},w_j} - \frac{\pi}{2}|$ portion of the equation quantifies how much the given point meets the criterion 2. If the point is a true vortex and is on the same vortex axis as its neighbouring point n_j then both of these terms will be minimised. When these terms are added over all points to give the K value as indicated in the above equation, K will be minimal if the point is a true vortex. The result of computing K for every point is pictured in Figure D.3. Here it can

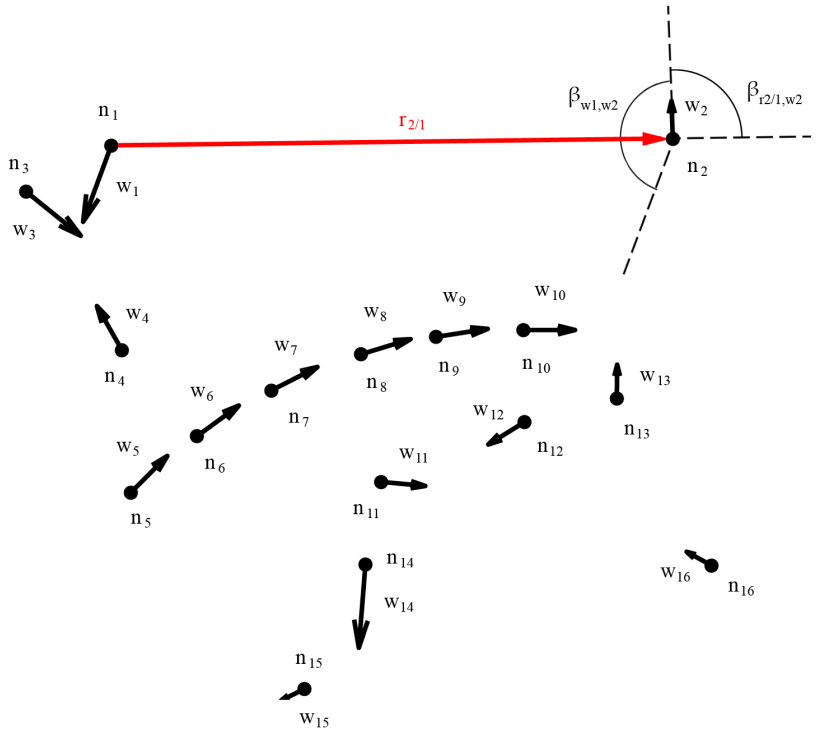

Figure D.2: Set of true and spurious vortex core points and their vorticity vectors

be seen that this method successfully reveals the true vortex core points $n_5 - n_{10}$, as they have a minimal K value.

Let us now apply this method to real experimental data. The result of computing K for all the points in Figure D.1 is shown in Figure D.4, where a long vortex axis becomes visible. In the calculation of K for each point, the ten closest neighbouring points were used, thus $m = 10$. The task now is to join these points that belong to the same vortex structure, which will be discussed next.

To join vortex axis points, the first step is to select manually the starting point of the vortex axis. This is done by computing the K value of all points as discussed previously to reveal the vortex axis, and then selecting a point on the end of this axis. For example, in Figure D.4 we would select the dark blue dot closest to the wing root. From this point, the following algorithm is employed:

let i = current point (i is initialised as the starting point mentioned previously)

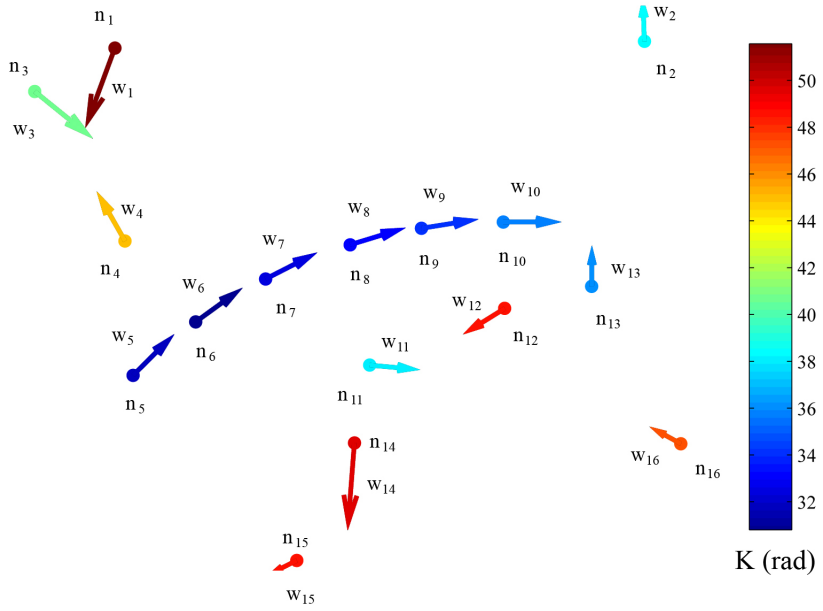

Figure D.3: Result of K value computation revealing the true vortex core points which have a minimal K

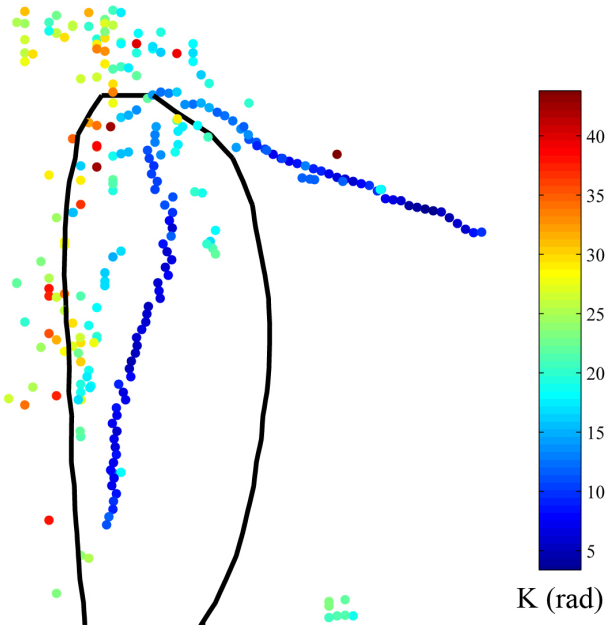

Figure D.4: Result of K value computation applied to experimental data revealing the true vortex core points which have a minimal K

let j = all points excluding the current point and any points joined to the vortex axis in a previous iteration

loop until break

flag = 0

loop over points j

construct a position vector $\mathbf{r}_{j/i}$ from the current point n_i to n_j

calculate the angle β_{w_i,w_j} between the vorticity vector $\mathbf{w}_i$ at the current point n_i and the vorticity vector $\mathbf{w}_j$ of point n_j

calculate the angle $\beta_{r_{j/i},w_i}$ between $\mathbf{r}_{j/i}$ and $\mathbf{w}_i$

calculate the angle $\beta_{r_{j/i},w_j}$ between $\mathbf{r}_{j/i}$ and $\mathbf{w}_j$

calculate magnitude $|r_{j/i}|$

if i > 1
calculate the angle $\beta_{r_{i/i-1},r_{j/i}}$ between $r_{i/i-1}$ and $r_{j/i}$
else
$\beta_{r_{i/i-1},r_{j/i}} = 0$
end if

if $(\frac{\pi}{2} - |\beta_{w_i,w_j} - \frac{\pi}{2}|) < threshold1$
and $(\frac{\pi}{2} - |\beta_{r_{j/i},w_j} - \frac{\pi}{2}|) < threshold2$
and $\beta_{r_{i/i-1},r_{j/i}} < threshold3$
and $|r_{j/i}| < threshold4$

flag = 1

calculate the perpendicular distance from the path of $\mathbf{w}_i$ to the path of $\mathbf{r}_{j/i}$, with $|\mathbf{r}_{j/i}|$ as the hypotenuse = $|\mathbf{r}_{j/i}|sin(\beta_{r_{j/i},w_i})$

calculate the perpendicular distance from the path of $\mathbf{w}_j$ to the

path of $\mathbf{r}_{j/i}$, with $|\mathbf{r}_{j/i}|$ as the hypotenuse = $|\mathbf{r}_{j/i}|sin(\beta_{r_{j/i},w_j})$

add these perpendicular distances to the magnitude of the position vector $\mathbf{r}_{j/i}$ to compute:
'distance sum' = $|\mathbf{r}_{j/i}| + |\mathbf{r}_{j/i}|sin(\beta_{r_{j/i},w_i}) + |\mathbf{r}_{j/i}|sin(\beta_{r_{j/i},w_j})$

end if

repeat loop for next point j

if flag = 0

break

else

the point j with the minimum 'distance sum' is considered to be the next point on the vortex axis and is then joined to the vortex axis

this point then becomes the current point i in the next iteration

end if

repeat loop for new point i

To complement this description, an illustration depicting the second iteration of this algorithm is given in Figure D.5. At this stage the vortex axis consists of points n_1 and n_2, and points $n_3 - n_m$ are being evaluated to determine which point to add next to the vortex axis. Thus $i = 2$ and $j = 3, 4, 5, ..m$, where m is the number of points (only points $n_1 - n_4$ are shown). All n_j points are then examined to determine which to include for further consideration using the four threshold tests indicated. The first test evaluates the angle between the vorticity vectors

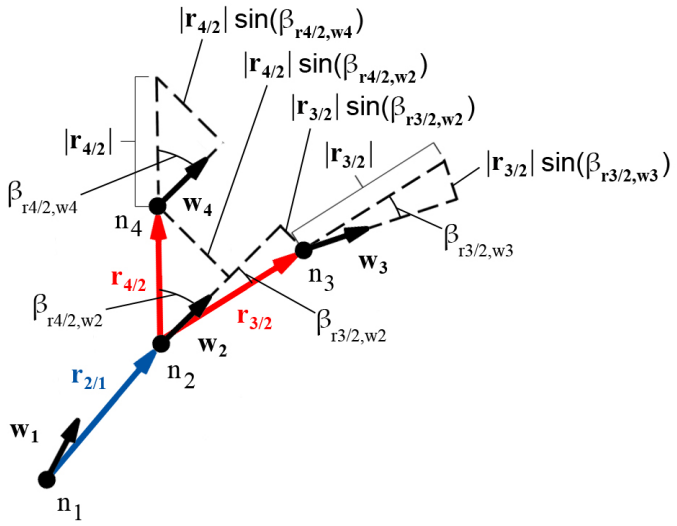

Figure D.5: Example of second iteration of vortex point-joining algorithm

at n_i and n_j, and ensures that the angle is below *threshold*1, so that it conforms to criterion 1 listed earlier. The second test determines if the angle between the position vector from n_i to n_j and the vorticity vector at n_j is below *threshold*2, to test its conformance to criterion 2. The next test ensures that the angle between the previous segment of the reconstructed vortex axis (position vector $r_{2/1}$) and the considered next segment ($r_{j/2}$) is below *threshold*3. This is used so that the reconstructed vortex axis does not take very sharp turns or reverse on itself. Finally, the last test allows only points that are sufficiently close by a distance of *threshold*4 or less to the current point n_2, to be considered for the next point on the axis. In this example points n_3 and n_4 both pass all four tests, and are now evaluated further to determine the appropriate point to add. For point n_3, 'distance sum' = $|\mathbf{r}_{3/2}| + |\mathbf{r}_{3/2}|sin(\beta_{r_{3/2},w_2}) + |\mathbf{r}_{3/2}|sin(\beta_{r_{3/2},w_3})$ and for point n_4 'distance sum' = $|\mathbf{r}_{4/2}| + |\mathbf{r}_{4/2}|sin(\beta_{r_{4/2},w_4}) + |\mathbf{r}_{4/2}|sin(\beta_{r_{4/2},w_2})$. It can be seen that 'distance sum' is minimised when point n_j is close to point n_i and $\mathbf{w}_i$ and $\mathbf{w}_j$ are parallel to the direction of $\mathbf{r}_{j/i}$. This way, finding the minimum 'distance sum' simultaneously finds a close point and the point that best meets criterion 2. Here 'distance sum' for point n_3 is less than that for point n_4, thus point n_3 is added to the vortex axis, and $i = 3$ and $j = 4, 5, 6, ...m$ for the next iteration. This continues and the loop ends when a scenario occurs where no points pass the four threshold tests.

When this algorithm is applied to the data in Figure D.4 and the dark blue dot

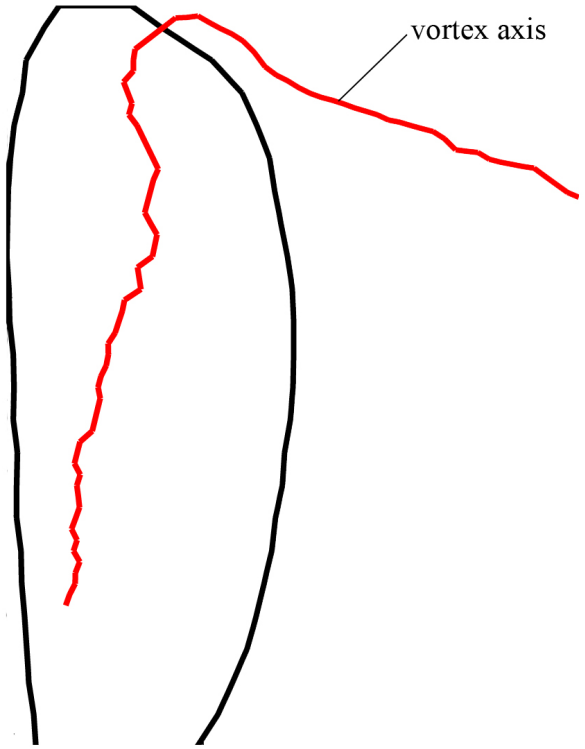

Figure D.6: Result of vortex axis joining algorithm applied to experimental data; the vortex axis is indicated by the solid red line; wing outline is indicated by the solid black line

closest to the wing root is selected as the starting point, an angle of 65° is used for threshold1 – 3, and a distance of 10 grid spacings (10mm) is used for threshold4, the result is that illustrated in Figure D.6. Here the vortex axis is shown by the red line. To illustrate how well this method identifies the true vortex axis, a comparison of the vorticity magnitude $|\mathbf{w}|$ along the curve to the component of the vorticity vector $\mathbf{w}_a$ (the axial vorticity) in the local direction of the curve is shown in Figure D.7. As discussed earlier, the vorticity vector at any point on a vortex axis will be tangent to the curve defining the vortex axis at that point. Thus, the magnitude of the 3D vorticity vector along a vortex axis should be equal to the component of the vorticity vector in the local direction of the vortex axis, which is virtually the case in Figure D.7. This is further shown in Figure D.8 which illustrates instantaneous streamlines released along the vortex axis in a vorticity vector field (w_x, w_y, w_z used instead of v_x, v_y, v_z). Here it can be seen that the paths of the streamlines largely coincide with the path of the vortex axis.

This developed method of joining vortex points is, however, somewhat ad hoc as it occasionally requires the threshold values to be adjusted to join an obvious

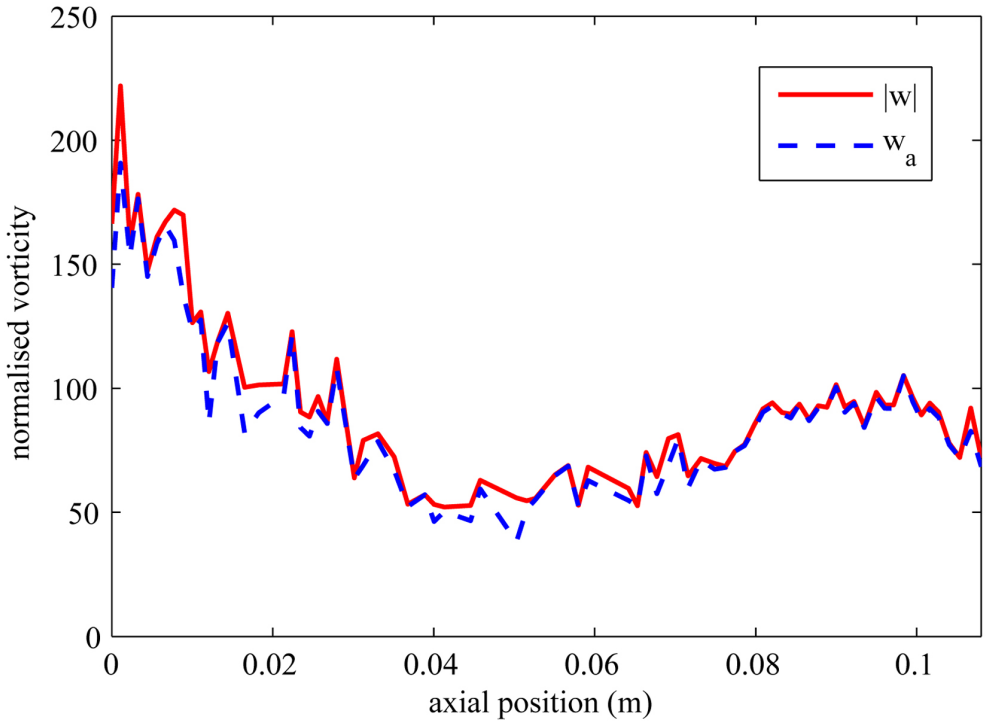

Figure D.7: Comparison of normalised vorticity magnitude $|\mathbf{w}|$ and axial vorticity $\mathbf{w}_a$ versus axial position on vortex axis; vorticity is normalised by the mean wing angular velocity ($79.7 rad/s$)

group of vortex points forming an axis. The threshold4 was always 10 grid spacings, whereas the threshold1-3 angles were varied in the range of $65° - 75°$. Also, at times points which were obviously not part of the vortex axis (indicated by a high K value) were incorrectly added to the axis, which would then cause the reconstructed axis trajectory to follow an erratic (incorrect) path. Such points had to be manually excluded from consideration in the algorithm.

A measure of how accurately the reconstructed vortex axis 'fits' the true vortex axis is provided by the comparison of the vorticity magnitude and axial vorticity along the axis. Along the true vortex axis, the vorticity magnitude will be equal to the axial vorticity. Therefore, the difference between the vorticity magnitude and axial vorticity along the reconstructed axis provides an 'error' of the axis fit. In the example shown in Figure D.7 which is a very good fit, the rms error from the differences of the normalised vorticities (normalised by the mean wing angular velocity $\bar{\Omega}_{wng}$) is 8. In the vortex axis reconstruction procedure, any required adjustment of the algorithm mentioned previously was performed until a similar level of axis fit was achieved. After computing the differences between

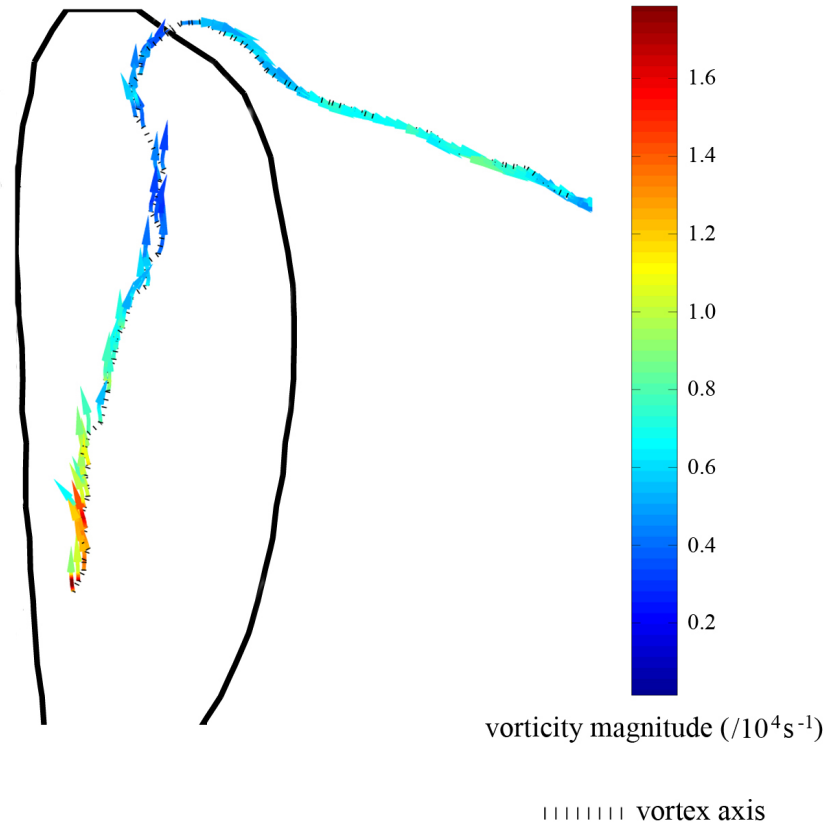

Figure D.8: Instantaneous streamlines coloured with vorticity magnitude released along vortex axis (dotted line) in a vorticity vector field; wing outline is indicated by the solid black line

the normalised axial vorticity and vorticity magnitude (both normalised by $\bar{w}_{wng}$) for all vortex axes identified in this thesis, the rms error was found to be 9.8. In addition, for each reconstructed axis, streamlines released in a vorticity field (as shown in Figure D.8) were used to verify that the vorticity streamlines followed the path of the axis. Furthermore, isosurfaces of Q were used to provide a secondary indication (and another confirmation) of the presence of a vortex.

It should be noted that inspiration for this vortex point-joining algorithm was drawn from the vortex axis identification algorithm of Singer & Banks (1994). This algorithm requires the user to input the starting point of the vortex axis, then a small step is made in the direction of the vorticity vector of the current point and then a plane is constructed perpendicular to the vorticity vector at the point one step away. The point with the local minimum pressure is then located in this plane, which is then added to the vortex axis and becomes the current point in the next iteration.

Appendix E

Calculation of Vortex Parameters

With a vortex axis identified using the procedure outlined in Appendix D, various characteristics of the vortex can then be obtained. These include axial and tangential vector quantities such as tangential velocity, and axial vorticity, helix angle, vortex diameter, and circulation. The method by which these quantities are obtained will be described in this Appendix, but first a local coordinate system fixed to the vortex axis must be introduced.

Characteristics of a vortex along its axis are obtained in a local $x_{va}y_{va}z_{va}$ coordinate system fixed at a given point n on the vortex axis. This is illustrated in Figure 6.1 (page 155) and is presented at the beginning of Chapter 6, but will be described again here for convenience. The frame is oriented such that at a given point n, the x_{va} axis points in the local direction of the curve defining the axis, towards the end of the axis without a white dot. The direction of x_{va} is obtained using coordinates on either side of point n and the central difference method. With an array of x_n, y_n, z_n values defining the xyz coordinates of a vortex axis, the unit direction vector $\mathbf{i}_{va}$ of the x_{va} axis for point n is obtained by:

$$\mathbf{i}_{va} = \begin{pmatrix} (x_{n+1} - x_{n-1}) / \sqrt{(x_{n+1} - x_{n-1})^2 + (y_{n+1} - y_{n-1})^2 + (z_{n+1} - z_{n-1})^2} \\ (y_{n+1} - y_{n-1}) / \sqrt{(x_{n+1} - x_{n-1})^2 + (y_{n+1} - y_{n-1})^2 + (z_{n+1} - z_{n-1})^2} \\ (z_{n+1} - z_{n-1}) / \sqrt{(x_{n+1} - x_{n-1})^2 + (y_{n+1} - y_{n-1})^2 + (z_{n+1} - z_{n-1})^2} \end{pmatrix} \quad \text{(E.1)}$$

With the $\mathbf{i}_{va}$ direction vector, the equation of a plane (the $y_{va}z_{va}$ plane) perpendicular to $\mathbf{i}_{va}$ (and x_{va}) at point n can then be formulated. With this equation, and the xyz coordinates of the wing edge, the coordinates of the intersections of the wing edge and this plane can be determined numerically. The two points where the wing edge intersects this plane (intersection at leading edge and trailing edge) are then used to formulate the direction of the y_{va} axis and its unit direction vector $\mathbf{j}_{va}$. This is performed using a similar formula to Equation E.1, but with the coordinates of intersection with the leading edge used in place of $x_{n+1}y_{n+1}z_{n+1}$, and coordinates for the intersection with the trailing edge used in place of $x_{n-1}y_{n-1}z_{n-1}$. Thus, the y_{va} axis is parallel to the line of intersection between the $y_{va}z_{va}$ plane

and the wing, and points towards the leading edge. The z_{va} axis and its direction vector $\mathbf{k}_{va}$ are then formulated by taking the cross product of $\mathbf{i}_{va}$ with $\mathbf{j}_{va}$. If at a given point on the axis the $y_{va}z_{va}$ plane does not intersect the wing then the z_{va} axis is oriented vertically such that the $x_{va}z_{va}$ plane is parallel to the z direction. The method in which various quantities are computed, will now be described.

E.1 Vector Quantities

Once the $x_{va}y_{va}z_{va}$ axes and direction vectors are defined, a grid of points in the $y_{va}z_{va}$ plane with the same grid spacing as in the $3D$ volume ($1mm$) is generated, where the local point n on the vortex axis is the origin. At each point in the grid, the three components of the desired vector quantities (velocity and vorticity) are interpolated from the volume of $3D$ vectors. For a given point, the interpolated $3D$ vector is then transformed to the $x_{va}y_{va}z_{va}$ frame by computing the components of the $3D$ vector in each of the x_{va},y_{va}, and z_{va} directions using the unit direction vectors. For example, the component in the x_{va} direction is computed by taking the dot product of the vector with $\mathbf{i}_{va}$. The resulting components in the x_{va} direction are the axial components, and components in the y_{va} direction are taken as the tangential components. Thus, axial velocity (v_a) and vorticity (w_a) are simply the components of these quantities in the x_{va} direction, while tangential velocity (v_t) is the velocity in the y_{va} direction. Tangential velocity is always plotted in this thesis along a vertical line through the vortex core and in the z_{va} direction, that is a vertical line at $y_{va} = 0$.

E.2 Helix Angle & Vortex Breakdown Location

Recall the expression for helix angle given in Equation 2.2 (page 34), where it is defined as the inverse tangent of the ratio of the tangential velocity to axial velocity at a point. Since tangential velocity is zero at the centre of a vortex, helix angle at the vortex centre for a given axial position was computed by calculating the helix angle at one grid point ($1mm$) on either side of the vortex core location

in both the z_{va} and $-z_{va}$ directions, and then averaging the result. Justification for calculating the helix angle in this manner, will be given next.

The maximum helix angle occurs at the edge of the vortex core since the tangential velocity rises towards the edge, while axial velocity falls. In the *LEV* on insect-like flapping wings, the helix angle at the edge of the vortex core is always beyond the critical angle of 50° (see § 2.2.8 for a description of this angle). This can be visualised by considering that flow emanating from the leading edge which is entrained into the *LEV*, originally has a direction roughly the same to that as the free-stream (i.e. no axial velocity, thus γ is close to 90°). Since the helix angle is always beyond critical at the edge of the *LEV* core, it would seem that the *LEV* is always in a state of breakdown along its entire length. However, this seems to be an inaccurate indication of breakdown, because regions where signs of breakdown are absent, such as those where axial velocity levels are high, and vortex diameter is small and grows very little, will be classified as being in a state of breakdown. It was stated by Délery (1994), that characterising breakdown with only one parameter is an oversimplification, and that the properties of the local velocity distributions must be taken into account. With this in mind, breakdown was not classified solely on helix angle, because using this criterion alone states that the entire *LEV* is always in breakdown. A more appropriate way of defining helix angle was to calculate its value very near the vortex centre in the manner explained above. This gives the lower bound of helix angles in the vortex, thus, if the helix angle near the centre has passed critical, then the helix angle is beyond critical everywhere in the vortex at that axial position. With this manner of calculating helix angle, and the comments of Délery (1994) in mind, breakdown was classified as the point where there was a rise in the helix above critical, a reversal in axial velocity, and a rise in vortex diameter.

E.3 Vortex Diameter

Vortex diameter was determined in the $y_{va}z_{va}$ plane by first plotting the tangential velocity along the line $y_{va} = 0$ through the vortex core (the z_{va} direction). The first absolute peak in v_t is found in this profile on either side of the vortex centre at $0, 0$. These absolute peaks are located by stepping through points from $0, 0$ in the z_{va} and $-z_{va}$ directions, and when the local rate of change of v_t in that direction

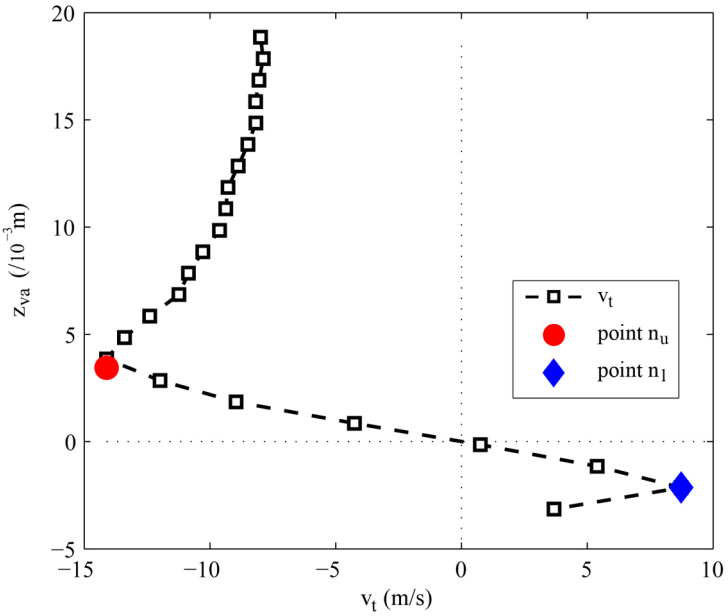

Figure E.1: Calculation of vortex diameter from tangential velocity profile through vortex core, where points n_u and n_l mark the extent of the rigid-body rotation region of the vortex

switches and the value of v_t changes by a certain threshold since the switch in the rate of change, then that point is an absolute peak. This threshold was taken as $0.5m/s$. For example, referring to Figure E.1, above the vortex centre, the first absolute peak occurs when v_t begins rising (after first declining from $0,0$) and the value of v_t rises by the threshold value or more since the switch in its rate of change with z_{va}. Similarly, below the vortex core, the first peak is located when the v_t begins declining, and declines by the threshold value or more. If however, the wing surface is reached before a peak in v_t is found below the vortex centre, then the peak location is taken as the location of the wing surface. Note that the vortex shown in Figure E.1 is clearly asymmetric, probably as a result of the proximity of the core to a solid surface (the wing). With the two absolute peak locations, a line is then fitted through the v_t, z_{va} points in between these peaks. The 'upper' point n_u on this line above this vortex axis is located at the v_t value of corresponding peak, and similarly a 'lower' point n_l is located on the line at the v_t value of the other peak. Thus, these points mark the extent of the solid-body rotation region of the vortex's tangential velocity profile, which represents the vortex core. The difference between z_{va} coordinates of points n_u and n_l gives the vortex diameter.

This method of fitting a line through the core points was employed because

the detected absolute peak locations on either side of the vortex core at times lay outside of the rigid-body rotation region of the profile. Therefore, simply using the z_{va} coordinates of the peak locations would give a less accurate measure of vortex diameter. In addition, when peak locations are outside of the rigid-body rotation region, the slope of the line through these peaks does not match the slope of the line through the points on the v_t profile at the core. These slopes should in fact match if the identified points are to represent the extent of the vortex diameter. By fitting a line through the vortex core points between the identified peak locations, and finding the points (n_u and n_l) on the line corresponding to the v_t values at the peak locations, the slopes through points n_u and n_l, and through the vortex core match much more closely. This results in a much better fit of points n_u and n_l to the rigid-body rotation region, and the measured diameter becomes much less sensitive to the identified absolute peak locations.

For a given point on the vortex axis, 16 points are made in the $y_{va}z_{va}$ plane defining a circle with the vortex diameter centred at the vortex core at $0, 0$. The coordinates of these points are then converted to the xyz frame, and the same process is performed at each point along the vortex axis. This results in a series of points in $3D$ which define the local outline of the vortex core as seen in the left of Figure E.2. These points are then joined into a surface, which provides a visualisation of the $3D$ vortex core, and its diameter.

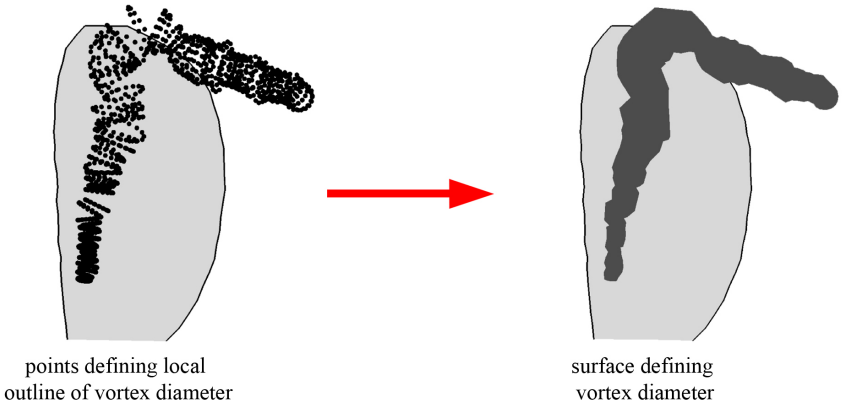

Figure E.2: Conversion of points defining local outline of vortex diameter to surface visualising the $3D$ vortex core

E.4 Circulation

Circulation was computed at a given point on the vortex axis using Equation 6.1 (page 179) combined with the computed vortex diameter, and the average of the absolute v_t values at the edges of the vortex core (v_t at n_u and n_l). It should be noted that when averaging the absolute v_t values as described, the result is given a positive sign if the velocities give a sense of rotation about the vortex centre in agreement with the right hand rule (i.e. clockwise rotation when viewed in the positive x_{va} direction). Conversely, if the v_t values give an anticlockwise rotation, then the average is given a negative sign.

Appendix F

Supplementary Figures

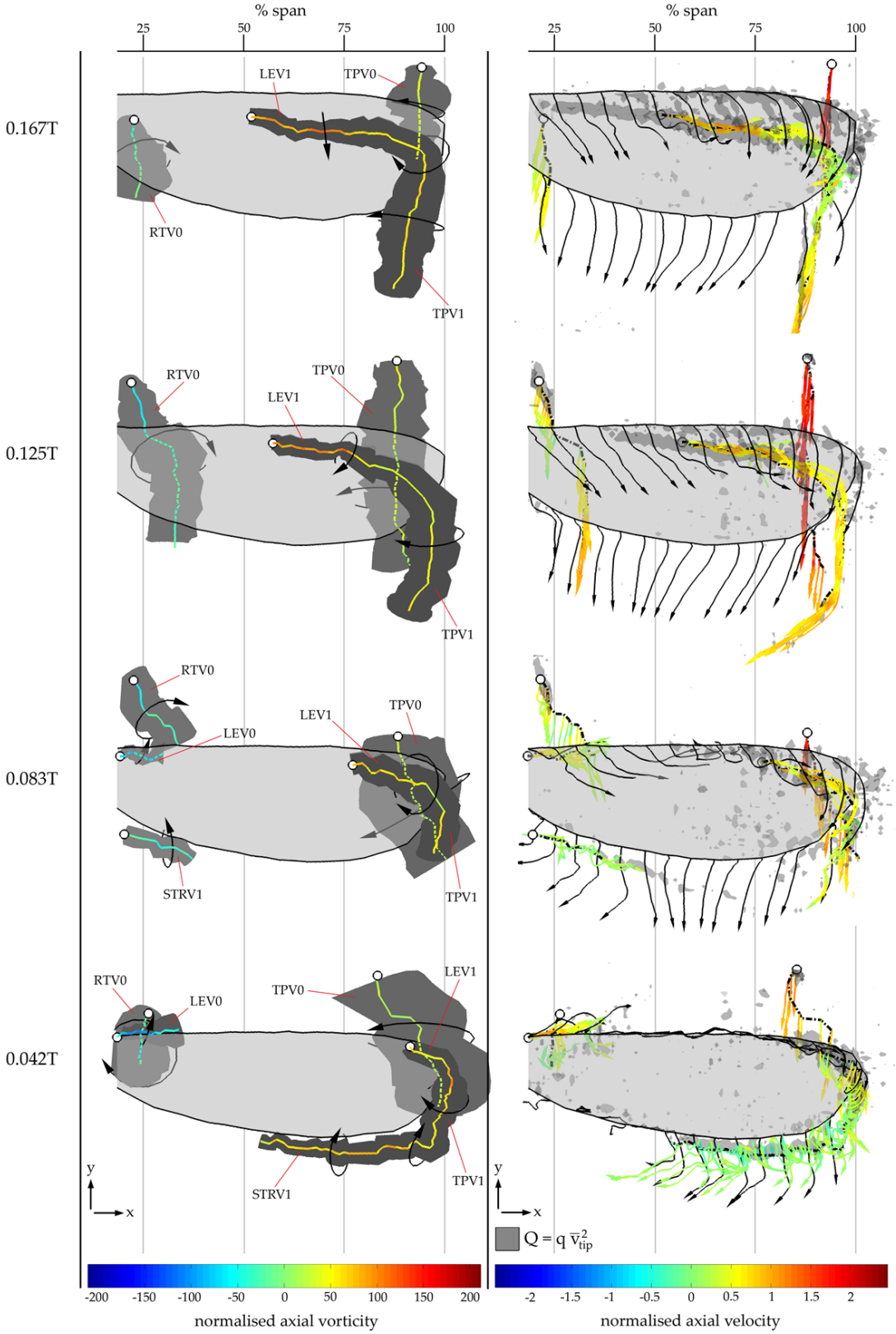

Figure F.1: Top views illustrating flow formation for the first third of a flapping half cycle; left column shows vortex core diameter (dark grey surfaces) and vortex axes coloured with axial vorticity normalised with respect to $\bar{\Omega}_{wng}$ ($79.7 rad/s$) (axes are dashed lines behind objects); right column shows instantaneous streamlines released from vortex axes coloured with axial flow normalised with respect to the mean wingtip speed ($8.4 m/s$), black streamlines released along the wing edge, and transparent grey isosurfaces of $Q = q\bar{v}^2_{tip}$ where $q \approx 8.5 \times 10^4 m^{-2}$; positive axial direction points along an axis towards the end without a white dot

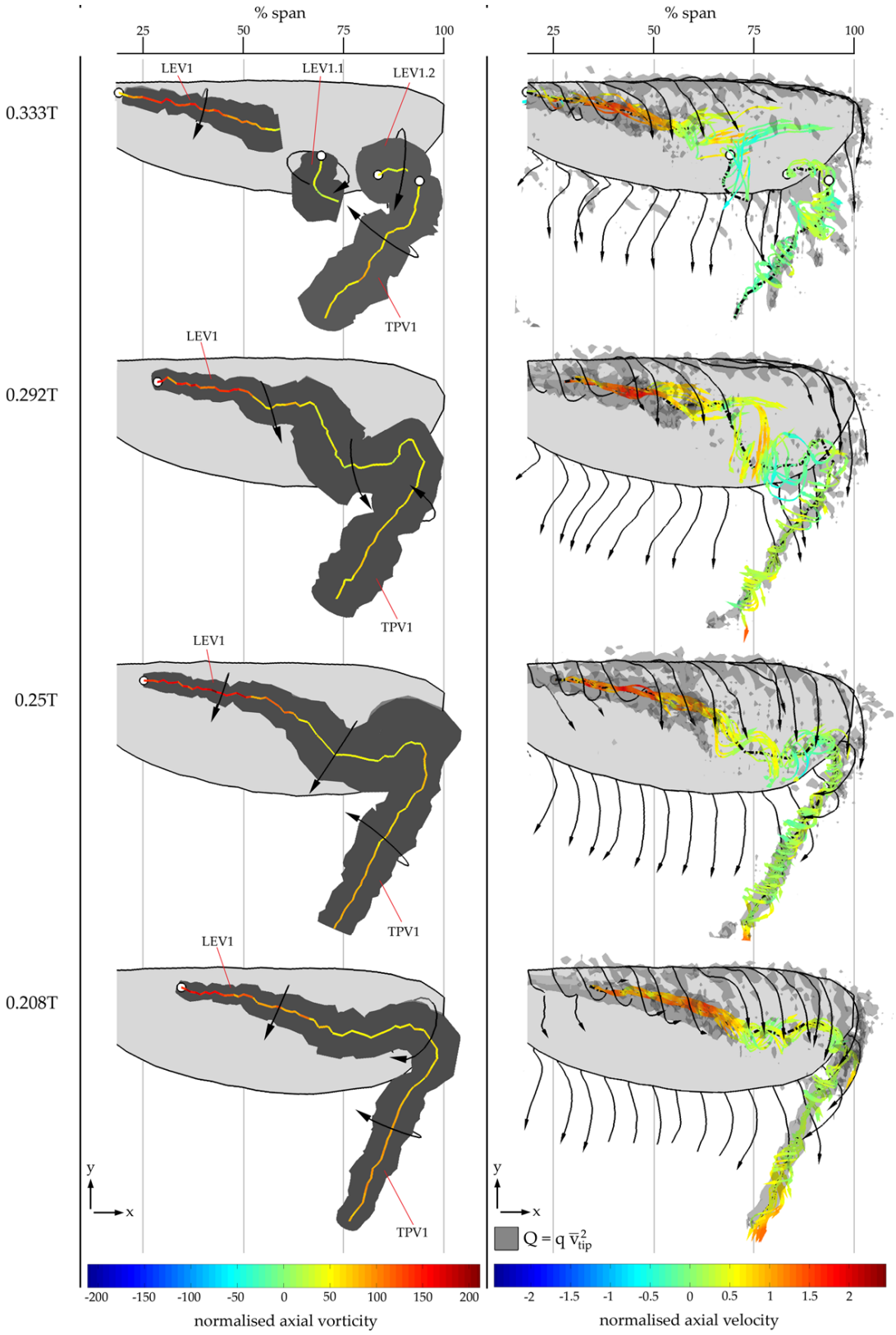

Figure F.2: Top views illustrating flow formation for the second third of a flapping half cycle; left column shows vortex core diameter (dark grey surfaces) and vortex axes coloured with axial vorticity normalised with respect to $\bar{\Omega}_{wng}$ ($79.7 rad/s$) (axes are dashed lines behind objects); right column shows instantaneous streamlines released from vortex axes coloured with axial flow normalised with respect to the mean wingtip speed ($8.4 m/s$), black streamlines released along the wing edge, and transparent grey isosurfaces of $Q = q\bar{v}^2_{tip}$ where $q \approx 8.5 \times 10^4 m^{-2}$; positive axial direction points along an axis towards the end without a white dot

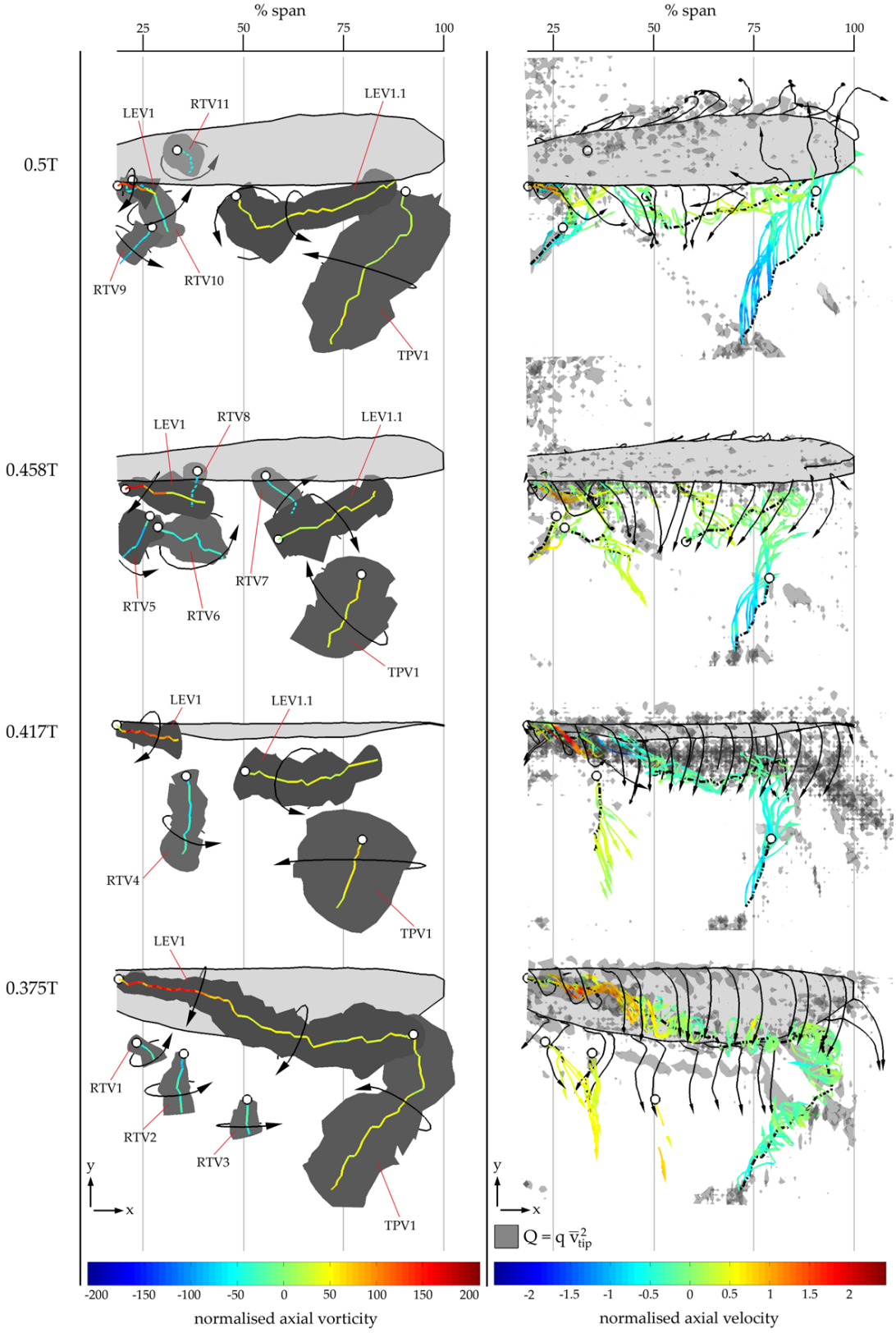

Figure F.3: Top views illustrating flow formation for the last third of a flapping half cycle; left column shows vortex core diameter (dark grey surfaces) and vortex axes coloured with axial vorticity normalised with respect to $\bar{\Omega}_{wng}$ ($79.7 rad/s$) (axes are dashed lines behind objects); right column shows instantaneous streamlines released from vortex axes coloured with axial flow normalised with respect to the mean wingtip speed ($8.4 m/s$), black streamlines released along the wing edge, and transparent grey isosurfaces of $Q = q\bar{v}^2_{tip}$ where $q \approx 8.5 \times 10^4 m^{-2}$; positive axial direction points along an axis towards the end without a white dot

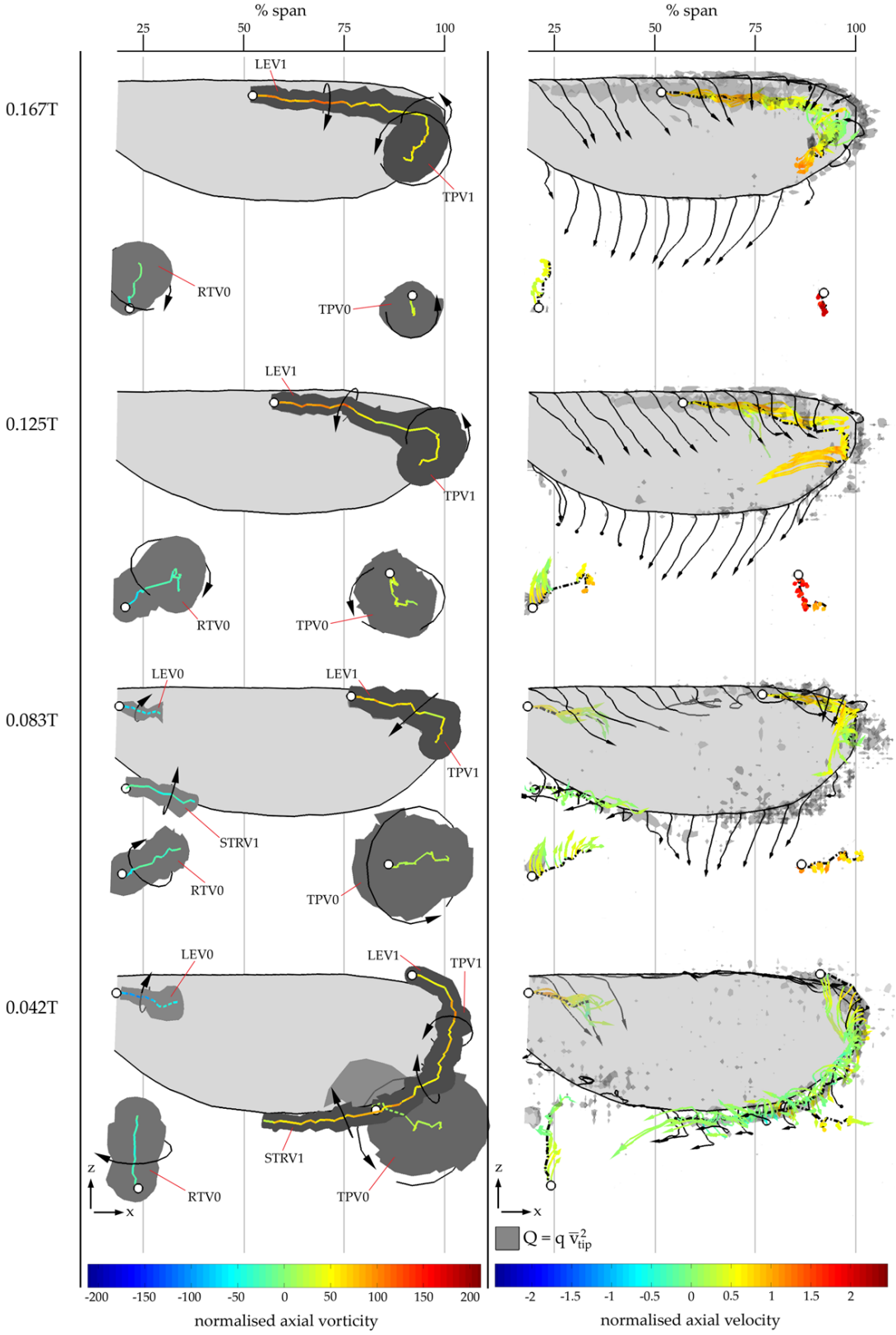

Figure F.4: Back views illustrating flow formation for the first third of a flapping half cycle; left column shows vortex core diameter (dark grey surfaces) and vortex axes coloured with axial vorticity normalised with respect to $\bar{\Omega}_{wng}$ ($79.7 rad/s$) (axes are dashed lines behind objects); right column shows instantaneous streamlines released from vortex axes coloured with axial flow normalised with respect to the mean wingtip speed ($8.4 m/s$), black streamlines released along the wing edge, and transparent grey isosurfaces of $Q = q\bar{v}^2_{tip}$ where $q \approx 8.5 \times 10^4 m^{-2}$; positive axial direction points along an axis towards the end without a white dot

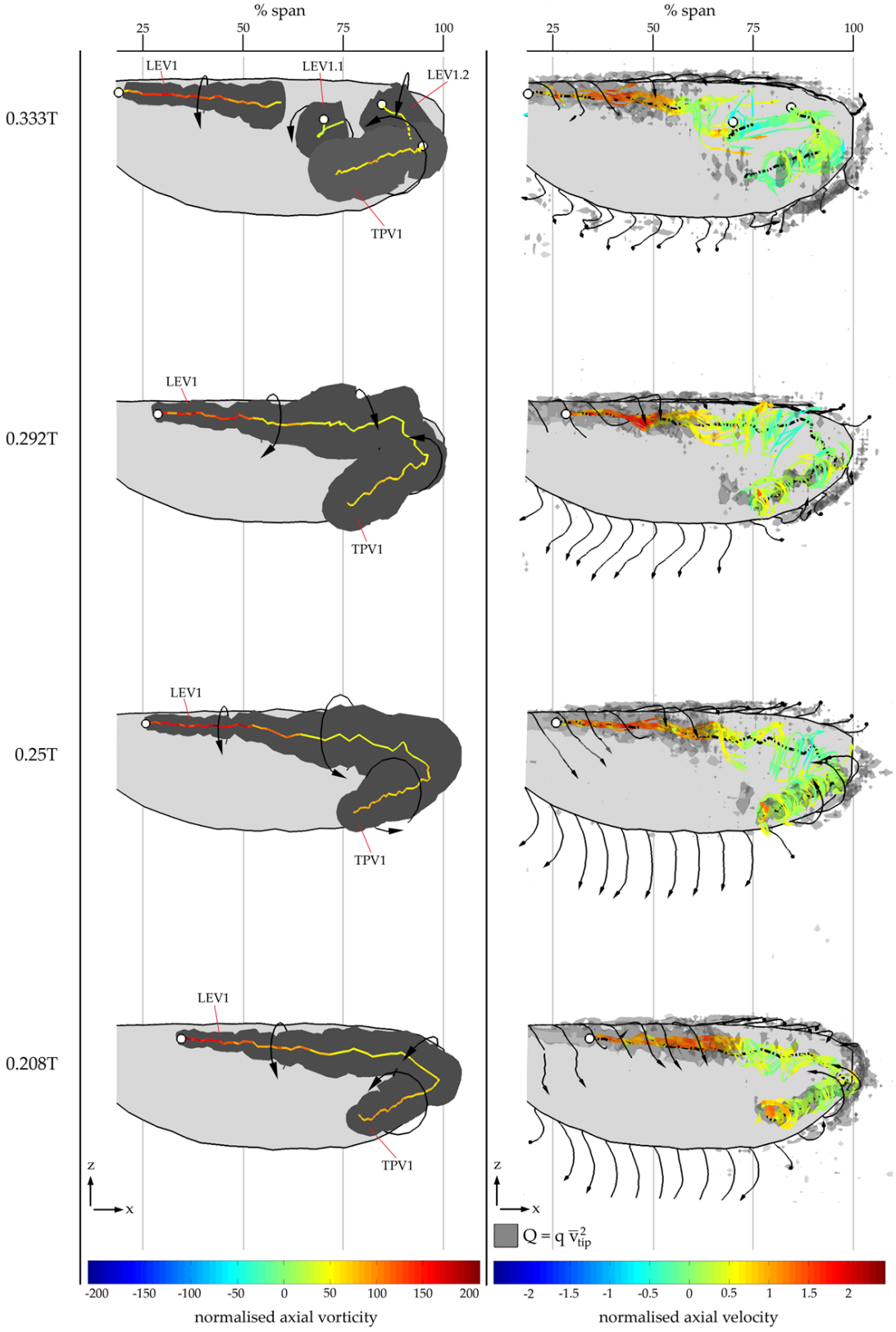

Figure F.5: Back views illustrating flow formation for the second third of a flapping half cycle; left column shows vortex core diameter (dark grey surfaces) and vortex axes coloured with axial vorticity normalised with respect to $\bar{\Omega}_{wng}$ ($79.7 rad/s$) (axes are dashed lines behind objects); right column shows instantaneous streamlines released from vortex axes coloured with axial flow normalised with respect to the mean wingtip speed ($8.4 m/s$), black streamlines released along the wing edge, and transparent grey isosurfaces of $Q = q\bar{v}^2_{tip}$ where $q \approx 8.5 \times 10^4 m^{-2}$; positive axial direction points along an axis towards the end without a white dot

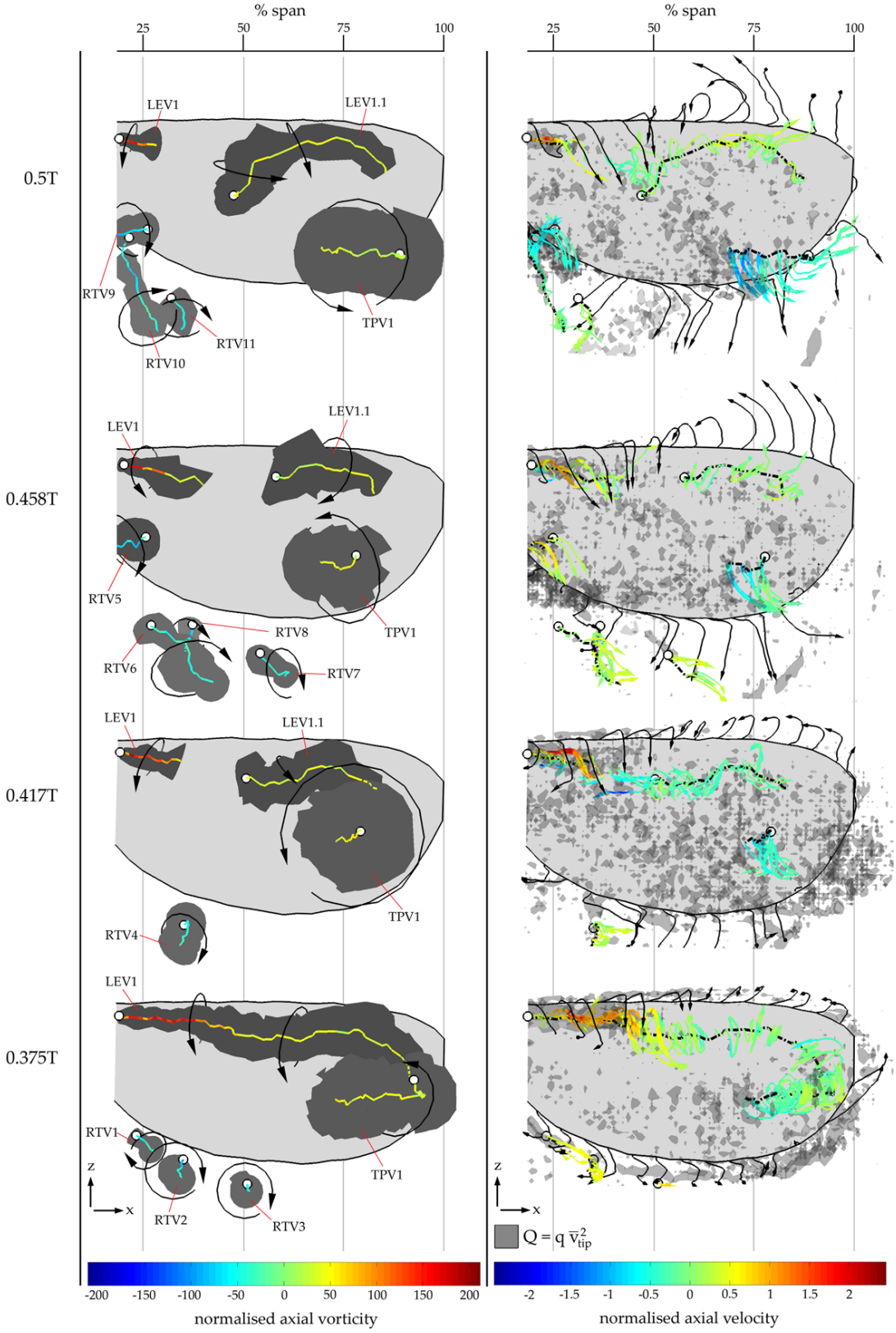

Figure F.6: Back views illustrating flow formation for the last third of a flapping half cycle; left column shows vortex core diameter (dark grey surfaces) and vortex axes coloured with axial vorticity normalised with respect to $\bar{\Omega}_{wng}$ $(79.7 rad/s)$ (axes are dashed lines behind objects); right column shows instantaneous streamlines released from vortex axes coloured with axial flow normalised with respect to the mean wingtip speed $(8.4 m/s)$, black streamlines released along the wing edge, and transparent grey isosurfaces of $Q = q\bar{v}^2_{tip}$ where $q \approx 8.5 \times 10^4 m^{-2}$; positive axial direction points along an axis towards the end without a white dot

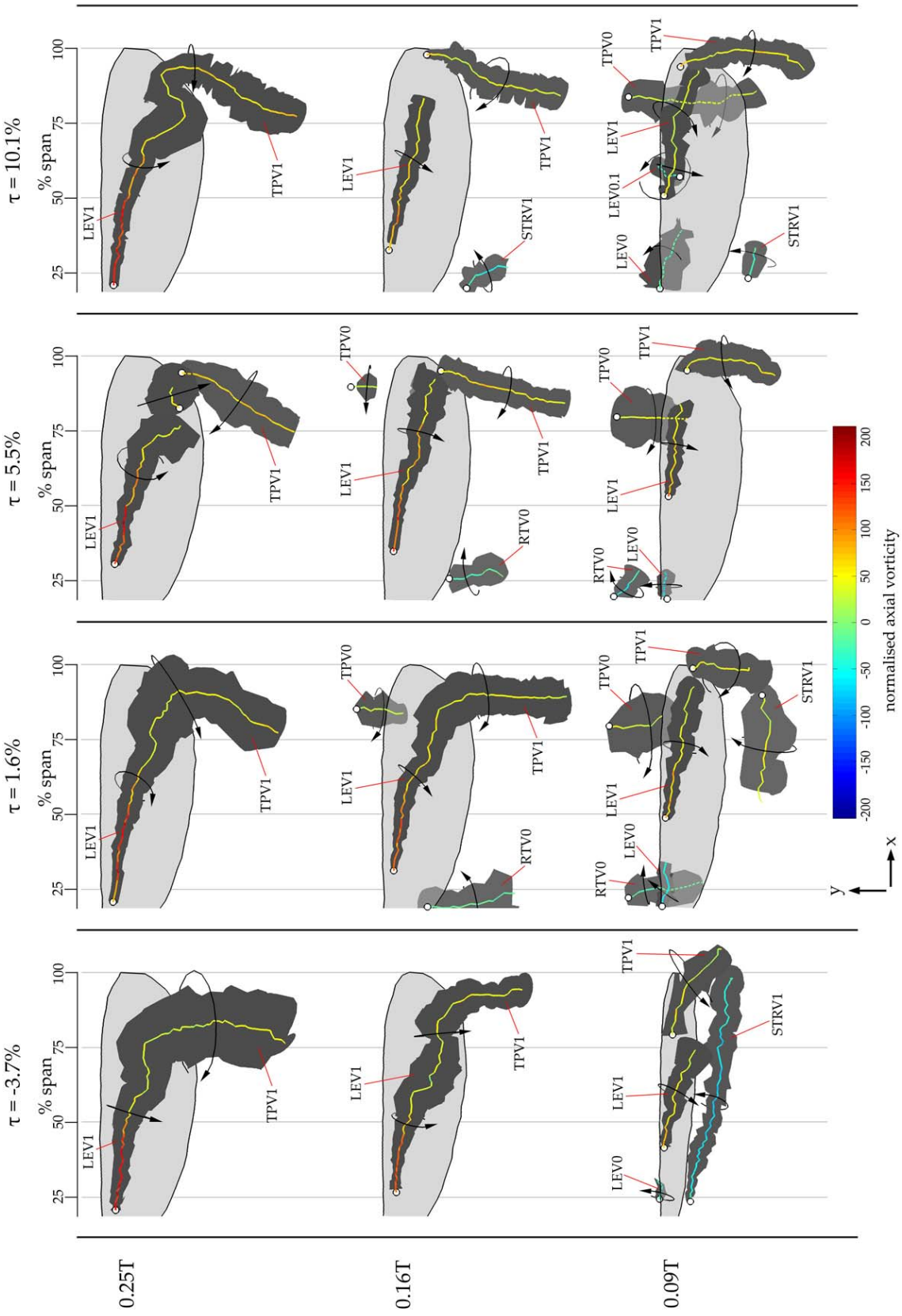

Figure F.7: Top views illustrating flow formation for the first half of a flapping half cycle for four rotation phases: $\tau = -3.7\%, 1.6\%, 5.5\%, 10.1\%$; vortex core diameter (dark grey surfaces) shown with vortex axes coloured with axial vorticity normalised with respect to $\bar{\Omega}_{wng}$ ($91.7 rad/s$) (axes are dashed lines behind objects); positive axial direction points along an axis towards the end without a white dot

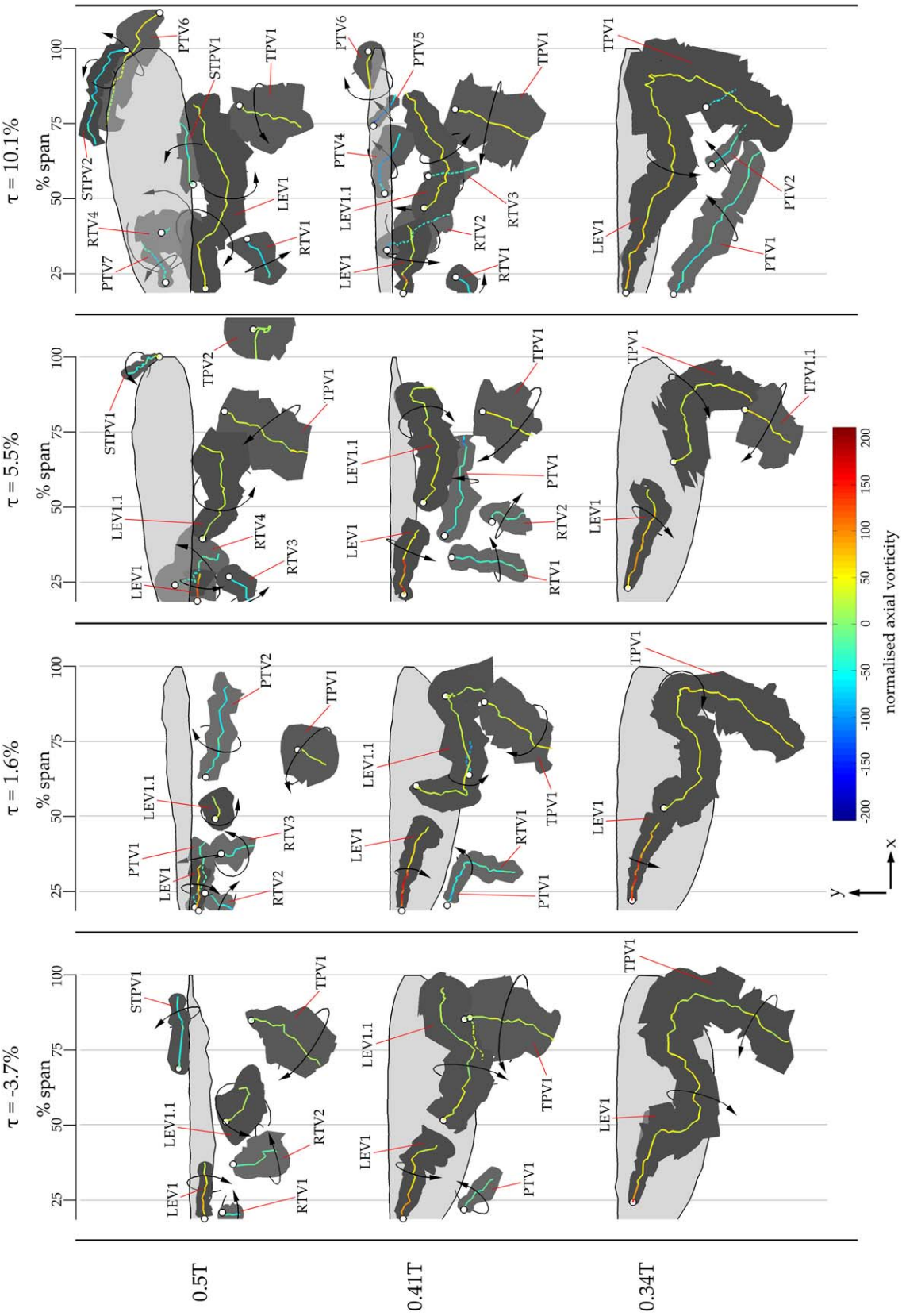

Figure F.8: Top views illustrating flow formation for the second half of a flapping half cycle for four rotation phases: $\tau = -3.7\%, 1.6\%, 5.5\%, 10.1\%$; vortex core diameter (dark grey surfaces) shown with vortex axes coloured with axial vorticity normalised with respect to $\bar{\Omega}_{wng}$ ($91.7 rad/s$) (axes are dashed lines behind objects); positive axial direction points along an axis towards the end without a white dot

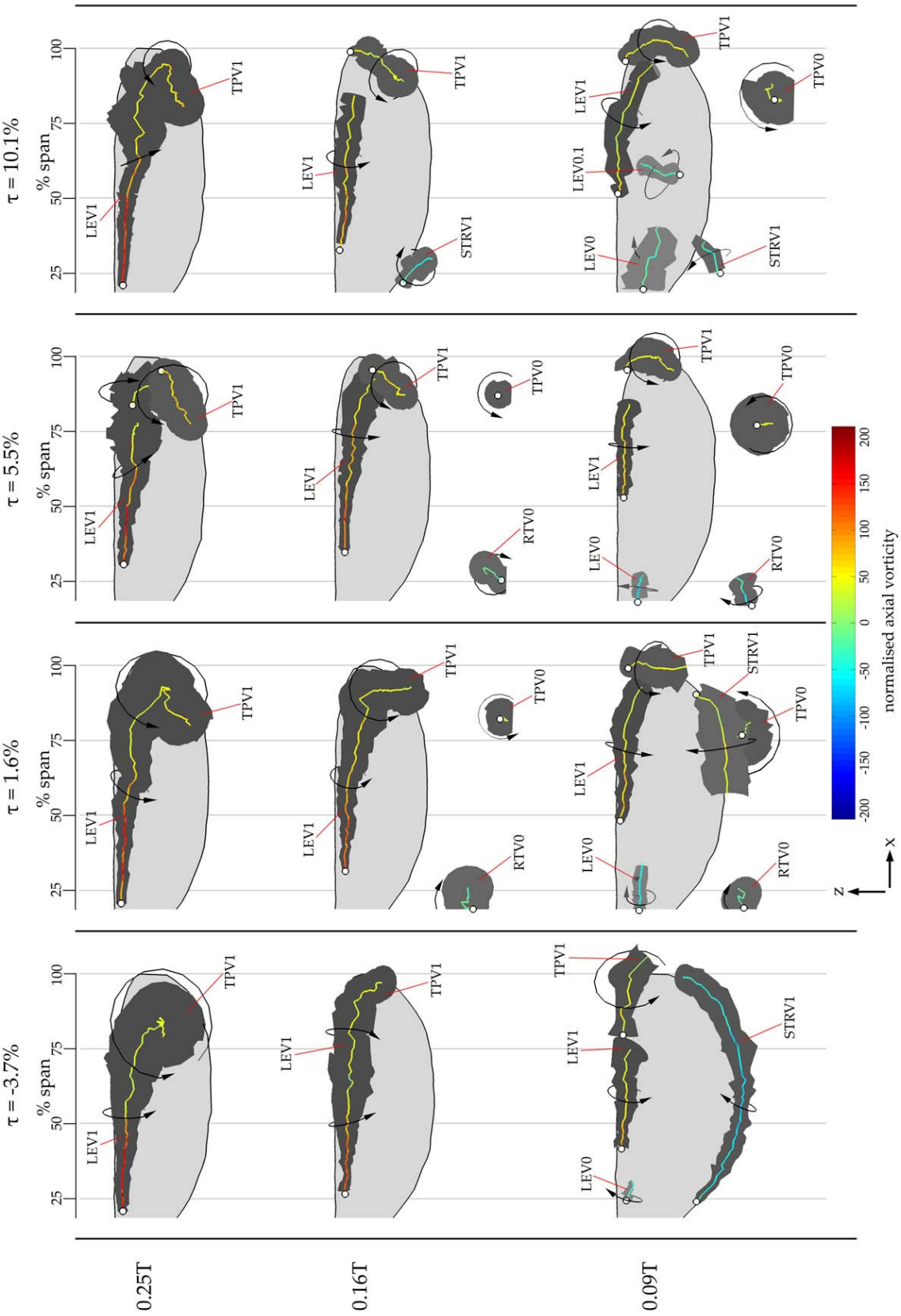

Figure F.9: Back views illustrating flow formation for the first half of a flapping half cycle for four rotation phases: $\tau = -3.7\%, 1.6\%, 5.5\%, 10.1\%$; vortex core diameter (dark grey surfaces) shown with vortex axes coloured with axial vorticity normalised with respect to $\bar{\Omega}_{wng}$ ($91.7 rad/s$) (axes are dashed lines behind objects); positive axial direction points along an axis towards the end without a white dot

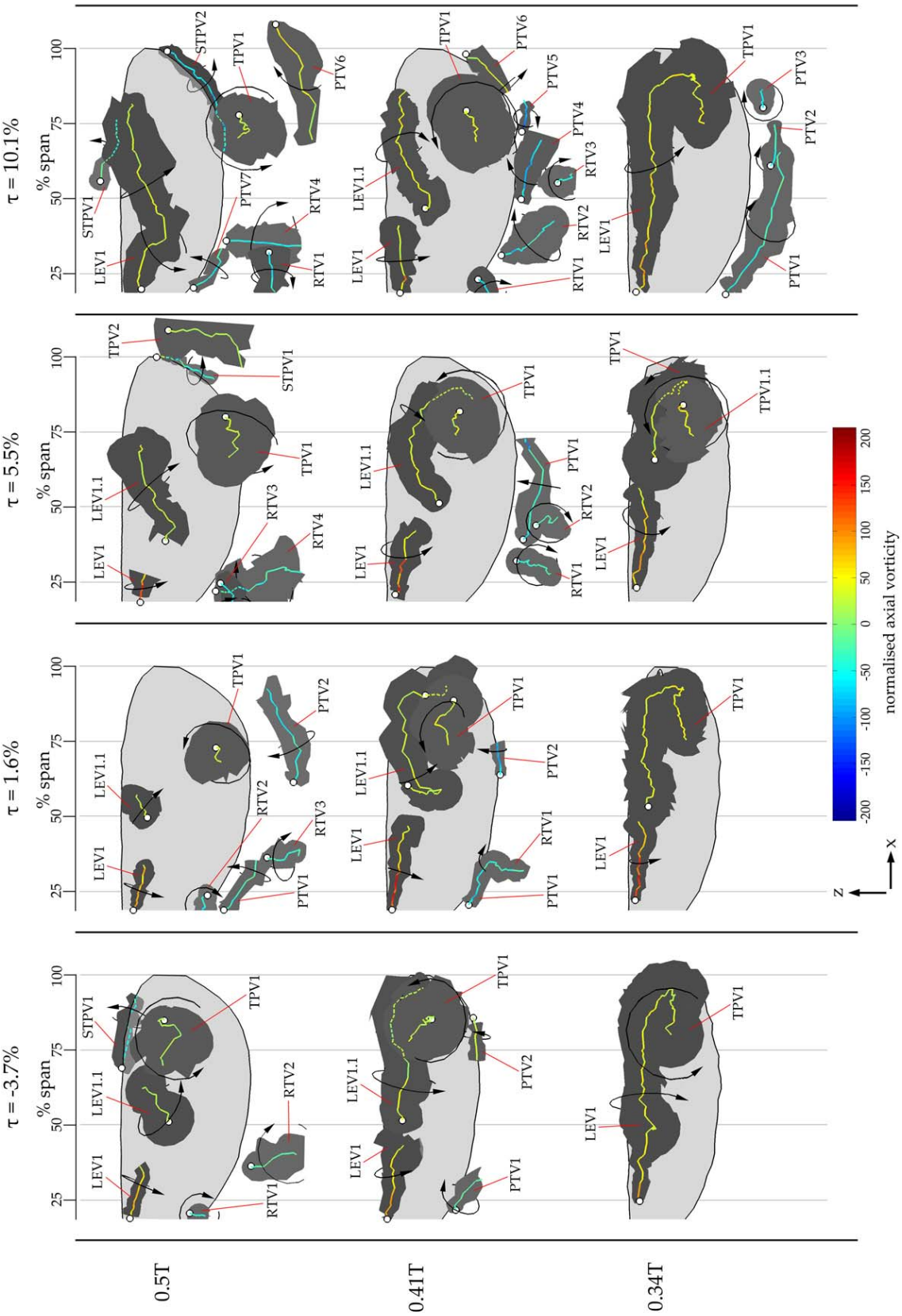

Figure F.10: Back views illustrating flow formation for the second half of a flapping half cycle for four rotation phases: $\tau = -3.7\%, 1.6\%, 5.5\%, 10.1\%$; vortex core diameter (dark grey surfaces) shown with vortex axes coloured with axial vorticity normalised with respect to $\bar{\Omega}_{wng}$ $(91.7 rad/s)$ (axes are dashed lines behind objects); positive axial direction points along an axis towards the end without a white dot

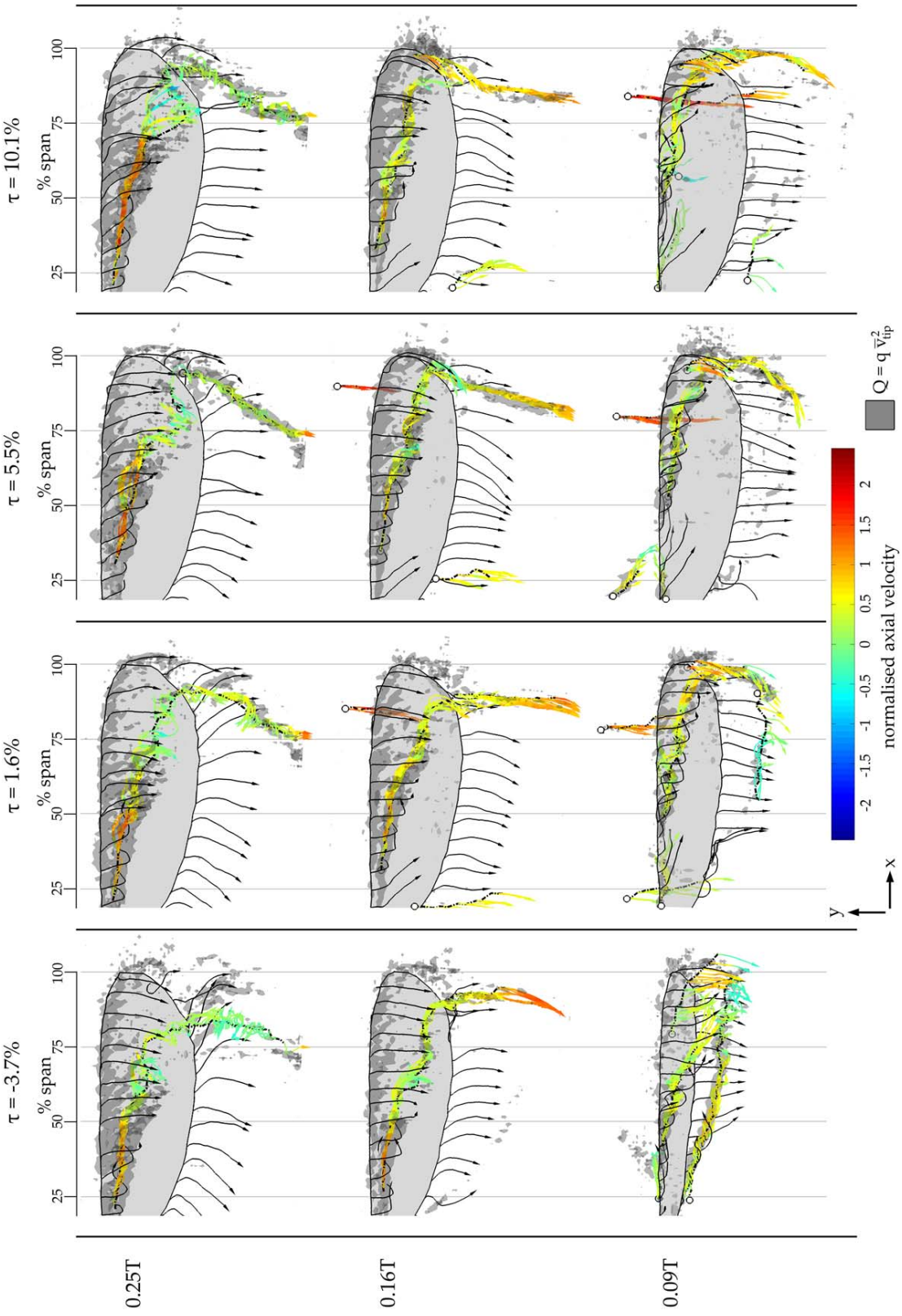

Figure F.11: Top views illustrating flow formation for the first half of a flapping half cycle for four rotation phases: $\tau = -3.7\%, 1.6\%, 5.5\%, 10.1\%$; instantaneous streamlines released from vortex axes coloured with axial velocity normalised with respect to the mean wingtip speed ($9.7m/s$); black streamlines are released along wing edge; transparent grey isosurfaces indicate areas where $Q = q\bar{v}_{tip}^2$ where $q \approx 8.5 \times 10^4 m^{-2}$; positive axial direction points along an axis towards the end without a white dot

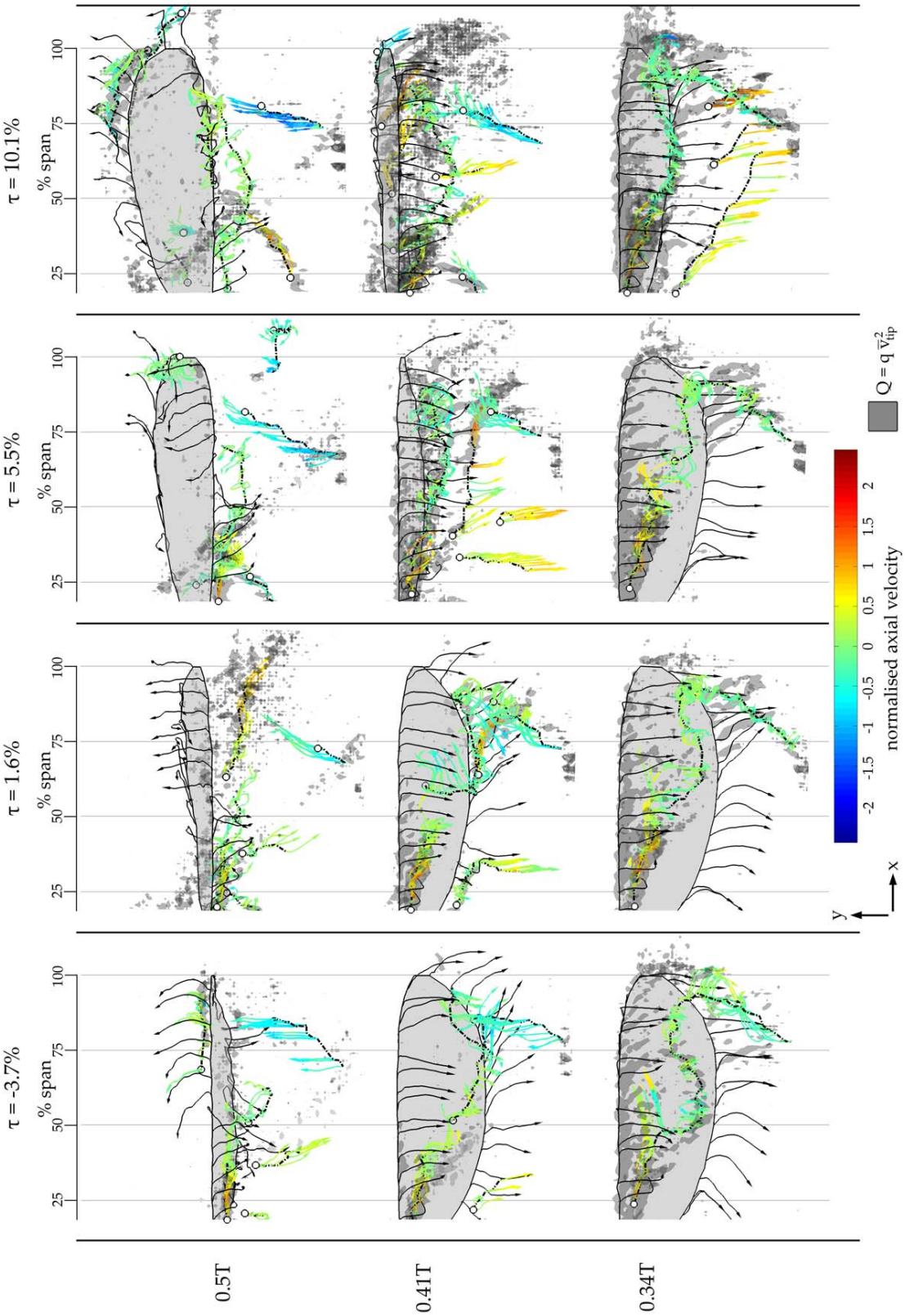

Figure F.12: Top views illustrating flow formation for the second half of a flapping half cycle for four rotation phases: $\tau = -3.7\%, 1.6\%, 5.5\%, 10.1\%$; instantaneous streamlines released from vortex axes coloured with axial velocity normalised with respect to the mean wingtip speed ($9.7m/s$); black streamlines are released along wing edge; transparent grey isosurfaces indicate areas where $Q = q\bar{v}_{tip}^2$ where $q \approx 8.5 \times 10^4 m^{-2}$; positive axial direction points along an axis towards the end without a white dot

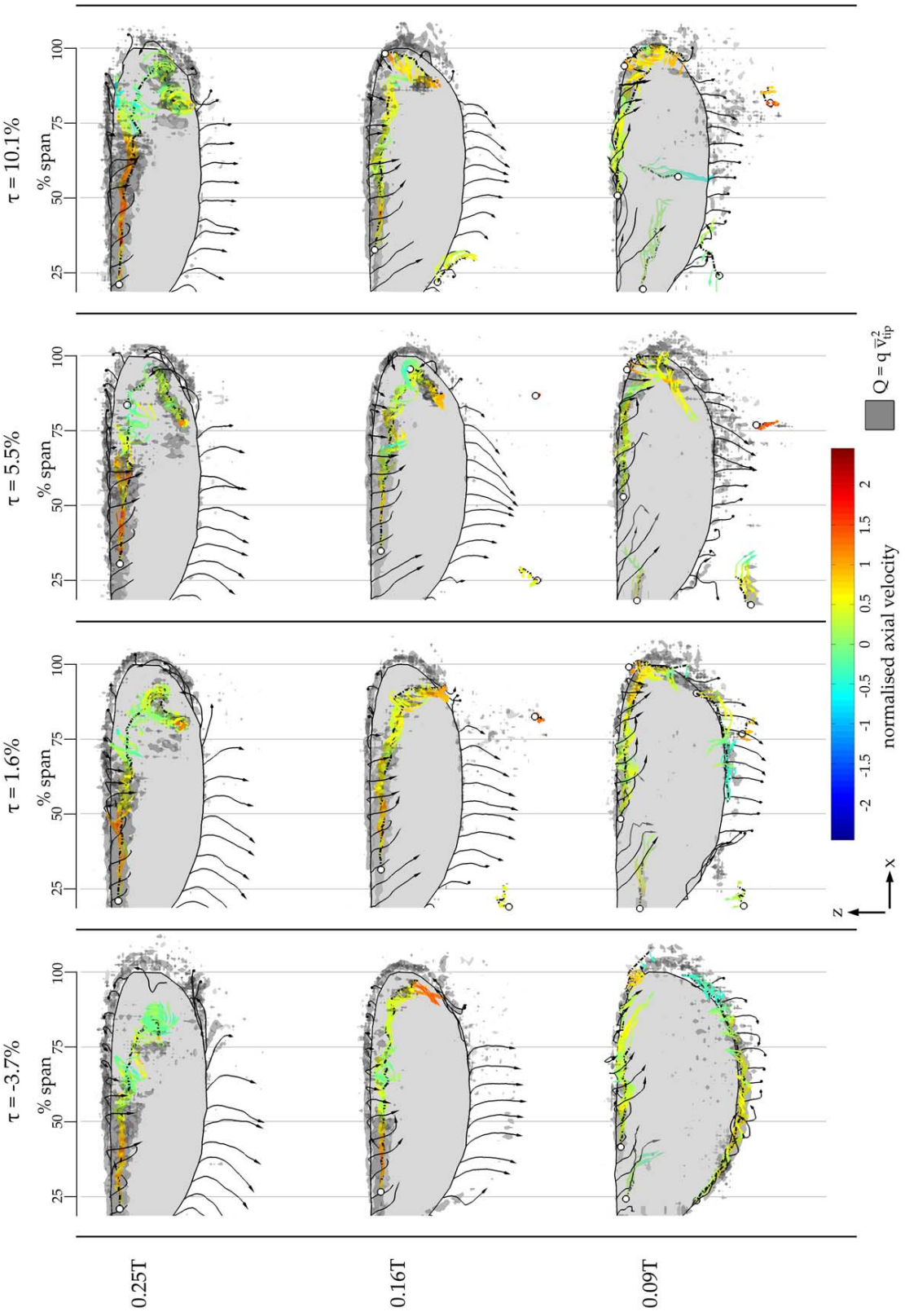

Figure F.13: Back views illustrating flow formation for the first half of a flapping half cycle for four rotation phases: $\tau = -3.7\%, 1.6\%, 5.5\%, 10.1\%$; instantaneous streamlines released from vortex axes coloured with axial velocity normalised with respect to the mean wingtip speed ($9.7m/s$); black streamlines are released along wing edge; transparent grey isosurfaces indicate areas where $Q = q\bar{v}_{tip}^2$ where $q \approx 8.5 \times 10^4 m^{-2}$; positive axial direction points along an axis towards the end without a white dot

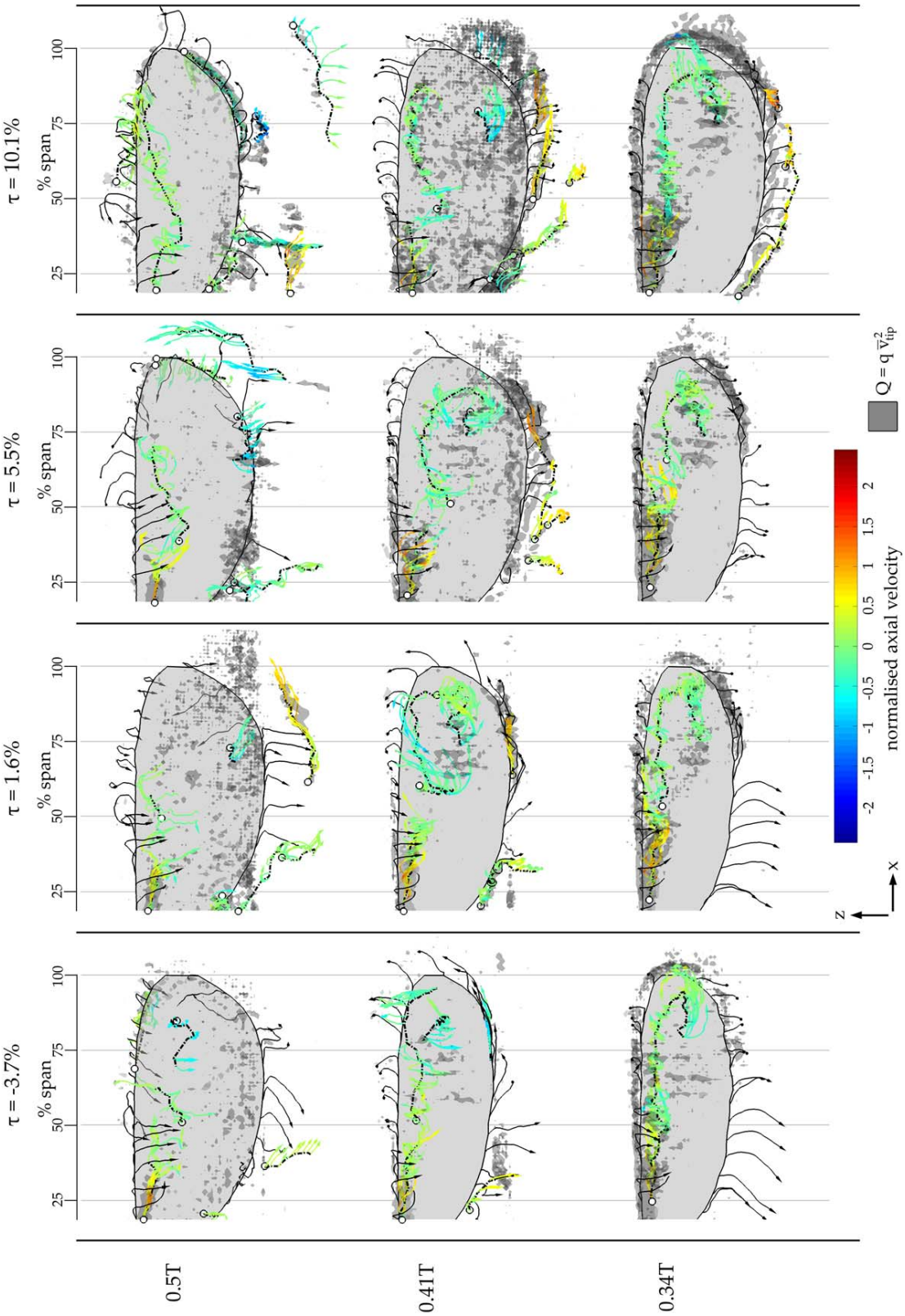

Figure F.14: Back views illustrating flow formation for the second half of a flapping half cycle for four rotation phases: $\tau = -3.7\%, 1.6\%, 5.5\%, 10.1\%$; instantaneous streamlines released from vortex axes coloured with axial velocity normalised with respect to the mean wingtip speed ($9.7m/s$); black streamlines are released along wing edge; transparent grey isosurfaces indicate areas where $Q = q\bar{v}_{tip}^2$ where $q \approx 8.5\times10^4 m^{-2}$; positive axial direction points along an axis towards the end without a white dot

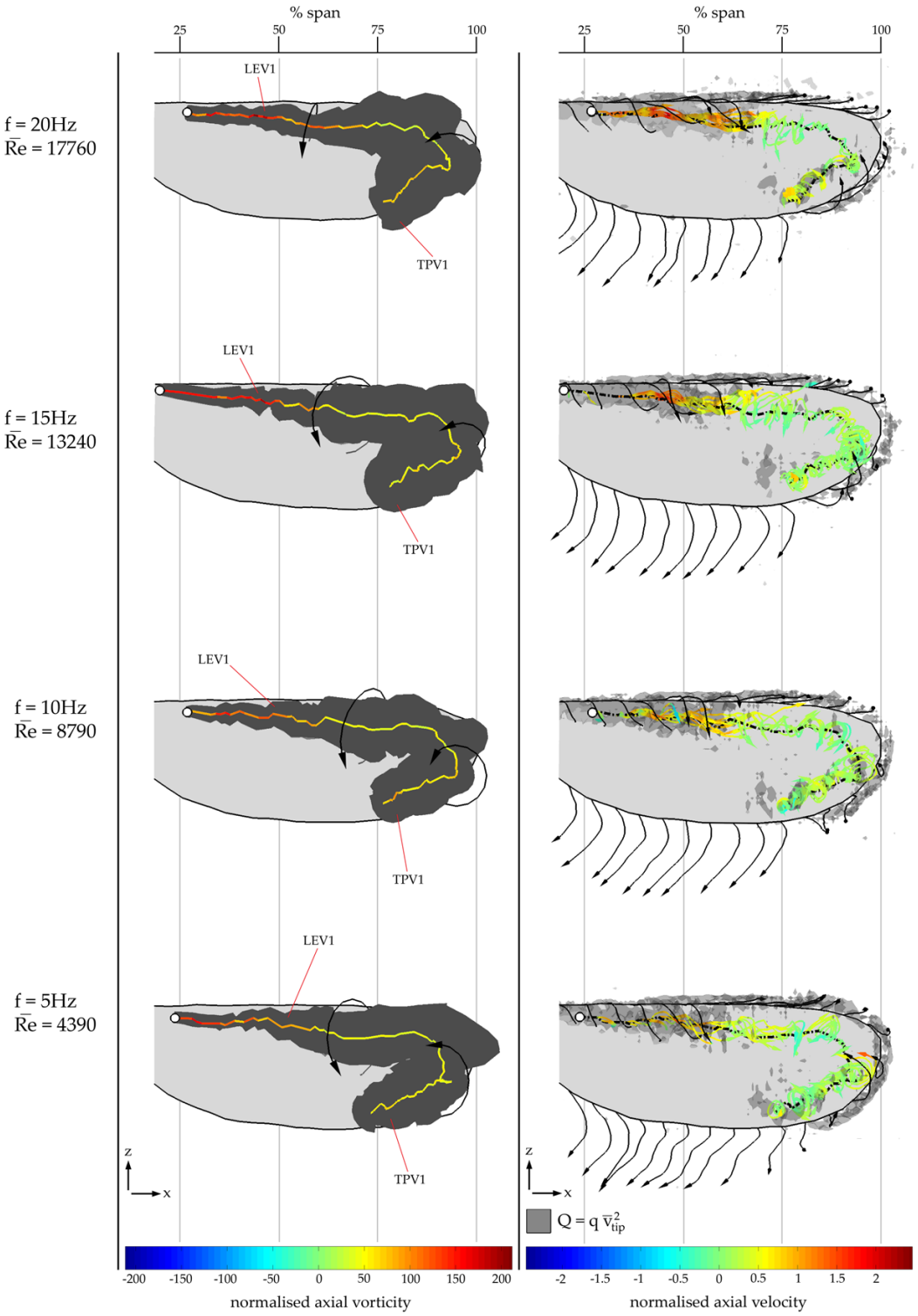

Figure F.15: Back views illustrating flow formation at mid-stroke for test cases with varying f ($\bar{Re}$) and constant Φ; left column shows vortex core diameter (dark grey surfaces) and vortex axes coloured with axial vorticity normalised with respect to $\bar{\Omega}_{wng}$ (23.1, 46.2, 69.6, 93.2rad/s); vortex axes become dashed when behind other objects; right column shows instantaneous streamlines released from vortex axes coloured with axial velocity normalised with respect to $\bar{v}_{tip}$ (2.4, 4.9, 7.4, 9.9m/s), black streamlines released along the wing edge, and transparent grey isosurfaces of $Q = q\bar{v}_{tip}^2$ where $q \approx 8.5 \times 10^4 m^{-2}$; positive axial direction points along an axis towards the end without a white dot

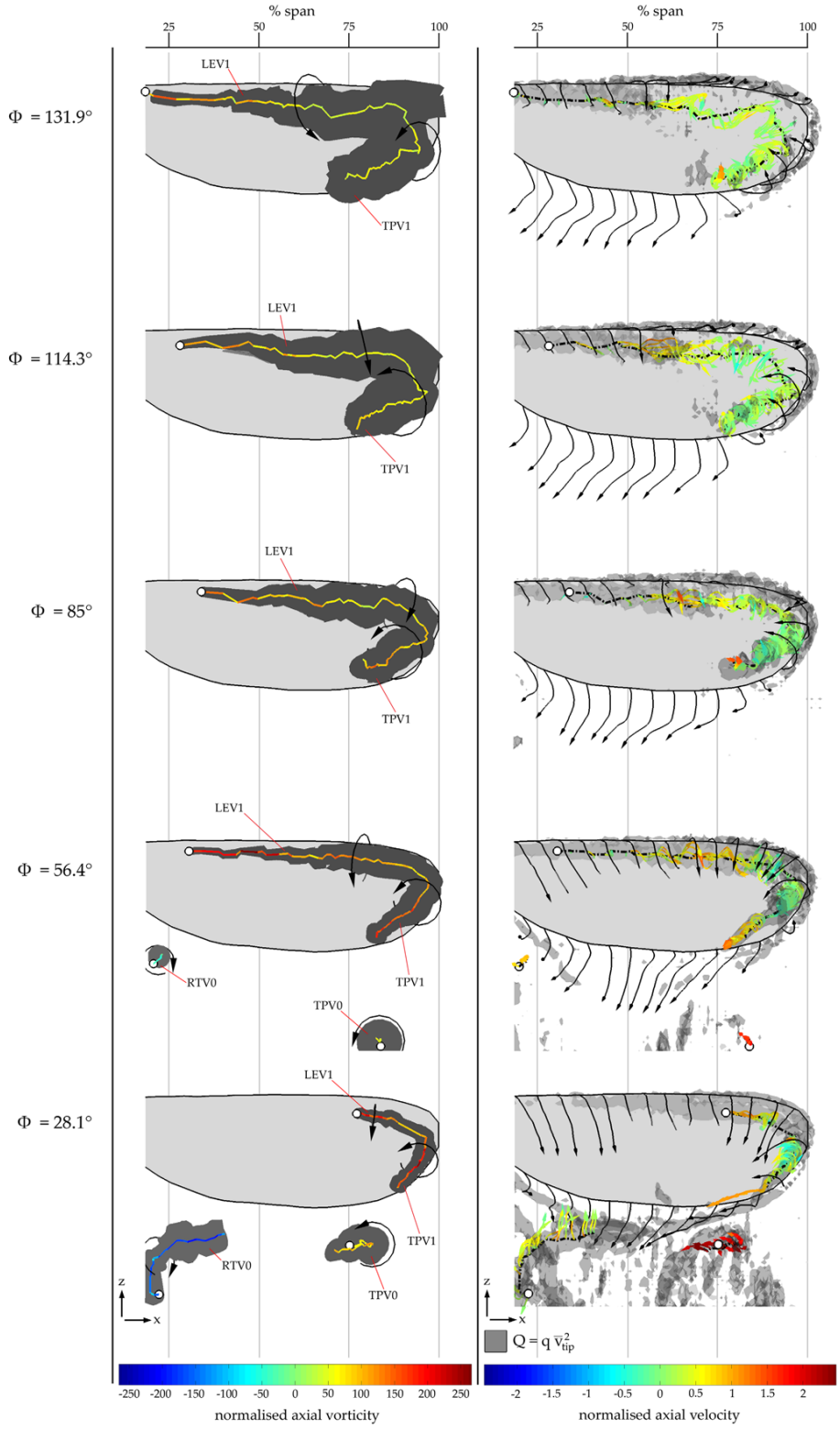

Figure F.16: Back views illustrating flow formation at mid-stroke for test cases with varying Φ and constant $\bar{R}e$; left column shows vortex core diameter (dark grey surfaces) and vortex axes coloured with axial vorticity normalised with respect to $\bar{\Omega}_{wng}$ $(19.8 rad/s)$; vortex axes become dashed when behind other objects; right column shows instantaneous streamlines released from vortex axes coloured with axial velocity normalised with respect to $\bar{v}_{tip}$ $(2.1 m/s)$, black streamlines released along the wing edge, and transparent grey isosurfaces of $Q = q\bar{v}^2_{tip}$ where $q \approx 8.5 \times 10^4 m^{-2}$; positive axial direction points along an axis towards the end without a white dot

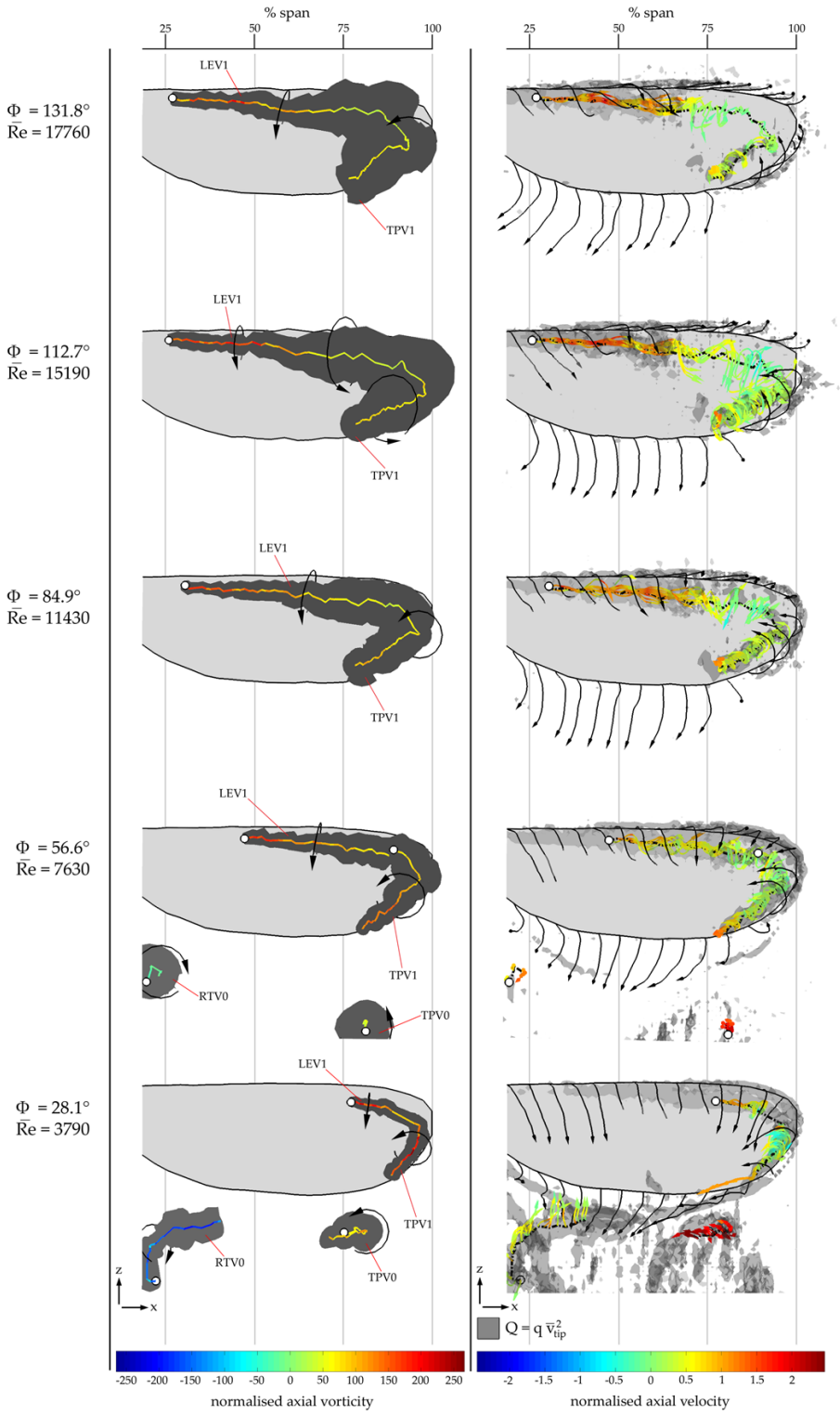

Figure F.17: Back views illustrating flow formation at mid-stroke for test cases with varying Φ and constant f; left column shows vortex core diameter (dark grey surfaces) and vortex axes coloured with axial vorticity normalised with respect to $\bar{\Omega}_{wng}$ (19.8, 40, 60, 79.7, 93.2rad/s); vortex axes become dashed behind other objects; right column shows instantaneous streamlines released from vortex axes coloured with axial velocity normalised with respect to $\bar{v}_{tip}$ (2.1, 4.2, 6.4, 8.4, 9.9m/s), black streamlines released along the wing edge, and transparent grey isosurfaces of $Q = q\bar{v}_{tip}^2$ where $q \approx 8.5 \times 10^4 m^{-2}$; positive axial direction points along an axis towards the end without a white dot

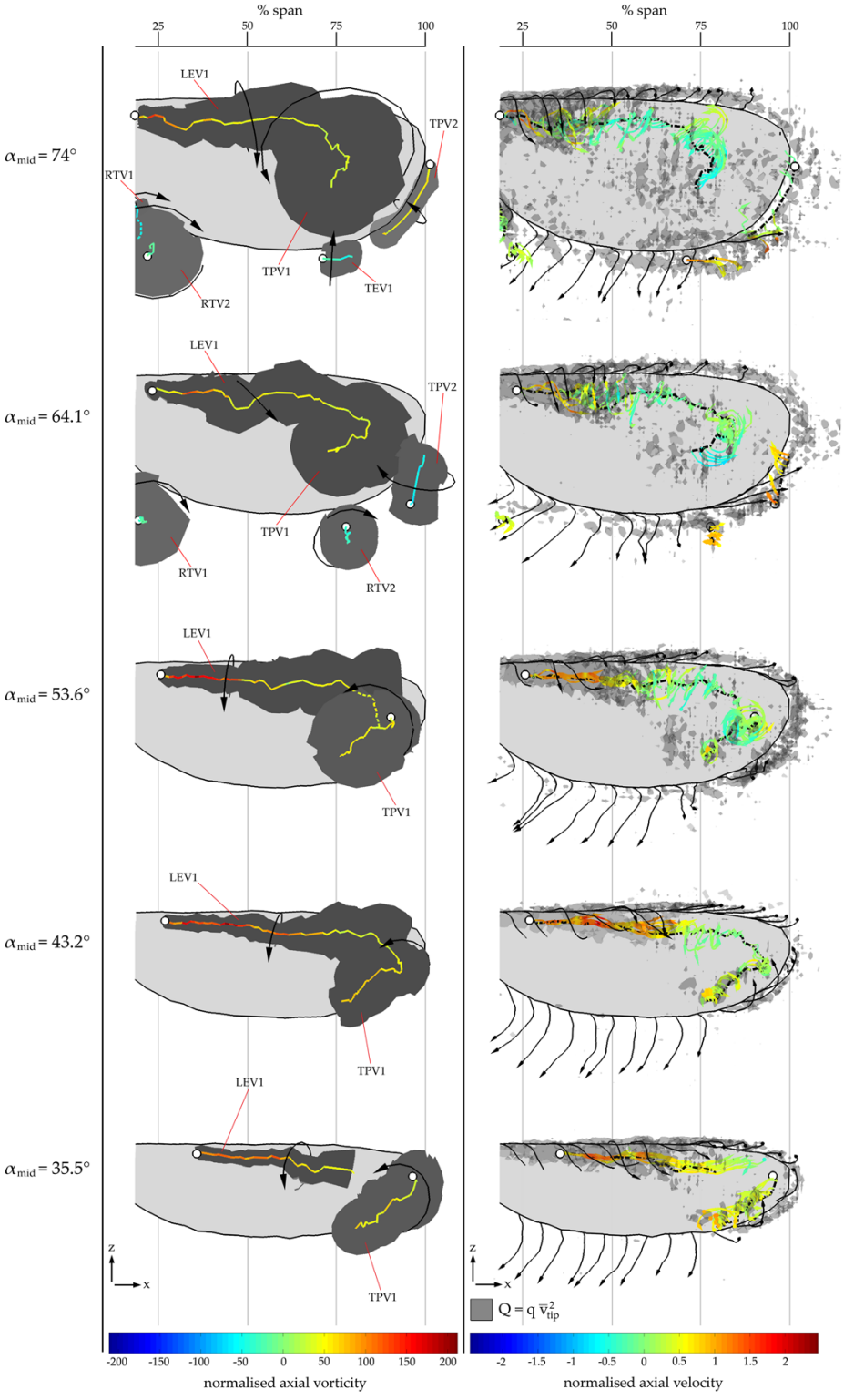

Figure F.18: Back views illustrating flow formation at mid-stroke for test cases with varying α_{mid}; left column shows vortex core diameter (dark grey surfaces) and vortex axes coloured with axial vorticity normalised with respect to $\bar{\Omega}_{wng}$ ($92.9 rad/s$); vortex axes become dashed behind other objects; right column shows instantaneous streamlines released from vortex axes coloured with axial velocity normalised with respect to $\bar{v}_{tip}$ ($9.7 m/s$), black streamlines released along the wing edge, and transparent grey isosurfaces of $Q = q\bar{v}_{tip}^2$ where $q \approx 8.5 \times 10^4 m^{-2}$; positive axial direction points along an axis towards the end without a white dot

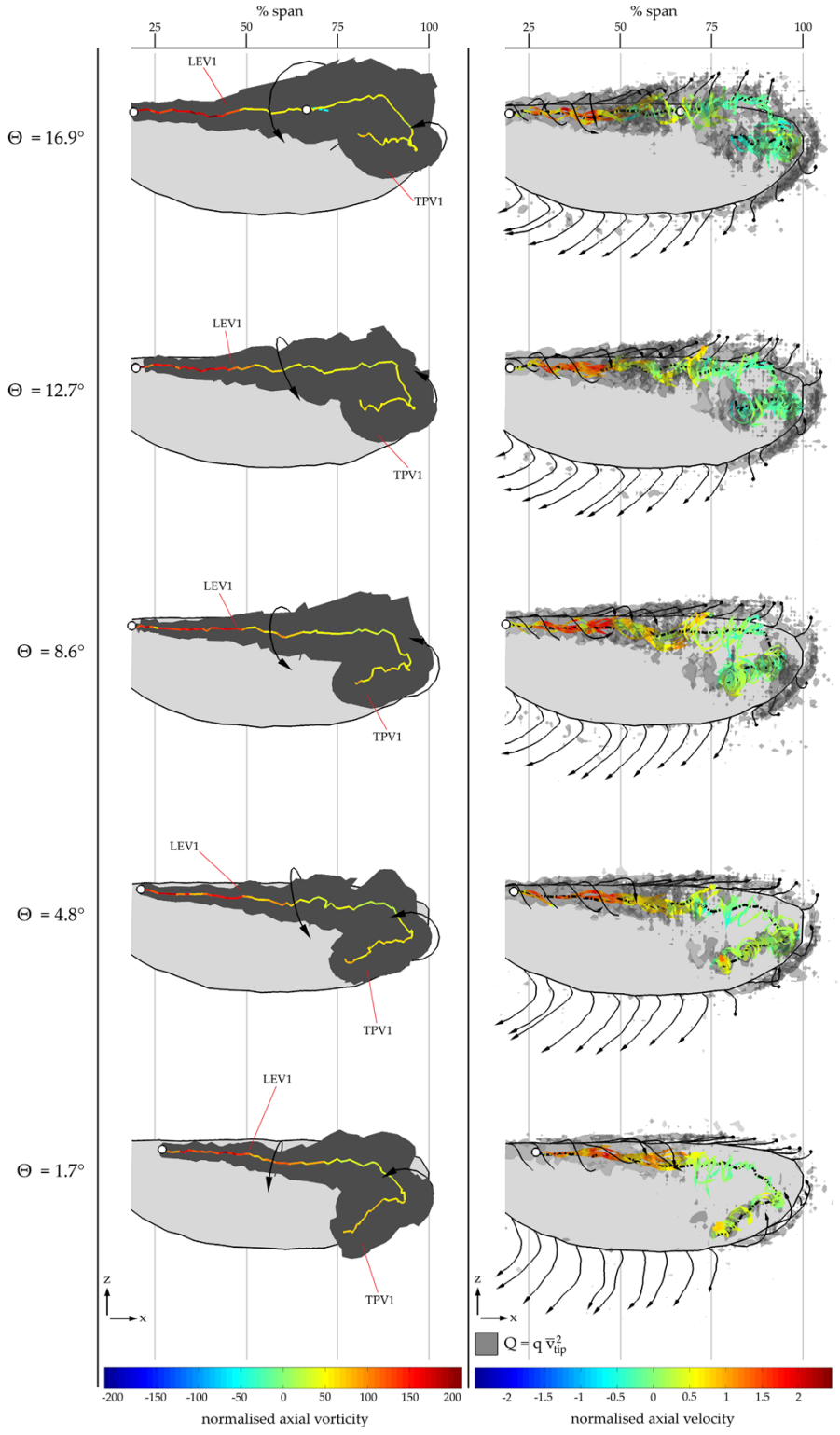

Figure F.19: Back views illustrating flow formation at mid-stroke for test cases with varying Θ with figure-of-eight kinematics; left column shows vortex core diameter (dark grey surfaces) and vortex axes coloured with axial vorticity normalised with respect to $\bar{\Omega}_{wng}$ (93.2, 94, 95.2, 97, 99rad/s); vortex axes become dashed behind other objects; right column shows instantaneous streamlines released from vortex axes coloured with axial velocity normalised with respect to $\bar{v}_{tip}$ (9.9, 9.9, 10.1, 10.3, 10.5m/s), black streamlines released along the wing edge, and transparent grey isosurfaces of $Q = q\bar{v}_{tip}^2$ where $q \approx 8.5 \times 10^4 m^{-2}$; positive axial direction points along an axis towards the end without a white dot

Appendix G

Navier-Stokes Equations for Flapping Flight

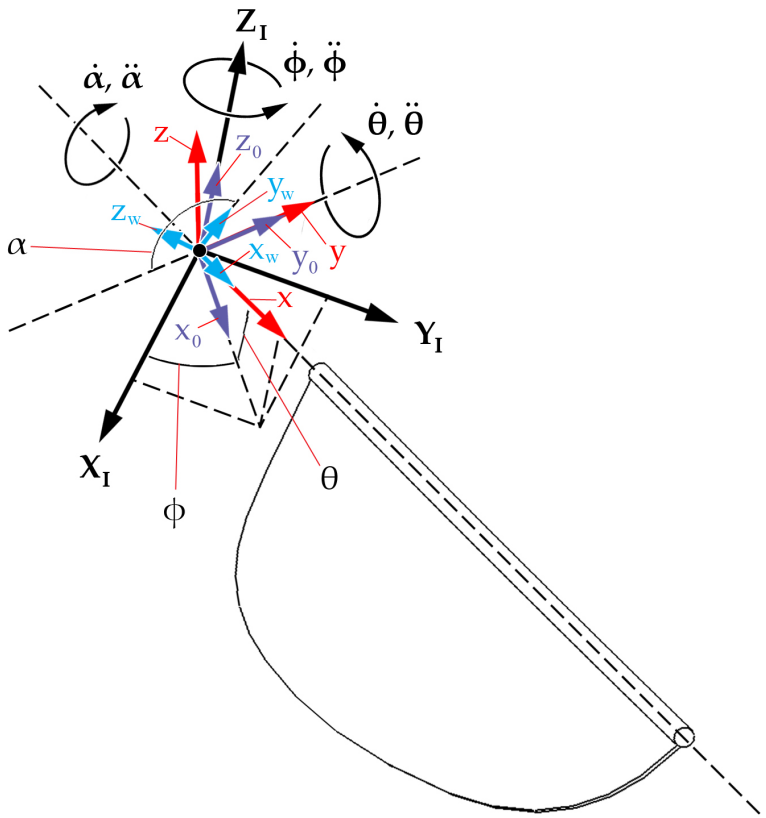

Figure G.1: Coordinate systems defining wing position

By their nature, flapping wings rotate back and forth about a centre of rotation in producing their flapping motion. This means that when the flow is viewed with respect to the wing, we are looking at it in a rotating frame of reference rather than an inertial (fixed) frame. In fact, such a frame of reference is not only rotating, but is also accelerating due to the fact that flapping wings constantly accelerate and decelerate. When viewing in a frame that rotates with a finite angular velocity and angular acceleration, extra terms arise in the Navier-Stokes equations which do not exist when viewing in an inertial frame. These extra terms will be derived here, using the derivation of the equations of motion in a rotating

frame of reference with a constant angular velocity (no angular acceleration) given in Kundu & Cohen (2008), which has been extended here for a frame that has a finite angular acceleration. Following this, expressions for these terms as a function of instantaneous kinematic parameters will be derived.

First consider the set of coordinate systems in Figure G.1. This is the same set of coordinate systems given in Figure 2.4 in § 2.1.2 (page 17), but with the addition of another coordinate system x_0, y_0, z_0. Here, the $x_0y_0z_0$ frame rotates about the Z_I axis by the stroke angle ϕ, the xyz frame rotates about the $-y_0$ axis by the plunge angle θ, and lastly the $x_wy_wz_w$ frame rotates about the $-x$ axis by the pitch angle α. The $x_wy_wz_w$ frame is fixed to the wing, and thus is the frame in which the equations of motion will be derived. In addition, all origins are placed at the centre of rotation.

We first define a vector $\mathbf{A}$ in the x_w, y_w, z_w frame:

$$\mathbf{A} = A_{xw}\mathbf{i}_w + A_{yw}\mathbf{j}_w + A_{zw}\mathbf{k}_w \tag{G.1}$$

Taking the time derivative gives:

$$(\dot{\mathbf{A}})_I = \dot{A}_{xw}\mathbf{i}_w + \dot{A}_{yw}\mathbf{j}_w + \dot{A}_{zw}\mathbf{k}_w + A_{xw}\dot{\mathbf{i}}_w + A_{yw}\dot{\mathbf{j}}_w + A_{zw}\dot{\mathbf{k}}_w \tag{G.2}$$

Here the subscript I denotes with respect to the inertial frame. The first half of Equation G.2 ($\dot{A}_{xw}\mathbf{i}_w + \dot{A}_{yw}\mathbf{j}_w + \dot{A}_{zw}\mathbf{k}_w$) is equal to $(\dot{\mathbf{A}})_w$ which is the rate of change of vector $\mathbf{A}$ with respect to the rotating frame $x_wy_wz_w$ (indicated by the subscript w). As for the second half of Equation G.2, the derivatives of the unit direction vectors are simply the cross products of the angular velocity vector of the $x_wy_wz_w$ frame Ω_w with the respective unit direction vectors (ie $\dot{\mathbf{i}}_w = \Omega_w \times \mathbf{i}_w$). Thus, the second half of Equation G.2 ($A_{xw}\dot{\mathbf{i}}_w + A_{yw}\dot{\mathbf{j}}_w + A_{zw}\dot{\mathbf{k}}_w$) is equal to $A_{xw}\Omega_w \times \mathbf{i}_w + A_{yw}\Omega_w \times \mathbf{j}_w + A_{zw}\Omega_w \times \mathbf{k}_w$ which itself is simply $\Omega_w \times \mathbf{A}$. Therefore Equation G.2 becomes:

$$(\dot{\mathbf{A}})_I = (\dot{\mathbf{A}})_w + \boldsymbol{\Omega}_w \times \mathbf{A} \tag{G.3}$$

Now substituting $\mathbf{A}$ with a position vector $\mathbf{r}$, gives an expression relating the velocity in an inertial frame to velocity in a frame rotating by the angular velocity Ω_w:

$$(\mathbf{v})_I = (\mathbf{v})_w + \boldsymbol{\Omega}_w \times \mathbf{r} \tag{G.4}$$

The time derivative of $(\mathbf{v})_I$ can be obtained by substituting $\mathbf{A}$ with $(\mathbf{v})_I$ in Equation G.3 to obtain:

$$(\dot{(\mathbf{v})_I})_I = (\dot{(\mathbf{v})_I})_w + \boldsymbol{\Omega}_w \times (\mathbf{v})_I \tag{G.5}$$

Substituting in Equation G.4:

$$(\mathbf{a})_I = \frac{d}{dt}((\mathbf{v})_w + \boldsymbol{\Omega}_w \times \mathbf{r})_w + \boldsymbol{\Omega}_w \times ((\mathbf{v})_w + \boldsymbol{\Omega}_w \times \mathbf{r}) \tag{G.6}$$

$$(\mathbf{a})_I = (\dot{\mathbf{v}})_w + (\dot{\boldsymbol{\Omega}}_w)_w \times \mathbf{r} + \boldsymbol{\Omega}_w \times (\dot{\mathbf{r}})_w + \boldsymbol{\Omega}_w \times (\mathbf{v})_w + \boldsymbol{\Omega}_w \times (\boldsymbol{\Omega}_w \times \mathbf{r}) \tag{G.7}$$

Substituting $\boldsymbol{\Omega}_w$ into Equation G.3, we see that $(\dot{\boldsymbol{\Omega}}_w)_I = (\dot{\boldsymbol{\Omega}}_w)_w$ (since $\boldsymbol{\Omega}_w \times \boldsymbol{\Omega}_w = 0$), thus the rate of change of the angular velocity vector is the same whether it is viewed in the rotating or inertial frame. Equation G.7 now becomes:

$$(\mathbf{a})_I = (\mathbf{a})_w + \dot{\boldsymbol{\Omega}}_w \times \mathbf{r} + 2\boldsymbol{\Omega}_w \times (\mathbf{v})_w + \boldsymbol{\Omega}_w \times (\boldsymbol{\Omega}_w \times \mathbf{r}) \tag{G.8}$$

This is the final result. The first term $(\mathbf{a})_w$ is the acceleration in the rotating frame, $\dot{\boldsymbol{\Omega}}_w \times \mathbf{r}$ is the Euler acceleration, $2\boldsymbol{\Omega}_w \times (\mathbf{v})_w$ is the coriolis acceleration and $\boldsymbol{\Omega}_w \times (\boldsymbol{\Omega}_w \times \mathbf{r})$ is the centripetal acceleration. We now want to include these terms in the Navier-Stokes equation, which is given for an incompressible fluid below:

$$\rho \frac{D\mathbf{v}}{Dt} = -\nabla p + \mu \nabla^2 \mathbf{v} \tag{G.9}$$

Substituting Equation G.8 into Equation G.9, and expanding the substantial derivative $\frac{D\mathbf{v}}{Dt}$ into its local and convective parts, we obtain the Navier-Stokes equation in the rotating frame of reference $x_w y_w z_w$.

$$\frac{d\mathbf{v}}{dt} + \mathbf{v} \cdot \nabla \mathbf{v} = -\frac{1}{\rho}\nabla p + \nu \nabla^2 \mathbf{v} - \dot{\mathbf{\Omega}}_w \times \mathbf{r} - 2\mathbf{\Omega}_w \times \mathbf{v} - \mathbf{\Omega}_w \times (\mathbf{\Omega}_w \times \mathbf{r}) \tag{G.10}$$

These new terms are the Euler acceleration $-\dot{\mathbf{\Omega}}_w \times \mathbf{r}$, the coriolis acceleration $-2\mathbf{\Omega}_w \times \mathbf{v}$, and the centrifugal acceleration $-\mathbf{\Omega}_w \times (\mathbf{\Omega}_w \times \mathbf{r})$. It would be useful to obtain expressions for these accelerations in the rotating frame as a function of the instantaneous kinematic parameters $(\phi, \dot{\phi}, \ddot{\phi}, \theta, \dot{\theta}, \ddot{\theta}, \alpha, \dot{\alpha}, \ddot{\alpha})$, which will be determined now.

First, the transformation matrices between subsequent frames will be determined, (let the xyz frame be denoted by the subscript 1):

$$T_{0/I} = \begin{pmatrix} cos(\phi) & sin(\phi) & 0 \\ -sin(\phi) & cos(\phi) & 0 \\ 0 & 0 & 1 \end{pmatrix} \tag{G.11}$$

$$T_{1/0} = \begin{pmatrix} cos(\theta) & 0 & sin(\theta) \\ 0 & 1 & 0 \\ -sin(\theta) & 0 & cos(\theta) \end{pmatrix} \tag{G.12}$$

$$T_{w/1} = \begin{pmatrix} 1 & 0 & 0 \\ 0 & -cos(\alpha) & sin(\alpha) \\ 0 & -sin(\alpha) & -cos(\alpha) \end{pmatrix} \tag{G.13}$$

We can now get the transformation matrices from the inertial and $x_0 y_0 z_0$ frames to the rotating frame $x_w y_w z_w$. First from the inertial:

$$T_{w/I} = T_{w/1} T_{1/0} T_{0/I} \tag{G.14}$$

$$T_{w/I} = \begin{pmatrix} [cos(\theta)cos(\phi)] & [cos(\theta)sin(\phi)] & [sin(\theta)] \\ [-sin(\theta)cos(\phi)sin(\alpha)+ \\ +sin(\phi)cos(\alpha)] & [-sin(\theta)sin(\phi)sin(\alpha)+ \\ -cos(\phi)cos(\alpha)] & [cos(\theta)sin(\alpha)] \\ [sin(\theta)cos(\phi)cos(\alpha)+ \\ +sin(\phi)sin(\alpha)] & [sin(\theta)sin(\phi)cos(\alpha)+ \\ -cos(\phi)sin(\alpha)] & [-cos(\theta)cos(\alpha)] \end{pmatrix} \quad \text{(G.15)}$$

From the $x_0 y_0 z_0$ frame:

$$T_{w/0} = T_{w/1} T_{1/0} \quad \text{(G.16)}$$

$$T_{w/0} = \begin{pmatrix} [cos(\theta)] & [0] & [sin(\theta)] \\ [-sin(\theta)sin(\alpha)] & [-cos(\alpha)] & [cos(\theta)sin(\alpha)] \\ [sin(\theta)cos(\alpha)] & [-sin(\alpha)] & [-cos(\theta)cos(\alpha)] \end{pmatrix} \quad \text{(G.17)}$$

Now define the angular velocity and angular acceleration vectors for all frames:

$$\mathbf{\Omega}_0 = \dot{\phi}\mathbf{k}_I \quad \text{(G.18)}$$

$$\dot{\mathbf{\Omega}}_0 = \ddot{\phi}\mathbf{k}_I \quad \text{(G.19)}$$

$$\mathbf{\Omega}_1 = \dot{\phi}\mathbf{k}_I - \dot{\theta}\mathbf{j}_0 \quad \text{(G.20)}$$

$$\dot{\mathbf{\Omega}}_1 = \ddot{\phi}\mathbf{k}_I - \ddot{\theta}\mathbf{j}_0 - \dot{\theta}\dot{\mathbf{j}}_0 \quad \text{(G.21)}$$

$$\mathbf{\Omega}_w = \dot{\phi}\mathbf{k}_I - \dot{\theta}\mathbf{j}_0 - \dot{\alpha}\mathbf{i}_1 \tag{G.22}$$

$$\dot{\mathbf{\Omega}}_w = \ddot{\phi}\mathbf{k}_I - \ddot{\theta}\mathbf{j}_0 - \dot{\theta}\dot{\mathbf{j}}_0 - \ddot{\alpha}\mathbf{i}_1 - \dot{\alpha}\dot{\mathbf{i}}_1 \tag{G.23}$$

Ultimately, we want $\mathbf{\Omega}_w$ and $\dot{\mathbf{\Omega}}_w$ written in components in the $x_w y_w z_w$ frame. Equation G.22 can be obtained in this frame using transformation matrices $T_{w/I}$, $T_{w/0}T_{w/1}$:

$$\mathbf{\Omega}_w = T_{w/I}\begin{pmatrix}0\\0\\\dot{\phi}\end{pmatrix} + T_{w/0}\begin{pmatrix}0\\-\dot{\theta}\\0\end{pmatrix} + T_{w/1}\begin{pmatrix}-\dot{\alpha}\\0\\0\end{pmatrix} \tag{G.24}$$

$$\mathbf{\Omega}_w = \begin{pmatrix}[\dot{\phi}sin(\theta) - \dot{\alpha}]\\[\dot{\phi}cos(\theta)sin(\alpha) + \dot{\theta}cos\alpha]\\[-\dot{\phi}cos(\theta)cos(\alpha) + \dot{\theta}sin\alpha]\end{pmatrix} \tag{G.25}$$

To obtain $\dot{\mathbf{\Omega}}_w$ in the $x_w y_w z_w$ frame we first need $\dot{\mathbf{j}}_0$ and $\dot{\mathbf{i}}_1$ in this frame. Starting with $\dot{\mathbf{j}}_0$:

$$\dot{\mathbf{j}}_0 = \mathbf{\Omega}_0 \times \mathbf{j}_0 \tag{G.26}$$

Notice that $\mathbf{\Omega}_0 = \dot{\phi}\mathbf{k}_0$ since $\mathbf{k}_I = \mathbf{k}_0$, thus:

$$\dot{\mathbf{j}}_0 = \dot{\phi}\mathbf{k}_0 \times \mathbf{j}_0 = -\dot{\phi}\mathbf{i}_0 \tag{G.27}$$

Converting to $x_w y_w z_w$ frame:

$$\dot{\mathbf{j}}_0 = T_{w/0}\begin{pmatrix}-\dot{\phi}\\0\\0\end{pmatrix} = \begin{pmatrix}[-\dot{\phi}cos\theta]\\[\dot{\phi}sin\theta sin\alpha]\\[-\dot{\phi}sin\theta cos\alpha]\end{pmatrix} \tag{G.28}$$

Now find $\dot{\mathbf{i}}_1$:

$$\dot{\mathbf{i}}_1 = \boldsymbol{\Omega}_1 \times \mathbf{i}_1 \tag{G.29}$$

Inserting Equation G.20 into Equation G.29 and transforming it to the $x_1y_1z_1$ frame (noting again that $\mathbf{k}_I = \mathbf{k}_0$):

$$\dot{\mathbf{i}}_1 = (T_{1/0}\begin{pmatrix} 0 \\ -\dot{\theta} \\ \dot{\phi} \end{pmatrix}) \times \mathbf{i}_1 = \dot{\phi}cos\theta\mathbf{j}_1 + \dot{\theta}\mathbf{k}_1 \tag{G.30}$$

Converting to $x_wy_wz_w$ frame:

$$\dot{\mathbf{i}}_1 = T_{w/1}\begin{pmatrix} 0 \\ \dot{\phi}cos\theta \\ \dot{\theta} \end{pmatrix} = \begin{pmatrix} [0] \\ [-\dot{\phi}cos(\theta)cos(\alpha) + \dot{\theta}sin(\alpha)] \\ [-\dot{\phi}cos(\theta)sin(\alpha) - \dot{\theta}cos(\alpha)] \end{pmatrix} \tag{G.31}$$

Now $\dot{\boldsymbol{\Omega}}_w$ can finally be obtained in the $x_wy_wz_w$ frame by substituting in Equation G.28, Equation G.31, and the appropriate transformation matrices into Equation G.23 to obtain:

$$\dot{\boldsymbol{\Omega}}_w = T_{w/I}\begin{pmatrix} 0 \\ 0 \\ \ddot{\phi} \end{pmatrix} + T_{w/0}\begin{pmatrix} 0 \\ -\ddot{\theta} \\ 0 \end{pmatrix} + \begin{pmatrix} [\dot{\phi}\dot{\theta}cos\theta] \\ [-\dot{\phi}\dot{\theta}sin\theta sin\alpha] \\ [\dot{\phi}\dot{\theta}sin\theta cos\alpha] \end{pmatrix} + T_{w/1}\begin{pmatrix} -\ddot{\alpha} \\ 0 \\ 0 \end{pmatrix} + \begin{pmatrix} [0] \\ [\dot{\alpha}(\dot{\phi}cos(\theta)cos(\alpha) - \dot{\theta}sin(\alpha))] \\ [\dot{\alpha}(\dot{\phi}cos(\theta)sin(\alpha) + \dot{\theta}cos(\alpha))] \end{pmatrix} \tag{G.32}$$

$$\dot{\boldsymbol{\Omega}}_w = \begin{pmatrix} [\ddot{\phi}sin(\theta) + \dot{\phi}\dot{\theta}cos(\theta) - \ddot{\alpha}] \\ [cos(\alpha)(\ddot{\theta} + \dot{\phi}\dot{\alpha}cos(\theta)) + sin(\alpha)(\ddot{\phi}cos(\theta) - \dot{\phi}\dot{\theta}sin(\theta) - \dot{\theta}\dot{\alpha})] \\ [sin(\alpha)(\ddot{\theta} + \dot{\phi}\dot{\alpha}cos(\theta)) - cos(\alpha)(\ddot{\phi}cos(\theta) - \dot{\phi}\dot{\theta}sin(\theta) - \dot{\theta}\dot{\alpha})] \end{pmatrix} \tag{G.33}$$

Using Equation G.25 and Equation G.33 in the following equations provides expressions for the euler, coriolis, and centrifugal accelerations denoted as $a_{eul}, a_{cor}, a_{cenf}$ respectively:

$$a_{eul} = -\dot{\mathbf{\Omega}}_w \times \mathbf{r} \tag{G.34}$$

$$a_{cor} = -2\mathbf{\Omega}_w \times \mathbf{v} \tag{G.35}$$

$$a_{cenf} = -\mathbf{\Omega}_w \times (\mathbf{\Omega}_w \times \mathbf{r}) \tag{G.36}$$

In summary, when viewing in a rotating frame of reference the Navier-Stokes equations include three extra terms defining an Euler, Coriolis and centrifugal acceleration, as given in Equation G.10. Equations G.25 and G.33 combined with Equations G.34 - G.36 provide expressions for the Euler, Coriolis and centrifugal accelerations as functions of instantaneous kinematic parameters.